

Daumantas Matulis *Editor*

Carbonic Anhydrase as Drug Target

Thermodynamics and Structure of
Inhibitor Binding

 Springer

Carbonic Anhydrase as Drug Target

Daumantas Matulis
Editor

Carbonic Anhydrase as Drug Target

Thermodynamics and Structure
of Inhibitor Binding

 Springer

Editor

Daumantas Matulis
Department of Biothermodynamics
and Drug Design
Vilnius University, Life Sciences Center,
Institute of Biotechnology
Vilnius, Lithuania

ISBN 978-3-030-12778-7 ISBN 978-3-030-12780-0 (eBook)
<https://doi.org/10.1007/978-3-030-12780-0>

© Springer Nature Switzerland AG 2019

This work is subject to copyright. All rights are reserved by the Publisher, whether the whole or part of the material is concerned, specifically the rights of translation, reprinting, reuse of illustrations, recitation, broadcasting, reproduction on microfilms or in any other physical way, and transmission or information storage and retrieval, electronic adaptation, computer software, or by similar or dissimilar methodology now known or hereafter developed.

The use of general descriptive names, registered names, trademarks, service marks, etc. in this publication does not imply, even in the absence of a specific statement, that such names are exempt from the relevant protective laws and regulations and therefore free for general use.

The publisher, the authors and the editors are safe to assume that the advice and information in this book are believed to be true and accurate at the date of publication. Neither the publisher nor the authors or the editors give a warranty, express or implied, with respect to the material contained herein or for any errors or omissions that may have been made. The publisher remains neutral with regard to jurisdictional claims in published maps and institutional affiliations.

This Springer imprint is published by the registered company Springer Nature Switzerland AG
The registered company address is: Gewerbestrasse 11, 6330 Cham, Switzerland

to Rex Lovrien

Dedication

I dedicate this book to the memory of my Ph.D. advisor Prof. Rex Eugene Lovrien (1928–2003), who has a special place in my life, and his teaching has shaped my path as a scientist in so many ways. He has introduced and taught me to apply biophysical and especially biothermodynamic techniques in protein studies resulting in this book, where we, a group of scientists, present the field of carbonic anhydrase interactions largely using biophysical methods.

Right after Lithuania became *de facto* independent from the USSR on September 6, 1991, he attended a conference in Germany and decided to travel to Poland and the Baltics in search of students to study in the Ph.D. program at the Biochemistry Department of the University of Minnesota. He gave a lecture at Vilnius University about the studies and how to take the necessary GRE and TOEFL exams and invited Lithuanian students to apply for the studies in the USA. He generously paid for my exams and the flight ticket, and in 1993, I ended up at the University of Minnesota as an Adult Specialist and entered the Ph.D. program at the Biochemistry Department in 1994. As a first-year student, I did three rotations: first under the supervision of Prof. Rex E. Lovrien in protein–ligand interactions; second under Prof. Douglas Ohlendorf in protein crystallography; and the third under Prof. Kevin Mayo in protein NMR. I decided to continue research with Prof. Rex E. Lovrien who has developed numerous ligands for protein stabilization and purification via coprecipitation.

Rex was born on a farm at Eagle Grove, Iowa, on January 25, 1928, where he attended a one-room country school. In 1939, he moved with his family to Sac City, Iowa, where he graduated from high school. He was a graduate of the University of Minnesota, received a Ph.D. from the University of Iowa in 1958, and then was a postdoctoral fellow at Yale University, the University of Indiana, and the University of Minnesota. In 1965, he became a professor in the Biochemistry Department at the University of Minnesota–St. Paul campus, where he worked so hard until his death on March 24, 2003, in St. Paul, Minnesota. During his academic career, he mentored many students and published over 60 papers.

Rex taught me the basics of thermodynamics, especially the mixing calorimetry, a technique to study protein–small-molecule interactions. It was my first practical grasp of the concept of enthalpy and its usefulness to gain fundamental insight into the mechanism of interaction. His contributions to our understanding of ion pairs

and their significance in the energetic dissection of protein–ligand binding were highly original and changed, for example, our understanding of the way how 1,8-anilino-naphthalene sulfonate binds to proteins. It was thought since the discovery of this probe in the 1960s that the sulfonate group simply keeps the probe in solution, but instead we showed that the group makes an ionic hydrogen bond primarily with the arginine guanidine group. Knowledge of the enthalpy was crucial in this demonstration because of its additivity principle, also known as Hess’s Law, most often used in the studies of gas combustion, but here applied to the protein–ligand binding.



Rex Eugene Lovrien

Rex influenced us beyond scientific discussions. When he was 17 in 1945, he enlisted in the US Army and was sent to the front against Japan. He was on a ship getting ready for the battle when the news of the atomic bomb on August 6 changed the course of history and instead he spent two years as a part of an occupying force and luckily did not have to experience the war. Unfortunately, as he told me, during that year on a ship he contracted the flu virus that damaged his heart valve. This may have been later the cause of his untimely death in 2003. We had spent many evenings discussing life, politics, and history or sometimes watched together the Monday-night football. During these times that I dearly miss, I have learned how much such an altruistic person as Rex contributes to the development of the world toward the better. I admire the whole USA not only for the highest-level science, but also for such wholehearted people as Rex, and I had a chance to meet many such persons while living in the USA.

Rex told me about scientists who started entire new scholar schools and developed new science trends. Among them were Charles Tanford, Julian Sturtevant, Rufus Lumry, and many more biological thermodynamicists, some of whom I met at the Gibbs Conference on Biothermodynamics, the Biophysical Society, and other meetings that Rex first took me and introduced to the community.

Rex had limited affection for computers and preferred direct exposure to chemistry via experimentation. He would urge me to leave the desk and go to the

bench, as he said. He did interesting experiments until his last days. He thought that my studies and experience gained in the USA should eventually be brought back to benefit our country, but he expressed his thoughts without ever pushing and instead helping me to make decisions on my own. Unfortunately, he did not see us go back. I did it only in 2005 after obtaining a Marie-Curie International Reintegration grant to establish a research laboratory at the Institute of Biotechnology in Vilnius.

Despite living in the city his entire adult life, he always retained the values and interests of his farmer beginnings, including a passion for polka music and farm machinery. I would like us to remember Rex E. Lovrien as a humble person, who did not try to become the first by pushing others, but has worked especially hard and made many significant contributions to the science of protein molecular biophysics. I will remember Rex for being a mentor and a close friend.

Vilnius, Lithuania
November 2018

Daumantas Matulis

Foreword

Carbonic anhydrase is a remarkable enzyme. Scientists at the end of the 1920s came to the conclusion that the release of carbon dioxide from carbonic acid (or rather bicarbonate) was too slow for the physiological needs. There had to be an enzyme to catalyze the reversible hydration of CO_2 to HCO_3^- and H^+ . Meldrum and Roughton were soon able to isolate and purify the proposed enzyme from ox blood and gave the enzyme its name. Little did they know how the magnitude of work to be devoted to this enzyme would expand. By further purification, variants of the enzyme were identified and understood to be isoenzymes. By now twelve isoforms of the enzyme are known in humans, all with their unique amino acid sequence, tissue distribution, and catalytic properties. In addition, there are three proteins in humans that are strongly related to carbonic anhydrases but lacking its catalytic activity but still expressed.

By analysis of a range of species, one has so far identified seven very different forms of the enzyme. Their amino acid sequence varies widely, as do their oligomeric states, but with regard to the basic three-dimensional structure they seem to belong to three different classes. The wheel has been invented three times, and we are confronted with three different proteins that have converged during evolution to perform the same catalytic reaction.

The enzyme was discovered early on to bind a zinc ion. Carbonic anhydrase is the first identified zinc enzyme. The zinc ion is the center of the active site. Its positive charge is essential to perturb the $\text{p}K_a$ of the catalytic water molecule, thereby greatly influencing the rate of catalysis. Interestingly, the convergent evolution is also evident in the active site. Not in an absolute way, but the groups participating see to that the reactants bind in a conserved manner, which may suggest that nature has three times identified in the same optimal way to perform the reaction. In these studies, several alternative metals have been found in different forms of the enzyme.

A range of small anions inhibit the enzyme by binding to the metal ion. However, a much more important class of inhibitors, identified in 1940, were the sulfonamides. A tremendous amount of work has since been done to optimize sulfonamides for treatment of different diseases related to the enzyme, early on primarily glaucoma and edema. With the discovery of cancer-related carbonic anhydrases, a strong activity focuses on cancer therapy and diagnostics using specific inhibitors of these isoenzymes.

A number of books have been produced on various aspects of carbonic anhydrase since its discovery. The current one gives a highly up-to-date and well-illustrated description of the enzyme itself and a wide coverage of currently used inhibitors and further design of novel drugs. Chapters also describe immunotherapy using specific carbonic anhydrases as targets to locate and treat cancer cells.

The editor of the book, Matulis, has collected a broad spectrum of specialists in a range of fields partly from the international scene but remarkable enough achieved collaboration by a local group of people doing an excellent job in composing the current overview.

Leksand, Sweden
November 2018

Anders Liljas

Preface

The carbonic anhydrase (CA) enzyme has captured the attention of researchers since its discovery in 1932. Probably the first book focused solely on the CA, *The Carbonic Anhydrases. Cellular Physiology and Molecular Genetics*, was published in 1991, edited by Susanna J. Dodgson. By that time the field has already expanded to seven CA isoforms that were discovered and described (CA I—CA VII), and it was hypothesized that not all of them are known yet. Today we know from genomic studies that humans contain 15 isoforms and 12 of them perform the catalytic function of CA, i.e., catalyze the reversible hydration of carbon dioxide. No additional isoforms of CA are expected to be discovered in humans in the future.

Further developments in the CA field were well presented in the books *The Carbonic Anhydrase. New Horizons* edited by W.Richard Chegwidden, Nicholas D. Carter, and Yvonne H. Edwards in 2000 and *Carbonic Anhydrase. Its Inhibitors and Activators* edited by Claudiu T.Supuran, Andrea Scozzafava, and Janet Conway in 2004. There have been many advances in the understanding of the CA role in the gastrointestinal tract and in the musculoskeletal, neurosensory, and reproductive systems. The CA became increasingly important in the clinic. Numerous inhibitors of CAs have been described in detail.

More recently, in 2014, Susan C. Frost and Robert McKenna edited a book *Carbonic Anhydrase: Mechanism, Regulation, Links to Disease, and Industrial Applications* where the field expanded from clinical to industrial applications, such as carbon sequestration and biofuel production. The importance of CA IX as an anticancer target has been further elaborated.

However, the design of high-affinity and high-selectivity ligands (small molecular weight compounds) still remains a challenging task. The fact that primary unsubstituted sulfonamides are strong inhibitors of CA has been known since the 1940s. The presence of such a pharmacophoric group is very helpful in the design of new compounds. However, building a ligand that would be highly selective and still possess picomolar affinity is challenging.

The CA enzyme is a well-described protein. It is relatively easy to recombinantly produce in large (milligram) amounts and quantitatively measure interactions with ligands using numerous biophysical and biochemical techniques, and some CA isoforms are quite easy to crystallize. Therefore, for example, the atomic resolution structure of CA II has been solved by X-ray crystallography and several hundreds of

them have been deposited to the Protein Databank, but there are human CA isoforms whose structure has never been solved. Most of the isoforms are relatively easy to produce in bacterial cultures, but some require mammalian cells for the production and some are very hard to obtain. Therefore, the CA enzyme family is still quite challenging to structural characterization.

Numerous drugs used in the clinic are CA inhibitors. Sometimes, it seems that the field is so popular and not much may be discovered here. However, there are no anticancer drugs among them that would target CA despite significant promise for the anticancer effect by inhibiting CA IX.

This book consists of four parts. The first part describes the human CA family of enzymes, their recombinant production, catalytic activity, inhibition, and the temperature stability of all twelve catalytically active human CA isoforms at various pHs. Despite numerous and well-prepared reviews of CA research, some additional information that we have gathered over the years working on the enzyme will be useful for researchers who make the proteins, especially for the application of various biophysical techniques.

The second part of the book focuses on the thermodynamics and kinetics of inhibitor binding to CAs. In addition to commonly used inhibition of enzymatic activity, we have studied the interaction by several techniques such as fluorescent thermal shift assay, isothermal titration calorimetry, and surface plasmon resonance and also by much less known techniques such as the pressure shift assay. Significant emphasis is put on the importance of the intrinsic thermodynamics and kinetics of inhibitor binding and dissection of the binding-linked protonation reactions.

The third part of the book describes the structural diversity of the chemical compounds that are synthesized by organic chemistry and are inhibitors of CAs and also of the proteins described by X-ray crystallography. The atomic-resolution structural characterization of the enzyme family together with the *in silico* modeling of the protein interaction and recognition of the compounds often provides insight and leads the way to the design of isoform-selective compounds.

Finally, the fourth part of the book attempts to describe the development of selected chemical compounds that exhibit exceptional affinity and selectivity toward several desired CA isoforms as drug candidates. The application of monoclonal antibodies for CA detection together with compound conjugates bearing reporter probes shows the possibilities to use them for diagnostics and therapy.

The book is primarily intended for the researchers in the field of protein molecular biophysical chemistry. However, I hope that it may be useful for master or doctoral students interested in drug design starting from the organic synthesis of small-molecule compounds, recombinant production of disease target proteins, determination of the interactions between compounds and proteins, biological testing of compound efficacy in cellular models, and finally, some aspects of compound development toward pharmaceuticals.

Acknowledgments

This book would not have been possible without the help, teaching, and collaboration of so many individuals whom I would like to thank, but it would be impossible to mention them all. My first affection with chemistry began thanks to teacher Veronika Paberžytė. The first mentor at the research laboratory, Prof. Jonas Rubikas, taught me the basics of scientific thinking, and a young mentor Rolandas Meškys helped with practical experimentation. My uncle Romas Šarmaitis, head of laboratory at the Institute of Chemistry, influenced me to take the chemistry path. I thank Prof. Jurgis Kadziauskas for teaching biochemistry.

In addition to my Ph.D. advisor Rex E. Lovrien, who introduced me to biothermodynamics, I thank postdoctoral advisor Victor A. Bloomfield, who taught me the biophysics of DNA, and Matthew J. Todd, supervisor at the 3-Dimensional Pharmaceuticals, later acquired by Johnson & Johnson, where I learned the principles of target-based drug discovery and used carbonic anhydrase for the first time—the CA II was routinely used there as a standard of protein melting temperature. I thank Matthew for the idea to make all 12 human CA isoforms and design compounds that would bind only one isoform.

I thank Algimantas Pauliukonis, the director of the Institute of Biotechnology, who accepted our proposed research program and helped to establish the Laboratory of Biothermodynamics and Drug Design, financed by two Marie-Sklodowska-Curie International Reintegration grants, given to me and independently to my wife Jurgita Matulienė, who established the Molecular and Cell Biology part of our joint laboratory. All departments of the institute were helpful to us, and there are so many people who I should thank, Prof. Saulius Klimašauskas for the use of the stopped-flow instrument to measure inhibition of CAs and the mass spectrometry measurements, Prof. Česlovas Venclovas for the computer modeling and advice, Prof. Virgis Šikšnys for the crystallography efforts, Arvydas Kanopka for the use of hypoxic camera, and Vytautas Smirnovas for helping to build our joint laboratory.

I am lucky to have such a wonderful group of dedicated researchers in our laboratory who have worked long hours to make our projects successful. The teams of recombinant protein production, organic synthesis, biothermodynamics, molecular modeling, and cell biology have all contributed to this book. Most of them are the coauthors, but others have also significantly contributed in many ways,

especially Piotras Cimperman, Miglė Kišonaitė, Eglė Maximowitsch, Povilas Norvaišas, Vilma Petrikaitė, Joana Smirnovienė, and many others.

I thank the authors of chapters in this book from other laboratories who joined this project. Without their contributions the book would not have been possible. I thank scientists who are not coauthors here, but have helped in various ways: Gaetano Angelici, Arieh Ben-Naim, Algirdas Brukštus, Inga Čikotienė, Per Hammarstrom, Heiko Heerklotz, Gerhard Klebe, Linas Labanauskas, Vincent J. LiCata, Nadine Martinet, Franz-Josef Meyer-Almes, Rytis Prekeris, Kannan Ramachandren, Martin Redhead, Catherine Ann Royer, Harun Said, Kirill Shubin, Vladimir Sirotkin, William Sly, Claudiu T. Supuran, Zigmantas Toleikis, Martti Tolvanen, Sigitas Tumkevičius, Abdul Waheed, Ala Yaromina, Reza Zolfaghari Eameh, members of the Carbonic Anhydrase Club, and also all who have performed research on this fascinating CA protein for so many years.

This book was primarily funded by the grant from the Research Council of Lithuania (Program on Healthy Aging, Grant No. SEN-04/2015).

I thank Silvia Herold who has contacted me from the publisher Springer and suggested to be an editor of a book on *Carbonic Anhydrase as a Drug Target* and Sethish Mahalakshmi and Saravanan Manogar who helped to publish it.

Vilnius, Lithuania
November 2018

Daumantas Matulis

Contents

Part I Carbonic Anhydrases—Preparation, Activity, Inhibition

- 1 **Overview of Human Carbonic Anhydrases** 3
Lina Baranauskienė and Daumantas Matulis
- 2 **Recombinant Production of 12 Catalytically Active Human CA Isoforms** 15
Aurelija Mickevičiūtė, Vaida Juozapaitienė, Vilma Michailovienė, Jelena Jachno, Jurgita Matulienė, and Daumantas Matulis
- 3 **Catalytic Activity and Inhibition of Human Carbonic Anhydrases** 39
Lina Baranauskienė and Daumantas Matulis
- 4 **Characterization of Carbonic Anhydrase Thermal Stability** 51
Asta Zubrienė and Daumantas Matulis

Part II Thermodynamics and Kinetics of Compound Binding to Carbonic Anhydrases

- 5 **Inhibitor Binding to Carbonic Anhydrases by Fluorescent Thermal Shift Assay** 63
Vytautas Petrauskas, Asta Zubrienė, Matthew J. Todd, and Daumantas Matulis
- 6 **Inhibitor Binding to Carbonic Anhydrases by Isothermal Titration Calorimetry** 79
Vaida Paketurytė, Asta Zubrienė, Wen-Yih Chen, Sandro Keller, Margarida Bastos, Matthew J. Todd, John E. Ladbury, and Daumantas Matulis
- 7 **Change in Volume Upon Inhibitor Binding to Carbonic Anhydrases by Fluorescent Pressure Shift Assay** 97
Gediminas Skvarnavičius, Daumantas Matulis, and Vytautas Petrauskas

8	<i>Observed Versus Intrinsic Thermodynamics of Inhibitor Binding to Carbonic Anhydrases</i>	107
	Asta Zubrienė and Daumantas Matulis	
9	<i>Kinetic Analysis of Carbonic Anhydrase–Sulfonamide Inhibitor Interactions</i>	125
	Vladimir O. Talibov, Vaida Linkuvienė, U. Helena Danielson, and Daumantas Matulis	
Part III Structure–Thermodynamics/Kinetics Correlations of Compound Binding to Carbonic Anhydrases		
10	<i>Organic Synthesis of Substituted Chlorinated Benzenesulfonamides as Selective Inhibitors of Several CA Isoforms</i>	143
	Edita Čapkauškaitė and Daumantas Matulis	
11	<i>Organic Synthesis of Substituted Fluorinated Benzenesulfonamides as Selective Inhibitors of CA IX and Other Isoforms</i>	153
	Virginija Dudutienė and Daumantas Matulis	
12	<i>Carbonic Anhydrase Inhibitors with Dual Targeting</i>	163
	Peteris Trapencieris, Anete Parkova, and Ineta Vendina-Birzniece	
13	<i>Structures of Human Carbonic Anhydrases and Their Complexes with Inhibitors</i>	179
	Alexey Smirnov, Elena Manakova, Saulius Gražulis, Robert McKenna, and Daumantas Matulis	
14	<i>X-Ray Crystallographic Structures of High-Affinity and High-Selectivity Inhibitor Complexes with CA IX That Plays a Special Role in Cancer</i>	203
	Kaspars Tars and Daumantas Matulis	
15	<i>In Silico Modeling of Inhibitor Binding to Carbonic Anhydrases</i>	215
	Visvaldas Kairys, Kliment Olechnovič, Vytautas Raškevičius, and Daumantas Matulis	
16	<i>Maps of Correlations Between Compound Chemical Structures and Thermodynamics of Binding to 12 Human Carbonic Anhydrases: Towards Isoform-Selective Inhibitors</i>	233
	Asta Zubrienė, Vaida Linkuvienė, and Daumantas Matulis	
17	<i>Correlations Between Inhibitor Binding Thermodynamics and Co-crystal Structures with Carbonic Anhydrases</i>	249
	Alexey Smirnov, Elena Manakova, and Daumantas Matulis	

Part IV Biological Development of Lead Compounds Toward Drugs Targeting Carbonic Anhydrases	
18 Efficacy of Novel CA IX Inhibitors in Biological Models	265
Justina Kazokaitė, Holger M. Becker, Harlan R. Barker, Ashok Aspatwar, Seppo Parkkila, Ludwig J. Dubois, and Daumantas Matulis	
19 Use of Carbonic Anhydrase IX Inhibitors for Selective Delivery of Attached Drugs to Solid Tumors	289
Spencer Gardeen and Philip S. Low	
20 Development of Therapeutic Antibodies Against Carbonic Anhydrases	305
Dovilė Stravinskienė and Aurelija Žvirblienė	
21 Detection of Carbonic Anhydrases	323
Aistė Imbrasaitė, Dovilė Stravinskienė, and Aurelija Žvirblienė	
22 Clinical Trials Involving Carbonic Anhydrase IX as a Target for Cancer Diagnosis and Treatment	335
Švitrigailė Grincevičienė and Daumantas Matulis	
Index	351

Contributors

Ashok Aspatwar Faculty of Medicine and Life Sciences, University of Tampere, Tampere, Finland

Lina Baranauskienė Department of Biothermodynamics and Drug Design, Institute of Biotechnology, Life Sciences Center, Vilnius University, Vilnius, Lithuania

Harlan R. Barker Faculty of Medicine and Life Sciences, University of Tampere, Tampere, Finland

Margarida Bastos CIQUP, Department of Chemistry & Biochemistry, Faculty of Sciences, University of Porto, Porto, Portugal

Holger M. Becker Department of Physiological Chemistry, University of Veterinary Medicine Hannover, Hannover, Germany

Edita Čapkuskaitė Department of Biothermodynamics and Drug Design, Institute of Biotechnology, Life Sciences Center, Vilnius University, Vilnius, Lithuania

Wen-Yih Chen Department of Chemical and Materials Engineering, National Central University, Taoyuan City, Taiwan

U. Helena Danielson Department of Chemistry - BMC, Science for Life Laboratory, Uppsala University, Uppsala, Sweden

Ludwig J. Dubois Department of Radiotherapy, The M-Lab Group, GROW - School for Oncology and Developmental Biology, Maastricht University Medical Centre, Maastricht, The Netherlands

Virginija Dudutienė Department of Biothermodynamics and Drug Design, Institute of Biotechnology, Life Sciences Center, Vilnius University, Vilnius, Lithuania

Spencer Gardeen Department of Chemistry and Purdue Institute for Drug Discovery, Purdue University, West Lafayette, IN, USA

Saulius Gražulis Department of Protein–DNA Interactions, Institute of Biotechnology, Life Sciences Center, Vilnius University, Vilnius, Lithuania

Švitrigailė Grincevičienė Department of Biothermodynamics and Drug Design, Institute of Biotechnology, Life Sciences Center, Vilnius University Vilnius, Lithuania

Aistė Imbrasaitė Department of Immunology and Cell Biology, Institute of Biotechnology, Life Sciences Center, Vilnius University, Vilnius, Lithuania

Jelena Jachno Department of Biothermodynamics and Drug Design, Institute of Biotechnology, Life Sciences Center, Vilnius University, Vilnius, Lithuania

Vaida Juozapaitienė Department of Biothermodynamics and Drug Design, Institute of Biotechnology, Life Sciences Center, Vilnius University, Vilnius, Lithuania

Visvaldas Kairys Department of Bioinformatics, Institute of Biotechnology, Life Sciences Center, Vilnius University, Vilnius, Lithuania

Justina Kazokaitė Department of Biothermodynamics and Drug Design, Institute of Biotechnology, Life Sciences Center, Vilnius University, Vilnius, Lithuania

Sandro Keller Molecular Biophysics, Technische Universität Kaiserslautern (TUK), Kaiserslautern, Germany

John E. Ladbury Department of Molecular and Cell Biology and Astbury Center for Structural Biology, University of Leeds, Leeds, UK

Vaida Linkuvienė Department of Biothermodynamics and Drug Design, Institute of Biotechnology, Life Sciences Center, Vilnius University, Vilnius, Lithuania

Philip S. Low Department of Chemistry and Purdue Institute for Drug Discovery, Purdue University, West Lafayette, IN, USA

Elena Manakova Department of Protein–DNA Interactions, Institute of Biotechnology, Life Sciences Center, Vilnius University, Vilnius, Lithuania

Jurgita Matulienė Department of Biothermodynamics and Drug Design, Institute of Biotechnology, Life Sciences Center, Vilnius University, Vilnius, Lithuania

Daumantas Matulis Department of Biothermodynamics and Drug Design, Institute of Biotechnology, Life Sciences Center, Vilnius University, Vilnius, Lithuania

Robert McKenna Department of Protein–DNA Interactions, Institute of Biotechnology, Life Sciences Center, Vilnius University, Vilnius, Lithuania

Vilma Michailovienė Department of Biothermodynamics and Drug Design, Institute of Biotechnology, Life Sciences Center, Vilnius University, Vilnius, Lithuania

Aurelija Mickevičiūtė Department of Biothermodynamics and Drug Design, Institute of Biotechnology, Life Sciences Center, Vilnius University, Vilnius, Lithuania

Kliment Olechnovič Department of Bioinformatics, Institute of Biotechnology, Life Sciences Center, Vilnius University, Vilnius, Lithuania

Vaida Paketurytė Department of Biothermodynamics and Drug Design, Institute of Biotechnology, Life Sciences Center, Vilnius University, Vilnius, Lithuania

Seppo Parkkila Faculty of Medicine and Life Sciences, University of Tampere, Tampere, Finland

Anete Parkova Latvian Institute of Organic Synthesis, Riga, Latvia

Vytautas Petrauskas Department of Biothermodynamics and Drug Design, Institute of Biotechnology, Life Sciences Center, Vilnius University, Vilnius, Lithuania

Vytautas Raškevičius Institute of Cardiology, Lithuanian University of Health Sciences, Kaunas, Lithuania

Gediminas Skvarnavičius Department of Biothermodynamics and Drug Design, Institute of Biotechnology, Life Sciences Center, Vilnius University, Vilnius, Lithuania

Alexey Smirnov Department of Biothermodynamics and Drug Design, Life Sciences Center, Institute of Biotechnology, Vilnius University, Vilnius, Lithuania

Dovilė Stravinskienė Department of Immunology and Cell Biology, Institute of Biotechnology, Life Sciences Center, Vilnius University, Vilnius, Lithuania

Vladimir O. Talibov Department of Chemistry - BMC, Uppsala University, Uppsala, Sweden

Kaspars Tars Latvian Biomedical Research and Study Center, Riga, Latvia

Matthew J. Todd Biophysical Solutions, Inc., Ambler, PA, USA

Peteris Trapencieris Latvian Institute of Organic Synthesis, Riga, Latvia

Ineta Vendina-Birzniece Latvian Institute of Organic Synthesis, Riga, Latvia

Asta Zubrienė Department of Biothermodynamics and Drug Design, Institute of Biotechnology, Life Sciences Center, Vilnius University, Vilnius, Lithuania

Aurelija Žvirblienė Department of Immunology and Cell Biology, Institute of Biotechnology, Life Sciences Center, Vilnius University, Vilnius, Lithuania

Acronyms

Abbreviations

ANS	1,8-anilinonaphthalene sulfonate
AZM	Acetazolamide (also commonly abbreviated as AZA, AAZ, ACTAZ)
CA	Carbonic anhydrase
DSC	Differential scanning calorimetry
DSF	Differential scanning fluorimetry
EZA	Ethoxzolamide
FPSA	Fluorescent (fluorescence-based) pressure shift assay, PressureFluor
FTSA	Fluorescent (fluorescence-based) thermal shift assay, alternatively termed ThermoFluor [®] or differential scanning fluorimetry, DSF
<i>int</i>	Intrinsic
ITC	Isothermal titration calorimetry
MZM	Methazolamide (also commonly abbreviated as METHZ)
NA	Not available (attempted but could not be conclusively determined)
ND	Not determined
NMR	Nuclear magnetic resonance
<i>obs</i>	Observed
SFA	Stopped-flow assay
SPR	Surface plasmon resonance
SULFA	Sulfanilamide
TFS	Trifluoromethanesulfonamide (also commonly abbreviated as TFMSA)

Variables

$\Delta\beta$	Isothermal compressibility
ΔC_p	Constant pressure heat capacity
ΔG	Standard Gibbs energy of binding (equivalent to ΔG°)
ΔG_{int}	Intrinsic standard Gibbs energy change on binding
ΔG_{obs}	Observed standard Gibbs energy change on binding
$\Delta G_{pr,CA}$	Standard Gibbs energy change on protonation of CA-Zn ^{II} -bound hydroxide

$\Delta G_{pr,SA}$	Standard Gibbs energy change on protonation of deprotonated sulfonamide amino group
ΔH	Standard enthalpy change on binding (equivalent to ΔH°)
ΔH_{int}	Intrinsic standard enthalpy change on binding
ΔH_{obs}	Observed standard enthalpy change on binding
$\Delta H_{pr,buf}$	Standard enthalpy change on buffer protonation
$\Delta H_{pr,CA}$	Standard enthalpy change on CA-Zn ^{II} -bound hydroxide protonation
$\Delta H_{pr,SA}$	Standard enthalpy change on protonation of deprotonated sulfonamide amino group
IC_{50}	Inhibitor concentration that inhibits 50% of enzymatic activity
k_a	Association rate constant
$k_{a,int}$	Intrinsic association rate constant
K_b	Equilibrium binding constant
$K_{b,int}$	Intrinsic equilibrium binding constant
$K_{b,obs}$	Observed equilibrium binding constant
K_d	Equilibrium dissociation constant
K_D	Equilibrium dissociation constant (used in kinetics (SPR), equivalent to K_d)
$K_{d,int}$	Intrinsic equilibrium dissociation constant
$K_{d,obs}$	Observed equilibrium dissociation constant
k_d	Dissociation rate constant
$k_{d,int}$	Intrinsic dissociation rate constant
K_i	Inhibition of enzymatic activity constant
K_M	Michaelis constant of an enzyme
pK_a	Negative logarithm of the dissociation constant of acid protons
$pK_{a,CA}$	Negative logarithm of the dissociation constant of acid protons from CA-Zn ^{II} -bound water molecule
$pK_{a,SA}$	Negative logarithm of the dissociation constant of acid protons from the protonated sulfonamide amino group
P_t	Total protein concentration
ΔS	Standard entropy change on binding (equivalent to ΔS°)
$\Delta S_{pr,CA}$	Standard entropy change on protonation of CA-Zn ^{II} -bound hydroxide
$\Delta S_{pr,SA}$	Standard entropy change on protonation of deprotonated sulfonamide amino group
T_m	Melting (unfolding, denaturation) temperature of a protein
ΔV	The standard change on binding of the volume of the protein–solvent–ligand system

Part I

**Carbonic Anhydrases—Preparation,
Activity, Inhibition**



Overview of Human Carbonic Anhydrases

1

Lina Baranauskienė and Daumantas Matulis

Abstract

In human body there are 15 proteins that possess highly homologous β -sheet-based structure called carbonic anhydrases (CAs) because 12 of them catalyze the reversible hydration of carbon dioxide to bicarbonate and acid protons using the Zn^{II} that is located in the active site of catalytically active CA. The remaining 3 CA isoforms do not possess this catalytic activity because they do not contain the Zn^{II} and thus are called carbonic anhydrase-related proteins (CARPs). The 12 catalytically active proteins are the proteins analyzed in this book from the perspective of drug targeting. The CA isoforms possess variable levels of catalytic activity, different cellular localization, patterns of multimerization, domain organization, and attachment to membranes. In this chapter we briefly review the CA research, beginning from the discovery of carbonic anhydrase enzyme through the development of specific CA inhibitors into human clinical drugs.

1.1 Introduction

Carbonic anhydrase (CA) is an enzyme (EC 4.2.1.1) which catalyzes the reversible hydration of carbon dioxide to bicarbonate and acid protons:



L. Baranauskienė · D. Matulis (✉)

Department of Biothermodynamics and Drug Design, Institute of Biotechnology, Life Sciences Center, Vilnius University, Vilnius, Lithuania

e-mail: lina.baranauskiene@bti.vu.lt; daumantas.matulis@bti.vu.lt

© Springer Nature Switzerland AG 2019

D. Matulis (ed.), *Carbonic Anhydrase as Drug Target*,
https://doi.org/10.1007/978-3-030-12780-0_1

3

This reaction occurs spontaneously in water but the rate is too slow to supply the needs of living cells. Therefore, all forms of life have developed various CAs that accelerate the reaction by up to approximately 1 million fold. There are many classes of CAs that are structurally very different in kingdoms from bacteria to animals, but their function is essential for every organism.

1.2 Discovery and Classification of Carbonic Anhydrases

Two research groups, N. U. Meldrum with F. J. W. Roughton in UK and W. C. Stadie with H. O'Brien in the USA, in 1932–1933 independently discovered an enzyme that catalyzed the hydration/dehydration of CO_2 to HCO_3^- [1–3]. Soon D. Keilin and T. Mann determined that this protein contains zinc and uses it to perform the enzymatic reaction, which can be inhibited by metal-complexing anions [4]. In 1940, the inhibition of CA by chemical compounds, containing unsubstituted primary sulfonamide group, was reported [5]. This discovery laid foundation for the later treatment of CA-linked diseases by applying sulfonamide drugs such as acetazolamide, brinzolamide, and dorzolamide.

Together with an increasing interest in animal CAs, the presence of these enzymes has been confirmed in numerous other organisms, such as in plants [6, 7], bacteria [8], archaea [9], and fungi [10]. The CAs have been found in all living organisms, where they were searched for [11]. The importance of CA function in accelerating the conversion between CO_2 and HCO_3^- is emphasized by the fact that the enzyme has been “re-invented” many times throughout the evolution. Currently, up to seven distinct classes of CAs are distinguished, namely the alpha (α), beta (β), gamma (γ), delta (δ), zeta (ζ), eta (η), and theta (θ) CA [1, 9, 12–16]. The enzymes belonging to these classes catalyze the same reaction but share no structural similarity. The α -CAs have been identified in animals, plant cytoplasm, algae, protozoa, and Gram-negative bacteria, the β -CAs—in bacteria, plant chloroplasts, fungi, and archaea, the γ -CAs—in bacteria, cyanobacteria, and archaea, the δ -CAs, ζ -CAs, and θ -CAs were detected in marine diatoms, while the η -CAs—in protozoa.

All known CAs are metalloproteins—most of them contain zinc ion in their active site, while in ζ -CAs it can be substituted with cadmium, in β -CAs—with iron, and in some α -CAs—with cobalt. In most CAs, the metal ion is coordinated by three amino acid ligands and a water molecule or hydroxide ion. However, the CAs from different classes have varying coordination pattern. The α , γ , and δ CAs use three His residues, the ζ and β -CAs have two Cys and one His ligand, but the β -CAs can also have two Cys, one His and one Asp (in closed active site form), while the η -CAs use two His and one Gln to coordinate the zinc ion [11, 17].

Due to complex evolutionary relationships, it is common that organisms would have multiple CA enzymes, sometimes even from different structural classes. An example could be the gastric pathogen, *Helicobacter pylori*, which has CAs both from the α and β classes [18, 19]. Humans have fifteen proteins that belong to the α -CA class and are called CA isoforms [20] as will be discussed throughout the book.

1.3 Structure and Catalytic Mechanism of Human α -CAs

In 1972, Anders Liljas and coworkers determined the first crystal structure of human CA II [21]. Currently, the number of different CA structures deposited to the Protein Data Bank (www.rcsb.org), both unliganded and with various ligands, is approximately 1000 [17, 22] and some of the structures are of ultrahigh resolution ($< 1 \text{ \AA}$).

All human α -CA isoforms have high structural similarity [23]. They have approximately 15 \AA -deep cone-shaped active site cleft, where the zinc ion is coordinated by three histidine residues His94, His96, and His119 (amino acids numerated according to CA II) at the bottom of the CA active site. The protein has a characteristic fold of ten-stranded anti-parallel β -sheet complemented with several α -helices and additional β -strands (Fig. 1.1).

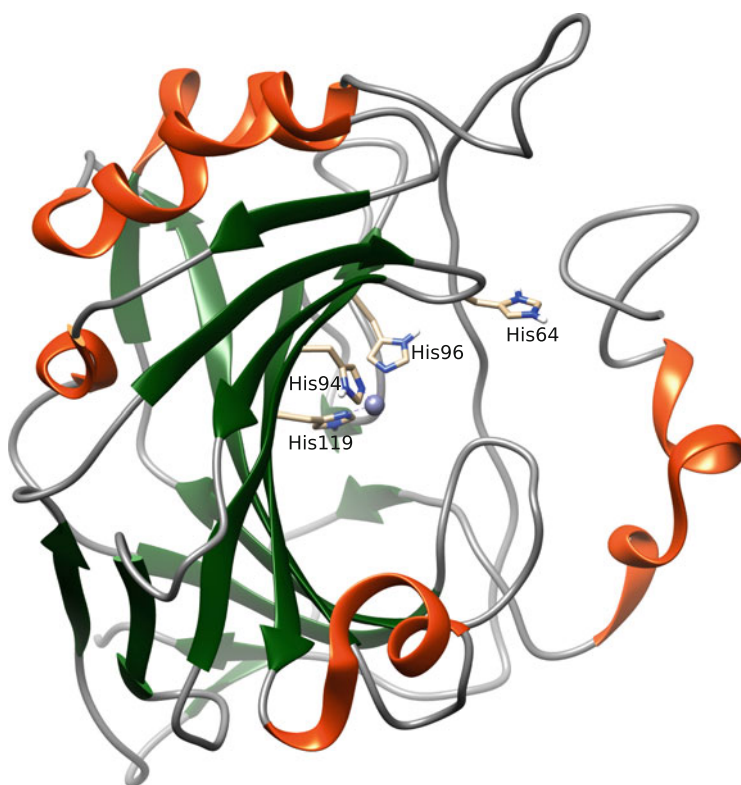
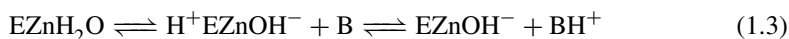
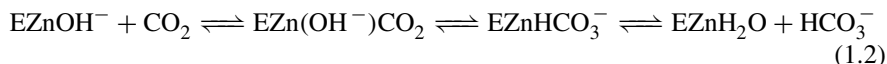


Fig. 1.1 The structure of human CA II. The β -strands are colored green, while the α -helices—in red. The zinc ion is shown as a blue sphere coordinated by the 3 histidine residues, His94, His96, and His119. The fourth nearby histidine, His64, does not bind the Zn^{II} , but is known as a proton-shuttle residue, depicted here in the “out” position

A characteristic feature of human CA active site is that one side of the cleft is hydrophobic, while the other is hydrophilic. This feature serves while performing the enzyme's catalytic function: CO_2 is highly hydrophobic molecule, exhibiting low aqueous solubility, and thus its entrapment and orientation benefits from the hydrophobic part of the active site, while the HCO_3^- and H^+ are hydrophilic entities and are transported via hydrophilic pathway [24].

The enzymatic catalysis is performed by the CA using the two-step ping-pong mechanism (where E denotes enzyme, and B—buffer or bulk solvent):



where ZnOH^- performs the nucleophilic attack on CO_2 , leading to the formation of HCO_3^- , while the water molecule remains bound to the zinc ion, and its conversion to OH^- is required to regenerate the active site for the next catalysis cycle. The proton transfer from the zinc ion-bound molecule to the bulk solvent is the limiting step of the overall catalysis rate [25]. In the fastest isoforms (such as CA II and CA IX), this step is assisted by the proton-shuttle residue His64.

1.4 Domain Organization, Cellular Localization, and Multimerization of Human CAs

There are fifteen CA isoforms in humans and they all belong to the α -CA class [20]. These proteins are highly homologous and have essentially the same 3D structure, but significantly different in the level of catalytic activity, oligomeric organization, tissue distribution, and the main function in the organism. Out of the 15 human CA isoforms, 12 are catalytically active, while the remaining three are acatalytic, also called carbonic anhydrase-related proteins (CARPs), namely CARP VIII, CARP X, and CARP XI. These three proteins lost their catalytic function due to mutations in the active site metal ion-coordinating residues (His was replaced by other amino acids) and thus they have no Zn^{II} in the active site and do not perform the carbon dioxide hydration reaction. The CARPs together with isoforms CA I, CA II, CA III, CA VII, and CA XIII are cytosolic proteins [26]. Two of CA isoforms, CA VA and CA VB, are mitochondrial, while CA VI is the only secreted isoform. Four isoforms are linked to the cell membrane with their active sites located outside of the cell, CA IV is held to the cellular membrane by the glycosylphosphatidylinositol anchor, while three isoforms—CA IX, CA XII, and CA XIV—are transmembrane proteins with their active sites oriented to the intercellular space, they all have single transmembrane helices and short intracellular fragments [11] (Fig. 1.2).

Most human CA isoforms are monomeric proteins and only three of them form dimers: CA VI and CA XII form noncovalent dimers, while the CA IX dimer is

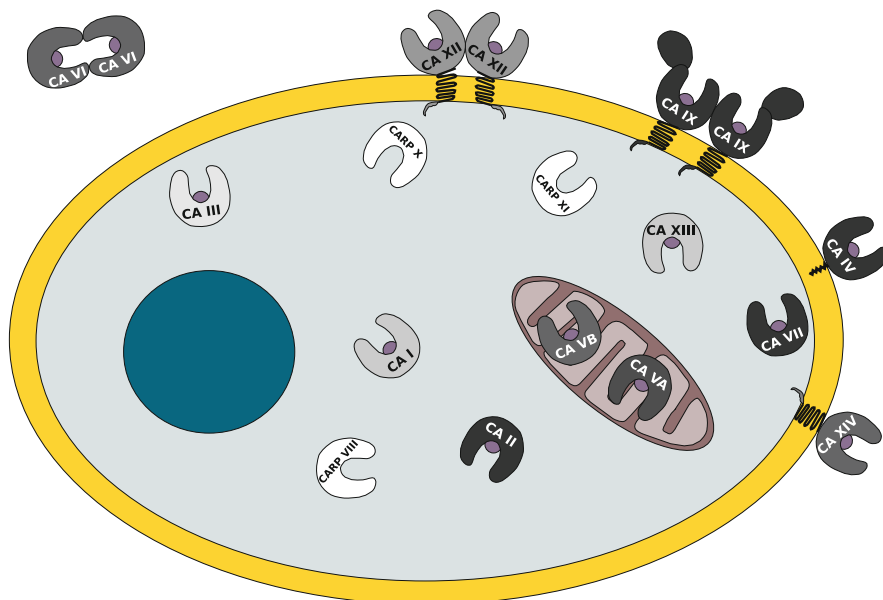


Fig. 1.2 Localization of human CA isoforms in the cell. Proteins are marked as horseshoe shaped figures with their color being proportional to the enzymatic activity. The acatalytic isoforms are shown in white. The zinc ions in the active sites of CAs are shown as small purple spheres

supported by the disulfide bond. The exact effect of dimerization on the function and catalytic activity of these isoforms is not fully clear.

The CAs are among the fastest known enzymes—their catalytic efficiency approaches the diffusion limit. However, this is true only for some human isoforms, the fastest ones are CA II and CA IX. For instance, the activity of CA I, the most abundant isoform in human blood is equivalent to approximately 10% of CA II, and the slowest is CA III reaching only 0.3% of CA II specific catalytic activity. The main features of human CA isoforms are summarized in Table 1.1.

Five cytosolic CA isoforms possess the CO_2 hydration catalytic activity, CA I, CA II, CA III, CA VII, and CA XIII. The primary function of cytosolic CAs is to maintain the intracellular pH and participate in maintaining of the blood pH. They can also interact with ion transporters forming transport metabolons.

The CA III is the least active isoform, expressed in skeletal muscle, adipose tissue, breast, and bones. The low CO_2 hydration activity is determined by the residue Phe 198 which restricts the free movement of substrate within the active site. It has other demonstrated or hypothesized biological functions, such as protection from oxidative stress, gene regulation, and participation in adipogenesis [27–29].

The CA VII together with CA III also functions in protection from oxidative stress [29]. This isoform participates in the transmission of neuro signal and is linked to seizures, neuropathic pain, and other disorders of neural system. It is expressed in brains, liver, colon, skeletal muscle, and some other organs/tissues [30, 31].

Table 1.1 Enzymatic activity, localization, and relation to diseases of human CA isoforms

Isoform	CO ₂ hydration activity	Localization in cell	Relation to diseases
CA I	Low	Cytosolic	Hemolytic anemia
CA II	High	Cytosolic	Glaucoma, edema, altitude sickness
CA III	Very low	Cytosolic	–
CA IV	High	Membrane-linked via GPI anchor	Glaucoma
CA VA	Moderate–high	Mitochondrial	Obesity
CA VB	Moderate	Mitochondrial	–
CA VI	Moderate	Secreted	Dental caries
CA VII	High	Cytosolic	Epilepsy, neuropathic pain
CARP VIII	None	Cytosolic	–
CA IX	High	Transmembrane	Cancer
CARP X	None	Cytosolic	–
CARP XI	None	Cytosolic	–
CA XII	Medium–low	Transmembrane	Glaucoma, cancer
CA XIII	Low	Cytosolic	Sterility
CA XIV	Moderate	Transmembrane	–

The CA XIII is expressed in kidney, liver, GI tract, brain, adipose tissue, reproductive system, and other organs/tissues. Its enzymatic activity is low and comparable to CA I, but its sensitivity to standard sulfonamide inhibitors is high and comparable to CA II [20].

There are two mitochondrial CAs: CA VA is expressed in liver, while CA VB has broad tissue distribution. They both are mainly responsible for the supply of bicarbonate ions for biosynthetic reactions in mitochondria. CA VA participates in glucose and lipid metabolism and is linked to obesity [32, 33].

CA VI is the only secreted isoform in this enzyme family. It is mainly detected in saliva and milk. This protein exists as a dimer. It has relatively low affinity to inhibitors compared to CA II. CA VI participates in perception of bitter taste [34]. Increased activity of this isoform is linked to the development of dental caries [35].

The CA IX and CA XII are the two dimeric cancer-linked membrane proteins with their active sites exposed to the extracellular space [36]. The CA IX has a unique structural feature in the human CA family, the proteoglycan-like domain, which has recently been classified as an intrinsically disordered protein element, increasing the stability of CA IX at acidic pH [37].

The CARP proteins (CARP VIII, CARP X, and CARP XI) lack the CO₂ hydration catalytic activity due to the mutation of one or more Zn^{II}-coordinating histidines. However, CARPs have other biological functions. They participate in the transmission of neuro signal, tumorigenesis, and other processes. For example, the CARP VIII inhibits IP₃ (inositol 1, 4, 5-trisphosphate) binding to its receptor (IPR₁), while CARP X and CARP IX bind to neurexins [26, 38, 39].

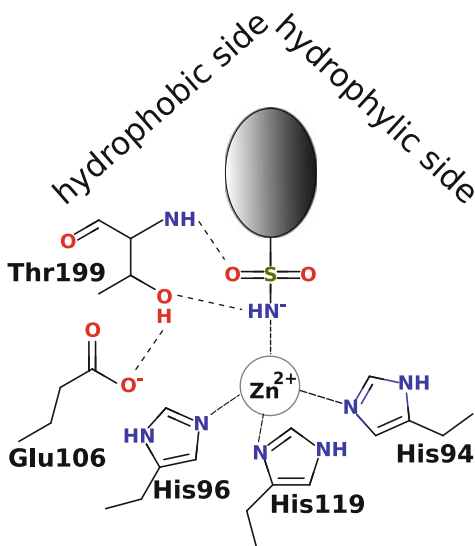
1.5 Clinical Drugs as Inhibitors of CA Catalytic Activity

CAs are clinically important enzymes, thus inhibition and activation of their catalytic activity by small molecule compounds is being extensively researched. Several different mechanisms of CA inhibition have been described [40]. The first synthetic inhibitors were identified soon after the discovery of CAs. They were aromatic compounds bearing the primary unsubstituted sulfonamide group [5]. Later, other classes of inhibitors were described. The CA inhibiting compounds could be broadly classified into two main groups, the zinc ion-binding compounds, and the compounds that do not form direct bond with the catalytic Zn^{II} .

The first group includes compounds, containing different zinc-binding groups, such as primary sulfonamides, sulfamates, sulfamides, carboxylates, hydroxamates, dithiocarbamates, xantanes, and phosphonates. The other group includes compounds that either anchor to the Zn^{II} -bound water molecule/hydroxide ion, such as phenols, polyamines, some carboxylates, sulfocoumarins, and 2-thioxocoumarins, or occlude the entrance of the substrate into enzyme's active site, for example, coumarins and fullerenes (predicted binding mode). Reported CA inhibition by antibodies is likely to occur via the occlusion of the active site. In addition to these groups, some compounds are supposed to bind outside of the active site of CA, while the binding mechanism of others has not been identified yet. Different inhibition types and mechanisms have been extensively described in [40].

The primary sulfonamides make direct coordination bond between the Zn^{II} and the sulfonamide nitrogen atom (Fig. 1.3). Several hydrogen bonds form too. However, the affinity and selectivity of various sulfonamides is largely determined by the functional groups attached to the sulfonamide moiety.

Fig. 1.3 Main interactions between sulfonamide inhibitors and the CA. The direct coordination bond between the sulfonamide nitrogen and the Zn^{II} plays a role of the main anchor orienting the inhibitor in the active site of the CA. Several hydrogen bonds also help orienting the inhibitor molecule. The affinity and selectivity of the compound is primarily determined by the remaining part of the inhibitor (shown as gray oval) that makes contacts with the hydrophilic and hydrophobic sides of the active site



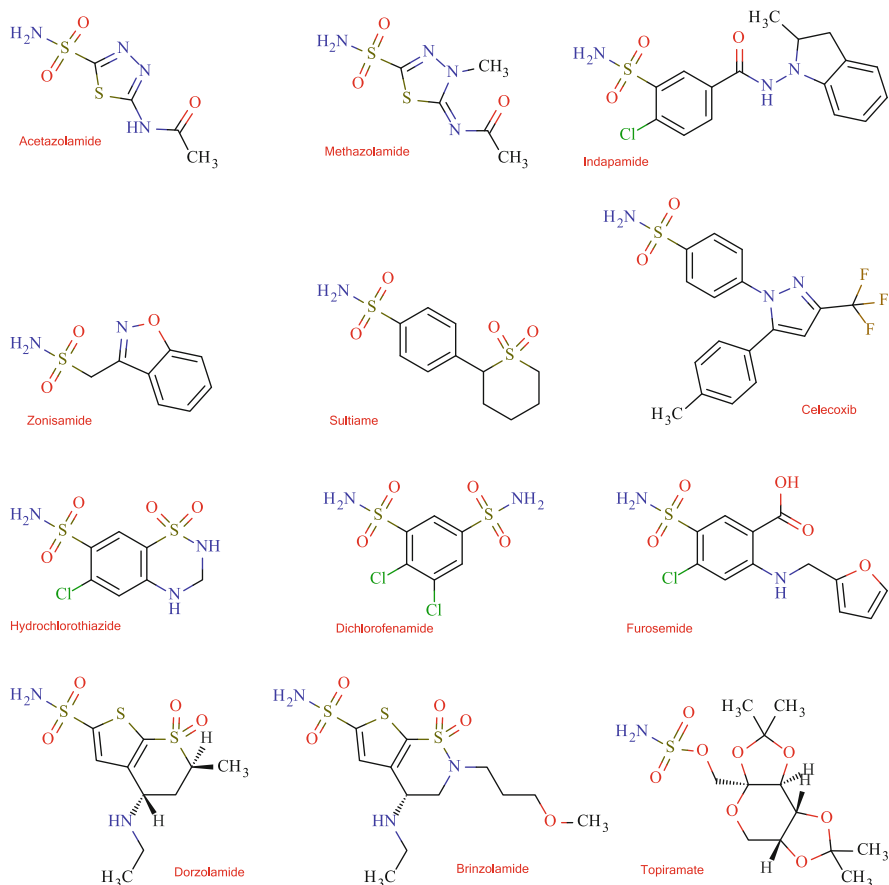


Fig. 1.4 Examples of some most popular drugs with the CA-inhibiting activity. Acetazolamide, methazolamide, and dichlorophenamide are used as systemic CA inhibitors for glaucoma, edema, and other CA-related diseases. Dorzolamide and brinzolamide are topical drugs for glaucoma management. Zonisamide, topiramate, and sulthiame are used to treat neurological disorders. Furosemide, hydrochlorothiazide, and indapamide are popular diuretics, while the celecoxib is an inhibitor of cyclooxygenase

Despite extensive research of different inhibition modes of CA, all currently clinically used drugs targeting CA activity are primary sulfonamides or their bioisosteres sulfamates. They are used to control diseases/disorders, such as glaucoma, edema, altitude sickness, metabolic alkalosis, and obesity, and there are currently ongoing clinical trials for cancer treatment [41, 42], summarized in Chapter 21.

There are more than 20 small molecule compounds (structures of some of them are presented in Fig. 1.4) that are being used as drugs for CA-related disease treatment. However, CAs are not necessarily the primary targets for some of them.

None of the currently marketed CA activity-perturbing drugs can be classified as highly selective—according to *in vitro* data, they inhibit several CA isoforms. Some of them are applied as topical drugs, such as brinzolamide and dorzolamide that act as CA inhibitors in the eye for glaucoma management. Systemic application of other drugs affects CAs in the entire organism, while the CA inhibiting effect, usually required for the treatment of selected disease/condition, is more local and specific organ/tissue-oriented [43, 44].

1.6 Carbonic Anhydrases as Model Proteins

In addition to the above-discussed clinically relevant features of human CAs, this group of enzymes, or at least some members (especially CA I and CA II), together with bovine CA II are regarded as model proteins, extensively reviewed by V. M. Krishnamurthy et al. [45]. The CAs are used as models in protein–ligand interaction, protein stability, protein fibrillation, and other protein-study areas. This is determined by the stable and relatively simple protein structure, inexpensive production and its commercial availability, well-defined catalytic and inhibition/ligand binding mechanisms, and the abundance of structural, ligand affinity, and other information. The CA has a rigid structure—no large structural rearrangements occur upon ligand binding. These and other properties make CA a good model, often used for technique validation and comparability of the results. For instance, repeatability/accuracy of isothermal titration calorimetry (ITC), analytical ultracentrifugation (AU), and surface plasmon resonance (SPR) was performed simultaneously in many laboratories using CA II binding to 4-carboxybenzenesulfonamide as a model reaction [46]. The bCA II binding to acetazolamide was used as a model interaction for large SPR comparability study to evaluate variation in establishing the binding affinity and binding kinetics between different laboratories [47]. Recently, bCA II binding to 4-carboxybenzenesulfonamide was employed for the validation of method to extract kinetic data from ITC experiment [48]. The CA I binding to sulfonamide group-bearing compounds of different affinity was used to compare the affinity constants obtained by mass spectrometry, ITC, and SPR methods. The CAs have been used for protein stability studies and determination of protein unfolding parameters [49–52].

1.7 Conclusions

Carbonic anhydrases have been studied for over 80 years and served as model proteins in numerous fields of protein research, including protein stability and ligand binding studies. Out of 15 highly homologous proteins in humans, the 12 isoforms possess the carbon dioxide hydration catalytic activity which varies among isoforms. The CAs have variable cellular localization, multimerization pattern, domain organization, and attachment to cell membrane. The primary function of CAs is pH regulation and they are involved in numerous physiological and

pathological processes and are thus drug targets in diseases such as glaucoma, obesity, altitude sickness, and even cancer.

References

1. Meldrum, N., Roughton, F.: Some properties of carbonic anhydrase, the CO₂ enzyme present in blood. *J. Physiol.* **75**, 15–16 (1932)
2. Meldrum N.U., Roughton F.J.W.: Carbonic anhydrase. Its preparation and properties. *J. Physiol.* **80**, 113–142 (1933)
3. Stadie, W.C., O'Brien, H.: The catalysis of the hydration of carbon dioxide and dehydration of carbonic acid by an enzyme isolated from red blood cells. *J. Biol. Chem.* **103**, 521–529 (1933)
4. Keilin, D., Mann, T.: Carbonic anhydrase. *Nature* **144**, 442–443 (1939)
5. Mann, T., Keilin, D.: Sulphanilamide as a specific inhibitor of carbonic anhydrase. *Nature* **146**, 164–165 (1940)
6. Neish, A.C.: Studies on chloroplasts. *Biochem. J.* **33**, 300–308 (1939)
7. Bradfield, J.R.G.: Plant carbonic anhydrase. *Nature* **159**, 467–468 (1947)
8. Veitch, F.P., Blankenship, L.C.: Carbonic anhydrase in bacteria. *Nature* **197**, 76–77 (1963)
9. Alber, B.E., Ferry, J.G.: A carbonic anhydrase from the archaeon *Methanosarcina thermophila*. *Proc. Natl. Acad. Sci. U. S. A.* **91**, 6909–6913 (1994)
10. Amoroso, G., Morell-Avrahov, L., Muller, D., Klug, K., Suttmeier, D.: The gene NCE103 (YNL036w) from *Saccharomyces cerevisiae* encodes a functional carbonic anhydrase and its transcription is regulated by the concentration of inorganic carbon in the medium. *Mol. Microbiol.* **56**, 549–558 (2005)
11. Supuran, C.T.: Structure and function of carbonic anhydrases. *Biochem. J.* **473**, 2023–2032 (2016)
12. Hewett-Emmett, D., Hopkins, P.J., Tashian, R.E., Czelusniak, J.: Origins and molecular evolution of the carbonic anhydrase isozymes. *Ann. N. Y. Acad. Sci.* **429**, 338–356 (1984)
13. Roberts, S.B., Lane, T.W., Morel, F.M.M.: Carbonic anhydrase in the marine diatom *Thalassiosira weissflogii* (Bacillariophyceae). *J. Phycol.* **33**, 845–850 (1997)
14. Lane, T.W., et al.: Biochemistry: a cadmium enzyme from a marine diatom. *Nature* **435**, 42 (2005)
15. Del Prete, S., et al.: Discovery of a new family of carbonic anhydrases in the malaria pathogen *Plasmodium falciparum*—the η -carbonic anhydrases. *Bioorg. Med. Chem. Lett.* **24**, 4389–4396 (2014)
16. Kikutani, S., et al.: Thylakoid luminal θ -carbonic anhydrase critical for growth and photosynthesis in the marine diatom *Phaeodactylum tricorutum*. *Proc. Natl. Acad. Sci. U. S. A.* **113**, 9828–9833 (2016)
17. Lomelino, C.L., Andring, J.T., McKenna, R.: Crystallography and its impact on carbonic anhydrase research. *Int. J. Med. Chem.* **2018** (2018)
18. Modak, J.K., Revitt-Mills, S.A., Roujeinikova, A.: Cloning, purification and preliminary crystallographic analysis of the complex of *Helicobacter pylori* α -carbonic anhydrase with acetazolamide. *Acta. Crystallogr. Sect. F Struct. Biol. Cryst. Commun.* **69**, 1252–1255 (2013)
19. Morishita, S., et al.: Cloning, polymorphism, and inhibition of β -carbonic anhydrase of *Helicobacter pylori*. *J. Gastroenterol.* **43**, 849–857 (2008)
20. Parkkila, S., et al.: Recent advances in research on the most novel carbonic anhydrases, CA XIII and XV. *Curr. Pharm. Des.* **14**, 672–678 (2008)
21. Liljas, A., et al.: Crystal structure of human carbonic anhydrase C. *Nat. New Biol.* **235**, 131–137 (1972)
22. Berman, H.M., et al.: The protein data bank. *Nucleic Acids Res.* **28**, 235–242 (2000)
23. Aggarwal, M., Boone, C.D., Kondeti, B., McKenna, R.: Structural annotation of human carbonic anhydrases. *J. Enzyme. Inhib. Med. Chem.* **28**, 267–277 (2013)

24. Liang, J.Y., Lipscomb, W.N.: Binding of substrate CO₂ to the active site of human carbonic anhydrase II: a molecular dynamics study. *Proc. Natl. Acad. Sci. U. S. A.* **87**, 3675–3679 (1990)
25. Silverman, D.N., Lindskog, S.: The catalytic mechanism of carbonic anhydrase: implications of a rate-limiting protolysis of water. *Acc. Chem. Res.* **21**, 30–36 (1988)
26. Aspatwar, A., Tolvanen, M.E.E., Ortutay, C., Parkkila, S.: *Carbonic Anhydrase: Mechanism, Regulation, Links to Disease, and Industrial Applications*, pp. 135–156. Springer, Dordrecht (2014)
27. Silagi, E.S., Batista, P., Shapiro, I.M., Risbud, M.V.: Expression of carbonic anhydrase III, a nucleus pulposus phenotypic marker, is hypoxia-responsive and confers protection from oxidative stress-induced cell death. *Sci. Rep.* **8**, 4856 (2018)
28. Monti, D.M., et al.: Insights into the role of reactive sulfhydryl groups of carbonic anhydrase III and VII during oxidative damage. *J. Enzyme Inhib. Med. Chem.* **32**, 5–12 (2017)
29. Di Fiore, A., Monti, D.M., Scaloni, A., De Simone, G., Monti, S.M.: Protective role of carbonic anhydrases III and VII in cellular defense mechanisms upon redox unbalance. *Oxidative Med. Cell. Longev.* **2018**, 2018306 (2018)
30. Buonanno, M., et al.: The crystal structure of a hCA VII variant provides insights into the molecular determinants responsible for its catalytic behavior. *Int. J. Mol. Sci.* **19**, 1571 (2018)
31. Bootorabi, F., et al.: Analysis of a shortened form of human carbonic anhydrase VII expressed in vitro compared to the full-length enzyme. *Biochimie* **92**, 1072–1080 (2010)
32. Scozzafava, A., Supuran, C.T., Carta, F.: Antiobesity carbonic anhydrase inhibitors: a literature and patent review. *Expert Opin. Ther. Pat.* **23**, 725–735 (2013)
33. Queen, A., Khan, P., Azam, A., Hassan, M.I.: Understanding the role and mechanism of carbonic anhydrase V in obesity and its therapeutic implications. *Curr. Protein Pept. Sci.* **19**, 909–923 (2018)
34. Patrikainen, M., Pan, P., Kuleskaya, N., Voikar, V., Parkkila, S.: The role of carbonic anhydrase VI in bitter taste perception: evidence from the Car6^{-/-} mouse model. *J. Biomed. Sci.* **21**, 82 (2014)
35. Picco, D.C.R., et al.: Children with a higher activity of carbonic anhydrase VI in saliva are more likely to develop dental caries. *CRE* **51**, 394–401 (2017)
36. Mboge, M.Y., Mahon, B.P., McKenna, R., Frost, S.C.: Carbonic anhydrases: role in pH control and cancer. *Metabolites* **8**, 19 (2018)
37. Langella, E., et al.: Biochemical, biophysical and molecular dynamics studies on the proteoglycan-like domain of carbonic anhydrase IX. *Cell. Mol. Life Sci.* 1–14 (2018)
38. Sterky, F.H., et al.: Carbonic anhydrase-related protein CA10 is an evolutionarily conserved pan-neurexin ligand. *PNAS* **114**, E1253–E1262 (2017)
39. Karjalainen, S.L., et al.: Carbonic anhydrase related protein expression in astrocytomas and oligodendroglial tumors. *BMC Cancer* **18**, 584 (2018)
40. Supuran, C.T.: How many carbonic anhydrase inhibition mechanisms exist? *J. Enzyme Inhib. Med. Chem.* **31**, 345–360 (2016)
41. Supuran, C.T.: Advances in structure-based drug discovery of carbonic anhydrase inhibitors. *Expert Opin. Drug Discovery* 1–28 (2016)
42. Supuran, C.T.: Applications of carbonic anhydrases inhibitors in renal and central nervous system diseases. *Expert Opin. Ther. Pat.* **28**, 713–721 (2018)
43. Swenson, E.R.: New insights into carbonic anhydrase inhibition, vasodilation, and treatment of hypertensive-related diseases. *Curr. Hypertens. Rep.* **16**, 1–11 (2014)
44. Swenson, E.R.: Safety of carbonic anhydrase inhibitors. *Expert Opin. Drug Saf.* **13**, 459–472 (2014)
45. Krishnamurthy, V.M., et al.: Carbonic anhydrase as a model for biophysical and physical-organic studies of proteins and protein-ligand binding. *Chem. Rev.* **108**, 946–1051 (2008)
46. Myszka, D.G., et al.: The ABRF-MIRG'02 study: assembly state, thermodynamic, and kinetic analysis of an enzyme/inhibitor interaction. *J. Biomol. Tech.* **14**, 247–269 (2003)
47. Cannon, M.J., et al.: Comparative analyses of a small molecule/enzyme interaction by multiple users of Biacore technology. *Anal. Biochem.* **330**, 98–113 (2004)

48. Li, D., Chen, L., Wang, R., Liu, R., Ge, G.: Synergetic determination of thermodynamic and kinetic signatures using isothermal titration calorimetry: a full-curve-fitting approach. *Anal. Chem.* **89**, 7130–7138 (2017)
49. Wahiduzzaman, et al.: Characterization of folding intermediates during urea-induced denaturation of human carbonic anhydrase II. *Int. J. Biol. Macromol.* **95**, 881–887 (2017)
50. Cimperman, P., et al.: A quantitative model of thermal stabilization and destabilization of proteins by ligands. *Biophys. J.* **95**, 3222–3231 (2008)
51. Lisi, G.P., Hughes, R.P., Wilcox, D.E.: Coordination contributions to protein stability in metal-substituted carbonic anhydrase. *J. Biol. Inorg. Chem.* **21**, 659–667 (2016)
52. Wright, T.A., Stewart, J.M., Page, R.C., Konkolewicz, D.: Extraction of thermodynamic parameters of protein unfolding using parallelized differential scanning fluorimetry. *J. Phys. Chem. Lett.* **8**, 553–558 (2017)



Recombinant Production of 12 Catalytically Active Human CA Isoforms

2

Aurelija Mickevičiūtė, Vaida Juozapaitienė, Vilma Michailovienė, Jelena Jachno, Jurgita Matulienė, and Daumantas Matulis

Abstract

Target-based drug design is based on the search of chemical compounds that would strongly and specifically bind to the target protein. The target protein is chosen based on biochemical and cellular investigation of a disease and a demonstration that chemical inhibitor/activator could be of help for the patient. Biochemical and biophysical interaction experiments require relatively large amount of the target protein. In this chapter, we overview recombinant production of the 12 catalytically active human carbonic anhydrase (CA) isoforms, beginning with the cloning of the CA gene sequences, construction of the catalytic domain encoding sequences, search for the best expression conditions in bacterial and mammalian cell cultures, and finally—the purification of the enzymes through Ni^{2+} -chelation chromatography or ligand-affinity chromatography using an immobilized benzenesulfonamide headgroup. The purity of every CA isoform has been confirmed by SDS-PAGE, HR-MS, and the specific activity determined by the stopped-flow inhibition of CO_2 hydration assay. Tens to hundreds of milligrams of highly purified CAs have been produced and subsequently used to crystallize the proteins and determine their interaction with synthetic compounds, and the inhibition of enzymatic activity as described in the following chapters.

A. Mickevičiūtė · V. Juozapaitienė · V. Michailovienė · J. Jachno · J. Matulienė · D. Matulis (✉)
Department of Biothermodynamics and Drug Design, Institute of Biotechnology, Life Sciences Center, Vilnius University, Vilnius, Lithuania
e-mail: mickeviciute@ibt.lt; jogaite@ibt.lt; roze@ibt.lt; elper@ibt.lt; matuliene@ibt.lt; matulis@ibt.lt

2.1 Introduction

Biophysical studies of proteins require quite a significant amount, usually milligram quantities of purified protein. Carbonic anhydrases are considered to be relatively easy to produce and especially the isoform CA II has been used as a model protein for many years. The protein served as a model of a globular well-behaving protein in the hands of many researchers using numerous techniques [1]. In our experience, the isoforms CA I, CA II, CA VII, CA XII, and CA XIII have proven to be quite easy to produce in bacterial cells and purify in large amounts. However, some other isoforms were hard to produce, especially CA VA, CA VB, and CA XIV. Furthermore, our group has not succeeded in repeating the procedure of CA IX production in bacterial cells as described in the literature [2] and instead we produced the catalytic domain of CA IX in mammalian cell cultures. Some other isoforms, such as CA III, CA IV, and CA VI, were also quite hard to make in large quantities in bacteria.

However, recombinant forms of CAs not always are identical to the native proteins as they are found in human body. Several isoforms were truncated by removing the signaling sequences or the trans-membrane regions. It was important to truncate them at a position that would ensure the catalytic domain to be in an enzymatically active form. Still, the truncated proteins seem to be functional and suitable for inhibitor design. First, all 12 isoforms caught the Zn^{2+} from the medium, as verified by the quantitative analysis of Zn. Second, the exact molecular weight of 11 isoforms has been confirmed by the HRMS analysis. The MW of CA IX could not be confirmed due to variable post-translational modifications, primarily glycosylation. Third, the specific catalytic activity and inhibition by conventional CA inhibitors such as acetazolamide and ethoxzolamide has been shown for each isoform.

The CA VI isoform occupies a special place because we have produced it in a fully native form from human saliva by affinity-ligand purification. We call it “native CA VI.” In addition, CA VI has been prepared recombinantly in bacteria and also in mammalian cell cultures. All three different preparations interacted with all tested inhibitors exhibiting essentially the same affinities thus showing that the recombinantly produced CA VI is a good model of the native CA VI isoform produced in human saliva. This example, in our opinion, confirms a general notion that the recombinantly made proteins are good models of their ligand binding profiles that resemble the properties in native body conditions.

However, it should be kept in mind that numerous differences between the recombinant proteins and the native ones may cause significant differences in compound binding. Such differences include but are not limited to: attachment to membrane via a trans-membrane domain or a lipid anchor (CA IV), posttranslational modifications such as phosphorylation or glycosylation, dimerization (possibly CA VI, CA IX, CA XII, and CA XIV), and the presence of additional domains such as the peptidoglycan (PG) domain in CA IX. Furthermore, some isoforms were purified using an artificially attached His₆-tag that may affect the protein characteristics.

The level of quality of protein preparations is finally indicated by the crystallizability of the proteins. We have attempted to crystallize all CA isoforms, but succeeded in crystallizing only half of them, namely, CA I, CA II, CA IV, CA VI, CA XII, and CA XIII. Compounds could be soaked into the CA crystals or had to be co-crystallized to solve the structures of compound-CA complexes. However, we never observed compounds bound to CA VI. The CA IX has been successfully co-crystallized with our compounds in the laboratory of Prof. Kaspars Tars as described in Chapter 14 on the crystallography of CA IX.

2.2 The Sequences of the Catalytically Active Human CAs

The multiple sequence alignment of all human α -CAs, made by MultAlin tool (<http://multalin.toulouse.inra.fr/multalin/>) is shown in Fig. 2.1. Protein sequences are from Uniprot database (<http://www.uniprot.org/>), their entry numbers are listed next to isoform name. High consensus (90% or more) areas are marked in red, while the low consensus (50% or more) are marked in blue, and the neutral ones are shown in black. The three His residues, that coordinate the Zn^{2+} in the active center, are marked in green. The catalytically inactive isoforms (CARPs), the CA VIII, CA X, and CA XI are marked in purple. They all miss at least one of the Zn^{2+} -coordinating His residue, and therefore do not perform the catalytic function.

The sequences of the recombinant proteins, prepared in our laboratory, were aligned with the proteins from Uniprot database (Fig. 2.2). Some recombinant proteins were made with His₆-tag (CA I, CA VA, CA VB, CA VI, CA VII, and CA XIV) to make them easier to purify via Ni^{2+} -chelation chromatography. The pET15b vector, which was used to make all His₆-tagged CAs except CA VA, has a thrombin cleavage site between the His₆-tag and the protein for His₆-tag removing. In Fig. 2.2, His₆-tags are marked in blue and the thrombin cleavage site in green. All tagged proteins, except CA VA, have the N-terminal His₆-tag. For CA VA and CA VB, different plasmids, containing either N-terminal or C-terminal His₆-tag were made. For CA VA, more protein was produced using the C-terminal His₆-tag, while for CA VB - with the N-terminal tag. Other CAs such as CA II, CA IV, CA XII, and CA XIII do not contain a tag. The CA II and CA XIII have enough His residues to bind Ni^{2+} without any additional sequences. For CA IV and CA XII, the proteins with His₆-tags were also made, but they didn't bind to the sorbent. Additional sequence potentially disturbs the protein structure. The CA I, CA II, CA III, and CA VII are full or almost full-length proteins. The CA I and CA III contain full domains, beginning at the 4th amino acid (Pro) and the 3rd amino acid (Lys), respectively. CA II and CA VII are also full-length proteins. The CA IV lacks the signal peptide and the C-terminal part, which is present in pro-peptide and removed during protein's maturation (marked in grey in Fig. 2.2). Since *Escherichia coli* does not make posttranslational modifications, the mentioned parts of the protein were removed during cloning. This idea came from [3] article. For CA VA, the idea was to remove the transit peptide (marked in grey in Fig. 2.2). However, that left the Cys residue at the very beginning of the protein. We made this protein, but it aggregated due to disulfide bond formation between proteins. To avoid this, several amino acids

```

CA_1_P00915 .....
CA_13_08N1Q1 .....
CA_2_P00918 .....
CA_3_P07451 .....
CA_7_P43166 .....
CA_5A_P35218 .....
CA_5B_Q9Y2D0 .....
CA_8_P35219 .....
CA_4_P22748 .....
CA_6_P23280 .....
CA_9_Q16790 MAPLCPSPWLPPLLIPAPAPGLTVQLLLSLLLVPVHPQRLFRMQEDSPLGGGSSGEDPDL
CA_12_Q43570 .....
CA_14_Q9ULX7 .....
CA_10_Q9NS85 .....
CA_11_Q75493 .....
consensus>50 .....

CA_1_P00915 .....
CA_13_08N1Q1 .....
CA_2_P00918 .....
CA_3_P07451 .....
CA_7_P43166 .....
CA_5A_P35218 .....
CA_5B_Q9Y2D0 .....
CA_8_P35219 .....
CA_4_P22748 .....
CA_6_P23280 .....
CA_9_Q16790 G E E D L P S E E D S P R E E D P P G E E D L P G E E D L P G E E D L P E V K P K S E E E G S L K L E D L P T V E A P F
CA_12_Q43570 .....
CA_14_Q9ULX7 .....
CA_10_Q9NS85 .....
CA_11_Q75493 .....
consensus>50 .....

CA_1_P00915 .....MASPDNGYDDKNGPEQ.....WSKLYPIANGNNQSPVDIKTSETKHDTSL
CA_13_08N1Q1 .....MSRLSNWGYREHNGPIH.....WKEFFPIADGDQSPLEIKTEKVKYDSSL
CA_2_P00918 .....MSHHNGYGKHNNGPEH.....WKKDFPIAKGERQSPVDDIDHTAKYDPSL
CA_3_P07451 .....MAKENGWYASHNGPDH.....WHELFPNAKERQSPVELHTKDIRHDPDL
CA_7_P43166 .....MTGHHGWYGGDDGPPSH.....WHKLYPIAOGDRQSPINIISQAVVSPSL
CA_5A_P35218 WSRSMRPFGRWCSCQASRCWAQTSNNTLHPL.....WTVPVSVPGGTRQSPINIQWRDVSVDPL
CA_5B_Q9Y2D0 QIPRFMPARPCSLYCTYKTRNRRLHPL.....WESVDLVPVGGDRQSPINIRWRDVSVDPL
CA_8_P35219 AFPEKKEDEEEEEEEVGEVWGYEEGVE.....WGLVFPDANGEYQSPINLNSREARYDPSL
CA_4_P22748 ARPSASAEHSHWCYEVQAESS..NYFC...LVPVKWGGNCQKDRQSPINIVTTRAKVKKL
CA_6_P23280 LGGQAQHVS DWTYSEGAL.....DE...AHWPQHYPACGGQKQSPINLQRTKVRYNPSL
CA_9_Q16790 DQPEPQNNARRHKEGDDQSHWRVGGD...PWPRVSPACAGRFQSPVDIRPQLAACPAL
CA_12_Q43570 SPA.PVNGSKWTYFGPD.....GE...NSWSKKYPCGGLLQSPIDLHSDILQYDASL
CA_14_Q9ULX7 ILA.ADGGQHWTYEGPH.....GQ...DHWPASYPECGNNAQSPIDIQTSVTFDPPDL
CA_10_Q9NS85 QNSPKIHGWWAYKEVVQGSFVVPVPSFWGLVNSAWNLCVSGKRQSPVNIETSHMIFDPL
CA_11_Q75493 IGPAPDPEDWWSYKDNLQGNFVPPFPFWGLVNAAWSLCVAGKRQSPVDVLELKRVLDFDPL
consensus>50 .....n.....w.....yp.gdrQSP!#i.....ydpSL

CA_1_P00915 KPISVS..YNPA.TAKEIINVGHFSFHVNFEDNDNRSVLRKGGPFS..DSYRLQFQFHWGS
CA_13_08N1Q1 RPLSIK..YDPS.SAKIISNSGHSFNVDFFDNTENKSVLRGGPFL..GSYRLRQVHLHWGS
CA_2_P00918 KPLSVS..YDQA.TSIRILNNGHAFNVEFDSDQKAVLKGGLD..GTYRLIQFHLHWGS
CA_3_P07451 QPWSVS..YDGC.SAKTILNNGKTCRVVFDYDTRMSLQGGPFL..GPYRLQFHLHWGS
CA_7_P43166 QPLELS..YEAC.MLSLITNNGHSVQVDFNDSDDRTVVTGGPFL..GPYRLKQFHLHWGK
CA_5A_P35218 KPLRVS..YEA.A.SCLYIWNNTGYLQVEFFDATEASGISGGPFL..NHYRLKQFHLHWGA
CA_5B_Q9Y2D0 KPLTIS..YDPA.TCLHVWNNGYSFLVEFEDSTDKSVKGGPFL..HNYRLKQFHLHWGA
CA_8_P35219 LDVRLSPNYVVC.RDCEVTDNGHTITQVILK...SKSVLSGGPFLPQGHFELEVEVFWHWG
CA_4_P22748 GRFFFSGYDKK..QWTMVQNNHGSVMMLLE...NKASISGGPFL.APYQAKLHLHWSD
CA_6_P23280 KGLNMTGYETQA.GEPPMVNNGHTVQISLP..STMRTVA.DG..TVYIAQQMHLHWGR
CA_9_Q16790 RPELELGFQPLPELRLRNNNGHSVQLTLP...PGLMAGL.PG..REYRALQLHLHWGA
CA_12_Q43570 TPLEFPQGYNLSANKQFLLTNNNGHSVKLNL...SDMHQ.G.LP..RKYVAAQLHLHWGN
CA_14_Q9ULX7 PALQPHGYDQPGTEPDLHNNNGHTVQLSLP...STLYL.G.LP..RKYVAAQLHLHWGQ
CA_10_Q9NS85 TPLRLNTGGRRKVSMTYNTGRHVSLRLDKE...HLVNISSGPMT..YSHRLEERLHLWGS
CA_11_Q75493 PPLRLSTGGPKLRGTLYNTGRHVSFLPAPR...PVMVNSGGPFL..YSHRLEERLHLWGA
consensus>50 .pl.s.yd.....l.i.nnghs.qvd.e.....d...l.ggppl.....yr1.#.hlhwg.

CA_1_P00915 TNEH..GSEHTVDGVKYSAELELVAHWNSA.KYSSLAEAASKADGLAVIGVLMKVGEA..N
CA_13_08N1Q1 ADDH..GSEHTVDGVSYAAELVHVHNSD.KYPSFVFAAHEPDLAVLGVFLQIGEP..N
CA_2_P00918 LDGQ..GSEHTVDKKKYAAELVHVHNT..KYGDGFKAQVQGLAVLGLIFLKVGA..K
CA_3_P07451 SDDH..GSEHTVDGVKYSAAELVHVHNP..KYNTFKBALQKRGJAVVIGFLIKIGE..H
CA_7_P43166 KHDV..GSEHTVDGKSFPSLELHVHNAK.KYSTVFKAASAPDGLAVVGVFLTGEDE..N
CA_5A_P35218 VNEG..GSEHTVDGHAYPAELVHVHNSV.KYQNYKBAVVNGEGLAVIGVFLKLGAAH..H
CA_5B_Q9Y2D0 IDAW..GSEHTVSKCFPAELVHVHNAV.RFENFEDAALBENGLAVIGVFLKLGKH..H
CA_8_P35219 ENQR..GSEHTVNFRAFPELLEIWNST.LFGSDEAVAKSPHGIAIHALFVQISKE..H
CA_4_P22748 L..PYKGSSEHSLDGEHFAMEMHIVHEKEKGTSRNVKQADPDEIAVLAFLVEAGTQ.VN
CA_6_P23280 ASSIISGSEHTVDGIRHVIIEIIVHYNSK..YKSYDIAQADPGLAVLAFLVEAKNYPEN
CA_9_Q16790 AGRP..GSEHTVGEHRFPAAELVHVHL.ST.AFARVDEALGRPPGLAVLAFLVEEGPE.EN
CA_12_Q43570 PNDP.HGSEHTVSGQHFAELVHVYNSD.LYPDASTASNKSEGLAVLAFLVEGFSF..N
CA_14_Q9ULX7 KGSP.GSEHQINSEATFAELVHVYSD.SYDSLSEAAERPPGGLAVLGLILEVGET.KN
CA_10_Q9NS85 EDSQ..GSEHLLNGQAFSGEVLIIHYNHE.LYTNVTEAASRPNGLVVVSIFFKVSDS.SN
CA_11_Q75493 RDGA..GSEHQINHGQFSAEVLIIHFNQE.LYGNFSAASRPNGLAIIISLFFNVAVT.SN
consensus>50 .d.....GSEHTvdg.f.aElhVHwns...y.f.eA.....pdgla!lgfv!evg...n

```

Fig. 2.1 Multiple sequence alignment of human CA isoforms from Uniprot

from the transit peptide were kept. For the same reason some amino acids were removed from CA VB domain together with the transit peptide (marked in gray in Fig. 2.2). The length of CA VI construct was chosen according to article [4].

Many studies of recombinant protein expression demonstrate that it may not be necessary to express the full-length protein to produce biochemically active enzyme, because, frequently the desired enzyme activity is supported by a discrete domain that can be used for the production of catalytically active recombinant enzyme [5]. Therefore, CA IX and CA XII were truncated and only catalytic domain was produced. The CA XII was cloned according to article [6]. The CA XIV preparation contains a truncated catalytic domain (lacks 10 last amino acids). The full domain was also produced, but truncated protein was easier to work with [7].

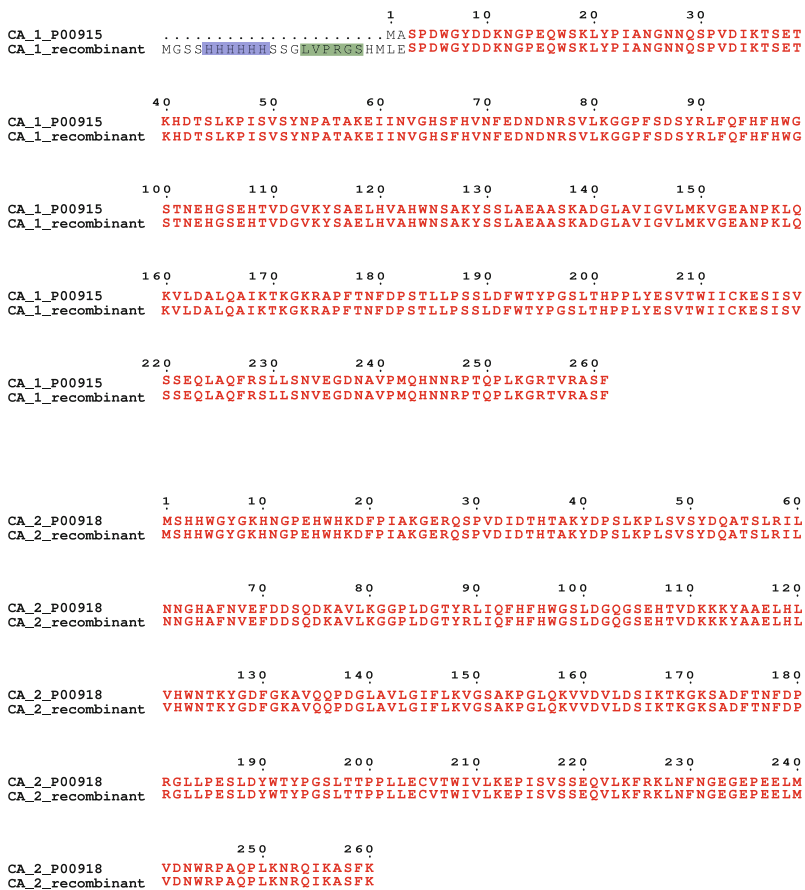


Fig. 2.2 The sequence alignment between the native human CA genomic sequences and our recombinantly produced CAs

```

                                1          10          20          30          40
CA_3_P07451      .....MAKEWGYASHNGPDHWHELFPPNAKGENQSPVELHTKDIRHD
CA_3_recombinant M6GSSHHHHHSSGTVPRGSHMLEWGYASHNGPDHWHELFPPNAKGENQSPIELHTKDIRHD

                                50          60          70          80          90          100
CA_3_P07451      PSLQPWSVSYDGGSAKITILNNGKTCRVVFDDTYDRSMLRGGPLPGPYRLRQFHLHWGSSD
CA_3_recombinant PSLQPWSVSYDGGSAKITILNNGKTCRVVFDDTYDRSMLRGGPLPGPYRLRQFHLHWGSSD

                                110         120         130         140         150         160
CA_3_P07451      DHGSEHTVDGVKYAAELHLVHWNPKYNTFKEALKQRDGIAVIGIFLKIGHENGEFQIFLD
CA_3_recombinant DHGSEHTVDGVKYAAELHLVHWNPKYNTFKEALKQRDGIAVIGIFLKIGHENGEFQIFLD

                                170         180         190         200         210         220
CA_3_P07451      ALDKIKTKGKEAPFTKFPDSCLFPACRDYWTYQGSFTTPPEECIVWLLLKEPMTVSSDQ
CA_3_recombinant ALDKIKTKGKEAPFTKFPDSCLFPACRDYWTYQGSFTTPPEECIVWLLLKEPMTVSSDQ

                                230         240         250         260
CA_3_P07451      MAKLRSLLSSAENEPVPVLSVNWRPPQPINNRVVRASFK
CA_3_recombinant MAKLRSLLSSAENEPVPVLSVNWRPPQPINNRVVRASFK

```

Signal peptide

```

                                1          10          20          30          40          50          60
CA_4_P22748      MRMLLLLLLLLLSAARPSASAESHWCYEVQAESSNYPCLVPVKWGGNCQKDROSPINIVTTK
CA_4_recombinant .....MAESHWCYEVQAESSNYPCLVPVKWGGNCQKDROSPINIVTTK
                                70          80          90          100         110         120
CA_4_P22748      AKVDKKLGRFFSGYDKKQTWTVQNNGHSVMLLENKASISGGLPAPYQAKQLHLHWSD
CA_4_recombinant AKVDKKLGRFFSGYDKKQTWTVQNNGHSVMLLENKASISGGLPAPYQAKQLHLHWSD

                                130         140         150         160         170         180
CA_4_P22748      LPYKGSEHSLDGEHFAMEMHIVHEKEKGTSRNVKEAQDPEDEIAVLAFLVEAGTQVNEGF
CA_4_recombinant LPYKGSEHSLDGEHFAMEMHIVHEKEKGTSRNVKEAQDPEDEIAVLAFLVEAGTQVNEGF

                                190         200         210         220         230         240
CA_4_P22748      QPLVEALSNIPKPEMSTTMAESSLDLLPKEEKLRHFRYLGSLTTPCDEKVVWTVFRE
CA_4_recombinant QPLVEALSNIPKPEMSTTMAESSLDLLPKEEKLRHFRYLGSLTTPCDEKVVWTVFRE

                                250         260         270         280         290         300
CA_4_P22748      FIQLHREQILAFSQKLYDKEQTVSMKDNVRPLQLGQRTVIKSGAPGRPLPWALPALLG
CA_4_recombinant FIQLHREQILAFSQKLYDKEQTVSMKDNVRPLQLGQRTVIKS.....

                                310
CA_4_P22748      FMLACLLAGFLR
CA_4_recombinant .....

```

Peptides sequence that is removed during proteins maturation

Fig. 2.2 (continued)

Transit peptide

	1	10	20	30	40	50	60
CA_5A_P35218	MLGRNTWKTSAFSFLVEQMWAPLWSRSMRPGRWCSQRS						CAWQTSNNTLHPLWTVVPSVPG
CA_5A_recombinantMSQRS						CAWQTSNNTLHPLWTVVPSVPG
	70	80	90	100	110	120	
CA_5A_P35218	GTRQSPINIQWRDSVYDPQLKPLRVSYEAASCLYIWNNGYLFQVEFDDATEASGISGGPL						
CA_5A_recombinant	GTRQSPINIQWRDSVYDPQLKPLRVSYEAASCLYIWNNGYLFQVEFDDATEASGISGGPL						
	130	140	150	160	170	180	
CA_5A_P35218	ENHYRLKQFHFWGAVNEGGSEHTVDGHAYPAELHLVHWNVSKYQNYKEAVVGENGLAVI						
CA_5A_recombinant	ENHYRLKQFHFWGAVNEGGSEHTVDGHAYPAELHLVHWNVSKYQNYKEAVVGENGLAVI						
	190	200	210	220	230	240	
CA_5A_P35218	GVFLKLGAAHQTLQRLVDILPEIKHKDARAAMRPFDPSTLLPTCWDYWTYAGSLTTPPLT						
CA_5A_recombinant	GVFLKLGAAHQTLQRLVDILPEIKHKDARAAMRPFDPSTLLPTCWDYWTYAGSLTTPPLT						
	250	260	270	280	290	300	
CA_5A_P35218	ESVTWIIQKEPVEVAPSQLSAFRTLLFSALGEEKMMVNNYRPLQPLMNRKVWASFQATN						
CA_5A_recombinant	ESVTWIIQKEPVEVAPSQLSAFRTLLFSALGEEKMMVNNYRPLQPLMNRKVWASFQATN						
CA_5A_P35218	EGTRS.....						
CA_5A_recombinant	EGTRSLERHHHHH						

Transit peptide

	1	10	20	30	40	50	60		
CA_5B_Q9Y2D0	MVMNLSLRVILQASPGKLLWRKFQIPRFMPARP						CCLYTC	TYKTRNRALHPLWESVDLVPG	
CA_5B_recombinantMGSS						HHHHH	SSGLVPRGSHM	TYKTRNRALHPLWESVDLVPG
	70	80	90	100	110	120			
CA_5B_Q9Y2D0	GDRQSPINIRWRDSVYDPGLKPLTISYDPATCLHVWNNGYSLFVEFEDSTDKSVIKGGPL								
CA_5B_recombinant	GDRQSPINIRWRDSVYDPGLKPLTISYDPATCLHVWNNGYSLFVEFEDSTDKSVIKGGPL								
	130	140	150	160	170	180			
CA_5B_Q9Y2D0	ENHYRLKQFHFWGAIDAWGSEHTVDSKCFPAELHLVHWNVAVRFENFEDAALAEENGLAVI								
CA_5B_recombinant	ENHYRLKQFHFWGAIDAWGSEHTVDSKCFPAELHLVHWNVAVRFENFEDAALAEENGLAVI								
	190	200	210	220	230	240			
CA_5B_Q9Y2D0	GVFLKLGKHKELQKLVDTLPSIKHKDALVEFGSFDPSCLMPTCPDYWTYSGSLTTPPLS								
CA_5B_recombinant	GVFLKLGKHKELQKLVDTLPSIKHKDALVEFGSFDPSCLMPTCPDYWTYSGSLTTPPLS								
	250	260	270	280	290	300			
CA_5B_Q9Y2D0	ESVTWIIKKQPVVDHDQLEQFRTLLFTSEGEKEKRMVDNFRPLQPLMNRTVRSSFRHDY								
CA_5B_recombinant	ESVTWIIKKQPVVDHDQLEQFRTLLFTSEGEKEKRMVDNFRPLQPLMNRTVRSSFRHDY								
	310								
CA_5B_Q9Y2D0	VLNVQAKPKPATSQATP								
CA_5B_recombinant	VLNVQAKPKPATSQATP								

Fig. 2.2 (continued)

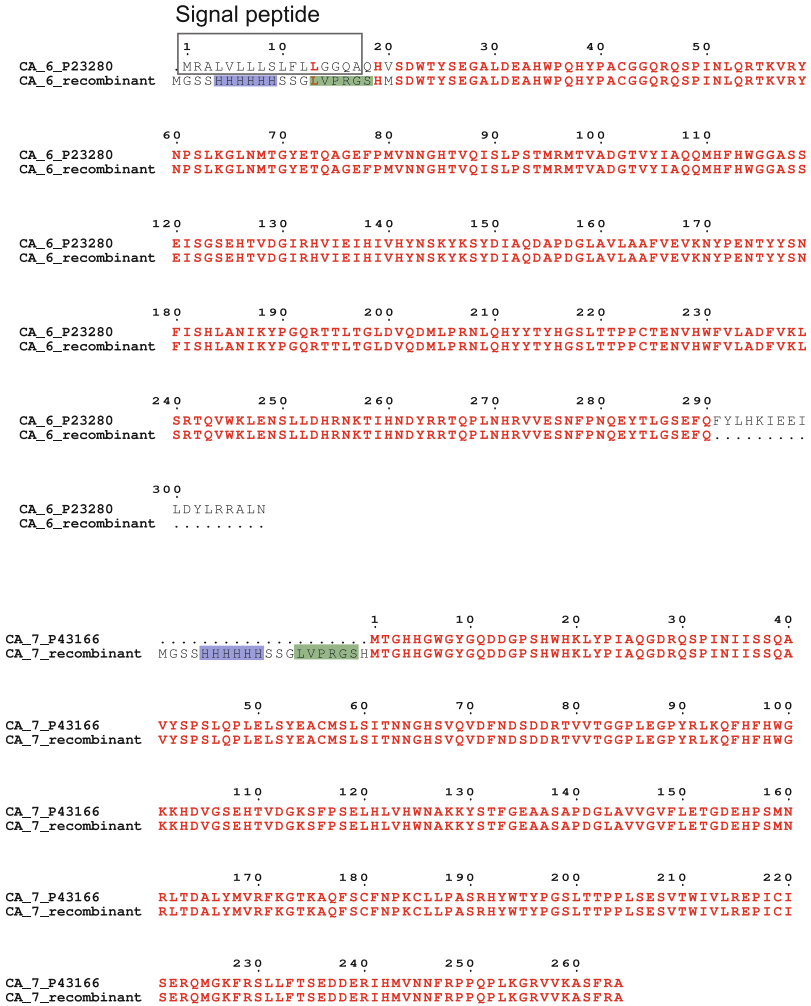


Fig. 2.2 (continued)

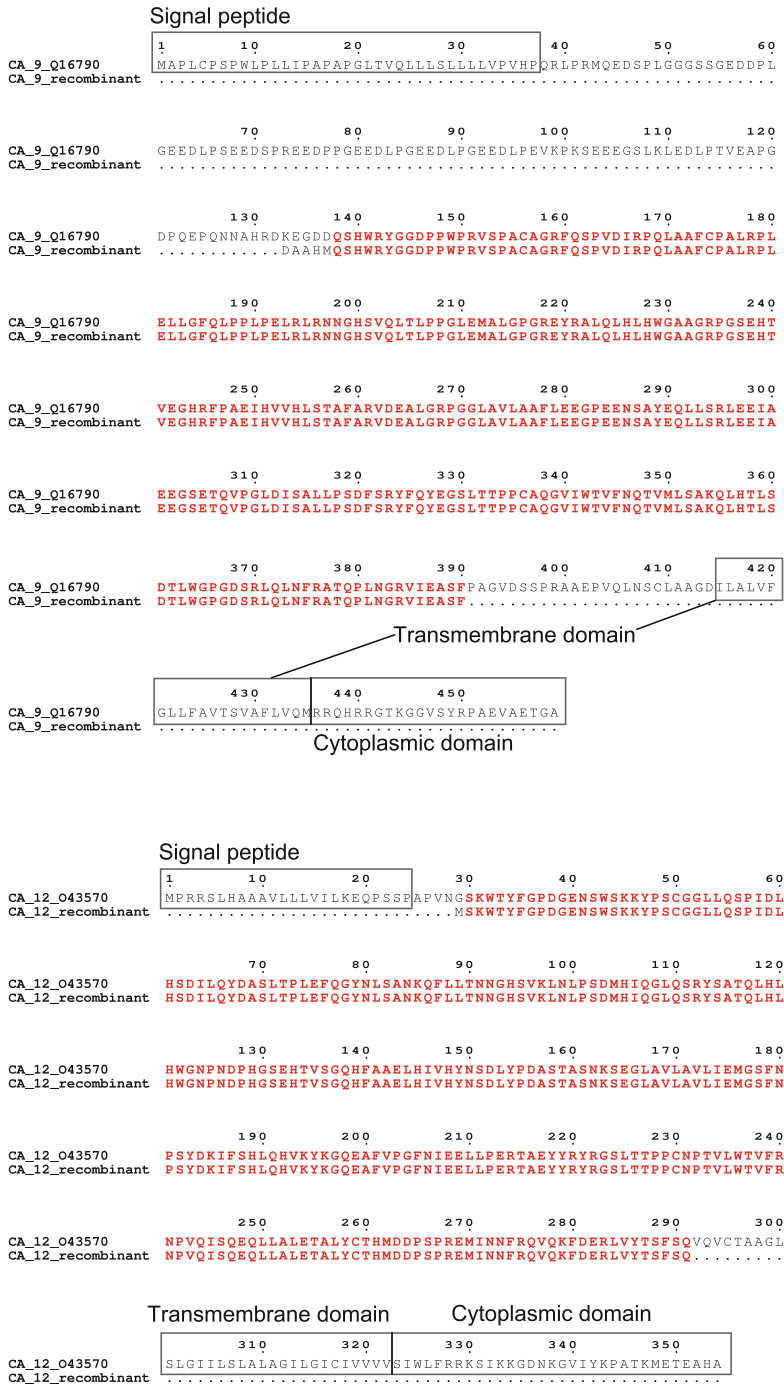


Fig. 2.2 (continued)


```

CA_13_Q8NIQ1      1      10      20      30      40      50
                  .MSRLSWGYREHNGPIHWKEFFPIADGDQQSPIEIKTKEVKYDSSLRPLSIKYDPSSAKI
CA_13_recombinant MMSRLSWGYREHNGPIHWKEFFPIADGDQQSPIEIKTKEVKYDSSLRPLSIKYDPSSAKI

CA_13_Q8NIQ1      60      70      80      90      100     110
                  INSGHSFNVDFDDTENKSVLRGGPLTGSYRLRQVHLHWSADDHGEHIVDGVSYAAEL
CA_13_recombinant INSGHSFNVDFDDTENKSVLRGGPLTGSYRLRQVHLHWSADDHGEHIVDGVSYAAEL

CA_13_Q8NIQ1      120     130     140     150     160     170
                  HVVHWNSDKYPSFVEAAHEPDGLAVLGVFLQIGEPNSQLQKITDTLDSIKEKGKQTRFTN
CA_13_recombinant HVVHWNSDKYPSFVEAAHEPDGLAVLGVFLQIGEPNSQLQKITDTLDSIKEKGKQTRFTN

CA_13_Q8NIQ1      180     190     200     210     220     230
                  FDLLSLLPPSWDYTYTPGSLTVPPLLESVTWIVLKQPINISSQLAKFRSLLCTAEGEAA
CA_13_recombinant FDLLSLLPPSWDYTYTPGSLTVPPLLESVTWIVLKQPINISSQLAKFRSLLCTAEGEAA

CA_13_Q8NIQ1      240     250     260
                  AFLVSNHRPPQPLKGRKVRASFH
CA_13_recombinant AFLVSNHRPPQPLKGRKVRASFH

```

Signal peptide

```

CA_14_Q9ULX7      1      10      20      30      40      50
                  . . . . . MLFSALLLEVIWILLAADGGQHWTYEGPHGQDHWPASYPECGNNAQSPIDIQTDS
CA_14_recombinant MGSSHHHHHSSSSGVFRGSHMADGGQHWTYEGPHGQDHWPASYPECGNNAQSPIDIQTDS

CA_14_Q9ULX7      60      70      80      90      100     110
                  VTFDPDLPALQPHGYDQPGTEPLDLLHNNGHTVQLSLPSTLYLGGLPRKYVAAQLHLHWGQ
CA_14_recombinant VTFDPDLPALQPHGYDQPGTEPLDLLHNNGHTVQLSLPSTLYLGGLPRKYVAAQLHLHWGQ

CA_14_Q9ULX7      120     130     140     150     160     170
                  KGSPGGSEHQINSEATFAELHIVHYDSDSYDSLSEAAERPQGLAVLGILIEVGETKNIAY
CA_14_recombinant KGSPGGSEHQINSEATFAELHIVHYDSDSYDSLSEAAERPQGLAVLGILIEVGETKNIAY

CA_14_Q9ULX7      180     190     200     210     220     230
                  EHILSHLEVRHKDQTSVPPFNLRELLPKQLGQYFRINGSLTTPPCYQSVLWTVFYRRS
CA_14_recombinant EHILSHLEVRHKDQTSVPPFNLRELLPKQLGQYFRINGSLTTPPCYQSVLWTVFYRRS

CA_14_Q9ULX7      240     250     260     270     280     290
                  QISMEQLEKLQGTLFSTEEEPSKLLVQNYRALQPLNQRMVFASFIQAGSSYTTGEMLSLG
CA_14_recombinant QISMEQLEKLQGTLFSTEEEPSKLLVQNYRALQPLNQRMVFASFIQAGSSYTTGEMLSLG

```

Transmembrane domain

```

CA_14_Q9ULX7      300     310     320     330
                  VGILVGCLCLLAVFYFIARKIRKRLENRKSVVFTSAQATTEA
CA_14_recombinant VGILVGCLCLLAVFYFIARKIRKRLENRKSVVFTSAQATTEA

```

Cytoplasmic domain

Fig. 2.2 (continued)

2.3 The Cloning of CA-Encoding Genes

The cloning of all CAs was done by using regular laboratory techniques, such as amplification of the desirable cDNA sequence by PCR, use of restriction endonucleases to create sticky ends on both the CA insert and a vector of choice, dephosphorylation, ligation, and transformation. A typical cloning procedure used for the cloning of CA IV is shown in Fig. 2.3. In our experiments we use a truncated form of protein (19–284 amino acids) without the N-terminal signal peptide and C-terminal peptide which is removed during the protein maturation. The PCR primers, which were used for cDNA amplification, had recognition sites of NdeI and XhoI restriction nucleases. The pET21a vector, which was used to create genetic construct, also had NdeI and XhoI restriction nuclease recognition sites in its multi-cloning site. This vector also encodes the C-terminal His₆-tag. Since a non-His₆-tagged protein was needed, the STOP codon was inserted to the reverse primer.

The cDNA, encoding full length CA IV, was purchased from RZPD Deutsches Ressourcenzentrum für Genomforschung (Berlin, Germany). After PCR, the restriction using NdeI and XhoI restriction nucleases was performed on both CA IV insert and vector. Then the linear vector was dephosphorylated. The vector and insert were ligated through sticky 5' and 3' ends and *E. coli* XLI-blue strain (Novagen) was transformed with the built genetic construct. The colonies from Petri dish were grown in small amounts of liquid media and the DNA was purified and sequenced.

2.4 Expression of Recombinant CAs

Various approaches for the production of sufficient amount of active recombinant CAs were used: (1) variation of the host, the *E. coli* strain, (2) variation of the vector and gene sequences, and (3) variation of the protein expression conditions (Table 2.1).

2.4.1 Variation of the Host

Numerous hosts are used for the production of recombinant proteins: bacterial, yeast, insect, and mammalian cells. Most recombinant CAs cloned in our laboratory were produced in *E. coli*, because it is easy and inexpensive to culture, it has short life cycle [8], and due to well-known genetics of *E. coli* it is possible to make some genetic modifications to improve the yield and solubility of recombinant proteins. Nevertheless, the need of post translational modifications, target protein toxicity for the host cell, tRNA bias between bacterial and mammalian cells can influence the expression of CAs, as well as other mammalian genes in *E. coli*.

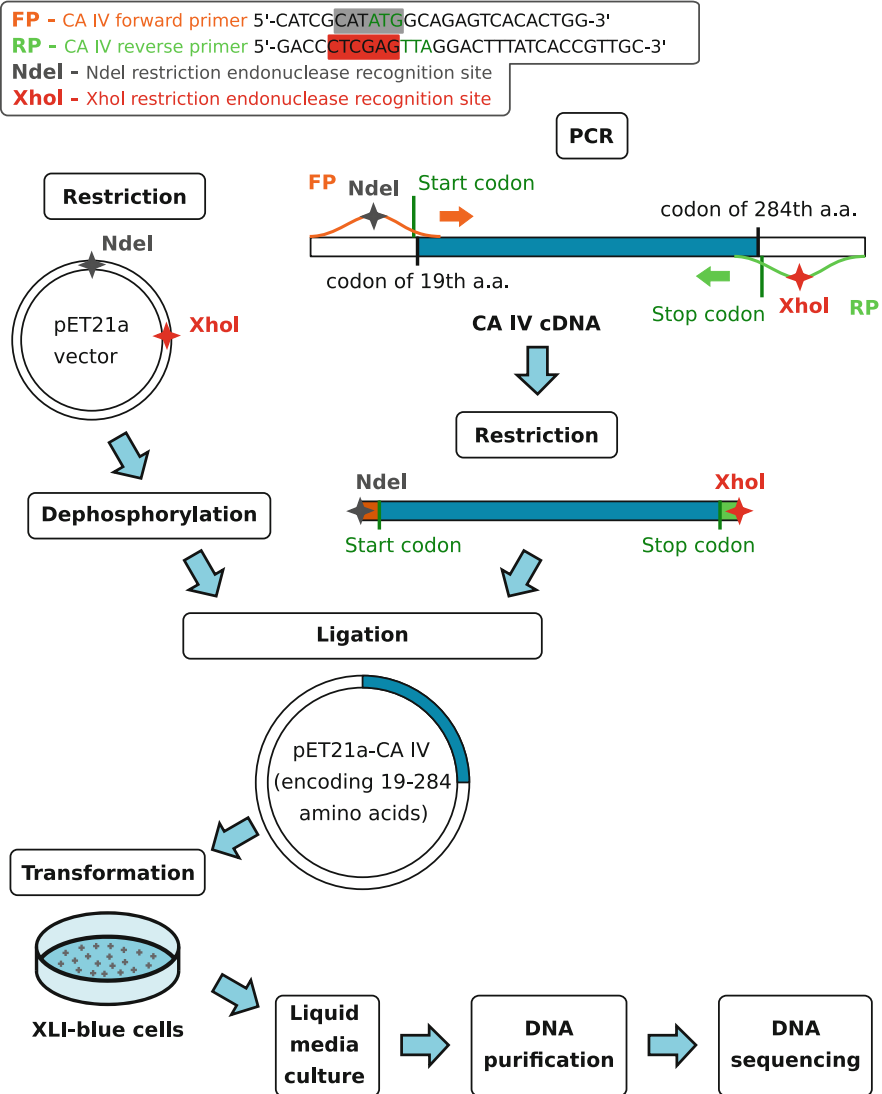


Fig. 2.3 A typical cloning procedure, the cloning of CA IV, beginning from the restriction of the vector plasmid, the PCR and restriction of the gene fragment, ligation of the two, transformation to bacteria, and finally the purification of the encoding DNA

Usually the CA expression experiments were started with the BL21(DE3) *E. coli* strain. This strain has advantage of being deficient in the *lon* and *ompT* proteases, lysogenic for λ prophage that contains an IPTG-inducible T7 RNA polymerase and is suitable for protein expression from pET vectors. The BL21(DE3) was used for full length CA II [9] and CA XIII [10], and parts of CA I (3-261 a.a.)

Table 2.1 An overview of the cloning and expression conditions of CA isoform production in *E. coli*

CA	Construct number ^a	Vector	Promotor	His ₆ -tag orientation	Region of CA (a.a.)	Strain	Zn ²⁺ source and concentration	IPTG	Temperature and time of CA expression	Target protein production ^P
I	pL0067	pET15b	T7	N-terminal	3-261	BL21(DE3)	0.4 mM ZnSO ₄	0.2 mM	30 °C, 4 h	High
II	pL0059	pET15b	T7	No	1-260 (Full)	BL21(DE3)	0.4 mM ZnSO ₄	0.2 mM	20 °C, o/n	High
III	pL0066	pET15b	T7	N-terminal	4-260	BL21(DE3)	0.4 mM ZnSO ₄	0.2 mM	30 °C, 4 h	Low
IV	pL0307	pET21a	T7	No	19-284	Origami B(DE3)	0.5 mM ZnCl ₂	1.0 mM	16 °C, o/n	Low
VA	pL0309	pET21b	T7	C-terminal	35-305	BL21trxB(DE3)	0.2 mM ZnSO ₄	0.1 mM	30 °C, 4 h	Low
VB	pL0173	pET15b	T7	N-terminal	40-317	Rosetta 2(DE3)	0.1 mM ZnSO ₄	0.1 mM	30 °C, 4 h	Low
VI	pL0229	pET15b	T7	N-terminal	21-290	Rosetta 2(DE3)	0.3 mM ZnSO ₄	1.0 mM	20 °C, o/n	Low
VII	pL0317	pET15b	T7	N-terminal	1-264 (Full)	BL21(DE3) CodonPlus-RIL	0.5 mM ZnSO ₄	1.0 mM	30 °C, 4 h	Low
XII	pL0119	pET21a	T7	No	30-291	Rosetta 2(DE3)	0.5 mM ZnSO ₄	1.0 mM	30 °C, 4 h	Medium
XIII	pL0058	pET15b	T7	No	1-262 (Full)	BL21(DE3)	0.4 mM ZnSO ₄	0.4 mM	30 °C, 4 h	High
XIV	pL0318	pET15b	<i>lac</i>	N-terminal	16-280	Origami B(DE3)	0.5 mM ZnCl ₂	0.5 mM	16 °C, o/n	Medium

The region of CA shows the amino acid numbers in the protein

^aConstruct number in laboratory plasmid list

^P — Visual estimation of target protein production in polyacrylamide gel; *Low*—band of target protein after expression induction is up to two times intensive than before, *Medium*—band of target protein after expression induction is up to four times intensive than before, *High*—band of target protein after expression induction is four or more times intensive than before

o/n—overnight cultivation

[11, 12] and CA III (4-260 a.a.) [13] recombinant protein expression. If the protein was not expressed or was expressed as inclusion bodies in *E. coli* cells, we used different *E. coli* strains with some genetic modifications: Rosetta (DE3), Rosetta gami TM 2(DE3), Arctic Express (DE3), C41 (DE3), BL21 CodonPlus-RIL (DE3), and others. The highest amount of soluble and active CA IV (19-284 a.a.) [14] and CA XIV (16-280) [7] were expressed in *E. coli* Origami B(DE3) strain that has mutations in thioredoxinreductase (*trx*B) and glutathione reductase (*gor*), which help the disulfide bond formation in recombinant CA in the cytoplasm. The CA VB (40-317 a.a.) [13], CA VI (21-290 a.a.) [15], and CA XII (30-291 a.a.) [16] were expressed in Rosetta 2(DE3) strain supplied with tRNA genes for seven codons, rarely used in *E. coli* gene expression: AUA, AGG, AGA, CUA, CCC, GGA, and CGG. The highest yield of CA VA (35-305 a.a.) was obtained from target protein expression in BL21 *trx*B(DE3) strain. This strain has the *trx*B mutation, which enables cytoplasmic disulfide bond formation. Recombinant full length CA VII was expressed in BL21 Codon Plus (DE3)-RIL strain containing copies of the Arg (AGA, AGG), Ile (AUA), Leu (CUA) tRNA genes.

2.4.2 Varying the Vector and Gene Sequences

Varying the vector involves changing the promoter, which controls expression of target gene or the fusion tag which influences the solubility and purification of target protein. In our laboratory, most CA genes were cloned in pET vector with the C- or N-terminal His₆-tag. Recombinant CAs with the N-terminal His₆-tag were CA I (3-261 a.a.), CA III (4-260 a.a.), CA VB (40-317 a.a.), CA VI (21-290 a.a.), full length CA VII, CA XIV (16-280 a.a.), and the C-terminal His₆-tag- CA VA (35-305 a.a.). His₆-tag is a relatively small part of the protein that can also be removed by a site-specific protease to ensure that it does not cause undesired effects. The histidine-tagged proteins can be purified using a relatively simple method of protein purification - immobilized metal affinity chromatography (IMAC). Some recombinant CAs have a large number of histidines (10–13) in the target protein sequence and can be purified using IMAC without an additional His₆-tag: full length CA II and full length CA XIII.

In order to increase the solubility of some recombinant CAs, the genes of interest were also cloned in vectors, providing tags of large-size protein—glutathione S-transferase (GST) (for the expression of catalytic domains of CA VB, CA VI, CA IX, CA XII, and CA XIV), small ubiquitin modifier (SUMO) (for the expression of catalytic domain of CA XIV), and N-utilization substance (NusA) (for the expression of the catalytic domain of CA IX). The drawback of protein tags is their large size (GST—211 a.a. (26 kDa), SUMO—100 a.a. (11 kDa), and NusA—495 a.a. (54.8 kDa)), and therefore the fusion tags can interfere with the activity of recombinant proteins and must be cleaved properly. Our experience shows that the tags (GST, SUMO, and NusA) fused with CAs did not change the solubility of recombinant CAs substantially or tag-fused CAs precipitated after the tag was cleaved.

Another important criterion for the selection of the vector is the strength of its promoter, which controls target protein expression in *E. coli* cells. The strength of the different promoters is determined by the relative frequency of transcription initiation [17]. This is influenced by the affinity of RNA polymerase to promoter sequence—the sequence of strong promoter match to RNA polymerase, resulting in efficient transcription initiation and elongation. Sequence of a weak promoter does not match exactly the RNA polymerase and therefore the transcription is less effective. This is particularly important if the protein of interest is toxic or harmful for the host cell. In these cases, weaker promoters may be preferred over stronger ones [17, 18]. Usually for recombinant human CA expression we used strong bacteriophage promoter T7, because we need high amount of target protein, but for CA XIV both bacterial weaker *tac* and bacteriophage stronger T7 promoters were used. However, CA XIV expression under both promoters revealed no obvious difference in the amount of the purified protein. This can be explained by relatively low differences between the strength of T7 and *tac* promoters [7]. While choosing the most optimal vector it is also very important to choose a proper length of protein itself - not too long so that *E. coli* would be able to produce it in stable and soluble way, but not too short so that it would not lose its catalytic activity. For every CA isoform, the optimal length of protein varies.

For the detection of optimal size of recombinant protein, several DNA constructs encoding proteins that vary in length by 2–10 amino acids at each end can be created [19]. For most of the isoforms, we did different constructs and tried to produce proteins of variable length. The best options were described earlier in section “The Sequences of the Catalytically Active Human CAs.”

2.4.3 Varying the Protein Expression Conditions

Culture conditions of *E. coli* may also increase the expression, solubility, and stability of a recombinant protein. Whereas the rate of polypeptide chain elongation is 4 to 10 times faster in prokaryotes than in eukaryotes, high translation rate in *E. coli* promotes aggregation of recombinant proteins by forming insoluble inclusion bodies. Thus cultivation of bacteria at lower temperatures slows down protein expression and increases their proper folding [20]. In our experience, the optimal temperatures for recombinant CA expression in *E. coli* were 16 °C (overnight expression), 20 °C (overnight expression), and 30 °C (four hours after expression induction).

Using vectors with T7 systems, the target protein expression can be induced either with isopropyl- β -D-thiogalactoside (IPTG) or by auto-induction medium. The optimal IPTG concentration for the expression of CAs should be optimized. In our laboratory, the *E. coli* cells were grown to optical density $OD_{600} \approx 0.6$ – 0.8 in Luria/Miller (LB) medium or Brain-Heart-Infusion Broth (BHI) and then the expression of CAs was induced with IPTG. The optimal IPTG concentration varied from 0.1 to 1 mM.

For catalytic activity of CAs, Zn^{2+} is important, because Zn^{2+} is located in the active site of CAs. $ZnSO_4$ and $ZnCl_2$ were added to the culture medium as a Zn^{2+} source. Both compounds are toxic for cells, therefore should be added at low concentrations. There was no significant difference which compound is used, but $ZnSO_4$ was preferred over $ZnCl_2$. The optimal concentration of $ZnSO_4$ varies from 0.1 to 0.5 mM, while the concentration of $ZnCl_2$ —0.5 mM.

2.4.4 Generation of Recombinant CA Proteins Using Mammalian Expression Systems

E. coli system is widely used for the expression of mammalian genes and generation of stable recombinant proteins. However, this system cannot be applied when these proteins require certain modifications, which occur only in eukaryotic cells. Good example of such protein is human CA IX. We could not produce stable recombinant CA IX in *E. coli* despite extensive efforts and experience, gained while generating other human CAs in prokaryotic systems. Therefore, we turned to mammalian cells for the production of this protein, as described in [13]. The expression systems used in mammalian cells are summarized in Table 2.2.

A FreeStyle MAX 293 Expression System from Invitrogen (ThermoFisher) was used, which contained suspension FreeStyle 293-F cells (derived from human HEK-923 cell line), complete chemically defined culture medium, and a cationic-lipid FreeStyle MAX transfection reagent. For the delivery of CA IX gene into mammalian cells an episomal expression vector pCEP4 (Invitrogen, ThermoFisher) was chosen, which combines the advantages of strong CMV promoter and extra-chromosomal replication for the high level of recombinant protein expression. Since the efficiency of protein production is highly dependent on the efficiency of transfection, and the latter is reduced by the size increase of DNA construct, we decided to reduce the size of the original pCEP4 vector by deleting ~2 kb region containing the Hygromycin B resistance gene. The modified vector was called pCEP4d (d stands for the deletion). Another modification, which took place, was an insertion of chemically synthesized DNA sequence, containing the secretion signal from the V-J2-C region of murine Ig kappa chain (modified vector called pCEP4dS, where S stands for the secretion). Secretion signal was placed at the beginning of a multicloning region to enable the secretion of the in-frame fused proteins into the growth medium of transfected cells. Taking into account that the FreeStyle culture medium does not contain a fetal bovine serum and is virtually protein-free, getting the recombinant protein secreted into the medium is very convenient because of a simple and efficient protein purification step. A one-step affinity chromatography using p-aminomethylbenzene sulfonamide-agarose was enough to get pure protein from the growth medium of transfected cells.

Table 2.2 Overview of conditions of CA production in *mammalian cells*

CA	Construct number ^a	Vector	Region of CA (a.a.) used in expression construct	Expression system	Hygromycin selection ^b	Amount of purified protein, mg/l ^c
IV	pL0200	pCEP4dS	19-284	FreeStyle Max 293	No	~9
VA	pL0205	pCEP4dS	34-297	FreeStyle Max 293	No	No expression
VI	pL0339	pCEP4dS	Full	FreeStyle Max 293	No	2-4
IX	pL0225	pCEP4dS	138-390	FreeStyle Max 293	No	10-15
IX-mut.	pL0226	pCEP4dS	138-392 (C41S)	FreeStyle Max 293	No	~45
PG-IX	pL0227	pCEP4dS	38-414	FreeStyle Max 293	No	~10
XII	pL0316	pCEP4dS	30-291	FreeStyle Max 293	No	~3
XIV	pL0228	pCEP4dS	16-285	FreeStyle Max 293	No	No expression
IX	pL0323	pCEP4S	138-390	FreeStyle Max 293	Yes	~10
IX-mut.	pL0324	pCEP4S	138-392 (C41S)	FreeStyle Max 293	Yes	~23
PG-IX	pL0315	pCEP4S	38-414	FreeStyle Max 293	Yes	~6
XII	pL0317	pCEP4S	30-291	FreeStyle Max 293	Yes	~2.5
XIV	pL0303	pCEP4S	16-285	FreeStyle Max 293	Yes	No expression
VI	pL0339	pCEP4dS	Full	Expi293F	No	~60
IX	pL0225	pCEP4dS	138-390	Expi293F	No	60-100
IX-mut.	pL0226	pCEP4dS	138-392 (C41S)	Expi293F	No	150-300
PG-IX	pL0227	pCEP4dS	38-414	Expi293F	No	15-20
IX	pL0323	pCEP4S	138-390	Expi293F	Yes	~50
IX-mut.	pL0324	pCEP4S	138-392 (C41S)	Expi293F	Yes	~100
PG-IX	pL0315	pCEP4S	38-414	Expi293F	Yes	~155

^a Construct number in laboratory plasmid list^b Culture was expanded after transfection using Hygromycin B selection^c Average amount of purified proteins, calculated in mg for 1 liter of expressing culture

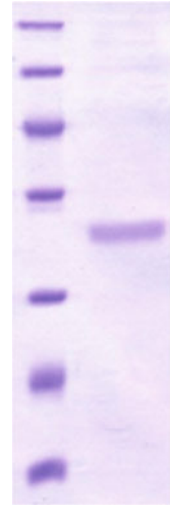
First batches of recombinant mammalian protein were obtained using pCEP4S-CA IX construct containing DNA sequence corresponding to the catalytic domain of CA IX (amino acids 138 to 390) and a FreeStyle MAX 293 Expression System following the manufacturer's recommendations for the suspension cell culturing and transfection conditions [13]. This method generated pure and very stable CA IX protein with an average gain of 10–15 mg of protein per 1 liter of culture. The same method was also used to express other CA IX constructs as well as other CAs, such as CA IV [14], CA VI [15], and CA XII [21]. However, this methodology had a serious limitation—a relatively high cost of protein production.

Original protocol of the FreeStyle MAX 293 Expression System is based on transient transfection, which is not time consuming and works very well when the small amounts of protein are needed. However, a large scale transient transfection may not be the method of choice considering the cost of the transfection reagent. Since stably transfected lines of suspension cells cannot be made without going through adhesive stage, we decided to increase the efficiency of transient transfection by making use of the Hygromycin resistance gene, present in the original pCEP4 vector. The secretion signal was inserted into pCEP4 vector and a small scale transfection with pCEP4S-CA IX construct was performed, adding Hygromycin B for selection of transfected cells 2 days after transfection [22]. The bulk selection with Hygromycin B turned out to be very useful not only because it increased the percentage of CA IX-expressing cells in the culture after transfection, but also because it supported the selective proliferation of these cells and allowed a possibility to dilute the culture several times until it reached ~ 10 times larger volume compared to the starting volume of transfection. This resulted in tenfolds lower consumption of the transfection reagent and much lower cost of protein production. Moreover, this method assured a healthy cell culture condition and low percentage of dead cells even at the end of cultivation (10–12 days after transfection), resulting in the absence of contaminating cell debris proteins in the growth medium. Therefore, secreted CA IX protein was always the major protein seen in SDS samples of the cell growth medium (Fig. 2.4). It made purification of CA IX simple and effective.

Although FreeStyle Max 293 expression system worked really well for several years, its efficiency unexpectedly dropped during the fifth year from the time of purchase. This drop was caused by decreased cell ability to recover from freezing in liquid nitrogen—after thawing cell culture remained very clumpy and could not reach single cell stage. This caused poor cell growth and low transfection efficiency. Therefore, we decided to adopt a new Expi293 Expression System developed by ThermoFisher.

Expi293 Expression System not only brings together a high-expressing 293 suspension cell line and a high-efficiency transfection reagent, but also includes specialized expression enhancers, that are added to the cell medium after transfection. This system proved to be very efficient and allowed us to get 5–10

Fig. 2.4 Expression of CA IX in the medium of pCEP4S-CA IX transfected cells. Left lane shows the protein marker. Right lane shows the CA IX protein seen in 20 μ l of the SDS sample of cell culture medium



times more of the CA IX protein from the same volume of culture medium (50–100 mg/l), compared to FreeStyle 293 Max system. Although selection with Hygromycin B did not give any advantage in this case, even without it, the new system provided the highest yields of protein production that we could achieve.

While discussing the expression of secreted recombinant proteins in human 293 cell culture systems, it is worth mentioning that the expression efficiency can be highly dependent on the length and the dimerization status of proteins that are produced. This can be illustrated by the example of three different CA IX constructs: pCEP4S—CA IX, pCEP4S—PG-CA IX, and pCEP4S—CA IX (C41S) [22]. While the average yield of CA IX protein, corresponding strictly to catalytic domain, in Expi293 system is about 50–100 mg/l, the presence of proteoglycan (PG) domain at the N terminus of catalytic domain (PG-CA IX) diminishes the protein yield about 4–5 folds, making it around 12–20 mg/l. However, if the cysteine in the catalytic domain of CA IX is changed to serine to prevent dimerization of these domains (CA IX (C41S)), the protein yield can increase up to 300 mg/l, showing that the monomeric proteins can be produced more efficiently.

Besides the differences in the expression level between various constructs of the same gene, we found that constructs of some genes, for example CA XIV and CA VA, could not be expressed at all in the above-mentioned systems. A likely reason for this is a presence of very strict protein quality control systems in mammalian cells, which cause the degradation of certain truncated or mutated proteins. However, the same systems guarantee a very high quality of recombinant

proteins that are produced. These proteins have all required modifications, are very stable and suitable for many kinds of different applications. In our laboratory, these proteins were successfully used for molecular biology, different biophysical assays (ITC, TSA, SPR, stopped flow inhibition, etc.), and antibody production, serving as a standard of the human recombinant proteins.

2.5 Purification of Recombinant CAs

The appearance of all 12 catalytically active CAs on an SDS-PAGE gel is shown in Fig. 2.5. The characteristics of the purified enzymes are listed in Table 2.3. In our experience, it was most practical to purify CA I, CA III, and CA VII by Ni^{2+} -metal chelation and ion-exchange chromatographies. The CA II and CA XIII are also purified the same way even though they did not contain the His₆-tag. The CA IV and CA XII were purified by ion-exchange and ligand-affinity chromatographies. The CA VA, CA VB, CA VI, and CA XIV were purified by Ni^{2+} -metal chelation and affinity chromatographies. The CA IX was produced in suspension culture of mammalian cells and purified using only the benzenesulfonamide-bearing affinity chromatography. The 12 prepared CAs were used in various biochemical and biophysical assays as described in the following chapters.

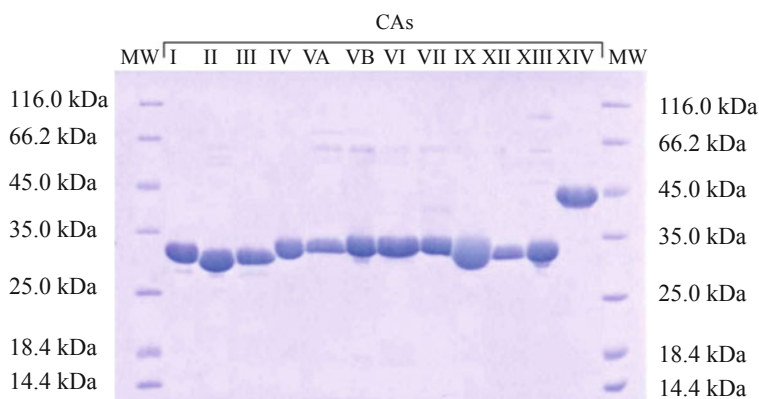


Fig. 2.5 SDS-PAGE of all 12 catalytically active CA isoforms was performed on a 12% resolving gel and a 4% stacking gel and the proteins were stained by Coomassie Brilliant Blue G250

Table 2.3 Characteristics of purified CA enzymes

CA	Construct number ^a	Protein amount mg/1 g biomass	Construct name	Remarks	Theoretical MW, Da	Obtained MW, Da
I	pL0067	5–6	pET15b-6H-CA I (3-261)	With N-terminal His ₆ -tag	28799.1	28799.6
II	pL0059	7–8	pET15b-CA II	Full length, without His ₆ -tag	29246.0	29115.1 ^b
III	pL0066	3–4	pET15b-6H-CA III (4-260)	With N-terminal His ₆ -tag	31648.8	31518.3 ^b
IV	pL0307	1–2	pET21a-CA IV (19-284)	Without His ₆ -tag	30454.6	30320.74 ^b
VA	pL0309	0.02–0.05	pET21a-CA VA-6H (35-305)	With N-terminal His ₆ -tag	31818.8	30320.74
VB	pL0173	0.4–0.5	pET15b-CA VB (40-317)	With N-terminal His ₆ -tag	34062.4	34062.2
VI	pL0176	0.9–1	pET15b-CA VI (21-290)	With N-terminal His ₆ -tag	33180.9	34062.7
VII	pL0137	1–2	pET15b-CA VII	Full length, with N-terminal His ₆ -tag	31821.7	32043.6
IX	pL0323	0.07–0.13 mg protein from 1 ml medium	pCEP4-CA IX (138-390)	Without proteoglycan domain, expressed in mammalian cells	28320.04	Was not obtained
XII	pL0119	4–5	pET21a-CA XII (30-291)	Without His ₆ -tag	29886.3	31690.0
XIII	pL0058	8–9	pET15b-CA XIII	Full length with additional N-terminal Met residue	29574.3	29574.2
XIV	pL0318	0.2–0.3	pET15b-CA XIV-6H (16-280)	With N-terminal His ₆ -tag	33114.7	32982.6 ^b

^aConstruct number in laboratory plasmids list^bThe difference between theoretical and measured MW is explained by the loss of Met without water (131.211 Da)

2.6 Conclusions

The catalytic domains of all 12 human catalytically active CA isoforms have been recombinantly prepared and purified in sufficient amounts for biophysical experiments. Some prepared CA isoforms fully resembled the native CAs. However, numerous other isoforms had to be truncated by removing trans-membrane and other regions. Some isoforms such as CA VA, CA VB, and CA XIV were especially hard to obtain in large amounts. All isoforms were prepared in bacterial cells except CA IX which was prepared in mammalian cell cultures. Sulfonamide-based affinity purification was necessary to obtain high-purity enzymes for biophysical interaction studies.

References

1. Krishnamurthy, V.M., et al.: Carbonic anhydrase as a model for biophysical and physical-organic studies of proteins and protein-ligand binding. *Chem. Rev.* **108**, 946–1051 (2008)
2. Vullo, D., Scozzafava, A., Pastorekova, S., Pastorek, J., Supuran, C.T.: Carbonic anhydrase inhibitors: inhibition of the tumor-associated isozyme IX with fluorine-containing sulfonamides. The first subnanomolar CA IX inhibitor discovered. *Bioorg. Med. Chem. Lett.* **14**, 2351–2356 (2004)
3. Okuyama, T., Waheed, A., Kusumoto, W., Zhu, X.L., Sly, W.S.: Carbonic anhydrase IV: role of removal of C-terminal domain in glycosylphosphatidylinositol anchoring and realization of enzyme activity. *Arch. Biochem. Biophys.* **320**, 315–322 (1995)
4. Pilka, E.S., Kochan, G., Oppermann, U., Yue, W.W.: Crystal structure of the secretory isozyme of mammalian carbonic anhydrases CA VI: implications for biological assembly and inhibitor development. *Biochem. Biophys. Res. Commun.* **419**, 485–489 (2012)
5. Klock, H.E., Koesema, E.J., Knuth, M.W., Lesley, S.A. Combining the polymerase incomplete primer extension method for cloning and mutagenesis with microscreening to accelerate structural genomics efforts. *Proteins: Struct., Funct., Bioinf.* **71**, 982–994 (2008)
6. Whittington, D.A., et al.: Crystal structure of the dimeric extracellular domain of human carbonic anhydrase XII, a bitopic membrane protein overexpressed in certain cancer tumor cells. *Proc. Natl. Acad. Sci. U. S. A.* **98**, 9545–9550 (2001)
7. Juozapaitienė, V., et al.: Purification, enzymatic activity and inhibitor discovery for recombinant human carbonic anhydrase XIV. *J. Biotechnol.* **240**, 31–42 (2016)
8. Fossum, S., Crooke, E., Skarstad, K.: Organization of sister origins and replisomes during multifork DNA replication in *Escherichia coli*. *EMBO J.* **26**, 4514–4522 (2007)
9. Cimperman, P., et al.: A quantitative model of thermal stabilization and destabilization of proteins by ligands. *Biophys. J.* **95**, 3222–3231 (2008)
10. Sūdžius, J., et al.: 4-[N-(Substituted 4-pyrimidinyl)amino]benzenesulfonamides as inhibitors of carbonic anhydrase isozymes I, II, VII, and XIII. *Bioorg. Med. Chem.* **18**, 7413–7421 (2010)
11. Baranauskienė, L., et al.: Inhibition and binding studies of carbonic anhydrase isozymes I, II and IX with benzimidazo[1,2-c][1,2,3]thiadiazole-7-sulphonamides. *J. Enzyme Inhib. Med. Chem.* **25**, 863–870 (2010)
12. Čapkauskaitė, E., et al.: Benzenesulfonamides with pyrimidine moiety as inhibitors of human carbonic anhydrases I, II, VI, VII, XII, and XIII. *Bioorg. Med. Chem.* **21**, 6937–6947 (2013)
13. Dudutienė, V., et al.: Discovery and characterization of novel selective inhibitors of carbonic anhydrase IX. *J. Med. Chem.* **57**, 9435–9446 (2014)
14. Mickevičiūtė, A., et al.: Intrinsic thermodynamics of high affinity inhibitor binding to recombinant human carbonic anhydrase IV. *Eur. Biophys. J.* **47**, 1–20 (2017)

15. Kazokaitė, J., Milinavičiūtė, G., Smirnovienė, J., Matulienė, J., Matulis, D.: Intrinsic binding of 4-substituted-2,3,5,6-tetrafluorobenzenesulfonamides to native and recombinant human carbonic anhydrase VI. *FEBS J.* **282**, 972–983 (2015)
16. Jogaitė, V., et al.: Characterization of human carbonic anhydrase XII stability and inhibitor binding. *Bioorg. Med. Chem.* **21**, 1431–1436 (2013)
17. Tegel, H., Ottosson, J., Hober, S. Enhancing the protein production levels in *Escherichia coli* with a strong promoter: protein production levels in *E. coli*. *FEBS J.* **278**, 729–739 (2011)
18. Ma, P., et al.: An efficient strategy for small-scale screening and production of archaeal membrane transport proteins in *Escherichia coli*. *PLoS ONE* **8**, e76913 (2013).
19. Gräslund, S., et al.: Protein production and purification. *Nat. Met.* **5**, 135–146 (2008)
20. Freigassner, M., Pichler, H., Glieder, A. Tuning microbial hosts for membrane protein production. *Microb. Cell Fact.* **8**, 69 (2009)
21. Dekaminaviciute, D., et al.: Development and characterization of new monoclonal antibodies against human recombinant CA XII. *BioMed Res. Int.* **2014**(00001), 1–11 (2014)
22. Linkuvienė, V., et al.: Intrinsic thermodynamics of inhibitor binding to human carbonic anhydrase IX. *Biochim. Biophys. Acta Gen. Subj.* **1860**, 708–718 (2016)



Catalytic Activity and Inhibition of Human Carbonic Anhydrases

3

Lina Baranauskienė and Daumantas Matulis

Abstract

Carbonic anhydrases, as any enzymes, possess the catalytic activity that can be measured experimentally using various techniques and approaches. The CAs have been shown to catalyze a series of non-native reactions, but here we primarily concentrate on the physiologically relevant activity of carbon dioxide hydration to bicarbonate anion and acid proton. The measurement of the esterase activity will also be described since it is a simple spectrophotometry-based method to demonstrate CA catalytic activity. The stopped-flow CO₂ hydratase activity assay is currently the most used assay of the CA catalytic activity. However, there are some limitations of the assay that will be discussed. The inhibition assay is the only direct demonstration that a compound is an inhibitor of the enzymatic activity. Numerous assays, such as isothermal titration calorimetry, thermal shift assay, and surface plasmon resonance, that will be discussed in further chapters, show the interaction, but the binding site may be different and thus the inhibition of enzymatic activity is essential for the demonstration of inhibition. However, if the compounds are structurally similar and possess a functional headgroup such as primary sulfonamide that has been shown to bind to the Zn^{II} in the active site, other techniques are more straightforward and may provide more accurate results than the assay of enzymatic activity.

L. Baranauskienė · D. Matulis (✉)

Department of Biothermodynamics and Drug Design, Institute of Biotechnology, Life Sciences Center, Vilnius University, Vilnius, Lithuania

e-mail: lina.baranauskiene@bti.vu.lt; matulis@ibt.lt

© Springer Nature Switzerland AG 2019

D. Matulis (ed.), *Carbonic Anhydrase as Drug Target*,
https://doi.org/10.1007/978-3-030-12780-0_3

39

3.1 Introduction

Carbonic anhydrases (CA, carbonic acid hydro-lyase, EC 4.2.1.1) are a family of enzymes, catalyzing interconversion between carbon dioxide and bicarbonate. In addition to carbon dioxide hydration reaction, some CA enzymes are reported to possess other enzymatic activities [1]. The physiological relevance of these is not fully understood, but the presence of additional activities enables industrial application of CAs for the catalysis of different reactions [2–4]. Members of this enzyme family are one of the fastest enzymes—they can increase reaction speed by up to 10^6 times. Due to the importance of the catalyzed reaction, all tested organisms have at least one enzyme with the CA properties. There are several evolutionary distinct classes of CAs, denoted by Greek letters: α , β , γ , δ , ζ , η , and θ . The enzymes have different folds and oligomeric structures, but all of them contain divalent metal ion (most often Zn^{II}) in their active sites [5, 6].

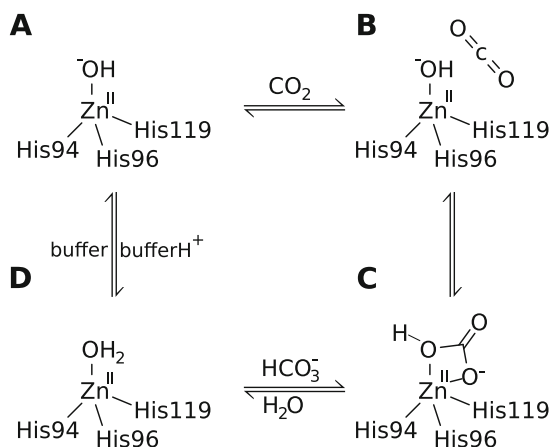
Humans have 15 CA isoforms and they all belong to α -class. Twelve of them have higher or lower CO_2 hydration enzymatic activity and three are acatalytic due to mutations in metal ion coordinating amino acids. All human CA isoforms are highly homologous and structurally similar [7, 8]. Since some members of human CAs are drug targets in various diseases and disorders, there is a need for selective inhibitors of target CA isoforms. Therefore, soon after the discovery of CAs in 1933, different methods for assaying the activity of this enzyme were introduced: manometric [9], colorimetric [10], electrometric [11, 12], etc. Different methods of catalytic activity and inhibition quantification are still used and some of them are described in this chapter.

3.2 Catalytic Mechanism

The active site of human CAs is in the center of protein molecule, where catalytically important zinc ion is coordinated by three histidine residues (His94, His96, and His119). The active site cavity is approximately 15 Å deep and has different affinity for water: one side of the cavity is formed mainly of hydrophobic amino acid residues, and the other is polar, made of hydrophilic residues [13].

The catalysis proceeds via two-step ping-pong mechanism [14]. When the CA active site has hydroxide ion bound to zinc ion (Fig. 3.1a), CO_2 enters the active site and binds to it (Fig. 3.1b). The hydroxyl group performs the nucleophilic attack to CO_2 forming HCO_3^- bound to the zinc ion (Fig. 3.1c). The bicarbonate anion is then displaced by a water molecule (Fig. 3.1d). The deprotonation of the water molecule is the rate limiting step in the catalysis reaction. The proton is transferred via ordered water network and in some isoforms via a proton-shuttle residue His64 to the bulk solvent.

Fig. 3.1 General scheme of the CO₂ hydration reaction catalyzed by carbonic anhydrase. The carbon atom of the CO₂ is nucleophilically attacked by the hydroxide of Zn^{II} forming bicarbonate which is displaced by the water molecule. The last step yielding the deprotonated hydroxide and preparing the enzyme for the next cycle is the slowest step of the entire cycle



3.3 Carbonic Anhydrase Esterase Activity Assay

It was demonstrated in 1964 that CAs have esterase activity [15]. Both the hydratase and esterase activities in CA use the same catalytic active site and have a similar mechanism. Despite the fact that the most commonly used substrate to test the esterase activity of various enzymes—the 4-nitrophenylacetate—is larger than CO₂, this method is often used for the primary inhibition studies (Fig. 3.2). This assay can be used for high throughput screening of enzymatic activity inhibitors—the esterase reaction is significantly slower as compared to the CO₂ hydration and can be easily monitored using a standard multi-well plate colorimetric assay. Due to its lower sensitivity, the lowest concentrations of the CA enzyme used for the inhibition studies in esterase activity assay are approximately 5–10 times higher than in the CO₂ hydration assays [16]. No direct quantitative correlation between inhibitor ranking obtained using the esterase and hydratase assays was observed using different compounds. However, the esterase assay was reported to be useful for the primary selection of inhibiting compounds / antibodies [16].

3.4 ¹⁸O Exchange Method (Membrane Inlet Mass Spectrometry)

Another method of measuring the CA catalytic activity and its inhibition is based on mass-spectrometric detection of ¹⁸O exchange from CO₂ to water during spontaneous or CA-catalyzed CO₂ hydration reaction [17]. Doubly labeled K₂¹³C¹⁸O₃ salt is used to prepare the solution of doubly labeled substrate ¹³C¹⁸O₂. The sample cuvette is coupled to mass spectrometer via membrane inlet system forming a closed system, and the concentrations of all gaseous CO₂ species are quantified according to their *m/z* values (Fig. 3.3).

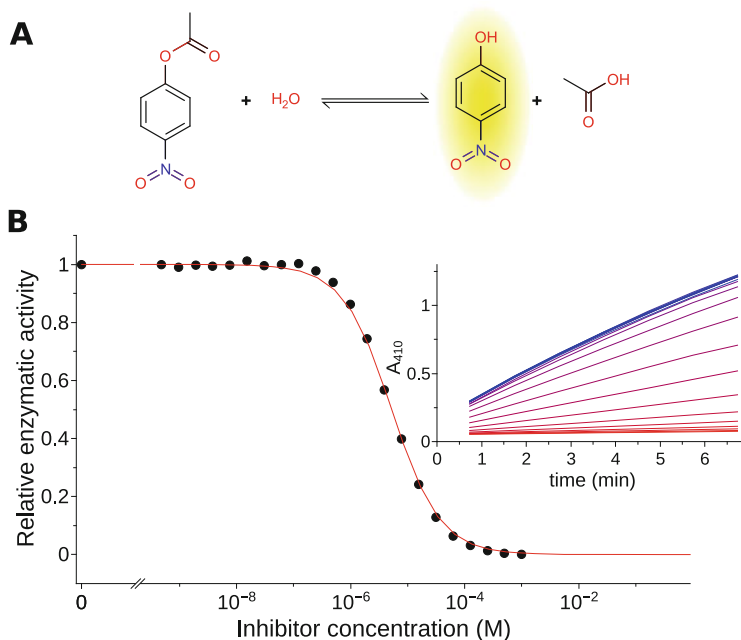


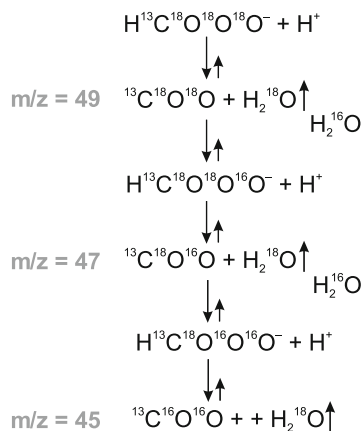
Fig. 3.2 Esterase activity assay of the CA enzyme: (a) The product of the most often used substrate, *p*-nitrophenyl acetate, hydrolysis is yellow and can be monitored spectrophotometrically, especially in slightly alkaline pH where the hydroxy group is deprotonated. (b) An example of an inhibitor dosing curve, the inhibition of CA II with weak inhibitor ($K_d = 5 \mu\text{M}$) zonisamide. The data points (black circles) show the experimental values that are proportional to the slopes of the raw data curves, while the red curve is the data fitting according to the Morrison model. The inset shows the raw data curves: blue-colored top curve corresponds to the fully active enzyme, while at the largest concentration of the inhibitor that results in full inhibition, the red-colored curve is observed. The slope of the curve is close to zero showing that no product is formed upon full inhibition of the enzyme

CA activity is linked to ^{18}O label disappearance from doubly labeled $^{13}\text{C}^{18}\text{O}_2$, the parameter, called atom percent enrichment [18], which is calculated using equation:

$$^{18}\text{O} \text{ atom fraction} = \log \frac{^{13}\text{C}^{18}\text{O} \times 100}{^{13}\text{CO}_2} \quad (3.1)$$

CA activity is calculated using the slope of ^{18}O atom fraction decrease over time. It is compared to non-catalyzed reaction. For calculation of inhibition constants, the inhibitor is dosed and the rate of ^{18}O atom fraction decrease is measured. The obtained slope vs. concentration data can be fitted using Hill or Morrison model to obtain inhibition parameters.

Fig. 3.3 Scheme of doubly labeled CO₂ disappearance and m/z values of the gas species detected by mass spectroscopy



The main advantages of this method to determine CA activity are: (1) the ability to use it with any required buffer or in the absence of any buffer because it is an equilibrium method and the exchange of ¹⁸O between CO₂ and water proceeds without a change of pH; (2) due to very high sensitivity of mass spectrometers, very small amounts of labeled atoms are detected enabling the use of enzyme concentrations down to tenths of picomolar, and accurate *K_i* determination for extremely tight-binding inhibitors.

3.5 Stopped-Flow Assay of CO₂ Hydration

Spontaneous CO₂ hydration reaction is quite fast (approximately 40 s to 100 s) and the reaction catalyzed by the CA is even much faster. Therefore, fast mixing and detection technique, such as stopped-flow apparatus, is required. This method for CA activity quantification has been described by Khalifah in 1971 [19]. Two solutions are prepared:

- first the solution that contains buffer (e.g., 20 mM Hepes, pH 7.5), pH indicator dye (e.g., Phenol Red, which has red color at pH 8.2 and above and yellow color at pH 6.4 or below, Fig. 3.4), enzyme (CA), and the inhibitor that can be added at various concentrations,
- second the CO₂ solution in ultra-pure water.

These two solutions are then quickly mixed in the stopped-flow cell, where the CO₂ is hydrated forming bicarbonate ion and proton, that acidifies the medium resulting in the change of indicator color (Fig. 3.5).

In the inhibition studies, a serial dilution of inhibitor is prepared while keeping the concentration of CA constant. Plotting the residual enzyme activity against the inhibitor concentration (in a logarithmic scale) results in a sigmoidal inhibition

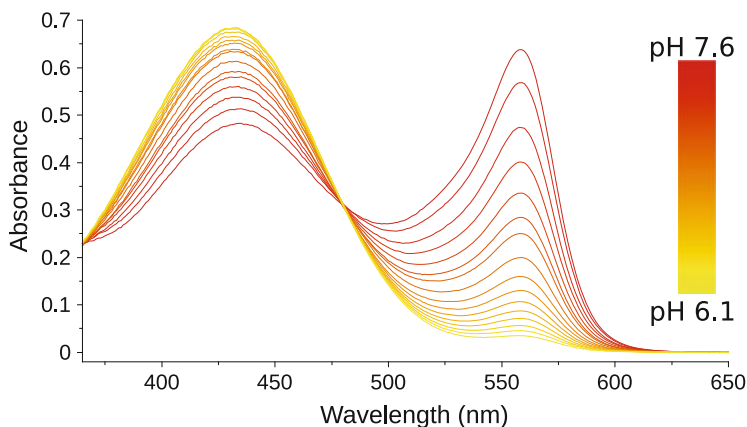


Fig. 3.4 Absorption spectra of Phenol Red at various pH showing how the spectrum changes decreasing the peak at 557 nm upon the drop in pH during the CO_2 hydration reaction catalyzed by CA. The indicated spectra correspond to pH interval from pH 7.6 to 6.1 changing by 0.1 pH unit

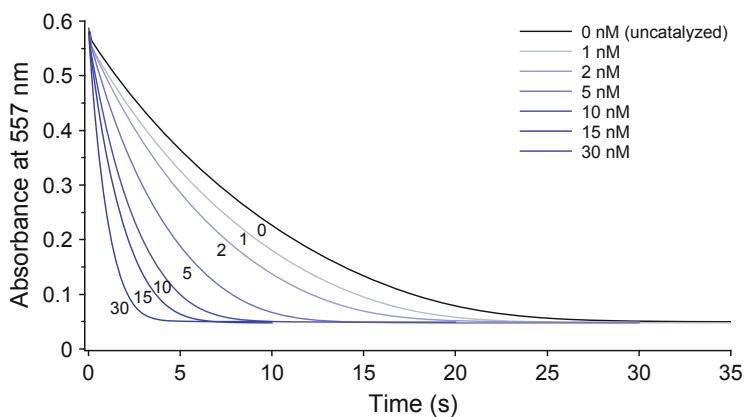


Fig. 3.5 Change of absorbance at 557 nm after mixing the CO_2 aqueous solution and the buffer of pH 7.5 with Phenol Red dye and different CA concentration. The black curve marks the spontaneous CO_2 hydration in the absence of the CA enzyme, while the other curves were obtained with increasing concentration of PG-CA IX protein (1 nM to 30 nM). In all cases, the reaction starts at approx. 0.58 absorbance units and ends at approx. 0.05. However, the time required for the reaction to complete differs from approx. 30 s for uncatalyzed reaction to approx. 5 s with the highest tested enzyme concentration

curve (Fig. 3.6). In most cases, the classical full-inhibition sigmoidal curve should be obtained with the Hill coefficient close to 1 and there should be no residual enzyme activity remaining at the highest inhibitor concentrations. In some cases, the compound solubility limits acquisition of full inhibition points, especially with low affinity compounds.

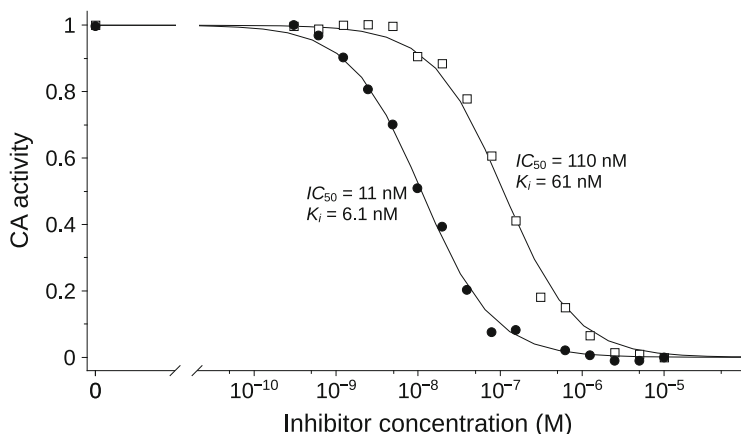


Fig. 3.6 Inhibitor dosing curves, inhibition of CA XII by two compounds with different affinity for the enzyme (black circles—compound VR16-05, open squares—VR16-09). Data points mark experimental values of enzyme activity, lines are fitted according to Hill model. The enzyme concentration was 20 nM, the K_m applied for the calculation of K_i was 21.5 mM

Inhibition parameters can be obtained by fitting experimental data such as in Fig. 3.6 to the Hill or Morrison model [20, 21]. The Hill model is much simpler and more often applied but it does not account for the enzyme concentration used in the experiment, while the Morrison model includes the enzyme concentration to obtain inhibition parameters and is more suitable for tight-binding inhibitors. We used Morrison quadratic equation to fit the inhibitor concentration-response data as explained in section 7.3 in the book by R.A. Copeland “Evaluation of Enzyme Inhibitors in Drug Discovery” [22, p. 254]. However, the term “Morrison” may not be fully accurate here as previously discussed by Kuzmic [23] because several different equations are used under the same name.

If the Hill model does not describe data using Hill coefficient 1, and the fit gets better while increasing this parameter, it is likely that this model should not be applied due to tight binding as illustrated in Fig. 3.7. The discussion on application of different analysis models and more details about method accuracy has been published recently [24].

Working with tight-binding inhibitors it is important to know the exact concentration of active enzyme used for inhibition studies. Therefore, the active site titration using standard well-characterized tight-binding inhibitor should be performed to verify the concentration of enzyme binding sites (Fig. 3.8).

Tightly-binding inhibitor K_i s cannot be accurately determined for the situations when the K_d is smaller than the protein concentration used in the assay. In other words, it is impossible to inhibit 10 nM enzyme by applying 10 pM inhibitor concentration despite the inhibitor possessing the $K_i = 10$ pM. Application of 10 pM inhibitor concentration would inhibit only 0.1 percent of the enzymatic activity. However, the addition of a sufficient amount of the inhibitor would yield a

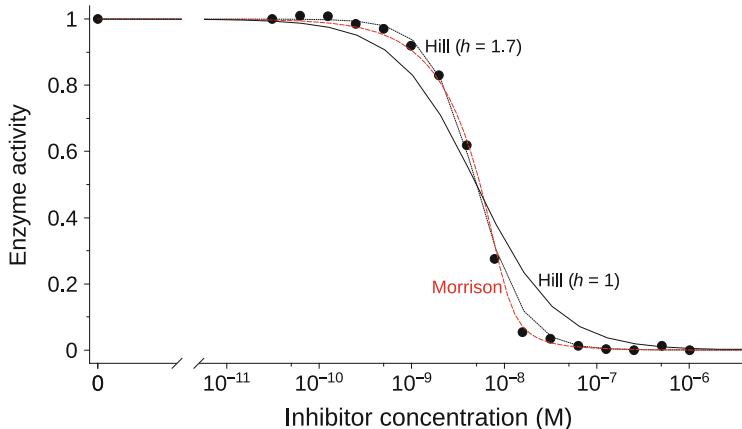


Fig. 3.7 Fitting of the tight-binding inhibitor dosing data curves by applying the Hill or Morrison model. The black solid curve shows application of the Hill model with the coefficient $h = 1$. This most-commonly applied model clearly does not fit the data. Increasing the Hill coefficient to 1.7 (black dotted curve) does increase the fit. However, the most accurate is the application of the quadratic Morrison model (red dashed curve) which accounts for the fact that the increase in curve steepness is due to the protein concentration

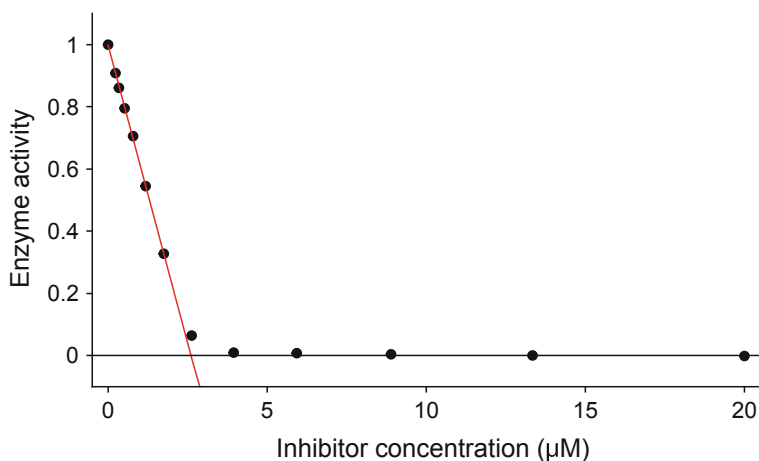


Fig. 3.8 Determination of the active site concentration of CA I by titration with tight-binding inhibitor ethoxzolamide (EZA). Concentration of CA I in all samples was $3 \mu\text{M}$ as determined by absorption at 280 nm . Concentration of EZA was varied from 0 to $20 \mu\text{M}$. Linear extrapolation using the first seven data points with the lowest inhibitor concentration showed that this protein preparation had 86.9% (or $2.6 \mu\text{M}$) of active CA I enzyme. The remaining fraction may have been misfolded or missing the Zn^{II} in the active site thus appearing in the concentration determination by A_{280} , but not showing in the inhibitor titration

dosing curve that would appear as if the IC_{50} is half of the protein concentration, i.e., 5 nM instead of 10 pM. Therefore, it is impossible to accurately characterize tight-binding (pM) inhibitors using the enzyme inhibition assay where the enzyme concentration must be kept at approximately 10 nM or higher for many CA isoforms.

Some additional complication is added by the necessity to apply the Cheng–Prusoff equation to convert from the middle point of the dosing curve (IC_{50}) to the inhibition constant K_i [25]:

$$K_i = \frac{IC_{50}}{1 + \frac{[CO_2]}{K_M}} \quad (3.2)$$

The equation allows to calculate the K_i when $IC_{50} \gg [E]$. If the total enzyme concentration is equal or higher than the IC_{50} , then the obtained K_i is not the real one, but the so-called apparent inhibition constant, since the observed process is the active site titration instead of real inhibition measurement. In other words, the IC_{50} that is lower than $[E]/2$ cannot be determined.

For the human CAs that possess the highest specific activity (CA II, CA IX), the lowest enzyme concentration that can be used to obtain a reliable signal is approximately 10 nM, while for the remaining isoforms that possess significantly lower activity this concentration is even higher. Therefore K_d s lower than 2 nM hardly could be determined using this method for the CAs.

Recently Zhao et al. reported a novel stopped-flow-based assay to determine the CA activity [26]. This assay measures the pH increase during CA-catalyzed or uncatalyzed reaction of H_2CO_3 dehydration at 10 °C. The assay was validated with two different pH indicators: absorbance-based analysis using Phenol Red (using absorbance ratio 570 nm/480 nm) and fluorescence-based assay using pyranine dye (ex. 415 nm, em. 460 nm). The main advantage of this method is using near-physiological experimental conditions. Thus, this assay is compatible with the intact red blood cells and the CA activity is used here as a marker of cell lysis [26].

3.6 Protonography

In 2014, a new method for the detection of CA activity in SDS-PAGE gels, termed protonography [27], was presented. Using this method, the protein is loaded into polyacrylamide gel with SDS but without a reducing agent and sample preheating. After running the gel, SDS is washed out from the gel, buffered at pH 8.2 and the CA activity is detected using pH indicator dye bromothymol blue when the gel is immersed into water saturated with CO_2 . The active CA then performs the catalytic reaction and acidifies the medium locally evident by the color change of the indicator from blue to yellow. This method allows direct relation of the catalytic activity to the protein molecular weight, identification of oligomeric forms, and the detection of CO_2 hydration activity in crude extracts.

3.7 Conclusions

Enzymatic activity inhibition methods directly demonstrate that the analyzed molecule not only binds to, but also perturbs the catalytic activity of a CA. For precise quantitative evaluation of ligand affinity, this method should be combined with other methods of affinity determination, such as surface plasmon resonance, isothermal titration calorimetry, or thermal shift assay. However, there is a possibility that a ligand will bind outside of the active site and have no effect on the catalytic activity. Thus, enzymatic assay is essential for the demonstration of inhibitory property of the ligand. The stopped-flow inhibition assay is suitable for the ranking of CA inhibitors up to the dissociation constant approximately 2 nM.

References

1. Supuran, C.T.: Structure and function of carbonic anhydrases. *Biochem. J.* **473**, 2023–2032 (2016)
2. Littlechild, J.A.: Improving the ‘tool box’ for robust industrial enzymes. *J. Ind. Microbiol. Biotechnol.* **44**, 711–720 (2017)
3. Höst, G., Mårtensson, L.-G. Jonsson, B.-H.: Redesign of human carbonic anhydrase II for increased esterase activity and specificity towards esters with long acyl chains. *Biochim. Biophys. Acta (BBA) - Proteins Proteomics* **1764**, 1601–1606 (2006)
4. Yoshimoto, M., Walde, P.: Immobilized carbonic anhydrase: preparation, characteristics and biotechnological applications. *World J. Microbiol. Biotechnol.* **34**, 151 (2018)
5. Supuran, C.T.: Carbonic anhydrases and metabolism. *Metabolites* **8**, 25 (2018)
6. Kupriyanova, E., Pronina, N., Los, D. Carbonic anhydrase—a universal enzyme of the carbon-based life. *Photosynthetica* **55**, 3–19 (2017)
7. Aggarwal, M., Boone, C.D., Kondeti, B., McKenna, R.: Structural annotation of human carbonic anhydrases. *J. Enzyme Inhib. Med. Chem.* **28**, 267–277 (2013)
8. Lomelino, C.L., Andring, J.T., McKenna, R.: Crystallography and its impact on carbonic anhydrase research. *Int. J. Med. Chem.* **2018**, 9419521 (2018)
9. Meldrum, N.U., Roughton, F.J.W.: Carbonic anhydrase. its preparation and properties. *J. Physiol.* **80**, 113–142 (1933)
10. Brinkman, R.: The occurrence of carbonic anhydrase in lower marine animals. *J. Physiol.* **80**, 171–173 (1993)
11. Stadie, W.C., O’Brien, H.: The catalysis of the hydration of carbon dioxide and dehydration of carbonic acid by an enzyme isolated from red blood cells. *J. Biol. Chem.* **103**, 521–529 (1933)
12. Wilbur, K.M., Anderson, N.G.: Electrometric and colorimetric determination of carbonic anhydrase. **176**, 147–154 (1948)
13. Liang, J.Y., Lipscomb, W.N.: Binding of substrate CO₂ to the active site of human carbonic anhydrase II: a molecular dynamics study. *Proc. Natl. Acad. Sci. U.S.A.* **87**, 3675–3679 (1990)
14. Silverman, D.N., Lindskog, S.: The catalytic mechanism of carbonic anhydrase: implications of a rate-limiting protolysis of water. *Acc. Chem. Res.* **21**, 30–36 (1988)
15. Tashian, R.E., Douglas, D.P., Yu, Y.-S.L.: Esterase and hydrase activity of carbonic anhydrase-I from primate erythrocytes. *Biochem. Biophys. Res. Commun.* **14**, 256–261 (1964)
16. Uda, N. R., et al.: Esterase activity of carbonic anhydrases serves as surrogate for selecting antibodies blocking hydratase activity. *J. Enzyme Inhib. Med. Chem.* **30**, 955–960 (2015)

17. Silverman, D.N. In: Purich, D.L. (ed.) *Methods in Enzymology*, pp. 732–752. Academic Press, New York (1982)
18. Sültemeyer, D.F., Fock, H.P., Canvin, D.T.: mass spectrometric measurement of intracellular carbonic anhydrase activity in high and low Ci cells of *Chlamydomonas*: studies using ^{18}O exchange with $^{13}\text{C}/^{18}\text{O}$ labeled bicarbonate. *Plant Physiol.* **94**, 1250–1257 (1990)
19. Khalifah, R.G.: The carbon dioxide hydration activity of carbonic anhydrase I. STOP-flow kinetic studies on the native human isoenzymes B and C. *J. Biol. Chem.* **246**, 2561–2573 (1971)
20. Hill, A.: The possible effects of the aggregation of the molecules of haemoglobin on its dissociation curves. *J. Physiol. (Lond.)* **40**, 4–7 (1910)
21. Williams, J.W., Morrison, J.F.: *Methods in enzymology*, 437–467. Academic Press, New York (1979)
22. Copeland, R.A.: *Evaluation of enzyme inhibitors in drug discovery a guide for medicinal chemists and pharmacologists*. John Wiley & Sons, Hoboken (2013)
23. Kuzmic, P.: History, variants and usage of the “Morrison equation” in enzyme inhibition kinetics, BioKin technical note TN-2015-01, BioKin Ltd., Watertown MA. www.Biokin.Com/TN/2015/01; <http://www.biokin.com/publications/technotes/TN201502015>
24. Smirnovienė, J., Smirnovas, V., Matulis, D.: Picomolar inhibitors of carbonic anhydrase: importance of inhibition and binding assays. *Anal. Biochem.* **522**, 61–72 (2017)
25. Yung-Chi, C., Prusoff, W.H.: Relationship between the inhibition constant (K_I) and the concentration of inhibitor which causes 50 per cent inhibition (I_{50}) of an enzymatic reaction. *Biochem. Pharmacol.* **22**, 3099–3108 (1973)
26. Zhao, P., Geyer, R.R., Boron, W.F.A.: Novel stopped-flow assay for quantitating carbonic-anhydrase activity and assessing red-blood-cell hemolysis. *Front. Physiol.* **8**, 169 (2017)
27. De Luca, V., Del Prete, S., Supuran, C.T., Capasso, C.: Protonography a new technique for the analysis of carbonic anhydrase activity. *J. Enzyme Inhib. Med. Chem.* **30**, 277–282 (2015)



Characterization of Carbonic Anhydrase Thermal Stability

4

Asta Zubrienė and Daumantas Matulis

Abstract

Proteins have different stabilities in various media. The twelve carbonic anhydrase (CA) isoforms have been recombinantly prepared and used in the search of high-affinity ligands. It was important to characterize their thermal stability and determine solution conditions where the biochemical inhibition and biophysical interaction experiments could be optimally performed. Optimal conditions for the thermal stability experiments were determined and used in the search of inhibitors as described in further chapters. The stability of the CAs could be enhanced by the presence of inhibitors depending on the affinity and compound concentration. The main method used to determine the affinities of compounds in this book was the thermal shift assay, based on the increased stability of the protein by the binding ligand as described in Chap. 5. Here we describe the stabilities of all 12 CA isoforms in various buffers, salts, pH, osmolytes, organic solvents, and other excipients that are not specific binders and inhibitors of CAs.

4.1 Introduction

Protein resistance against various physical and chemical factors, e.g., temperature, pH, or addition of other substances, determines its stability. Stability of the correctly folded native structure is essential for successful purification, storage, crystallization, and many other practical applications. Proteins used in the experiments must be of sufficient stability both thermodynamically and kinetically, and survive in the native conformation until the end of experiment. Since all 12 CA isoforms were

A. Zubrienė · D. Matulis (✉)

Department of Biothermodynamics and Drug Design, Institute of Biotechnology, Life Sciences Center, Vilnius University, Vilnius, Lithuania
e-mail: astzu@ibt.lt; matulis@ibt.lt

used in the search of high-affinity ligands (small MW compounds), it was important to determine the limits of stability of all isoforms.

Numerous techniques may be used to determine the stability of proteins. For the analysis of protein unfolding, spectroscopic methods such as fluorescence, UV spectrophotometry, and circular dichroism (CD) may be applied. Differential scanning calorimetry (DSC) and fluorescent thermal shift assay (FTSA) methods can be used to assess the thermal stability by determining the protein melting temperature T_m , at which exactly half of the protein is unfolded, i.e., the concentrations of the native and unfolded protein are equal. Conditions that increase the T_m stabilize the protein. In addition, the calorimetric technique, DSC, determines the thermodynamic parameters of protein unfolding, the enthalpy change ΔH and the heat capacity change ΔC_p upon unfolding. The thermal stability of a protein may also be determined by using the FTSA, a method that consumes significantly less material than DSC and can be applied in a high-throughput plate format. This enables performing stability measurements at various experimental conditions, such as pH, ionic strength, salt chemical composition, osmolytes, detergents, and numerous biochemicals simultaneously in a rather high throughput. In this chapter, the stability of the 12 catalytically active CA isoforms is compared. The use of FTSA method for the identification of stabilizing and destabilizing conditions for recombinant CAs is described.

4.2 Stability of Human CA Isoforms

Previous studies of denaturation and refolding of human CAs were primarily focused on two isoforms, CA I and CA II, and these studies have been extensively reviewed [3]. These two proteins have also been often used as model systems due to numerous advantages, including their easy expression in high yield from *E. coli*, monomeric, stable, and rigid structures. However, the characterization of stabilities of the remaining CA isoforms has gotten less attention [4].

The resistance of CAs to thermal denaturation is reflected in the measured T_m of the DSC thermograms or FTSA-derived protein melting curves. There are not so many studies in the literature which used DSC in studying human CA stability. Most of the studies were related to the rational design of a thermally stabilized variant of CA II, which would maintain high catalytic efficiency [5–8]. For example, the inclusion of a conserved disulfide bridge led to a stabilized variant of CA II with comparable catalytic activity to the wild-type CA II. The T_m increased by 15 °C at pH 7.8 [5].

DSC directly measures the heat absorption associated with the protein unfolding and a thermodynamic analysis of thermogram yields not only the T_m , but also the ΔH_{unf} (Fig. 4.1). The DSC profile showed that CA XIII was more stable than CA II and CA VII at pH 7.0 in phosphate buffer, the T_m of CA XIII was 5 °C higher than CA VII and about 2 °C higher than CA II. The thermal stability of CA II in our study is similar ($T_m = 56.5$ °C) as compared with previous results performed by McKenna group (T_m is about 57 °C and 59 °C). The difference can be attributed to different

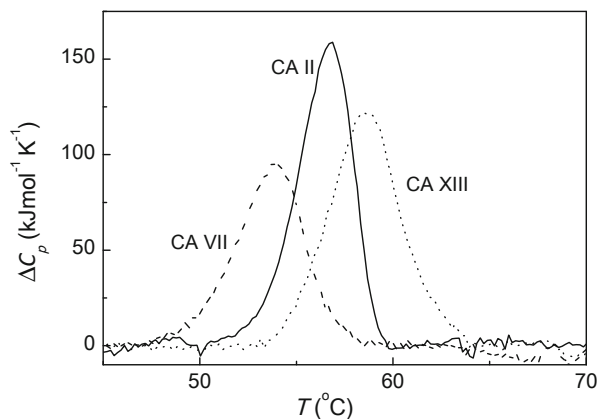


Fig. 4.1 The DSC scans of CA II (100 μ M), CA VII (41 μ M), and CA XIII (50 μ M), all in sodium phosphate buffer, pH 7.0. The T_m of CA II = 56.5 °C, the enthalpy of unfolding was equal to 570 kJ/mol. The T_m of CA VII = 53.4 °C, the enthalpy of unfolding was equal to 420 kJ/mol. The CA XIII exhibited the T_m equal to 58.6 °C and the enthalpy of unfolding was equal to 570 kJ/mol. The data has been described in [1,2]

experimental conditions (higher pH, Tris buffer, and CA II concentration). However, the unfolding enthalpies of CA II differed significantly, the $\Delta H=570$ kJ/mol in our study and about 1000 kJ/mol in [7].

The thermal unfolding of CA III has been determined to be biphasic. The T_m for the less-stable part was equal to 48 °C and for the more-stable part 53.3 °C [9]. The same authors [9] found CA VI and CA VII to be less-stable proteins with temperature transition midpoints at 41.6 °C and 41.2 °C, respectively. Interestingly, the recombinant CA VII was about 12 °C less stable than the CA VII produced in our laboratory (Fig. 4.1). This discrepancy may be attributed to different solution conditions used by the two laboratories.

Human CA IX displayed a $T_m = 59.3$ °C at pH 7.0, $T_m = 51.9$ °C at pH 4.0, $T_m = 38.4$ °C pH 3.0, and a $T_m = 30.1$ °C at pH 2.0 as determined by DSC [10]. Moreover, the structural dynamics and the state of CA IX at low pH remained unchanged as determined by the CD. The retaining of enzymatic activity and stability at low pHs explains the role of CA IX, which is abundant in the stomach, but not other CAs, in the effective pH control in acidic tumor microenvironment.

In our previous studies, the thermal stability of CA IV [12], CA VB [13], CA VI [14], CA VII [13], the catalytic CA IX domain (CA IXCD, residues 138-390) [15], and CA XII [16] was investigated at various conditions. We applied the FTSA method for the determination of optimal stabilizing buffer compositions for each CA isoform. The three-component universal buffer (containing sodium phosphate, sodium acetate, and sodium borate) allowed a wide pH range (pH 4–11) to be screened without altering the composition of the buffering chemicals. Our results showed (Fig. 4.2) that CA IV was the most stable protein among all twelve

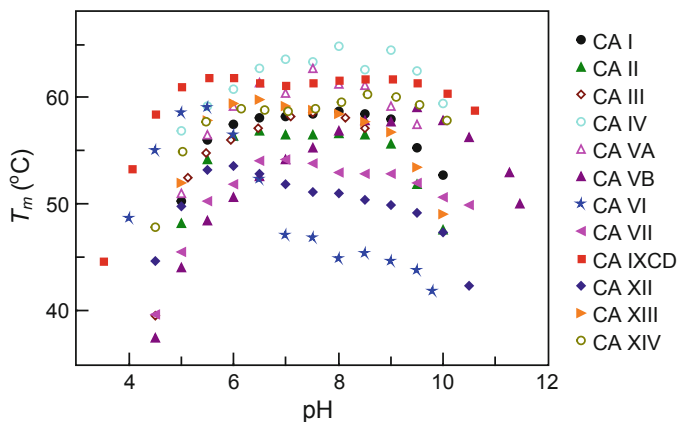


Fig. 4.2 Characterization of stability of all twelve CA isoforms in the universal buffer as a function of pH. Experiments were performed in the presence of 1% DMSO. Most isoforms have rather flat stability profiles in the pH region of 5–9. However, some isoforms such as CA VI are noticeably more stable in acidic pH, while others, such as CA VB, are more stable in alkaline pH. The CA IV appears to be the most stable isoform. However, these stabilities are valid for recombinant proteins and may not be fully valid for the proteins in human body due to different domain organization and multimerization

catalytically active CAs at pHs from 6.5 to 9.5. The protein melting temperature was between 62 °C and 65 °C at these pHs. It was previously observed that CA IV, differently from other CAs, was stable at higher SDS concentrations [17]. The presence of two disulfide linkages in CA IV between 6–18 and 28–211 cysteines could account for the high thermal stability and enhanced resistance to denaturation with SDS [18]. The disulfide linkage 28–211 is conserved in CA VI, CA IX, CA XII, and CA XIV [19–22]. However, these isoforms are less resistant to SDS than CA IV.

The stability of CA IX catalytic domain (CA IXCD) is slightly lower than CA IV. However, the enzyme is very stable at wider pH ranges (pH 5–10) with the T_m around 61 °C (Fig. 4.2). The denaturation profile of recombinant CA IX form CA IX PG, which consists of the N-terminal proteoglycan-like domain (PG) and a CA catalytic domain splits into two melting transitions, showing that the protein is composed of monomers and dimers. The dimeric form (the second transition of CA IX PG denaturation curve) is much more stable with the T_m around 70 °C (Fig. 4.3), while the T_m s of the first transitions are similar to the T_m s of the CA IX catalytic domain at various pHs. The substitution of cysteine by serine (CA IXC174S) decreased the protein thermal stability by about 5 °C.

Comparing all CAs the lowest stabilities at pHs 7–10 are of CA VI and CA XII. However, CA VI is very stable protein at acidic pHs with the T_m optimum at pH 5.5 equal to 59 °C. The CA XII is most stable at pH 6.0, the $T_m = 53$ °C. The stabilities of most CAs drop below pH 5.0, but the CA IX remains the most stable isoform at low pH.

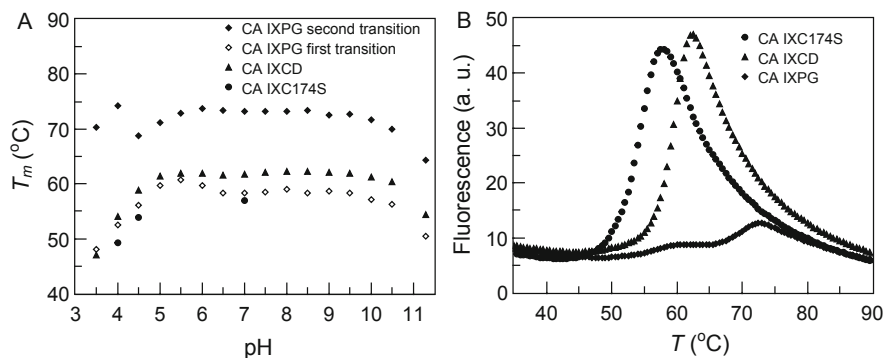


Fig. 4.3 Thermal stabilities of several CA IX proteins in the universal buffer (containing 50 mM sodium phosphate, 50 mM sodium acetate, 25 mM sodium borate, and 50 mM NaCl) as a function of pH. Panel (a) The dependence of T_m on pH for three constructs of CA IX: the CA IX PG—the CA IX catalytic domain together with the PG domain, CA IX CD—the catalytic domain of CA IX alone, CA IX C174S—the mutant C174S of the catalytic domain of CA IX. Panel (b) Denaturation profiles of CA IX at pH 4.5 as a function of temperature. The T_m of several CA IX proteins at 5 μ M was determined by FTSA in the universal buffer, containing 1% DMSO

The effect of various buffer solutions on CA stabilities was examined with sodium phosphate, sodium acetate, sodium citrate, Tris-HCl, HEPES, Mes, and Pipes (Fig. 4.4). Many CAs demonstrated better thermostability in acetate than in citrate buffer at low pHs 4.5–5.5. The CA VI was the most stable in acetate buffer at pH 5.0 with the $T_m = 60.9^\circ\text{C}$. The CA III, CA IV, CA VB, CA VII, CA XII, and CA XIV were the most stable in sodium phosphate buffer. The highest stabilities of CA I, CA II, and CA XIII were in HEPES and Tris buffers, the melting temperatures in these buffers at the pH ranges from 6.5 to 9.0 were about 59°C , 58°C , and 60°C , respectively. The CA IX was the most stable in Mes buffer at pH 5.0 ($T_m = 70^\circ\text{C}$), while at higher pHs the T_m was lower. The CA IX is quite stable between pH 5 and 9 in Mes, Tris, Pipes, HEPES, and acetate buffers, but significantly destabilized by the sodium citrate buffer.

The studies of denaturation of human CA I and CA II in concentrated solutions of denaturing osmolytes such as urea and guanidine hydrochloride showed that the CA I is more stable than the CA II, and the concentrations of guanidine hydrochloride giving 50% inactivation in 24 h were approximately 0.95 M for the CA II and 1.5 M for the CA I [23–25]. These two isoforms were more resistant to higher urea concentrations, with the midpoint concentration of CA I and CA II unfolding at 5 M and 4.4 M urea, respectively [23]. Sodium chloride significantly stabilized the molten-globule intermediate in the denaturation of CA II by urea, leading to a three-state unfolding behavior (N–I transition is shifted from 4.4 to 3.0 M urea and the I–U transitions from 4.4 to 6.4 M urea) [25].

The investigation of the concentration-dependent thermal denaturation of CAs in the presence of inorganic salts NaCl and Na_2SO_4 demonstrated the stabilization of membrane-bound CA isoforms by the increasing Na_2SO_4 concentrations from 5 to

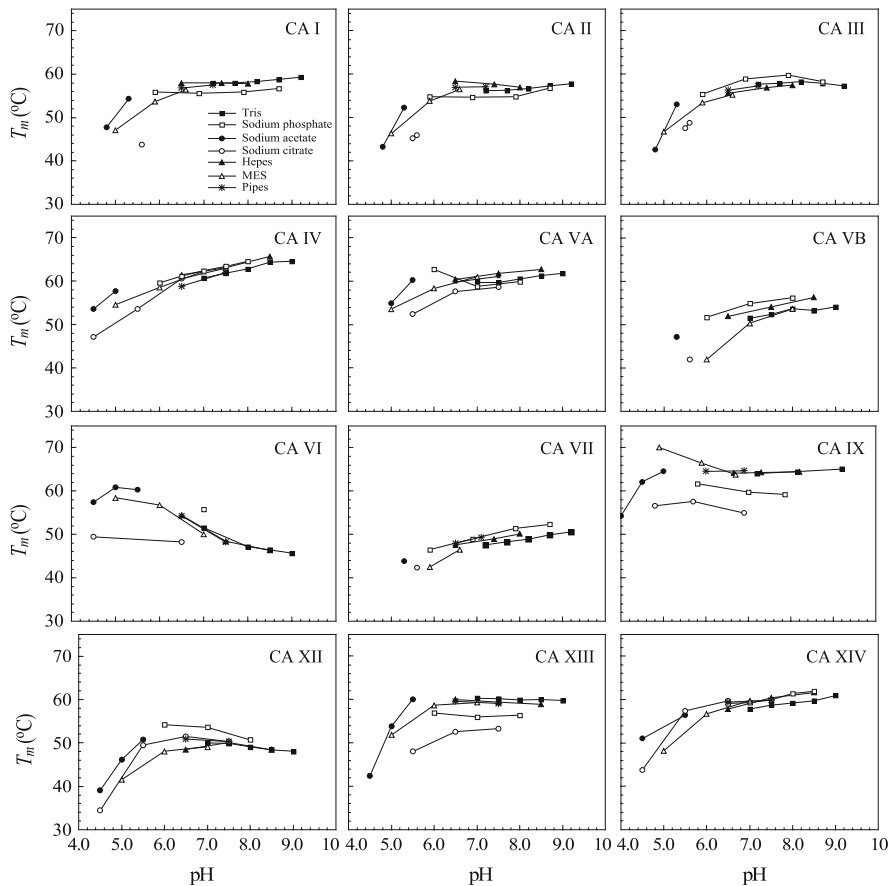


Fig. 4.4 Comparison of CA isoform thermal stability in different buffers as a function of pH. Experiments were performed in 100 mM buffer (listed in the legend of the CA I panel), containing 2 mM NaCl and 0.5% DMSO. Some buffers stabilize while others may strongly destabilize many isoforms, notably the sodium citrate buffer. The figure is taken from [11]

1000 mM (Figs. 4.5 and 4.6). The salt NaCl had low effect on the stabilization of CA IV, CA IX, and CA XIV, whereas CA XII stability increased by more than 6 °C by adding 1 M NaCl. The NaCl also stabilized CA III and CA VB isoforms, while destabilized all other CA isoforms (Fig. 4.7).

Glycerol, a commonly used cryoprotectant, had no or minor effect on CA I, CA II, CA III, CA IV, CA VI, CA VII, CA VII, CA IX, CA XII, CA XIII, and CA XIV stability at concentration of 2–10% (v/v) (Fig. 4.7). Addition of 10% of glycerol increased the T_m of CA VA and CA VB by about 2 °C. Glycerol is essential component of CA VB storage buffer. Without glycerol this CA isoform aggregates. Addition of dimethylsulfoxide (DMSO) at comparable concentrations destabilized CA I, CA II, CA III, CA VII, and CA IX isoforms by about 4 °C.

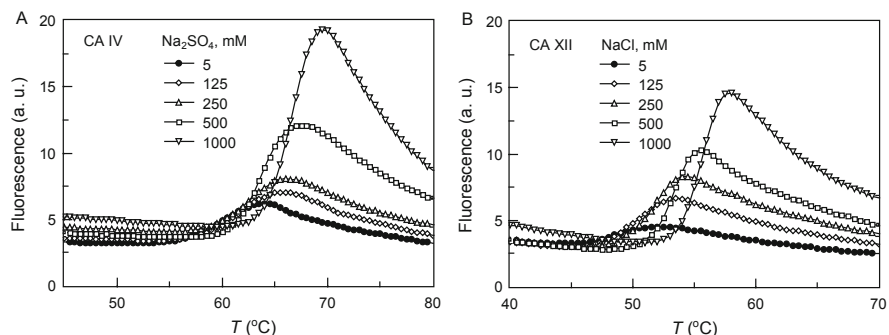


Fig. 4.5 Thermal melting fluorescence curves of CA IV (a) and CA XII (b) in 2.5 mM sodium phosphate buffer, pH 7.0, in the presence of various Na₂SO₄ (a) and NaCl (b) concentrations. Both salts significantly increased the stability of both isoforms

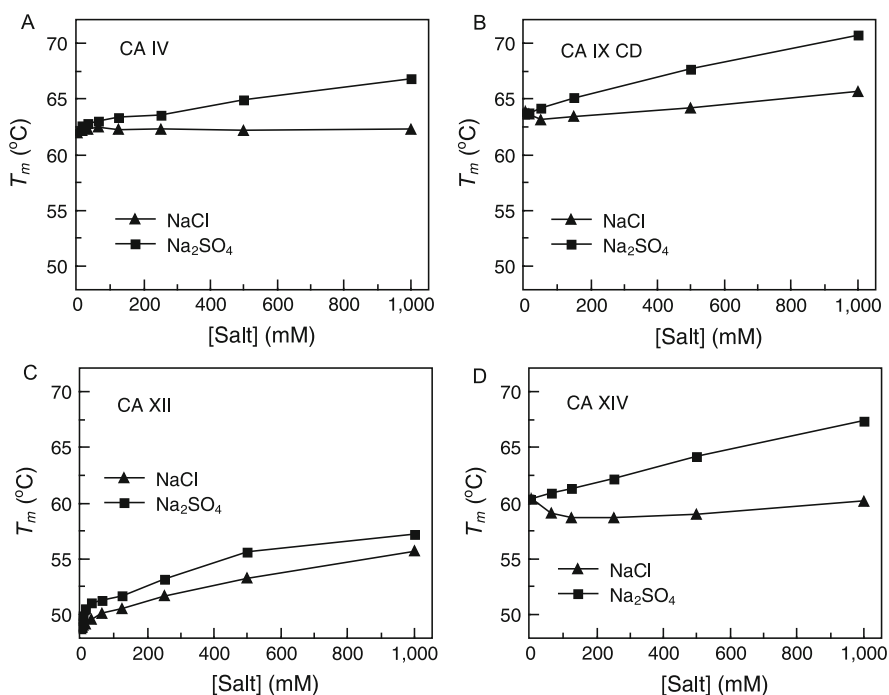


Fig. 4.6 Thermal stability of the catalytic domains of the membrane-bound CA isoforms, CA IV, CA IX, CA XII, and CA XIV as a function of NaCl and Na₂SO₄ concentrations

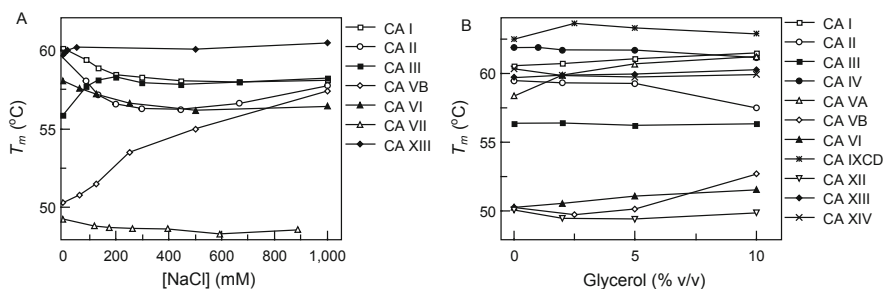


Fig. 4.7 Thermal stabilities of CAs as a function of NaCl (a) and glycerol (b) concentrations. The CA VB stability increased significantly with increasing NaCl concentration. However, apparently this was the only isoform so strongly affected by NaCl. Addition of glycerol up to 10% somewhat stabilized only the CA VA and CA VB isoforms

4.3 Conclusions

Thermal stability studies of the twelve human CA isoforms showed that these enzymes have different melting temperatures that depend on buffer, pH, and numerous other additives. The isoforms differed in their physicochemical properties and aggregation behavior. The FTSA assay permitted simultaneous screening of the stabilizing and destabilizing conditions of all CA isoforms.

References

1. Barauskienė, L., Matulis, D.: Intrinsic thermodynamics of ethoxzolamide inhibitor binding to human carbonic anhydrase XIII. *BMC Biophys.* **5**, 12 (2012)
2. Zubrienė, A., et al.: Measurement of nanomolar dissociation constants by titration calorimetry and thermal shift assay—radicolol binding to Hsp90 and ethoxzolamide binding to CAII. *Int. J. Mol. Sci.* **10**, 2662–2680 (2009)
3. Krishnamurthy, V. M., et al.: Carbonic anhydrase as a model for biophysical and physical-organic studies of proteins and protein-ligand binding. *Chem. Rev.* **108**, 946–1051 (2008)
4. Aggarwal, M., Boone, C. D., Kondeti, B., McKenna, R.: Structural annotation of human carbonic anhydrases. *J. Enzyme Inhib. Med. Chem.* **28**, 267–277 (2013)
5. Boone, C.D., Habibzadegan, A., Tu, C., Silverman, D.N., McKenna, R.: Structural and catalytic characterization of a thermally stable and acid-stable variant of human carbonic anhydrase II containing an engineered disulfide bond. *Acta Crystallogr. D Biol. Crystallogr.* **69**, 1414–1422 (2013)
6. Boone, C.D., Gill, S., Tu, C., Silverman, D.N., McKenna, R.: Structural, catalytic and stabilizing consequences of aromatic cluster variants in human carbonic anhydrase II. *Arch. Biochem. Biophys.* **539**, 31–37 (2013)
7. Boone, C.D., Rasi, V., Tu, C., McKenna, R.: Structural and catalytic effects of proline substitution and surface loop deletion in the extended active site of human carbonic anhydrase II. *FEBS J* **282**, 1445–1457 (2015)
8. Mikulski, R., et al.: Structure and catalysis by carbonic anhydrase II: role of active-site tryptophan 5. *Arch. Biochem. Biophys.* **516**, 97–102 (2011)

9. Durdagi, S., et al.: Protein–protein interactions: inhibition of mammalian carbonic anhydrases I–XV by the murine inhibitor of carbonic anhydrase and other members of the transferrin family. *J. Med. Chem.* **55**, 5529–5535 (2012)
10. Mahon, B.P., et al.: The structure of carbonic anhydrase IX is adapted for low-pH catalysis. *Biochemistry* **55**, 4642–4653 (2016)
11. Linkuvienė, V., et al.: Thermodynamic, kinetic, and structural parameterization of human carbonic anhydrase interactions toward enhanced inhibitor design. *Q. Rev. Biol.* **51**, e10 (2018)
12. Mickevičiūtė, A., et al.: Intrinsic thermodynamics of high affinity inhibitor binding to recombinant human carbonic anhydrase IV. *Eur. Biophys. J.* **7**, 271–290 (2018)
13. Kasiliauskaitė, A., et al.: Thermodynamic characterization of human carbonic anhydrase VB stability and intrinsic binding of compounds. *J. Therm. Anal. Calorim.* **123**, 2191–2200 (2016)
14. Kazokaitė, J., Milinavičiūtė, G., Smirnovienė, J., Matulienė, J., Matulis, D.: Intrinsic binding of 4-substituted-2,3,5,6-tetrafluorobenzene-sulfonamides to native and recombinant human carbonic anhydrase VI. *FEBS J.* **282**, 972–983 (2015)
15. Linkuvienė, V., et al.: Intrinsic thermodynamics of inhibitor binding to human carbonic anhydrase IX. *Biochim. Biophys. Acta Gen. Subj.* **1860**, 708–718 (2016)
16. Jogaitė, V., et al.: Characterization of human carbonic anhydrase XII stability and inhibitor binding. *Bioorg. Med. Chem.* **21**, 1431–1436 (2013)
17. Waheed, A., Okuyama, T., Heyduk, T., Sly, W.S.: Carbonic anhydrase IV: purification of a secretory form of the recombinant human enzyme and identification of the positions and importance of its disulfide bonds. *Arch. Biochem. Biophys.* **333**, 432–438 (1996)
18. Waheed, A., Sly, W.S.: Membrane associated carbonic anhydrase IV (CA IV): a personal and historical perspective. *Subcell. Biochem.* **75**, 157–179 (2014)
19. Alterio, V., et al.: Crystal structure of the catalytic domain of the tumor-associated human carbonic anhydrase IX. *Proc. Natl. Acad. Sci. U.S.A.* **106**, 16233–16238 (2009)
20. Alterio, V., et al.: The structural comparison between membrane-associated human carbonic anhydrases provides insights into drug design of selective inhibitors. *Biopolymers* **101**, 769–778 (2014)
21. Pilka, E.S., Kochan, G., Oppermann, U., Yue, W.W.: Crystal structure of the secretory isozyme of mammalian carbonic anhydrases CA VI: implications for biological assembly and inhibitor development. *Biochem. Biophys. Res. Commun.* **419**, 485–489 (2012)
22. Whittington, D.A., et al.: Crystal structure of the dimeric extracellular domain of human carbonic anhydrase XII, a bitopic membrane protein overexpressed in certain cancer tumor cells. *Proc. Natl. Acad. Sci. U.S.A.* **98**, 9545–9550 (2001)
23. Carlsson, U., Henderson, L.E., Lindskog, S.: Denaturation and reactivation of human carbonic anhydrases in guanidine hydrochloride and urea. *Biochim. Biophys. Acta Protein Struct.* **310**, 376–387 (1973)
24. Edsall, J.T.: Multiple molecular forms of carbonic anhydrase in erythrocytes. *Ann. N.Y. Acad. Sci.* **151**, 41–63 (1968)
25. Borén, K., Grankvist, H., Hammarström, P., Carlsson, U.: Reshaping the folding energy landscape by chloride salt: impact on molten-globule formation and aggregation behavior of carbonic anhydrase. *FEBS Lett.* **566**, 95–99 (2004)

Part II

Thermodynamics and Kinetics of Compound Binding to Carbonic Anhydrases



Inhibitor Binding to Carbonic Anhydrases by Fluorescent Thermal Shift Assay

5

Vytautas Petrauskas, Asta Zubrienė, Matthew J. Todd,
and Daumantas Matulis

Abstract

In this chapter we describe the model that quantifies interactions between proteins and ligands applying the thermal shift assay. When combined with fluorescence-based measurements of protein thermal unfolding, this model forms the basis of the fluorescent thermal shift assay—a widely applicable and cost-effective technique to quantify ligand affinity towards proteins. Most ligands stabilize proteins against thermal denaturation and shift their melting points towards higher temperatures. Equations that relate the shift in protein melting temperature with the ligand concentration are presented. The assay has been used to determine affinities of various sulfonamide inhibitor binding to carbonic anhydrase isoforms. The results illustrate applicability and limitations of the fluorescent thermal shift assay.

5.1 Introduction

Pharmaceutical industry often relies on thermal shift assays—a biophysical technique used to search for a strongly binding small molecule to a protein-target [1]. Thermal shift assays based on fluorescence carry various names: fluorescent thermal shift assay (FTSA) [2]; differential scanning fluorimetry (DSF) [3, 4]; or ThermoFluor[®], if performed in plate format in high-throughput [5, 6]. These

V. Petrauskas · A. Zubrienė · D. Matulis (✉)
Department of Biothermodynamics and Drug Design, Institute of Biotechnology, Life Sciences
Center, Vilnius University, Vilnius, Lithuania
e-mail: vytautas.petrauskas@bti.vu.lt; astzu@ibt.lt; matulis@ibt.lt

M. J. Todd
Biophysical Solutions, Inc., Ambler, PA, USA
e-mail: matthew.todd@biophysical-solutions.com

techniques allow to estimate compound binding affinity towards a protein-target and to screen thousands of compounds in a relatively short time-scale. Although these techniques are widely applicable and yield a quantitative measure of many thermodynamic parameters, most laboratories limit their application to observation of qualitative shifts in protein melting temperature. Actually, only the dissociation constant is being determined in the assay with sufficient accuracy for practical application. However, additional parameters such as the enthalpy of ligand binding may also be obtained with the help of orthogonal techniques such as isothermal titration calorimetry.

Fluorescent thermal shift assay measures the change in fluorescence upon protein unfolding. The fluorescence may be intrinsic (tryptophan fluorescence) or extrinsic (solvatochromic fluorescent probe). Figure 5.1 shows a typical fluorescence curve observed upon a protein unfolding achieved by heating the protein sample. We often assume that a native-to-unfolded transition is a single-step process. However, proteins may undergo intermediate states and the unfolded protein may aggregate. Although protein unfolding may be a reversible process, in practice many heat-denatured proteins aggregate and precipitate, resulting in an irreversible transition. Despite the “apparent irreversibility,” thermal shift assays still provide ligand dissociation constants that match the ones obtained by equilibrium isothermal techniques. It is probable that in thermal shift assays the proteins in diluted solutions can reach equilibrium before they aggregate.

The fluorescence yield may be followed by observing the fluorescence of extrinsic probes such as 1,8-anilinonaphthalene sulfonate (ANS). This is a highly solvatochromic probe that has been used as a probe of hydrophobic protein surfaces for many years [7, 8]. Matulis and colleagues have shown that electrostatic ion pair formations between the negatively charged sulfonate group of ANS and the positively charged Arg, Lys, and His residues of the protein are necessary for

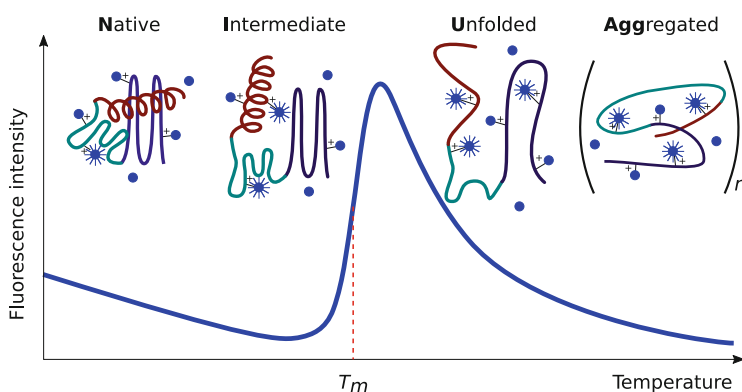


Fig. 5.1 Profile of protein thermal unfolding determined by FTSA. Blue dots represent extrinsic fluorescence probes (e.g., ANS molecules): with rays—fluorescent probes, without rays—non-fluorescent probes. When temperature is increased, the hydrophobic surfaces of a protein become accessible to ANS and this results in increased fluorescence intensity of the probe

binding [9] and that such a probe may significantly affect the protein structure [10]. However, the mechanism of ANS binding to proteins is still not fully understood, but the probe is one of the best reporters of the protein unfolding. Out of nearly 100 tested compounds, we believe that ANS is the most suitable probe to report on protein unfolding [2]. The fluorescence of ANS molecules is effectively quenched if the non-polar anilinonaphthalene groups are exposed to water. ANS becomes fluorescent, when anilinonaphthalene groups of bound ANS anions are buried from water in the hydrophobic or hydrophilic environment of the semi-unfolded protein. This process is illustrated in Fig. 5.1. In addition to ANS, other fluorescent dyes such as Sypro Orange are also often being used for the screening of compound binding to proteins [11] and CA inhibitors among them [12]. However, in our opinion Sypro Orange exhibits significantly stronger affinity to proteins than ANS and thus may interfere with the binding of studied compound.

5.2 Model for Fluorescence Yield Upon Protein Unfolding

In this section, mathematical equations are provided that describe the thermal unfolding of a protein. Quantitative characterization of the fluorescence yield, f , can be described by equation $f = \sum_i f_i X_i$, where f_i and X_i are fluorescence yield and molar fraction of the i -th state of protein, respectively. For most practical purposes it is sufficient to consider only two states of a protein—native (hereafter denoted as N) and unfolded (or denatured, denoted as U). By omitting all intermediate and aggregated states of the protein we can use the following equation to describe the fluorescence yield:

$$f = f_N X_N + f_U X_U. \quad (5.1)$$

Here f_N and X_N are the fluorescence yield and fraction of the native form of a protein, while f_U and X_U are those of the unfolded form. In the two-state approach the molar fractions of native and unfolded protein forms are given by equations

$$X_N = \frac{[N]}{[N] + [U]}, \quad (5.2)$$

$$X_U = \frac{[U]}{[N] + [U]}. \quad (5.3)$$

The molarities of native ([N]) and denatured ([U]) protein states are also used to define the equilibrium constant of protein unfolding

$$K_U = \frac{[U]}{[N]}, \quad (5.4)$$

which describes the reaction $N \xrightleftharpoons{K_U} U$. The fluorescence yield Eq. (5.1) can be given a different form by substituting X_N and X_U variables from Eqs. (5.2) and (5.3) and by using the definition of K_U from Eq. (5.4):

$$f = f_N + \frac{f_U - f_N}{1 + \frac{1}{K_U}}. \quad (5.5)$$

This equation is used to evaluate the fluorescence yield during the process of protein unfolding, if parameters f_N and f_U are constant at various levels of denaturing factor. However, decaying apparent fluorescence yields of both native and unfolded forms of protein are usually observed with an increase of temperature. A typical example is shown in Fig. 5.2; it was obtained by monitoring the fluorescence yield of a globular protein in the assay of thermal denaturation.

Temperature-dependent fluorescence yields in the native and unfolded states are usually approximated by a set of linear equations:

$$f_N = f_{N_{T_m}} + m_N(T - T_m), \quad (5.6)$$

$$f_U = f_{U_{T_m}} + m_U(T - T_m), \quad (5.7)$$

where m_N and m_U are the slopes in the pre- and post-transition states, while $f_{N_{T_m}}$ and $f_{U_{T_m}}$ are the levels of fluorescence yields of the native and unfolded protein

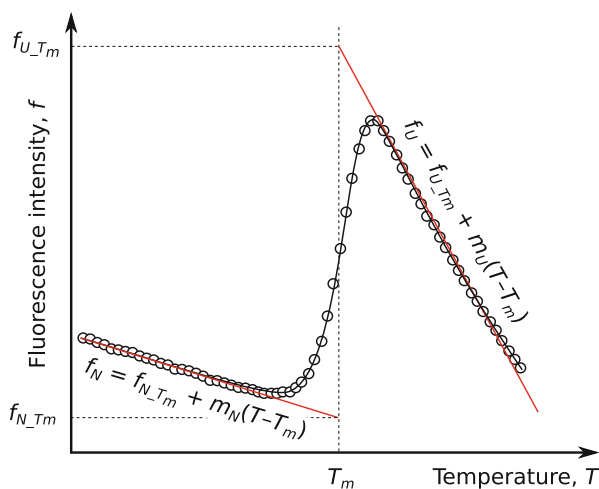


Fig. 5.2 A simulated unfolding curve of a globular protein visualized by fluorescence as a function of temperature. The fluorescence signal can come from intrinsic tryptophan or extrinsic probe such as 1,8-anilinonaphthalene sulfonate. The temperature axis point corresponding to the midpoint of unfolding curve (when half of the protein is unfolded) is called melting temperature, T_m

states at the melting temperature T_m . Parameters $f_{N_{-T_m}}$ and $f_{U_{-T_m}}$ are visualized in Fig. 5.2. The final equation for fluorescence yield is obtained by substituting f_N and f_U terms in Eq. (5.5) by their temperature dependencies (Eq. (5.6) and (5.7)):

$$f = f_{N_{-T_m}} + m_N(T - T_m) + \frac{f_{U_{-T_m}} - f_{N_{-T_m}} + (m_U - m_N)(T - T_m)}{1 + \frac{1}{K_U}}. \quad (5.8)$$

In general, K_U is a function of temperature. This dependency and K_U 's constitutional terms will be discussed in the following section.

5.3 Model for Ligand-Induced Protein Stability Against Thermal Denaturation

In this section, we will describe a model for ligand-induced protein stabilization against thermal denaturation. The protein stabilization can be described quantitatively by the shift in its melting temperature with an addition of a ligand. Here, we will derive an equation, relating the concentration of added ligand with the changes in Gibbs energy, enthalpy, and entropy of protein unfolding and protein–ligand binding.

We start the derivation using a set of four equations:

$$[P]_t = [N] + [P \cdot L] + [U], \quad (5.9)$$

$$[L]_t = [L] + [P \cdot L], \quad (5.10)$$

$$K_U = \frac{[U]}{[N]}, \quad (5.11)$$

$$K_b = \frac{[P \cdot L]}{[N][L]}. \quad (5.12)$$

The first two Eqs. (5.9) and (5.10) describe the mass conservation of protein and ligand, K_b —equilibrium constant of protein–ligand binding, $[P \cdot L]$ denotes the concentration of protein–ligand complex, $[P]_t$ and $[L]_t$ —initial molarities of protein and ligand, respectively. Unbound ligand molarity $[L]$ term in Eq. (5.10) can be substituted by $[L] = \frac{[P \cdot L]}{K_b[N]}$ from Eq. (5.12). We also make use of the relation

$[N] = \frac{[U]}{K_U}$ from Eq. (5.11), which leads to

$$[L]_t = \frac{K_U[P \cdot L]}{K_b[U]} + [P \cdot L] = [P \cdot L] \left(\frac{K_U}{K_b[U]} + 1 \right). \quad (5.13)$$

Equations (5.9) and (5.11) are combined to obtain the molarity of protein–ligand complex

$$[P \cdot L] = [P]_t - [U] - \frac{[U]}{K_U}. \quad (5.14)$$

Substitution of the $[P \cdot L]$ term into Eq. (5.13) results in:

$$[L]_t = \left([P]_t - [U] - \frac{[U]}{K_U} \right) \left(\frac{K_U}{K_b[U]} + 1 \right). \quad (5.15)$$

We describe the temperature dependencies of equilibrium constants K_U and K_b in terms of the standard Gibbs energies ΔG_U° and ΔG_b° of the corresponding protein unfolding and protein–ligand binding processes:

$$K_U(T) = \exp\left(-\frac{\Delta G_U^\circ}{RT}\right), \quad (5.16)$$

$$K_b(T) = \exp\left(-\frac{\Delta G_b^\circ}{RT}\right), \quad (5.17)$$

where R is the molar gas constant. The change in Gibbs energy has two constituent parts—enthalpy (ΔH) and entropy (ΔS). Both terms are temperature-dependent and their standard values at a particular temperature, T , can be calculated using equations

$$\Delta H_x^\circ = \Delta H_{x_{T_r}}^\circ + \int_{T_r}^T \Delta C_{p-x} dT, \quad (5.18)$$

$$\Delta S_x^\circ = \Delta S_{x_{T_r}}^\circ + \int_{T_r}^T \left(\frac{\Delta C_{p-x}}{T} \right) dT, \quad (5.19)$$

where T_r is a reference (initial) temperature, $\Delta H_{x_{T_r}}^\circ$ and $\Delta S_{x_{T_r}}^\circ$ —standard enthalpy and entropy at T_r , ΔC_{p-x} —the change in constant pressure heat capacity. The changes in enthalpy and entropy associated with either binding or unfolding have the same mathematical form of temperature dependency. Thus, Eqs. (5.18) and (5.19) are used to describe both binding ($x \equiv b$) and unfolding ($x \equiv U$) processes. If ΔC_p is constant in the temperature range from T_r to T_m , we can integrate Eqs. (5.18) and (5.19) and the resulting Gibbs energy is

$$\begin{aligned} \Delta G_x^\circ &= \Delta H_x^\circ - T_m \Delta S_x^\circ = \\ &= \Delta H_{x_{T_r}}^\circ + \Delta C_{p-x}(T_m - T_r) - T_m \left(\Delta S_{x_{T_r}}^\circ + \Delta C_{p-x} \ln \frac{T_m}{T_r} \right). \end{aligned} \quad (5.20)$$

The reference temperatures for binding and unfolding can be different. Reference temperature for the binding can be given an arbitrary value (e.g., 25 °C or 37 °C) and hereafter will be denoted as T_0 . T_r for unfolding process is usually considered to be melting temperature of ligand-free protein.

In the FTSA experiment, protein melting temperatures are determined at various increasing concentrations of added ligand. According to the definition, folded and unfolded fractions of a protein are equal at melting temperature, T_m , thus $[U] = \frac{[P]_f}{2}$ at T_m . At melting temperature we can simplify Eq. (5.15) that together with Eqs. (5.16) and (5.17) forms the mathematical background of FTSA:

$$\left\{ \begin{array}{l} [L]_f = (K_U - 1) \left(\frac{1}{K_b} + \frac{[P]_f}{2K_U} \right), \\ K_U = \exp \left(- \frac{\Delta H_{U_{T_r}}^\circ + \Delta C_{p_{U_{T_r}}}(T_m - T_r) - T_m \left(\Delta S_{U_{T_r}}^\circ + \Delta C_{p_{U_{T_r}}} \ln \frac{T_m}{T_r} \right)}{RT_m} \right), \\ K_b = \exp \left(- \frac{\Delta H_{b_{T_0}}^\circ + \Delta C_{p_{b_{T_0}}}(T_m - T_0) - T_m \left(\Delta S_{b_{T_0}}^\circ + \Delta C_{p_{b_{T_0}}} \ln \frac{T_m}{T_0} \right)}{RT_m} \right). \end{array} \right. \quad (5.21)$$

Here we used Eq. (5.20) to expand the Gibbs energy terms in K_U and K_b . This system of equations describes protein melting temperature as a function of added ligand concentration and is commonly referred to as a dosing curve. In the absence of ligand $K_U = 1$, addition of stabilizing ligand shifts the T_m towards higher values, and thus K_U increases. Note that the first equation of the system (5.21) describes protein melting temperature as a function of added ligand concentration, despite it is written in the form as if L_f would be a function of T_m . From the mathematical point of view it is more convenient to keep the T_m dependence on L_f in the unexplicit form, since the explicit dependency would give a transcendental function.

Figure 5.3 shows a dosing curve obtained by FTSA. Temperature dependencies of ANS fluorescence yields are measured at increasing values of added ligand. Stabilizing ligands shift the T_m s to the higher temperatures. The values of T_m generate the dosing curve, and non-linear regression analysis should be used to obtain the protein unfolding and protein–ligand binding parameters as described previously.

5.4 Thermal Stabilization of CAs by Ligands

CA inhibitors such as sulfonamides and their isosteres (sulfamates, sulfamides) specifically bind to the active site of the enzyme. Most ligands stabilize CAs upon binding and therefore the protein T_m increases. The shift in T_m with an

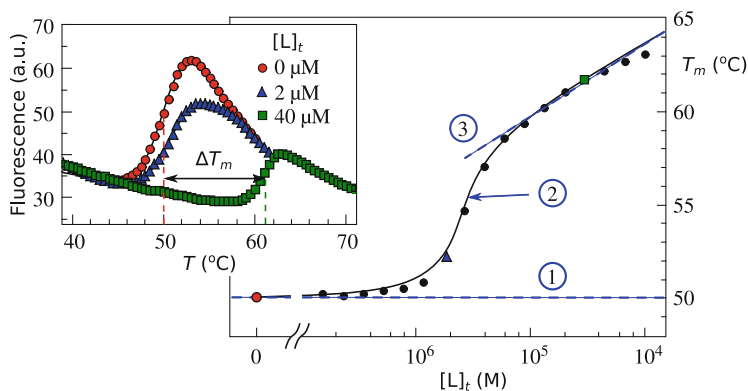


Fig. 5.3 An example of a dosing curve obtained by FTSA. The inset shows the temperature dependencies of ANS fluorescence yield at three different concentrations of added ligand. Encircled numbers indicate the main properties of the dosing curve: (1) ligand-free value of protein T_m , (2) curve inflection point that indicates the total concentration of the protein, (3) slope of the curve at saturating values of $[L]_t$ is proportional to the protein unfolding enthalpy

addition of the ligand (ΔT_m) serves as a quantitative measure of protein stability and allows to determine the protein–ligand binding affinity as it was described in the previous section. Here, we present several examples of the applicability of FTSA for affinity measurements of sulfonamide binding to recombinant and native CA isoforms. We show examples of the effect of protein and ligand concentration on the thermal denaturation of CAs, FTSA data for tight-binding inhibitors, the independence of compound binding affinity of the production source of CA isoform (e.g., recombinant *vs* native CA), and the measurements of the binding affinity at different pH.

FTSA can be performed using standard real-time PCR instruments such as Corbett Rotor-Gene 6000, which makes this assay rapid and cost-effective. Usually we dose 8–16 different concentrations of ligand in a buffer solution containing 2% DMSO (one with no ligand), and dispense to the tubes filled with protein solution. The amount of protein per one data point can vary from 1.5 μg to 3 μg per tube (5 μl to 10 μl of 10 μM CA solution). Protein-to-compound ratio depends on the expected affinity (K_d) and is usually about 1:40 if the K_d is in the range of 1 μM –1 nM.

Ligand stabilizes the CA and shifts its melting temperature. A higher ligand concentration induces a bigger T_m shift (Fig. 5.4a). We use Eq. (5.21) to fit the experimental T_m dependencies on ligand concentration. The fitted parameters provide an estimate of protein–ligand binding affinity (K_b). The higher concentrations of the CA increase the fluorescence signal, but do not affect the binding constant. For example, each of four AZM dosing curves in Fig. 5.4 yielded the same binding constant to human CA II isoform ($K_d = 25$ nM at 25 $^\circ\text{C}$, pH 7.5). The observed sigmoidal dependence of T_m on the ligand concentration allows to determinate the binding stoichiometry between ligand and protein.

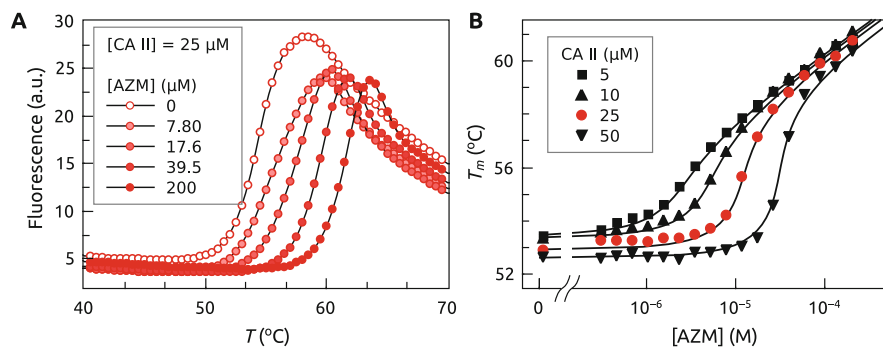


Fig. 5.4 Determination of acetazolamide (AZM) compound binding affinity by FTSA. Here, the CA II unfolding was followed at various added concentrations of AZM. (a) Denaturation profiles of CA II (25 μM) in 50 mM phosphate buffer, 100 mM NaCl (pH 7.5) with different concentrations of AZM. (b) The melting temperatures of ligand-free and ligand-bound CA II at four protein concentrations: 5, 10, 25, and 50 μM . The dissociation constant of AZM obtained at all four protein concentrations was equal to 25 nM (at 25 °C)

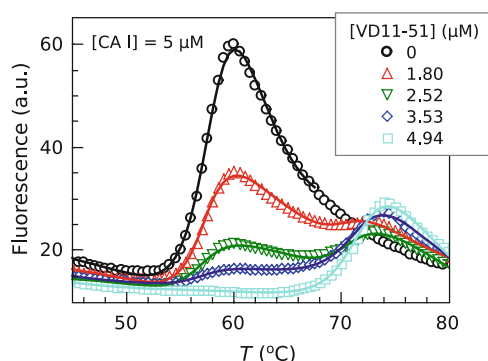


Fig. 5.5 Denaturation profile of CA I in the presence of a tight-binding compound VD11-51. Two melting transitions are observed when the ligand concentration is lower than the protein concentration. Heights of both transition peaks are proportional to the fraction of saturation by the ligand. Symbols represent the experimental data while the lines are fits according to the model described by Zubriené et al [13]

When ligand binds to CA with high affinity (nanomolar or picomolar K_{ds}) the melting transition of CA may split into two parts, if ligand concentration is lower than protein concentration (Fig. 5.5). In this case two transitions are observed: the first peak corresponds to the unfolding of ligand-free protein fraction, the second one—to the unfolding of ligand-bound fraction. The height of transition peak is proportional to the ligand-bound fraction of the protein. When the ligand concentration becomes equal to the protein concentration, the first transition peak disappears. The binding affinities can be determined using equations described in [13]. However, the binding affinity can be also determined using Eq. (5.21), if only

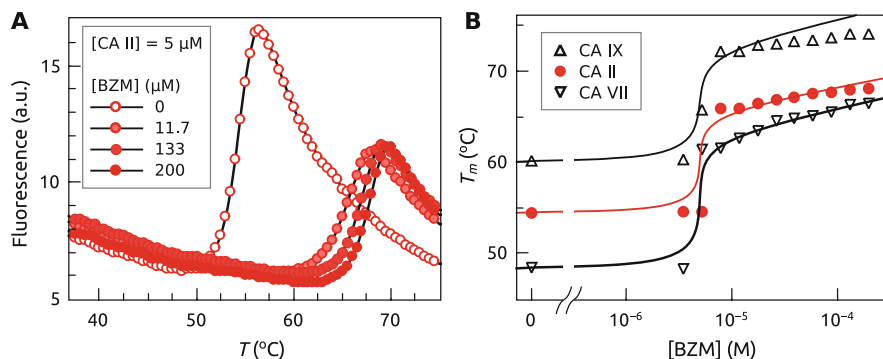


Fig. 5.6 Brinzolamide (BZM) binds to CA II, CA VII, and CA IX with high affinity. **(a)** FTSA fluorescence raw data of BZM binding to CA II. **(b)** The dose response curves: T_m values of CA isoforms plotted as a function of added BZM concentration

second (ligand-bound fraction) transition peak is used in calculations. Protein–ligand binding stoichiometry is determined with higher precision in the presence of two transitions than from one transition.

The fitted ligand-dosing curves did not always match the experimental data points, especially for tight-binding ligands (Fig. 5.6b). The T_m shifted dramatically at low ligand concentration and in some cases did not increase further as predicted by the model (Fig. 5.6a). The binding affinity value cannot be determined from such data accurately, nevertheless, such ligand dose curve behavior indicates that the ligand is a tight binder and the constant is above some well-determined value. We hypothesize that the origin of the saturation effect may be (1) low solubility of the ligand; (2) ligand binding to the unfolded state of the protein, or (3) extremely slow dissociation kinetics that prevent to achieve the equilibrium.

Most inhibition and binding studies are performed using recombinant CA isozymes. To date, only two native CA isozymes—CA I and CA II—purified from human erythrocytes are commercially available. We have compared the binding affinities of various compounds to the native and recombinant CA I (Fig. 5.7a) and the native in-house produced CA VI from human saliva with two forms of recombinant CA VI from *E. coli* and mammalian FreeStyle 293-F cells (Fig. 5.7b). Our goal was to assess whether the recombinant proteins are appropriate models of the native CA isozymes for ligand binding reactions. The binding affinities of tested sulfonamides to recombinant and native CA I isozymes were essentially identical, even the T_m s of recombinant and native CA I were the same, equal to 57.4°C (Fig. 5.7a). Similarly, there were no significant differences in affinities of many tested benzenesulfonamides binding to recombinant and native CA VI (Fig. 5.7b) [14]. These data demonstrated the suitability of recombinant proteins as a model of native CA isoforms.

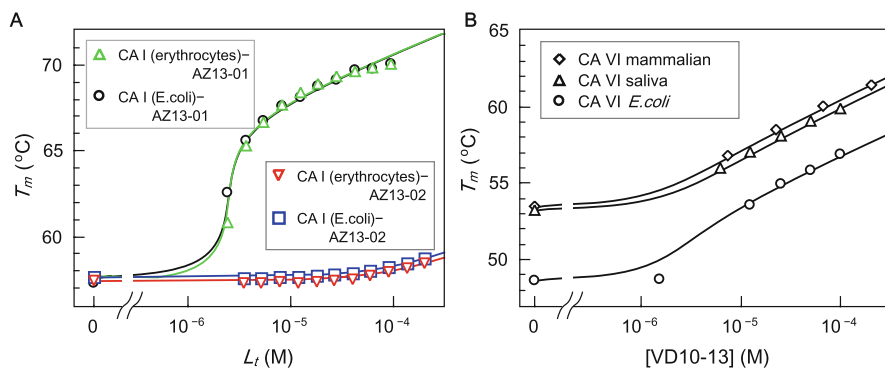


Fig. 5.7 Ligand binding to human CAs as determined by FTSA. (a) Comparison of compound binding to recombinant CAI produced from *E. coli* and CAI from human erythrocytes. (b) The binding affinities of compound VD10-13 towards CA VI from mammalian cells, saliva, and *E. coli* are equal to 380, 500, and 200 nM, respectively

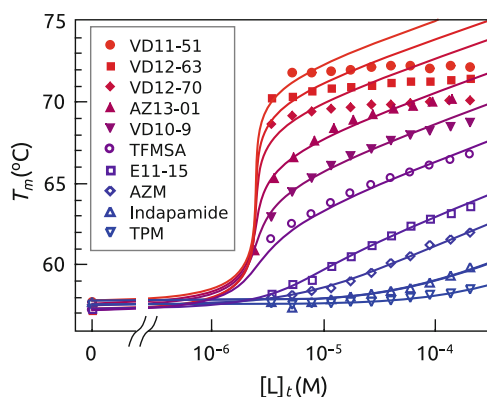


Fig. 5.8 Wide ranges of compound binding affinities towards CAI from 34 μM for TPM to 0.05 nM for VD11-51

FTSA has vast ranges of measurement of binding affinities. Since ligand concentrations must be several times higher than the estimated affinity, the ligand solubility can be the only limiting factor for the measurement of weak binding affinity. The binding of various ligands to CAI of different affinities is shown in Fig. 5.8. Topiramate (TPM) binds to CA I with 34 μM K_d and stabilizes the protein only by about 1 °C at concentration of 200 μM , whereas compound VD11-51 binds with $K_d = 0.05$ nM stabilizing CAI by more than 14 °C at the concentration of 5 μM .

Figure 5.9 shows the selectivity of AZM binding to several CA isoforms. AZM binds much stronger to CA VII than to other isoforms. The determination of selectivity between CA isoforms solely by ΔT_m is not fully correct, as the

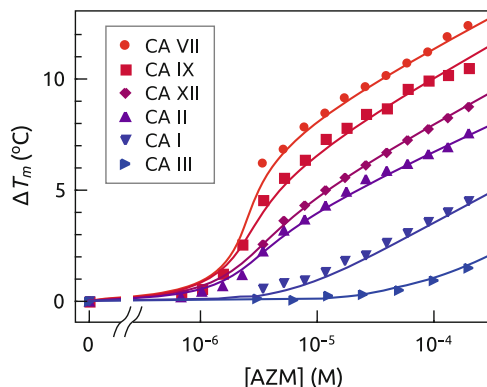


Fig. 5.9 AZM binds with different affinities to various CA isoforms. Data points show the ΔT_m as a function of the total added AZM concentration

thermal stabilization of these isoforms is not equal, i.e., the enthalpy of unfolding and the T_m of CA isoforms differ.

We compared sulfonamide binding to three recombinant CA IX proteins: catalytic domain of CA IX (CA IX CD, residues 138–390), the mutant CA IX CD protein (CA IX CDC174S), and an extracellular part of CA IX bearing the PG domain (CA IX PG, residues 38–414). These proteins bind sulfonamides with similar binding affinities. Figure 5.10 shows FTSA data of VD11-4-2—selective CA IX inhibitor—binding to different CA IX domains and the K_d values ranged from 2.5 nM to 10 nM.

The binding affinity for CA-sulfonamide complex depends on pH. In the first study by Taylor et al in 1970 [15], the binding of sulfonamides to human CA II by stopped flow technique showed a bell-shaped association rate constant dependence on pH. The FTSA analysis of a number of CA isoform (CA I [16], CA II [16], CA IV [17], CA VB [18], CA VI [14], CA VII [19], CA IX [20], CA XII [21], CA XIII [22], and CA XIV [23]) binding with commercial compounds EZA and trifluoromethanesulfonamide also demonstrated the pH-dependence of binding constant as shown in Fig. 5.11. There is a region of maximal affinity of EZA for CA XIII between pH 7.5 and pH 8.5. At those pH values, the affinity is close to 2 nM. The affinity decreased at low pH (due to the protonation of sulfonamide group of the compound) and at high pH (due to the deprotonation of Zn-bound water in the active site of CA XIII). Such U-form profile of binding constant dependence on pH enables the determination of intrinsic binding constant, which will be discussed in Chap. 8.

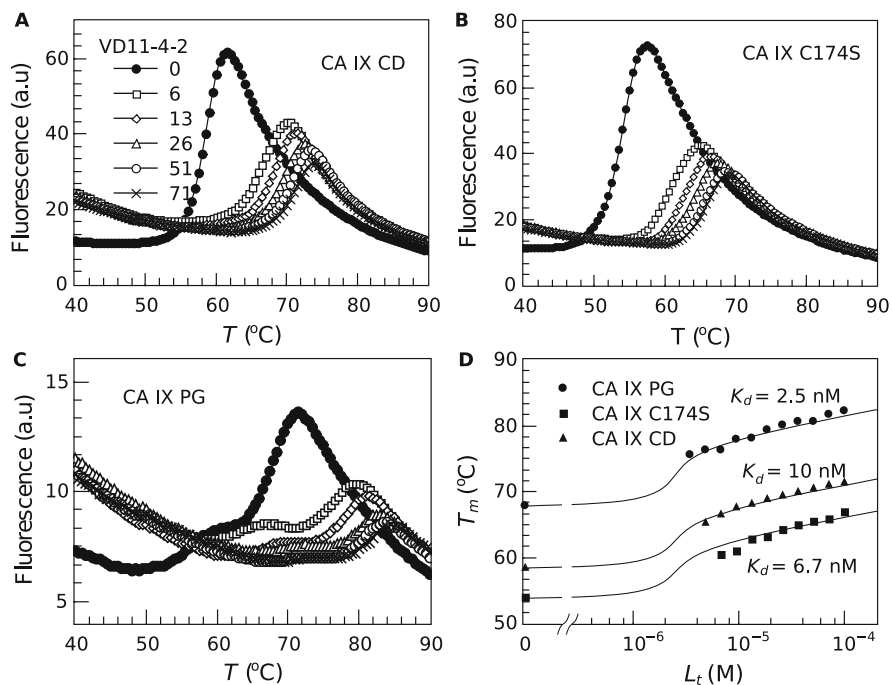


Fig. 5.10 Thermal melting fluorescence curves of three CA IX variants at various concentrations of inhibitor VD11-4-2. (a) The melting curves of the recombinant form of the catalytic domain of CA IX (CA IXCD). (b) The melting curves of mutant (C174S) protein CA IX CDC174S. (c) Thermal melting curves of recombinant CA IX containing the PG domain. (d) The dosing curves of CA IXPG (filled circles), CA IXCD (filled square), and CA IX CDC174S (filled triangle). Data points are fitted according to the model (Eq. (5.21))

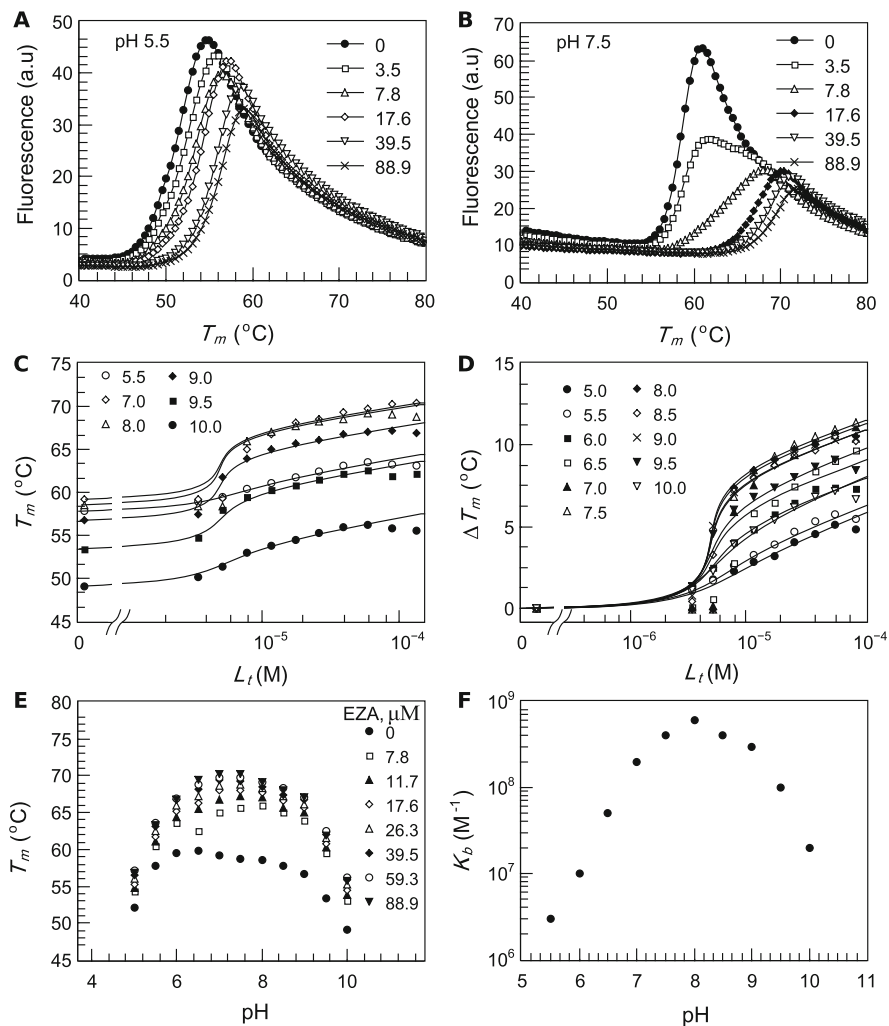


Fig. 5.11 The dependence of ligand binding affinity on pH. Thermal melting fluorescence curves of CA XIII (10 μM) in universal buffer, pH 5.5 (a) and 7.5 (b) in the presence of various EZA concentrations comparing relatively weak and strong binding conditions. (c) The dose response curves as a function of added concentration of EZA at different pHs. (d) EZA binds with different affinities to CA XIII at various pHs. Data points show the ΔT_m as a function of the total added EZA concentration. It is easier to compare stabilization by ligand on a relative scale showing ΔT_m rather than actual melting temperatures shown in panel C. (e) CA XIII T_m dependence on pH at various added EZA concentrations. The shift is largest in the middle pH range. (f) The dependence of the EZA binding constants to CA XIII on pH at 25 $^{\circ}\text{C}$ exhibits a bell-shaped curve

5.5 Conclusions

Fluorescent thermal shift assay is a method to determine the thermal stability of proteins and to obtain the affinity constants from the stabilization effect on the protein caused by ligand binding. The assay is highly robust and in our opinion is the method of first choice to determine the affinities of small molecule compound binding to human CA isoforms. The 1,8-anilino-naphthalene sulfonate solvatochromic fluorescent compound is a probe of choice to follow the protein unfolding. Here we provide the equations to fit both the protein thermal melting curves and the inhibitor dosing T_m curves to obtain the dissociation constants.

References

1. Lo, M.-C., et al.: Evaluation of fluorescence-based thermal shift assays for hit identification in drug discovery. *Anal. Biochem.* **332**, 153–159 (2004)
2. Cimmperman, P., Matulis, D. In: Podjarny, A., Dejaegere, A. P., Kieffer, B. (eds.) *RSC Biomolecular Sciences*, pp. 247–274. Royal Society of Chemistry, Cambridge (2011)
3. Vivoli, M., Novak, H.R., Littlechild, J.A., Harmer, N.J.: Determination of protein-ligand interactions using differential scanning fluorimetry. *J. Vis. Exp.* **91**, e51809 (2014)
4. Niesen, F.H., Berglund, H., Vedadi, M.: The use of differential scanning fluorimetry to detect ligand interactions that promote protein stability. *Nat. Protoc.* **2**, 2212–2221 (2007)
5. Pantoliano, M. W., et al.: High-density miniaturized thermal shift assays as a general strategy for drug discovery. *J. Biomol. Screen.* **6**, 429–440 (2001)
6. Kranz, J.K., Schalk-Hihi, C.: Protein thermal shifts to identify low molecular weight fragments. *Methods Enzymol.* **493**, 277–298 (2011)
7. Slavik, J., Horak, J., Rihova, L., Kotyk, A.: Anilino-naphthalene sulfonate fluorescence and amino acid transport in yeast. *J. Membr. Biol.* **64**, 175–9 (1982)
8. Daniel, E., Weber, G.: Cooperative effects in binding by bovine serum albumin. I. The binding of 1-anilino-8-naphthalenesulfonate. *Fluorimetric titrations. Biochemistry* **5**, 1893–1900 (1966)
9. Matulis, D., Lovrien, R.: 1-anilino-8-naphthalene sulfonate anion-protein binding depends primarily on ion pair formation. *Biophys. J.* **74**, 422–429 (1998)
10. Matulis, D., Baumann, C.G., Bloomfield, V.A., Lovrien, R.E.: 1-anilino-8-naphthalene sulfonate as a protein conformational tightening agent. *Biopolymers* **49**, 451–458 (1999)
11. Rogez-Florent, T., et al.: Label-free characterization of carbonic anhydrase-novel inhibitor interactions using surface plasmon resonance, isothermal titration calorimetry and fluorescence-based thermal shift assays. *J. Mol. Recognit.* **27**, 46–56 (2014)
12. Krasavin, M., et al.: Discovery of Strecker-type α -aminonitriles as a new class of human carbonic anhydrase inhibitors using differential scanning fluorimetry. *J. Enzyme Inhib. Med. Chem.* **31**, 1707–1711 (2016)
13. Zubrienè, A., et al.: Measurement of nanomolar dissociation constants by titration calorimetry and thermal shift assay—radicicol binding to Hsp90 and ethoxzolamide binding to CAII. *Int. J. Mol. Sci.* **10**, 2662–2680 (2009)
14. Kazokaitè, J., Milinavičiūtė, G., Smirnovienė, J., Matulienė, J. & Matulis, D.: Intrinsic binding of 4-substituted-2,3,5,6-tetrafluorobenzene-sulfonamides to native and recombinant human carbonic anhydrase VI. *FEBS J.* **282**, 972–983 (2015)
15. Taylor, P.W., King, R.W., Burgen, A.S.V.: Influence of pH on the kinetics of complex formation between aromatic sulfonamides and human carbonic anhydrase. *Biochemistry* **9**, 3894–3902 (1970)

16. Morkūnaitė, V., et al.: Intrinsic thermodynamics of sulfonamide inhibitor binding to human carbonic anhydrases I and II. *J. Enzyme Inhib. Med. Chem.* **30**, 204–211 (2015)
17. Mickevičiūtė, A., et al.: Intrinsic thermodynamics of high affinity inhibitor binding to recombinant human carbonic anhydrase IV. *Eur. Biophys. J.* **47**, 271–290 (2018)
18. Kasiliauskaitė, A., et al.: Thermodynamic characterization of human carbonic anhydrase VB stability and intrinsic binding of compounds. *J. Therm. Anal. Calorim.* **123**, 2191–2200 (2016)
19. Pilipuitytė, V., Matulis, D.: Intrinsic thermodynamics of trifluoromethanesulfonamide and ethoxzolamide binding to human carbonic anhydrase VII: thermodynamics of TFS and EZA binding to CA VII. *J. Mol. Recognit.* **28**, 166–172 (2015)
20. Linkuvienė, V., et al.: Intrinsic thermodynamics of inhibitor binding to human carbonic anhydrase IX. *Biochim. Biophys. Acta Gen. Subj.* **1860**, 708–718 (2016)
21. Jogaitė, V., et al.: Characterization of human carbonic anhydrase XII stability and inhibitor binding. *Bioorg. Med. Chem.* **21**, 1431–1436 (2013)
22. Baranauskienė, L., Matulis, D.: Intrinsic thermodynamics of ethoxzolamide inhibitor binding to human carbonic anhydrase XIII. *BMC Biophys.* **5**, 12 (2012)
23. Juozapaitienė, V., et al.: Purification, enzymatic activity and inhibitor discovery for recombinant human carbonic anhydrase XIV. *J. Biotechnol.* **240**, 31–42 (2016)



Inhibitor Binding to Carbonic Anhydrases by Isothermal Titration Calorimetry

6

Vaida Paketurytė, Asta Zubrienė, Wen-Yih Chen, Sandro Keller,
Margarida Bastos, Matthew J. Todd, John E. Ladbury,
and Daumantas Matulis

Abstract

Small-molecule drug-candidate compounds are ranked by their capability, primarily described as affinity, to bind a target protein, for example, human carbonic anhydrase (CA), a subject of this book. One of the methods of choice to determine the affinity is isothermal titration calorimetry (ITC), a biophysical technique that enables the determination of the thermodynamic parameters of binding between a protein and a small molecule, both unmodified

V. Paketurytė · A. Zubrienė · D. Matulis (✉)

Department of Biothermodynamics and Drug Design, Institute of Biotechnology, Life Sciences Center, Vilnius University, Vilnius, Lithuania

e-mail: vaيدا.paketuryte@gmc.vu.lt; astzu@ibt.lt; daumantas.matulis@bti.vu.lt

W.-Y. Chen

Department of Chemical and Materials Engineering, National Central University, Taoyuan City, Taiwan

e-mail: wychen@ncu.edu.tw

S. Keller

Molecular Biophysics, Technische Universität Kaiserslautern (TUK), Kaiserslautern, Germany

e-mail: mail@sandrokeller.com

M. Bastos

CIQUP, Department of Chemistry and Biochemistry, Faculty of Sciences, University of Porto, Porto, Portugal

e-mail: mbastos@fc.up.pt

M. J. Todd

Biophysical Solutions, Inc., Ambler, PA, USA

e-mail: matthew.todd@biophysical-solutions.com

J. E. Ladbury

Department of Molecular and Cell Biology and Astbury Center for Structural Biology, University of Leeds, Leeds, UK

e-mail: J.E.Ladbury@leeds.ac.uk

and free in solution—the change in Gibbs energy, enthalpy, entropy, and heat capacity—through the direct measurement of the heat exchange upon binding. ITC is the only technique that directly determines the change in enthalpy upon binding at isothermal and isobaric conditions providing additional information on the mechanism of interaction and thus plays an important role in drug design. In this chapter we describe the main principles, advantages, and disadvantages of the ITC technique, as well as its use to determine the enthalpy change upon sulfonamide inhibitor binding to catalytically active CA isoforms.

6.1 Introduction

Calorimetry is an experimental technique that relies on the observation that heat is absorbed or released in essentially any chemical reaction or a biophysical process. Even the simple dilution of an aqueous solution into water (or buffer) is also associated with the evolution or uptake of heat. The heat exchanged is measured at constant pressure, and thus equals the thermodynamic parameter, the change in enthalpy, which is measured in Joules (according to the International System, SI, of Units), but calories are also still used (CGI system). Both units are often used in the literature and can be easily converted: 1 calorie (cal) = 4.184 Joule (J).

Isothermal titration calorimetry (ITC) involves the titration of one binding partner contained in a syringe into another which is in the calorimeter cell. Three main parameters are determined in a single experiment—the change in Gibbs energy (ΔG), in enthalpy (ΔH), and in entropy ($T\Delta S$ (multiplied by T —temperature)) upon interaction, determined at equilibrium conditions in units of J/mol (or cal/mol) [1].

The Gibbs energy change describes the change in Gibbs energy between the bound and free states. The equilibrium association constant can be calculated from this thermodynamic term. The binding reaction is spontaneous (exergonic) when the ΔG is negative at constant temperature and pressure.

The ΔG° at standard conditions (often also referred in our manuscripts as ΔG) can be calculated using this relationship [2, 3]:

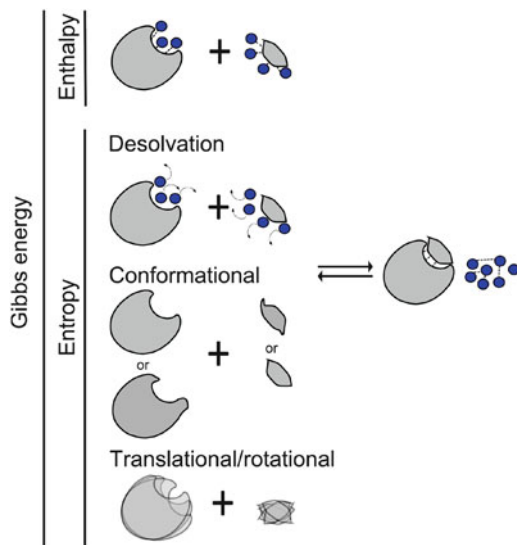
$$\Delta G_{non_standard} = \Delta G^\circ + RT \ln(K_b) = \Delta G^\circ - RT \ln(K_d), \quad (6.1)$$

where $\Delta G_{non_standard} = 0$ and R is the universal gas constant (8.3144 J/K mol), T is the absolute temperature (273.15 K = 0 °C), and K_d is the dissociation constant. Therefore:

$$\Delta G^\circ = -RT \ln(K_b) = RT \ln(K_d), \quad (6.2)$$

All thermodynamic parameters throughout the book refer to standard conditions and should be denoted with the naught symbol. The symbol is not used here for simplicity of the terms.

Fig. 6.1 The main enthalpic (top panel) and entropic (bottom panel) contributions to the Gibbs energy of a protein–ligand binding process. Enthalpic contributions arise primarily from desolvation of the ligand and the protein and the contacts between the ligand and the protein, while the entropic contributions relate to the water that is released to bulk solvent, but also include additional factors such as conformational and translational/rotational degrees of freedom



The binding constant (K_b) is the reciprocal of the dissociation constant (K_d). Both constants reflect the affinity of the two partners, protein and ligand.

$$K_b = \frac{1}{K_d} = \frac{[PL]}{[P][L]} \quad (6.3)$$

where [P], [L], [PL] represent equilibrium molar concentrations of the protein, ligand, and complex, respectively.

The Gibbs energy change has two components, enthalpic (ΔH) and entropic (ΔS) contributions (Fig. 6.1):

$$\Delta G = \Delta H - T \Delta S \quad (6.4)$$

The entropy change can be calculated by using the equation for Gibbs energy change (6.4):

$$\Delta S = \frac{\Delta H - \Delta G}{T} \quad (6.5)$$

The ΔH and ΔS give additional information about the characteristics of the binding event that cannot be extracted directly from ΔG alone [4–6], and are thus fundamental thermodynamic parameters for a more complete understanding of the binding process.

The enthalpy change upon binding is primarily associated with the molecular interactions between the protein, ligand, and solvent molecules, but also with conformational changes and buffer reactions. The enthalpy change results from

the net making or breaking of non-covalent bonds when the binding partners go from the free to the bound state. These bonds include macromolecule-solvent and ligand-solvent interactions which are broken and solvent-solvent interactions that are formed upon the binding event. The ΔH can be negative or positive, depending on whether the overall binding process is exothermic (system releases heat to the surroundings) or endothermic (the system absorbs heat from the surroundings; heat is equal to the enthalpy if pressure $P = \text{const}$).

Compound binding to protein takes place in at least two stages:

- Water molecules, ions, or other molecules that are bound to the protein and ligand unbind (at least partially) the protein and ligand. $\Delta H_{\text{desolvation}}$ —usually positive.
- The ligand binds to the protein. $\Delta H_{\text{binding}}$ can be positive or negative, but most commonly is negative.

$$\Delta H = \Delta H_{\text{binding}} - \Delta H_{\text{desolvation}} \quad (6.6)$$

However, enthalpy is also associated with other processes such as conformational rearrangements and buffer/pH related reactions thus Eq. (6.6) is not fully complete should be substituted by may contain other terms. ITC measures directly the sum of all processes and is called experimentally the observed enthalpy change, ΔH .

Entropy change is defined as a change in molecular degrees of freedom between the bound and free states of the protein and ligand. The binding entropy change (ΔS) is the sum of the solvation ($\Delta S_{\text{solvation}}$), conformational ($\Delta S_{\text{conformational}}$), and translational/rotational ($\Delta S_{\text{translational/rotational}}$) entropy changes:

$$\Delta S = \Delta S_{\text{solvation}} + \Delta S_{\text{conformational}} + \Delta S_{\text{translational/rotational}} \quad (6.7)$$

ITC does not measure these parameters, but the entropy change upon binding, ΔS , can be calculated from the experimentally determined ΔG and ΔH using the Eq. (6.5) [7].

ITC has been used in a number of applications [8], such as determination of affinity of intermolecular interactions (protein–DNA, protein–protein, etc. [9, 10]), the measurement of binding kinetics [11], enzyme inhibition kinetics [12, 13], heat capacity changes upon binding [14], displacement reactions to determine extremely tight interactions [15, 16], among others [17–19]. Moreover, the popularity of the ITC technique has been constantly growing [20]: in 1990, only 32 articles, while in 2017, already 650 articles with “isothermal titration calorimetry” content have been published.

6.2 The Principles of ITC Experiment

There are several commercially available ITC instruments [21] that differ in their technical characteristics, but the calorimetric principle of the microcalorimeter models more commonly used to study biological systems is of the power compensation, overflow type. Their main characteristics are shown in Fig. 6.2a [22]:

- there are two identical cells, with volumes from $\sim 200\ \mu\text{L}$ to $\sim 1.4\ \text{mL}$, surrounded by an adiabatic jacket:
 - Sample cell—usually filled with a protein solution (in the context of protein–ligand binding), but may also be a solution of the ligand.

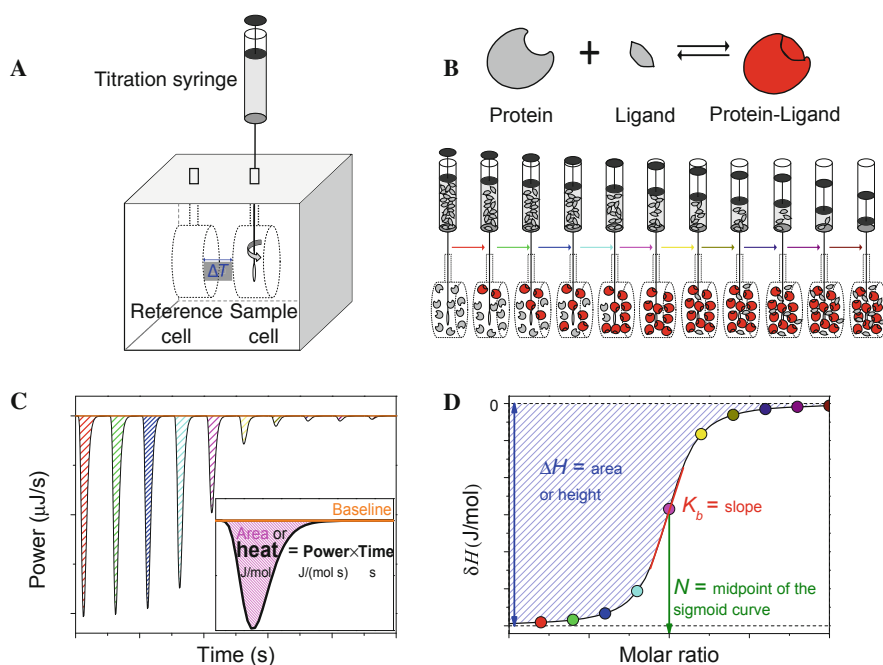


Fig. 6.2 The principle of an ITC experiment. (a) Titration calorimeter contains 2 cells (sample cell that usually contains the protein and reference cell filled with water or solvent media) and syringe used to inject the ligand solution to the sample cell. (b) Saturation of the protein binding sites by a ligand during titration. The experiment is planned so that most protein is saturated around the middle of the titration. The protein–ligand complex is colored red. (c) The power compensation between the sample and reference cells yields the raw ITC data peaks. Each peak represents a change in electric power needed to keep the temperature constant in the cell where a reaction has taken place. The area of the peak (product of time and power) is transformed into the heat evolved upon one injection by appropriate calibration. (d) Binding isotherm, a set of datapoints obtained by integrating the raw ITC data peak areas. A single-binding-site model can be used to fit the data, yielding the affinity (K_b) and the change in enthalpy (ΔH) upon the interaction. In some cases (see text) the stoichiometry can also be estimated from the N

- Reference cell—filled with water or the same solvent that is used for protein preparation. This is particularly important if a fraction of organic solvent is used.
- the titration syringe is filled with one of the components, in the same solvent medium. This is usually the smaller molecule, e.g. drug, peptide, because the compound needs to be stable to the large dilution effects experienced in the early injections. The titration syringe is placed into the sample cell and it titrates the solution with precise volumes at certain time intervals and mixes the solutions by rotating at a certain speed.

The instrument is designed to minimize the temperature difference between the sample and reference cells. Two heaters are constantly providing a small amount of heat to both sample and reference cells (power compensation) which maintain both cells at the experimental temperature (e.g. 25°C). When an injection is made, the heat is evolved or absorbed as a result of the interactions in the sample cell. To minimize the temperature difference between the cells, a change in the heat input to the sample cell is required. Changing of the heat input (or power over a time period) results in rapid restoration of the temperature difference between the cells to maintain the experimental temperature. In a binding experiment with high binding constant most injected compound interacts with the protein in the cell and equilibrium is rapidly attained. Subsequent injections result in further interactions and the concomitant heat absorption or release. As the binding sites of the protein in the cell are gradually saturated, the amount of heat exchange is reduced and further injections of interacting compound will result in lower heat exchange (Fig. 6.2b). Even with a fully saturated target, a small amount of heat exchange is observed that is mainly due to the heat of dilution of the component in the syringe, but to a smaller extent also reflects the temperature difference between the cell and the syringe and the heat of friction caused by the injection.

The area of each peak under the baseline (Fig. 6.2c) is integrated and plotted as a function of molar ratio between ligand and protein (Fig. 6.2d). The raw data derived from the titration run need to be corrected for the heats of dilution, mostly of the ligand into the calorimetric cell. There are several ways to treat the heat of dilution, namely: (a) it can be determined in an independent “control experiment” (titration of the ligand in the syringe into the solvent in the cell, and (less significant) titration of solvent media into the protein in the cell), and thereafter the heats from the integrated peaks are subtracted from the integrated data for the titration run data; (b) take the average of the last, constant heat injections, and then subtract this value from the integrated data for the titration run; or (c) fit the dilution heat together with the model fitting. After correction for the heat of dilution a model can be fitted to the obtained data [21], and both the enthalpy change (ΔH) and the binding constant (K_b), also sometimes referred to as association or affinity constant (K_a), are obtained. In cases where the concentration of the protein and ligand is known with high certainty, the stoichiometry (obtainable from the N) of the interaction can also be estimated from the fitting in most available programs. It should be noted, however, that errors in the concentrations of the interacting species will lead to N

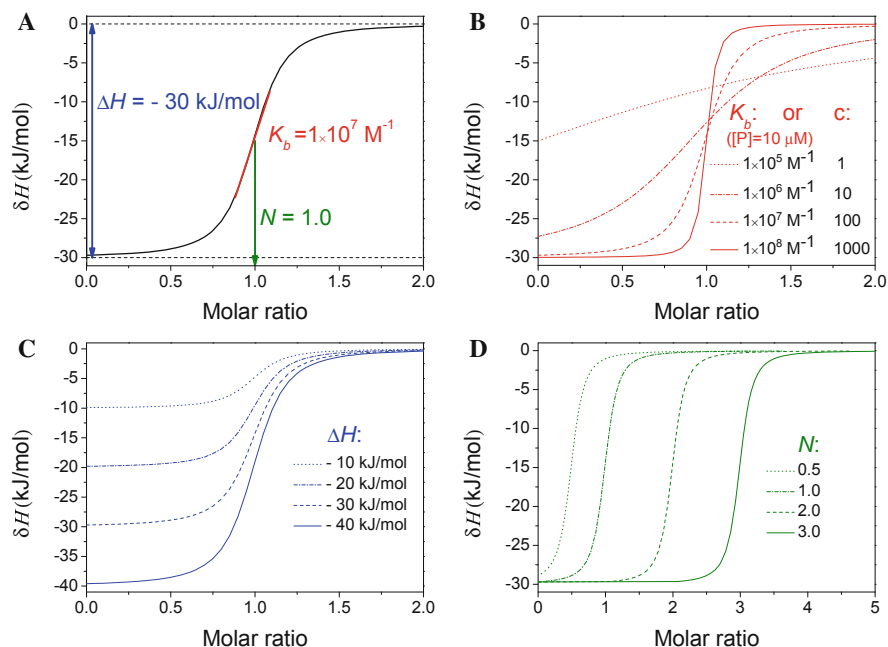


Fig. 6.3 Simulated ITC binding isotherms. (a) Simulated binding isotherm for a 1:1 binding model showing the change in enthalpy (blue arrow), degree of saturation (green arrow), and affinity (proportional to the steepness of the curve, shown in red). (b) Simulated binding isotherms for 1:1 model with varying affinities or c -value, red. (c) Simulated binding isotherms for 1:1 model with varying enthalpy changes, blue. (d) Simulated binding isotherms with varying stoichiometries (for four different protein–ligand systems) or alternatively degrees of saturation (for the same protein–ligand system at various concentrations), green

values different from 1 (in the case of a 1:1 interaction), although the stoichiometry can be 1:1. That is the reason why some software fit for the so-called incompetent fraction, instead of N , to avoid misleading by directly providing the stoichiometry of the interaction. From these parameters (ΔH and K_b), the Gibbs energy (ΔG) and entropy changes (ΔS) can be determined using Eqs. (6.2) and (6.5).

In Fig. 6.3a, the simulation parameters were $K_b = 1 \times 10^7 \text{ M}^{-1}$, $\Delta H = -30 \text{ kJ/mol}$ and $N = 1.0$ (one ligand molecule interacts with one protein molecule, the model usually referred to as “a single binding site model”). Figure 6.3b–d shows simulated binding isotherms by varying one of these 3 parameters while the remaining ones are kept constant.

In Fig. 6.3b, in addition to the binding constants, the c -values (also called Wiseman parameter) [23–26] are also highlighted. This parameter is related to the steepness of the ITC isotherm and to the detection limit of each ITC, and can be calculated according to:

$$c = K_b[\text{P}]N \quad (6.8)$$

where $[P]$ is the molar protein concentration. When the c -value is small (usually stated as being less than 10), the curve is too flat, and when it is too large ($c > 500$), the curve is too steep [24]. In both cases, the binding constant, K_b , cannot be accurately determined, but in the second case the enthalpy change can be obtained with high precision. In order to obtain both thermodynamic parameters accurately, K_b , and ΔH , the experiment must be performed using a protein concentration that leads to a c -value between approximately 10 and 500. If this is not possible, some alternative methods such as displacement ITC methodology may work for very high K_b values [15].

Figure 6.3c shows plots where ΔH is varied. The ΔH component can be related to all non-covalent interactions, and its magnitude varies with temperature, as well as with the buffer. Therefore, in some cases, where the observed ΔH is small or zero, the reaction can be sometimes studied, by varying the temperature and/or choosing buffers of different protonation enthalpy (for more details, see Sect. 6.4).

Different binding molar ratios of the complex (equivalent to stoichiometry) or saturation are shown in Fig. 6.3d. For the same system, the stoichiometry is the same (e.g., one sulfonamide molecule interacts with a single CA molecule), but the N value retrieved from an ITC experiment can vary due to errors in protein or ligand concentration but should not be misled with a stoichiometry. The N value of, e.g., 0.8 would most likely mean that the stoichiometry of the system is 1:1, but some 20% of the protein in the cell is unable to bind the ligand or concentration estimation was not fully accurate.

6.3 ITC Determines the Binding Affinity and the Enthalpy Change of Intermolecular Interactions

As described above, the main thermodynamic parameters characterizing protein–ligand interaction can be directly measured by ITC and used in drug design. Correlation maps of the compound chemical structures with the intrinsic binding parameters, as described in Chap. 16, are very helpful for this purpose. The binding information is even more useful when structural data (e.g., obtained by X-ray crystallography) is also known. Structural and thermodynamic information on the binding event are complementary [27, 28] (for more details, see Chaps. 13 and 17), and can contribute to lead compound optimization in rational drug design [29].

Figure 6.4 shows raw (Fig. 6.4a and c) and integrated (Fig. 6.4b and d) data of compound VD11-4-2 binding to CA IX and CA I. CA IX is known as potential drug target or marker for cancer therapy [30–32], while CA I is responsible for gas exchange and pH balance [33] in normal tissues and thus should not be inhibited. Furthermore, in the human body, there are another 10 isozymes of CA, which are also responsible for many physiological functions. Thus, a potential drug (chemical compound) should selectively inhibit only CA IX, but not the other isoforms. ITC data provided significant information that the compound VD11-4-2 exhibited selective binding to CA IX while avoiding CA I.

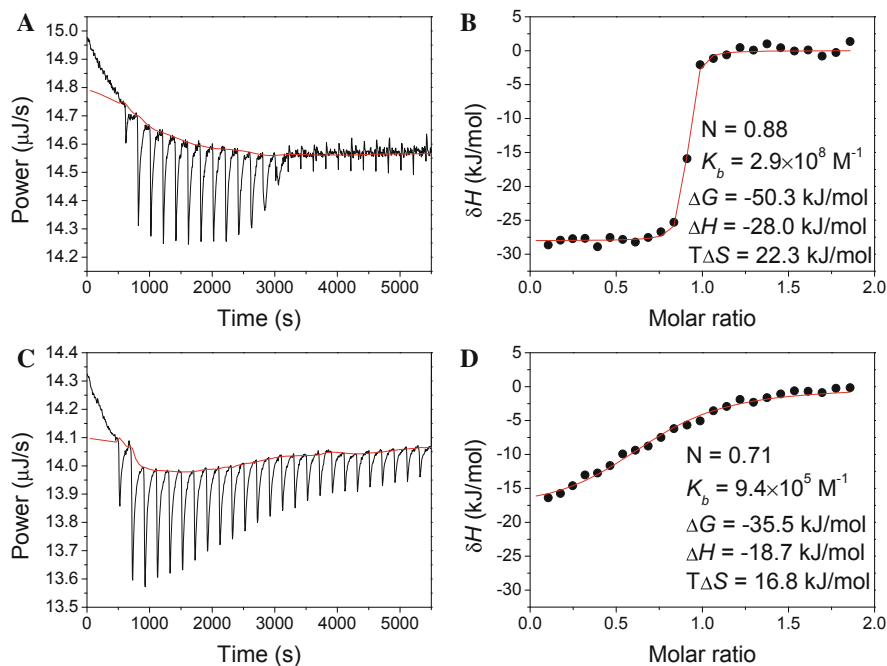


Fig. 6.4 The ITC data of compound VD11-4-2 binding to (a, b) CAIX and (C, D) CAI. Left panels show the raw ITC data while the panels on the right—the integrated ITC isotherms. The experiments were performed by VP-ITC calorimeter in 50 mM TRIS-HCl buffer (pH 7.0) containing 100 mM NaCl at 37 °C. The compound binds to CAIX with a significantly greater affinity than to CAI and thus exhibited selectivity towards CAIX over CAI

The ITC data in Fig. 6.4 yields not only the affinities, but also the change in enthalpies upon compound VD11-4-2 interaction with CAIX and CAI. The enthalpies can be obtained from the fits of the integrated curves. However, it should be kept in mind that the obtained values have little practical usefulness because they are “non-intrinsic” as will be explained in Chap. 8.

6.4 Binding-Linked Protonation Reactions

Baker and Murphy described the binding-linked protonation effect (proton linkage) in 1996 [34]. This phenomenon should be considered in ITC ligand binding studies as protonation/deprotonation upon binding can contribute a significant heat effect that is measured together with the binding event. There are several examples of reported data in the CA literature in which protonation effects are not considered and therefore show only the observed binding parameters, which allow only incomplete and even misleading conclusions about the effect of compound structure on the binding affinity. As highlighted above, the binding parameters obtained from ITC

experiments often include contributions from protonation effects which accompany the binding event and can be derived for both interacting components and the solvent. For an accurate description of the binding event the following terms need to be individually assessed:

- Enthalpy change of the observed binding reaction may depend on buffer because buffers have different enthalpies of protonation (Fig. 6.5g).
- Enthalpy and Gibbs energy change of the observed binding reaction could depend on pH due to the different fractions of the protein and ligand in their binding-ready forms.

Figure 6.5 shows the same protein–ligand binding reaction measured by ITC under different buffers: sodium phosphate (Fig. 6.5a and c) and TRIS (Fig. 6.5b and d), and varied pH values: 6.0, 7.5, and 8.5. Clearly, both the buffer type and buffer pH affect the results as shown in Fig. 6.5e and f. This is caused by the linked protonation effects that occur upon CA interaction with a sulfonamide compound. Plotting the observed enthalpy of binding as a function of the buffer protonation enthalpy (47.5 kJ/mol of TRIS and 5.1 kJ/mol of phosphate buffer at 25 °C [35]) at various pHs yields three lines of different slopes (Fig. 6.5g). These slopes represent a number of net protons either uptaken by the protein–ligand complex from the buffer (positive slope) or released to the buffer (negative slope). The net number of protons is plotted as a function of pH (Fig. 6.5h). Full understanding of all binding-linked reactions is necessary in order to account for the linked protonation events and calculate the *intrinsic* binding constant as explained in Chap. 8.

6.5 Troubleshooting in ITC

Even the simplest ITC titrations may yield erroneous results if performed with insufficient care. The most common reasons for obtaining poor thermograms and the problems with ITC data are described below.

Large Heat of Dilution If the buffers in the cell and syringe match, the heat of dilution is small and arises mainly from the dilution of the ligand in the syringe. If that dilution heat is not significant, the last titration peaks resemble water–water titration (Fig. 6.6a). Nevertheless, if the buffers do not match, the heat of dilution may be very high, masking the true heat of binding [36]. A common cause may be a mismatch in the concentration of DMSO (Fig. 6.6b), because most ligands are prepared with DMSO (typically several % (v/v) in ITC) due to their low solubility in water. In this case the same concentration of DMSO must be present in the protein solution as in the ligand solution.

Unstable Baseline and Peak Jumps (Fig. 6.7) The cause is not always clear and there may be several reasons: air bubbles; poorly washed cell and/or syringe; denaturation of the protein; or precipitation of the ligand or protein upon binding.

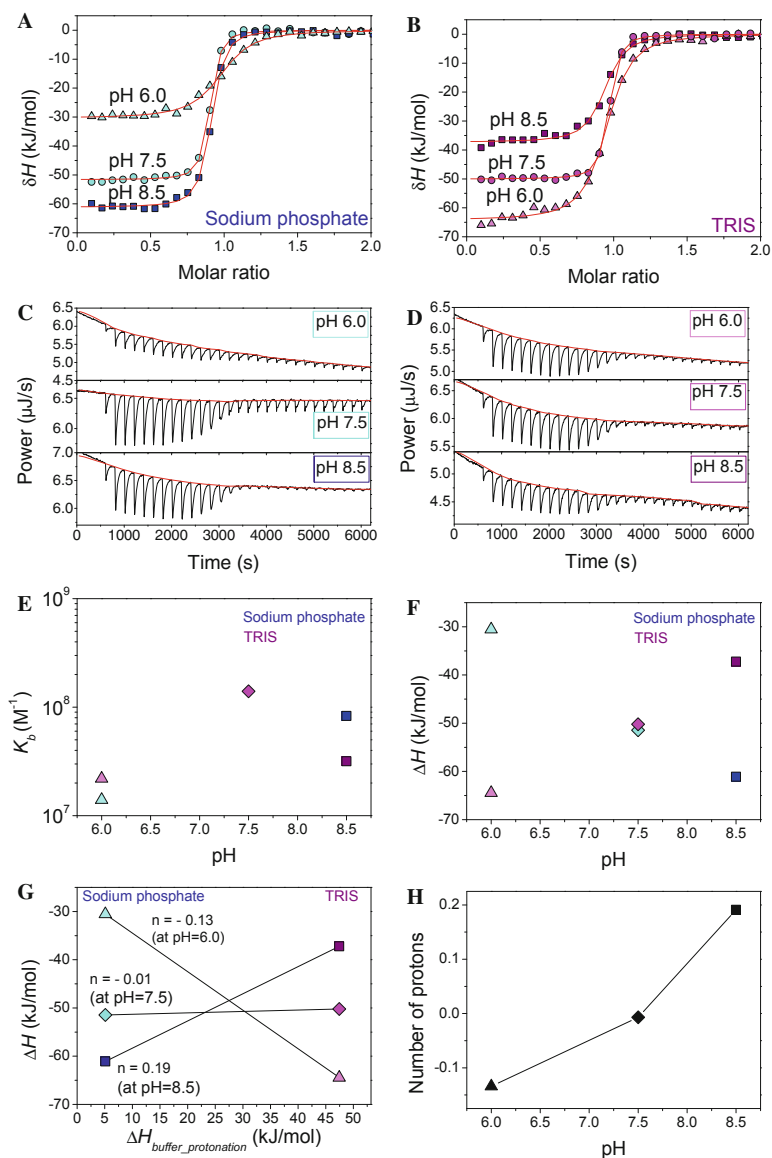


Fig. 6.5 An example of ITC binding isotherms obtained in different buffers and at various pH values. The thermograms show the titration of ethoxzolamide into CA XII in 50 mM sodium phosphate (a, c) and 50 mM TRIS-Cl (b, d) buffers at pH 6.0, 7.5, and 8.5. (e) and (f) show the K_b and ΔH dependence on pH in both buffers. (g) Plot of the observed enthalpies as a function of buffer protonation enthalpy. At pH 6.0 the slope is positive while at pH 8.5 the slope is negative. These slopes are equal to the net number of protons, n , being uptaken from the buffer or released to the buffer upon binding. (h) The number of protons uptaken from the buffer (positive) or released to the buffer (negative) as a function of pH. It is obvious that the enthalpy is highly dependent both on buffer and pH and thus must be accounted for by calculating the *intrinsic* enthalpy which is independent of linked protonations as explained in Chap. 8

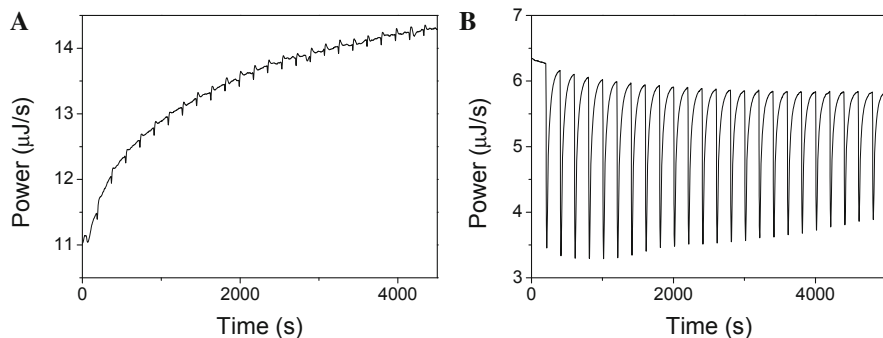


Fig. 6.6 (a) Raw ITC data of water–water titration. The peaks are relatively small showing the small heats of titration of water into water. The baseline is rather unstable. (b) Raw ITC data show large heats obtained when 1% DMSO was added to the syringe, but was not added to the solvent in the cell, resulting in “solvent mismatch,” due to the strongly exothermic heat of dilution of DMSO

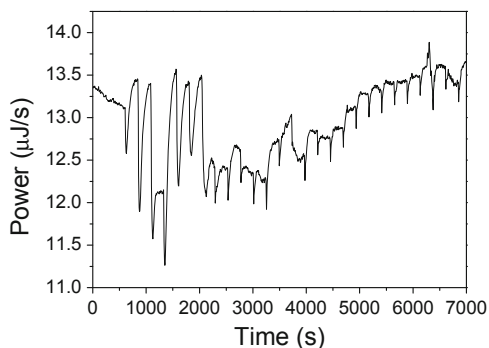


Fig. 6.7 Example of a thermogram with a very unstable baseline. Such thermograms should not be used to obtain the enthalpy of interaction and instead the experiment should be repeated after extensive cleaning of the cell and syringe, degassing the solutions, and centrifugation of the samples

Thus, degassing of the sample and taking care not to introduce air bubbles is fundamental. Care should be taken when degassing the sample for extended periods of time as it leads to water evaporation and thus a change in concentration. Therefore weighing the sample before and after degassing is recommended so this can be detected and corrected [37]. Centrifugation may also be helpful to get rid of aggregates and also bubbles.

Furthermore, it is also important to mention that even in a properly performed experiment, the baseline is not perfectly straight as in Fig. 6.2c. Some software packages provide the possibility to plot the raw data already corrected for the baseline, but such presentation alone is highly unrecommended in the scientific literature [20] because it hides baseline instability from the reader.

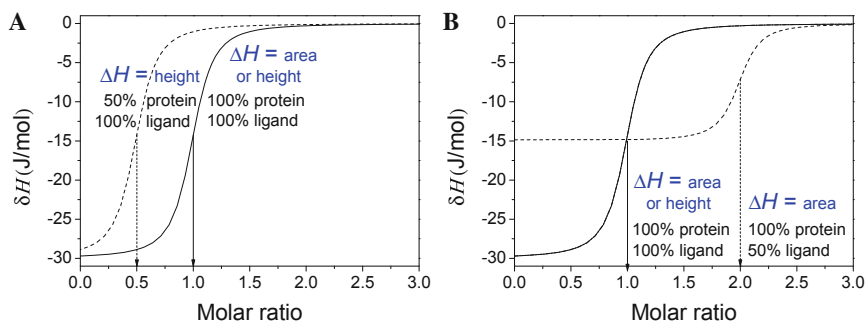


Fig. 6.8 Simulated ITC data showing the cases, when (a) protein and (b) ligand are only 50% pure. Incorrect concentration of the component in the cell will yield accurate enthalpy and the association constant. However, incorrect concentration of the component in the syringe would not permit to see the end of a standard titration because it would be visible only if titration is continued to reach the ratio of 4. Furthermore, the observed enthalpy would be two times smaller than the real value if the compound is only 50% pure

The Molar Ratio in the Complex Does Not Match the Expected Stoichiometry

This applies to well-characterized systems, but is especially important when working with unstable proteins or compounds. The impurities of the protein and compound, or the fact that not all protein present is in “competent” for binding has a large impact on the values retrieved from ITC experiments. Even very stable proteins, such as CA II, are not 100% pure/active. Therefore, the molar ratio of such ITC data is typically close to but smaller than 1.0 (typically 0.8–0.9).

Figure 6.8 shows simulated ITC curves for cases when the protein (Fig. 6.8a) or the ligand (Fig. 6.8b) is impure or not fully active. When the solution contains only 50% of pure or active protein and correct concentration of the ligand, the titration appears complete at a lower molar ratio (Fig. 6.8a, dashed line) i.e., the saturation level achieves only 0.5. In this case, the change in enthalpy from the height difference is correct, but the value obtained from the area is not (Fig. 6.2d). On the other hand, when we have only 50% of the ligand and 100% of competent protein, the titration will have the inflection point at a higher molar ratio (Fig. 6.8b, dashed line) i.e., 2.0. In this case, the determination of the enthalpy change from a height difference is inaccurate, and the one derived from the area should be used instead [37].

6.6 Accuracy and Precision of ITC Measurements

As with any experimental technique, it is important to know the accuracy of the instruments and the repeatability of the resultant ITC data. The issues related to the accuracy, precision, and standard errors in ITC experiments [25, 38–48] and calibration issues [26, 49, 50] have been analyzed in detail to achieve the highest accuracy and precision in ITC. It is important to distinguish whether

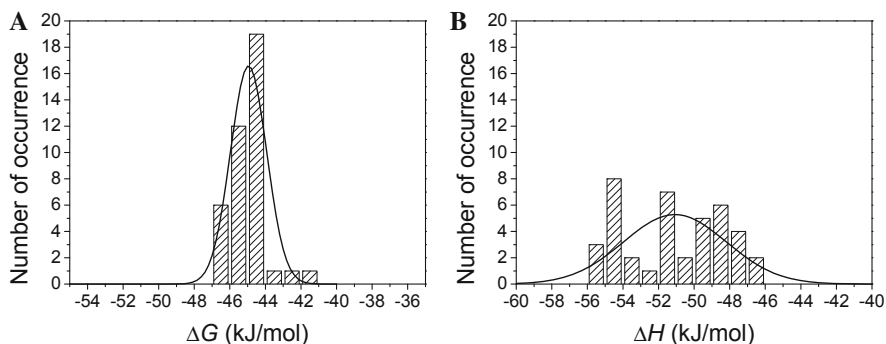


Fig. 6.9 Normal distribution of the ΔG (a) and ΔH (b) of CA II—acetazolamide binding data obtained by repeating the same ITC titration 40 times, 10 times with 4 ITC instrument models. The bin widths are the same for ΔG and ΔH to help visual comparison and it is obvious that the Gibbs energy is determined with a smaller standard error window than the enthalpy

two ligands have significantly different thermodynamic parameters for binding or if their differences do not exceed the combined uncertainties of the respective measurements. It is very important to correctly report the precision of the obtained parameters.

To determine the uncertainty of sulfonamide-CA ITC measurements, the same ITC experiment (acetazolamide binding to human carbonic anhydrase II) was performed a large number of times with several instruments (Affinity ITC, PEAQ-ITC, ITC200, VP-ITC, and MCS-ITC), as reported in [51]. The resulting histograms of the distribution of ΔG and ΔH are shown in Fig. 6.9. Data were obtained from 40 ITC experiments by Affinity ITC, PEAQ-ITC, ITC200, and VP-ITC calorimeters with uniformly prepared samples (100 μM of acetazolamide and 10 μM of recombinant human CA II). The data was analyzed by NITPIC and SEDPHAT software [52, 53]. The averaged values together with their confidence intervals (at $\alpha = 0.95$) were $\Delta H = -51.1 \text{ kJ/mol} \pm 0.9 \text{ kJ/mol}$ and $\Delta G = -44.9 \text{ kJ/mol} \pm 0.3 \text{ kJ/mol}$. This study shows that thermodynamic parameters retrieved from ITC data may not have precision higher than approximately 1 kJ/mol. Individual experiments involving reagents of lower stability or purity could have even larger errors. Therefore, it is important to perform repeated experiments to enable the calculation of the statistical uncertainty of the obtained data. The precision of our ITC data [54] has an uncertainty of 1 kJ/mol–4 kJ/mol. This indicates that typically differences in thermodynamic parameters for binding reactions involving the same protein with different ligands that are smaller than 1 kJ/mol should be considered within the statistical noise of the data, and not revealing significant differences in affinity [55].

6.7 Conclusions

ITC is a universal label- and immobilization-free method for determining the thermodynamics of molecular interactions in aqueous solution. It is the prime method for the determination of the change in enthalpies and entropies of protein–ligand interactions, and the only experimental technique allowing a direct determination of the change in enthalpy of binding and a full thermodynamic characterization of the binding reaction from a single titration. Experiments should always be carefully performed, even for a well-characterized system such as carbonic anhydrase interaction with sulfonamide inhibitors. ITC is indispensable in the demonstration and quantitative characterization of binding-linked protonation reactions.

Acknowledgements D. M. thanks the Research Council of Lithuania (project TAP LLT-1/2016). M. B. thanks Fundação para a Ciência e Tecnologia (FCT-Portugal) (project UID/QUI/0081/2013 and NORTE-01-0145-FEDER-000028 (Sustainable Advanced Materials (SAM), Programa Operacional Regional do Norte (Norte 2020).

References

1. Leavitt, S., Freire, E.: Direct measurement of protein binding energetics by isothermal titration calorimetry. *Curr. Opin. Struct. Biol.* **11**, 560–566 (2001)
2. Gurney, R.W.: *Ionic Processes in Solution*. McGraw-Hill Book Company, Inc, New York (1953)
3. Kauzmann, W.: Some factors in the interpretation of protein denaturation. *Adv. Protein Chem.* **14**, 1–63 (1959)
4. Schön, A., Freire, E.: Enthalpy screen of drug candidates. *Anal. Biochem.* **513**, 1–6 (2016)
5. Chodera, J.D., Mobley, D.L.: Entropy-enthalpy compensation: role and ramifications in biomolecular ligand recognition and design. *Annu. Rev. Biophys.* **42**, 121–142 (2013)
6. Klebe, G., Böhm, H.-J.: Energetic and entropic factors determining binding affinity in protein–ligand complexes. *J. Recept. Signal Transduct.* **17**, 459–473 (1997)
7. Bronowska, A.K.: Thermodynamics of ligand–protein interactions: implications for molecular design. In: *Thermodynamics - Interaction Studies - Solids, Liquids and Gases* (2011)
8. Bastos, M.: *Biocalorimetry: Foundations and Contemporary Approaches*. CRC Press, Boca Raton (2016)
9. Jelesarov, I., Bosshard, H.R.: Isothermal titration calorimetry and differential scanning calorimetry as complementary tools to investigate the energetics of biomolecular recognition. *J. Mol. Recognit.* **12**, 3–18 (1999)
10. Chaires, J.B., et al.: Biocalorimetry. *Methods* **76**, 1–2 (2015)
11. Trani, J.M.D., et al.: Rapid measurement of inhibitor binding kinetics by isothermal titration calorimetry. *Nat. Commun.* **9**, 893 (2018)
12. Di Trani, J.M., Moitessier, N., Mittermaier, A.K.: Complete kinetic characterization of enzyme inhibition in a single isothermal titration calorimetric experiment. *Anal. Chem.* **90**, 8430–8435 (2018)
13. Frasca, V.: Using isothermal titration calorimetry techniques to quantify enzyme kinetics. *Ind. Biotechnol.* **12**, 207–211 (2016)
14. Prabhu, N.V., Sharp, K.A.: Heat capacity in proteins. *Annu. Rev. Phys. Chem.* **56**, 521–548 (2005)
15. Sigurskjold, B.W.: Exact analysis of competition ligand binding by displacement isothermal titration calorimetry. *Anal. Biochem.* **277**, 260–266 (2000)

16. Krainer, G., Keller, S.: Single-experiment displacement assay for quantifying high-affinity binding by isothermal titration calorimetry. *Methods (San Diego, Calif.)* **76**, 116–123 (2015)
17. Atri, M.S., Saboury, A.A., Ahmad, F.: Biological applications of isothermal titration calorimetry. *Phys. Chem. Res.* **3**, 319–330 (2015)
18. Jayanthi, S.: The versatility of isothermal titration calorimetry in modern biology. *J. Anal. Bioanal. Tech.* **06**, e121 (2015)
19. Ladbury, J.E., Chowdhry, B.Z.: Sensing the heat: the application of isothermal titration calorimetry to thermodynamic studies of biomolecular interactions. *Chem. Biol.* **3**, 791–801 (1996)
20. Falconer, R.J.: Applications of isothermal titration calorimetry - the research and technical developments from 2011 to 2015: review of isothermal titration calorimetry from 2011 to 2015. *J. Mol. Recognit.* **29**, 504–515 (2016)
21. Perozzo, R., Folkers, G., Scapozza, L.: Thermodynamics of protein-ligand interactions: history, presence, and future aspects. *J. Recept. Signal Transduct. Res.* **24**, 1–52 (2004)
22. Freyer, M.W., Lewis, E.A.: In: *Methods in Cell Biology*, pp. 79–113. Academic Press, Cambridge (2008)
23. Wiseman, T., Williston, S., Brandts, J.F., Lin, L.N.: Rapid measurement of binding constants and heats of binding using a new titration calorimeter. *Anal. Biochem.* **179**, 131–137 (1989)
24. Turnbull, W.B., Daranas, A.H.: On the value of C: can low affinity systems be studied by isothermal titration calorimetry? *J. Am. Chem. Soc.* **125**, 14859–14866 (2003)
25. Broecker, J., Vargas, C., Keller, S.: Revisiting the optimal C value for isothermal titration calorimetry. *Anal. Biochem.* **418**, 307–309 (2011)
26. Demarse, N.A., Quinn, C.F., Eggett, D.L., Russell, D.J., Hansen, L.D.: Calibration of nanowatt isothermal titration calorimeters with overflow reaction vessels. *Anal. Biochem.* **417**, 247–255 (2011)
27. Chaires, J.B.: Calorimetry and thermodynamics in drug design. *Annu. Rev. Biophys.* **37**, 135–151 (2008)
28. Renaud, J.-P., et al.: Biophysics in drug discovery: impact, challenges and opportunities. *Nat. Rev. Drug Discov.* **15**, 679–698 (2016)
29. Ladbury, J.E., Klebe, G., Freire, E.: Adding calorimetric data to decision making in lead discovery: a hot tip. *Nat. Rev. Drug Discov.* **9**, 23–27 (2010)
30. Mboge, M.Y., Mahon, B.P., McKenna, R., Frost, S.C.: Carbonic anhydrases: role in pH control and cancer. *Metabolites* **8**, 19 (2018)
31. Pastorekova, S., Zatovicova, M., Pastorek, J.: Cancer-associated carbonic anhydrases and their inhibition. *Curr. Pharm. Des.* **14**, 685–698 (2008)
32. Supuran, C.T., Winum, J.-Y.: Carbonic anhydrase IX inhibitors in cancer therapy: an update. *Future Med. Chem.* **7**, 1407–1414 (2015)
33. Maren, T.H.: Carbonic anhydrase: chemistry, physiology, and inhibition. *Physiol. Rev.* **47**, 595–781 (1967)
34. Baker, B.M., Murphy, K.P.: Evaluation of linked protonation effects in protein binding reactions using isothermal titration calorimetry. *Biophys. J.* **71**, 2049–2055 (1996)
35. Goldberg, R.N., Kishore, N., Lennen, R.M.: Thermodynamic quantities for the ionization reactions of buffers. *J. Phys. Chem. Ref. Data* **31**, 231–370 (2002)
36. Bian, X., Lockless, S.W.: Preparation to minimize buffer mismatch in isothermal titration calorimetry experiments. *Anal. Chem.* **88**, 5549–5553 (2016)
37. Williams, M.A., Daviter, T. (eds.): *Protein-Ligand Interactions*. Humana Press, Totowa (2013)
38. Boyce, S.E., Tellinghuisen, J., Chodera, J.D.: Avoiding accuracy-limiting pitfalls in the study of protein-ligand interactions with isothermal titration calorimetry. *bioRxiv*, 023796 (2015)
39. Hansen, L.D., Fellingham, G.W., Russell, D.J.: Simultaneous determination of equilibrium constants and enthalpy changes by titration calorimetry: methods, instruments, and uncertainties. *Anal. Biochem.* **409**, 220–229 (2011)
40. Kantonen, S.A., Henriksen, N.M., Gilson, M.K.: Evaluation and minimization of uncertainty in ITC binding measurements: heat error, concentration error, saturation, and stoichiometry. *Biochim. Biophys. Acta (BBA)* **1861**, 485–498 (2017)

41. Krimmer, S.G., Klebe, G.: Thermodynamics of protein–ligand interactions as a reference for computational analysis: how to assess accuracy, reliability and relevance of experimental data. *J. Comput. Aided Mol. Des.* **29**, 867–883 (2015)
42. Tellinghuisen, J.: In: *Methods in Enzymology*, pp. 245–282 (2004)
43. Tellinghuisen, J.: Volume errors in isothermal titration calorimetry. *Anal. Biochem.* **333**, 405–406 (2004)
44. Tellinghuisen, J.: Statistical error in isothermal titration calorimetry: variance function estimation from generalized least squares. *Anal. Biochem.* **343**, 106–115 (2005)
45. Tellinghuisen, J.: Optimizing experimental parameters in isothermal titration calorimetry. *J. Phys. Chem. B* **109**, 00062, 20027–20035 (2005)
46. Tellinghuisen, J.: Optimizing experimental parameters in isothermal titration calorimetry: variable volume procedures. *J. Phys. Chem. B* **111**, 11531–11537 (2007)
47. Tellinghuisen, J., Chodera, J.D.: Systematic errors in isothermal titration calorimetry: concentrations and baselines. *Anal. Biochem.* **414**, 297–299 (2011)
48. Wadsö, I., Wadsö, L.: Systematic errors in isothermal micro-and nanocalorimetry. *J. Therm. Anal. Calorim.* **82**, 553–558 (2005)
49. Tellinghuisen, J.: Calibration in isothermal titration calorimetry: heat and cell volume from heat of dilution of NaCl(Aq). *Anal. Biochem.* **360**, 47–55 (2007)
50. Baranauskienė, L., Petrikaitė, V., Matulienė, J., Matulis, D.: Titration calorimetry standards and the precision of isothermal titration calorimetry data. *Int. J. Mol. Sci.* **10**, 00029, 2752–2762 (2009)
51. Linkuvienė, V., Krainer, G., Chen, W.-Y., Matulis, D.: Isothermal titration calorimetry for drug design: precision of the enthalpy and binding constant measurements and comparison of the instruments. *Anal. Biochem.* **515**, 61–64 (2016)
52. Brautigam, C.A., Zhao, H., Vargas, C., Keller, S., Schuck, P.: Integration and global analysis of isothermal titration calorimetry data for studying macromolecular interactions. *Nat. Protoc.* **11**, 882–894 (2016)
53. Zhao, H., Piszczek, G., Schuck, P.: SEDPHAT – a platform for global ITC analysis and global multi-method analysis of molecular interactions. *Methods* **76**, 137–148 (2015)
54. Linkuvienė, V., et al.: Thermodynamic, kinetic, and structural parameterization of human carbonic anhydrase interactions toward enhanced inhibitor design. *Q. Rev. Biophys.* **51** (2018)
55. Nguyen, T.H., et al.: Bayesian analysis of isothermal titration calorimetry for binding thermodynamics. *PLoS One* **13**, e0203224 (2018)



Change in Volume Upon Inhibitor Binding to Carbonic Anhydrases by Fluorescent Pressure Shift Assay

7

Gediminas Skvarnavičius, Daumantas Matulis,
and Vytautas Petrauskas

Abstract

High-pressure studies of protein–ligand system in aqueous solution provide volumetric information about the increase or decrease in compactness of the interacting counterparts. Volumetric parameters complement the thermodynamic picture of protein–ligand interaction. Here we describe fluorescent pressure shift assay—a technique that addresses volume-related parameters of protein–ligand system. Carbonic anhydrase (CA) and their ligands were useful objects that extended our knowledge about the applicability of this method.

7.1 Thermodynamic Parameters of Protein–Ligand Interaction

The majority of experimental techniques, which are dedicated to describe interactions between a protein and a ligand, exploit temperature as a thermodynamic variable. Gibbs energy (G) and enthalpy (H) are among the most used parameters in the field of macromolecule–ligand interaction. Although pressure is a rarely exploited thermodynamic variable, if compared to temperature, it addresses the protein–volume-related properties of protein–ligand system.

Energy of any reaction at equilibrium is evaluated using at least one thermodynamic function (parameter) listed in Fig. 7.1. This list establishes connections between various thermodynamic parameters and their derivatives. Only part of the listed parameters can be measured directly in experiments; others must be calculated. Without volume-related parameters, several connections in this thermo-

G. Skvarnavičius · D. Matulis · V. Petrauskas (✉)
Department of Biothermodynamics and Drug Design, Institute of Biotechnology,
Life Sciences Center, Vilnius University, Vilnius, Lithuania
e-mail: skvarnavicius@ibt.lt; matulis@ibt.lt; vytautas.petrauskas@bti.vu.lt

$$\begin{array}{rcccl}
 A \rightarrow & \begin{array}{l} \text{1st free energy derivative} \\ -\left(\frac{\partial(A/T)}{\partial T}\right)_p T^2 \\ \left(\frac{\partial A}{\partial T}\right)_v \\ \left(\frac{\partial G}{\partial T}\right)_p \\ \left(\frac{\partial G}{\partial p}\right)_T \end{array} & \begin{array}{l} \rightarrow \\ \searrow \\ \nearrow \\ \rightarrow \\ \searrow \\ \nearrow \end{array} & \begin{array}{l} U \rightarrow \\ -S \rightarrow \\ V \rightarrow \\ H \rightarrow \end{array} & \begin{array}{l} \text{2nd free energy derivative} \\ \left(\frac{\partial U}{\partial T}\right)_v \\ -T\left(\frac{\partial S}{\partial T}\right)_p \\ -\frac{1}{V}\left(\frac{\partial S}{\partial p}\right)_T \\ \frac{1}{V}\left(\frac{\partial V}{\partial T}\right)_p \\ -\frac{1}{V}\left(\frac{\partial V}{\partial p}\right)_T \\ \left(\frac{\partial H}{\partial T}\right)_p \end{array} & \begin{array}{l} \rightarrow \\ \rightarrow \\ \rightarrow \\ \rightarrow \\ \rightarrow \\ \rightarrow \\ \rightarrow \end{array} & \begin{array}{l} C_V \\ C_p \\ \alpha_V \\ \beta_T \\ C_p \end{array}
 \end{array}$$

Fig. 7.1 The derivative–integral relationships between thermodynamic parameters. A and G are Helmholtz and Gibbs energies, respectively, $Y = G/T$ —Planck function. The first derivatives of A , G , and Y yield internal energy (U), entropy (S), volume (V), and enthalpy (H) as indicated by the arrows. The only shown derivative by pressure yields the volume. The last column of thermodynamic parameters—the constant-volume and constant-pressure heat capacities (C_V and C_p), isochoric thermal expansion coefficient (α_V), and the isothermal compressibility factor (β_T)—is obtained by derivation of the second column thermodynamic parameters U , S , V , and H [1]

dynamic list would be missing. For example, the first pressure and temperature derivatives of volume are proportional to compressibility and thermal expansion coefficients, respectively. Full thermodynamic description of a biological reaction should include all these parameters. However, in many cases reactions are characterized solely by the Gibbs energy. We expect that volumetric information could improve the models that predict protein–ligand interaction energies.

7.2 Pressure is a Key to Protein Volumetric Properties

Researchers attribute the changes in protein volume upon unfolding to the change of its native conformation. This transition rearranges protein cavities, clefts, and subsequently the hydration shell. Many scientists dedicated their efforts to reveal structural and volumetric properties of proteins by denaturing in high-pressure environment [2–9].

A substantial change in volume is also related to protein–ligand binding [10–17]. The change in protein volume upon ligand binding is called protein–ligand binding volume (ΔV_b). In some literature sources ΔV_b was termed as reaction or interaction volume. The above definition of ΔV_b is not precise, because the hydration shells of protein and ligand have been ignored. Thus, the ΔV_b should be defined as the

$$V_{\{\text{hydrated P}\}} + V_{\{\text{hydrated L}\}} = V_{\{\text{hydrated PL}\}} + V_{\{\text{excess hydration}\}} + \Delta V_b$$

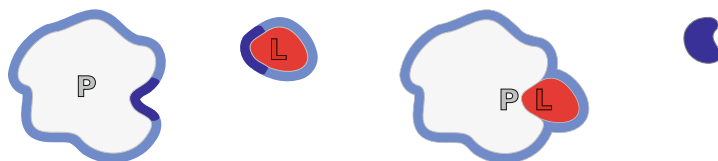


Fig. 7.2 Schematic representation of protein–ligand binding volume

difference between two sums of volumes: hydrated protein–ligand complex plus the excess hydration water molecules and the volumes of hydrated protein and ligand

$$\Delta V_b = (V_{\{\text{hydrated P-L}\}} + V_{\{\text{excess hydration}\}}) - (V_{\{\text{hydrated P}\}} + V_{\{\text{hydrated L}\}}). \quad (7.1)$$

Figure 7.2 sketches the graphical representation of the binding volume. The ΔV_b can be either positive or negative. The sign depends on whether protein–ligand complex together with its hydration shell occupies bigger or smaller volume than the unbound protein and ligand with their hydration shells. The absolute magnitude of ΔV_b for various proteins is comparable or even higher than the change in the unfolding volume [15].

Pressure affects both—unfolding and ligand-binding-induced—volume changes of proteins. Together with other physical and chemical perturbation methods, high-pressure studies complement our knowledge about protein–ligand interactions [10, 11, 18–22].

7.3 Carbonic Anhydrase Unfolding at Elevated Pressure

Proteins can lose their native conformation under high pressure. Both intrinsic—protein’s tryptophan and tyrosine residues—and extrinsic fluorescent probes can be used to monitor protein unfolding. If we consider only two protein states—native (N) and unfolded (U)—pressure-dependent fluorescence signal $f(p)$ is described by equation

$$f(p) = f_N + \frac{f_U - f_N}{1 + \exp(\Delta G_U/RT)}, \quad (7.2)$$

where ΔG_U is the change in Gibbs energy associated with pressure-induced protein unfolding, R —universal molar gas constant, and T —absolute temperature. Parameters f_N and f_U in Eq. (7.2) denote the experimental fluorescence yields for the native and unfolded protein states, respectively. The following equation describes the Gibbs energy as a function of pressure, p , at a constant temperature:

$$\Delta G_U = \Delta G_U^\circ + \Delta V_U^\circ(p - p_0) + \frac{\Delta\beta_U^\circ}{2}(p - p_0)^2. \quad (7.3)$$

ΔG_U° , ΔV_U° , and $\Delta\beta_U^\circ$ denote changes in the standard state thermodynamic parameters of protein unfolding—the Gibbs energy, volume, and compressibility factor, respectively [23, 24], and p_0 —initial pressure. By definition $\Delta G_U = 0$ at the midpoint of protein unfolding curve, i.e., when both native and unfolded protein concentrations are equal. The pressure value at this midpoint is referred to as the melting pressure, p_m [2, 10].

We used fluorescence intensity signals at a fixed wavelength ($\lambda = 332$ nm) to determine unfolding profiles of human heat shock protein 90 [13, 15, 17] and human serum albumin proteins [25]. However, for some isoforms of carbonic anhydrases, this technique can provide inaccurate melting pressures. Panels b, d, and f in Fig. 7.3 show unfolding profiles (also termed as melting curves) of CA I, CA II, and CA XIII proteins, respectively. Fluorescence intensity data, recorded at $\lambda = 332$ nm (solid triangles), provide unambiguous native-to-unfolded transition for CA II (Fig. 7.3d), but this transition is blurred for CA I and CA XIII isoforms (Fig. 7.3b and f).

The uncertainty of p_m values can be reduced if we monitor the native-to-unfolded transition following the shift of spectral mass center (abbreviated as CSM), which is defined as

$$\lambda_{\text{CSM}} = \frac{\sum_i f_i \lambda_i}{\sum_i f_i}. \quad (7.4)$$

Here f_i is the fluorescence intensity at a wavelength λ_i and the summation is over entire spectrum range [26, 27]. Panels a, c, and e in Fig. 7.3 show intrinsic tryptophan fluorescence spectra at pressures ranging from 0.1 MPa (atmospheric) to 380 MPa. At low pressures spectral maxima are concentrated at approximately 332 nm—dominating fluorescence emission wavelength of tryptophan in hydrophobic environment [28]. Increasing pressures start to unfold the protein, which is manifested by the shift of spectral maxima towards 353 nm—a tryptophan emission peak in polar environments [28]. These spectral shifts generate the unfolding profiles that are shown in Fig. 7.3b, d, and f as open-circle curves. Although it takes longer to measure the tryptophan fluorescence spectra than its intensity at a fixed wavelength, the CSM-based profiles provided unambiguous transition midpoints for all investigated CA isoforms [27]. Our data showed that fluorescence intensity measurements at a fixed wavelength can also be reliable (CA II case), but they are more sensitive to a particular spatial arrangement of fluorescent probes and could be blurred (CA I case) or even misleading (CA XIII case).

7.4 Protein–Ligand Binding Volume

Several experimental techniques have been used to determine the binding volumes of various protein–ligand and protein–protein systems: high-pressure NMR [17, 29, 30], vibrating tube densitometry [12, 16, 17, 31–33], and high-pressure fluorescence-based assays [13, 15, 17, 25, 27, 34–37]. Here we describe how to determine ΔV_b by following protein fluorescence at elevated pressures. We termed this technique

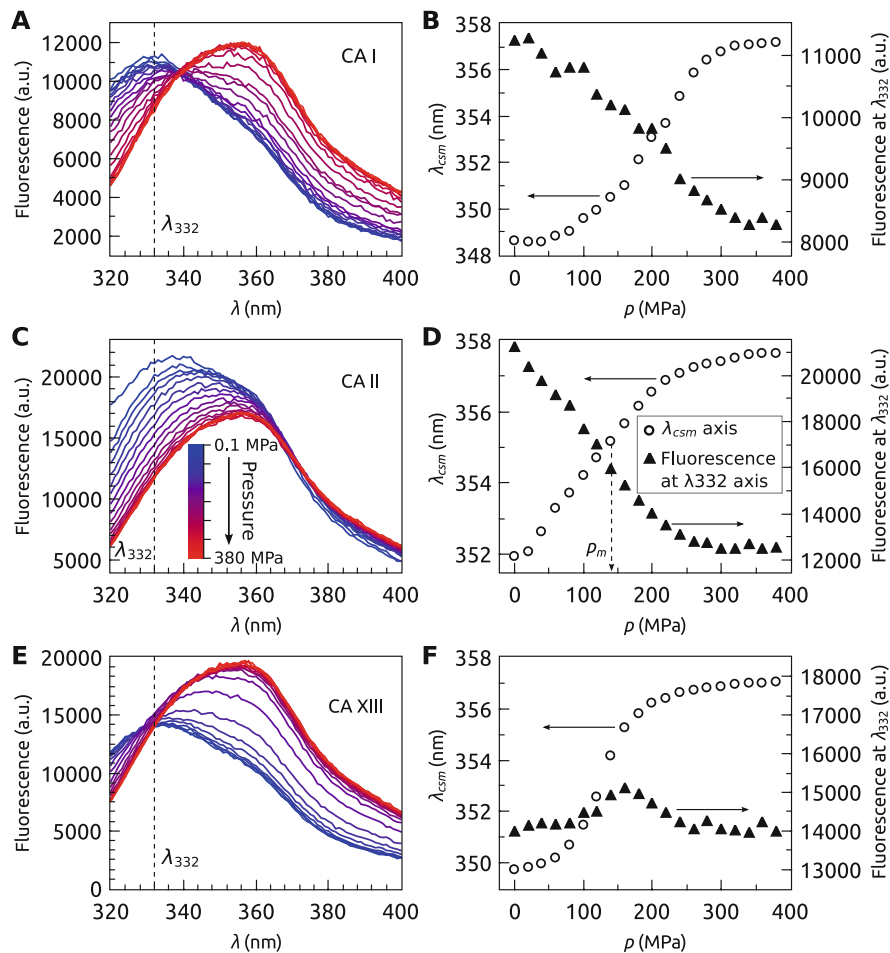


Fig. 7.3 Unfolding of carbonic anhydrase proteins at elevated pressures. Panels **a**, **c**, and **e**: intrinsic tryptophan fluorescence spectra of CA I, CA II, and CA XIII isoforms at pressures up to 380 MPa. Panels **b**, **d**, and **f**: pressure-induced unfolding profiles of CA I, CA II, and CA XIII obtained from fluorescence intensities at $\lambda = 332$ nm (solid triangles, right axis labels) and shifts of spectral mass centers (open circles, left axis labels)

fluorescent pressure shift assay (FPSA) and applied it to various protein–ligand systems, including several CA isoforms [1, 13, 15, 17, 25, 27].

As listed in Fig. 7.1, the change in volume upon ligand binding to protein is

$$\Delta V_b = \left(\frac{\partial \Delta G_b}{\partial p} \right)_T, \quad (7.5)$$

where ΔG_b is the change in standard Gibbs energy upon ligand binding to protein at constant temperature. If we consider only pressure as a thermodynamic variable, the ΔG_b is described similarly to ΔG_U in Eq. (7.3), but all unfolding-related

parameters are substituted with binding parameters: ΔG_b° , ΔV_b° , and $\Delta\beta_b^\circ$

$$\Delta G_b = \Delta G_b^\circ + \Delta V_b^\circ(p - p_0) + \frac{\Delta\beta_b^\circ}{2}(p - p_0)^2, \quad (7.6)$$

where $\Delta\beta_b^\circ$ is the isothermal compressibility change upon protein–ligand binding.

In drug design field scientists search for ligands that alter protein catalytic functions. Enzymatic activity determination techniques should be used to directly demonstrate the inhibition of activity. However, in many cases it is sufficient to test the protein stability against various denaturing factors upon addition of ligand. As previously mentioned, high pressure can unfold a protein, but the addition of binding compounds usually works in the opposite way—the inhibitors stabilize proteins and higher pressure is required to unfold them. If we measure the p_m at various concentrations of added ligand, we obtain a *dosing curve*—a relationship, which gives protein melting pressure as a function of added ligand concentration. Figure 7.4b shows an example of a dosing curve: the increased stability of CA II (increased values of its p_m) upon addition of acetazolamide (AZM).

Mathematical description of FPSA is similar to fluorescent thermal shift assay (FTSA), derived in Chap. 5. Here we provide a final system of equations that relates the concentration of added ligand ($[L]_t$) with the total protein concentration ($[P]_t$) and the melting pressure (p_m) [1]:

$$\left\{ \begin{array}{l} [L]_t = (K_U - 1) \left(\frac{1}{K_b} + \frac{[P]_t}{2K_U} \right), \\ K_U = \exp \left(-\frac{\Delta G_U^\circ + \Delta V_U^\circ(p_m - p_0) + \frac{\Delta\beta_U^\circ}{2}(p_m - p_0)^2}{RT} \right), \\ K_b = \exp \left(-\frac{\Delta G_b^\circ + \Delta V_b^\circ(p_m - p_0) + \frac{\Delta\beta_b^\circ}{2}(p_m - p_0)^2}{RT} \right). \end{array} \right. \quad (7.7)$$

These equations are used to fit the p_m versus ligand concentration data (Fig. 7.4b). The curve fitting reveals binding parameters—changes in the standard Gibbs energy, volume, and compressibility. Toleikis et al. described potential challenges and solutions of many-parameter models [17].

7.5 Protein Stability in the Pressure–Temperature Phase Diagram

Figure 7.4 allows to compare fluorescent pressure shift assay and fluorescent thermal shift assay techniques. FTSA exploits temperature to probe protein stability and is much more widely used than FPSA. Although both assays probe protein

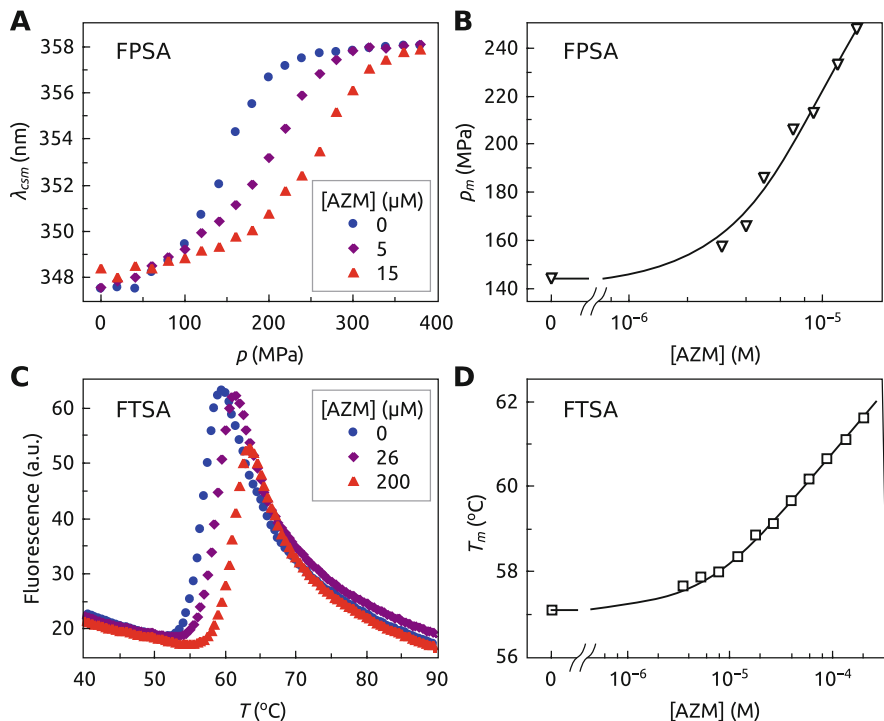


Fig. 7.4 Comparison between the fluorescent pressure shift assay (**a** and **b**) and fluorescent thermal shift assay (**c** and **d**). Panel **a** shows pressure-induced, while panel **c**—temperature-induced unfolding profiles of CA II at different concentrations of AZM. Resultant shift in p_m (**b**) and T_m (**d**) is fitted to the model and reveals the thermodynamic parameters of AZM binding to CA II

stability, their output complements each other and can be combined to obtain a protein stability diagram in both pressure and temperature coordinates. Hawley [23] described the Gibbs energy change between native and unfolded states with p and T variables by equation

$$\begin{aligned} \Delta G = & \Delta G_U^{\circ} + \Delta V_U^{\circ}(p - p_0) + \frac{\Delta\beta_U^{\circ}}{2}(p - p_0)^2 + \\ & + \Delta\alpha(p - p_0)(T - T_0) + \Delta H^{\circ} + \Delta C_p(T - T_0) \\ & - T \left(\Delta S^{\circ} + \Delta C_p \ln \frac{T}{T_0} \right), \end{aligned} \quad (7.8)$$

where T_0 is the reference temperature, ΔH° and ΔS° —changes in standard enthalpy and entropy at T_0 , ΔC_p and $\Delta\alpha$ —the changes in constant pressure heat capacity and thermal expansion coefficient. This equation yields an elliptical-shape curve (Fig. 7.5) also referred to as $p - T$ phase diagram [3]. Internal part of

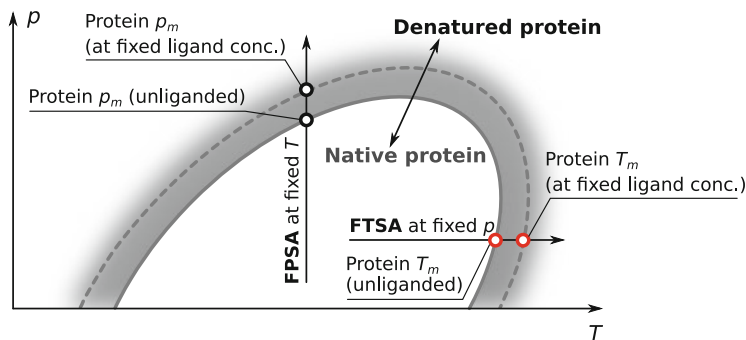


Fig. 7.5 The diagram of protein unfolding in pressure and temperature coordinates. Increased concentration of the ligand usually stabilizes the protein and shifts the native-to-unfolded boundary towards higher T_m and p_m values as determined by FTSA and FPSA

the ellipse corresponds to the native state protein while the outside area—the denatured (unfolded) state. Position of the transition boundary between the native and denatured states depends on the ligand concentration. The higher protein–ligand affinity, the bigger ellipse is obtained as illustrated by the gray area in Fig. 7.5. The dashed line corresponds to one particular concentration of added ligand.

Not all parts of the $p - T$ diagram are experimentally accessible. In FPSA we increase pressure at several constant temperatures to measure protein p_m values (vertical path in Fig. 7.5), while in FTSA we increase temperature at several fixed pressures to obtain the T_m s (horizontal path in Fig. 7.5). Although both temperature and pressure tend to unfold protein, the $p - T$ diagram reveals that at moderately elevated pressure a protein is more stable against thermal unfolding than at atmospheric pressure as observed for several globular proteins [15, 23]. Furthermore, a protein may withstand higher pressure at moderately elevated temperature.

In addition to heat denaturation temperature, proteins also have the cold denaturation temperature. It is usually in the range from $-70\text{ }^\circ\text{C}$ to $-20\text{ }^\circ\text{C}$, thus practically inaccessible due to freezing of aqueous solution. However, as predicted by the model (Eq. (7.8)), the cold denaturation temperature may be above $0\text{ }^\circ\text{C}$ at moderately elevated pressure.

7.6 Concluding Remarks

Experiments at high pressure reveal volumetric properties of protein unfolding and protein–ligand binding. Additional parameters—the changes in volume and compressibility of a protein–ligand system—complement the thermodynamic description of protein–ligand interactions. However, relatively low amount of data on volumetric properties still keep the question open whether the high-pressure approaches will find broader applications in drug design.

References

1. Petrauskas, V., Baranauskienė, L., Zubrienė, A., Matulis, D.: In: *Biocalorimetry*, pp. 261–280. CRC Press, Boca Raton (2016)
2. Zipp, A., Kauzmann, W.: Pressure denaturation of metmyoglobin. *Biochemistry* **12**, 4217–4228 (1973)
3. Heremans, K., Smeller, L.: Protein structure and dynamics at high pressure. *Biochim. Biophys. Acta Protein Struct. Mol. Enzymol.* **1386**, 353–370 (1998)
4. Royer, C.A.: Revisiting volume changes in pressure-induced protein unfolding. *Biochim. Biophys. Acta Protein Struct. Mol. Enzymol.* **1595**, 201–209 (2002)
5. Ribó, M., et al.: Pressure as a tool to study protein-unfolding/refolding processes: the case of ribonuclease A. *Biochim. Biophys. Acta, Proteins Proteomics* **1764**, 461–469 (2006)
6. Rouget, J.-B., et al.: Unique features of the folding landscape of a repeat protein revealed by pressure perturbation. *Biophys. J.* **98**, 2712–2721 (2010)
7. Roche, J., et al.: Cavities determine the pressure unfolding of proteins. *Proc. Natl. Acad. Sci. U. S. A.* **109**, 6945–6950 (2012)
8. Fossat, M.J., et al.: High-resolution mapping of a repeat protein folding free energy landscape. *Biophys. J.* **111**, 2368–2376 (2016)
9. Espada, R., Sánchez, I.E., Ferreira, D.U.: Detailing protein landscapes under pressure. *Biophys. J.* **111**, 2339–2341 (2016)
10. Li, T.M., Hook III, J.W., Drickamer, H.G., Weber, G.: Plurality of pressure-denatured forms in chymotrypsinogen and lysozyme. *Biochemistry* **15**, 5571–5580 (1976)
11. Chalikian, T.V.: Volumetric properties of proteins. *Annu. Rev. Biophys. Biomol. Struct.* **32**, 207–235 (2003)
12. Filfil, R., Chalikian, T.V.: Volumetric and spectroscopic characterizations of glucose–hexokinase association. *FEBS Lett.* **554**, 351–356 (2003)
13. Toleikis, Z., Cimmerman, P., Petrauskas, V., Matulis, D.: Determination of the volume changes induced by ligand binding to heat shock protein 90 using high-pressure denaturation. *Anal. Biochem.* **413**, 171–178 (2011)
14. Son, I., Shek, Y.L., Dubins, D.N., Chalikian, T.V.: Volumetric characterization of Tri- *N* -acetylglucosamine binding to lysozyme. *Biochemistry* **51**, 5784–5790 (2012)
15. Petrauskas, V., Gyltė, J., Toleikis, Z., Cimmerman, P., Matulis, D.: Volume of Hsp90 ligand binding and the unfolding phase diagram as a function of pressure and temperature. *Eur. Biophys. J.* **42**, 355–362 (2013)
16. Son, I., Selvaratnam, R., Dubins, D.N., Melacini, G., Chalikian, T.V.: Ultrasonic and densimetric characterization of the association of cyclic amp with the camp-binding domain of the exchange protein Epac1. *J. Phys. Chem. B* **117**, 10779–10784 (2013)
17. Toleikis, Z., et al.: Volume of Hsp90 protein–ligand binding determined by fluorescent pressure shift assay, densitometry, and NMR. *J. Phys. Chem. B* **120**, 9903–9912 (2016)
18. Chalikian, T.V., Breslauer, K.J.: On volume changes accompanying conformational transitions of biopolymers. *Biopolymers* **39**, 619–626 (1996)
19. Dellarole, M., et al.: Probing the physical determinants of thermal expansion of folded proteins. *J. Phys. Chem. B* **117**, 12742–12749 (2013)
20. Meersman, F., McMillan, P.F.: High hydrostatic pressure: a probing tool and a necessary parameter in biophysical chemistry. *Chem. Commun.* **50**, 766–775 (2014)
21. Luong, T.Q., Kapoor, S., Winter, R.: Pressure-A gateway to fundamental insights into protein solvation, dynamics, and function. *ChemPhysChem* **16**, 3555–3571 (2015)
22. Pandharipande, P.P., Makhatadze, G.I.: Applications of pressure perturbation calorimetry to study factors contributing to the volume changes upon protein unfolding. *Biochim. Biophys. Acta, Gen. Subj.* **1860**(5), 1036–1042 (2015)
23. Hawley, S.A.: Reversible pressure-temperature denaturation of chymotrypsinogen. *Biochemistry* **10**, 2436–2442 (1971)

24. Meersman, F., Smeller, L., Heremans, K.: Protein stability and dynamics in the pressure-temperature plane. *Biochim. Biophys. Acta, Proteins Proteomics* **1764**, 346–354 (2006)
25. Toleikis, Z., Cimperman, P., Petrauskas, V., Matulis, D.: Serum albumin ligand binding volumes using high pressure denaturation. *J. Chem. Thermodyn* **52**, 24–29 (2012)
26. Royer, C.A., Weber, G., Daly, T.J., Matthews, K.S.: Dissociation of the lactose repressor protein tetramer using high hydrostatic pressure. *Biochemistry* **25**, 8308–8315 (1986)
27. Skvarnavičius, G., et al.: High pressure spectrofluorimetry—a tool to determine protein-ligand binding volume. *J. Phys. Conf. Ser.* **950**, 042001 (2017)
28. Reshetnyak, Y.K., Burstein, E.A.: Decomposition of protein tryptophan fluorescence spectra into log-normal components. II. The statistical proof of discreteness of tryptophan classes in proteins. *Biophys. J.* **81**, 1710–1734 (2001)
29. Wilton, D.J., Kitahara, R., Akasaka, K., Pandya, M.J., Williamson, M.P.: Pressure-dependent structure changes in barnase on ligand binding reveal intermediate rate fluctuations. *Biophys. J.* **97**, 1482–1490 (2009)
30. Dellarole, M., Roumestand, C., Royer, C., Lecomte, J.T.J.: Volumetric properties underlying ligand binding in a monomeric hemoglobin: a high-pressure NMR study. *Biochim. Biophys. Acta, Proteins Proteomics* **1834**, 1910–1922 (2013)
31. Gekko, K., Yamagami, K.: Compressibility and volume changes of lysozyme due to inhibitor binding. *Chem. Lett.* **27**, 839–840 (1998)
32. Dubins, D.N., Filfil, R., Macgregor, R.B., Chalikian, T.V.: Role of water in protein-ligand interactions: volumetric characterization of the binding of 2'-Cmp and 3'-Cmp to ribonuclease A. *J. Phys. Chem. B* **104**, 390–401 (2000)
33. Barbosa, S., Taboada, P., Mosquera, V.: Protein-ligand interactions: volumetric and compressibility characterization of the binding of two anionic penicillins to human serum albumin. *Langmuir* **19**, 1446–1448 (2003)
34. Li, T.M., Hook, J.W., Drickamer, H.G., Weber, G.: Effects of pressure upon the fluorescence of the riboflavin binding protein and its flavin mononucleotide complex. *Biochemistry* **15**, 3205–3211 (1976)
35. Carey, F.G., Knowles, F., Gibson, Q.H.: Effect of hydrostatic pressure on ligand binding to hemoglobin. *J. Biol. Chem.* **252**, 4102–4107 (1977)
36. Torgerson, P.M., Drickamer, H.G., Weber, G.: Inclusion complexes of poly- β -cyclodextrin: a model for pressure effects upon ligand-protein complexes. *Biochemistry* **18**, 3079–3083 (1979)
37. Panick, G., et al.: Exploring the temperature-pressure phase diagram of staphylococcal nuclease. *Biochemistry* **38**, 4157–4164 (1999)



Observed Versus Intrinsic Thermodynamics of Inhibitor Binding to Carbonic Anhydrases

8

Asta Zubrienė and Daumantas Matulis

Abstract

When primary sulfonamide inhibitors bind to carbonic anhydrases, several reactions occur simultaneously. These binding-linked reactions significantly reduce the affinity of sulfonamides towards CAs. Therefore, we observe significantly lower binding constants in any assay, including SFA, FTSA, ITC, and SPR, than they are in reality. For the sulfonamide–CA interaction, the discrepancy in K_d may reach 1000 or even 1 million-fold. It is therefore very important to account for the linked reactions and distinguish between the *observed* and *intrinsic* thermodynamic parameters. Only the intrinsic binding parameters are meaningful in the structure–thermodynamics correlation analysis. In the literature we mostly see the analysis performed using the observed parameters. Such analysis may lead to erroneous assignment of the reasons for increased or decreased affinity due to manipulation with compound chemical structure. Examples of such incorrect assignments will be provided.

8.1 Introduction

Consider a case when a protein has two conformations, P, that is capable of binding a ligand and P*—not capable of binding the same ligand (Fig. 8.1). Furthermore, in solution at physiological conditions the conformation P* is highly dominant. The ligand will then bind only to P effectively depleting its concentration. Then P* will partially convert to P in order to retain equilibrium between P* and P. Newly available P will be able to again bind the ligand. Process will continue until all

A. Zubrienė · D. Matulis (✉)

Department of Biothermodynamics and Drug Design, Institute of Biotechnology, Life Sciences Center, Vilnius University, Vilnius, Lithuania
e-mail: astzu@ibt.lt; matulis@ibt.lt

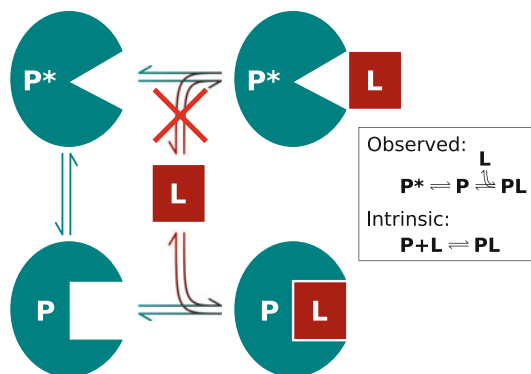


Fig. 8.1 If a protein P exists in two forms, P and P^* , and only P is capable of binding ligand L , then the *intrinsic* reaction is the binding between P and L , while the *observed* reaction is the sum of both the binding and the conversion reaction between P^* and P . If the P^* form is highly prevalent at experimental conditions, then the observed binding affinity will be weakened by the amount of energy needed for the conversion between P^* and P . If the P form is highly prevalent, then the observed and intrinsic energies will be equal

protein is converted to P and it is completely saturated by the ligand. The conversion may be invisible by an experimental technique and appear as if all of the protein bound ligand with a 1:1 stoichiometry.

However, the conversion between P^* and P may require quite a bit of energy and thus the observed K_d would be significantly different if the ligand binds the dominating form of the protein and no conversion would be needed for the binding to occur. In order to determine the influence and energetic contribution to the “real” intrinsic K_d , it is important to analyze these linked reactions and calculate the intrinsic $K_{d,int}$ that may not be possible to observe experimentally. However, we emphasize that it is essential to use the “real” $K_{d,int}$ when comparing various compounds and trying to draw correlations between their chemical structures and the thermodynamic parameters of their binding to protein targets.

When sulfonamide inhibitor binds to carbonic anhydrase, several binding-linked protonation–deprotonation reactions occur. These reactions significantly reduce sulfonamide affinity to CAs. Despite the fact that all biochemical and biophysical techniques such as stopped-flow assay of inhibition of CA enzymatic activity (SFA), fluorescent thermal shift assay (FTSA), and isothermal titration calorimetry (ITC) always determine the *observed* dissociation constants, the techniques could be used to dissect the linked protonation reactions from the sulfonamide ligand binding by performing the experiments at different pH in one buffer and in various buffers at the same pH.

The observed affinity of sulfonamide binding to CAs depends on pH and has a U-shape. The $K_{d,obs}$ strongly depends on pH, while the $K_{d,int}$ is independent of pH (Fig. 8.2). Furthermore, ITC measurements in the presence of different buffers also show linked protonation effects to the binding enthalpy. The determination of

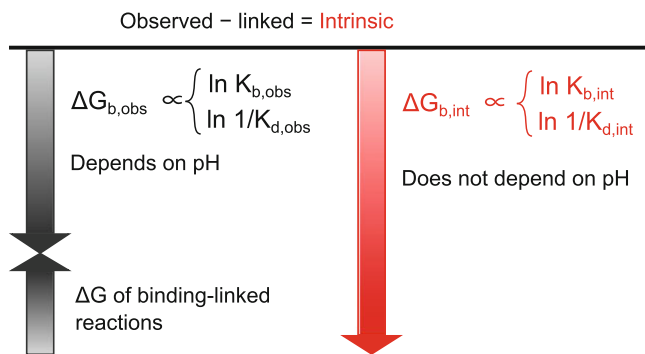


Fig. 8.2 Distinction between the *observed* and *intrinsic* Gibbs energy change upon binding. The standard *observed* Gibbs energy of a protein–ligand binding depends on experimental conditions such as pH if there are binding-linked protonation/deprotonation reactions. The standard *intrinsic* Gibbs energy of binding is obtained by summation of the energies from those linked reactions. The intrinsic energy is thus always greater than the observed. The same argument applies to all thermodynamic and kinetic parameters where the binding-linked protonation reactions occur. The figure is adapted from [1]

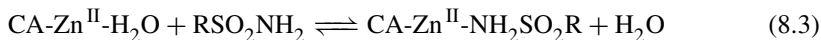
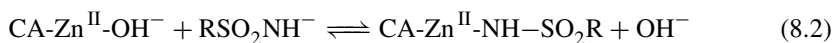
the enthalpies of protonation and pK_a s of both interacting partners enables the calculation of intrinsic binding enthalpies which represented the actual reaction between the sulfonamide anion and the Zn^{II} -bound water form of CA.

Since 1940, when Thaddeus Mann for the first time showed the inhibitory effect of p-aminobenzenesulfonamide (sulfanilamide) on the activity of CA [2], many compounds bearing primary sulfonamide group were synthesized as CA inhibitors. However, the mechanism of binding to CA remains uncertain. As first identified by Taylor et al. [3] in 1970, the association rate constants for complex formation between benzenesulfonamide derivative and human CA II are dependent on pH, whereas the dissociation rate constants are pH-independent.

Application of biophysical techniques such as FTSA, ITC, and SPR also showed that the binding affinity has U-shape dependence on pH and the binding is strongest near neutral pH. The affinity decreases exactly tenfold with one pH unit both in the acidic and alkaline regions. This indicates that the CA–sulfonamide binding reaction is linked to at least two protonation–deprotonation reactions.

There are four possible ways for the sulfonamide to bind the CA, shown in Eqs. (8.1)–(8.4). First possibility is that the electrostatically neutral (protonated) sulfonamide replaces the OH^- bound to the Zn^{II} in the active site of CA (Eq. (8.1)). Second, that the negatively charged (deprotonated) sulfonamide replaces the OH^- (Eq. (8.2)). Third, that neutral sulfonamide displaces water molecule (Eq. (8.3)), and the fourth, that the deprotonated sulfonamide (negatively charged SO_2NH^-) replaces the H_2O molecule coordinated by the Zn^{II} in the active site of CA (Eq. (8.4)). The second and third reactions have been already shown [3, 4] to be inconsistent with the U-shape dependence on pH. However, both the first and the

fourth reactions are thermodynamically indistinguishable.



Currently we think that only the fourth reaction (Eq. (8.4)) takes place when sulfonamides bind to a CA. The first indication that the deprotonated sulfonamide binds to the Zn-bound water form of CA was the spectral data on Co-containing CA enzyme [5]. The most unambiguous evidence came from the neutron-diffraction crystal structure of acetazolamide bound to CA II from McKenna laboratory [6] that directly demonstrated that the sulfonamide amino group is in its deprotonated form and the inhibitor is bound in the active site of CA II as an anion. The binding of other sulfonamides such as methazolamide, dorzolamide, ethoxzolamide, and brinzolamide to CA II in their deprotonated (anionic) form was confirmed later by the same group using neutron crystallography [7, 8]. Our thermodynamic and kinetic data is consistent with this conclusion. Based on neutron crystallography and thermodynamics we think that only the fourth reaction (Eq. (8.4)) takes place when sulfonamides bind to a CA (Fig. 8.3).

Reactions that occur upon sulfonamide binding to CA:

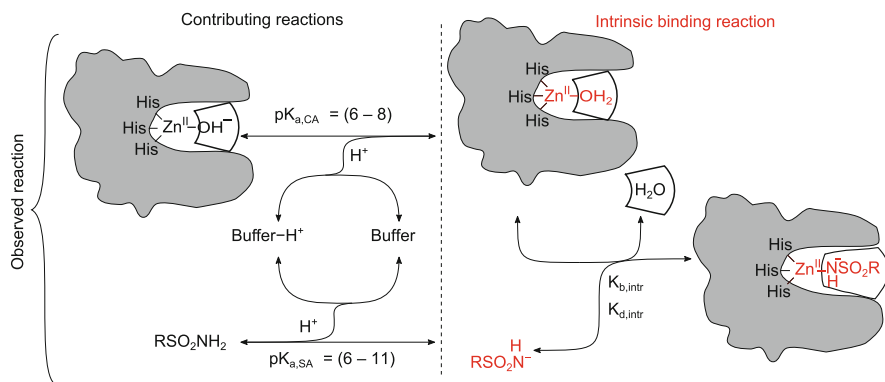
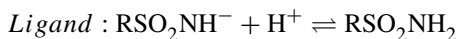
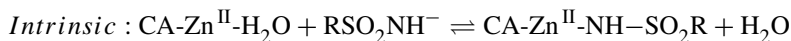
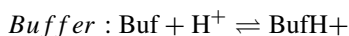


Fig. 8.3 The model of the linked protonation reactions (Eq. (8.5)), occurring in buffer solution upon sulfonamide binding to CA. The contributions from all linked reactions must be accounted to obtain the intrinsic reaction, representing sulfonamide anion binding to the Zn^{II}-bound water form of CA. The figure is adapted from [1]



Observed : Intrinsic + Ligand + Protein + Buffer

Most sulfonamides have $\text{p}K_a$ s between 8 and 11. Therefore, at neutral pH 7, they are almost fully protonated and only a small fraction is in the deprotonated form capable of binding CA. When the deprotonated form is depleted upon binding, additional sulfonamide deprotonates to keep the fraction unchanged. This additional fraction continues to bind the CA until the enzyme is fully saturated with the inhibitor.

The $\text{p}K_a$ of the Zn^{II} -bound water in the active site of human CA isoforms is between 6 and 8 (Table 8.1). Thus, approximately half of CA is in its protonated form capable of binding the sulfonamide anion. However, similarly to how this works for the ligand, the CA is also fully saturated by depleting the deprotonated form. The protein uptakes protons, while the ligand releases them, but non-equal amounts. The remaining protons are absorbed or released by the buffer.

8.2 Intrinsic Binding Affinity

To calculate the intrinsic affinity, we first estimate the fraction of deprotonated sulfonamide that depends on the sulfonamide amino group $\text{p}K_{a,SA}$ and is calculated using Eq. (8.6):

$$f_{\text{RSO}_2\text{NH}^-} = \frac{10^{\text{pH}-\text{p}K_{a,SA}}}{1 + 10^{\text{pH}-\text{p}K_{a,SA}}} \quad (8.6)$$

The fraction of Zn^{II} -bound water form of CA depends on pH and the $\text{p}K_{a,CA}$ of the water molecule bound to Zn ion in the active site is calculated using Eq. (8.7):

$$f_{\text{CAZnH}_2\text{O}} = \frac{10^{\text{p}K_{a,CA}-\text{pH}}}{1 + 10^{\text{p}K_{a,CA}-\text{pH}}} \quad (8.7)$$

The observed affinity of binding depends on the fractions of both binding partners in their active forms. The intrinsic $K_{b,int}$ is calculated using Eq. (8.8):

$$K_{b,int} = \frac{K_{b,obs}}{f_{\text{CAZnH}_2\text{O}} \times f_{\text{RSO}_2\text{NH}^-}} \quad (8.8)$$

In turn, the intrinsic Gibbs energy change upon binding is calculated using Eq. (8.9):

$$\Delta G_{int} = -RT \ln(K_{b,int}) \quad (8.9)$$

Table 8.1 Standard thermodynamic parameters of protonation of CA-Zn^{II}-bound OH⁻ for twelve catalytically active human CA isoforms

CA isoform	p <i>K</i> _{a,CA}	p <i>K</i> _{a,CA}		$\Delta G_{pr,CA}$ (kJ mol ⁻¹)		$\Delta H_{pr,CA}$ (kJ mol ⁻¹)		$T\Delta S_{pr,CA}$ (kJ mol ⁻¹)	
		25 °C	37 °C	25 °C	37 °C	25 °C	37 °C	25 °C	37 °C
Method	Inhibition	FTSA, ITC							
CA I [9]	8.1 [10]	8.4 ± 0.2	8.1	-47.9	-48.2	-41.0	-38.5	6.9	9.7
	6.9 [11]								
	7.1 [12]								
	7.3 [13, 14]								
CA II [9]	6.9 [15, 16]	7.1	6.9	-40.5	-41.1	-26.0	-23.5	14.5	17.6
	7.1 [11]								
	6.8 [17]								
CA III	5 [17]	6.6	6.5	-37.7	-38.6	ND	ND	ND	ND
	5 [18, 19]								
	<6 [20]								
<i>E. coli</i> CA IV [21]	6.2 [22]	6.8	6.6	-38.8	-39.0	-33.0	-30.5	5.8	8.5
Murine CA IV	6.6 [23]								
CA VA		7.3	7.3	-41.7	-43.3	ND	ND	ND	ND
CA VB [24]		7.2	7.0	-41.1	-41.5	-30.0	-27.5	11.1	14.0
<i>E. coli</i> CA VI [25]		6.2	6.0	-35.4	-35.6	-32.0	-29.0	3.4	6.6
Saliva CA VI [25]		5.5		-31.4					
Mammalian CA VI [25]		5.5		-31.4					
CA VII [26]		7.0	6.8	-40.0	-40.2	-33.0	-30.5	7.0	9.7
Murine CA VII	6.2[27]								
CA IX [28]	6.3[29]	6.8	6.6	-38.8	-39.4	-24.0	-21.5	14.8	17.9
CA IX (catalytic domain)	7.01[11]								
CA IX (full length)	6.49[11]								
CA XII [30]	7.1[31]	7.0	6.8	-40.0	-40.4	-28.0	-25.5	12.0	14.9
CA XII	6.9[11]								
CA XIII [32]		8.3	8.0	-47.4	-47.5	-44.0	-41.5	3.4	6.0
CA XIV [33]	6.92[11]	6.8	6.8	-38.8	-40.4	ND	ND	ND	ND

The p*K*_as determined by various methods and taken from earlier literature are listed in the second column together with the references. The values determined by FTSA and ITC by our group are listed in the following columns with the references in the first column next to the CA isoforms. The uncertainty of the p*K*_a values determined by FTSA and ITC is up to 0.2 pH units, while for the change in Gibbs energies and enthalpies it is up to 2 kJ mol⁻¹. ND not determined

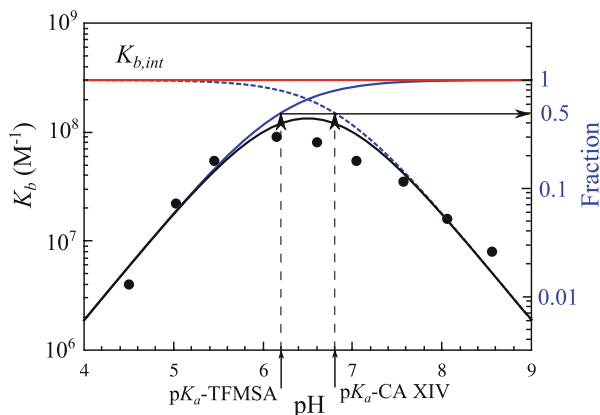


Fig. 8.4 Relationship between the intrinsic (independent of pH, shown as horizontal red line) and observed affinities (filled circles fit by the solid line of overturned U-shape) of TFMSA binding to CA XIV. The observed affinity is lower both at acidic and alkaline pHs due to smaller fractions of available binding-ready species (negatively charged sulfonamide, shown as blue line, and CA, bearing the neutral water molecule, shown as a dotted blue line). The blue lines correspond to the fractions shown on the right axis of the plot. The fractions are equal to half (0.5 or 50%) when the pH is equal to the corresponding pK_a s

The intrinsic and observed affinities are shown in Fig. 8.4. The intrinsic affinity is independent of pH, but since there is an increasingly smaller fraction of each interacting component at acidic and alkaline pH, energy is needed to overcome this linked reaction and therefore the observed affinity is smaller at both the acidic and alkaline pH. Note that the observed affinity does not reach the intrinsic value at any pH, though get quite close at near-neutral pH.

The change in the standard Gibbs energy of ligand binding dependence on pH has a U-shape, similar to the K_d , but upside down as K_b . Figure 8.5 shows that the U-shapes are obtained for all catalytically active human CAs. All experimental techniques (FTSA, ITC, and SPR) yield the U-shaped inhibitor binding Gibbs energy dependence on pH. In all cases the affinity is strongest in near-neutral pH range and decreases in both directions. The observed affinity comes closest to the intrinsic value at near-neutral pH, but usually does not reach it and thus is almost never observed experimentally.

8.3 Intrinsic Enthalpy of Binding

The change in the standard *observed* enthalpy upon binding, similarly to ΔG , has contributions from all binding-linked processes, including inhibitor deprotonation, protonation of the CA-bound OH^- , minus the compensating buffer effects (8.10):

$$\Delta H_{obs} = \Delta H_{int} + n_{SA} \Delta H_{pr,SA} + n_{CA} \Delta H_{pr,CA} - n_{buf} \Delta H_{pr,buf} \quad (8.10)$$

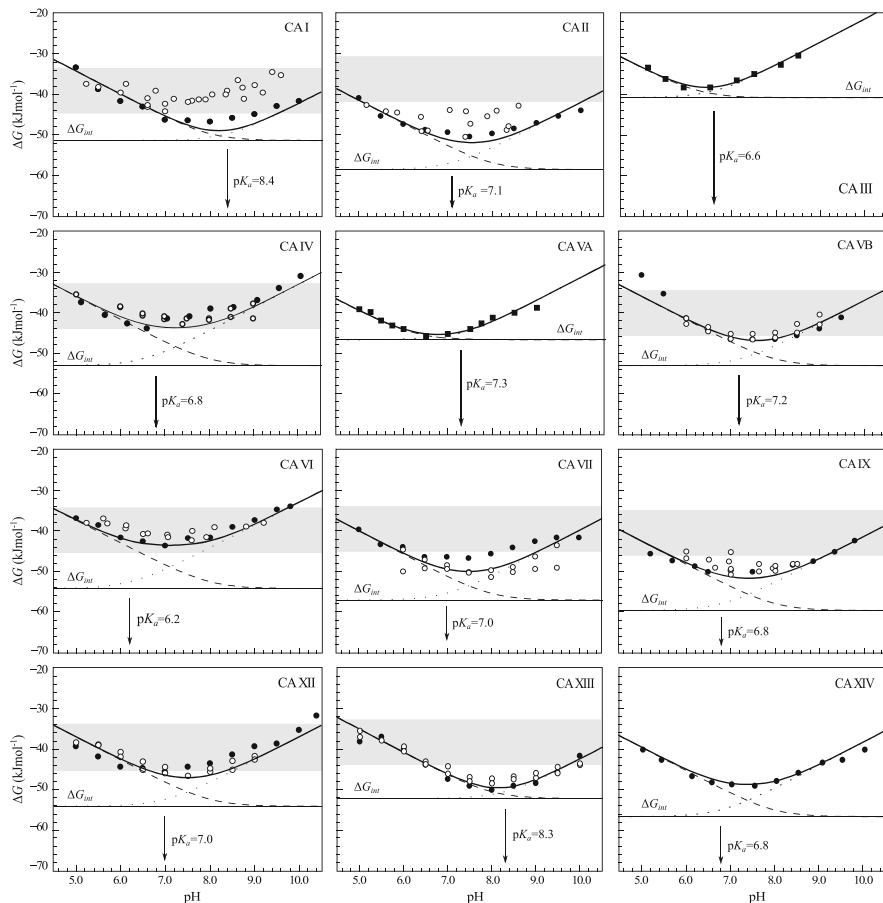


Fig. 8.5 Plots of ΔG_{obs} dependence on pH determined by FTSA (filled circles) and ITC (open circles) at 25 °C. Circles show the binding of EZA and squares of TFMSA (to CA III and CA VA). Solid curve is a fit to the model, solid line is the intrinsic standard Gibbs energy change upon binding, dashed line is a fraction of ligand, dotted line is a fraction of protein, and gray zone shows the 5–500 range of c -value (Wiseman factor). Experiments were performed in universal buffer made of 50 mM sodium phosphate, 50 mM sodium acetate, and 25 mM sodium borate containing 100 mM NaCl and up to 2 % DMSO as previously described in: CA I and CA II [9], CA IV [21], CA VB [24], CA VI [25], CA VII [26], CA IX [28], CA XII [30], CA XIII [32], and CA XIV [33]. All panels are drawn at the same scale to help visualize the differences in affinities of binding. The figure is adapted from [1]

Therefore, to get the change in *intrinsic* enthalpy of binding, it is necessary to subtract all linked processes from the observed reaction as shown in Eq. (8.11):

$$\Delta H_{int} = \Delta H_{obs} - n_{SA} \Delta H_{pr,SA} - n_{CA} \Delta H_{pr,CA} + n_{buf} \Delta H_{pr,buf} \quad (8.11)$$

where ΔH_{obs} —the observed enthalpy of binding obtained by direct ITC titration, $\Delta H_{pr,SA}$ —the enthalpy of protonation of deprotonated sulfonamide inhibitor, $\Delta H_{pr,CA}$ —the enthalpy of protonation of the CA-bound OH^- , and $\Delta H_{pr,buf}$ —the enthalpy of buffer protonation. The n_s denote the numbers of protons uptaken or released:

$$n_{SA} = f_{\text{RSO}_2\text{NH}^-} - 1 \quad (8.12)$$

is the number of protons released from the inhibitor to buffer ($n_{inh} = -1$ to 0),

$$n_{CA} = 1 - f_{\text{CAZnH}_2\text{O}} \quad (8.13)$$

is the number of protons uptaken by the CA-bound OH^- ($n_{CA} = 0$ to 1), and

$$n_{buf} = n_{SA} + n_{CA} \quad (8.14)$$

is the *net* number of protons uptaken by the buffer both from the ligand and protein or released by the buffer to the ligand or protein ($n_{buf} = -1$ to 1).

If we perform sulfonamide–CA ITC titrations in various buffers at various pHs as shown in Fig. 8.6, the observed enthalpies will depend both on the buffer and on the pH. X-shape dependence is obtained when plotting the observed enthalpies as a function of pH as shown in Fig. 8.7. At low pH, the observed enthalpies (ΔH_{obs}) in phosphate buffer are low in magnitude, while in TRIS—significantly more exothermic. The difference between the observed enthalpies is equal to the difference between the enthalpies of protonation of the two buffers. The enthalpy

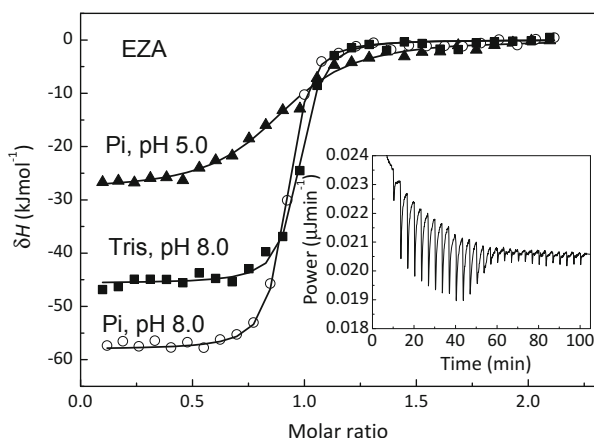


Fig. 8.6 ITC data of EZA binding to CA XII in TRIS and phosphate buffers at several pHs at 25 °C. The *observed* enthalpies of binding, directly determined from each ITC curve, depended both on the buffer and on buffer pH. The inset shows ITC raw data curve of EZA binding in TRIS buffer at pH 8.0

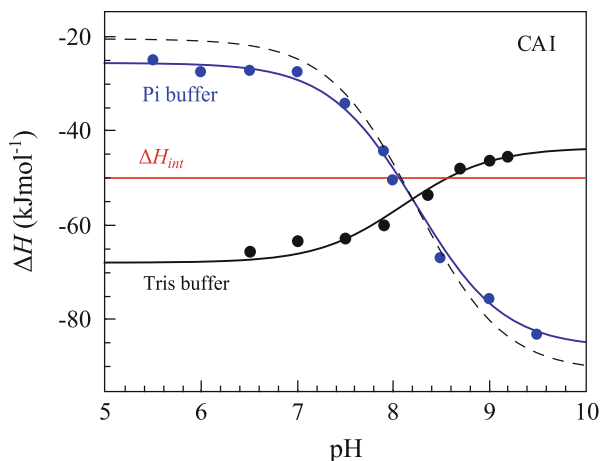


Fig. 8.7 The plot of enthalpies obtained by ITC of EZA binding to CAI in sodium phosphate or TRIS chloride buffer as a function of pH at 25 °C. Blue datapoints show the ΔH_{obs} in phosphate buffer, while black in TRIS. Solid black and blue lines are global fits to the above described model (fit in the way where the pK_a s are consistent with the FTSA data for each isoform) yielding the intrinsic enthalpy of binding (ΔH_{int} , red line) that is independent of pH. Dashed line shows a situation how the observed enthalpy dependence should look if a hypothetical buffer was used whose enthalpy of protonation was equal to zero

of protonation of TRIS base is $-47.45 \text{ kJ mol}^{-1}$ and of HPO_4^{2-} is -5.1 kJ mol^{-1} at 25 °C [34].

In the alkaline region, situation is reversed—the enthalpies in phosphate are much more exothermic, while in TRIS—less exothermic. The red solid line shows the position of the intrinsic enthalpy (ΔH_{int}) of EZA binding to CAI. The intrinsic enthalpy is independent of pH. The dashed line shows a hypothetical situation for the observed enthalpy dependence on pH if the buffer had enthalpy of protonation equal to zero ($\Delta H_{pr,buf} = 0$). The difference between the dashed line and the intrinsic enthalpy in the acidic region is equal to the enthalpy of inhibitor protonation ($\Delta H_{pr,SA}$), while in the alkaline region—to the enthalpy of protonation of the CA-bound OH^- ($\Delta H_{pr,CA}$).

The same procedure has been performed for every purified CA isoform and the data is shown in Fig. 8.8. All of the 9 isoforms where data has been obtained exhibited similar X-shaped curves, but since the protein pK_a s were slightly different and the intrinsic enthalpies of binding also varied among isoforms, slightly different curves are obtained. It should be noted that despite significant efforts to achieve high precision, there were discrepancies between the observed data and the model curves, especially at the acidic and alkaline pH. We assume that these discrepancies were due to protein destabilization.

Most researchers have based the choosing of the lead compound for development on the *observed* parameters, primarily observed affinity, but also observed enthalpy. It may seem that it is sufficient to experimentally determine compound affinities at

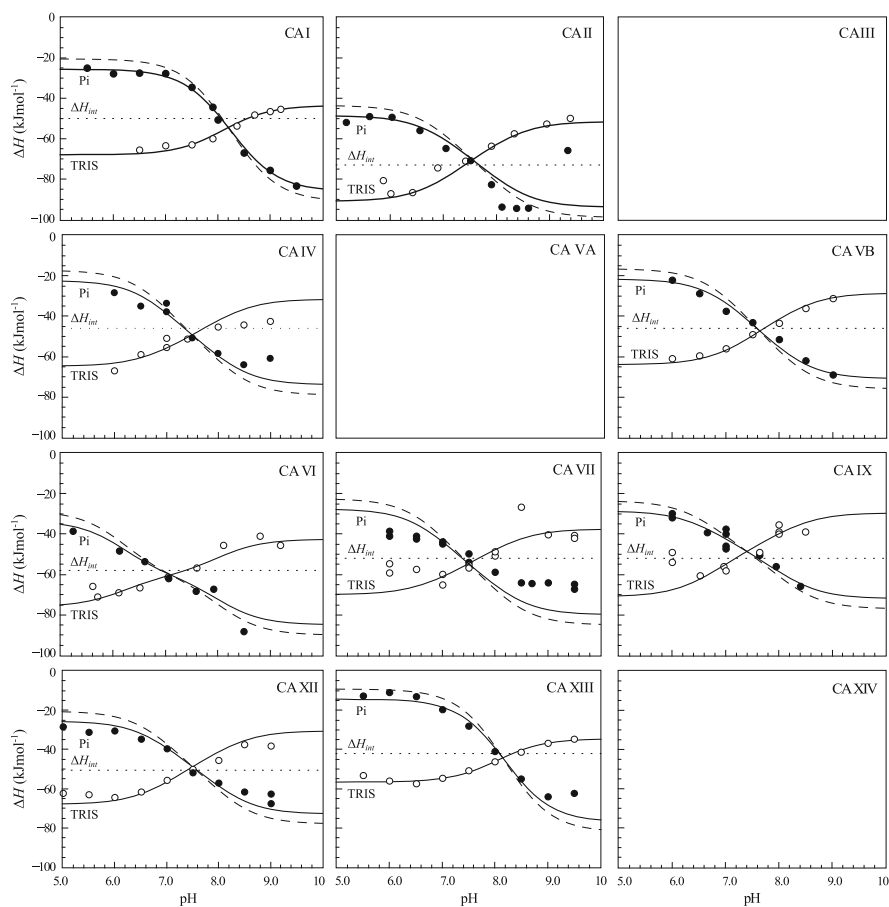


Fig. 8.8 ITC data of EZA binding to CA isoforms at 25 °C. Filled circles— ΔH_{obs} determined in sodium phosphate buffer, open circles— ΔH_{obs} determined in TRIS buffer, dotted line shows value of ΔH_{int} of EZA binding, solid curves are fits of experimental data, while the dashed curve is a fit of a hypothetical situation if there were no buffer or the enthalpy of buffer protonation ($\Delta H_{pr,buf}$) was equal to zero. The fits were global together with the FTSA U-shapes keeping the sulfonamide and CA pK_a s the same. Experiments were performed in either 50 mM sodium phosphate or 50 mM TRIS chloride buffer containing 100 mM NaCl and up to 2% DMSO as previously described in: CAI and CAII [9], CAIV [21], CA VB [24], CA VII [25], CA IX [28], CA XII [30], and CA XIII [32]. All panels are drawn at the same scale to help visualize the differences in the standard observed and intrinsic enthalpies upon binding. No data has been determined at comparable conditions for CA III, CA VA, and CA XIV. The overall pattern of the X-shapes is similar, but details are different due to different $pK_{a,CA}$ and ΔH_{int} for each isoform. The figure is taken from [1]

physiologically relevant conditions. One may be interested in the affinities observed at pH 7.4. It may seem that it is most relevant to correlate the compound chemical structures with the binding data obtained at such pH.

However, this is only partially true and may lead to erroneous conclusions. For example, if the binding affinities of two compounds are compared where the compounds have highly different pK_a s (e.g., 8 and 11), then if the compound with the pK_a 8 is 1000-fold stronger binder than the compound with pK_a 11, one may assume that the first compound is better attached to the CA. This conclusion is incorrect because the higher observed affinity is entirely explained by the difference in the pK_a s and both compounds would exhibit identical intrinsic affinity.

The observed enthalpies are even much less informative than affinities. Only the intrinsic enthalpy change describes the interaction. Buffer, ligand, and protein contributions may be so large that they may overwhelm the enthalpy data and the compounds would thus be ranked in a completely wrong order. Therefore, it is essential to determine the mechanism and calculate intrinsic enthalpies to rank compounds in the order of increasingly exothermic enthalpy.

8.4 Protonation pK_a and Enthalpy of CA-Zn^{II}-OH⁻ of 12 Human CA Isoforms

It is not possible to determine the pK_a and the enthalpy of protonation of the CA Zn^{II}-bound hydroxide/water molecule in the active site of CA isoform by a direct ITC titration. Differently from the compounds, it is not possible to pH-titrate the protein and record with spectrophotometer or titration calorimeter. In order to determine the pK_a , researchers have measured the pH dependence of CA activity inhibition or replaced Zn with Co that exhibited visible spectral changes upon the change in pH. However, it is disputable to what extent such non-natural Co-containing CA represents the native CA.

We determined the pK_a s of all 12 CA isoforms by fitting the inhibitor affinities at various pHs as explained earlier in the discussion of U-shaped plots. The enthalpies of protonation were determined via the global fit of the X-shaped curves obtained by ITC titrations in two buffers. Both the pK_a and the enthalpy of protonation had to be obtained only once with one inhibitor and then can be applied for other inhibitors to obtain the intrinsic energetics of binding to the CA isoform. The thermodynamic parameters of protonation of the hydroxide anion bound to catalytically active CA isoforms are summarized in Table 8.1.

The pK_a s of human CAs that have been determined previously by other research groups using numerous spectroscopic and inhibition techniques are listed in Table 8.1. Their values span between approximately 5.0 and 8.1. The values determined by us using FTSA and ITC were close. However, there were several outliers of up to 1 pK_a unit. It seems that CA I and CA XIII have rather high pK_a s, above 8.0. Remaining ones are essentially the same as determined previously. The standard deviation of combined FTSA and ITC determinations in the pH dependencies described above did not exceed 0.2 pH or pK_a units. This accuracy was highly dependent on proper calibration of the pH-meters and standard buffer preparations. The Gibbs energy changes of protonation were recalculated according to Eq. (8.9). The enthalpies were obtained via the global fit of ITC titrations of each

CA isoform with EZA at a series of pH as explained above. The entropies were obtained by subtracting the Gibbs energy changes from enthalpies:

$$\Delta S_{pr,CA} = (\Delta H_{pr,CA} - \Delta G_{pr,CA})/T \quad (8.15)$$

The entropy values carry a largest standard deviation, a sum of deviations of the enthalpy and Gibbs energy.

8.5 Determination of pK_a and the Change of Protonation Enthalpy of Ligand Sulfonamide Group

If we would like to calculate the intrinsic affinity of sulfonamide inhibitor binding to CA, it is necessary to determine its pK_a . Sulfonamide inhibitor amino group usually deprotonates with a pK_a between 6 and 11. Actual value depends on the chemical structure of the compound, especially the presence of electron-withdrawing and donating groups, the size of the aromatic conjugated system, and other factors.

The pK_a of the sulfonamide can be determined by preparing the compound solution in a series of buffers and recording the UV spectrum of the solution at each pH [35]. The spectrum changes at pH around the pK_a and it is easy to find the wavelengths of a largest change (Fig. 8.9a). The absorbance values at those pH are then plotted as a function of pH and normalized to unit as shown in Fig. 8.9b.

The enthalpies of sulfonamide amino group protonation may be determined by titrating the compound solution with acid in an ITC calorimeter at a constant temperature. The compound in a solid pure form exists as a protonated electrostatically neutral sulfonamide. Therefore, it must be deprotonated by applying sufficient amount of base to achieve the pH sufficiently above the pK_a for accurate determination. We usually apply 50% surplus of base and therefore the resultant ITC curves appear as two-step ITC reactions (Fig. 8.9c). Titration of such solution with a strong acid, such as HNO_3 , provides direct measurement of the enthalpy of protonation as shown in Fig. 8.9d.

8.6 Importance of the Correlation of Compound Structure with Intrinsic Binding Thermodynamics

Most of the studies examining sulfonamide binding to CAs discuss only the experimentally observed binding parameters without the dissection of binding-linked protonation effects. In structure–activity relationship analysis only intrinsic binding parameters provide valuable information about the nature of protein–ligand recognition. The calculated intrinsic thermodynamic parameters for the binding of sulfonamide anion with the $\text{Zn}^{\text{II}}\text{-H}_2\text{O}$ form of CA allow determination of the contributions of particular atoms or compound functional groups to the binding energetics. In some cases, when studied ligands are very similar and induce the same change in their protonation states (the same enthalpy of protonation and pK_a

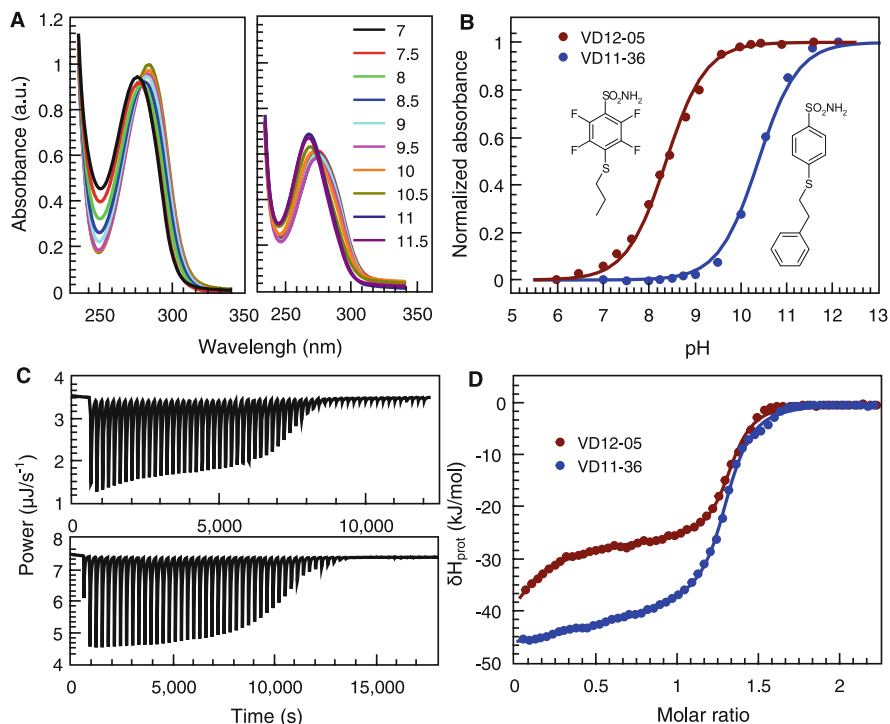


Fig. 8.9 Determination of the $pK_{a,SA}$ and enthalpy of protonation ($\Delta H_{pr,SA}$) of the sulfonamide amino group. Panels **a** and **b** show the spectrophotometric, while **c** and **d**—ITC data. (**a**) UV–Vis spectra of compounds VD12-05 (left) and VD11-36 (right) solution in buffers of various pH. (**b**) The normalized absorbance change at a ratio of values at two wavelengths. (**c**) ITC raw data of titrating an alkaline (added 1.5 equiv.) sulfonamide with HNO_3 . (**d**) Integrated ITC curves of the alkaline sulfonamide with acid

of the series of ligands), the observed binding parameters can be used for a relative comparison [36]. In such cases, the binding-linked effects will be similar and in a relative comparison across the series of ligands the protonation contributions will cancel. It should be kept in mind that only relative changes of observed binding parameters will be of value in such case, and not their absolute values.

Figure 8.10 shows the observed and intrinsic K_d s for a series of sulfonamides binding to human recombinant CA VI (produced from *E. coli*). The compounds were arranged in the order of increasing intrinsic $K_{d,int}$. The binding data shows that there is no correlation between the observed and intrinsic binding affinities. The $K_{d,obs}$ for compounds VD12-10 and VD10-21a were almost the same, but the intrinsic affinities differed by more than 300-fold. Not knowing the intrinsic values would yield completely wrong conclusions about the structural determinants of the compounds that cause the affinity to be greater or smaller.

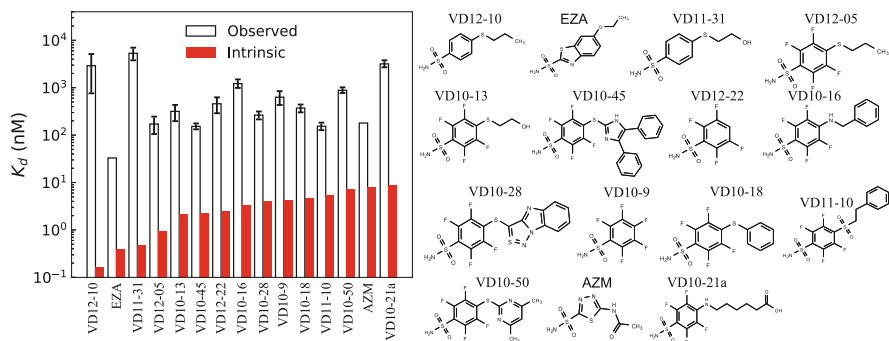


Fig. 8.10 Comparison of the observed and intrinsic K_d of a series of sulfonamide compound interaction with CA VI [25]. The observed $K_{d,obs}$ values for the ligand binding to the recombinant CA VI produced from *Escherichia coli* were determined by FTSA at pH 7.0. Data are presented with average standard deviation (SD) of three independent experiments

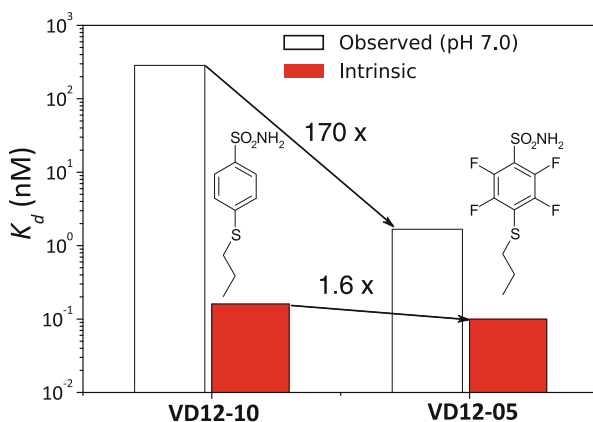


Fig. 8.11 The observed and intrinsic K_d of two benzenesulfonamide interaction with CA XIII. The compounds differ only in four fluorines on the benzene ring. The $K_{d,obs}$ for fluorine bearing compound VD12-05 was 150-times lower than for non-fluorinated compound VD12-10. Fluorines significantly reduced the pK_a of benzenesulfonamide and therefore $K_{d,obs}$ was lower than for non-fluorinated compound. The intrinsic affinities were practically the same for both compounds indicating that the recognition of fluorine and hydrogen atoms by the protein surface is similar

Another example (Fig. 8.11) shows a different situation from Fig. 8.10 when the observed binding constants for two compounds are quite different, but the intrinsic ones are nearly the same. From the $K_{d,obs}$ one can expect that fluorines would make favorable contacts with the protein because the $K_{d,obs}$ decreases by 170-fold upon fluorination of VD12-10. However, the reduction of $K_{d,obs}$ is due to the higher fraction of fluorinated compound VD12-05 in deprotonated form than VD12-10. Fluorines as electron-withdrawing substituents decrease the pK_a of the compound and contribute favorably to the observed binding affinity for CA. However, similar

intrinsic affinities of both compounds revealed no impact of fluorines on protein recognition.

8.7 Conclusions

Protein–ligand binding may be linked to various reactions such as conformational changes or protonations. Upon sulfonamide inhibitor binding to CA, the sulfonamide amino group must deprotonate and the OH^- bound to the Zn^{II} of CA must protonate. Only then the inhibitor will bind the CA. These linked reactions strongly affect both the affinity and the enthalpy of binding and should be accounted for by subtraction from the experimentally observed values in order to obtain the intrinsic values that can be used for structure–thermodynamics correlations in the design of compounds with improved binding capabilities.

References

1. Linkuvienė, V., et al.: Thermodynamic, kinetic, and structural parameterization of human carbonic anhydrase interactions toward enhanced inhibitor design. *Q. Rev. Biophys.* **51**, 1–48 (2018)
2. Mann, T., Keilin, D.: Sulphanilamide as a specific inhibitor of carbonic anhydrase. *Nature* **146**, 164–165 (1940)
3. Taylor, P.W., King, R.W., Burgen, A.S.V.: Influence of pH on the kinetics of complex formation between aromatic sulfonamides and human carbonic anhydrase. *Biochemistry* **9**, 3894–3902 (1970)
4. Krishnamurthy, V.M., et al.: Carbonic anhydrase as a model for biophysical and physical-organic studies of proteins and protein-ligand binding. *Chem. Rev.* **108**, 946–1051 (2008)
5. Engberg, P., Lindskog, S.: Effects of pH and inhibitors on the absorption spectrum of cobalt(II)-substituted carbonic anhydrase III from bovine skeletal muscle. *FEBS Lett.* **170**, 326–330 (1984)
6. Fisher, S.Z., Aggarwal, M., Kovalevsky, A.Y., Silverman, D.N., McKenna, R.: Neutron diffraction of acetazolamide-bound human carbonic anhydrase II reveals atomic details of drug binding. *J. Am. Chem. Soc.* **134**PDB ID: 4G0C, 14726–14729 (2012)
7. Kovalevsky, A., et al.: “To Be or Not to Be” Protonated: atomic details of human carbonic anhydrase-clinical drug complexes by neutron crystallography and simulation. *Structure* **26**, 383–390 (2018)
8. Aggarwal, M., et al.: Neutron structure of human carbonic anhydrase II in complex with methazolamide: mapping the solvent and hydrogen-bonding patterns of an effective clinical drug. *IUCrJ* **3**, 319–325 (2016)
9. Morkūnaitė, V., et al.: Intrinsic thermodynamics of sulfonamide inhibitor binding to human carbonic anhydrases I and II. *J. Enzyme Inhib. Med. Chem.* **30**, 204–211 (2015)
10. Coleman, J.E.: Mechanism of action of carbonic anhydrase substrate, sulfonamide, and anion binding. *J. Biol. Chem.* **242**, 5212–5219 (1967)
11. Innocenti, A., et al.: The proteoglycan region of the tumor-associated carbonic anhydrase isoform IX acts as an intrinsic buffer optimizing CO_2 hydration at acidic pH values characteristic of solid tumors. *Bioorg. Med. Chem. Lett.* **19**, 5825–5828 (2009)
12. Engstrand, C., Jonsson, B.-H., Lindskog, S.: Catalytic and inhibitor-binding properties of some active-site mutants of human carbonic anhydrase I. *Eur. J. Biochem.* **229**, 696–702 (1995)

13. Whitney, P.L., Brandt, H.: Effects of two ionizing groups on the active site of human carbonic anhydrase B. *J. Biol. Chem.* **251**, 3862–3867 (1976)
14. Khalifah, R.G.: Histidine-200 alters inhibitor binding in human carbonic anhydrase B. A Carbon-13 nuclear magnetic resonance identification. *Biochemistry* **16**, 2236–2240 (1977)
15. Duda, D., et al.: Structural and kinetic analysis of the chemical rescue of the proton transfer function of carbonic anhydrase II. *Biochemistry* **40**, 1741–1748 (2001)
16. Mikulski, R., et al.: Structure and catalysis by carbonic anhydrase II: role of active-site tryptophan 5. *Arch. Biochem. Biophys.* **516**, 97–102 (2011)
17. Tu, C., et al.: Kinetic analysis of multiple proton shuttles in the active site of human carbonic anhydrase. *J. Biol. Chem.* **277**, 38870–38876 (2002)
18. Jewell, D.A., et al.: Enhancement of the catalytic properties of human carbonic anhydrase III by site-directed mutagenesis. *Biochemistry* **30**, 1484–1490 (1991)
19. Qian, M., Tu, C., Earnhardt, J.N., Laipis, P.J., Silverman, D.N.: Glutamate and aspartate as proton shuttles in mutants of carbonic anhydrase. *Biochemistry* **36**, 15758–15764 (1997)
20. Elder, I., et al.: Structural and kinetic analysis of proton shuttle residues in the active site of human carbonic anhydrase III. *Proteins* **68**, 337–343 (2007)
21. Mickevičiūtė, A., et al.: Intrinsic thermodynamics of high affinity inhibitor binding to recombinant human carbonic anhydrase IV. *Eur. Biophys. J.* **47**, 271–290 (2017)
22. Baird, Jr, T., Waheed, A., Okuyama, T., Sly, W.S., Fierke, C.A.: Catalysis and inhibition of human carbonic anhydrase IV. *Biochemistry* **36**, 2669–2678 (1997)
23. Hurt, J.D., Tu, C., Laipis, P.J., Silverman, D.N.: Catalytic properties of murine carbonic anhydrase IV. *J. Biol. Chem.* **272**, 13512–13518 (1997)
24. Kasiliauskaitė, A., et al.: Thermodynamic characterization of human carbonic anhydrase VB stability and intrinsic binding of compounds. *J. Therm. Anal. Calorim.* **123**, 2191–2200 (2016)
25. Kazokaitė, J., Milinavičiūtė, G., Smirnovienė, J., Matulienė, J., Matulis, D.: Intrinsic binding of 4-substituted-2,3,5,6-Tetrafluorobenzene-sulfonamides to native and recombinant human carbonic anhydrase VI. *FEBS J.* **282**, 972–983 (2015)
26. Pilipuitytė, V., Matulis, D.: Intrinsic thermodynamics of trifluoromethane-sulfonamide and ethoxzolamide binding to human carbonic anhydrase VII: Thermodynamics of TFS and EZA Binding to CA VII. *J. Mol. Recognit.* **28**, 166–172 (2015)
27. Earnhardt, J.N., et al.: The catalytic properties of murine carbonic anhydrase VII. *Biochemistry* **37**, 10837–10845 (1998)
28. Linkuvienė, V., et al.: Intrinsic thermodynamics of inhibitor binding to human carbonic anhydrase IX. *Biochimica et Biophysica Acta (BBA) - General Subjects* **1860**, 708–718 (2016)
29. Wingo, T., Tu, C., Laipis, P.J., Silverman, D.N.: The catalytic properties of human carbonic anhydrase IX. *Biochem. Biophys. Res. Commun.* **288**, 666–669 (2001)
30. Jogaitė, V., et al.: Characterization of human carbonic anhydrase XII stability and inhibitor binding. *Bioorg. Med. Chem.* **21**, 1431–1436 (2013)
31. Ulmasov, B., et al.: Purification and kinetic analysis of recombinant CA XII, a membrane carbonic anhydrase overexpressed in certain cancers. *Proc. Natl. Acad. Sci. U.S.A.* **97**, 14212–14217 (2000)
32. Baranauskienė, L., Matulis, D.: Intrinsic thermodynamics of ethoxzolamide inhibitor binding to human carbonic anhydrase XIII. *BMC Biophys.* **5**, 12 (2012)
33. Juozapaitienė, V., et al.: Purification, enzymatic activity and inhibitor discovery for recombinant human carbonic anhydrase XIV. *J. Biotechnol.* **240**, 31–42 (2016)
34. Goldberg, R.N., Kishore, N., Lennen, R.M.: Thermodynamic quantities for the ionization reactions of buffers. *J. Phys. Chem. Ref. Data* **31**, 231–370 (2002)
35. Snyder, P.W., et al.: Mechanism of the hydrophobic effect in the biomolecular recognition of arylsulfonamides by carbonic anhydrase. *Proc. Natl. Acad. Sci. U.S.A.* **108**, 17889–17894 (2011)
36. Krimmer, S.G., Klebe, G.: Thermodynamics of protein–ligand interactions as a reference for computational analysis: how to assess accuracy, reliability and relevance of experimental data. *J. Comput. Aided Mol. Des.* **29**, 867–883 (2015)



Kinetic Analysis of Carbonic Anhydrase–Sulfonamide Inhibitor Interactions

9

Vladimir O. Talibov, Vaida Linkuvienė, U. Helena Danielson, and Daumantas Matulis

Abstract

Interactions between CAs and their inhibitors can be extensively characterized by equilibrium-based methods, described in previous chapters, or by kinetic methods that characterize interactions as a function of time. One of the main techniques for characterization of biomolecular interactions, surface plasmon resonance (SPR) biosensor technology, has been used to measure association and dissociation rate constants of sulfonamide inhibitors with numerous CA isoforms. The ratio of rate constants yields a thermodynamic equilibrium dissociation constant (K_d), equivalent to the K_d values obtained by orthogonal techniques. The results demonstrate that highly selective and high-affinity inhibitors may be developed, with certain kinetic signatures to be expected from a potent inhibitor. The *intrinsic* association and dissociation rate constants can also be determined by a novel SPR-based approach, using chemodynamic analysis of the binding-linked pH-dependent effects, with similar results to the thermodynamic studies described in previous chapters. The kinetic data demonstrated that the observable association rate constants are pH-dependent,

V. O. Talibov
Department of Chemistry - BMC, Uppsala University, Uppsala, Sweden
e-mail: vladimir.talibov@kemi.uu.se

V. Linkuvienė · D. Matulis (✉)
Department of Biothermodynamics and Drug Design, Institute of Biotechnology,
Life Sciences Center, Vilnius University, Vilnius, Lithuania
e-mail: morkunaite@ibt.lt; matulis@ibt.lt

U. H. Danielson
Department of Chemistry - BMC, and Science for Life Laboratory, Uppsala University, Uppsala, Sweden
e-mail: helena.danielson@kemi.uu.se

while the dissociation rate constants are pH-independent, suggesting that the association and dissociation mechanisms are inherently different.

9.1 Introduction

The previous chapters have had a focus on the description of systems at equilibrium, i.e., with a strong focus on the thermodynamics of interactions and on methods to address them. However, living organisms and the biochemical machinery within are dynamic systems that rarely exists in an equilibrium state. Kinetic characterization of biological systems reveals not only the pathways convoluted in the transition between two different states, but also certain fine details of the molecular recognition events, which can be directly translated to a phenomenological level.

The kinetic theory utilized in biomolecular interaction analyses is based on the law of mass action. A reversible association reaction is represented with the following scheme, where k_a and k_d are constants whose role is clarified further on [1]:



Equation (9.1) describes the simplest reversible recognition event in biological systems, but is not valid for all systems per se, although the vast majority of interactions follow this on an apparent level.

Defining the reaction rate as a change in the concentration of any component per moment of time, the following non-linear ordinary differential equation is postulated as a rate equation:

$$\frac{d[AB]}{dt} = k_a([A]_0 - [AB])([B]_0 - [AB]) - k_d[AB] \quad (9.2)$$

Parameters k_a and k_d are association and dissociation rate constants, fundamental interaction parameters that together with known starting conditions provide an accurate description of the system on a time-scale; $[A]_0$ and $[B]_0$ are initial concentrations of the reactants. Equation (9.2) has an analytical solution, but on an experimental level, most progress curves are obtained at conditions that simplify their analysis.

There are numerous techniques that allow kinetic experiments, with surface plasmon resonance-based (SPR) biosensors, among others, taking the lion's share of early stage drug design applications [2]. It should be noted that other flow biosensor setups and different detection principles exist. However the kinetic principles, assay designs, and interpretations are the same or relatively similar as those found for SPR-based biosensors. SPR itself is a phenomena of induced surface electron oscillation in an electron-rich metal (usually gold in sensing instruments). Understanding the underlying physics and the general instrument construction is important for

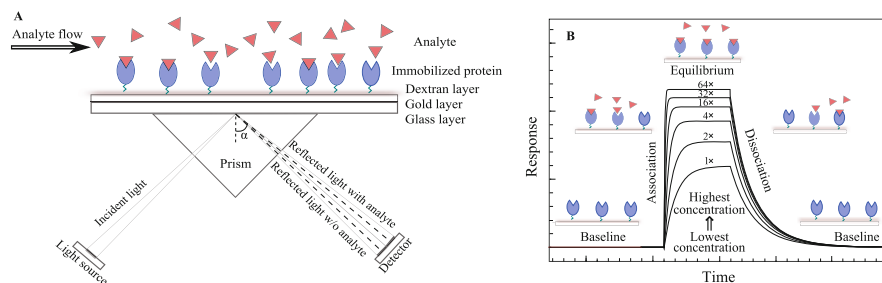


Fig. 9.1 Schematic representation of SPR biosensor and data output. **(a)** The sensing element and the detection system. The analyte solution is handled by the microfluidic system to accurately address the immobilized target. The photomultiplier records the reflected light and the resonance angle θ at which the incident light is dissipated due to excitation of plasmon electrons oscillation. This angle is changed upon changes in the refractivity of the surface layer at the phase interface. **(b)** A set of interaction kinetic curves (sensorgrams), obtained during a kinetic experiment using a series of different analyte concentrations. The curves consist of two phases: the association phase (analyte injection) and the dissociation phase (complex dissociation)

both refined assay design and interpretation of results, and can be found elsewhere [3, 4]. In short, the angle at which incident light induces plasmon oscillations in a thin golden layer depends on the refractivity at the phase interface and can be optically monitored in a time-resolved manner. Through functionalization with a linker matrix and immobilization of one of the interaction partners, the gold layer forms a recognition (sensing) element, Fig. 9.1a. Another interaction partner, being injected as an analyte over the surface, changes the refractive index of the interface upon interaction with the immobilized counterpart. SPR biosensors designed for biomolecular interaction studies have a microfluidic format, with built-in autosampling and pump modules. Monitoring the time dependency of the change in resonance excitation angle (usually denoted as θ) upon injections of analytes over an immobilized target translates into sensorgrams (progress curves, reaction curves, or interaction kinetic curves) describing the formation and decay of a complex, Fig. 9.1.

Sensorgrams consist of two phases—the association phase that corresponds to the injection of a molecule of interest (analyte) and the dissociation phase—dissociation of the complex into the flow of a running buffer, as shown in Fig. 9.1b. Since the refractive index is proportional to the abundance of a constituent, the change in instrument response dR/dt is proportional to the change in concentration. In a flow setup, the concentration of the analyte $[B]$ is constant and Eq. (9.2) can be simplified to a pseudo-first-order rate equation. Therefore, the association phase of the progress curve can be approximated with an integral form of modified Eq. (9.2):

$$R = R_{eq}(1 - e^{-(k_a[B] + k_d)t}) \quad (9.3)$$

The dissociation phase is dominated by complex decay and re-association events are often negligible. Therefore, complex decay can be treated as a first-order

reaction and dissociation can be approximated by a simple exponential decay function:

$$R = R' e^{-k_d t} \quad (9.4)$$

The typical outcome of SPR-based kinetic experiments is a set of progress curves acquired at different concentrations of the analyte (Fig. 9.1b). A global non-linear regression analysis of the curves using Eqs. (9.3) and (9.4) allows the quantification of the dissociation and association rate constants, as well as their ratio—the thermodynamic dissociation constant K_d . Alternatively, K_d can be assessed independently through an analysis of report points taken at steady-state and the Langmuir isotherm.

SPR biosensors are suitable for studying almost all types of biomolecular interactions, providing that experiments are based on a well-developed expertise concerning the characteristics of the proteins. While evaluation of protein–protein and protein–ligand interactions nowadays has become a trivial task, current instruments and methodology improvements allow the detection limit to be pushed to extremely small organic molecules [5] and even ions [6, 7]. The technique can determine association rate constants in the range from $10^3 \text{ M}^{-1} \text{ s}^{-1}$ to $10^8 \text{ M}^{-1} \text{ s}^{-1}$, dissociation rate constants from 10^{-5} s^{-1} to 1 s^{-1} [8, 9], and equilibrium dissociation constant from 1 nM to 500 μM [2]. Another advantage of biosensor analyses is that interaction parameters can be determined using very small amounts of protein and ligands in a medium-throughput and a highly robust manner. Unlike common beliefs, the running costs of experiments are not that high: a well-developed and optimized assay allows the study of hundreds of interactions with one surface preparation. Modern applications of the method include not only detailed characterization of selected interactions, but also screening of compound libraries. This is especially suitable for fragment-based lead discovery [10]. Some examples of SPR-based interaction analyses of carbonic anhydrases will be shown in this chapter.

9.2 Interaction Kinetic Analysis of Carbonic Anhydrases

Carbonic anhydrases constitute a well-characterized enzyme family. Some isoforms have been used extensively for interaction kinetic analysis using different flow biosensors. A majority of such studies include instrument benchmarking [11, 12], method development [13], and assay validation [5]. They have mostly involved CA I and CA II, of human or bovine origin. The low complexity of CAs and the large number of homologies allow the CA family to serve as a suitable model system. Several isoforms (i.e., CA IX and CA XII [14, 15]) are clinically relevant and therefore also stimulate pharmacological research on this enzyme family.

Sulfonamides represent the largest class of CA ligands, being a well-known type of potent CA inhibitors. Despite the existence of other classes of CA ligands, here we will focus on sulfonamides as they are specific active site probes that exist in various protonation states and can be evolved to extremely potent compounds with K_i (K_D) values approaching the pM range.

SPR experiments start out with the preparation of the sensing surface by means of target immobilization. Basically, any common approach in bioconjugation [16] can be exploited for biosensor surface setup. The standard and first-try approach is typically a simple amine immobilization—chemical linkage between protein primary amines and activated esters of carboxylic groups of the matrix. Carbonic anhydrases are stable over a broad range of pH values and do not have lysine residues close to the active site. Amine coupling of CAs to the surface consequently results in surface functionality high enough for analysis of interactions even with the smallest ligands, e.g., with methylsulfonamide. According to our previously published data, the apparent binding activity (functionality) of the immobilized protein depends on the isoform used [17]. But it can, for example, approach 100% for CA IX, an isoform that exposes only one lysine residue. Also, most CA isozymes except CA I exhibit an outstanding stability after being chemically immobilized on the surface, with no strong loss of sulfonamide binding activity over the course of 3–4 days at 25 °C. This indicates that CAs can maintain their conformation, withhold oxidative stress, and keep the active site zinc cation over a prolonged period of time under non-equilibrium conditions.

The buffer of choice plays a crucial role in SPR experiments. Fortunately, human CAs do not require reduction equivalents or supplement of specific co-factors for analytical experiments. In our hands, standard phosphate-based buffers (e.g., PBS) [17], as well as Tris- and acetate-based buffers [18], and HEPES buffers (unpublished data) are equally well suited for the interaction studies. Worth noting is that their high pH stability allows the buffer pH to be chosen outside a normal physiological range [18]. Furthermore, human CAs can tolerate relatively high concentrations of organic co-solvents. The only practical limitation when studying CAs comes to their requirement for normal salt concentration. However, the unsatisfactory quality of the interaction kinetic curves obtained under low ionic strength may be attributed to experimental artifacts, rather than protein degradation (unpublished observation).

Analyte sample preparation, preparation of concentration series, and generic setups for analytical runs are usually not different from standard biosensor procedures. Briefly, it is recommended that concentration series span a range of 0.1–10 of the expected K_D value for the complex. For screening purposes and pilot experiments, we recommend the highest analyte concentration to be prepared maximally at 200 μM . From our experience, this statement applies not only for characterization of drug-like molecules, but also for fragments. Even for well-behaving interaction assays using CAs, concentrations of ligands above 200 μM result in multiple ligand-induced artifacts.

9.3 Observed Kinetics

In one of our previous studies [17], we analyzed interaction kinetics between 18 selected sulfonamides and 6 CA isoforms, CA I, CA II, CA VII, CA IX, CA XII, and CA XIII. It involved 3 groups of structurally similar phenylsulfonamide derivatives (N-alkylated benzimidazolyl, S-alkylated 2-thiopyrimidyl, and fluorine-substituted benzenesulfonamides; Fig. 9.2). The analyte molecules employed were well-developed inhibitors, some with a high potency and extremely low dissociation constants for their complexes with CAs. The initial aim was not only to take a look at the QSAR and selectivity of the sulfonamides towards various isozymes, but also to dissect the interaction into kinetic components and to find the potency-defining parameters.

Upon setting up the kinetic experiments, the first observations highlighted certain features of this ligand class relative to the CA target. The data analysis revealed that all analyzed interactions could be described on a phenomenological level, using a simple single-step reversible interaction model, as represented by Eq. (9.1). This implies that the association rate is limited by the active encounter between a protein and a ligand, and that there are no intermediates with a half-life high enough to affect association and dissociation kinetics. Surprisingly, sulfonamides acted as “slow” binders—their association rate constants k_a were consistently within the range of $10^5 \text{ M}^{-1} \text{ s}^{-1}$ to $10^6 \text{ M}^{-1} \text{ s}^{-1}$. Taking into account the small size of the ligands (300 Da to 400 Da) and the morphology of the interaction site (a relatively large cavity), one would expect a faster association rate. Interestingly enough, the apparent association rates for CA IX and XII, enzymes with an easier access to the prosthetic group (as judged from the solvent accessibility), were slightly higher in comparison with the other tested isozymes.

For the studied interactions, when it was possible to quantify kinetic parameters from the acquired sensorgrams, thermodynamic dissociation constants were also quantified and compared to the K_d values, obtained using FTSA. The equilibrium binding data obtained using the two different methods was reasonably close, as shown in Fig. 9.3. The orthogonal methods thus gave similar results, testifying a good quality of the developed assay. The largest discrepancies between the data obtained by the two techniques were found for interactions with extremely slow dissociation rates.

Unfortunately, certain challenges arose from the nature of the ligands and method limitations. Since a very slow dissociation translates into inability to quantify the rate constant uniquely, SPR biosensor analysis is severely limited for studies involving very stable complexes. Moreover, the saturation of the surface by a potent ligand blocks it for subsequent analytical cycles. There are several experimental methodologies to overcome such a limitation. The first one is to force dissociation under non-native conditions, e.g., via injections of potent surfactants, chaotropes, or buffers forcing a large change in pH. In our experience, while being a valid methodology for surface regeneration in protein–protein interaction assays, it is hard to induce dissociation of a very stable protein–ligand complex

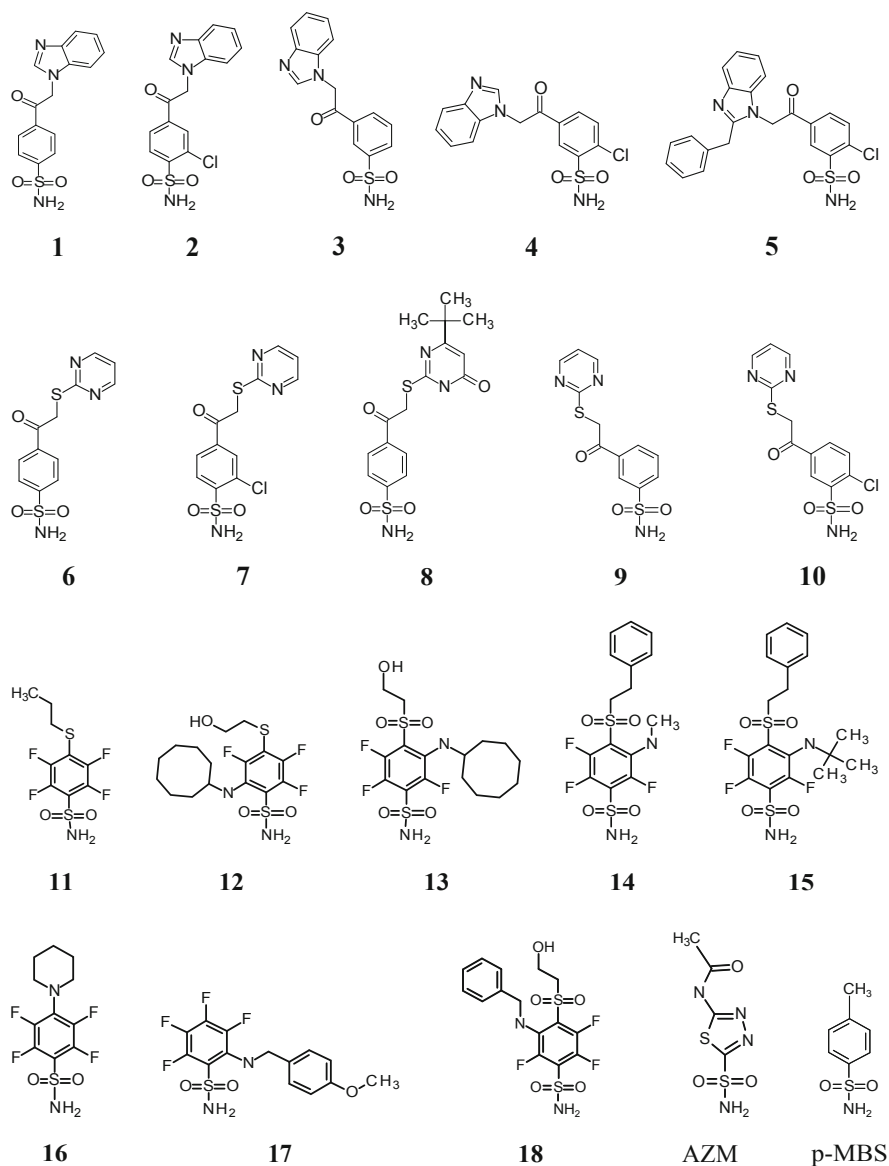


Fig. 9.2 Structures of benzenesulfonamides used in experiments by Talibov et al. [17] and Linkuviene et al. [18]. AZM—acetazolamide and p-MBS—*para*-methylbenzenesulfonamide. The synthesis and activity evaluation of other compounds can be found elsewhere: N-alkylated benzimidazole derivatives **1–5** [19, 20], S-alkylated 2-thiopyrimidine derivatives **6–10** [20, 21], and fluorine-substituted benzenesulfonamides **11–18** [22–24]

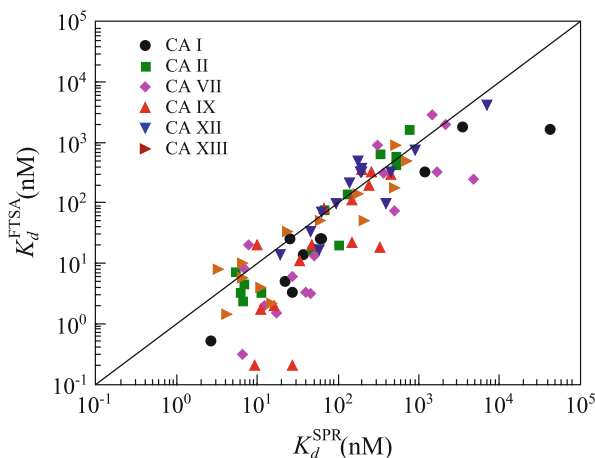


Fig. 9.3 Comparison of equilibrium binding constants obtained by two techniques, SPR-based biosensor technology and FTSA. Data was taken from Talibov et al. [17]. Only the K_d values, quantified from global curve analysis, were used to build the bivariate correlation plot. Different colors and data point shapes represent different CA isoforms

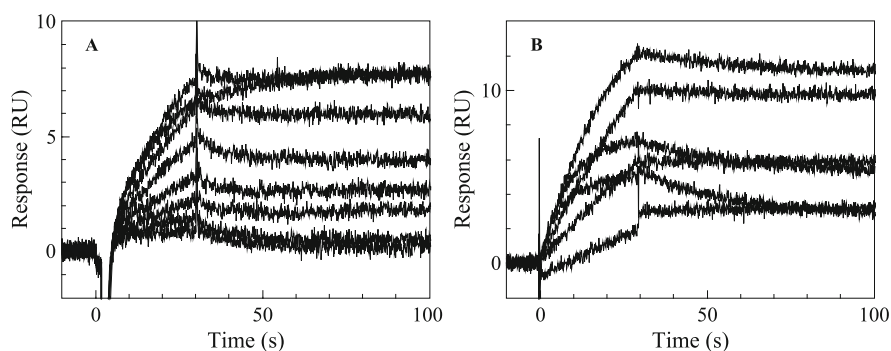


Fig. 9.4 Sensorgrams of CA–sulfonamide interactions that exhibit extremely low dissociation rates. Panel (a) shows the interaction of CA VII with compound **15**, and panel (b)—the interaction of CA XII with compound **13**

without a significant loss of surface functionality. An alternative approach was employed in Talibov et al. [17], where we used a high concentration of a low-affinity orthosteric compound to out-compete potent ligands. For some interactions, injections of 200 μM of sulphanilamide ($k_a = 3.7 \times 10^4 \text{ M}^{-1} \text{ s}^{-1}$, $k_d = 0.1 \text{ s}^{-1}$, and $K_d = 3.1 \times 10^{-6} \text{ M}$ [12]) allowed the regeneration of certain surfaces, possibly by reducing re-binding effects. Unfortunately, this approach did not help to resolve the kinetics of the most potent ligands, whose interactions were treated as “essentially irreversible.” In Fig. 9.4 examples of interaction kinetic curves obtained with tight-binding compounds are shown.

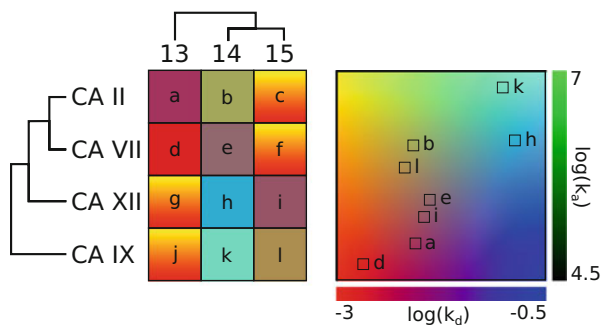


Fig. 9.5 Chemical phylogenetic analysis for selected interactions. Entries in the rectangular array correspond to individual interactions; a color barcode is assigned to each set of kinetic parameters. Interactions (c), (f), (g), and (j) are considered to be essentially irreversible

An overview on the correlation between the chemical structures of inhibitors and interaction parameters for different CA isoforms has been extensively discussed [17] and is briefly outlined below. However, it should be kept in mind that the observed parameters may be misleading since they include linked protonation effects (see the following section). The quantified parameters showed that *p*-substituted acetylated heterocyclic derivatives of the studied benzenesulfonamides are stronger binders than *m*-substituted derivatives. In most cases, the contribution of the benzimidazole heterocyclic moiety within the benzenesulfonamide structure was more favorable than the pyrimidine. The chlorine group at the *ortho* position reduced the K_d for the interaction for all isoforms except for CA IX, within the compound groups of N-substituted benzimidazole derivatives and S-substituted 2-thiopyrimidine derivatives. The highest affinities and lowest k_d values were found for the fluorine-containing derivatives.

Additionally, we developed an approach called chemical phylogenetic interaction kinetics analysis to simplify evaluation of a large set of kinetic data that involves several members of the same enzyme family and structurally related compounds. The compounds and enzymes were grouped in a bidirectional manner, with kinetic parameters being color-barcoded, as exemplified in Fig. 9.5 for four CA isozymes and three fluorinated benzenesulfonamides. As shown in the figure, while compound **13** interacted essentially irreversibly with CA IX and XII, the complexes were less stable for more distant paralogues. Upon substitutions at the *meta*- and *para*-positions, the ligand selectivity changed in the opposite direction, towards the formation of more stable complexes with carbonic anhydrases II and VII. Yet, for compounds **14** and **15** the general QSAR trend remained the same for all four isozymes. A methyl- to *tert*-butyl substitution at the aromatic amino group caused a considerable decrease of the k_d value, increasing the stability of the protein–ligand complex.

Interaction kinetic analysis of CA-inhibitor interactions highlighted the importance of the dissociation rate constant k_d in the ranking of the ligands. Judging

from the ligand chemotype, it was expected that there would not be an outstanding selectivity towards various CA isoforms, as the sulfonamide functional group serves as an efficient “warhead” and is a pharmacophore that provides the majority of the binding energy for all tested complexes. However, while the order of magnitude of association rate constants for a selected ligand and a set of different human CAs was approximately the same, the ligand potency, and, in turn, selectivity towards different isozymes was well-defined by the k_d . To exemplify, fluorinated compounds bearing bulky hydrophobic functional groups such as a cyclooctyl (**12** and **13**) demonstrated the lowest dissociation rate constants for the interaction with CA IX. It thus confirmed the potential of these compounds to be developed as selective drugs targeting CA IX. These compounds are efficient enough in blocking the active site of the enzyme to “solvent inaccessible” state, which increases the stability of the complex by both entropic and mechanistic factors, as proposed below. The importance of residence time in ligand evolution, especially for developing efficient enzyme inhibitors, has been a subject for several reviews [25, 26] and has been proposed as an efficient metric for ligand quality [27]. Here we want to highlight that k_d is a valid criterion for selectivity analysis, especially since a drug–target interaction in in vivo system cannot be treated by means of thermodynamics only.

9.4 Intrinsic Interaction Kinetics

Although Eq. (9.1) describes experimental results well, it should be clear that there is a difference between the interaction mechanism and the phenomenological observation of the interaction. As stated above, we found no indication that there are any long-living intermediates or additional significant steps involved in a formation of stable complex during the association between studied ligands and proteins. The previous chapters stated and rationalized clearly the influence of pH on the observed thermodynamic parameters, in terms of a mathematical model based on *intrinsic* constants. In this section, a similar logic will be applied to the interaction kinetics.

This book gives an extensive overview of the structure of human carbonic anhydrases, its prosthetic group, and the influence of pH on ionization states of both the sulfonamide ligand and the enzyme. Briefly, this section is based on a mechanism involving the interaction between the deprotonated sulfonamide group of the ligand and the protonated prosthetic group of the enzyme, resulting in the substitution of a water molecule from the zinc coordination sphere by the sulfonamide. We postulate that neither the protonated sulfonamide in its neutral form nor the deprotonated prosthetic group with a hydroxide anion as the fourth ligand of the zinc cation can associate and form a complex, Fig. 9.6a.

On apparent level, rate equation for carbonic anhydrase (CA) and sulfonamide (SA) interaction (Eq. (9.2)) can be rewritten in the following way (concentrations are functions of time):

$$v = k_a[\text{CA}][\text{SA}] - k_d[\text{CA-SA}] \quad (9.5)$$

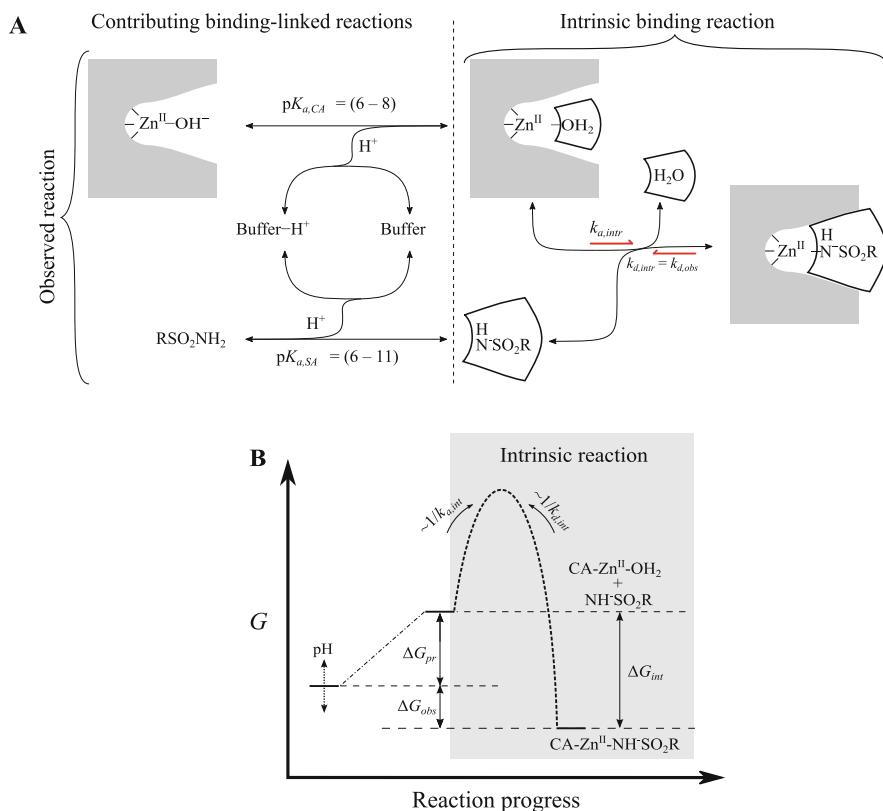


Fig. 9.6 The model of an interaction between a sulfonamide inhibitor and carbonic anhydrase. Panel (a) left part, illustrates the contribution of the binding-linked protonation reactions. Upon their subtraction, the intrinsic interaction reaction can be obtained, as shown on the right part of the same panel. Panel (b) shows the energy diagram for both observable and intrinsic reactions

As the van't Hoff expression of the law of mass action states, the rate is proportional to the concentration of reactants. In Eq. (9.5), the concentrations are expressed as sums of both interaction-competent (reactive) and incompetent species, and are in turn pH-independent. Therefore, the nature of association rate constant should be pH-dependent. Knowing the pK_a values of the zinc-coordinated water of an enzyme and of the amide of sulfonamide group, the real concentrations of reactive species can be accurately quantified at any pH value. Thus, Eq. (9.5) can be transformed into a more accurate one:

$$v = k_{a,int} f_{CA} f_{SA} [CA][SA] - k_{d,int} [CA-SA] \quad (9.6)$$

In Eq. (9.6), $k_{a,int}$ and $k_{d,int}$ are intrinsic (pH-independent in this context) rate constants, and f are fractions of the corresponding interaction-competent species,

derived through pK_a and pH as it was shown in the previous chapters. The second linear components in Eqs. (9.5) and (9.6) are not different, because (for the given model) the dissociation reaction cannot be pH-dependent and the observable dissociation rate constant is equal to the intrinsic rate constant.

9.5 Influence of pH on Interaction Kinetics

Originally, the pH-dependency of CA–SA interaction kinetics was examined in the second part of twentieth century using stopped-flow kinetic experiments [28, 29]. However, it was not rationalized from a ligand discovery point of view and did not involve evaluation of the influence of pH on dissociation rate constants. The potential usefulness of intrinsic kinetics was highlighted once the atomic details of sulfonamide–carbonic anhydrase interaction were revealed [30], as the role of the amide pK_a on QSAR became obvious. We proposed the intrinsic kinetics concept (described in a section above) in our first study of CAs [17]. Nevertheless, its verification required a more sophisticated experimental design and was explored specifically in a later study [18]. To determine the pH-dependency of interaction rate constants, and their consistencies with the model, SPR-based interaction analyses were performed at different pH. A set of ligands with various sulfonamide pK_a values was analyzed against three different CA isoforms (CA II, CA IX, and CA XIII) at a range of pH values from 5 to 9 with a 0.5 increment. An example of sensorgrams is given in Fig. 9.7.

A simple graphic analysis of the extracted data highlighted a clear pH-dependency of the association rate constants, as indicated in Fig. 9.8a and d. The observed U-shape of pH-dependent values was found to be similar to the pH-dependency of affinity constants obtained using equilibrium-based methods

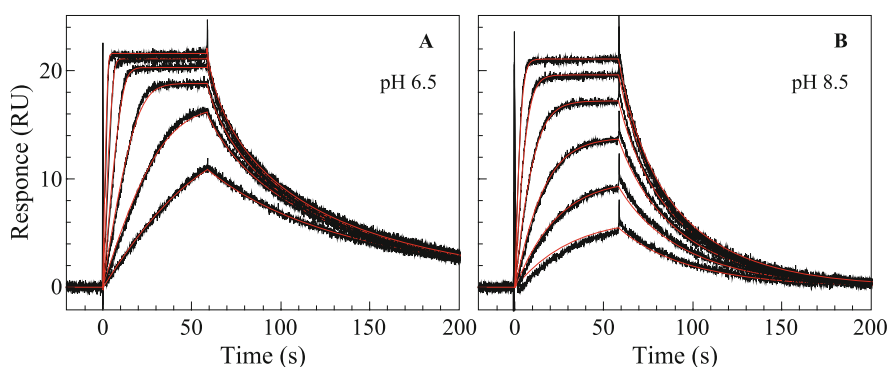


Fig. 9.7 Example of kinetic analysis of CA–sulfonamide performed at different pH values, showing the interactions between AZM and immobilized CA II at pH 6.5 (a) and 8.5 (b). Red lines represent the progress curve approximation using a reversible 1:1 interaction model (Eqs. (9.1), (9.3), and (9.4))

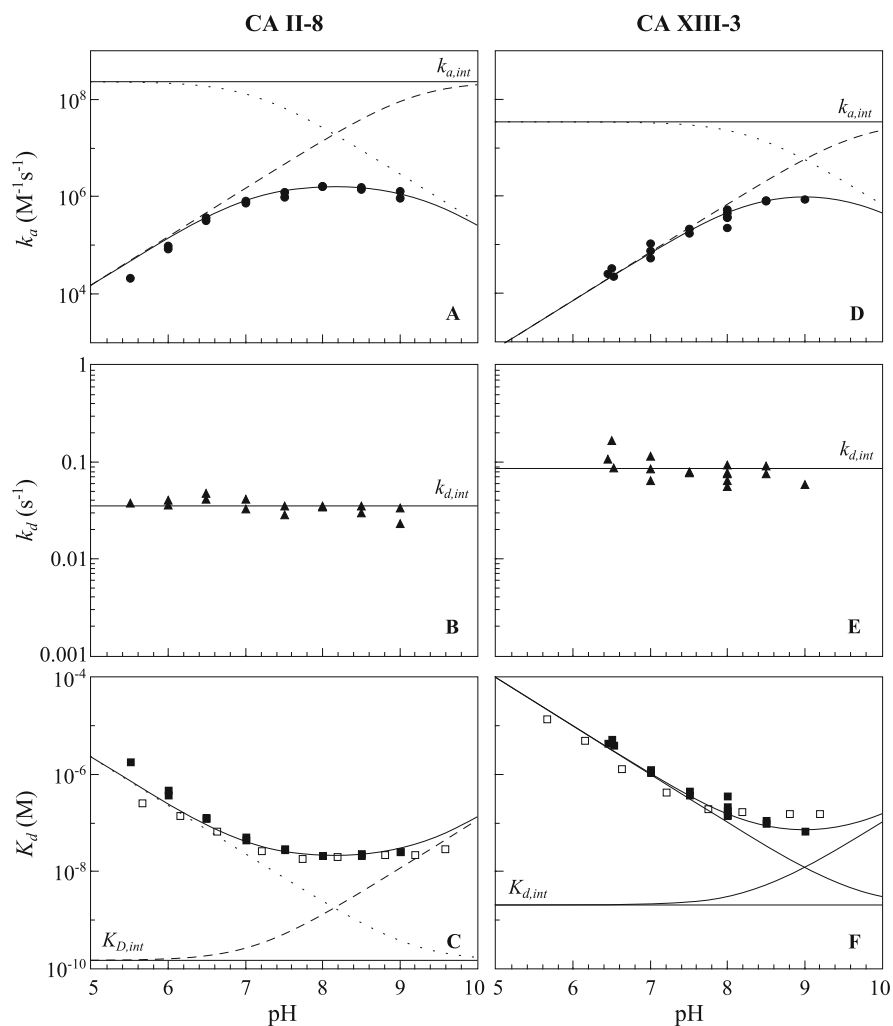


Fig. 9.8 Observed interaction kinetic parameters, kinetic-derived dissociation constant K_d as functions of pH for interactions between CA II-compound **8** and CA XIII-compound **3**. The association rate constants are shown in the top panels (**a** and **d**). Intrinsic values of k_a are shown as solid lines following the data approximation with Eq. (9.7). Dashed and dotted lines represent the fractions of binding-competent CA and sulfonamide, respectively. The middle panels (**b** and **e**) show that the dissociation rate constants are pH-independent. The bottom panels (**c** and **f**) show the K_d dependence on pH. K_d values obtained through interaction kinetic analysis are shown as solid squares, while the K_d values, obtained by FTSA, are included as open squares

(Fig. 9.8c and f, open squares), and is consistent with the opposite influence of pH on the concentration of interaction-competent species. For the given hyperbolic dependency, the critical points were found in the near-neutral pH region and the values of k_a diminished five- to tenfold with every pH unit towards alkaline or acidic areas. On an apparent level, the pH of the interaction medium had almost no influence on the dissociation rate constant k_d , Fig. 9.8b and e.

Since the observations were consistent with the model described in this chapter, a numerical analysis of the obtained interaction parameters was performed. Following Eq. (9.6), the pH-dependency of the apparent on-rate constant k_a should adhere to the following expression:

$$k_a = k_a^{int} f_{CA} f_{SA} \quad (9.7)$$

Using Eq. (9.7), we quantified the intrinsic association rate constants, $k_{a,int}$. The estimated intrinsic values differed drastically from the maximum obtained observable values, up to two orders of magnitude, and approached $10^8 \text{ M}^{-1} \text{ s}^{-1}$.

Certain important conclusions could be drawn from the kinetic analysis of intrinsic interactions between carbonic anhydrases and sulfonamides. The unexpectedly slow association of sulfonamide ligands is not mediated by inefficient or kinetically controlled recognition events. CAs are known to be among the fastest enzymes with k_{cat} value of 10^6 s^{-1} and diffusion-limited reaction kinetics. For the bovine CA II orthologue, the second-order rate constant for the Michaelis complex formation is expected to be around $10^{10} \text{ M}^{-1} \text{ s}^{-1}$ for its inorganic substrate [31, 32], and is only two orders of magnitude lower on the intrinsic level for the studied sulfonamide inhibitors. The moderate association rate is attributed to the acid–base equilibrium and binding-linked protonation events, but not to the obstacles in recognition per se.

The absence of pH-dependency for the off-rate constant k_d , despite being expected to be independent based on the proposed model, is of high interest. Our studies did not resolve the dissociation mechanism, and it is unclear if an amide in the zinc coordination sphere is protonated prior to dissociation, or if it dissociates in a negatively charged form. Moreover, it is not clear if the synthetic ligand is substituted by a water molecule or a hydroxide anion. It is evident that none of these events define the reverse reaction, as the rate-limiting step for the dissociation is pH-independent. A possible explanation includes the solvent accessibility of tetracoordinated zinc with a sulfonamide in its coordination sphere. In this paradigm, a fluctuation in a conformation of a bound ligand is required to let the water molecule access the prosthetic group and to initiate the complex dissociation.

Prima facie, the determination of intrinsic kinetic parameters for a sulfonamide–CA system requires the execution of a relatively large series of kinetic experiments, and cannot satisfy the requirements of an early stage drug discovery campaign. Yet, an accurate estimation of the values can be done with a single-point analysis employing a low complexity of Eqs. (9.6) and (9.7). Knowing the acid dissociation constants of the reactants, experimental details, and the observed values, one can easily calculate the intrinsic parameters. [18].

Intrinsic rate constants are important in a context of quantitative structure–activity relationships. The apparent values of the activity modulation criteria, in terms of either inhibition constants or interaction parameters, are well suited for screening purposes or for a characterization of a panel of chosen leads. However, they can be misleading in structure-guided lead design. An apparent gain in the potency of a sulfonamide compound can be attributed not only to an improved interaction network, but also to an increased fraction of the interaction-competent form. On the other hand, it increases the importance of k_d values for ranking. As a crystal structure is a snapshot of the interaction network in its ground state, and for sulfonamides the intrinsic dissociation rate constants do not differ from the apparent constant, its rationalization can deepen the understanding of an actual recognition that stabilizes the protein–ligand complex.

9.6 Conclusions

Interaction kinetic analysis casts an additional dimension on lead characterization, showing the dynamics of complex formation and its stability under non-equilibrium conditions. The carbonic anhydrase–sulfonamide system is suitable for such studies, and kinetic experiments can produce data of high value. It both helps to understand the interaction mechanism better and adds extra criteria to choose compounds with desired properties. Similarly to equilibrium-based methods, SPR analysis can provide intrinsic interaction parameters—quantities that genuinely reflect the molecular recognition events.

References

1. Atkins, P., De Paula, J., Keeler, J.: *Atkins' Physical Chemistry*. Oxford University Press, Oxford (2018)
2. Renaud, J.-P., et al. Biophysics in drug discovery: impact, challenges and opportunities. *Nat. Rev. Drug Discov.* **15**, 679–698 (2016)
3. Huber, W., Mueller, F.: Biomolecular interaction analysis in drug discovery using surface plasmon resonance technology. *Curr. Pharm. Des.* **12**, 3999–4021 (2006)
4. Cooper, M.A.: Optical biosensors in drug discovery. *Nat. Rev. Drug Discov.* **1**, 515–528 (2002)
5. Nordstrom, H., et al.: Identification of MMP-12 inhibitors by using biosensor based screening of a fragment library. *J. Med. Chem.* **51**, 3449–3459 (2008)
6. Seeger, C., Talibov, V.O., Danielson, U.H.: Biophysical analysis of the dynamics of calmodulin interactions with neurogranin and Ca^{2+} /calmodulin-dependent kinase II. *J. Mol. Recognit.* **30**, e2621 (2017)
7. Christopheit, T., Gossas, T., Danielson, U.H.: Characterization of Ca^{2+} and phosphocholine interactions with C-reactive protein using a surface plasmon resonance biosensor. *Anal. Biochem.* **391**, 39–44 (2009)
8. Myszka, D.G., Rich, R.L.: Implementing surface plasmon resonance biosensors in drug discovery. *Pharm. Sci. Technol. Today* **3**, 310–317 (2000)
9. Kemp, M.M., We wer, M., Koehler, A.N.: Unbiased binding assays for discovering small-molecule probes and drugs. *Bioorg. Med. Chem.* **20**, 1979–1989 (2012)
10. Giannetti, A.M.: *Methods in Enzymology*, pp. 169–218. Elsevier, Amsterdam (2011)

11. Cannon, M. J., et al.: Comparative analyses of a small molecule/enzyme interaction by multiple users of biacore technology. *Anal. Biochem.* **330**, 98–113 (2004)
12. Papalia, G.A., et al.: Comparative analysis of 10 small molecules binding to carbonic anhydrase II by different investigators using biacore technology. *Anal. Biochem.* **359**, 94–105 (2006)
13. Navratilova, I., Hopkins, A.L.: Fragment screening by surface plasmon resonance. *ACS Med. Chem. Lett.* **1**, 44–48 (2010)
14. Ivanov, S., et al.: Expression of hypoxia-inducible cell-surface transmembrane carbonic anhydrases in human cancer. *Am. J. Pathol.* **158**, 905–919 (2001)
15. Swietach, P., Vaughan-Jones, R.D., Harris, A.L.: Regulation of tumor pH and the role of carbonic anhydrase 9. *Cancer Metastasis Rev.* **26**, 299–310 (2007)
16. Hermanson, G.T.: *Bioconjugate Techniques*. Academic Press, London (2013)
17. Talibov, V.O., Linkuvienė, V., Matulis, D., Danielson, U.H.: Kinetically selective inhibitors of human carbonic anhydrase isozymes I, II, VII, IX, XII, and XIII. *J. Med. Chem.* **59**, 2083–2093 (2016)
18. Linkuvienė, V., Talibov, V.O., Danielson, U.H., Matulis, D.: Introduction of intrinsic kinetics of protein–ligand interactions and their implications for drug design. *J. Med. Chem.* **61**, 2292–2302 (2018)
19. Zubrienė, A., et al.: Benzenesulfonamides with benzimidazole moieties as inhibitors of carbonic anhydrases I, II, VII, XII and XIII. *J. Enzyme Inhib. Med. Chem.* **29**, 124–131 (2014)
20. Čapkauskaitė, E., et al.: Indapamide-like benzenesulfonamides as inhibitors of carbonic anhydrases I, II, VII, and XIII. *Bioorg. Med. Chem.* **18**, 7357–7364 (2010)
21. Čapkauskaitė, E., et al.: Design of [(2-pyrimidinylthio)acetyl]benzenesulfonamides as inhibitors of human carbonic anhydrases. *Eur. J. Med. Chem.* **51**, 259–270 (2012)
22. Dudutienė, V., et al.: Discovery and characterization of novel selective inhibitors of carbonic anhydrase IX. *J. Med. Chem.* **57**, 9435–9446 (2014)
23. Dudutienė, V., et al.: 4-substituted-2,3,5,6-tetrafluorobenzenesulfonamides as inhibitors of carbonic anhydrases I, II, VII, XII, and XIII. *Bioorg. Med. Chem.* **21**, 2093–2106 (2013)
24. Dudutienė, V., et al.: Functionalization of fluorinated benzenesulfonamides and their inhibitory properties toward carbonic anhydrases. *ChemMed-Chem.* **10**, 662–687 (2015)
25. Copeland, R.A., Pompliano, D.L., Meek, T.D.: Drug–target residence time and its implications for lead optimization. *Nat. Rev. Drug Discov.* **5**, 730 (2006)
26. Copeland, R.A.: The drug–target residence time model: a 10-year retrospective. *Nat. Rev. Drug Discov.* **15**, 87 (2016)
27. Murray, J.B., Roughley, S.D., Matassova, N., Brough, P.A.: Off-Rate screening (ORS) by surface plasmon resonance. an efficient method to kinetically sample hit to lead chemical space from unpurified reaction products. *J. Med. Chem.* **57**, 2845–2850 (2014)
28. Kernohan, J.: A method for studying the kinetics of the inhibition of carbonic anhydrase by sulphonamides. *Biochim. Biophys. Acta (BBA) - Enzymol. Biol. Oxid.* **118**, 405–412 (1966)
29. Taylor, P.W., King, R.W., Burgen, A.S.V.: Influence of pH on the kinetics of complex formation between aromatic sulfonamides and human carbonic anhydrase. *Biochemistry* **9**, 3894–3902 (1970)
30. Fisher, Z., et al.: Neutron structure of human carbonic anhydrase II: a hydrogen-bonded water network “switch” is observed between pH 7.8 and 10.0. *Biochemistry* **50**, 9421–9423 (2011)
31. Kernohan, J.: The pH-activity curve of bovine carbonic anhydrase and its relationship to the inhibition of the enzyme by anions. *Biochim. Biophys. Acta (BBA) - Enzymol. Biol. Oxid.* **96**, 304–317 (1965)
32. Koenig, S.H., Brown, R.D.: H_2CO_3 as substrate for carbonic anhydrase in the dehydration of HCO_3^- . *Proc. Natl. Acad. Sci.* **69**, 2422–2425 (1972)

Part III

Structure–Thermodynamics/Kinetics Correlations of Compound Binding to Carbonic Anhydrases



Organic Synthesis of Substituted Chlorinated Benzenesulfonamides as Selective Inhibitors of Several CA Isoforms

10

Edita Čapkauskaitė and Daumantas Matulis

Abstract

Among a wide range of synthetic compounds that have been demonstrated to possess CA inhibitory activity, the benzene sulfonamides take a central place. The active site shapes of various CA isoforms are very similar, but possess some important differences that enable to design inhibitors exhibiting selectivity towards one or another CA isoform. Small structural changes in the structure of the chemical compound can sometimes cause thousand-or-greater-fold change in affinity to a particular isoform. The changes may be as small as a single methylene group that may make a compound not able to fit in the pocket of one isoform, but fit well to another isoform. However, in most cases, small changes cause only slight changes in the affinity and selectivity profiles of the compounds. In this chapter, we discuss the organic synthesis and spectral identification of a series of halogenated, primarily chlorinated substituted benzenesulfonamides.

10.1 Variation of Substituents in the Benzenesulfonamide and on the Tail

The “ring” and “tail” approach has been used to design many CAs inhibitors [1, 2]. The “ring” represents hetero/aromatic ring bearing sulfonamide group, which binds to the zinc ion, and the electron acceptor substituent, which increases the acidity of the sulfonamide group consequently increasing the binding capability. The “tail” is a flexible fragment that improves aqueous solubility or participates in additional

E. Čapkauskaitė · D. Matulis (✉)

Department of Biothermodynamics and Drug Design, Institute of Biotechnology, Life Sciences Center, Vilnius University, Vilnius, Lithuania

e-mail: edita.capkauskaite@chf.stud.vu.lt; matulis@ibt.lt

© Springer Nature Switzerland AG 2019

D. Matulis (ed.), *Carbonic Anhydrase as Drug Target*,
https://doi.org/10.1007/978-3-030-12780-0_10

143

interplay between the CA and a ligand by interacting with active site part located further away from the zinc ion.

In the search of higher selectivity and binding affinity substituents were varied on the benzene ring. Small substituents were compared with the relatively large “tails” that were constructed from aromatic/heteroaromatic fragment connected by a flexible linker. Four classes of inhibitors which will be referred as **A**, **B**, **C**, and **D** were synthesized by alkylation of various hetero/aromatic compounds with four bromoacetophenones (Fig. 10.1) [3–7].

All alkylation reactions were carried out using sodium acetate as a base in tetrahydrofuran (THF) at room temperature with the exception of imidazoles, when

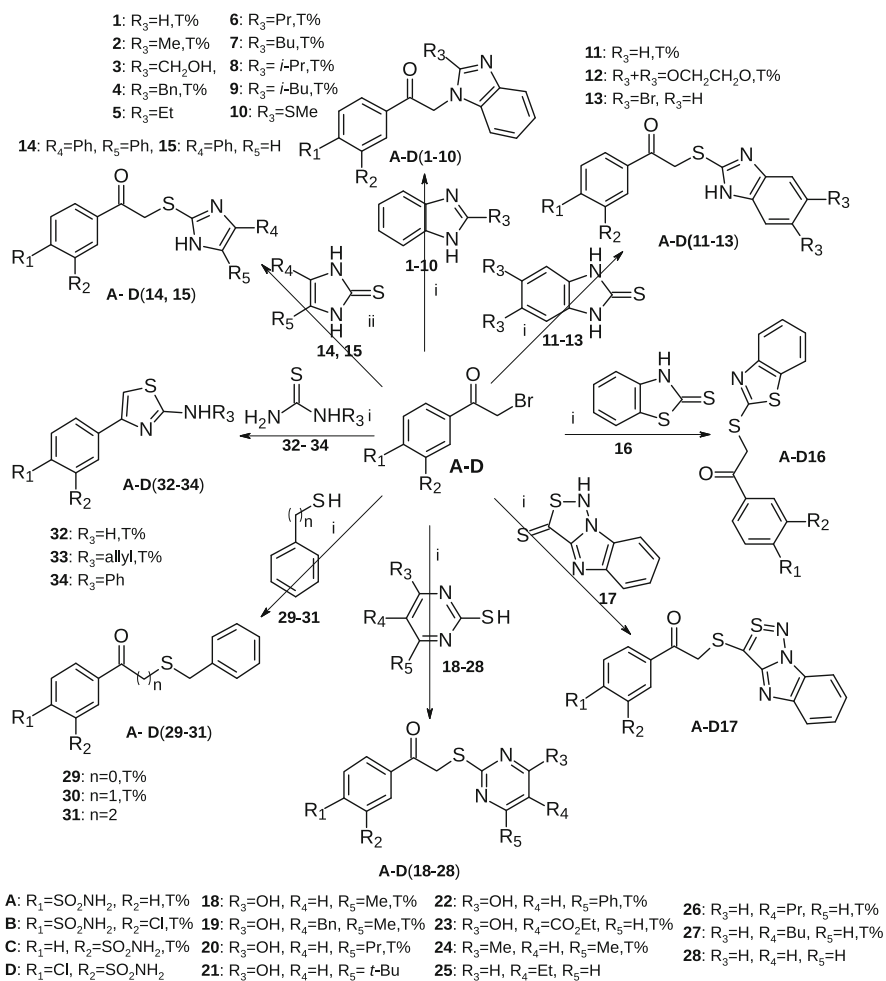


Fig. 10.1 Synthesis of compounds **A–D** (1–34) via two major routes: (i) NaOAc, THF, r.t., 24 h, (ii) NaOAc, toluene, r.t., 72 h

better yield was obtained using toluene as a solvent. Using the strongest bases such as sodium methanolate in methanol and potassium carbonate in acetone led to the formation of various by-products, reducing the product yield in the N-alkylated benzimidazole synthesis. Choosing a weaker base, sodium acetate, led to avoid the formation of undesired side compounds [7,8]. It should be noted that better results in the N-alkylation reaction were obtained when a 1.5 equivalent of the corresponding benzimidazole **1–10** was used. Contrary, the employment of an excess of alkylating reagent results in the dialkylation of the benzimidazole ring. For example, in the case of bromoacetophenone **1** and benzimidazole **D** ratio 1:2, the compound **D1a** was obtained as the main reaction product (Fig. 10.2) [7].

For the synthesis of S-alkylated compounds (benzimidazoles **A–D** (**11–13**) [7], imidazoles **A–D** (**14–15**), benzothiazoles **A–D16** [4], benzimidazo[1,2-c][1,2,3]thiadiazoles **A–D17**, pyrimidines **A–D** (**18–28**) [5,6], and phenylalkylthiols **A–D** (**29–31**) [6], the excess of thione derivative is not necessary.

An investigation of the S-substituted pyrimidine derivative structures **A–D** (**18–28**) by NMR spectroscopy showed that the ^1H and ^{13}C NMR spectra of pyrimidinones **A–D** (**18–23**) in DMSO- d_6 solution contained two sets of signals (Fig. 10.3). These results suggest that compounds **A–D** (**18–23**) in DMSO- d_6 solution exist in two forms: open chain **I** and cyclic **II** (Fig. 10.4) [5,6].

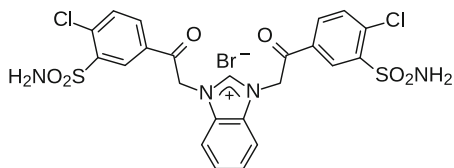
Notably large differences were observed for signals of SCH_2 group protons in the ^1H NMR spectra. This signal of open chain form **I** appeared as a singlet in the 4.72–4.97 ppm region, while SCH_2 group protons of cyclic form **II** were observed as doublets with $J = (12.0\text{--}12.9)$ Hz at 3.54–3.79 ppm. The geminal-type spin–spin coupling of SCH_2 protons arises from their non-equivalency in the cyclic form **II**.

The ^{13}C NMR spectra of compounds **A–D** (**18–23**) gave additional evidence for the existence of two forms of compounds **A–D** (**18–23**) in DMSO- d_6 solution. The signal for carbon of the SCH_2 group in open chain form **I** was observed at 37.3–39.3 ppm. In the ^{13}C NMR spectra of cyclic form **II**, a signal for this carbon was observed in the 42.1–43.0 ppm region.

Furthermore, the open chain isomers **A–D** (**18–23**) were characterized by the $\text{C}=\text{O}$ group carbon signal ranging from 192.2 ppm to 194.1 ppm. The $\text{C}-\text{OH}$ group carbon signal of cyclic form **II** was observed in the 95.5–97.8 ppm.

It was found that the **B**-type compounds are more involved in cyclic form (the ratio **I**: **II** was 1:0.83 as calculated from integral intensities of SCH_2 signals of the ^1H NMR spectra), as compared to the others (type **D**—1:0.30, type **A**—1:0.29, and type **C**—1:0.21). These differences can be explained by the influence of electron withdrawing substituents in the benzene ring on the carbonyl group.

Fig. 10.2 The structure of compound **D1a** that appears as a main undesired product if excess alkylating agent is used



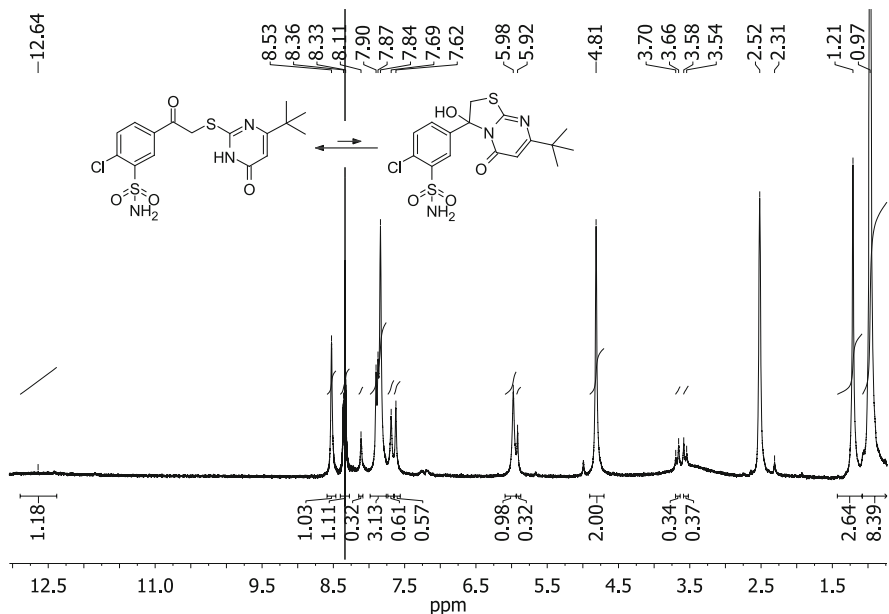


Fig. 10.3 The ^1H NMR spectrum of 5-[2-[(4-tert-butyl-6-oxo-1H-pyrimidin-2-yl)sulfanyl]acetyl]-2-chloro-benzenesulfonamide (**D21**)

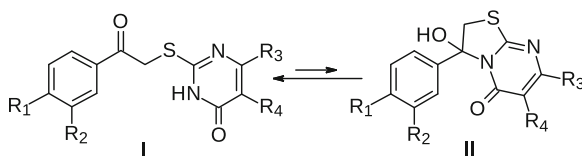


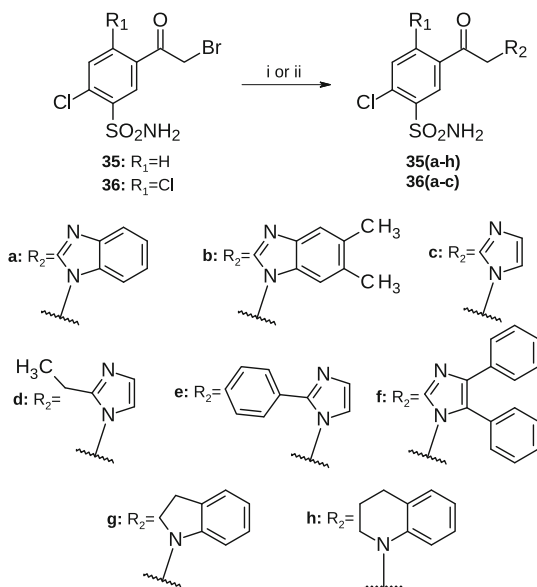
Fig. 10.4 Open chain **I** and cyclic **II** forms of compounds **A–D** (**18–23**)

Thiazolylbenzenesulfonamides **A–D** (**32–34**) were synthesized from thiocarbamides **32–34** and bromoacetophenones **A–D** according to the Hantzsch thiazole synthesis (Fig. 10.1). The reaction conditions used were the same as in the S-alkylation reaction.

10.2 Design of CA VA-Selective Compounds

It was observed that 5-[2-(benzimidazol-1-yl)acetyl]-2-chloro-benzenesulfonamide **35a** (**D1**) that is different from 2-chloro-5-[(2-methyl-1H-benzimidazol-1-yl)acetyl]benzenesulfonamide **D2** by only one methyl group showed higher binding affinity to CA VA than **35a** and possessed significant selectivity against all CA isoforms [9]. A number of **35a** analogs—2-chloro- and 2,4-dichlorobenzenesulfonamides, bearing different heterocyclic moieties, were

Fig. 10.5 Synthesis of compounds **35(a–h)** and **36(a–c)**. Reagents and conditions: (i) benzimidazole or imidazole (1.5 eq), NaOAc, THF, room temperature, 24 h (for **35(a–f)** and **36(a–c)**); (ii) 1,2,3,4-tetrahydroquinoline or indoline (2 eq), THF, room temperature, 48 h (for **35g** and **35h**)



synthesized to explore the influence of substituents on the binding affinity to CA VA [3].

As shown in Fig. 10.5, the synthesis of *N*-alkylated heterocycle derivatives **35(a–h)** and **36(a–c)** was performed by the alkylation of appropriate heterocycle with 5-(bromoacetyl)-2-chlorobenzene sulfonamide (**35**) and 5-(bromoacetyl)-2,4-dichlorobenzene sulfonamide (**36**) in the presence of NaOAc in THF at room temperature. The dialkylation of the benzimidazole/imidazole ring can be avoided by using the excess of the heterocycle. An excess of 1,2,3,4-tetrahydroquinoline and indoline was applied instead of NaOAc for the synthesis of **35g** and **35h**.

The protection of sulfonamide group with an *N,N*-dimethylaminomethylidene residue led to obtain the compound **41** with good yield, when direct acylation of 1-aminobenzimidazole with 2,4-dichloro-5-sulfamoyl-benzoyl chloride (**37**) led to the formation of a mixture of products.

The protected sulfonamide **38** was synthesized from initial 2,4-dichloro-5-sulfamoyl-benzoic acid (**37**) using dimethylformamide and thionyl chloride and subsequently converted to acyl chloride **39**. The following formation of amide **40** using pyridine in THF at 80 °C and removal of the sulfonamide-protecting group using NaOH(aq) resulted in the desired *N*-(benzimidazol-1-yl)-2,4-dichloro-5-sulfamoyl-benzamide (**41**) (Fig. 10.6). The 2-chloro-4,5-disubstituted benzenesulfonamides (**42–45**) were synthesized from 2,4-dichloro-5-substituted benzenesulfonamides **36a**, **36b**, and **41** by using appropriate thiol in DMSO or methanol in the presence of Et₃N as shown in Fig. 10.7.

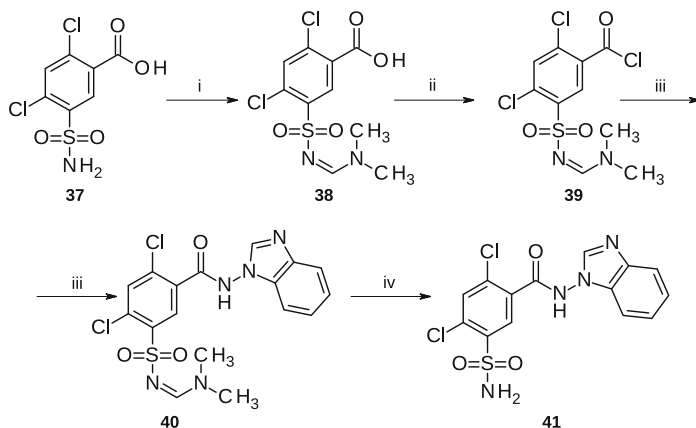


Fig. 10.6 Synthesis of compound **41**. Reagents and conditions: (i) DMF, SOCl_2 , -10°C , then r.t., 2 h; (ii) SOCl_2 , toluene, reflux, 2 h; (iii) 1-aminobenzimidazole, pyridine, THF 80°C , 3 h, then overnight at r.t.; (iv) 2 M NaOH(aq), r.t., 48 h, then 2 M HCl(aq)

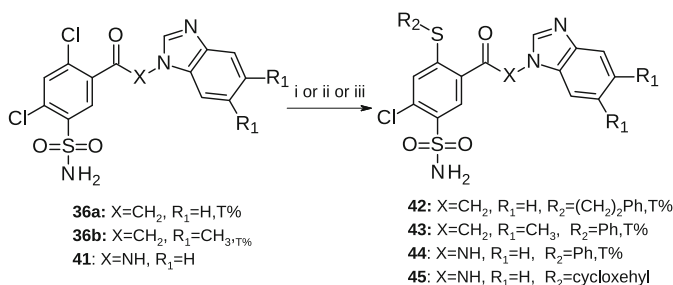


Fig. 10.7 Synthesis of 2-chloro-4,5-disubstituted benzenesulfonamides (compounds **42–45**). Reagents and conditions: (i) 2-phenylethanethiol, Et_3N , DMSO, r.t., 24 h; (ii) thiophenol, Et_3N , MeOH, reflux, 3 h; (iii) thiophenol or cyclohexanethiol, Et_3N , DMSO, r.t., 7 days

10.3 Design of Two-Tailed Compounds With Rotationally Fixed Benzenesulfonamide Ring While Within the CA Active Site That Bound Specific Pockets of the Target Isoforms

The arrangement of amino acids in the CA active site cavity leads to distinguish hydrophobic pocket with Phe131 side chain (CA II) [10, 11] and hydrophilic wall [12] which are situated against each other. Design of two-tailed compounds which could engage both CA pockets proposes new perspective for selective CA inhibitor design [13–19].

The flexibility and mobility of the compound is a disadvantage of this approach due to its ability to adapt to each CA's active site, thus reducing selectivity. A solution of this problem could be the restriction of the rotation of the benzene ring. The 2-halo-benzenesulfonamide scaffold was chosen as a background for

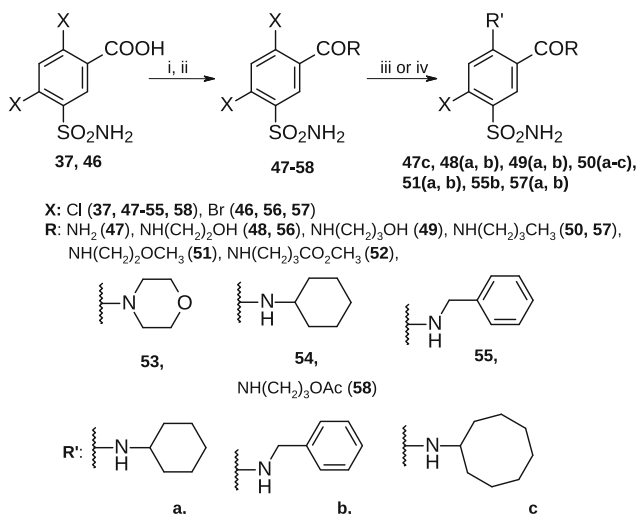


Fig. 10.8 The synthesis of 2-halo-4,5-disubstitutedbenzenesulfonamides **47–58**, **47c**, **48a–b**, **49a–b**, **50a–c**, **51a–b**, **55b**, and **57a–b**. (i) SOCl₂, toluene, reflux; (ii) appropriate amine RH, THF, 0 °C–20 °C; (iii) excess of appropriate amine R'H, reflux; (iv) appropriate amine R'H, dioxane, reflux

compound's synthesis due to the 2-Cl group's ability to fix the benzene ring of the ligand molecule in one known position in all CA isoforms [20].

The syntheses of mono and two-tailed compounds were performed starting from 2,4-dihalo-5-sulfamoylbenzoic acids **37** and **46**. First, one tail was introduced by amidation of the carboxyl group. Then the second tail was attached by the nucleophilic displacement of chlorine group [21, 22].

The synthesis of dihalosulfamoylbenzamides **47–58** is shown in Fig. 10.8. Acids **37** and **46** were converted to amides by refluxing with thionyl chloride and subsequent treatment with an appropriate amine, using as the base the excess of amine or triethylamine. Propanolamide **49** showed strong tendency to form *O*-acetylated derivative **58** during purification by concentrating ethyl acetate extract unlike ethanolamide **48** which formed only trace of *O*-acetylated compound.

Obtained one-tail containing compounds dichlorobenzamides **47–55** were amidated at 120 °C without solvent using amine excess according to the procedure previously reported in the literature [23]. The formation of by-products in the synthesis of dibromobenzamides **56** and **57** was avoided by performing the reaction in boiling dioxane for 7 days.

Dihalobenzamides **47–58** were subjected to reaction with various thiol-bearing derivatives (Fig. 10.9). As expected, the nucleophilic substitution occurs in the 4-position (*para*) relative to the sulfonamide group. Reaction conditions, using boiling methanol and triethylamine, are satisfactory for thiophenol. However, syntheses using other thiol derivatives required the replacement of a polar protic solvent MeOH to a polar aprotic solvent DMSO and a base triethylamine to

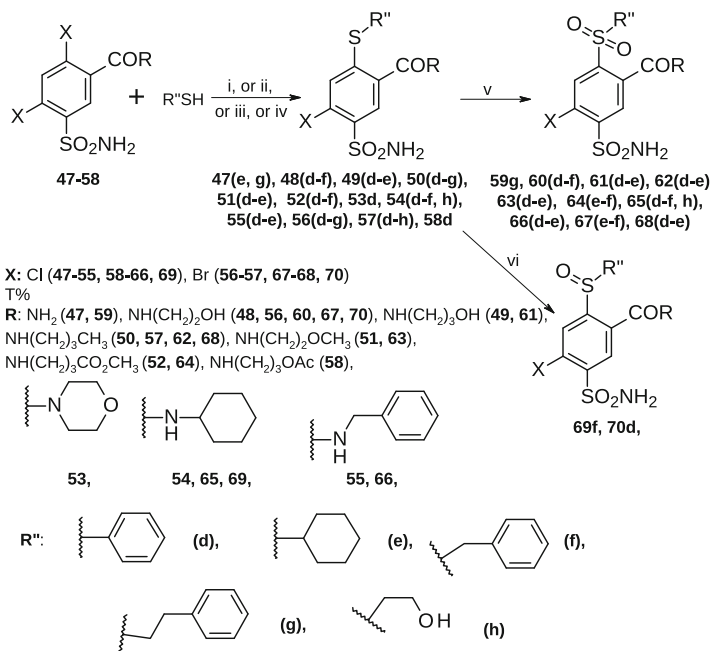


Fig. 10.9 The synthesis of 2-halo-4,5-disubstitutedbenzenesulfonamides. (i) TEA, MeOH, reflux; (ii) Cs₂CO₃, DMSO, 120 °C; (iii) K₂CO₃, DMSO, 60 °C; (iv) TEA, DMSO, 60 °C; (v) H₂O₂, AcOH, 75 °C; (vi) PAA, AcOH, 50 °C

potassium carbonate or even applying strict reaction condition (Cs₂CO₃, 120 °C for morpholinyl derivative **53**).

The sulfides **47–52** and **54–57** were oxidized to sulfonyl- and sulfinyl-derivatives using in situ generated peracetic acid (Fig. 10.9). A tendency of the hydroxyl group containing compound (**60d–f**, **61d–e**, **65h**, and **67e–f**) susceptibility to *O*-acetates formation was observed. Therefore, the reaction product mixture subsequently was subjected to deacetylation by boiling in diluted HCl.

The geminal coupling between the non-equivalent protons of the benzylic methylene group was observed in compound **69f** ¹H NMR spectra (DMSO-d₆: 4.05 (1H_A, d, *J* = 12.4 Hz, CH₂Ph) and 4.51 (1H_B, d, *J* = 12.4 Hz, CH₂Ph)) [24].

Several benzoic acids **37(c, e, g)** were synthesized from benzamides **47(c, e, g)** by performing hydrolysis by boiling in an acidic medium in order to avoid chlorine substitution. Alkaline medium at room temperature was more suitable to ester **52**, **52d–f**, and **64f** hydrolysis due to the ability to avoid attendant hydrolysis of the amide as suggested by TLC (Fig. 10.10).

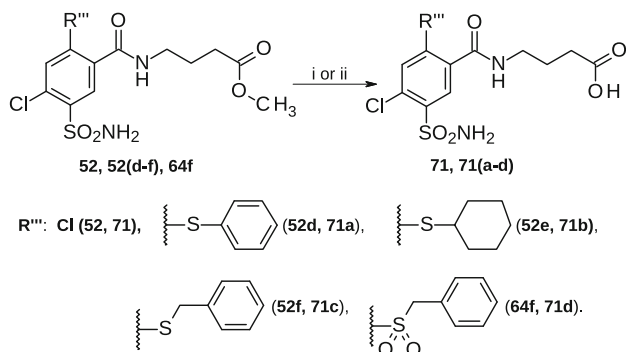


Fig. 10.10 The synthesis of 4-[(2,4-disubstituted-5-sulfamoyl-benzoyl)amino]butanoic acids **71**, **71a–d**. (i) conc. HCl(aq), MeOH, reflux; (ii) 10% NaOH(aq), MeOH, r.t.

10.4 Conclusions

Application of several benzenesulfonamide ring-based and tail-based approaches yielded a series of chlorinated substituted inhibitors of CAs. The chlorine in the benzene ring increased the acidity of the sulfonamide group. A series of CA VA-selective inhibitors were designed. The synthesis routes and the analysis of final products were described.

References

- Krishnamurthy, V.M., et al.: Carbonic anhydrase as a model for biophysical and physical-organic studies of proteins and protein-ligand binding. *Chem. Rev.* **108**, 946–1051 (2008)
- Supuran, C.T., Scozzafava, A., Casini, A.: Carbonic anhydrase inhibitors. *Med. Res. Rev.* **23**, 146–189 (2003)
- Čapkauskaitė, E., et al.: Benzimidazole design, synthesis, and docking to build selective carbonic anhydrase VA Inhibitors. *Bioorg. Med. Chem.* **26**, 675–687 (2018)
- Čapkauskaitė, E., et al.: Thiazole-substituted benzenesulfonamides as inhibitors of 12 human carbonic anhydrases. *Bioorg. Chem.* **77**, 534–541 (2018)
- Čapkauskaitė, E., et al.: Benzenesulfonamides with pyrimidine moiety as inhibitors of human carbonic anhydrases I, II, VI, VII, XII, and XIII. *Bioorg. Med. Chem.* **21**, 6937–6947 (2013)
- Čapkauskaitė, E., et al.: Design of [(2-pyrimidinylthio)acetyl]benzenesulfonamides as inhibitors of human carbonic anhydrases. *Eur. J. Med. Chem.* **51**, 259–270 (2012)
- Čapkauskaitė, E., et al.: Indapamide-like benzenesulfonamides as inhibitors of carbonic anhydrases I, II, VII, and XIII. *Bioorg. Med. Chem.* **18**, 7357–7364 (2010)
- Zubrienė, A., et al.: Benzenesulfonamides with benzimidazole moieties as inhibitors of carbonic anhydrases I, II, VII, XII and XIII. *J. Enzyme Inhib. Med. Chem.* **29**, 124–131 (2014)
- Čapkauskaitė, E., et al.: Combinatorial design of isoform-selective N-alkylated benzimidazole-based inhibitors of carbonic anhydrases. *ChemistrySelect* **2**, 5360–5371 (2017)
- Boriack, P.A., Christianson, D.W., Kingery-Wood, J., Whitesides, G.M.: Secondary interactions significantly removed from the sulfonamide binding pocket of carbonic anhydrase II influence inhibitor binding constants. *J. Med. Chem.* **38**, 2286–2291 (1995)

11. Pacchiano, F., et al.: Selective hydrophobic pocket binding observed within the carbonic anhydrase II active site accommodate different 4-substituted-ureido-benzenesulfonamides and correlate to inhibitor potency. *Chem. Commun.* **46**, 8371–8373 (2010)
12. Domsic, J.F., et al.: Entrapment of carbon dioxide in the active site of carbonic anhydrase II. *J. Biol. Chem.* **283**, 30766–30771 (2008)
13. Vernier, W., et al.: Thioether benzenesulfonamide inhibitors of carbonic anhydrases II and IV: structure-based drug design, synthesis, and biological evaluation. *Bioorg. Med. Chem.* **18**, 3307–3319 (2010)
14. Congiu, C., Onnis, V., Balboni, G., Supuran, C.T.: Synthesis and carbonic anhydrase I, II, IX and XII inhibition studies of 4-*N,N*-disubstituted sulfanilamides incorporating 4,4,4-trifluoro-3-oxo-but-1-enyl, phenacylthiourea and imidazol-2(3*H*)-one/thione moieties. *Bioorg. Med. Chem. Lett.* **24**, 1776–1779 (2014)
15. Tanpure, R.P., et al.: Carbonic anhydrase inhibitors with dual-tail moieties to match the hydrophobic and hydrophilic halves of the carbonic anhydrase active site. *J. Med. Chem.* **58**, 1494–1501 (2015)
16. Vaškevičienė, I., et al.: *N*-sulfamoylphenyl- and *N*-sulfamoylphenyl-*N*-thiazolyl- β -alanines and their derivatives as inhibitors of human carbonic anhydrases. *Bioorg. Chem.* **75**, 16–29 (2017)
17. Hou, Z., et al.: Dual-tail approach to discovery of novel carbonic anhydrase IX inhibitors by simultaneously matching the hydrophobic and hydrophilic halves of the active site. *Eur. J. Med. Chem.* **132**, 1–10 (2017)
18. Supuran, C.T.: How many carbonic anhydrase inhibition mechanisms exist? *J. Enzyme Inhib. Med. Chem.* **31**, 345–360 (2016)
19. Dudutienė, V., et al.: Discovery and characterization of novel selective inhibitors of carbonic anhydrase IX. *J. Med. Chem.* **57**, 9435–9446 (2014)
20. Scott, A.D., et al.: Thermodynamic optimisation in drug discovery: a case study using carbonic anhydrase inhibitors. *ChemMedChem* **4**, 1985–1989 (2009)
21. Matulis, D., Čapkauskaitė, E., Zakšauskas, A., Morkūnaite, V.: Selective inhibitors of carbonic anhydrase. WO2017017505 (A1) (2017)
22. Zakšauskas, A., et al.: Design of two-tail compounds with rotationally fixed benzenesulfonamide ring as inhibitors of carbonic anhydrases. *Eur. J. Med. Chem.* **156**, 61–78 (2018)
23. Sturm, K., Siedel, W., Weyer, R., Ruschig, H.: Zur chemie des furosemids, I. Synthesen von 5-sulfamoyl-anthranilsäure-derivaten. *Eur. J. Inorg. Chem.* **99**, 328–344 (1966)
24. Nishio, M.: Nuclear magnetic resonance studies of sulfur compounds. II. The substituent effect on geminal coupling constants and on magnetic nonequivalence of the methylene protons of sulfoxides. *Chem. Pharm. Bull.* **15**, 1669–1676 (1967)



Organic Synthesis of Substituted Fluorinated Benzenesulfonamides as Selective Inhibitors of CA IX and Other Isoforms

11

Virginija Dudutienė and Daumantas Matulis

Abstract

Numerous chemical compounds have been previously shown to be efficient inhibitors of human CAs. However, the primary-sulfonamide-group-bearing compounds have always stood as exceptionally strong binders. The binding affinity can be significantly increased by introducing electron-withdrawing groups near the sulfonamide group in order to increase the acidity of the amino group. Fluorine substituent is one of the strongest available electron-withdrawing groups that increase the acidity by several pH units. In this chapter, we describe the design and organic synthesis of a series of fluorine-substituted benzenesulfonamides. Furthermore, the compounds possess one or more additional bulky functional groups that determine compound selectivity towards a particular CA isoform. Such compounds have been designed to not fit the active site cavity of every CA except the targeted isoform. In some cases, the fluorine-bearing compounds reached thousand-to-million-fold selectivities and thus are expected to exhibit much smaller side effects than the non-selective compounds.

11.1 *para*-Substituted Tetrafluoro Benzenesulfonamides

A wide range of compounds have been reported to inhibit the enzymatic activity of CAs. Many of the classical CA inhibitors are primary benzenesulfonamides bearing various substituents designed using the “tail approach” that targets hydrophobic or

V. Dudutienė · D. Matulis (✉)

Department of Biothermodynamics and Drug Design, Institute of Biotechnology, Life Sciences Center, Vilnius University, Vilnius, Lithuania
e-mail: virginija.dudutiene@bti.vu.lt; matulis@ibt.lt

hydrophilic regions of CAs. Furthermore, it is known that the pK_a of sulfonamide amino group has to be reduced to increase inhibitor affinity towards CA [1]. The pK_a should be near the pH of the medium (≈ 7.4) [1], while the pK_a of unsubstituted benzenesulfonamide is 10.1 [2]. The presence of electron-withdrawing substituents on a benzene ring decreases the pK_a of sulfonamide and increases affinity to CAs.

For this purpose we synthesized a series of benzenesulfonamides bearing fluorine atoms immediately on the sulfonamide-holding benzene ring. The pentafluorobenzenesulfonamide was chosen as a starting reference compound. The synthesis of pentafluorobenzenesulfonamide (compound **1**) via amination of pentafluorobenzenesulfonyl chloride (purchased from Alfa Aesar) with aqueous ammonia was performed. The synthesis of pentafluorobenzenesulfonamides from appropriate sulfonyl chloride has been previously reported in the literature [3]. However, this path yielded substantial amounts of disulfonimide that was obtained as a by-product. We found that the formation of imide can be avoided by keeping the reaction medium near neutral pH. The formation of imide is due to low pK_a of pentafluorobenzenesulfonamide. Deprotonation of sulfonamide occurs in the basic medium and deprotonated sulfonamide reacts readily with the starting material—sulfonyl chloride. The starting compound pentafluorobenzenesulfonamide readily underwent nucleophilic substitution reaction and formed the 4-substituted-2,3,5,6-tetrafluorobenzenesulfonamides [4]. The 4-substituted-2,3,5,6-tetrafluorobenzenesulfonamides **2–24** were obtained from compound **1** by using the appropriate nucleophile in ethanol, methanol, or DMSO in the presence of Et_3N or K_2CO_3 (excess of nucleophile was used in several cases instead of the mentioned bases) (Fig. 11.1). The compounds bearing SO_2R groups were synthesized by oxidation of appropriate thiol derivatives.

The spectral elucidation of purified products showed that substitution occurred in the *para* position. In the ^{13}C NMR spectra of isolated products there were triplets for carbons ($C-SO_2NH_2$, $C-R$) due to the coupling of two identical fluorines to *ortho* carbons and the coupling constants of 14–21 Hz. The two doublets of doublets occurred for two pairs of carbons. The fluorine coupling to directly substituted carbons (*ipso*) was very large and the coupling constants were 228–258 Hz. The ^{13}C NMR (DMSO) of 2,3,5,6-tetrafluoro-4-[(2-hydroxyethyl)sulfonyl] benzenesulfonamide is given as an example in Fig. 11.2. In the ^{19}F NMR spectra of isolated products there were two sets of signals because of two pairs of fluorine atoms.

The *para*-substituted tetrafluoro benzenesulfonamides have exhibited extremely high affinity to some CA isoforms, primarily to CA I, that was a non-desired target for most therapeutic applications. Therefore, it was considered that the substitution of one or two fluorines with groups that would recognize protein surface pockets of desired targets such as CA IX could yield selective inhibitors for the desired CA isoforms.

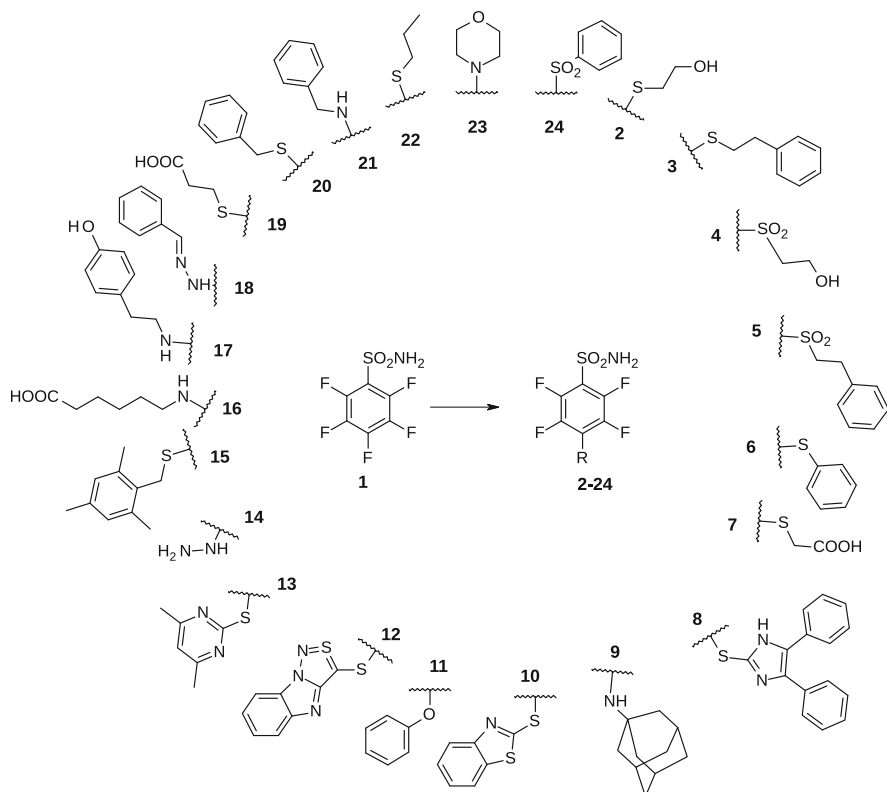


Fig. 11.1 A general scheme shows the synthesis path and the diversity of substituents yielding the *para*-substituted tetrafluoro benzenesulfonamides. Compound synthesis has been previously described in [4]

11.2 *ortho-para*-Substituted Trifluoro Benzenesulfonamides

The 4-substituted-2,3,5,6-tetrafluorobenzenesulfonamides can be subjected to further aromatic nucleophilic substitution reactions. A series of 2,4-substituted-3,5,6-trifluorobenzenesulfonamides (**25a–g** and **26a–o**), 3,4-substituted-2,5,6-trifluorobenzenesulfonamides (**27a–f, h, k; 28a–k, p–s**), and 3,4,5-substituted-2,6-difluorobenzenesulfonamides (**29dd, at, au; 30bb**) were synthesized (Fig. 11.3) [5, 6].

The 2,3,5,6-tetrafluoro-4-[(2-hydroxyethyl)sulfonyl]benzenesulfonamide (**2**) and 2,3,5,6-tetrafluoro-4-[(2-phenylethyl)thio]benzenesulfonamide (**3**) were chosen as main substances for aromatic nucleophilic substitution reactions occurring in the *ortho* position. Some other compounds bearing propylthio-, [2(4-hydroxyphenyl)ethyl]thio-, or simply hydrogen were investigated as substrates for aromatic nucleophilic substitution reactions [5]. Also 4-(2-mercaptoethyl)benzoic acid derivative was involved in aromatic nucleophilic substitution reactions [7]. Here we explain the synthesis of the majority of compounds, bearing particular

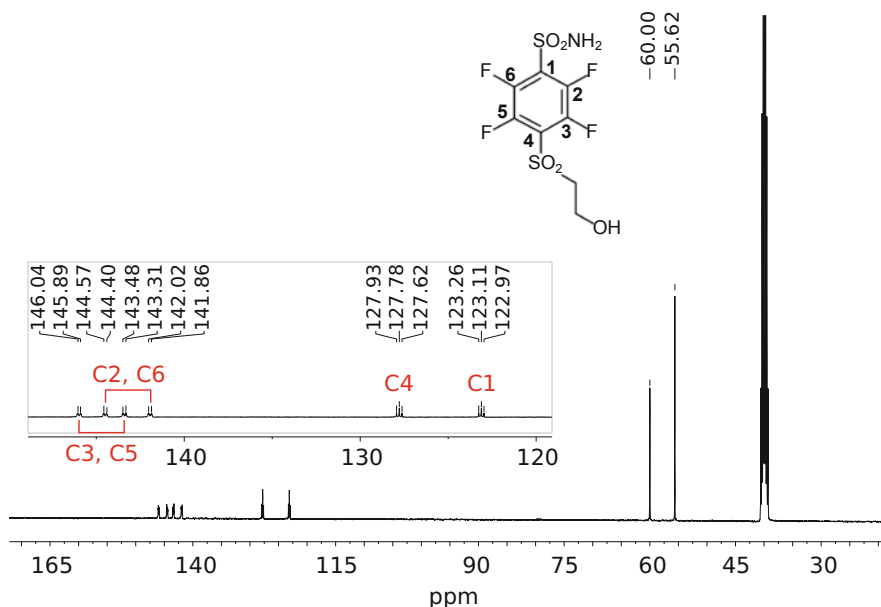


Fig. 11.2 The ^{13}C NMR (DMSO) spectrum of 2,3,5,6-tetrafluoro-4-[(2-hydroxyethyl)sulfonyl]benzenesulfonamide (**4**)

para-substituents (compounds **2** and **3**). Reactions of compounds **2** and **3** with various nitrogen-centered nucleophiles were performed in DMSO in the presence of Et_3N . The *ortho* substituted (relative to the sulfonamide group) products **25a–g**, **26a–o** were obtained. The formation of *ortho* substituted products is due to sulfonamide group *ortho*-directing ability.

The spectral elucidation of purified products showed that the *ortho* substitution occurred [5, 6]. In the ^{13}C NMR (CDCl_3 , DMSO) spectra of isolated products **25a–g**, **26a–o**, there were triplets for methylene groups ($\text{SCH}_2\text{CH}_2\text{Ph}$, $\text{SCH}_2\text{CH}_2\text{OH}$) at 35–37 ppm due to the coupling of two identical fluorines to carbon and the coupling constants of 2–4 Hz. These fluorines are in the *ortho* position relative to $\text{SCH}_2\text{CH}_2\text{Ph}$, $\text{SCH}_2\text{CH}_2\text{OH}$ groups. The substituents which appeared from incoming N-centered nucleophiles exhibited similar C–F couplings. The signals of carbons (N–C) appeared as doublets due to one fluorine coupling to carbon at 40–60 ppm with the coupling constants of 10–12 Hz. The H, C HETCOR spectrum of compound **25b** (VD12-09) confirmed our assignment of carbon signals (Fig. 11.4). In ^{13}C NMR (DMSO) spectra, the triplet at 36.86 ppm belongs to the carbon of group $\text{SCH}_2\text{CH}_2\text{OH}$ and the doublet at 55.65 ppm belongs to the carbon of fragment NHCH. Additional valuable information about the substitution profile can be obtained from the ^{13}C NMR spectra. The ^{13}C NMR (DMSO) spectrum of 2-(cyclooctylamino)-3,5,6-trifluoro-4-[(2-hydroxyethyl)thio]benzenesulfonamide (**25b**, VD12-09) is given in Fig. 11.5 as an example. Carbons directly substituted

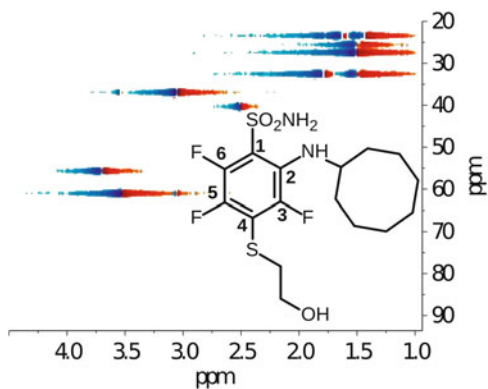


Fig. 11.4 The H–C HETCOR (DMSO) spectrum of 2-(cyclooctylamino)-3,5,6-trifluoro-4-[(2-hydroxyethyl)thio] benzenesulfonamide (compound **25b**, VD12-09)

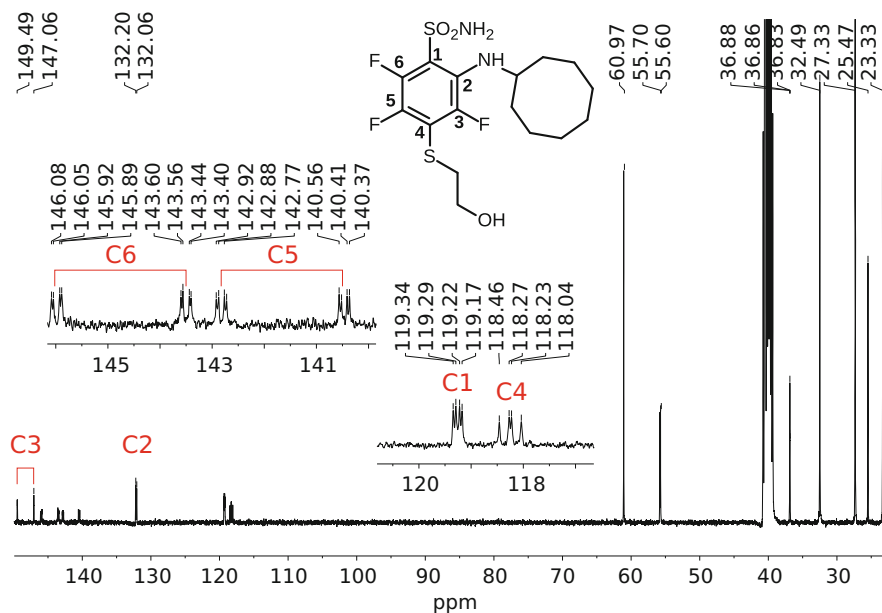


Fig. 11.5 The ^{13}C NMR (DMSO) spectrum of 2-(cyclooctylamino)-3,5,6-trifluoro-4-[(2-hydroxyethyl)thio]benzenesulfonamide (compound **25b**, VD12-09)

this inhibitor. The position of the substituent was well resolved in the electron density of the compound bound in active centers of CAs.

11.3 *meta-para*-Substituted Trifluoro Benzenesulfonamides

The 4-substituted-2,3,5,6-tetrafluoro benzenesulfonamides bearing fully oxidized sulfur functional groups in the *para* position can be handy in further aromatic nucleophilic substitution reactions, but in this case the substitution reaction occurs in the *meta* position (relatively to the sulfonamide group). Reactions of 2,3,5,6-tetrafluoro-4-[(2-hydroxyethyl)sulfonyl]benzenesulfonamide (**4**) and 2,3,5,6-tetrafluoro-4-[(2-phenylethyl)sulfonyl]benzenesulfonamide (**5**) with various nitrogen-centered nucleophiles were accomplished and the *meta* substituted products **27a–f, h, k**; **28a–k, p–s** were obtained (Fig. 11.3) [5, 6]. The groups $\text{SO}_2\text{CH}_2\text{CH}_2\text{Ph}$ and $\text{SO}_2\text{CH}_2\text{CH}_2\text{OH}$ exhibit stronger electron-withdrawing properties than SO_2NH_2 and direct nucleophile in *meta* position according to SO_2NH_2 group. Reactions of compounds **4** and **5** with various nitrogen-centered nucleophiles were carried out in DMSO in the presence of Et_3N . The compound **4** bearing (2-hydroxyethyl)sulfonyl “tail” was sensitive to such bases as Et_3N or K_2CO_3 and instead of these bases the equivalent of nitrogen-centered nucleophile was used.

The spectral elucidation of purified products led us to conclude that the nucleophilic substitution for the compounds bearing (2-phenylethyl)sulfonyl and (2-hydroxyethyl)sulfonyl “tails” took place at the *meta* position. In the ^{13}C NMR spectra of isolated products, there were doublets for the methylene group ($\text{SO}_2\text{CH}_2\text{CH}_2\text{Ph}$ and $\text{SO}_2\text{CH}_2\text{CH}_2\text{OH}$) at 53–62 ppm with the coupling constants of 4–2 Hz. The splitting was due to the coupling of one fluorine atom to carbon. This fluorine is in the *ortho* position relative to $\text{SO}_2\text{CH}_2\text{CH}_2\text{Ph}$ and $\text{SO}_2\text{CH}_2\text{CH}_2\text{OH}$ groups. This splitting was observed just for minority of compounds recorded using the 300–75 MHz spectrometer. However, when some compounds which did not show such splitting were repeatedly recorded with the 400–100 MHz spectrometer, then the splitting appeared. The substituents which appeared from incoming N-centered nucleophiles similarly to *ortho* substituted compounds exhibit C–F couplings. The signals of carbons (N–C) appeared as doublets (due to one fluorine coupling to carbon) at 34–66 ppm with coupling constants 11–13 Hz. H, C HETCOR spectrum of compound **27b** (VD11-4-2) confirmed our assignment of carbon signals where the doublet at 60.03 ppm belongs to carbon of group $\text{SO}_2\text{CH}_2\text{CH}_2\text{OH}$ and the doublet at 55.91 ppm belongs to the carbon of fragment NHCH (Fig. 11.6). Furthermore, valuable information about the substitution profile can be obtained from the ^{13}C NMR spectra. ^{13}C NMR (DMSO) of **27b** (VD11-4-2) as an example is given in Fig. 11.7. Carbons directly substituted with fluorines (ipso carbons—C2, C5, C6) possess large coupling constants 247–254 Hz and appear as a doublet (C2) at 144.54 ppm and a doublet of doublet of doublets (C5, C6) at 146.06 and 137.16 ppm. The doublet at 144.54 ppm can be assigned to C2 as none of the fluorine atoms exists in the neighborhood. The carbon C3 appears as a doublet at 135 ppm due to F coupling to the *ortho*-position with the coupling constant

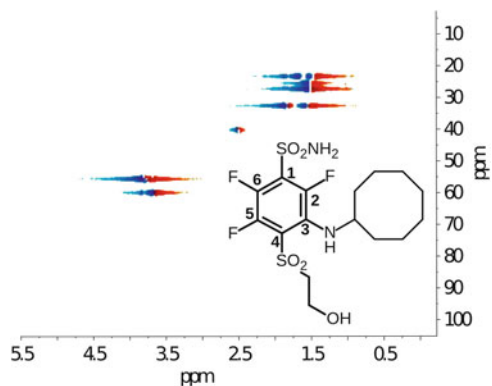


Fig. 11.6 The H–C HETCOR (DMSO) spectrum of 3-(cyclooctylamino)-2,5,6-trifluoro-4-[(2-hydroxyethyl)thio]benzenesulfonamide (**27b**, VD11-4-2)

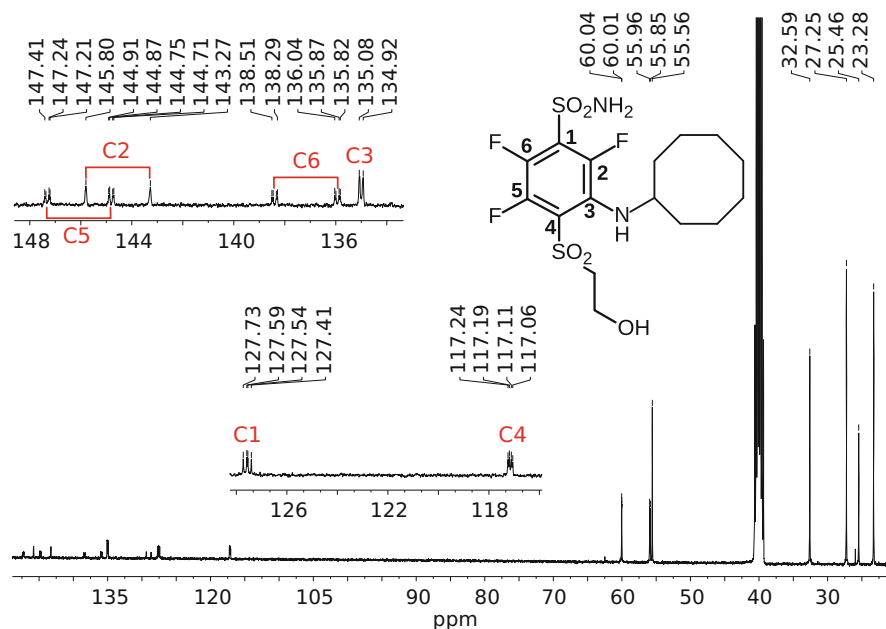


Fig. 11.7 The ^{13}C NMR (DMSO) spectrum of 3-(cyclooctylamino)-2,5,6-trifluoro-4-[(2-hydroxyethyl)thio]benzenesulfonamide (**27b**, VD11-4-2)

of 13 Hz. The doublet of doublets at 127.57 and 117.15 ppm can be assigned to carbons C1 and C4. Carbon C1 appears as almost a triplet due to two fluorines in the *ortho* position.

In the ^{19}F NMR spectra of isolated products there were three sets of signals because of three fluorine atoms. Furthermore, the *meta* substitution for compounds

27b, **g**, **h**, and **28i** was demonstrated by the X-ray structures of CA crystals soaked with these inhibitors. The position of the substituent was well resolved in the electron density of the compounds bound in the active centers of CAs.

The 3-substituted compounds bearing (2-phenylethyl)sulfonyl and (2-hydroxyethyl)sulfonyl “tails” are activated towards a nucleophilic attack and thus the 3,5-substituted compounds **29dd**, **at**, **au**; **30bb** were obtained [5]. The second nucleophilic substitution occurred in the *meta* position again. Such substitution profile is confirmed primarily by the ^{19}F NMR spectra. We observe one singlet in ^{19}F NMR spectra for 3,5-substituted compounds bearing the same substituents at positions 3 and 5. Also, the ^{13}C NMR spectra verify di *meta* substitution. This is particularly visible in ^{13}C NMR spectra of compounds bearing the same substituents at positions 3 and 5. There are two symmetric carbons directly substituted with fluorines and in the ^{13}C NMR spectra we observe one signal which possesses a large coupling constant of 244–247 Hz. The carbon substituted with the sulfonamide group appears as a triplet due to two identical fluorines in the *ortho* position with the coupling constant of 16 Hz. The carbon substituted with the (2-phenylethyl)sulfonyl and (2-hydroxyethyl)sulfonyl groups appears as a triplet due to two identical fluorines in the *meta* position with the coupling constant of 3–5 Hz. The symmetric carbons substituted with amines appear as a doublet of doublets due to two fluorines in the *ortho* and *para* positions with the coupling constants of 10 and 6 Hz.

11.4 Conclusions

Synthesis routes, purification techniques, and the analytical methods of the final obtained products have been described for tetrafluoro *para*-substituted benzenesulfonamides, trifluoro *para* and *meta* or *ortho*-substituted benzenesulfonamides. The fluorine atoms on the ring adjacent to sulfonamide group were essential for increase in acidity of the compounds by electron withdrawing, thus making the compounds bind with greater affinity to carbonic anhydrases.

References

1. Krishnamurthy, V.M., et al.: Carbonic anhydrase as a model for biophysical and physical-organic studies of proteins and protein-ligand binding. *Chem. Rev.* **108**, 946–1051 (2008)
2. Krishnamurthy, V.M., et al.: Thermodynamic parameters for the association of fluorinated benzenesulfonamides with bovine carbonic anhydrase II. *Chem. Asian J.* **2**, 94–105 (2007)
3. Robson, P., Smith, T.A., Stephens, R., Tatlow, J.C.: Aromatic polyfluoro-compounds. Part XIII. derivatives of penta- and 2,3,5,6-tetra-fluorothiophenol. *J. Chem. Soc.* **1963**, 3692–3703 (1963)
4. Dudutienė, V., et al.: 4-Substituted-2,3,5,6-tetrafluorobenzenesulfonamides as inhibitors of carbonic anhydrases I, II, VII, XII, and XIII. *Bioorg. Med. Chem.* **21**, 2093–2106 (2013)
5. Dudutienė, V., et al.: Functionalization of fluorinated benzenesulfonamides and their inhibitory properties toward carbonic anhydrases. *ChemMed-Chem* **10**, 662–687 (2015)
6. Dudutienė, V., et al.: Discovery and characterization of novel selective inhibitors of carbonic anhydrase IX. *J. Med. Chem.* **57**, 9435–9446 (2014)
7. Kazokaitė, J., et al.: Novel fluorinated carbonic anhydrase IX inhibitors reduce hypoxia-induced acidification and clonogenic survival of cancer cells. *Oncotarget* **9**, 26800–26816 (2018)



Carbonic Anhydrase Inhibitors with Dual Targeting

12

Peteris Trapencieris, Anete Parkova, and Ineta Vendina-Birzniece

Abstract

Rational design of pharmaceutically active small molecules is usually based on a paradigm where one small molecule targets a single protein molecule and this way exhibits its medically relevant effect. This paradigm has recently changed toward the idea that design to affect several targets instead of one can provide superior therapeutic effect. Here we provide a series of examples where carbonic anhydrase inhibition may or may not be the main function of the drugs and dual targeting may have additional advantages. Inhibitors of COX-2, such as valdecoxib, are also good inhibitors of CAs due to the presence of sulfonamide moiety that may not be crucial for the binding of COX-2. Dual inhibitors of matrix metalloproteinases (MMPs) and CAs are also discussed.

12.1 Introduction

Diseases are complex biological processes. In the 1970s of the twentieth century, the main strategy for drug design was monotherapy. This strategy—one ligand (key) compound might fit and operate to a single target (lock)—has failed mainly for one reason. Most diseases are molecularly complex and develop via dysregulation of more than one target enzyme and they are more difficult to “unlock.” When technological advances in genomics and high-throughput screening (HTS) developed during the last 2 decades, “dirty drugs” paradigm has changed. Fifteen years ago it was stated that balanced modulation of several targets can provide superior therapeutic effect [1]. At the early stages authors proposed the term “designed

P. Trapencieris (✉) · A. Parkova · I. Vendina-Birzniece
Latvian Institute of Organic Synthesis, Riga, Latvia
e-mail: peteris@osi.lv; anete@osi.lv; ineta@osi.lv

multiple” (DM) ligands. Shifting from the single to the multitarget paradigm in drug discovery will discover a route to solution of problems with complex diseases [2].

In fact, there are two distinct approaches: rational design of pharmacophores and screening of compound libraries of known drugs. Pharmacophore combination approach would lead to search for cleavable conjugates. For example, nitric oxide release functionalities for ibuprofen [3] or conjugated pharmacophores, and of thrombin inhibitor linked to antithrombin III-mediated factor Xa [4].

As a rule, these active compounds are larger in molecular size and are more complex. Alternative structures are highly integrated, because proteins are much more similar and inhibitors have closer structural similarities, for example, angiotensin-1 (AT₁) and endothelin-A (ET_A) receptor DM ligands [5]. Already in 2004 Morphy [1] proposed ten aspirations for DM ligands: similar targets; multiple lead generation approaches; clear in vitro and in vivo relationship; “designing in” activities; structure–activity relationship (SAR) should indicate places of overlapping; good physicochemical and pharmacokinetic properties; common functional activities; metabolites should be the same in vitro profile or be inactive; ligand and protein models; and a single enantiomer should be responsible for all desired activities.

With more complex diseases like cancer, inflammation, cardiovascular and central nervous system (CNS) diseases good results with monotherapy approaches are difficult to achieve. In some cases the usage of several drugs so far is the best choice. With the development of personalized medicine in the nearest future, polypharmacology may be the solution of a problem partly. Better way to solve the problems is the use of the proteochemometrics (PCM) [6], a method which enables to explore ligand–ligand, protein–ligand, and protein–protein interactions by the usage of target, ligand, and ligand–target descriptors. In addition, advances in the current development of hybrid anticancer drug discovery have been reviewed [7] and provided a clear view of future directions.

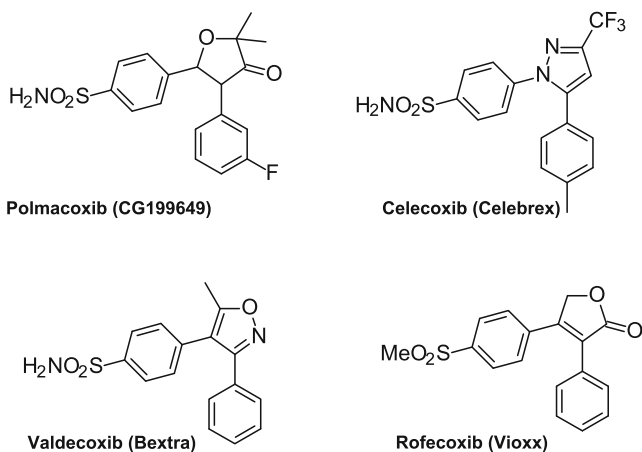
12.2 Known Drugs as CA Inhibitors

Carbonic anhydrase (CA) is a naturally abundant and a very important enzyme regulating a very simple reaction—interconversion of carbon dioxide to bicarbonate anion [8]. Due to the presence of CA, this reaction is one of the fastest of proton exchange enzymes. In humans 15 isoforms of CAs are located in different parts of cells—cytosol, mitochondria, and membranes—and may be applied as good targets for treatment of different diseases. Thus, regulation of cytosolic CA II may be helpful for the treatment of glaucoma, while membrane proteins CA IX and CA XII—for the treatment of different forms of cancer.

12.2.1 Inhibitors of COX-2

The first group of compounds checked as dual inhibitors were related to known drugs, which were tested on CA activity. Inhibitors of COX-2, non-steroidal anti-

inflammatory drugs (NSAIDs), have been applied quite often. Tricyclic “coxibs” differ and possess methyl sulfone (rofecoxib) and sulfonamide (celecoxib and valdecoxib) moieties. These structural differences are responsible for inhibition of activity of CA isoforms CA I, CA II, CA IV, CA IX, and CA XII. Thus, inhibition of CA II by celecoxib (Celebrex), but not rofecoxib (Vioxx), could be responsible for diuretic effect that could counteract renal hypertension induced by COX-2 inhibitors. This explains why patients treated with Vioxx, but not celecoxib, demonstrate increased incidence of hypertension and edema. Polmacoxib (CG100649) is an NSAID, approved in South Korea in February 2015 to treat osteoarthritis. It characterizes with long life in plasma and whole blood (half-life of 100–160h) [9]. It seems that inhibitor sulfonamide moiety is responsible for CA inhibition, also stabilizes the inhibitor, and reduces cardiovascular risks.

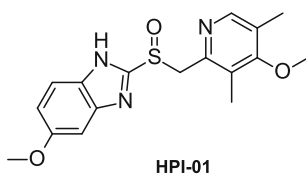


This dual CA-COX-2 activity may help to explain differences in clinical observation between sulfonamide and methyl sulfone COX-2 inhibitors [10]. Moreover, activity of CA II, CA IX, and CA XII may be critical for development and invasion of cancer cells.

12.2.2 H⁺K⁺ATPase

Changes in ion flows mainly are regulated by H⁺K⁺ATPase inhibitors and omeprazole (HPI-01) is a selective and irreversible proton pump inhibitor (HPI). It suppresses stomach acid secretion in the final step of production by specific inhibition of the H⁺K⁺ATPase system. It was shown that omeprazole has dual

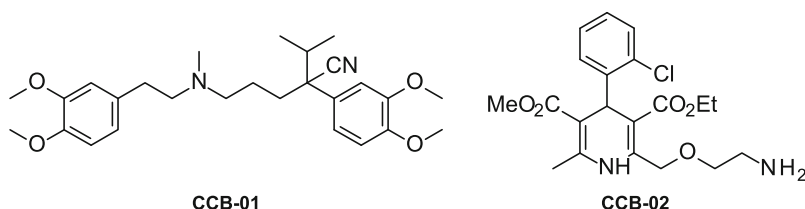
mechanism of action: besides the known H^+K^+ ATPase inhibition, it showed gastric mucosa CA inhibition [11]. These both enzymes may be functionally coupled.



This mechanism of action (antisecretory and vasodilating), which does not occur in other therapies, may explain the greater effectiveness of substituted benzimidazoles.

12.2.3 Calcium Channel Blockers (CCB)

Verapamil and amlodipine are two famous generic calcium channel blockers (CCBs), both are used for the treatment of high blood pressure and both are in the list of WHO Essential Medicines. Verapamil (CCB-01) has been used since 1981 and amlodipine (CCB-02) has been used since 1990 and it was assumed that both inhibit vascular smooth muscle CA I activity in vitro and in vivo in a dose-dependent manner [12].

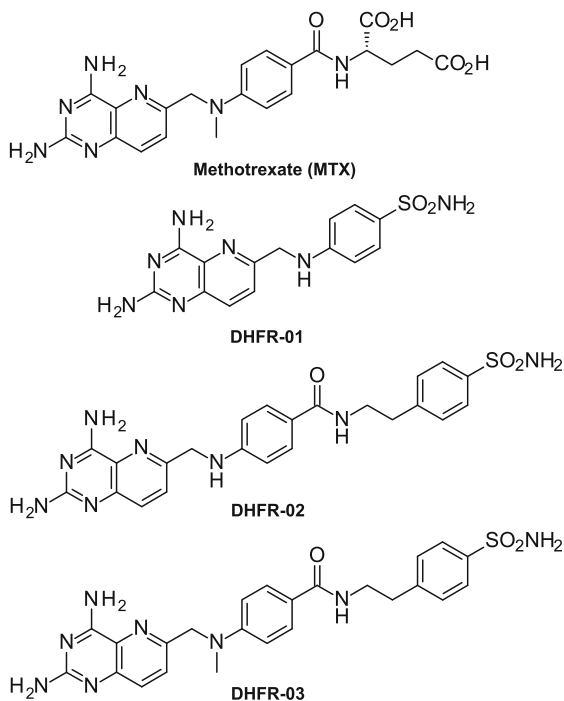


These data suggest verapamil and amlodipine dual mechanism of action: the former consists of action on calcium channels and the latter inhibition of smooth muscle CA I. Consecutive pH increase might be an additional factor involved in intracellular influx through calcium channels.

12.3 Modification of Known Drugs

The second group of compounds checked as dual inhibitors were also related to known drugs, which were modified chemically and checked as potential CA inhibitors. Thus, antifolate *methotrexate* (MTX) is one of the oldest anticancer drugs, based on the blockage of folate pathways by inhibiting dihydrofolate reductase

(DHFR). Some new hybrid compounds as dual inhibitors for DHFR and CAs were developed [13]. Pteridine and sulfonamide fragments were selected as key moieties and were combined in the same molecular entity.



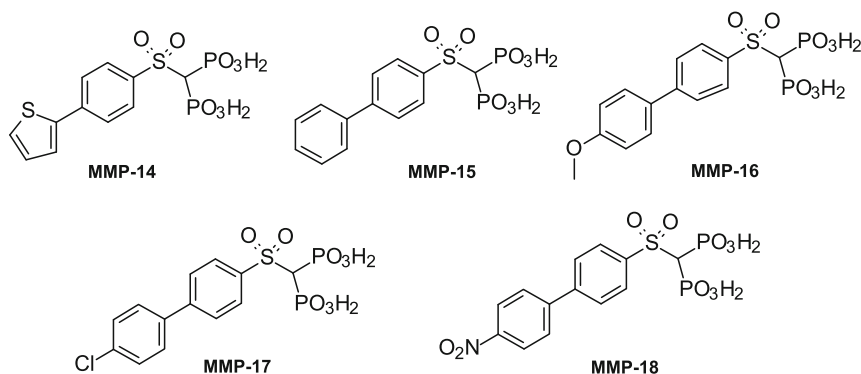
At the beginning MTX molecule was simplified and a spacer (NH) was used the same way as in the structure DHFR-01. Structural changes in the spacer improved CA IX/CA II selectivity up to two orders (compounds DHFR-02 and DHFR-03). Unfortunately activity against DHFR is weak (low micromolar range) in comparison with the basic structure MTX. Antiproliferative activities against two cancer cell lines (A549 and PC3) were in the millimolar range due to deficiency of inhibitor transport inside the cancer cells.

12.4 New Dual CA Inhibitors in New Classes of Compounds

The third group of compounds used as dual inhibitors are recognized as active compounds for one enzyme system and new materials for CA inhibition or hybrid materials where pharmacophores for both activities are coupled in a one molecule.

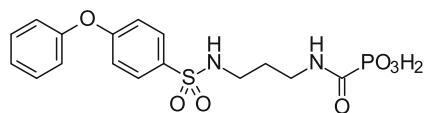
The most attempts for finding inhibitors in this area are devoted to MMP-CA dual inhibition and STS-CA dual inhibition.

12.4.1 Matrix Metalloproteinase (MMP)

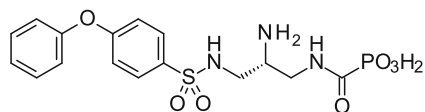


MPP-2 inhibitor activity was shown in the class of bisphosphonic acid derivatives (compounds MMP-14 to MMP-18) [14]. But Cl-derivative (MMP-17) exhibited more visible MMP-2 selectivity, which is connected with successful treatment of patients with debilitating bone metastases. Three years later the same bisphosphonic acid derivatives were tested on binding to several CA isoforms (CA I, CA II, CA IX, CA XII, and CA XIV) [15]. The best nanomolar dual inhibition against MMP-2 and selected CA isoforms was shown for compounds with diatomic functionality. This class of compounds characterizes with some interesting selectivity—4-methoxy derivative MMP-16 has nanomolar binding on all five tested CA isoforms, 4-Cl derivative MMP-17 is active in submicromolar range only on CA XII, but MMP-15 inhibited membrane-bounded isoforms CA IX and CA XII. Thienyl group containing MMP-14 showed the same inhibition profile as parent phenyl isosteric derivative MMP-15.

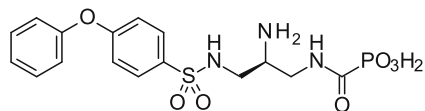
Aminoalkylcarbamoylphosphonates MMP-19 to MMP-21 inhibition of MMPs and CAs in some cases showed submicromolar binding [16]. Changes in chiral center geometry (MMP-20 vs. MMP-21) did not make noticeable changes in CA's submicromolar binding or did make small changes in MMP micromolar binding.



MMP-19

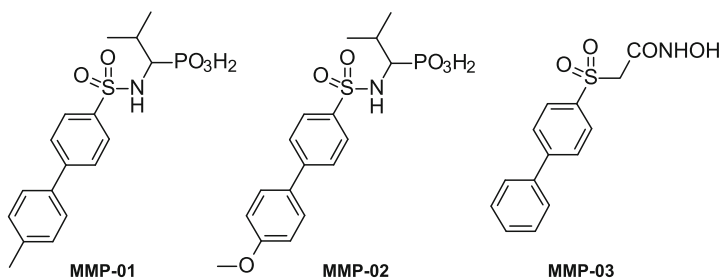


MMP-20



MMP-21

Chiral phosphonates (R-MMP-01 and R-MMP-02) have the potential as dual inhibitors of selected isoforms of MMP and CA, both involved in tumor formation, invasion, and metastasis [17]. (R)-MMP-02 is presenting the best isoform-selectivity toward CA IX. Thus, (R)-MMP-01 has IC_{50} 93 nM for CA IX, 475 nM for CA XII, 2.3 nM for MMP-2, and 0.4 nM for MMP-8. (R)-MMP-02 has IC_{50} 84 nM for CA IX, 6220 nM for CA XII, 1.5 nM for MMP-2, and 1.4 nM for MMP-8. MMP-03 has IC_{50} 527 nM for CA IX, 8862 nM for CA XII, 6.0 nM for MMP-2, and 24 nM for MMP-8. All three inhibitors are not affecting CA isoforms I and II. Biaryl chiral phosphonates ((R)-MMP-01 and (R)-MMP-02) are more active than corresponding hydroxamic acids (MMP-03).

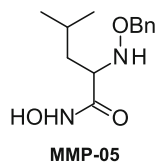
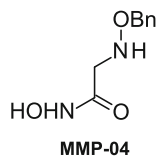


MMP-01

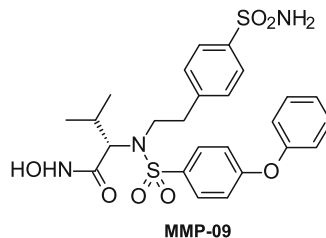
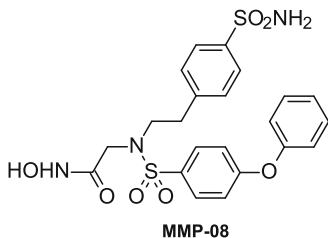
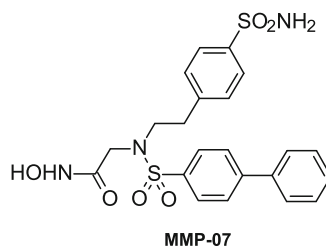
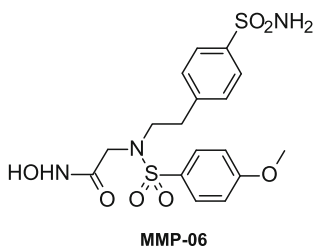
MMP-02

MMP-03

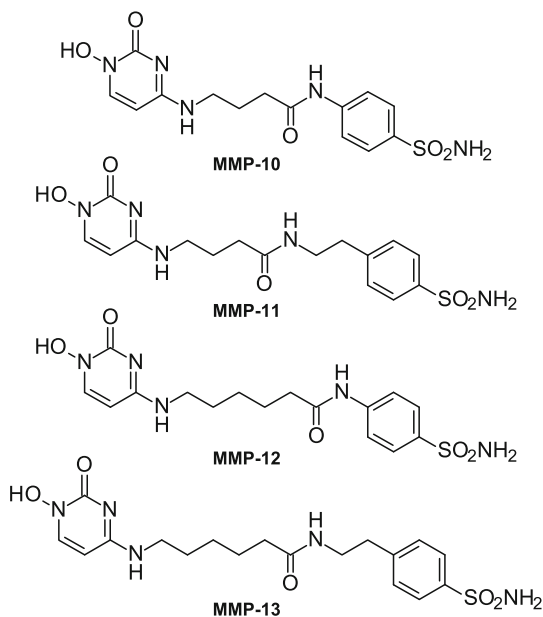
Some sulfonylated hydroxamates proved to be potent dual CA-MMP inhibitors. Only 2 compounds (MMP-04 and MMP-05) have a better binding to CA IX than CA I and CA II in the micromolar range [18].



Introduction of sulfamoylphenylethyl (SPE) moiety (compounds MMP-06 to MMP-09) led to increase of activity to all MMPs isoforms [19]. At the same time selectivity of MMP-08 to cancer-related MMP2 was decreased. These best results were obtained for compound MMP-09, where besides high MMP and CA binding, additional high activity to TACE (IC_{50} 55 nM) was observed.



Thus, SPE moiety in iminodiacetic scaffold maintains MMP inhibitory potency and also provides good activity for CA II and CA IX, at the same time showing good selectivity against CA I.

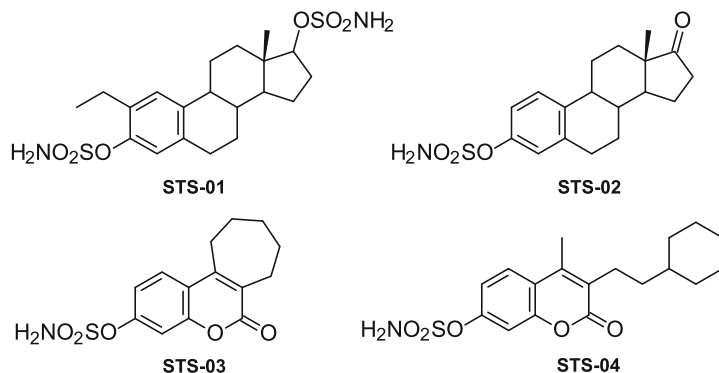


New hydroxypyrimidinones containing two Zn^{II}-binding groups (hydroxamate and sulfonamide) exhibited CA binding selectivity in low nanomolar range [20]. Hydroxypyrimidine fragment itself did not show good CA inhibition, but more simple sulfonamides acted as MMP inhibitors.

12.4.2 Steroid Sulfatases (STS)

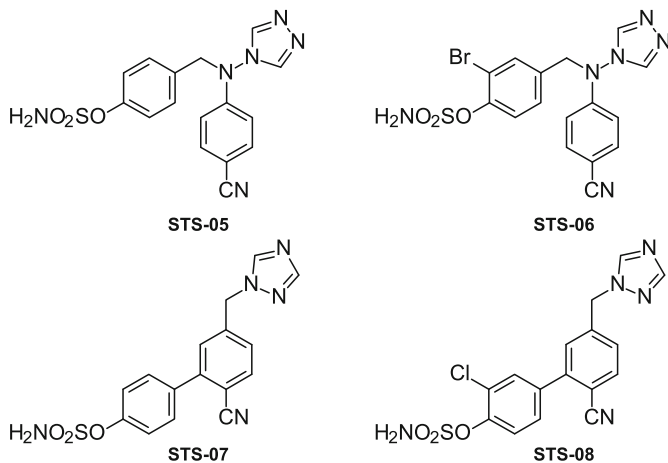
Steroid sulfatases (STS) is a key therapeutic target for treatment of estrogen-dependent tumors. This enzyme catalyzes hydrolysis of steroid sulfates, which is the main source of estrogens in tumors [21].

Several groups investigated CA inhibitory properties of the steroid sulfatase inhibitors (STSIs) on novel therapies for hormone-dependent tumors [22,23]. Some of them are derivatives of natural coumarin sulfamates or terpene sulfamates. Their CA II inhibition capacity IC₅₀ possesses 290 nM (STS-01), 9 nM (STS-02; EMATE), 17 nM (STS-03; 667COUMATE), and 15 nM (STS-04), respectively.



EMATE (STS-02) showed non-specific strong nanomolar binding activity on three CA isoforms. X-ray crystal structure of CA II with EMATE showed very short (1.78 Å) bond between Zn ion and the coordinated nitrogen in sulfamate moiety [24]. Steroidal scaffold part of the inhibitor interacts with the hydrophobic part of the CA active site accommodating several water molecules not present in the uncomplexed enzyme, which may explain very high affinity. In addition EMATE was found to be a potent CA IX inhibitor [25]. STS-03 (Irosustat) was developed and as the first STS inhibitor has reached Phase II clinical trials for the treatment of breast cancer to overcome some EMATE's side effects. It was terminated from Phase II studies in 2016.

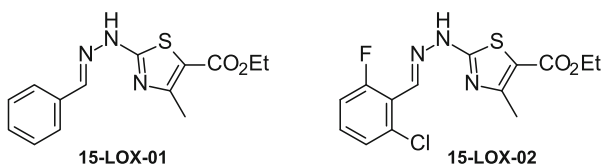
Interesting approach of administering an STS inhibitor with aromatase inhibitor in dual aromatase–steroid sulfatase inhibitor (DASI) was proposed by Lloyd group in the UK [26]. They have used triazole moiety as pharmacophore in this design and proposed two structures STS-05 and STS-06 as perspective DASI inhibitors. Introduction of bromine in molecule STS-06 cardinaly increased by 1–2 orders steroid sulfatase and aromatase affinity, keeping CA inhibition affinity in the same order. Both compounds were more stable than reference 667COUMATE. Thus, binding of sulfamate-based drugs to CA II could be a general method for increasing their stability.



It is known that hormone-dependent breast cancer (HDBC) is more efficiently treated with dual inhibition of aromatase and steroid sulfatase. Introduction of aromatase pharmacophore into biphenyl STS inhibitor led to new DASIs [27]. From differently combined biphenyl and triazole structural fragments in biphenyls STS-07 and STS-08 were found to be the most potent as aromatase (IC_{50} 2.0 and 0.5 nM) and STS (IC_{50} 35.0 and 5.5 nM) inhibition, correspondingly. Chlorine function in STS-09 increased binding capacity for both enzymes. Compound STS-09 is nonestrogenic and potently inhibits CA II (IC_{50} 86 nM) to be sequestered into CA II in erythrocytes.

12.4.3 15-LOX

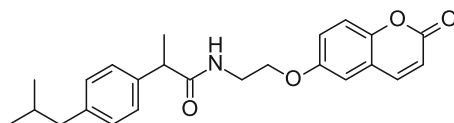
Overexpression of 15-LOX is related with some specific carcinomas (pancreatic, gastric, and brain). Similarly CA II is expressed in pancreatic, gastric carcinomas and brain tumors. Some thiazole carboxylates (15-LOX-01 and 15-LOX-02) showed dual inhibition, which consists of moderate 15-LOX binding activity (IC_{50} 0.12 to 0.69 μ m) and weak bovine CA II inhibitor activity (IC_{50} 1.26 to 2.93 μ m) [28].



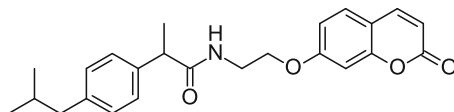
Thus, dual inhibitors of CAII and 15-LOX are perspective for anticancer drug discovery.

12.4.4 NSAID-CAI Hybrids

Two different fragments (aromatic sulfonamides or coumarins) of CA inhibitors were used to make low molecular weight hybrid compounds to improve existing NSAIDs. Increased stability of these compounds, to reach the target tissues unmodified, would open new perspective in the treatment of inflammation [29]. CA inhibitor fragment was chosen as 6- or 7-substituted coumarins. All tested NSAID-CA I hybrids coming from 8 well-known inflammation drugs—indomethacin, sulindac, ketoprofen, ibuprofen (NSAID-01 and NSAID-02), diclofenac, flurbiprofen, ketorolac, and naproxen—were stable.

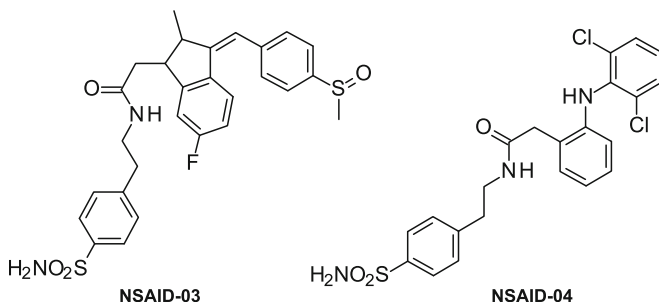


NSAID-01



NSAID-02

7-Coumarin hybrid with ibuprofen NSAID-02 showed potent and persistent antihyperalgesic effect up to 60 min after administration [30]. Among synthesized hybrid compounds in the series of aromatic sulfonamides NSAID-03 and NSAID-04 showed potent antinociceptive effects lasting up to 60 minutes after administration [31]. The antihyperalgesic activity was assessed by tests using in vivo rheumatoid arthritis (RA) model.



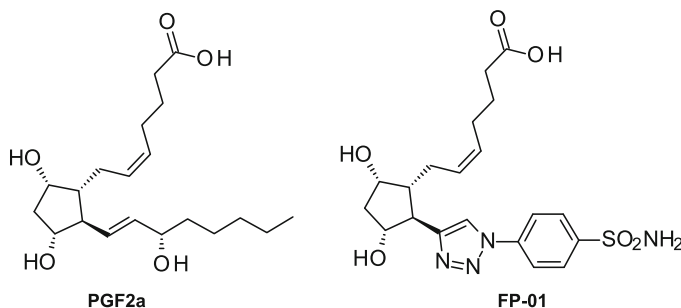
NSAID-03

NSAID-04

Majority of the hybrids were effective in inhibiting CA I and CA II as well as RA overexpressed CA IX and CA XII isoforms with K_i values in low-medium nanomolar range.

12.4.5 Prostaglandin F Receptor (FP)

A number of prostaglandin $\text{PGF}_2\alpha$ analogs were approved in the USA for treatment as antiglaucoma agents. Alternative approach is connected with CA II inhibition. Dual pharmacology of prostaglandin F receptor (FP) agonist together with CA II inhibitor may be the best solution in glaucoma treatment. So far the best ligand for this purpose is cyclopentane derivative FP-01 [32], exhibiting high CA inhibition value and weak potency as an FP agonist.



The α -chain functionality is likely necessary for potent FP antagonism. Modification of ω -chain with triazole fragment indicates that weak FP agonist activity can be reached in tandem with high CA II inhibition.

12.5 Future Prospects

Epigenetics is playing the most important role in the regulation of natural compounds. So far only two articles [33,34] are reviewing the new concept of multitarget epigenetic drugs for anticancer treatment where one of the enzymes is from field of epigenetics. Only in the recent 5 years some publications in the field of cancer epigenetics showed a connection with carbonic anhydrases. Thus, for the first time were shown tumor-suppressive role of CA IV in colorectal cancer (CRC) [35], and the mechanisms involved in cell cycle arrest and apoptosis induction. The CA IV hypermethylation may serve as a biomarker for predicting occurrence of CRC. In addition, CA VIB is essential for host defense against *Listeria monocytogenes* infection by epigenetically promoting interleukin-12 (IL-12) expression both in vitro and in vivo [36]. Mechanistically, CA VIB selectively interacts with arginine N-methyltransferase (PRMT5), which reduces symmetrical methylation of H3R8Me2sat IL-12 promoters.

Natural products, recently found as EZH2 inhibitors [37], are mainly multitarget ligands and are in the most comprehensive source of new drug searches [38]. We propose a new concept of multitarget epigenetic drugs for anticancer treatment and offer to check a sort of dual inhibitors, where both of them are influencing

epigenetic reactions—phosphorylation, methylation, or acetylation and binding to CA to improve molecule stability.

12.6 Conclusions

Multitarget paradigm in drug discovery for treatment of complex (cancer, inflammation, cardiovascular, and CNS) diseases may be effective only in the cases with appropriate drug targets. Choice of carbonic anhydrases as a one target for dual inhibition has perspective future, because they are changing some properties of known drugs, including increased stability and longevity in the host organism. This strategy may be useful in construction of new drugs or making changes in the known drug structure, resulting in a decrease of some bad side effects. Alternative route in a new drug design is an addition of next appropriate pharmacophore to the existing CA inhibitor. This method may provide a way to the next generation of hybrid anticancer drugs.

References

1. Morphy, R., Kay, C., Rankovic, Z.: From magic bullets to designed multiple ligands. *Drug Discov. Today* **9**, 641–651 (2004)
2. Medina-Franco, J.L., Giulianotti, M.A., Welmaker, G.S., Houghten, R.A.: Shifting from the single to the multitarget paradigm in drug discovery. *Drug Discov. Today* **18**, 495–501 (2013)
3. Lolli, M.L., et al.: A new class of Ibuprofen derivatives with reduced gastrotoxicity. *J. Med. Chem.* **44**, 3463–3468 (2001)
4. Buijsman, R.C., et al.: Design and synthesis of a novel synthetic NAPAP-penta-saccharide conjugate displaying a dual antithrombotic action. *Bioorg. Med. Chem. Lett.* **9**, 2013–2018 (1999)
5. Murugesan, N., et al.: Discovery of N-isoxazolyl biphenylsulfonamides as potent dual angiotensin II and endothelin A receptor antagonists. *J. Med. Chem.* **45**, 3829–3835 (2002)
6. Cortés-Ciriano, I., et al.: Polypharmacology modelling using proteochemo-metrics (PCM): recent methodological developments, applications to target families, and future prospects. *MedChemComm* **6**, 24–50 (2015)
7. Fortin, S., Bérubé, G.: Advances in the development of hybrid anticancer drugs. *Expert Opin. Drug Discovery* **8**, 1029–1047 (2013)
8. Supuran, C. T., Winum, J.-Y. (eds): *Drug Design of Zinc-Enzyme Inhibitors: Functional, Structural, and Disease Applications*. Wiley, Hoboken, (2009)
9. Hirankarn, S., Barrett, J.S., Alamuddin, N., FitzGerald, G.A., Skarke, C.: GCG100649, A novel cyclooxygenase-2 inhibitor, exhibits a drug disposition profile in healthy volunteers compatible with high affinity to carbonic anhydrase-I/II: preliminary dose-exposure relationships to define clinical development strategies. *Clin. Pharmacol. Drug Dev.* **2**, 379–386 (2013)
10. Dogne, J.M., Thiry, A., Pratico, D., Masereel, B., Supuran, C.T.: Dual carbonic anhydrase–cyclooxygenase-2 inhibitors. *Curr. Top Med. Chem.* **7**, 885–91 (2007)
11. Puscas, I., Coltau, M., Baican, M., Domuta, G.: Omeprazole has a dual mechanism of action: it inhibits both H(+)K(+)ATPase and gastric mucosa carbonic anhydrase enzyme in humans (in vitro and in vivo experiments). *J. Pharmacol. Exp. Ther.* **290**, 530–534 (1999)
12. Puscas, I., et al.: Hypotensive effect of calcium channel blockers is parallel with carbonic anhydrase I inhibition. *Clin. Pharmacol. Ther.* **68**, 443–449 (2000)

13. Marques, S.M., et al.: Pteridine-sulfonamide conjugates as dual inhibitors of carbonic anhydrases and dihydrofolate reductase with potential antitumor activity. *Bioorg. Med. Chem.* **18**, 5081–5089 (2010)
14. Rubino, M.T., et al.: Biphenyl sulfonylamino methyl bisphosphonic acids as inhibitors of matrix metalloproteinases and bone resorption. *ChemMed-Chem.* **6**, 1258–1268 (2011)
15. Tauro, M., Loiodice, F., Ceruso, M., Supuran, C.T., Tortorella, P.: Dual carbonic anhydrase/matrix metalloproteinase inhibitors incorporating bis-phosphonic acid moieties targeting bone tumors. *Bioorg. Med. Chem. Lett.* **24**, 2617–2620 (2014)
16. Veerendhar, A., et al.: Synthesis of enantiomeric aminoalkylcarbamoylphosphonates and their evaluation as dual-action anticancer MMP and carbonic anhydrase inhibitors. *Heteroat. Chem.* **26**, 257–269 (2015)
17. Luisi, G., et al.: Dual targeting of cancer-related human matrix metalloproteinases and carbonic anhydrases by chiral N-(biarylsulfonyl)-phosphonic acids. *J. Enzyme Inhib. Med. Chem.* **32**, 1260–1264 (2017)
18. Nuti, E., et al.: Carbonic anhydrase and matrix metalloproteinase inhibitors. Inhibition of human tumor-associated isozymes IX and cytosolic isozyme I and II with sulfonylated hydroxamates. *Bioorg. Med. Chem.* **15**, 2298–311 (2007)
19. Marques, S.M., et al.: Dual inhibitors of matrix metalloproteinases and carbonic anhydrases: iminodiacetyl-based hydroxamate-benzenesulfonamide conjugates. *J. Med. Chem.* **51**, 7968–79 (2008)
20. Esteves, M.A., et al.: New hydroxypyrimidinone-containing sulfonamides as carbonic anhydrase inhibitors also acting as MMP inhibitors. *Bioorg. Med. Chem. Lett.* **20**, 3623–3627 (2010)
21. Reed, M.J., Purohit, A., Woo, L.W.L., Newman, S.P., Potter, B.V.L.: Steroid sulfatase: molecular biology, regulation, and inhibition. *Endocr. Rev.* **26**, 171–202 (2005)
22. Vicker, N., et al.: Docking studies of sulphamate inhibitors of estrone sulphatase in human carbonic anhydrase II. *Bioorg. Med. Chem. Lett.* **13**, 863–865 (2003)
23. Ho, Y.T., et al.: Inhibition of carbonic anhydrase II by steroidal and non-steroidal sulphamates. *Biochem. Biophys. Res. Commun.* **305**, 909–914 (2003)
24. Abbate, F., et al.: Carbonic anhydrase inhibitors: X-ray crystallographic structure of the adduct of human isozyme II with EMATE, a dual inhibitor of carbonic anhydrases and steroid sulfatase. *Bioorg. Med. Chem. Lett.* **14**, 231–234 (2004)
25. Winum, J.Y., et al.: Carbonic anhydrase inhibitors. Inhibition of cytosolic isozymes I and II and transmembrane, tumor-associated isozyme IX with sulfamates including EMATE also acting as steroid sulfatase inhibitors. *J. Med. Chem.* **46**, 2197–204 (2003)
26. Lloyd, M.D., et al.: First crystal structures of human carbonic anhydrase II in complex with dual aromatase-steroid sulfatase inhibitors. *Biochemistry* **44**, 6858–6866 (2005)
27. Woo, L.W.L., et al.: Highly potent first examples of dual aromatase-steroid sulfatase inhibitors based on a biphenyl template. *J. Med. Chem.* **53**, 2155–2170 (2010)
28. Saeed, A., et al.: Substituted (E)-2-(2-benzylidenehydrazinyl)-4-methylthiazole-5-carboxylates as dual inhibitors of 15-lipoxygenase & carbonic anhydrase II: synthesis, biochemical evaluation and docking studies. *Biochem. Biophys. Res. Commun.* **482**, 176–181 (2017)
29. Menicatti, M., et al.: Resolution of co-eluting isomers of anti-inflammatory drugs conjugated to carbonic anhydrase inhibitors from plasma in liquid chromatography by energy-resolved tandem mass spectrometry. *J. Enzyme Inhib. Med. Chem.* **33**, 671–679 (2018)
30. Bua, S., et al.: Design and synthesis of novel nonsteroidal anti-inflammatory drugs and carbonic anhydrase inhibitors hybrids (NSAIDs–CAIs) for the treatment of rheumatoid arthritis. *J. Med. Chem.* **60**, 1159–1170 (2017)
31. Akgul, O., et al.: Discovery of novel nonsteroidal anti-inflammatory drugs and carbonic anhydrase inhibitors hybrids (NSAIDs–CAIs) for the management of rheumatoid arthritis. *J. Med. Chem.* **61**, 4961–4977 (2018)

32. Long, D.D., et al.: A multivalent approach towards linked dual-pharmacology prostaglandin F receptor agonist/carbonic anhydrase-II inhibitors for the treatment of glaucoma. *Bioorg. Med. Chem. Lett.* **23**, 939–943 (2013)
33. Ganesan, A.: Multitarget drugs: an epigenetic epiphany. *Chem. Med. Chem.* **11**, 1227–1241 (2016)
34. de Lera, A.R., Ganesan, A.: Epigenetic polypharmacology: from combination therapy to multitargeted drugs. *Clin. Epigenetics* **8**, 105 (2016)
35. Zhang, J., et al.: Carbonic anhydrase IV inhibits colon cancer development by inhibiting the Wnt signalling pathway through targeting the WTAP-WT1-TBL1 axis. *Gut* **65**(9), 1482–1493 (2015)
36. Xu, J., et al.: Nuclear carbonic anhydrase 6B associates with PRMT5 to epigenetically promote IL-12 expression in innate response. *Proc. Natl. Acad. Sci. U. S. A.* **114**, 8620–8625 (2017)
37. Shahabipour, F., et al.: Naturally occurring anti-cancer agents targeting EZH2. *Cancer Lett.* **400**, 325–335 (2017)
38. Harvey, A.L.: Natural products in drug discovery. *Drug Discov. Today* **13**, 894–901 (2008)



Structures of Human Carbonic Anhydrases and Their Complexes with Inhibitors

13

Alexey Smirnov, Elena Manakova, Saulius Gražulis,
Robert McKenna, and Daumantas Matulis

Abstract

The structures of human carbonic anhydrases (CA) have been fairly well characterized, with approximately 1000 structures deposited to the PDB. However, most of the structures are of human isoform II. So far only 10 out of 12 active human CA isoforms have been solved by X-ray crystallography. Mitochondrial isoforms CA VA and CA VB have not been determined yet. Neutron diffraction structures of CA II have provided crucial information on the protonation states of catalytically important water molecules in the active site thus deepening our knowledge of the catalytic mechanism. They have also demonstrated that the amino group of sulfonamide is in a deprotonated state when bound to the Zn^{II} of CA. Numerous structures of inhibitors bound to various CA isoforms have helped to design inhibitors that would exhibit high affinity and significant selectivity towards a particular CA over the remaining isoforms.

A. Smirnov · D. Matulis (✉)

Department of Biothermodynamics and Drug Design, Institute of Biotechnology, Life Sciences Center, Vilnius University, Vilnius, Lithuania
e-mail: Alexey.smirnov@bti.vu.lt; matulis@ibt.lt

E. Manakova · S. Gražulis

Department of Protein–DNA Interactions, Institute of Biotechnology, Life Sciences Center, Vilnius University, Vilnius, Lithuania
e-mail: lena@ibt.lt; grazulis@ibt.lt

R. McKenna

Department of Biochemistry and Molecular Biology, College of Medicine, University of Florida, Gainesville, FL, USA
e-mail: rmckenna@ufl.edu

13.1 X-ray Crystallography of Proteins

Protein crystallography along with nuclear magnetic resonance (NMR) spectroscopy and cryo-electron microscopy (Cryo-EM) allows the determination of the atomic coordinates of biological macromolecules. In protein crystallography the coordinates of atoms are obtained processing the X-ray scattering pattern of the crystal. Short X-ray wavelengths (0.8 Å to 1.54 Å) used in the protein crystallography are comparable with the interatomic distances (1 Å to 2 Å) in protein molecules. In a typical data collection experiment the protein crystal is usually cooled to 100 K, placed on rotating goniometric head and exposed to the focused X-ray beam, and scattering pattern is captured by a detector.

Protein crystals, like inorganic and small molecule crystals, are made of identical repeating blocks that are called unit cells. Each unit cell contains one or several macromolecules that could or could not be related by symmetry operators. Protein crystals usually contain 40 % to 70 % solvent that occupies space between macromolecules. This feature makes protein crystals rather delicate but high solvent content makes it possible to introduce desired small molecules into protein crystals by soaking. This feature is used widely in the crystallographic studies of carbonic anhydrases complexed with various ligands.

The X-ray diffraction pattern and the scattered intensities provide information on the unit cell, the symmetry of the molecules packed in the crystal, and is characteristic for the symmetry of the crystal. The detectors are able to record the scattered intensities, whereas the phase information of the diffracted X-rays is lost. This is referred to as a phase problem, and there are many methods in modern protein crystallography to address this problem. There are two principal ways to obtain phases: molecular replacement method that calculates initial phases from a previously determined structure of the same or similar protein, and the introduction of few strongly scattering heavy atoms into the protein crystal and comparing modified and native datasets. Nowadays the most popular way to the *ab initio* phasing is to use anomalous scattering at the wavelengths that are close to the absorption edge of X-rays by heavy atoms (SAD or MAD from single- or multi-wavelength anomalous dispersion), which is possible at the tunable X-ray synchrotron beam lines. A popular way to introduce anomalous scatterer into the protein is *in vivo* labeling using Se-methionine substituting methionine.

Protein crystallography is a main source of our knowledge about the protein structure at atomic resolution. The fraction of protein structures obtained by NMR spectroscopy and Cryo-EM is still rather small in the Protein Data Bank (PDB), but these methods are indispensable because they provide structural information on proteins or protein complexes that could not be crystallized, such as intrinsically disordered peptides or large multiprotein complexes. Currently there are 150 000 protein structures determined by crystallography, NMR, and Cryo-EM in the PDB [1] making an immense impact on our understanding of protein function and the development of structural bioinformatics.

The PDB database is not just a comprehensive open access collection of protein structures, but also provides other information including statistics on data collection and structure refinement. The most important of these parameters is the resolution of the structure. At the high resolution 1 Å or better, the hole in benzene ring is visible and carbon atoms are separated while at resolution greater than 3.5 Å it is difficult to even distinguish between amino acid side chains. Recently, on-line tools calculating electron density map have been made available [2]. The quality of the electron density map depends on resolution of collected data. During the refinement of the initial model, calculated phases reveal electron density corresponding to the structural fragments absent in the initial models (ligands, water molecules, etc.) (Fig. 13.1). It is important to examine the electron density of the corresponding part of the protein or ligand before making far-reaching conclusions.

The quality of the protein model during refinement can be tracked by *R*-factors parameters. The R_{cryst} parameter reflects the agreement between a diffraction pattern derived from the protein model and the observed diffraction data. The goal

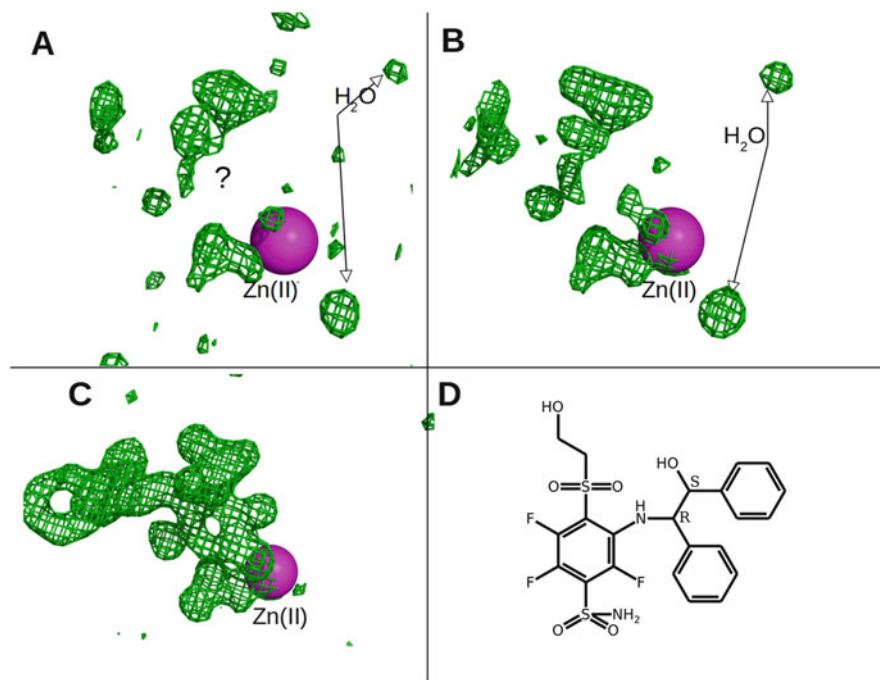


Fig. 13.1 Improvement of the electron density in the active site of CA II. The difference electron density map ($F_{obs} - F_{calc}$) is contoured at 3.0σ . (a) The initial difference electron density map after molecular replacement containing no Zn atom. (b) The initial model refined, the zinc ion is included into the model, small peaks in active site could be interpreted as solvent molecules. (c) Addition of solvent molecules resulted in high quality electron density of the sulfonamide ligand bound in the active site. (d) The chemical structure of ligand which was built in the electron density (PDB ID: 4QIY)

is to produce a model PDB coordinate file that best accounts for the observed diffraction data while obeying the restrictions of chemical geometry (bond lengths, angles, torsion angles, etc.). The protein models obtained for high resolution structures usually are of better quality in terms of accuracy and geometry restraints. Hence, for low resolution structures correct restraints are very important, because the electron density does not provide enough details and the protein chain has some degree of conformational freedom. The rule of thumb in a correctly solved structure: R_{cryst} in percent corresponds approximately to the resolution of the structure multiplied by 10. The R_{free} parameter is also important showing the discrepancy between crystallographic model and refinement bias. It is the same parameter reflecting errors in the structure as R_{cryst} , but it is calculated using a small portion (5% to 10%) of reflections that are excluded from the refinement of the model. In an ideal case at high resolution both R-factors are close to each other. In reliable structures the difference between R_{cryst} and R_{free} is less than 5%. High R_{cryst} values, however, do not necessarily reflect poor crystallographer's performance as there could be also some experimental reasons for the poor agreement. Many proteins contain disordered regions, even whole subunits in multisubunit complexes could be poorly resolved or the diffraction data could be noisy, the crystal could have high mosaicity (disorder) (Fig. 13.2).

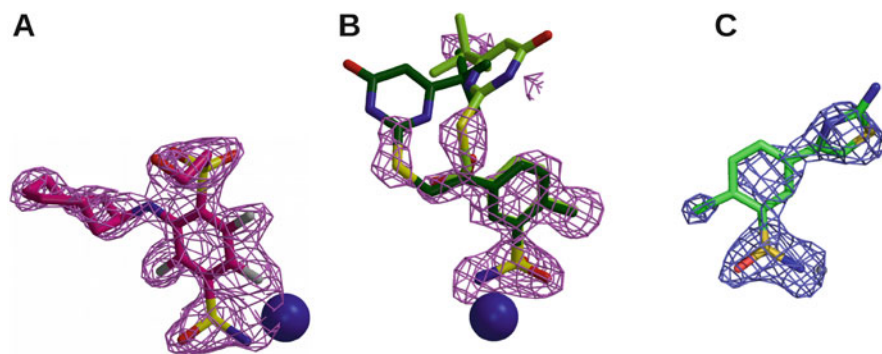


Fig. 13.2 The quality of electron density of ligands in the active site of CA in crystal structures that have similar ($\approx 2\text{\AA}$) resolution and certain problems with overall completeness of the dataset or conformational mobility of ligand. (a) Ligand VD11-4-2 in CA XII is bound in a single conformation, the ligand is well-ordered despite the low overall completeness of the dataset—75% (PDB ID: 4Q0L). (b) Ligand E52 bound to CA II demonstrated alternate conformations of the pyrimidine ring, whereas the chlorinated benzene ring is in the same position due to interactions of chlorine substituent in the hydrophobic pocket. Thus the electron density seems to be highly incomplete. (c) Electron density of a ligand E35 bound in CA IV (PDB ID 5IPZ). The overall completeness of the dataset was 85% but resulted in only partial electron density of the ligand

13.2 Neutron Crystallography

The positions of hydrogen (H) atoms in macromolecules are difficult to visualize using X-ray crystallographic techniques, even when atomic resolution ($\leq 1.0 \text{ \AA}$) diffraction is obtained. This is because the interpretation of the electron density maps when assigning the positions of H atoms of water molecules with high ($>20 \text{ \AA}^2$) thermal parameters can be ambiguous [3]. However, neutron crystallographic data at medium ($\sim 2.0 \text{ \AA}$) resolution can complement medium-to-high resolution (~ 2.0 to 1.0 \AA) X-ray crystallographic data and allow the placement and analysis of key H atoms [4–8].

The two methods are therefore very complementary, requiring the same experimental setup, with the difference being that neutrons are used instead of X-rays. This complicates the experimental setup, which includes generating the neutron beam and the design of detectors to record the diffraction pattern. Also as neutron beams have less flux than traditional X-ray sources, the crystals have to be larger and it takes considerably more time and is expensive to collect the complete diffraction data.

Neutron scattering can provide the position of H atoms, as H has a neutron-scattering length ($-3.7 \times 10^{-15} \text{ m}$ or -3.7 fm) similar in magnitude but opposite in sign to other atoms found in proteins (O, 5.8 fm ; N, 9.4 fm ; C, 6.6 fm ; S, 2.8 fm) and they can be detected. Also, deuterium (D) has a positive scattering length (6.7 fm) compared to protium (H) and a significantly smaller incoherent neutron-scattering cross-section (2.0 barns vs. 80 barns for H), and therefore the signal-to-noise diffraction data can be greatly improved in neutron scattering when D atoms are substituted instead of H atoms.

In contrast to neutrons, the diffraction of X-rays depends on the number of electrons and since as H and D are relatively electron-poor, compared to heavier atoms found in proteins, they diffract very weakly and appear practically invisible in X-ray crystallography. In neutron crystal structure the H atoms are typically exchanged by D atoms. These factors taken together make it much easier to locate D or H in resulting nuclear density maps in neutron compared to X-ray crystallography [9]. Therefore neutron crystallography can readily provide information on the protonation states of amino acid residues, ligands, and the nature of bonds involving hydrogen [10]. Neutron crystallography can also be used to identify H atoms that are exchanged with D and the extent of this replacement, thus providing a tool for identifying isotopically labeled structural features, for studying solvent accessibility and macromolecular dynamics, and for identifying minimal protein folding domains [11].

Neutron crystallography is also useful for studying the hydration of macromolecules, especially when it is combined with X-ray crystallography in joint (X-ray and Neutron) refinement procedures. In X-ray crystallography, the electron density maps depict water molecules as a spherical density peak corresponding to the position of the oxygen (O) atom. However, in neutron-scattering density maps, due to the strong scattering contribution from D, the density associated with D_2O

may no longer be spherical but rather shaped to indicate the position of the D atoms. It can often be difficult to interpret these extended neutron-scattering density peaks. However, we have found that using both X-ray and neutron data together can greatly help in this interpretation, by allowing placement of the O atom and the subsequent interpretation of the extended neutron-scattering density peak as either one or two D atoms. For this kind of analysis it is ideal to have neutron data to 2.0 Å or better. Both the ability to accurately place and orient D₂O and viewing the resulting hydrogen bonded patterns they participate in can give enormous advantages in understanding how enzymes work [7].

13.3 Protein Crystallography and Drug Design

Role of crystallography in the structural biology and bioinformatics has been critical for our understanding of biology. Also, since the introduction of the third generation synchrotron beam (X-ray source) lines that made possible collection of full dataset from the crystal in minutes [12] and recent methodical advances of protein crystallography, this method became to be routinely used not only in the fields of pure scientific research, but also as part of the drug design workflow. Two approaches of ligand design rely on the high throughput crystallographic studies: structure-based [13, 14] and fragment-based drug design [15].

In these studies protein crystallography is evaluative because it allows to visualize a selection of compounds bound to the protein of interest and aid in the design of next generation inhibitors. Also crystallographic results can be used for training of computer algorithms that can aid chemists to predict chemical structures of putative inhibitors [16].

Therefore protein crystallography has played an important role in pharmaceutical research, namely in the structure-based drug design [17]. Visualization of the ligand bound in the active site of a target protein is an evidence of the binding by itself, and analysis of the interactions between the protein and ligand helps to understand the binding mechanism. On the other hand, concentration of the protein used in crystallization is of a millimolar range and even very weakly bound ligand can be observed in the crystal structures. Crystallography cannot provide information on the binding affinity of the ligand but provides the structure of the binding pocket. The crystal structure is a static view of a bound ligand, therefore it is not necessarily the only possible conformation of the compound of interest, showing only its energy-minimized orientation. Analysis of several crystal structures or comparison of the ligand binding between subunits if those are present in the asymmetric cell often reveals several alternative binding modes. Alternate conformations of the ligands and protein side chains are also detected.

Recent advances in protein crystallography have allowed to determine a crystal structure in a less than an hour using automated computation pipelines linked to fast data collection at modern synchrotrons. The main limitation for the use of protein crystallography is the difficulties associated with the crystallization of a protein and improving of the diffraction quality of crystals. Not all proteins can be crystallized

within reasonable time and available resources. However, if the crystals of a target protein diffract good enough to see and identify the bound compound of interest, protein crystallography is a useful tool for such drug design project.

13.4 Crystal Structures of Carbonic Anhydrase Isoforms

The first X-ray crystal structures of CA reported in 1970s were the structures α -CA isoforms of CA I and CA II purified from human erythrocytes [18–21]. CA I crystals usually form the $P2_12_12_1$ symmetry and contain two protein subunits in the asymmetric unit. There are 29 crystal structures of CA I in PDB with bound inhibitors [22–29]. The active site of CA I does not differ much from CA II, and this may be the reason why this isoform is not well represented in the PDB. Both isoforms are very similar in tissue location and specific catalytic activity being blood CAs. Crystals of CA I are usually of very good quality, but are not in use for soaking with inhibitors due to the fact that in the crystal the entrances into the active site are blocked by crystallographic packing by neighboring subunits (Fig. 13.3). Therefore in the case of CA I the pre-mixed complexes of CA I with inhibitors have to be prepared prior to crystallization [26, 28, 29]. Since the active site of CA I is similar to CA II, inhibitors that bind with high affinity to CA II usually also bind with high affinity to CA I.

CA II is by far the most represented CA isoform in PDB (with approximately 700 structures in PDB). The first crystal structure of CA II was published in 1972 [19, 30] along with CA I. The protein crystallized usually in $P2_1$ (such symmetry is one of the “most common” between proteins). Variations in CA II crystal form ($P2_12_12_1$, $P1$, and $C2$) have been described in several studies [27, 29, 31–36]. CA II is not only the model protein for the CA inhibition studies, but CA II crystal structures were also used in numerous theoretical studies of protein–ligand interactions as well as in elucidation of the mechanism of CO_2 hydration catalyzed by CAs.

The crystal structure of CA III was first described in 2005 [37]. The enzyme possesses much lower specific activity than CA II and other highly active CA isoforms. The crystal structure revealed that Phe198 could be the main reason for the lower activity of CA III and this hypothesis was tested by mutation of Phe198 to leucine (numbered according to CA II). The resulting mutant protein was 10-times more active than the wild-type CA III. The proton transfer pathway was analyzed further [37, 38] and when Lys64 was replaced by His64 in CA III, the enzyme almost reached the level of CA II activity.

Membrane-bound CA IV is located outside the cell and is also one of the most active human CA isoforms. Twelve crystal structures of this isoform are available currently in the PDB. The first structure of the secreted domain of CA IV was published in 1996 [39]. The protein is monomeric and stabilized by two intramolecular disulfide bonds. Among other structural features unique for this isoform is the positive surface potential at the C-terminus. This is connected with the membrane anchor of the enzyme. Crystals of CA IV diffract to the medium resolution 1.7 Å to 2.8 Å. The loop formed by residues 126–138 is disordered

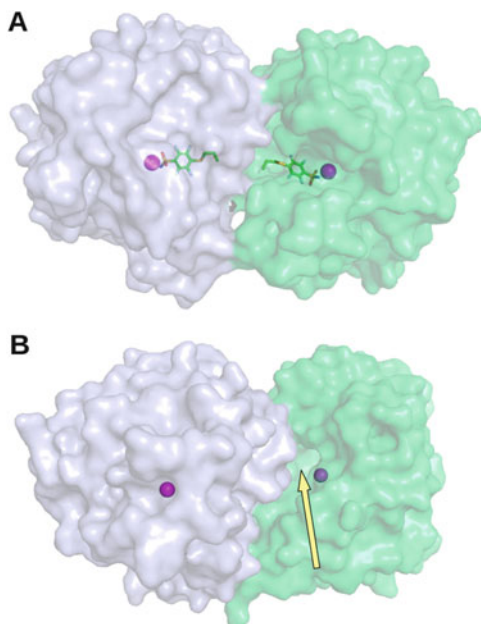


Fig. 13.3 Crystal structures of CA I and CA XIII illustrate how protein packing in the crystal blocks the entrance of an inhibitor into the active site. The protein–ligand complexes can be obtained only by co-crystallization or by use of crystals with other packing mode of protein molecules that would allow soaking. Zinc atoms are shown as magenta spheres. (a) Two neighboring molecules in the crystal structure of CA I crystallized in the $P2_12_12_1$ symmetry. The entrance into the active site cavity is blocked by crystal packing, subunits blocking the entrance preventing the diffusion of inhibitor VD12-05, shown as ball-and-stick, into the active site (PDB ID: 4WR7). (b) Two crystallographically related protein molecules of CA XIII crystallized in the $P4_12_12$ symmetry when the subunits partially block the entrance into the active site cavity (shown with yellow arrow). Such packing of CA XIII molecules is not presented in the PDB database

or demonstrates varied conformations in different crystal structures, allowing the binding of larger inhibitors by this isoform as compared to other CA isoforms [40,41].

The dimeric secreted isoform **CA VI** is represented in PDB by a single crystal structure of the catalytic domain [42]. The intramolecular dimer formed by CA VI is stabilized by a disulfide bond that is characteristic for membrane-bound CA isoforms. The dimerization interface of CA VI differs from CA IX and CA XII. Surprisingly, magnesium ion forming an octahedral coordination pattern was present in the active site instead of zinc.

Only three crystal structures of **CA VII** are present in PDB containing clinical drugs ethoxzolamide and acetazolamide bound in the active site. An intramolecular disulfide bond (Cys54–Cys178) was present in the structure of CA VII with acetazolamide [43]. Recently, ordered water network has been analyzed in CA VII crystal structure [44] and compared with CA II.

CA VIII represents an inactive isoform, also referred to as CARP (CA-related proteins), and only one crystal structure has been published of this isoform [45]. This CA demonstrates an extensive negatively charged surface, absent in other CA isoforms. The cavity of the active site is narrow compared to other structurally characterized isoforms due to the presence of arginine and isoleucine side chains. The residue Arg116 structurally coincides with His94 in CA II, whereas Ile224 replaced Thr200 in CA II. A chlorine atom was found in the position that is normally occupied by the zinc in enzymatically active CA isoforms.

Since the membrane-associated **CA IX** has been shown to be associated with certain tumors [46], the protein has attracted significant attention from crystallographers. The first crystal structure of the catalytic domain was determined in 2009 [47]. The catalytic domains of CA IX form a homodimer like other membrane-bound CA isoforms, but the structure revealed that dimerization mode of CA IX differs from CA XII.

The interest to crystallographic studies of CA IX in connection with search of isoform-selective inhibitors resulted in design of engineered CA II forms that could “mimic” the active site of CA IX. Six amino acids in the active site cavity differ between these isoforms (Table 1 in Chap. 14), and the proposed mimics have 2–8 mutations [48–56]. On the other hand, significant progress was made in the optimization of CA IX expression system [57] and its crystallization as described in Chap. 14.

CA XII is another dimeric membrane-bound isoform and its overexpression is also associated with various cancers. The crystal structure of the catalytic domain was first published in 2001 [58]. The protein is a dimer, linked through the disulfide bond Cys23–Cys203. The main difference of the active site of CA XII from other CAs is the absence of phenylalanine within the active site, instead it has an alanine at the equivalent 131 position. The absence of this bulky hydrophobic side chain makes the CA XII active site more spacious, providing ligands the possibility to adopt more conformations upon binding. This feature makes CA XII a very interesting reference protein in search of the CA IX isoform-specific inhibitors [29, 33, 36, 56, 59, 60]. A mimic of CA XII was made by introducing several point mutations in CA II for comparison of ligand binding in the mimic protein, CA II and CA XII [56].

CA XIII is a monomeric isoform that is located in the cytosol and is expressed in several human tissues. The CA XIII preferred crystallization space group is $P2_1$ or $P2_12_12_1$. Crystal structures of unliganded CA XIII and its complex with acetazolamide were the first crystal structures [61] of CA XIII. Twelve crystal structures of this enzyme have been published as a part of comparative studies in the designing of isoform-selective inhibitors [28, 33, 36, 59, 60, 62].

The last discovered human CA was the membrane-associated **CA XIV**. The extracellular domain of this human enzyme was crystallized in complex with acetazolamide [63]. The protein is monomeric and contained an intramolecular disulfide bridge. As the baculovirus expression system was used for crystallization, the protein contains pentasaccharide N-linked to Asn195m that was clearly visible in the electron density. The disulfide bond supports the loop containing Thr199. Similarly to other CA isoforms the active site cavity also is divided into two regions:

hydrophobic part formed by residues Ala91, Val121, Leu131, Ala135, Leu141, Val143, Leu198, Val207, and Trp209 and the hydrophilic part formed by Tyr7, His60, Asn62, His64, Thr65, Gln67, and Gln92. The second published crystal structure of CA XIV was the complex with biphenyl-contained inhibitor [64].

13.5 Structural Studies of Carbonic Anhydrase Catalytic Mechanism

The crystal structures revealed that human CAs are similar not only at the level of primary sequence, but share a similar fold. All human CAs, including the membrane-associated isoforms, have similar catalytic domains made of 10-stranded β -sheet as the main structural element. Three conserved histidine side chains coordinate the Zn^{II} in tetragonal coordination sphere (His94, His96, and His119 in CA II). The fourth ligand of the zinc is a water molecule or hydroxide ion. Conformations of histidines are stabilized by aromatic residues located in the “secondary coordination sphere” and mutations of these residues influence the affinity of CA II to zinc or other metal ions [65–67].

Catalytic reaction mechanism of human CA II was elucidated in great detail with the help of numerous crystal structures of CA I and CA II. Crystallography was combined with mutational analysis aimed to clarify the roles of particular residues. The zinc can be removed from CA II but the stability then significantly decreases [68]. Zinc has been replaced by other metals, such as copper, cobalt, and nickel [69, 70], the protein could accommodate metals with different coordination sphere. Replacement of Zn-coordinating histidines also caused the distortion of the stability and catalytic properties of CA II [71–75].

The protein (CA II) active site contains one wall that is highly hydrophobic to help the binding of CO_2 and the opposite wall is hydrophilic to alleviate HCO_3^- binding thus making the catalytic reaction most efficient. The limiting step in the hydration of CO_2 by CA is the regeneration of the zinc-bound water to hydroxyl which assumed the transfer of the proton from the protein side chain to bulk solvent. The most probable candidate residue for the role of proton donor, discovered in the crystal structures of CA II, was His64 and this hypothesis was tested and proven by crystallographic characterization of the His64 mutant CA II [76–85].

Neutron crystallography has also added to our understanding of the CA catalytic mechanism [86–90] as neutron crystallography allowed the visualization of protonation state of the active site side chains and water molecule H atoms. This is due to the fact that neutrons are directly interacting with atomic nuclei, and not with the electrons, as X-rays do.

The bicarbonate ion as a product of CO_2 hydration reaction was found as a zinc ligand in several CA I and CA II crystal structures [91–95]. The CO_2 bound in CA II was seen in CO_2 -pressured and cryo-cooled crystals [96–100].

Small inorganic anions inhibit CA II and are therefore often seen in the crystal structures: acetate [101, 102], azide and bromide [103], and sulfide and nitrate [104]. The SCN^- at pH 8.5 displaced the deep water [105].

Small organic molecules that do not contain sulfonamide group were also found bound to zinc occupying the substrate position, among them triazoles [106] and dithiocarbamates [107, 108]. In contrast, hydroxybenzoic acid and phenol-based inhibitors described in [109], as well as other zinc-binding groups, like polyamines [110] were found bound to Zn^{II} -bound water without direct contact with the metal.

13.6 CA Crystallography in Protein Biophysical Studies

Human CAs, especially CA I, CA II, CA XII, and CA XIII, are good examples of proteins that can be readily crystallized and diffract X-ray to high resolution [111, 112]. The robustness of good quality of CA II crystals has been exploited to visualize various bound ligands [35, 113].

There are hundreds of high quality crystal structures of CA II complexed with benzene- or heterocyclic-sulfonamides bearing various tails and substituents. Compounds can be divided into a series that differ minimally from each other. Comparison of crystal structures of CA with homologous ligands has resulted in numerous studies aimed to understand and explain parameters of binding with structural details. Such series have also been used for software training used in drug design, like the “Combinatorial small molecule growth algorithm” [16, 114].

The CA II crystal structures of ultra-high resolution [112, 115, 116] have been described. A comparison of several high resolution structures of CA II was used to reveal variable parts of otherwise very robust protein [111]. Analysis of numerous CA II crystal structures revealed that active site cavity can contain various small molecular weight ligands bound to zinc or zinc-bound water/hydroxyl. These observations were used in the publication, where Hofmeister series was correlated with crystal structures of four inorganic anions in CA II [117].

Numerous crystallographic and thermodynamic studies investigated the dependence of sulfonamide-based ligand with CA II on substituent structure. For example, the hydrophobic effect was studied in a series of benzenesulfonamides with fluorinated and aliphatic tails [118–122].

Crystallization of sulfonamide derivatives can also be used for visualization of various interesting compounds, like synthetic foldamers interacting with protein surfaces [113]. These synthetic protein analogs also could oligomerize when bound to CA. Another example was the crystal structure of Xe-caging agent cryptophane [123].

Interesting attempt to use CA II in zinc biosensors was presented in [124, 125]. The fluorophore dansylamide was bound hydrophobically in the active site. Fluorescein-containing compounds were also crystallized in CA II [126], aimed to detect hypoxic tumors. In the complex of a bifunctional compound a complex with Xe was used for the detection by hyperpolarized ^{129}Xe NMR [127]. Another

example is the crystal structure of fluorescein-derivatized aryl-benzenesulfonamide with CA II, as part of zinc biosensor [125].

13.7 Structures of Carbonic Anhydrase–Inhibitor Complexes

Most crystal structures of CAs address a problem of recognition by small molecular weight inhibitors. By far the largest part of inhibitors are primary sulfonamides and the largest number of structures are of isoform CA II (Fig. 13.4). Other isoforms are represented by significantly lower number of crystal structures and there are no structures deposited to the PDB of isoforms CA VA, CA VB, CA X, and CA XI. The isoforms CA IV, CA XII, and CA XIII are represented by complexes with inhibitors allowing to compare ligand binding in the active site of several isoforms in search of isoform-selective inhibitors.

Currently, one of the main goals in CA research is the search of CA IX-selective inhibitors, because it plays a central role in the development of hypoxic tumors [128]. Another direction is the search of selective inhibitors for ubiquitous CA I and CA II isoforms, targets of anti-glaucoma, anti-obesity, anti-epileptic drugs that could be used against other disorders [70, 129–131]. Numerous studies combining inhibition measurements with the crystallographic description of various compounds have been performed by Supuran group. These include a search for inhibitors of CA II, isoform-selective inhibitors as promising anti-cancer agents, and anti-bacterial compounds as selective inhibitors of bacterial CAs. The group has also investigated crystallographically a great variety of non-sulfonamide (non-classical) compounds that bind to CA, reviewed in [53, 132, 133].

“Classical” CA inhibitors include sulfonamide derivatives and their isosteres: sulfamates and sulfamides [134]. Most ligands reported in the literature are based

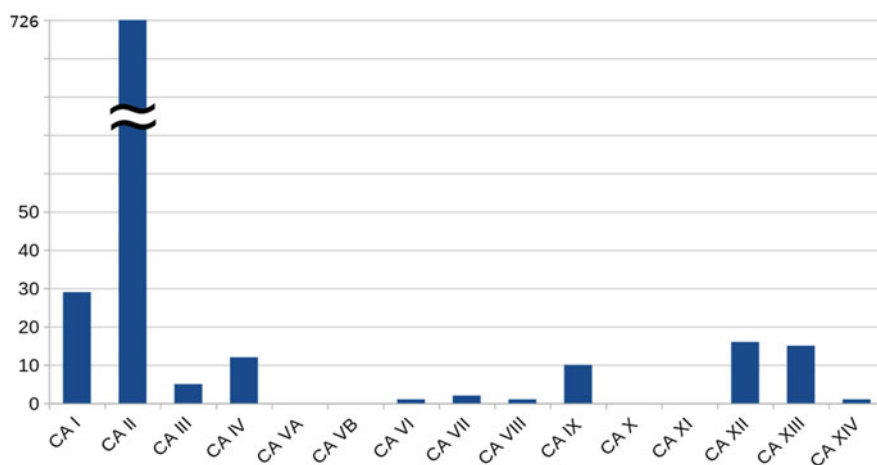


Fig. 13.4 The number of crystal structures of human CA isoforms in PDB database

on the primary sulfonamide group. There are also sulfamide-based compounds represented by anticancer steroid and non-steroid drugs [135–137]. It was found that some buffer components and amino acids could stimulate CA activity increasing the efficiency of the proton-shuttle mechanism [116, 138–141].

The main difficulty in designing isoform-specific inhibitors of human CAs is the active sites which are highly similar in amino acid composition. Many compounds have been screened in search of leads that would bind weakly to the ubiquitously expressed CA II and CA I but strongly to CA IX. The CA IX-specific compounds have been used not only for the inhibition of CA IX isoform, but also as markers of hypoxic tumors or as sensibilization agents [142–145]. Benzenesulfonamide with positively charged *para*-substituent has been tested for anti-tumor activity and crystallized in CA II [146]. Such modification prevented the transport of the compound across the cell membrane. The usual approach in search of isoform-specific CA inhibitors includes the scanning series of homologous compounds according to the inhibition or binding to several CA isoforms and analysis of the binding within the active site of one or more isoforms, usually CA II [143, 147–150].

We have attempted to correlate binding thermodynamics with the structural details of compounds bound in the active sites of several CA isoforms. One investigated group of CA inhibitors were 2,4-, 3,4-, or 4-substituted fluorinated benzenesulfonamides [28, 29, 33, 56, 151].

The crystal structures of *para*-substituted fluorinated benzenesulfonamides bound in CA I, CA II, CA XII, and CA XIII have been described in [59] and [29]. These compounds have high selectivity towards CA I. Positions of ligands in different isoforms were compared and two main orientations of the benzene ring were described. Positions of benzene ring in CA I and CA II were different. These studies were continued with *meta*- and *para*-substituted compounds bound in CA II, CA XII, and CA XIII [33].

Several designed compounds demonstrated unusually high affinity towards CA IX, especially the *ortho*- and *meta*-cyclooctyl-substituted *para*-substituted fluorinated benzenesulfonamides, VD12-09 and VD11-4-2, respectively [56]. The structures of VD11-4-2 bound to several CAs that are compared with compound VD12-05 that does not possess a second *meta*-substituent are shown in Fig. 13.5. The structure of VD11-4-2 bound to CA IX is described in the next chapter. High selectivity of these compounds towards CA IX could be inferred from the good fit of the cyclooctyl group to the hydrophobic pocket of CA IX. The binding to CA IX was modeled by multiple mutations of CA II making it to resemble the active site of CA IX. A similar CA XII mimic was also constructed to compare the switch of the ligand binding mode between CA II and CA XII isoforms. The binding of both compounds in the CA IX mimic was different. The CA XII mimic based on published data [56] was concluded to be a good “working” model of CA XII.

In contrast, the binding constants of VD11-4-2 to CA IX and its mimic differed substantially. Therefore, the crystal structures of CA IX mimic should be used with care when trying to mimic actual CA IX. In conclusion, it was stated that it is not enough to design a single *para*-substituent to achieve the desired selectivity

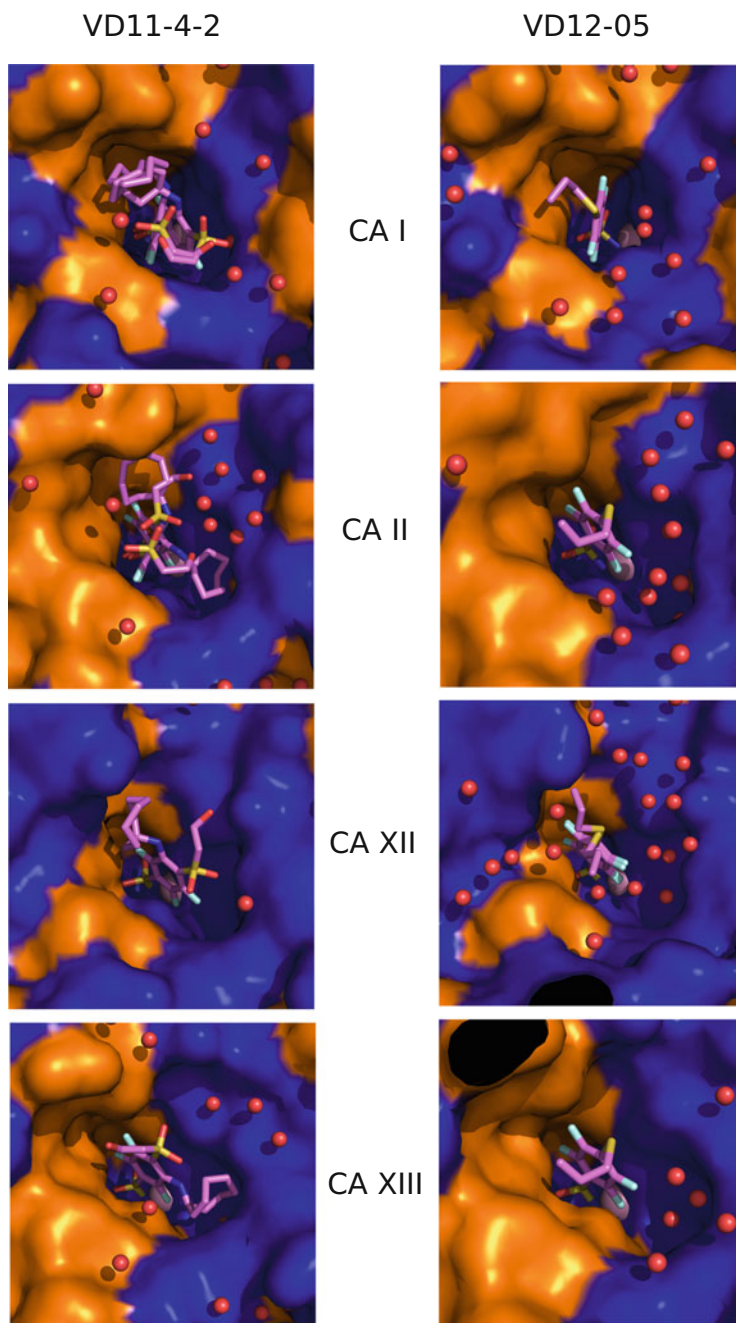


Fig. 13.5 Positions of compounds VD11-4-2 (left column) and VD12-05 (right column) in the active sites of CA I, CA II, CA XII, and CA XIII isoforms. Hydrophilic amino acid surface is depicted blue and hydrophobic—yellow. Compounds are drawn as pink sticks, water molecules—as red circles. The structures are drawn with Pymol

for CA IX, but at least two substituents, *ortho*-/*para*- or *meta*-/*para*-, are needed. Selectivity and high affinity should be balanced and it is always a compromise.

In [33] the binding modes of three *para*-*meta*-trifluorobenzenesulfonamides, VD11-28, VD10-39a, and VD12-25-2 in the active sites of CA II, CA XII, and CA XIII were analyzed crystallographically. Two compounds, VD10-39a and VD11-28, showed variable binding modes in the three tested isoforms. In contrast, VD12-25-2 has a bulky and rigid *meta*-group [(1R,2S)-2-hydroxy-1,2-diphenylethyl]amino which was found in all crystal structures towards the hydrophobic pocket of the active site. In one of alternate conformations, the substituent displaced Phe133 of CA XIII. The sulfonyl linker made H-bonds with the hydrophilic part of the active site, namely with Asn37 structural counterparts (Lys69 in CA XII and Asn69 in CA XIII). This compound was selective towards CA XIII.

In another study, benzenesulfonamide groups differed by the presence of chlorine in the position 2 of the benzene ring [59, 62, 152–154]. Structures of three indapamide-like compounds bound to CA II were presented in [154]. All these compounds are *meta*-substituted 2-Cl-benzenesulfonamides. The presence of chlorine usually fixed the position of benzene ring (that is similar to that of indapamide and chlorthalidone) and the *meta*-substituents defined the higher affinity of synthesized compounds.

The selectivity and binding properties of *meta*- and *para*-substituted 2-Cl-benzenesulfonamides were compared with *meta*- and *para*-substituted benzenesulfonamides in [153] and [60]. Their binding to CA II, CA XII, and CA XIII was analyzed crystallographically. The *para*-substituted compounds demonstrated higher affinities, but the *meta*-substituted compounds containing Cl were usually more selective between isoforms. The full matrix of four tailgroups combined with four variants of benzenesulfonamide scaffolds was analyzed crystallographically and thermodynamically in [62].

13.8 Neutron Structure Demonstrated the Deprotonated State of Bound Sulfonamide

Neutron diffraction studies by visualizing the positions of H(D) atoms have provided crucial information on the protonation state of the NH₂ group in the sulfonamide. The second deuterium is not visible in the neutron structures showing both acetazolamide and ethoxzolamide bound to CA II (Fig. 13.6). This evidence that is essential to confirm the amino group becomes deprotonated in order to bind the Zn^{II} of CA.

The neutron structures were important to demonstrate the positions of all water molecules involved in the catalytic mechanism [90, 100]. Positions of water molecules are visible by X-ray crystallography, but the positions of H atoms and thus the orientation of waters are visible only in the neutron diffraction structures [90]. It is also important to visualize water molecules occupying the active site both in the absence and in the presence of the inhibitor compound. This difference in

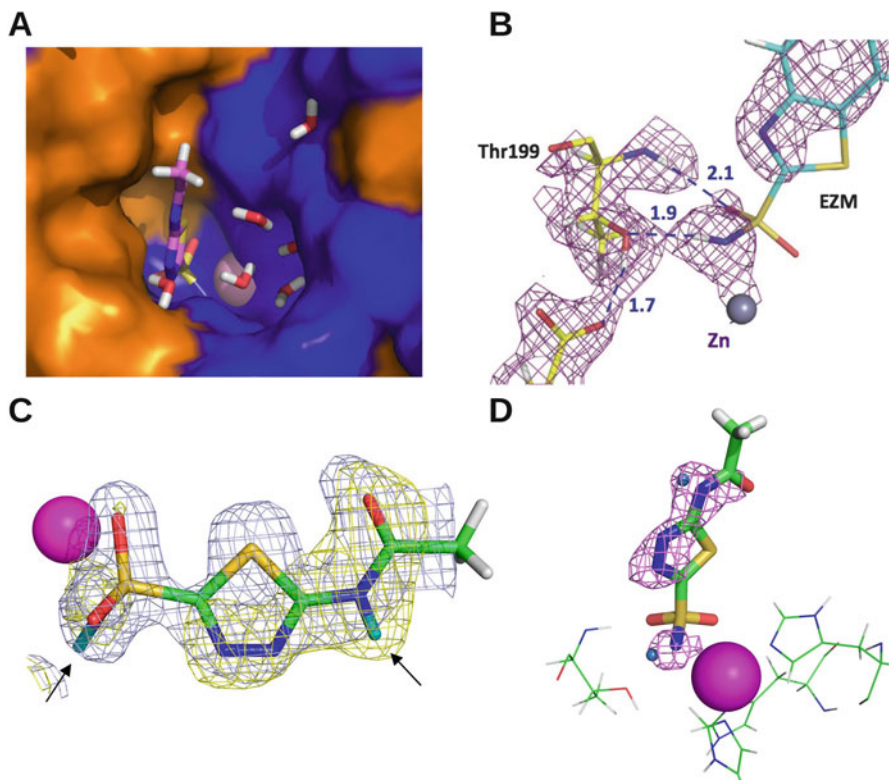


Fig. 13.6 Neutron diffraction studies have demonstrated the positions of deuterium atoms thus enabling visualization of the orientation of water molecules (a) and the absence of the second proton in the NH_2 group of the bound sulfonamide group of ethoxzolamide (EZA, EZM) (b) and AZM (c and d). (a). Orientations of water molecules drawn with Pymol based on PDB 4g0c, AZM are bound to CA II. (b). There is no density at the position where the second deuterium (protium) is supposed to be in the NH_2 group if it was protonated [90]. (c). The electron density of acetazolamide (AZM, PDB 4g0c) is shown in gray mesh, neutron density shown in yellow. The Zn^{II} is shown as a pink sphere. (d). Different orientation of AZM to show the absence of the second proton in the NH_2 group of sulfonamide. Reprinted with permission from [90] (b) and [88] (c)

the solvation pattern may yield answers of the energetics and recognition by the compounds of the protein active site.

13.9 Conclusions

Structural studies showing the position of every atom in the CA–inhibitor complex provide essential information for our understanding of the recognition between the CA protein and a sulfonamide inhibitor. X-ray crystallography shows the positions of all atoms except hydrogens, while the application of neutron diffraction fills this

gap and enables visualization of deuterium atoms thus providing the orientations of water molecules in the active site and demonstrating that the amino group of sulfonamide is in a deprotonated state when bound to the CA.

References

1. Rose, P.W. et al.: The RCSB protein data bank: integrative view of protein, gene and 3D structural information. *Nucleic Acids Res.* **45**, D271–D281 (2017)
2. Rose, A.S., Hildebrand, P.W. NGL viewer: a web application for molecular visualization. *Nucleic Acids Res.* **43**, W576–W579 (2015)
3. Gutberlet, T., Heinemann, U., Steiner, M.: Protein crystallography with neutrons—status and perspectives. *Acta Crystallogr. D Biol. Crystallogr.* **57**, 349–354 (2001)
4. Katz, A.K., et al.: Locating active-site hydrogen atoms in d-xylose isomerase: time-of-flight neutron diffraction. *Proc. Natl. Acad. Sci. U. S. A.* **103**, 8342–8347 (2006)
5. Bennett, B., et al.: Neutron diffraction studies of *Escherichia coli* dihydro-folate reductase complexed with methotrexate. *Proc. Natl. Acad. Sci. U. S. A.* **103**, 18493–18498 (2006)
6. Coates, L., et al.: The catalytic mechanism of an aspartic proteinase explored with neutron and x-ray diffraction. *J. Am. Chem. Soc.* **130**, 7235–7237 (2008)
7. Blum, M.-M., et al.: Rapid determination of hydrogen positions and protonation states of diisopropyl fluorophosphatase by joint neutron and x-ray diffraction refinement. *Proc. Natl. Acad. Sci. U. S. A.* **106**, 713–718 (2009)
8. Blakeley, M.P., et al.: Quantum model of catalysis based on a mobile proton revealed by subatomic x-ray and neutron diffraction studies of h-aldoase reductase. *Proc. Natl. Acad. Sci.* **105**, 1844–1848 (2008)
9. Shu, F., Ramakrishnan, V., Schoenborn, B.P.: Enhanced visibility of hydrogen atoms by neutron crystallography on fully deuterated myoglobin. *Proc. Natl. Acad. Sci.* **97**, 3872–3877 (2000)
10. Blakeley, M.P., Langan, P., Niimura, N., Podjarny, A.: Neutron crystallography: opportunities, challenges, and limitations. *Curr. Opin. Struct. Biol.* **18**, 593–600 (2008)
11. Bennett, B.C., Gardberg, A.S., Blair, M.D., Dealwis, C.G.: On the determinants of amide backbone exchange in proteins: a neutron crystallographic comparative study. *Acta Crystallogr. D Biol. Crystallogr.* **D64**, 764–783 (2008)
12. Pathuri, P., Norton, D., Willems, H., Tisi, D., Jhoti, H.: In: Neidle, S. (ed.) *Cancer Drug Design and Discovery*, 2nd edn., pp. 121–141. Academic Press, Cambridge (2014)
13. Huang, H.-J., et al.: Current developments of computer-aided drug design. *J. Taiwan Inst. Chem. Eng.* **41**, 623–635 (2010)
14. Śledź, P., Caffisch, A.: Protein structure-based drug design: from docking to molecular dynamics. *Curr. Opin. Struct. Biol.* **48**, 93–102 (2018)
15. Chilingaryan, Z., Yin, Z., Oakley, A.J.: Fragment-based screening by protein crystallography: successes and pitfalls. *Int. J. Mol. Sci.* **13**, 12857–12879 (2012)
16. Grzybowski, B.A., et al.: Combinatorial computational method gives new picomolar ligands for a known enzyme. *Proc. Natl. Acad. Sci. U. S. A.* **99**, 1270–1273 (2002)
17. Rondeau, J.-M., Schreuder, H. In: Wermuth, C.G., Raboisson, P., Aldous, D., Rognan, D. (eds.) *The Practice of Medicinal Chemistry*, pp. 511–537. Academic Press, Cambridge (2015)
18. Kannan, K.K., et al.: Crystal structure of human erythrocyte carbonic anhydrase B. Three-dimensional structure at a nominal 2.2 Å resolution. *Proc. Natl. Acad. Sci. U. S. A.* **72**, 51–55 (1975)
19. Liljas, A., et al.: Crystal structure of human carbonic anhydrase C. *Nat. New Biol.* **235**, 131–137 (1972)
20. Kannan, K.K., et al.: Structure of human carbonic anhydrase B. I. Crystallization and heavy atom modifications. *J. Mol. Biol.* **63**, 601–604 (1972). PDB ID: 1CAB, 2CAB

21. Kannan, K.K., Ramanadham, M., Jones, T.A.: Structure, refinement, and function of carbonic anhydrase isozymes: refinement of human carbonic anhydrase I. *Ann. N. Y. Acad. Sci.* **429**, 49–60 (1984). PDB ID: 2CAB
22. Chakravarty, S., Kannan, K.K.: Drug-protein interactions. Refined structures of three sulfonamide drug complexes of human carbonic anhydrase I enzyme. *J. Mol. Biol.* **243**, 298–309 (1994). PDB ID: 1AZM, 1BZM, 1CZM
23. Jude, K.M., et al.: Ultrahigh resolution crystal structures of human carbonic anhydrases I and II complexed with “Two-Prong” inhibitors reveal the molecular basis of high affinity. *J. Am. Chem. Soc.* **128**, 3011–3018 (2006)
24. Srivastava, D.K., et al.: Structural analysis of charge discrimination in the binding of inhibitors to human carbonic anhydrases I and II. *J. Am. Chem. Soc.* **129**, 5528–5537 (2007)
25. Temperini, C., et al.: Phosph(on)ate as a zinc-binding group in metalloenzyme inhibitors: x-ray crystal structure of the antiviral drug foscarnet complexed to human carbonic anhydrase I. *Bioorg. Med. Chem. Lett.* **17**, 2210–2215 (2007). PDB ID: 2IT4
26. Alterio, V., et al.: The first example of a significant active site conformational rearrangement in a carbonic anhydrase-inhibitor adduct: the carbonic anhydrase I-topiramate complex. *Org. Biomol. Chem.* **8**, 3528–3533 (2010). PDB ID: 3LXE
27. Kim, H.T., Cha, H., Hwang, K.Y.: Structural insight into the inhibition of carbonic anhydrase by the COX-2-selective inhibitor polmacoxib (CG100649). *Biochem. Biophys. Res. Commun.* **478**, 1–6 (2016)
28. Zubrienė, A., et al.: Intrinsic thermodynamics and structures of 2,4- and 3,4- substituted fluorinated benzenesulfonamides binding to carbonic anhydrases. *ChemMedChem* **12**, 161–176 (2017)
29. Zubrienė, A., et al.: Intrinsic thermodynamics of 4-substituted-2,3,5,6-tetrafluorobenzenesulfonamide binding to carbonic anhydrases by isothermal titration calorimetry. *Bio-Phys Chem* **205**, 51–65 (2015)
30. Kannan, K.K., et al.: Crystal structure of human erythrocyte carbonic anhydrase C. VI. The three-dimensional structure at high resolution in relation to other mammalian carbonic anhydrases. *Cold Spring Harb. Symp. Quant. Biol.* **36**, 221–231 (1972)
31. Robbins, A. H., Domsic, J.F., Agbandje-McKenna, M., McKenna, R.: Structure of a monoclinic polymorph of human carbonic anhydrase II with a doubled a axis. *Acta. Crystallogr. D Biol. Crystallogr.* **66**, 628–634 (2010)
32. Fisher, Z., et al.: Kinetic and structural characterization of thermostabilized mutants of human carbonic anhydrase II. *Protein Eng. Des. Sel.* **25**, 347–355 (2012). PDB ID: 3V3F, 3V3G, 3V3H, 3V3I, 3V3J
33. Dudutienė, V., et al.: Functionalization of fluorinated benzenesulfonamides and their inhibitory properties toward carbonic anhydrases. *ChemMed-Chem* **10**(4), 662–687 (2015)
34. Boone, C.D., Rasi, V., Tu, C., McKenna, R.: Structural and catalytic effects of proline substitution and surface loop deletion in the extended active site of human carbonic anhydrase II. *FEBS J* **282**, 1445–1457 (2015)
35. Jewginski, M., et al.: Self-assembled protein-aromatic foldamer complexes with 2:3 and 2:2:1 stoichiometries. *J. Am. Chem. Soc.* **139**, 2928–2931 (2017)
36. Čapkauskaitė, E., et al.: Combinatorial design of isoform-selective N-alkylated benzimidazole-based inhibitors of carbonic anhydrases. *ChemistrySelect* **2**, 5360–5371 (2017)
37. Duda, D.M., et al.: Human carbonic anhydrase III: structural and kinetic study of catalysis and proton transfer. *Biochemistry* **44**, 10046–10053 (2005)
38. Elder, I., et al.: Structural and kinetic analysis of proton shuttle residues in the active site of human carbonic anhydrase III. *Proteins* **68**, 337–343 (2007)
39. Stams, T., et al.: Crystal structure of the secretory form of membrane-associated human carbonic anhydrase IV at 2.8-Å resolution. *Proc. Natl. Acad. Sci. U. S. A.* **93**, 13589–13594 (1996)
40. Vernier, W., et al.: Thioether benzenesulfonamide inhibitors of carbonic anhydrases II and IV: structure-based drug design, synthesis, and biological evaluation. *Bioorg. Med. Chem.* **18**, 3307–3319 (2010)

41. Mickevičiūtė, A., et al.: Intrinsic thermodynamics of high affinity inhibitor binding to recombinant human carbonic anhydrase IV. *Eur. Biophys. J.* **47**, 271–290 (2018)
42. Pilka, E.S., Kochan, G., Oppermann, U., Yue, W.W.: Crystal structure of the secretory isozyme of mammalian carbonic anhydrases CA VI: implications for biological assembly and inhibitor development. *Biochem. Bio-phys. Res. Commun.* **419**, 485–489 (2012)
43. Di Fiore, A., et al.: Crystal structure of the C183S/C217S mutant of human CA VII in complex with acetazolamide. *Bioorg. Med. Chem. Lett.* **20**, 5023–5026 (2010)
44. Buonanno, M., et al.: The crystal structure of a hCA VII variant provides insights into the molecular determinants responsible for its catalytic behavior. *Int. J. Mol. Sci.* **19**, 1571 (2018)
45. Picaud, S.S., et al.: Crystal structure of human carbonic anhydrase-related protein VIII reveals the basis for catalytic silencing. *Proteins* **76**, 507–511 (2009). PDB ID: 2W2J
46. Pastorekova, S., Zatovicova, M., Pastorek, J.: Cancer-associated carbonic anhydrases and their inhibition. *Curr. Pharm. Des.* **14**, 685–698 (2008)
47. Alterio, V., et al.: Crystal structure of the catalytic domain of the tumor-associated human carbonic anhydrase IX. *Proc. Natl. Acad. Sci. U. S. A.* **106**, 16233–16238 (2009)
48. Genis, C., et al.: Design of a carbonic anhydrase IX active-site mimic to screen inhibitors for possible anticancer properties. *Biochemistry* **48**, 1322–1331 (2009)
49. Sippel, K.H., et al.: Characterization of carbonic anhydrase isozyme specific inhibition by sulfamated 2-ethylestra compounds. *Lett. Drug Des. Discovery* **8**, 1–25 (2011). PDB ID: 3OIK, 3OIL, 3OIM, 3OKU, 3OKV
50. Tars, K., et al.: Sulfocoumarins (1,2-benzoxathiine-2,2-dioxides): a class of potent and isoform-selective inhibitors of tumor-associated carbonic anhydrases. *J. Med. Chem.* **56**, 293–300 (2013)
51. Pinard, M.A., Boone, C.D., Rife, B.D., Supuran, C.T. McKenna, R.: Structural study of interaction between brinzolamide and dorzolamide inhibition of human carbonic anhydrases. *Bioorg. Med. Chem.* **21**, 7210–7215 (2013). PDB ID: 4M2R, 4M2U, 4M2W, 4M2V
52. Moeker, J., et al.: Structural insights into carbonic anhydrase IX isoform specificity of carbohydrate-based sulfamates. *J. Med. Chem.* **57**, 8635–8645 (2014)
53. Pinard, M.A., Aggarwal, M., Mahon, B.P., Tu, C., McKenna, R.: A sucrose-binding site provides a lead towards an isoform-specific inhibitor of the cancer-associated enzyme carbonic anhydrase IX. *Acta Crystallogr. F Struct. Biol. Commun.* **71**, 1352–1358 (2015). PDB ID: 4YWP 4ZAO
54. Mahon, B.P., et al.: Saccharin: a lead compound for structure-based drug design of carbonic anhydrase IX inhibitors. *Bioorg. Med. Chem.* **23**, 849–854 (2015)
55. Mahon, B.P., et al.: Mapping selective inhibition of the cancer-related carbonic anhydrase IX using structure-activity relationships of glucosyl-based sulfamates. *J. Med. Chem.* **58**, 6630–6638 (2015). PDB ID: 4ZWX 4ZWY 4ZWZ 4ZX0 4ZX1
56. Dudutienė, V., et al.: Discovery and characterization of novel selective inhibitors of carbonic anhydrase IX. *J. Med. Chem.* **57**, 9435–9446 (2014)
57. Leitans, J., et al.: Efficient expression and crystallization system of cancer-associated carbonic anhydrase isoform IX. *J. Med. Chem.* **58**, 9004–9009 (2015)
58. Whittington, D.A., et al.: Crystal structure of the dimeric extracellular domain of human carbonic anhydrase XII, a bitopic membrane protein over-expressed in certain cancer tumor cells. *Proc. Natl. Acad. Sci. U. S. A.* **98**, 9545–9550 (2001)
59. Dudutienė, V., et al.: 4-Substituted-2,3,5,6-tetrafluorobenzenesulfonamides as inhibitors of carbonic anhydrases I, II, VII, XII, and XIII. *Bioorg. Med. Chem.* **21**(7), 2093–2106 (2013)
60. Čapkauskaitė, E., et al.: Benzenesulfonamides with pyrimidine moiety as inhibitors of human carbonic anhydrases I, II, VI, VII, XII, and XIII. *Bioorg. Med. Chem.* **21**(22), 6937–6947 (2013)
61. Fiore, A.D., et al.: Crystal structure of human carbonic anhydrase XIII and its complex with the inhibitor acetazolamide. *Proteins* **74**, 164–175 (2009)
62. Kišonaitė, M., et al.: Intrinsic thermodynamics and structure correlation of benzenesulfonamides with a pyrimidine moiety binding to carbonic anhydrases I, II, VII, XII, and XIII. *PLoS ONE* **9**(12), e114106 (2014)

63. Alterio, V., et al.: The structural comparison between membrane-associated human carbonic anhydrases provides insights into drug design of selective inhibitors. *Biopolymers* **101**, 769–778 (2014)
64. La Regina, G., et al.: Discovery of 1,1'-biphenyl-4-sulfonamides as a new class of potent and selective carbonic anhydrase XIV inhibitors. *J. Med. Chem.* **58**, 8564–8572 (2015)
65. Lesburg, C., Christianson, D.: X-ray crystallographic studies of engineered hydrogen bond networks in a protein-zinc binding site. *J. Am. Chem. Soc.* **117**, 6838–6844 (1995). PDB ID: 1CNK, 1CNI, 1CNJ, 1CNH, 1CNG
66. Huang, C.C., Lesburg, C.A., Kiefer, L.L., Fierke, C.A., Christianson, D.W.: Reversal of the hydrogen bond to zinc ligand histidine-119 dramatically diminishes catalysis and enhances metal equilibration kinetics in carbonic anhydrase II. *Biochemistry* **35**, 3439–3446 (1996). PDB ID: 1ZSA, 1ZSB, 1ZSC
67. Cox, J.D., Hunt, J.A., Compber, K.M., Fierke, C.A., Christianson, D.W.: Structural influence of hydrophobic core residues on metal binding and specificity in carbonic anhydrase II. *Biochemistry* **39**, 13687–13694 (2000)
68. Avvaru, B.S., et al.: Apo-human carbonic anhydrase II revisited: implications of the loss of a metal in protein structure, stability and solvent network. *Biochemistry* **48**, 7365–7372 (2009). PDB ID: 3GZ0
69. Haakansson, K., Carlsson, M., Svensson, L.A., Liljas, A.: Structure of native and apo carbonic anhydrase II and structure of some of its anion-ligand complexes. *J. Mol. Biol.* **227**, 1192–1204 (1992). PDB ID: 2CBA 2CBB 2CBC 2CBD 2CBE
70. Krishnamurthy, V.M., et al.: Carbonic anhydrase as a model for biophysical and physical-organic studies of proteins and protein-ligand binding. *Chem. Rev.* **108**, 946–1051 (2008)
71. Kiefer, L., Ippolito, J., Fierke, C., Christianson, D.: Redesigning the zinc-binding site of human carbonic anhydrase-II - structure of a His₂Asp-Zn²⁺ metal coordination polyhedron. *J. Am. Chem. Soc.* **115**, 12581–12582 (1993). PDB ID: 1CVK
72. Alexander, R.S., Kiefer, L.L., Fierke, C.A., Christianson, D.W.: Engineering the zinc binding site of human carbonic anhydrase II: structure of the His-94->Cys apoenzyme in a new crystalline form. *Biochemistry* **32**, 1510–1518 (1993)
73. Lesburg, C.A., Huang, C., Christianson, D.W. Fierke, C.A.: Histidine->Carboxamide ligand substitutions in the zinc binding site of carbonic anhydrase II alter metal coordination geometry but retain catalytic activity. *Biochemistry* **36**, 15780–15791 (1997). PDB ID: 1H4N, 1H9N, 1H9Q, 2H4N
74. Ippolito, J.A., Christianson, D.W.: Structural consequences of redesigning a protein-zinc binding site. *Biochemistry* **33**, 15241–15249 (1994). PDB ID: 1CNB, 1CNC, 1CVD, 1CVE, 1CVF, 1CVH
75. Ippolito, J.A., Baird, T.T., McGee, S.A., Christianson, D.W., Fierke, C.A.: Structure-assisted redesign of a protein-zinc-binding site with femtomolar affinity. *Proc. Natl. Acad. Sci. U. S. A.* **92**, 5017–5021 (1995). PDB ID: 1CCS, 1CCT, 1CCU
76. Nair, S.K., Christianson, D.W.: Unexpected pH-dependent conformation of His-64, the proton shuttle of carbonic anhydrase II. *J. Am. Chem. Soc.* **113**, 9455–9458 (1991). PDB ID: 1CA3, 1HCA
77. Scolnick, L., Christianson, D.: X-ray crystallographic studies of alanine-65 variants of carbonic anhydrase II reveal the structural basis of compromised proton transfer in catalysis. *Biochemistry* **35**, 16429–16434 (1996). PDB ID: 1UGA, 1UGB, 1UGC, 1UGD, 1UGE, 1UGF, 1UGG
78. Tu, C., et al.: Kinetic analysis of multiple proton shuttles in the active site of human carbonic anhydrase. *J. Biol. Chem.* **277**, 38870–38876 (2002)
79. Fisher, Z., et al.: Structural and kinetic characterization of active-site histidine as a proton shuttle in catalysis by human carbonic anhydrase II. *Biochemistry* **44**, 1097–1105 (2005)
80. Bhatt, D., et al.: Proton transfer in a Thr200His mutant of human carbonic anhydrase II. *Proteins* **61**, 239–245 (2005). PDB ID: 1Y00, 1Y01, 1Y02
81. Fisher, S.Z., et al.: Speeding up proton transfer in a fast enzyme: kinetic and crystallographic studies on the effect of hydrophobic amino acid substitutions in the active site of human

- carbonic anhydrase II. *Biochemistry* **46**, 3803–3813 (2007). PDB ID: 2NWO, 2NWP, 2NWX, 2NWZ, 2NXR, 2NXS, 2NXT
82. Zheng, J., Avvaru, B.S., Tu, C., McKenna, R., Silverman, D.N.: Role of hydrophilic residues in proton transfer during catalysis by human carbonic anhydrase II. *Biochemistry* **47**, 12028–12036 (2008). PDB ID: 3DV7, 3DVB, 3DVC, 3DVD
83. Domsic, J.F., et al.: Structural and kinetic study of the extended active site for proton transfer in human carbonic anhydrase II. *Biochemistry* **49**, 6394–6399 (2010)
84. Mikulski, R., et al.: Structure and catalysis by carbonic anhydrase II: role of active-site tryptophan 5. *Arch. Biochem. Biophys.* **516**, 97–102 (2011)
85. Mikulski, R., et al.: Water networks in fast proton transfer during catalysis by human carbonic anhydrase II. *Biochemistry* **52**, 125–131 (2013)
86. Fisher, S.Z., et al.: Neutron structure of human carbonic anhydrase II: implications for proton transfer. *Biochemistry* **49**, 415–421 (2010). PDB ID: 3KXX
87. Fisher, Z., et al.: Neutron structure of human carbonic anhydrase II: a hydrogen-bonded water network “Switch” is observed between pH 7.8 and 10.0. *Biochemistry* **50**, 9421–9423 (2011). PDB ID: 3TMJ
88. Fisher, S.Z., Aggarwal, M., Kovalevsky, A.Y., Silverman, D.N., McKenna, R.: Neutron diffraction of acetazolamide-bound human carbonic anhydrase II reveals atomic details of drug binding. *J. Am. Chem. Soc.* **134**, 14726–14729 (2012). PDB ID: 4G0C
89. Michalczyk, R., et al.: Joint neutron crystallographic and NMR solution studies of Tyr residue ionization and hydrogen bonding: implications for enzyme-mediated proton transfer. *Proc. Natl. Acad. Sci. U. S. A.* **112**, 5673–5678 (2015). PDB ID: 4Q49, 4Y0J
90. Kovalevsky, A., et al.: “To Be or Not to Be” protonated: atomic details of human carbonic anhydrase-clinical drug complexes by neutron crystallography and simulation. *Structure* **26**(3), 383–390.e3 (2018)
91. Kumar, V. & Kannan, K.K.: Enzyme-substrate interactions. Structure of human carbonic anhydrase I complexed with bicarbonate. *J. Mol. Biol.* **241**, 226–232 (1994). PDB ID: 1HCB
92. Haakansson, K., Wehnert, A.: Structure of cobalt carbonic anhydrase complexed with bicarbonate. *J. Mol. Biol.* **228**, 1212–1218 (1992). PDB ID: 1CAH
93. Xue, Y., Liljas, A., Jonsson, B., Lindskog, S.: Structural analysis of the zinc Hydroxide-Thr-199-Glu-106 hydrogen-bond network in human carbonic anhydrase II. *Proteins* **17**, 93–106 (1993). PDB ID: 1CAI, 1CAJ, 1CAK, 1CAL, 1CAM
94. Xue, Y., et al.: Crystallographic analysis of Thr-200→His human carbonic anhydrase II and its complex with the substrate, HCO₃⁻. *Proteins* **15**, 80–87 (1993). PDB ID: 1BIC
95. Huang, S., Sjöblom, B., Sauer-Eriksson, A.E., Jonsson, B.-H.: Organization of an efficient carbonic anhydrase: implications for the mechanism based on structure-function studies of a T199P/C206S mutant. *Biochemistry* **41**, 7628–7635 (2002). PDB ID: 1LG5, 1LG6, 1LGD
96. Domsic, J. F., et al.: Entrapment of carbon dioxide in the active site of carbonic anhydrase II. *J. Biol. Chem.* **283**, 30766–30771 (2008)
97. Domsic, J.F., McKenna, R.: Sequestration of carbon dioxide by the hydrophobic pocket of the carbonic anhydrases. *Biochim. Biophys. Acta* **1804**(2), 326–331 (2009)
98. West, D., et al.: Structural and kinetic effects on changes in the CO₂ binding pocket of human carbonic anhydrase II. *Biochemistry* **51**, 9156–9163 (2012)
99. Sjöblom, B., Polenturutti, M., Djinović-Carugo, K.: Structural study of x-ray induced activation of carbonic anhydrase. *PNAS* **106**, 10609–10613 (2009)
100. Kim, J.K., et al.: Active-site solvent replenishment observed during human carbonic anhydrase II catalysis. *IUCrJ* **5**, 93–102 (2018)
101. Haakansson, K., Briand, C., Zaitsev, V., Xue, Y., Liljas, A.: Wild-type and E106Q mutant carbonic anhydrase complexed with acetate. *Acta Crystallogr. D Biol. Crystal.* **50**, 101–104 (1994). PDB ID: 1CAX, 1CAZ
102. Mazumdar, P.A., Kumaran, D., Swaminathan, S., Das, A.K.: A novel acetate-bound complex of human carbonic anhydrase II. *Acta Crystallogr. F Struct. Biol. Cryst. Commun.* **64**, 163–166 (2008)

103. Jonsson, B.M., Hakansson, K., Liljas, A.: The structure of human carbonic anhydrase II in complex with bromide and azide. *FEBS Lett.* **322**, 186–190 (1993). PDB ID: 1RAY, 1RAZ
104. Mangani, S., Hakansson, K.: Crystallographic studies of the binding of protonated and unprotonated inhibitors to carbonic anhydrase using hydrogen sulphide and nitrate anions. *Eur. J. Biochem.* **210**, 867–871 (1992). PDB ID: 1CAN, 1CAO
105. Eriksson, A.E., Kylsten, P.M., Jones, T.A., Liljas, A.: Crystallographic studies of inhibitor binding sites in human carbonic anhydrase II: a pentacoordinated binding of the SCN⁻ ion to the zinc at high pH. *Proteins* **4**, 283–293 (1988). PDB ID: 3CA2, 2CA2
106. Mangani, S., Liljas, A.: Crystal structure of the complex between human carbonic anhydrase II and the aromatic inhibitor 1,2,4-triazole. *J. Mol. Biol.* **232**, 9–14 (1993). PDB ID: 1CRA
107. Carta, F., et al.: Dithiocarbamates: a new class of carbonic anhydrase inhibitors. Crystallographic and kinetic investigations. *Chem. Commun. (Camb.)* **48**, 1868–1870 (2012)
108. Carta, F., et al.: Dithiocarbamates strongly inhibit carbonic anhydrases and show antiglaucoma action in vivo. *J. Med. Chem.* **55**, 1721–1730 (2012). PDB ID: 3P5A
109. Martin, D.P., Cohen, S.M.: Nucleophile recognition as an alternative inhibition mode for benzoic acid based carbonic anhydrase inhibitors. *Chem. Comm.* **48**, 5259–5261 (2012)
110. Carta, F., et al.: Polyamines inhibit carbonic anhydrases by anchoring to the zinc-coordinated water molecule. *J. Med. Chem.* **53**, 5511–5522 (2010)
111. Behnke, C.A., et al.: Atomic resolution studies of carbonic anhydrase II. *Acta Crystallogr. D* **66**, 616–627 (2010)
112. Avvaru, B.S., et al.: A short, strong hydrogen bond in the active site of human carbonic anhydrase II. *Biochemistry* **49**, 249–251 (2010). PDB ID: 3KS3
113. Buratto, J., et al.: Structure of a complex formed by a protein and a helical aromatic oligoamide foldamer at 2.1 Å resolution. *Angew. Chem. Int. Ed. Engl.* **53**, 883–887 (2014). PDB ID: 4LP6, 4MTY
114. Wischeler, J.S., et al.: Stereo- and regioselective azide/alkyne cycloadditions in carbonic anhydrase II via tethering, monitored by crystallography and mass spectrometry. *Chemistry* **17**, 5842–5851 (2011). PDB ID: 3KIG, 3KNE
115. Fisher, S.Z., et al.: Atomic crystal and molecular dynamics simulation structures of human carbonic anhydrase II: insights into the proton transfer mechanism. *Biochemistry* **46**, 2930–2937 (2007). PDB ID: 2ILI
116. Duda, D., et al.: The refined atomic structure of carbonic anhydrase II at 1.05 Å resolution: implications of chemical rescue of proton transfer. *Acta Crystallogr. D Biol. Crystal.* **59**, 93–104 (2003). PDB ID: 1MOO
117. Fox, J.M., et al.: Interactions between Hofmeister anions and the binding pocket of a protein. *J. Am. Chem. Soc.* **137**, 3859–3866 (2015)
118. Mecinović, J., et al.: Fluoroalkyl and alkyl chains have similar hydrophobicities in binding to the “Hydrophobic Wall” of carbonic anhydrase. *J. Am. Chem. Soc.* **133**, 14017–14026 (2011)
119. Kim, C., et al.: Contribution of fluorine to protein-ligand affinity in the binding of fluoroaromatic inhibitors to carbonic anhydrase II. *J. Am. Chem. Soc.* **122**, 12125–12134 (2000). PDB ID: 1G3Z, 1G4O, 1G45, 1G46, 1G48, 1G4J, 1G1D, 1G52, 1G53, 1G54
120. Kim, C.Y., Chandra, P.P., Jain, A., Christianson, D.W.: Fluoroaromatic-fluoroaromatic interactions between inhibitors bound in the crystal lattice of human carbonic anhydrase II. *J. Am. Chem. Soc.* **123**, 9620–9627 (2001). PDB ID: 1I9L, 1I9M, 1I9N, 1I9O, 1I9P, 1I9Q
121. Snyder, P.W., et al.: Mechanism of the hydrophobic effect in the biomolecular recognition of arylsulfonamides by carbonic anhydrase. *Proc. Natl. Acad. Sci. U. S. A.* **108**, 17889–17894 (2011)
122. Lockett, M.R., et al.: The binding of benzoarylsulfonamide ligands to human carbonic anhydrase is insensitive to formal fluorination of the ligand. *Angew. Chem. Int. Ed. Engl.* **52**, 7714–7717 (2013)
123. Aaron, J.A., et al.: Structure of a 129Xe-cryptophane biosensor complexed with human carbonic anhydrase II. *J. Am. Chem. Soc.* **130**, 6942–6943 (2008). PDB ID: 3CYU
124. Nair, S.K., Elbaum, D., Christianson, D.W.: Unexpected binding mode of the sulfonamide fluorophore 5-dimethylamino-1-naphthalene sulfonamide to human carbonic anhydrase II.

- Implications for the development of a zinc biosensor. *J. Biol. Chem.* **271**, 1003–1007 (1996). PDB ID: 1OKL
125. Elbaum, D., Nair, S., Patchan, M., Thompson, R., Christianson, D.: Structure-based design of a sulfonamide probe for fluorescence anisotropy detection of zinc with a carbonic anhydrase-based biosensor. *J. Am. Chem. Soc.* **118**, 8381–8387 (1996). PDB ID: 1OKM, 1OKN
 126. Alterio, V., et al.: Carbonic anhydrase inhibitors: x-ray and molecular modeling study for the interaction of a fluorescent antitumor sulfonamide with isozyme II and IX. *J. Am. Chem. Soc.* **128**, 8329–8335 (2006). PDB ID: 2F14
 127. Wang, Y., Roose, B.W., Philbin, J.P., Doman, J.L., Dmochowski, I.J.: Programming a molecular relay for ultrasensitive biodetection through (129) Xe NMR. *Angew. Chem. Int. Edt. Engl.* **55**, 1733–1736 (2016). PDB ID: 5EKH, 5EKJ, 5EKM
 128. Supuran, C.T.: Structure-based drug discovery of carbonic anhydrase inhibitors. *J. Enzyme. Inhib. Med. Chem.* **27**, 759–772 (2012)
 129. Supuran, C.T.: Advances in structure-based drug discovery of carbonic anhydrase inhibitors. *Expert Opin. Drug. Discov.* **12**, 61–88 (2017)
 130. Supuran, C.T.: Carbonic anhydrases—an overview. *Curr. Pharm. Des.* **14**, 603–14 (2008)
 131. Hassan, M.I., Shajee, B., Waheed, A., Ahmad, F., Sly, W.S.: Structure, function and applications of carbonic anhydrase isozymes. *Bioorg. Med. Chem.* **21**, 1570–1582 (2013)
 132. Lomelino, C.L., Mahon, B.P., McKenna, R., Carta, F., Supuran, C.T.: Kinetic and x-ray crystallographic investigations on carbonic anhydrase isoforms I, II, IX and XII of a thioureido analog of SLC-0111. *Bioorg. Med. Chem.* **24**, 976–981 (2016)
 133. Supuran, C.T.: Carbonic anhydrase inhibitors and activators for novel therapeutic applications. *Future Med. Chem.* **3**, 1165–1180 (2011)
 134. Supuran, C.T.: Inhibition of carbonic anhydrase IX as a novel anticancer mechanism. *World J. Clin. Oncol.* **3**, 98–103 (2012)
 135. Winun, J.Y., Scozzafava, A., Montero, J.L., Supuran, C.T.: New zinc binding motifs in the design of selective carbonic anhydrase inhibitors. *Mini Rev. Med. Chem.* **6**, 921–36 (2006)
 136. Recacha, R., Costanzo, M.J., Maryanoff, B.E., Chattopadhyay, D.: Crystal structure of human carbonic anhydrase II complexed with an anti-convulsant sugar sulphamate. *Biochem. J.* **361**, 437–441 (2002). PDB ID: 1EOU
 137. Woo, L.W.L., et al.: Highly potent first examples of dual aromatase-steroid sulfatase inhibitors based on a biphenyl template. *J. Med. Chem.* **53**, 2155–2170 (2010). PDB ID: 2WD3
 138. Temperini, C., Scozzafava, A., Puccetti, L., Supuran, C.T.: Carbonic anhydrase activators: x-ray crystal structure of the adduct of human isozyme II with L-histidine as a platform for the design of stronger activators. *Bioorg. Med. Chem. Lett.* **15**, 5136–5141 (2005). PDB ID: 2ABE
 139. Temperini, C., et al.: Carbonic anhydrase inhibitors. Interaction of 2-N,N-Dimethylamino-1,3,4-Thiadiazole-5-Methanesulfonamide with 12 mammalian isoforms: kinetic and x-ray crystallographic studies. *Bioorg. Med. Chem. Lett.* **18**, 999–1005 (2008). PDB ID: 3BL0
 140. Bhatt, D., Fisher, S.Z., Tu, C., McKenna, R., Silverman, D.N.: Location of binding sites in small molecule rescue of human carbonic anhydrase II. *Biophys. J.* **92**, 562–570 (2007). PDB ID: 2FNK, 2FNM, 2FNN
 141. Aggarwal, M., et al.: Structural insight into activity enhancement and inhibition of H64A carbonic anhydrase II by imidazoles. *IUCrJ* **1**, 129–135 (2014). PDB ID: 4HEW, 4HEY, 4HEZ, 4HF3
 142. D'Ambrosio, K., et al.: Carbonic anhydrase inhibitors: bioreductive nitro-containing sulfonamides with selectivity for targeting the tumor associated isoforms IX and XII. *J. Med. Chem.* **51**, 3230–3237 (2008)
 143. De Simone, G., et al.: Carbonic anhydrase inhibitors: hypoxia-activatable sulfonamides incorporating disulfide bonds that target the tumor-associated isoform IX. *J. Med. Chem.* **49**, 5544–51 (2006)
 144. Gitto, R., et al.: Synthesis, structure-activity relationship studies, and x-ray crystallographic analysis of arylsulfonamides as potent carbonic anhydrase inhibitors. *J. Med. Chem.* **55**, 3891–3899 (2012). PDB ID: 3V7X, 3VBD

145. Buemi, M.R., et al.: Carbonic anhydrase inhibitors: design, synthesis and structural characterization of new heteroaryl-N-carbonylbenzenesulfonamides targeting druggable human carbonic anhydrase isoforms. *Eur. J. Med. Chem.* **102**, 223–232 (2015)
146. Menchise, V., et al.: Carbonic anhydrase inhibitors: stacking with Phe131 determines active site binding region of inhibitors as exemplified by the x-ray crystal structure of a membrane-impermeant antitumor sulfonamide complexed with isozyme II. *J. Med. Chem.* **48**, 5721–5727 (2005). PDB ID: 1ZE8
147. Güzel-Akdemir, Ö., Akdemir, A., Isik, S., Vullo, D., Supuran, C.: T O-Benzenedisulfonimido–Sulfonamides are potent inhibitors of the tumor-associated carbonic anhydrase isoforms CA IX and CA XII. *Bioorg. Med. Chem. Carb. Anhyd.* **21**, 1386–1391 (2013)
148. Hen, N., et al.: Anticonvulsant 4-aminobenzenesulfonamide derivatives with branched-alkylamide moieties: x-ray crystallography and inhibition studies of human carbonic anhydrase isoforms I, II, VII, and XIV. *J. Med. Chem.* **54**, 3977–3981 (2011). PDB ID: 3OY0, 3OQY, 3OYS
149. Pacchiano, F., et al.: Selective hydrophobic pocket binding observed within the carbonic anhydrase II active site accommodate different 4-substituted-ureido-benzenesulfonamides and correlate to inhibitor potency. *Chem. Com-mun. (Camb.)* **46**, 8371–8373 (2010). PDB ID: 3MZC, 3N0N, 3N2P, 3N3J, 3N4B
150. Carta, F., et al.: Sulfonamides incorporating 1,3,5-triazine moieties selectively and potently inhibit carbonic anhydrase transmembrane isoforms IX, XII and XIV over cytosolic isoforms I and II: solution and x-ray crystallographic studies. *Bioorg. Med. Chem.* **19**, 3105–3119 (2011)
151. Smirnov, A., Zubrienè, A., Manakova, E., Grazulis, S., Matulis, D.: Crystal structure correlations with the intrinsic thermodynamics of human carbonic anhydrase inhibitor binding. *PeerJ* **6**, e4412 (2018)
152. Rutkauskas, K., et al.: 4-Amino-substituted benzenesulfonamides as inhibitors of human carbonic anhydrases. *Molecules* **19**(11), 17356–17380 (2014)
153. Čapkauskaitė, E., et al.: Design of [(2-Pyrimidinylthio)Acetyl]Benzenesulfonamides as inhibitors of human carbonic anhydrases. *Eur. J. Med. Chem.* **51**, 259–270 (2012)
154. Čapkauskaitė, E., et al.: Indapamide-like benzenesulfonamides as inhibitors of carbonic anhydrases I, II, VII, and XIII. *Bioorg. Med. Chem.* **18**, 7357–7364 (2010)



X-Ray Crystallographic Structures of High-Affinity and High-Selectivity Inhibitor Complexes with CA IX That Plays a Special Role in Cancer

14

Kaspars Tars and Daumantas Matulis

Abstract

Carbonic anhydrase IX (CA IX) is an isoform of CAs that is highly overexpressed in numerous human cancers and found essentially only in the stomach in healthy humans. Therefore, it is considered to be a target both for cancer therapy and cancer diagnostics. The CA IX is primarily found on the surface of cancer cells, it acidifies the environment and alleviates the progression of metastases. To rationally design inhibitors of CA IX that would bind and inhibit the enzyme with high affinity but at the same time would not bind or bind weakly to the remaining 11 catalytically active CA isoforms is a difficult task that requires a high-resolution crystal structure of the enzyme and its complexes with inhibiting compounds. Oppositely to many CA isoforms, the CA IX enzyme has proven to be very difficult to crystallize. Only several crystal structures of the enzyme have been previously described. Here we describe the crystal structures of CA IX with a series of inhibitors that bear fluorine for increased affinity and a hydrophobic moiety that makes it highly selective for CA IX. The crystal structures describe how the compounds recognize the enzyme and provide clues to the structure–thermodynamics correlations that are necessary for compound design with desired binding properties.

K. Tars

Latvian Biomedical Research and Study Center, Riga, Latvia

e-mail: kaspars@biomed.lu.lv

D. Matulis (✉)

Department of Biothermodynamics and Drug Design, Institute of Biotechnology, Life Sciences Center, Vilnius University, Vilnius, Lithuania

e-mail: matulis@ibt.lt

© Springer Nature Switzerland AG 2019

D. Matulis (ed.), *Carbonic Anhydrase as Drug Target*,

https://doi.org/10.1007/978-3-030-12780-0_14

203

14.1 Introduction

Carbonic anhydrase IX (CA IX) is one of the twelve enzymatically active CA isoforms found in human organism. CA IX is a trans-membrane protein, rarely found on a surface of normal cells and limited to the tissue of gastrointestinal tract [1], but frequently overexpressed in human hypoxic tumors. Cells of many solid tumors are facing hypoxic conditions and therefore are developing various strategies to adopt their metabolism. Under hypoxic conditions, the cells obtain most of their energy from glycolysis, resulting in accumulation of pyruvate and lactate—organic acids, which are lowering intracellular pH. Produced hydrogen ions may react with bicarbonate, forming carbon dioxide, which escapes the cell and again is converted to bicarbonate and proton. The net result is that the intracellular pH is maintained within physiological range, but extracellular space gets acidified. In order to enhance the conversion of carbon dioxide to bicarbonate, hypoxic cells tend to overproduce the membrane-associated carbonic anhydrases. Notably, CA IX is overproduced in many hypoxic tumors including renal cell carcinoma [2], breast cancer [3], and numerous others. Furthermore, high expression of CA IX generally correlates with poor prognosis and is related to a decrease in the disease-free interval following successful therapy [4]. Apart from its role in pH regulation, CA IX modulates tumor growth, survival, and malignancy by several other mechanisms which do not seem to be directly related to enzymatic activity. These include interference with the Rho/ROCK signaling pathway [5], and binding to beta-catenin, resulting in weakening of intercellular contacts [6].

14.2 Utilization of CA IX as Anti-Cancer Therapeutic Target

Specific presence of CA IX on the surface of tumor cells can be targeted in two distinct ways [7]. First, enzymatic activity of CA IX can be inhibited, thereby reducing the fitness of tumor cells in hypoxic environment. Second strategy is to use CA IX as a cancer cell-targeting molecule. This can be accomplished either by targeting toxic or radio-labeled compounds or marking the CA IX- expressing cells for attack by immune system. For example, specific anti-CA IX antibodies can mediate cancer cell destruction by antibody-dependent cell-mediated cytotoxicity (ADCC), complement-dependent cytotoxicity (CDC), and antibody-dependent cellular phagocytosis (ADCP) [8]. Several monoclonal anti-CA IX antibodies have been shown to reduce tumor size in animal models. Anti-CA IX monoclonal antibody girentuximab (known also as G250) displayed promising results in Phase I and Phase II clinical trials [9] but failed to display significant benefit in Phase III trials [10]. A less well-explored strategy is the induction of auto-anti-CA IX immune response. One study demonstrated that dendritic cells, presenting CA IX, are efficient anti-cancer vaccine candidates in animal models [11]. In this case, the cancer cell destruction was achieved by T-cell mediated CA IX-specific inhibition of tumor growth rather than by any mechanism involving antibodies.

Specific CA IX targeting is not restricted to the use of anti-CA IX antibodies. The CA IX-targeting peptides have been obtained by phage display [12–14]. Furthermore, it is possible to use CA inhibitors as targeting molecules by fusing them to toxic compounds [15, 16] or nanoparticles [17].

14.3 Structure of CA IX and the Properties of Non-Catalytic Domains

CA IX is a multi-domain membrane protein, containing extracellular, trans-membrane, and intracellular parts [18] (Fig. 14.1). The first 37 residues consist of the signal peptide, which is absent in the mature protein. Extracellular part is composed of the N-terminal proteoglycan-like domain (PG), followed by the catalytic domain. After a short linker region, there is a single trans-membrane helix, followed by a short intracytoplasmic (intracellular) tail.

While the catalytic domain and trans-membrane helix fulfill the obvious functions of catalytic activity and membrane anchoring, the exact biological roles of the other parts of the protein are less well defined, although several functions have been attributed to both PG and intracellular domains. Residues 53 to 111 of the PG domain display sequence homology to keratan sulfate region of aggrecan, which is a part of proteoglycan assembly, hence the name “proteoglycan-like domain” [18], although the presence of carbohydrate units has never been observed in the CA IX PG except for a single O-glycosylation site at Thr78 [19]. The PG domain has a remarkably high content of negatively charged residues (35 out of 99) and contains a 6-fold tandem repeat of consensus sequence GEEDLP. Structurally, the PG domain seems to belong to the intrinsically disordered proteins, possibly with some regions adapting polyproline II-type helix conformation [20].

The PG domain appears to have several functions. First, it plays a role in cancer cell adhesion, spreading, and migration [21]. The PG domain has also been shown to influence the catalytic activity of the enzyme. It has been demonstrated that the enzyme without PG domain is roughly 2 to 3 times less active compared to the full-length enzyme [19]. Furthermore, the addition of recombinant PG domain to PG-less CA IX also enhances the enzymatic activity [20]. The presence of PG domain also shifts the optimum pH value for the enzyme from 7.0 in the PG-less variant to 6.5 in the full-length protein, therefore making CA IX more efficient in acidic environments, typical for hypoxic cancer tissue [22]. The mechanism for PG domain action on the catalytic activity is unclear, but, judging from the structure of catalytic domain, the PG domain lies at the border of the active site, and it is thought that the negatively charged residues of PG domain might interact with the positively charged residues lining the active site of the catalytic domain [23]. More recently it has been demonstrated that the PG domain has yet another function—it mediates the facilitation of lactate transport in cancer cells [24].

The intracellular domain is very short, comprising just 26 residues. No direct experimental data is available regarding its structure, but modeling studies suggest that the intracellular part is in helical conformation [25]. The intracellular tail has

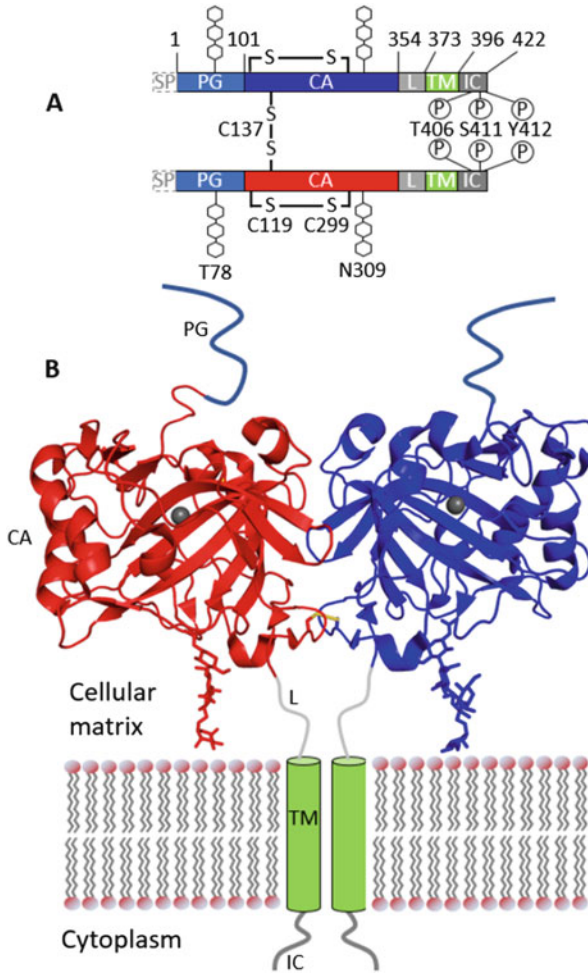


Fig. 14.1 The structure of CA IX. (a) Domain organization and covalent structure of CA IX dimer. Signal peptide (SP) is absent in mature protein. *PG* proteoglycan-like domain, *CA* catalytic domain of carbonic anhydrase, *L* linker region, *TM* trans-membrane helix, *IC* intracytoplasmic tail. Inter- and intra-monomer disulfides, two glycosylation sites, and three phosphorylation sites are shown along with the respective residue numbers. Residues are numbered as for mature protein, excluding signal peptide. (b) Three-dimensional model of CA IX, based on known structure of catalytic domain and predicted trans-membrane helix. Coloring of domains is the same as in panel (a). The catalytic zinc ions are shown as gray spheres. Sugar moieties at N309 are shown as stick models

three phosphorylation sites—T406, S411, and Y412. The first two seem to regulate the enzymatic activity of CA IX, while the last one is involved in EGFR-induced signal transduction to PI3/Akt kinase pathway. The intracellular tail has also been shown to interact with cullin-associated NEDD8-dissociated protein 1 (CAND1). It

appears that CAND1 is stabilizing the CA IX structure, since the cells with lower CAND1 expression also have lower CA IX content [25].

14.4 Structure and Function of the Catalytic Domain of CA IX

Due to technical challenges of the work with trans-membrane proteins, most in vitro inhibition and structural studies of CA IX have been limited to the use of catalytic domain, which can be produced in soluble form and retains at least a part of the catalytic activity of full-length CA IX [19,26]. The CA IX in its physiological form makes a homo-dimer, where the catalytic domain is making all known inter-dimer interactions. Both catalytic domains are linked by a single disulfide bond, but the dimeric structure is also retained in the absence of the covalent linkage, as demonstrated by the site-directed mutagenesis, where the disulfide-forming cysteine was replaced by a serine [23].

The carbonic anhydrase XII (CA XII) is also a dimer in its physiological form. However, the dimer-forming interface of CA XII is completely different from that of CA IX [23]. As of now, it remains unknown if the dimerization of CA IX has any biological function, such as the cross-talk between both active sites.

The catalytic domain of CA IX is homologous to other human CAs, being 34% identical to that of CA II. Despite the relatively high similarity to CA II and other “easy-going” carbonic anhydrases, the catalytic domain of CA IX is notoriously difficult to produce in soluble form and crystallize, which is often the case for mammalian non-cytosolic proteins. To circumvent this problem, a number of CA IX active site mimics have been reported earlier, based on CA II scaffold, but with active site residues to some extent representing those of CA IX [27,28]. However, none of the active site mimics is a perfect model for drug design. In the best available mimic, all active site residues along with several nearby residues were converted to those of CA IX and the resulting 3D structure of the active site was indeed very similar to that of CA IX [27].

However, later structural studies with inhibitors revealed that in some cases there are modest, yet significant changes in the exact positions of bound inhibitors among CA IX and CA IX mimic structures [29]. The first successful structure of the catalytic domain of CA IX was obtained from the enzyme produced in insect cells [23]. Apart from the lack of intracellular, trans-membrane, and PG parts, the protein had an additional change—a cysteine, able to form the intra-dimer covalent disulfide bond was mutated to serine, resulting in a substantially higher resolution. The overall structure of CA IX catalytic domain is very similar to that of other alpha class CAs, forming an α - β - α sandwich, where 10-stranded anti-parallel β -sheet forms the protein core (Fig. 14.2). The secondary structure elements of the catalytic domain of CA IX are essentially the same as in CA II and even most of the loop structures are quite similar. Largest differences are found in a hairpin loop region, which forms the inter-monomer interface in CA IX dimer, in part accounting for the fact that CA IX can form a dimer, but CA II cannot.

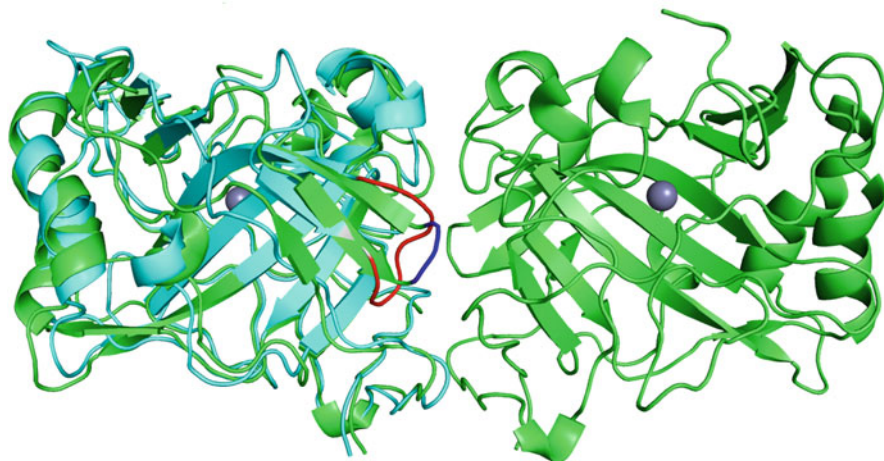


Fig. 14.2 Comparison of overlaid catalytic domain of CA IX (green) and CA II (cyan) overall structures. The biggest differences are found in the loop region (red for CA II and blue for CA IX), involved in the dimer contacts in CA IX. The catalytic zinc ions are shown as gray spheres

Despite the obtained structure, the production of the catalytic domain of CA IX in insect cell production system was rather challenging. Therefore, an alternative system of production in *Pichia pastoris* was introduced, utilizing a cleavable N-terminal MBP fusion protein tag [26]. The obtained protein was essentially the same as in the insect production system, except that the asparagine Asn309 was replaced with a glutamine to avoid potential overglycosylation problems, since Asn309 is known to be glycosylated in insect cell production system.

14.5 Design of High-Affinity and Specific CA IX Inhibitors

Since human genome encodes twelve catalytically active CAs with a considerable degree of homology, specific targeting of a particular CA is challenging. As illustrated in Fig. 14.3 and Table 14.1, the active sites of human CAs are indeed very similar. In fact, out of about 23 residues lining the active site, only six are substantially variable among the CA isoforms. Therefore, to achieve meaningful selectivity, the inhibitor must make contact with some of those six residues.

Furthermore, the residues which are different among isoforms are located relatively far from the catalytic zinc ion. Therefore, small, zinc-binding molecules, such as acetazolamide or ethoxzolamide, are unlikely to be isoform-specific and distinguish between CA II and CA IX.

Like in many other CAs, the active site of CA IX is composed of polar and hydrophobic sides (Figs. 14.3 and 14.4). It is thought that this is due to the extremely different nature of CA substrate vs products. CO_2 is a hydrophobic gas, poorly soluble in water, while HCO_3^- and H^+ ions are highly soluble in water. Therefore,

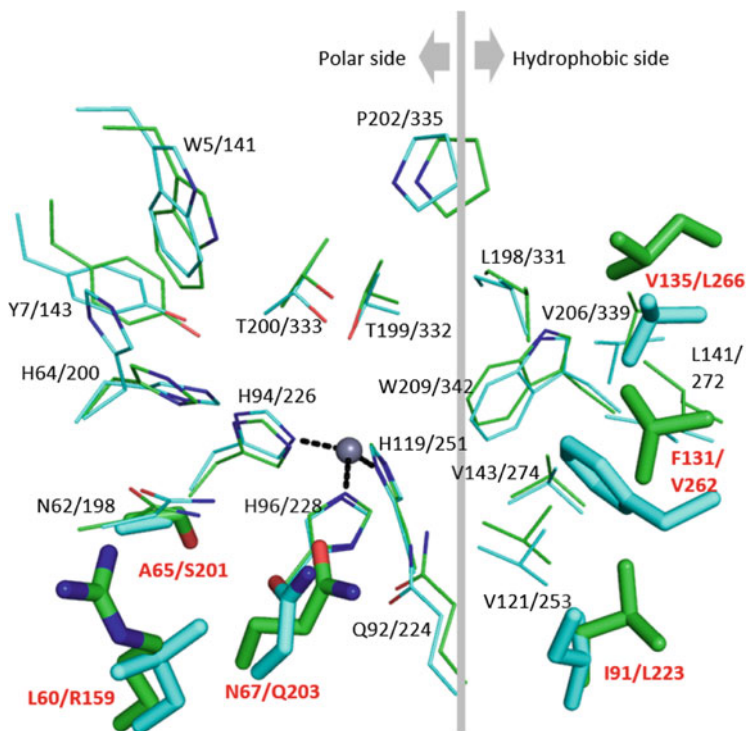


Fig. 14.3 Comparison of the active sites of CA II and CA IX. The CA II residues are shown with cyan carbons, while the CA IX residues—with green carbons. The catalytic zinc ion is shown as a gray sphere. The residues, which are different between CA II and CA IX are shown as thick stick models and labeled in red. Approximate boundary between the polar and hydrophobic sides is shown with a gray vertical line

the substrate enters via the hydrophobic side, while the product leaves via the polar one. This property can be utilized in the design of specific “dual-tail” inhibitors, interacting with both polar and hydrophobic parts of the active site.

Currently, a vast number of different CA IX inhibitors have been reported belonging to many different compound classes, including sulfonamides, sulfamates [30], sulfocoumarins [31], and saccharine derivatives [32] (see [33] and [34] for reviews). However, most of the reported CA IX inhibitors are not highly isoform-specific and many of them bind to CA I and/or CA II even better than to CA IX. Nevertheless, one inhibitor, ureidobenzenesulfonamide SLC-0111, has reached clinical trials (<https://clinicaltrials.gov/ct2/show/NCT02215850>). The SLC-0111 is reported to exhibit $K_i = 45$ nM for CA IX and display 10-fold selectivity over CA II [35]. In our opinion, the 10-fold selectivity is insufficient for the compound to be considered truly selective and fully inhibit target isoform while leaving the remaining eleven isoforms untouched. The 10 thousand-fold selectivity is required to achieve 99% inhibition of the target while leaving 99% of the undesired isoform

Table 14.1 Structural alignment of the amino acid residues in the active sites of catalytically active human CAs

Residue	CA isoforms											
	I	II	III	IV	Va	Vb	VI	VII	IX	XII	XIII	XIV
5/141	W	W	W	W	W	Y	W	W	W	W	W	W
7/143	Y	Y	Y	Y	W	Y	Y	Y	Y	Y	Y	Y
60/159	I	L	L	Q	W	W	V	T	R	T	S	H
62/198	N	N	N	N	N	N	N	N	N	N	N	N
64/200	H	H	K	H	Y	Y	H	H	H	H	H	H
65/201	S	A	T	S	L	S	T	S	S	S	S	T
67/203	H	N	R	M	Q	L	Q	Q	Q	K	N	Q
91/223	F	I	R	K	K	K	Q	K	L	T	R	A
92/224	Q	Q	Q	Q	Q	Q	Q	Q	Q	Q	Q	Q
<i>94/226</i>	<i>H</i>	<i>H</i>	<i>H</i>	<i>H</i>	<i>H</i>	<i>H</i>	<i>H</i>	<i>H</i>	<i>H</i>	<i>H</i>	<i>H</i>	<i>H</i>
<i>96/228</i>	<i>H</i>	<i>H</i>	<i>H</i>	<i>H</i>	<i>H</i>	<i>H</i>	<i>H</i>	<i>H</i>	<i>H</i>	<i>H</i>	<i>H</i>	<i>H</i>
<i>119/251</i>	<i>H</i>	<i>H</i>	<i>H</i>	<i>H</i>	<i>H</i>	<i>H</i>	<i>H</i>	<i>H</i>	<i>H</i>	<i>H</i>	<i>H</i>	<i>H</i>
121/253	A	V	V	V	V	V	V	V	V	V	V	V
131/262	L	F	F	V	Y	F	Y	F	V	A	F	L
135/266	A	V	L	Q	V	A	Q	A	L	S	A	A
141/272	L	L	I	I	L	L	L	L	L	L	L	L
143/274	V	V	V	V	V	V	V	V	V	V	V	V
198/331	L	L	F	L	L	L	L	L	L	L	L	L
199/332	T	T	T	T	T	T	T	T	T	T	T	T
200/333	T	T	T	T	T	T	T	T	T	T	V	T
202/335	P	P	P	P	P	P	P	P	P	P	P	P
206/339	V	V	I	V	V	V	V	V	V	V	V	V
209/342	W	W	W	W	W	W	W	W	W	W	W	W

The residue numbers are shown for CA II/CA IX. Invariant Zn-coordinating histidines are shown in italic. The main variable residues, different in some or many CA isoforms, that could be utilized in the design of isoform-selective inhibitors, are shown in bold

activity. It is really difficult to achieve when the inhibitor is supposed to inhibit only one isoform such as CA IX but leaves all remaining isoforms active.

However, recently we have reported a series of sulfonamide based CA IX inhibitors with substantially better affinities and selectivities [27, 36]. For example, inhibitor VR16-09 has $K_i = 160$ pM and more than million-fold selectivity over CA II. The reported inhibitors have fluorinated benzenesulfonamide scaffold, ensuring tight binding to zinc ion due to low pK_a value of the sulfonamide group, induced by strong electronegative properties of the fluorine atoms. Additionally, there are two tails attached to the fluorinated benzene ring—one hydrophobic and another polar which occupy the corresponding hydrophobic and polar parts of the CA IX active site, ensuring high selectivity over other CA isoforms.

In the case of VR16-09, the selectivity of the compound is rather obvious from the crystallographic studies (Fig. 14.4). The bulky 12-member carbon ring occupies

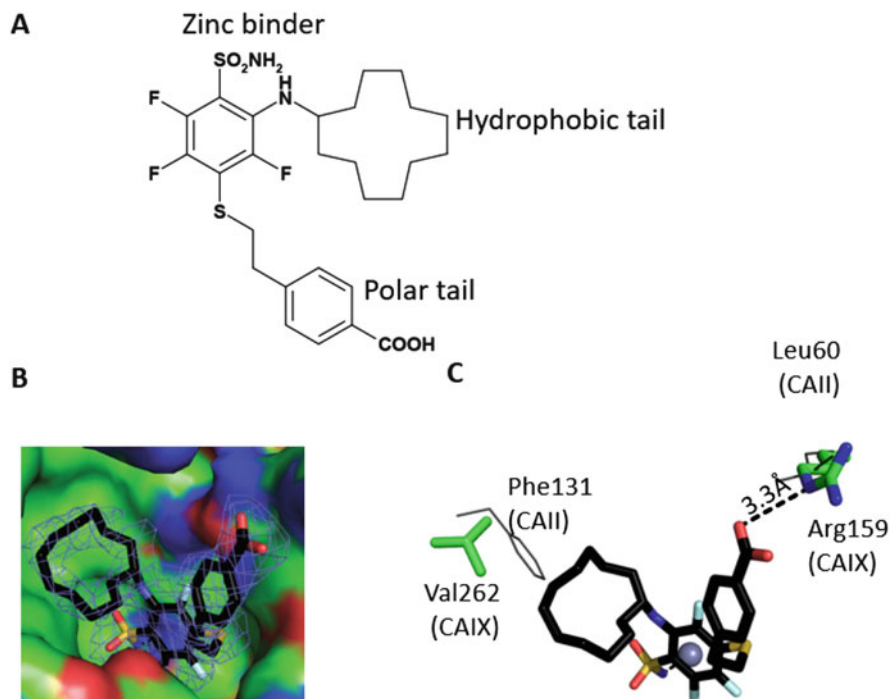


Fig. 14.4 The binding mode of the compound VR16-09 in the active site of CA IX. (a) Chemical formula of VR16-09, indicating the polar, hydrophobic, and zinc-binding parts of the molecule, (b) the CA IX surface model, shown with carbon atoms in green, oxygens in red, and nitrogens in blue. As it can be seen, the inhibitor (black carbon atoms) is occupying both the hydrophobic and polar parts of the active site cavity. The Fo–Fc omit map is contoured at 3σ . (c) The inhibitor is making two contacts with residues which are different between CA II and CA IX. The Phe131 in CA II would collide with the carbon atom ring of VR16-09, while there is no collision with the smaller valine residue in CA IX. The salt bridge of carboxyl group of VR16-09 is making a charged interaction with Arg159, while the corresponding residue in CA II is Leu that is incapable of making the charged interaction

the hydrophobic part of the CA IX active site. Binding of the same 12-member ring in CA II would be problematic due to the collision with Phe131. The benzoic acid moiety of VR16-09 is making a CA IX-specific charged interaction with Arg159. Therefore, VR16-09 is an example of successfully designed high-affinity dual-tail CA IX inhibitor.

However, inhibitors with even higher affinities and selectivities may have to be designed in the future to fully address the requirements for the affinity and selectivity. Furthermore, to be a candidate for drug development, the compound should possess various physico-chemical properties within the required range. Such properties as compound solubility, octanol–water partition coefficient, resistance to enzyme modification in human body, and many other would have to be optimized.

14.6 Conclusions

High-resolution X-ray crystallographic structure of CA IX complex with bound inhibitor VD11-4-2 and other similar inhibitors has explained the structural origins of the selectivity when the compound binds to CA IX significantly more strongly than to CA II. The cyclooctyl ring of the compound would not fit as easily in CA II due to the presence of bulky Phe131, which is absent in CA IX. In addition, an ion pair is formed between the carboxylic group of VR16-09 and Arg159 in CA IX, where Leu60 is present in CA II.

Acknowledgements D. M. thanks the Research Council of Lithuania (project TAP LLT-1/2016).

References

1. Pastoreková, S., et al.: Carbonic anhydrase IX, MN/CA IX: analysis of stomach complementary DNA sequence and expression in human and rat alimentary tracts. *Gastroenterology* **112**, 398–408 (1997)
2. Bismar, T.A., et al.: Quantification of G250 mRNA expression in renal epithelial neoplasms by real-time reverse transcription-PCR of dissected tissue from paraffin sections. *Pathology* **35**, 513–517 (2003)
3. Chia, S.K., et al.: Prognostic significance of a novel hypoxia-regulated marker, carbonic anhydrase IX, in invasive breast carcinoma. *J. Clin. Oncol. Off. J. Am. Soc. Clin. Oncol.* **19**, 3660–3668 (2001)
4. Bui, M.H.T., et al.: Carbonic anhydrase IX is an independent predictor of survival in advanced renal clear cell carcinoma: implications for prognosis and therapy. *Clin. Cancer Res.* **9**, 802–811 (2003)
5. Shin, H.-J., et al.: Carbonic anhydrase IX (CA9) modulates tumor-associated cell migration and invasion. *J. Cell Sci.* **124**, 1077–1087 (2011)
6. Svastová, E., et al.: Carbonic anhydrase IX reduces E-cadherin-mediated adhesion of MDCK cells via interaction with beta-catenin. *Exp. Cell Res.* **290**, 332–345 (2003)
7. Pastorek, J., Pastorekova, S.: Hypoxia-induced carbonic anhydrase IX as a target for cancer therapy: from biology to clinical use. *Semin. Cancer Biol.* **31**, 52–64 (2015)
8. Chang, D.-K., et al.: Human anti-CAIX antibodies mediate immune cell inhibition of renal cell carcinoma in vitro and in a humanized mouse model in vivo. *Mol. Cancer* **14**, 119 (2015)
9. Bleumer, I., et al.: A phase II trial of chimeric monoclonal antibody G250 for advanced renal cell carcinoma patients. *Br. J. Cancer* **90**, 985–990 (2004)
10. Haas, N.B., et al.: Adjuvant treatment for high-risk clear cell renal cancer: updated results of a high-risk subset of the ASSURE randomized trial. *JAMA Oncol.* **3**, 1249–1252 (2017)
11. Birkhäuser, F.D., et al.: Dendritic cell-based immunotherapy in prevention and treatment of renal cell carcinoma: efficacy, safety, and activity of AdGM-CAIX in immunocompetent mouse models. *J. Immunother. (Hagerstown, Md.: 1997)* **36**, 102–111 (2013)
12. Askoxylakis, V., et al.: A new peptide ligand for targeting human carbonic anhydrase IX, identified through the phage display technology. *PLoS One* **5**, e15962 (2010)
13. Rana, S., et al.: Screening of a novel peptide targeting the proteoglycan-like region of human carbonic anhydrase IX. *Mol. Imaging* **12**(8), 7290–2013 (2013)
14. Rana, S., et al.: Optimization of a novel peptide ligand targeting human carbonic anhydrase IX. *PLoS One* **7**, e38279 (2012)
15. Krall, N., et al.: A small-molecule drug conjugate for the treatment of carbonic anhydrase IX expressing tumors. *Angew. Chem. Int. Ed. Engl.* **53**, 4231–4235 (2014)

16. Krall, N., Pretto, F., Neri, D.: A bivalent small molecule-drug conjugate directed against carbonic anhydrase IX can elicit complete tumour regression in mice. *Chem. Sci.* **5**, 3640–3644 (2014)
17. Stiti, M., et al.: Carbonic anhydrase inhibitor coated gold nanoparticles selectively inhibit the tumor-associated isoform IX over the cytosolic isozymes I and II. *J. Am. Chem. Soc.* **130**, 16130–16131 (2008)
18. Opavský, R., et al.: Human MN/CA9 gene, a novel member of the carbonic anhydrase family: structure and exon to protein domain relationships. *Genomics* **33**, 480–487 (1996)
19. Hilvo, M., et al.: Biochemical characterization of CA IX, one of the most active carbonic anhydrase isozymes. *J. Biol. Chem.* **283**, 27799–27809 (2008)
20. Langella, E., et al.: Biochemical, biophysical and molecular dynamics studies on the proteoglycan-like domain of carbonic anhydrase IX. *Cell. Mol. Life Sci.* **75**, 3283–3296 (2018)
21. Csaderova, L., et al.: The effect of carbonic anhydrase IX on focal contacts during cell spreading and migration. *Front. Physiol.* **4**, 271 (2013)
22. Innocenti, A., et al.: The proteoglycan region of the tumor-associated carbonic anhydrase isoform IX acts as an intrinsic buffer optimizing CO₂ hydration at acidic pH values characteristic of solid tumors. *Bioorg. Med. Chem. Lett.* **19**, 5825–5828 (2009)
23. Alterio, V., et al.: Crystal structure of the catalytic domain of the tumor associated human carbonic anhydrase IX. *Proc. Natl. Acad. Sci. U. S. A.* **106**, 16233–16238 (2009)
24. Ames, S., Pastorekova, S., Becker, H.M.: The proteoglycan-like domain of carbonic anhydrase IX mediates non-catalytic facilitation of lactate transport in cancer cells. *Oncotarget* **9**, 27940–27957 (2018)
25. Buonanno, M., et al.: Disclosing the interaction of carbonic anhydrase IX with cullin-associated NEDD8-dissociated protein 1 by molecular modeling and integrated binding measurements. *ACS Chem. Biol.* **12**, 1460–1465 (2017)
26. Leitans, J., et al.: Efficient expression and crystallization system of cancer-associated carbonic anhydrase isoform IX. *J. Med. Chem.* **58**, 9004–9009 (2015)
27. Dudutienė, V., et al.: Discovery and characterization of novel selective inhibitors of carbonic anhydrase IX. *J. Med. Chem.* **57**, 9435–9446 (2014)
28. Genis, C., et al.: Design of a carbonic anhydrase IX active-site mimic to screen inhibitors for possible anticancer properties. *Biochemistry* **48**, 1322–1331 (2009)
29. Kazokaitė, J., et al.: Novel fluorinated carbonic anhydrase IX inhibitors reduce hypoxia-induced acidification and clonogenic survival of cancer cells. *Oncotarget* **9**, 26800–26816 (2018)
30. Winum, J.-Y., et al.: Carbonic anhydrase inhibitors. Inhibition of cytosolic isozymes I and II and transmembrane, tumor-associated isozyme IX with sulfamates including EMATE also acting as steroid sulfatase inhibitors. *J. Med. Chem.* **46**, 2197–2204 (2003)
31. Tars, K., et al.: Sulfocoumarins (1,2-benzoxathiine-2,2-dioxides): a class of potent and isoform-selective inhibitors of tumor-associated carbonic anhydrases. *J. Med. Chem.* **56**, 293–300 (2013)
32. Ivanova, J., et al.: X-ray crystallography-promoted drug design of carbonic anhydrase inhibitors. *Chem. Commun.* **51**, 7108–7111 (2015)
33. McDonald, P.C., Winum, J.-Y., Supuran, C.T., Dedhar, S.: Recent developments in targeting carbonic anhydrase IX for cancer therapeutics. *Oncotarget* **3**, 84–97 (2012)
34. Kazokaitė, J., Aspatwar, A., Parkkila, S., Matulis, D.: An update on anti-cancer drug development and delivery targeting carbonic anhydrase IX. *PeerJ* **5**, e4068 (2017)
35. Pacchiano, F., et al.: Ureido-substituted benzenesulfonamides potently inhibit carbonic anhydrase IX and show antimetastatic activity in a model of breast cancer metastasis. *J. Med. Chem.* **54**, 1896–1902 (2011)
36. Kazokaitė, J., et al.: Novel fluorinated carbonic anhydrase IX inhibitors reduce hypoxia-induced acidification and clonogenic survival of cancer cells. *Oncotarget* **9**, 26800–26816 (2018)



In Silico Modeling of Inhibitor Binding to Carbonic Anhydrases

15

Visvaldas Kairys, Kliment Olechnovič, Vytautas Raškevičius,
and Daumantas Matulis

Abstract

The ability to model carbonic anhydrase (CA) receptor and its inhibitors *in silico* is important because it can save valuable resources and help to rationalize the mode of binding, and to design better inhibitors. In this chapter, we briefly review the existing literature on molecular modeling of CA and its binders, with a particular emphasis on molecular docking and quantitative structure–activity relationship (QSAR) methods. We also demonstrate some of the difficulties encountered when trying to model CAs.

15.1 Introduction

Carbonic anhydrases (CAs) (E.C. number 4.2.1.1) comprise an important class of enzymes catalyzing reversible hydration of carbon dioxide to bicarbonate [1]. In this chapter, our focus will be on selected aspects of computational modeling of CAs. First, we will overview applications of molecular docking to study CA and its inhibitors. Some issues encountered when docking into the CAs will also be touched upon, such as the presence of the metal ion and the ligand rotamer problem.

V. Kairys · K. Olechnovič

Department of Bioinformatics, Institute of Biotechnology, Vilnius University, Vilnius, Lithuania
e-mail: visvaldas.kairys@bti.vu.lt; kliment.olechnovic@bti.vu.lt

V. Raškevičius

Institute of Cardiology, Lithuanian University of Health Sciences, Kaunas, Lithuania
e-mail: Vytautas.Raskevicius@lsmuni.lt

D. Matulis (✉)

Department of Biothermodynamics and Drug Design, Institute of Biotechnology,
Vilnius University, Vilnius, Lithuania
e-mail: matulis@ibt.lt

We will briefly overview the existing literature on molecular dynamics (MD) and quantum mechanics (QM) calculations with CA as a target. Finally, the successes and shortcomings of quantitative structure–activity relationship (QSAR) method will be discussed.

15.2 Molecular Docking

Molecular docking, or simply docking, is a popular method of determination of the optimal geometry of the ligand/protein complex. The idea of docking is based on the intuitively simple “lock and key” theory suggested by Emil Fischer more than 120 years ago [2]. “Virtual screening” is a selection of compounds, active against a certain receptor, from a large compound database, commonly by means of the molecular docking. Docking and/or virtual screening are often used to analyze the CA inhibitor interactions within the binding site, and to predict new and hopefully better binders.

A search in Scopus database (<https://www.scopus.com/>) for articles containing “carbonic anhydrase” together with “docking” or “virtual screening” in their title, abstract, or keywords leads to 245 hits (end of March 2018). After a manual examination of the list, it was reduced to about 200 papers directly dealing with the molecular docking of the small molecules (ligands) into CA. It should be noted that this list does not include papers in which CA is a part of a wide selection of docking targets, and therefore not specifically listed in the abstract of keywords, for example, when testing performance of docking programs and/or scoring functions (e.g., GOLD [3], FlexX [4], and Glide [5]), or as a part of specially designed ligand/receptor sets, such as Astex diverse test set [6].

Further analysis of the list of the 200 papers shows that docking into CA receptor is becoming progressively more widely used in research: 11, 23, and 38 papers were published in 2011, 2014, and 2017, correspondingly. The first relevant paper related to the development of the first molecular docking program DOCK goes back to 1988 [7]. Probably the most usual application for the docking procedure is the rationalization of the observed inhibition results. The examples are too numerous so we will just mention several. Docking was used to investigate binding to CA of 5-aryl-1*H*-pyrazole-3-carboxylic acids [8], bisindolylmethanes [9], isatin analogs [10], indolin-2-one-based sulfonamides [11], carbohydrazones [12], coumarin derivatives [13], and so on.

It would be interesting to analyze which docking programs were used the most. In about 195 papers to which we had access and where the used docking program was explicitly named, about 20 docking programs have been employed. AutoDock [14] or its variants were used in 54 papers, followed by GOLD [3]—48 papers, Glide [5]—46, MOE-Dock [15]—18, FlexX [4]—7, CDOCKER [16]—5, and DOCK [17]—5 papers. It should be noted that some papers employ several docking programs. Here we did not analyze the use of the scoring functions used to evaluate docking quality, because the scoring functions usually have multitude of variants, and they tend to develop much more dynamically than the docking engines. The

frequencies of the use of the first three abovementioned programs are consistent with the trends observed in the general docking literature [18]. Interestingly, MOE-Dock [15] was used about three times more often when docking to the CAs compared to the general use [18].

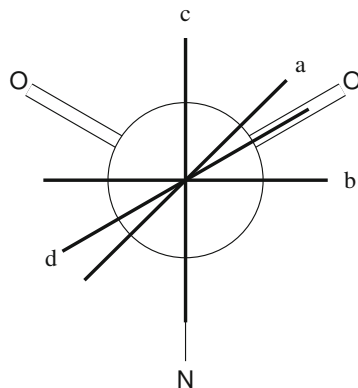
Comparing performances of the docking programs when dealing with CAs is especially interesting, but the performance seems to be inhibitor dependent. Tuccinardi et al. found that GOLD yielded better docked conformations compared to AutoDock for a series of CA II sulfonamide inhibitors [19]. Mori et al. tested four programs to dock to CA II a non-sulfonamide inhibitor, and found AutoDock to perform best [20]. Kontoyianni et al. tested the performance of 5 docking programs on many targets, including CA, and out of 25 CA dockings, only in 2 cases, one using Glide, and the other using GOLD, the top ranked conformation (pose) was characterized as being “close” to the experimental structure [21]. This shows that the success of docking to CA is not guaranteed. Below, we will briefly analyze some of the issues which are encountered during docking.

The most important CA isoforms contain a metal ion, usually zinc. Zinc ion requires a special care in order to be able to use the receptor for any meaningful computer simulations, including docking. For example, in the AutoDock program the proper handling of Zn, named AutoDock4_{Zn} force field, was implemented only relatively recently [22]. This is especially important for sulfonamide inhibitors since only the sulfonamide nitrogen is being ligated to the metal, but the sulfonamide oxygens are similar to the nitrogen from the viewpoint of simple electrostatics and therefore could confuse the docking algorithm. In Vdocking docking program [23] the proper coordination with zinc can be most easily ensured by fixing the ligating atom in space by setting the dimensions of the translational box to zeros [24]. Other docking programs deal with the metal ion issue in their own way, for example, in GOLD program metal coordination is modeled by “pseudohydrogen bonding,” and metals bind to H-bond acceptors. In addition, the ion can be set to a particular coordination geometry, e.g., tetrahedral [25]. At any rate, some caution and a bit of a common sense is required when docking, and probably some sort of validation of the program using known structures as well. For example, in a paper by Suthar et al., docking using AutoDock, apparently the version without the patch to treat the zinc, missed sulfonamide ligation to zinc, which seems to be not likely [26].

It is important to use the correct structures when doing docking simulations (in fact, any kind of simulations), and especially when validating simulation results. For example, Hartshorn et al. pointed out that in the Protein Data Bank (PDB) entry **1jd0**, the ligand rotamer is probably incorrect (*cis* amide instead of *trans*) [6]. This makes this particular ligand/protein complex slightly tainted when used for validating the program or comparing docking program results. The rotamers in the experimental structures could also be incorrect not only in the ligand but also in the protein [27]. However, most often simulation errors arise not from the experimental data but from the theoretical framework, e.g., force fields.

Sulfonamide derivatives are by far the most common inhibitors of the carbonic anhydrases. The importance of the correct energy profile of the S–C dihedral angle in the substituted sulfonamides to interpret the experimental results has been shown

Fig. 15.1 Newman projection of the aryl sulfonamide S–C torsion angle. Conformation **a** corresponds to the average dihedral angle for *ortho* unsubstituted sulfonamides in CA; angle **b** is most often found in unbound sulfonamides; and angles **b** and **c** are found in 2,3,5,6-tetrafluorobenzenesulfonamides bound to CAs in the Protein Data Bank



[28, 29]. A survey by Morkūnaitė et al. showed that in the PDB the majority of carbonic anhydrases bound sulfonamides, where the sulfonamide is connected to phenyl ring with H at *ortho* positions, the phenyl ring plane forms average 14.7° angle with one of the S=O bonds, i.e., it is slightly off from being aligned with S=O (position **a** in Fig. 15.1) [30]. Interestingly, in most molecular (i.e., not bound to receptor) sulfonamide X-ray crystal structures the phenyl plane is rotated in such way so that *p*-orbital of the *ipso* carbon divides O=S=O angle in half (position **b** in Fig. 15.1) [31, 32]. However, docking of the ligands parameterized using CHARMM force field [33] had a strong tendency of aligning phenyl ring with S–N bond which was clearly incorrect [30]. To overcome this, a constraint on the S–C torsion was imposed during the docking. A more proper way to handle the problem should involve the improvement of the force field parameters. Indeed, CGenFF force field [34], which similarly to CHARMM is also compatible with CHARMM [35], contains improved arylsulfonamide torsional angle parameters.

Another example of CA inhibitor rotamer problem is related to 4-substituted 2,3,5,6-tetrafluorobenzenesulfonamides. A quick PDB survey finds 14 structures containing compounds belonging to this series, complexed with various CA isoforms. Some of the PDB entries have several chains; moreover, ligands in several PDB chains have two alternative positions. Within these 14 structures there are 33 instances of tetrafluorobenzenesulfonamides bound to Zn. This includes molecules bound to different chains, as well as their alternative conformations.

Seven conformations out of 33 are bound to Zn in the CA II isoform. In the **4ww6** PDB entry one of the conformers is bound outside of the binding site; therefore, this conformation is not included into this analysis. While the non-fluorinated benzyisulfonamides tend to have the phenyl plane nearly aligned with S=O as illustrated *vide supra*, in 3 cases out of 7 the fluorinated phenyl ring is aligned with S–N, and in the rest of 4 cases it is aligned with S=O (conformations **c** and **d** in Fig. 15.1, correspondingly). Notably, probably due to the bulkiness of the fluorines, S–N and S=O rotamers are somewhat tilted with respect to each other

Fig. 15.2 Two superposed CA II structures with different tetrafluorobenzenesulfonamide rotamers (**4ht0**: pink protein and purple ligand and **5lle**: salmon protein and orange ligand). Zinc is shown as a grayish sphere. Possibly important water molecule in **4ht0** (small red sphere) is also shown

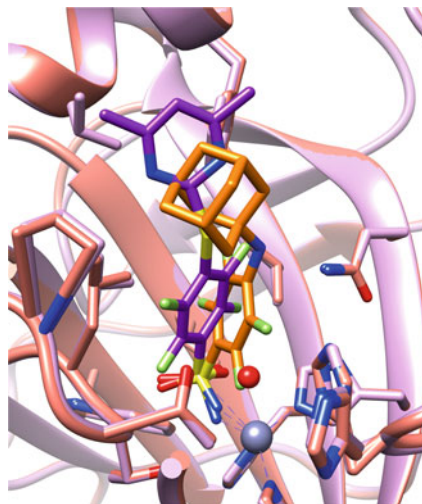


(Fig. 15.2). This is most likely due to the bulkiness of the fluorines, and this tilt could be important for the drug design.

Examination of Fig. 15.2 shows that the conformations of protein sidechains near the ligand are quite similar in both cases; therefore, answering a question of why one rotamer is preferred over the other one is not trivial. Interestingly, preliminary exploration of rotamer interaction energies with the protein using CHARMM/CHARMm force fields for the S–N and S=O rotamers of **4ht0** ligand shows a high energetic preference (by at least 10 kcal/mol, and mostly due to van der Waals clashes) for the S–N rotamer. This raises a question of the reason of the existence of the S=O aligned rotamer in **4ht0**. The most rational explanation would be the presence of the water molecule near the S=O rotamer, almost at the same position where one of the fluorines of the S–N rotamer is situated. Probably this water molecule, which makes a hydrogen bond with the sulfonamide nitrogen, is forcing the phenyl plane into the S=O rotamer. Modeling of the S=O rotamer in **4ht0** without the relevant explicit water molecule or without constraining of the dihedral angle would be quite challenging. An even bigger challenge is predicting which rotamer, S=O or S–N, will be prevalent for a particular ligand. Because of the apparent role of the water influencing the rotamer choice, it comes as no surprise then that the rotamer preference can be directly correlated with the enthalpy or entropy being the driving force for binding [36].

Interestingly, different CA isoforms show different rotamer preferences for this series of ligands. Three ligand instances in CA I exhibit only the S=O rotamer, and in five instances in CA XIII the ligand adopts exclusively the S–N rotamer. In the case of CA XII, the situation is mixed: out of 17 instances, 10 and 7 belong to the S–N and S=O rotamers, respectively. Moreover, different rotamers happen to be in the same PDB (**4ht2**, **5msa**, and **5msb**). This behavior is puzzling especially since hydrogenated analogs of these compounds (benzenesulfonamides) essentially have

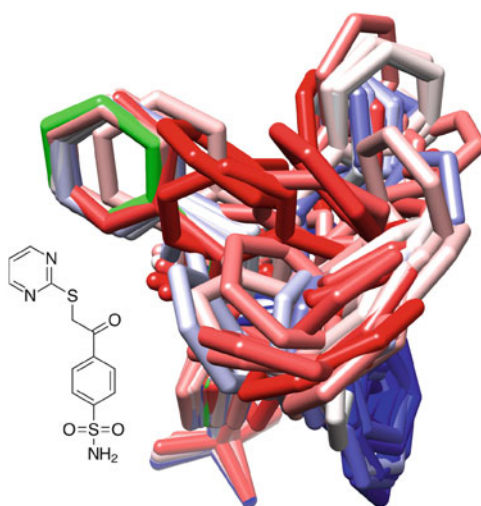
a preference for the S=O rotamer (Fig. 15.1). Incidentally, in **4ww6** the ligand of this series bound off-site (i.e., not bound to Zn) has the S=O rotamer.

This analysis shows the importance of rotamers when targeting different CA isozymes. It might well be that the rotamer preferences for the ligands could be solved only when entropy and enthalpy interplay for a given ligand/receptor is fully understood; therefore, these inhibitor/receptor complexes are good systems to test proposed thermodynamic energy component calculation algorithms. At the very least, when performing docking validation tests, one should also be aware of how well the key torsional angles are reproduced.

The flexibility of the protein often needs to be taken into account. Fortunately, CA does not undergo *gross* conformational changes upon inhibitor binding [37]. However, one should always watch out for the rotamers of some sidechains such as Gln, Asn, and His, in which the X-ray crystallography cannot distinguish between C, N, and O atoms [27], so there could always be ambiguity in atom assignment.

To further illustrate the problems arising during docking into CA, we performed a docking of **3sbi** ligand into the CA II receptor from the same PDB id [24]. The pyrimidine tail of the ligand is partly hydrophobic, partly hydrophilic (structure shown in Fig. 15.3) yet it is bound to an extremely hydrophobic site lined by residues Phe131, Val135, Leu198, Pro202, and Leu204. A majority of CA inhibitors of sufficient length present in the Protein Data Bank are bound to that site, hence we consider this as an exemplary test. The docking used CHARMM [35] and CHARMM [33] force fields for proteins and the ligand, correspondingly. The solvent effects were modeled using a simplistic distance-dependent dielectric approximation $\epsilon = 4r_{ij}$ [38], in which the electrostatic force between two charges is divided by the distance between the charges (with the additional scaling factor). This essentially mimics electrostatic shielding of water molecules between two remote charges, but does not include other effects such as desolvation, or entropy

Fig. 15.3 120 docked conformations of **3sbi** ligand (structure depicted on the left), docked with the genetic algorithm switched off to enhance sampling of the binding pocket. The conformations are colored by the rank according to the docked energy: from blue (the best) to red (the worst). The X-ray conformation is shown in green. Note the self-folded conformations in the lower right of the picture. See text for more explanations



of the solvent. Also, due to reasons which were already discussed, the sulfonamide atom was fixed in space at the correct position, and the torsional angle of the bond connecting the phenyl ring with the sulfonamide group was constrained to $\pm 15^\circ$ around the experimental value. Since we wanted to explore the conformational space within the whole binding site, the genetic algorithm was switched off. One hundred conformations were generated using this setup. In addition, to explore the conformations near the X-ray conformation, additional 20 docked minima were generated where all torsional angles had $\pm 15^\circ$ constraints around the experimental values.

The 120 docked conformations (sometimes also called “poses”) are shown in Fig. 15.3. Each conformation is colored according to the docked score, blue being the best and red being the worst. Perhaps strikingly, the poses close to the native X-ray conformation, pictured green, have a relatively poor score. The best scores belong to the self-folded conformations of the ligand (Fig. 15.3, lower right) in which the pyrimidine ring is stacked against the phenyl ring. While the feasibility of the self-folded conformations will not be discussed here, we will note in passing that these conformations probably would be penalized because they would have to push out one or two water molecules out of the binding site. Nevertheless, ligands have been found to bind to CA in a self-stacked binding mode, but only for fluorinated compounds [36, 39].

For the other, presumably more realistic, non-self-folded conformations, the scoring function seems to underestimate the hydrophobic effect of the attraction of the ligand tail into the hydrophobic pocket. The funnel-like binding site of CA is hydrophobic only in one part of the pocket, and mostly hydrophilic in the rest; therefore, the docking program tends to bind ligand pyrimidine nitrogens to the opposite, hydrophilic part of the binding pocket. The hydrophobic effect of the ligand bound into its proper location is therefore underestimated by the force field (including the apparently insufficiently adequate distance-dependent dielectric approximation for the estimation of the solvent effects).

The hydrophobicity and hydrophilicity of the CA II binding site is illustrated in Fig. 15.4. The picture was generated using Voronota program [40] by drawing Voronoi cell faces between the receptor and the conformations of the ligand in Fig. 15.3. Voronoi cells are cells taken by an individual atom in space, and are enclosed by planes (or spheres because of the different radii of the atoms, to be exact) which divide the distance between the atoms exactly in half. Alternatively, Voronoi cell of an atom can be comprehended as a zone in the space consisting of points that are closest to that atom but not to the others. The yellow and blue colors signify hydrophobic and hydrophilic surfaces. The hydrophobicity of the subpocket which is holding the tail of the ligand is very obvious, and the mismatch between the hydrophobicity of the pocket and the hydrophilic nitrogen atom pointing downwards is also apparent.

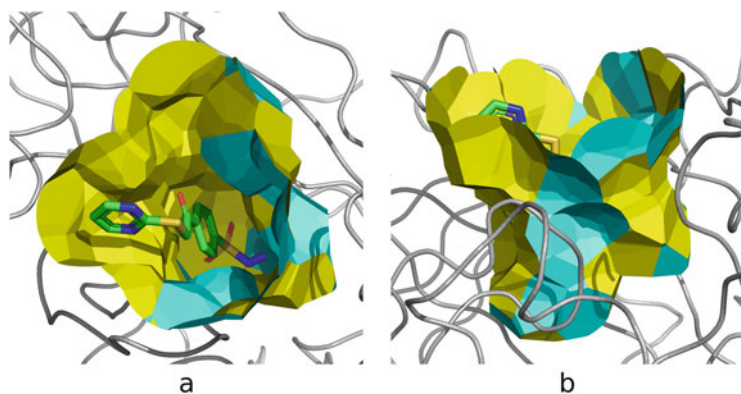


Fig. 15.4 The binding site of CA II, shown as Voronoi cell faces drawn between the CA II receptor and the ligand conformations from Fig. 15.3. The faces are colored based on the hydrophobicity (yellow) or hydrophilicity (cyan) of the receptor atoms. Two views are shown (a and b). The X-ray conformation of the **3sbi** ligand is shown as colored sticks

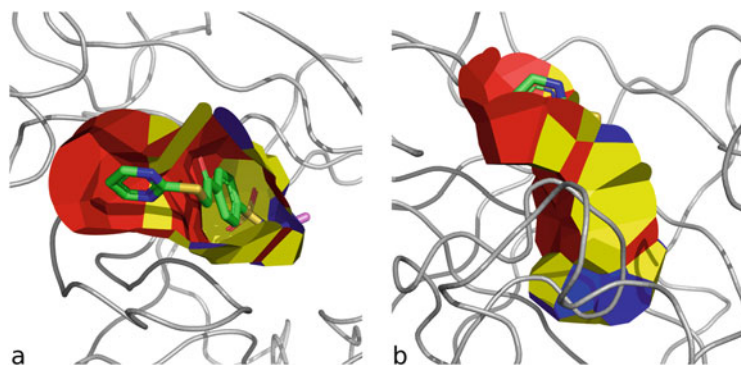


Fig. 15.5 Voronoi cell faces between the X-ray structure of the **3sbi** ligand (shown as sticks) and the CAII receptor. The faces are colored based on the hydrophobicity of the ligand and receptor atoms. Red color signifies that both atoms (ligand and receptor) are hydrophobic (i.e., carbons), blue—both are hydrophilic (heteroatoms), and yellow denotes a “mismatch”: one atom is hydrophilic, and the other atom is hydrophobic. Two views are shown (a and b)

The concept of mismatching hydrophobicities and hydrophilicities between the receptor and the ligand is further explored in Fig. 15.5 using Voronoi cells. This time, only the X-ray conformation is analyzed. The Voronoi cell faces are colored based on the hydrophobicity/hydrophilicity of the atoms which are separated by that face. The red and blue colors signify a match between the atom types (both receptor and ligand atoms are hydrophobic and hydrophilic, correspondingly), and the yellow color represents a mismatch: one atom is hydrophobic, and the other atom is hydrophilic, or *vice versa*. Note that the pyrimidine ring nitrogens are causing a surface mismatch inside the hydrophobic pocket (cf. Fig. 15.4). Perhaps it is then not

surprising that the docking tries to place the ligand tail in the more hydrophilic parts of the binding site. A “perfect match” between the ligand and the protein formally would have to contain no “mismatching” atom types, with an important caveat: this scheme does not show interactions with the bulk solvent.

First of all, in the “open” surface area on the top of the ligand in Fig. 15.5 the ligand is interacting not with the protein but with the bulk solvent (water). Since by definition water solvent is hydrophilic, for the formation of good hydrogen bonding network with water it is advantageous that at least some of ligand atoms which are exposed to the solvent are hydrophilic, such is one of the pyrimidine nitrogens in the **3sbi** ligand. If the free (unbound) ligand in the water makes hydrogen bonds, it is important that these hydrogen bonds are not lost when the ligand is bound to the protein [41], i.e., the hydrogen bonds should also be formed between the ligand and the protein upon desolvation of the ligand and/or protein. Also, the hydrophobic surfaces of both unbound ligand and the protein (they bind poorly to the water) will improve the binding energy if they match when they are bound. Many sophisticated scoring functions are trying to address desolvation and other ligand binding to protein issues [42, 43].

It should be kept in mind that the whole framework of interactions valid for one receptor could change, sometimes dramatically, if the ligand is modified, or if one CA isoform is replaced by another isoform. A simple change of the rotamer or a change of the overall binding mode can have far reaching enthalpic and entropic effects on the binding affinities [36].

Several papers by our group, for example [36, 44–46], are using intrinsic binding affinities for their analysis of inhibitor binding, which are very important for ionizable inhibitors such as sulfonamides because they lose a proton when binding to zinc. In short, because of the involvement of protons in the enzymatic reaction, the observed binding affinities are dependent on the pH of the reaction environment. The intrinsic binding constants $K_{b,int}$ are pH- and buffer-independent and are calculated as the observed binding constant $K_{b,obs}$ divided by the fractions of the deprotonated inhibitor f_{SA^-} and the protonated Zn-bound water form of CA f_{CAZnH_2O} [36]:

$$K_{b,int} = \frac{K_{b,obs}}{(f_{SA^-})(f_{CAZnH_2O})} \quad (15.1)$$

One of the consequences of this is that the deprotonated form of inhibitor is the active form. Hence, more acidic sulfonamides will tend to be better inhibitors, because a larger fraction of them will be in the anionic form in the solution. Moreover, because of the independence from the pH, the thermodynamic analysis of the binding, especially when considering reaction enthalpy and entropy, is more robust and more meaningful. Therefore it would be advantageous to use intrinsic thermodynamic parameters by the computational approaches covered in this chapter.

15.3 Molecular Dynamics

Molecular dynamics (MD) method, along with some related methods such as Monte Carlo approach, offers a detailed picture of the development of molecular systems in time. While being able to give very useful insights, it is also much more computer-demanding compared to docking. A quick Scopus search showed up to 200 papers in which MD was applied to study carbonic anhydrases. Without going into too much detail, we will briefly mention some of the MD applications.

In many papers, MD was used after the molecular docking to further improve (refine) the predicted pose of the ligand, and to allow for the more thorough relaxation of the protein. For example, Özgeriş et al. used MD to further explore docking results of 2-aminotetralins and tacrine into CA I and acetylcholinesterase (AChE): MD was employed to investigate the effect of the ligand on the protein rigidity, and the interactions within the binding site of both receptors [47]. Similarly, Costa et al. used MD to examine interactions between the CA VA binding site residues and docked compounds from essential oils and acetazolamide [48].

An important application of molecular dynamics is exploration of the dynamics of the protein. For example, Prakash et al. investigated unfolding of CA IX in urea solutions of various concentrations [49]. Maupin and Voth explored variability of orientations of His64 sidechain in CA II [50]. MD was also used to explore ligand tail conformations [51].

To perform successful MD simulations, a reasonable set of force field parameters for zinc (as well as for other with components of the protein/ligand complex) is necessary. CA has been used to derive force field parameters for zinc bound to the protein, and the parameters were further validated using molecular dynamics simulations [52]. The obtained improved parameters are used to perform simulations not only on CA but also on other zinc proteins. Often parameter derivation also requires use of *ab initio* (quantum mechanical) calculations as well as validation using MD calculations, so these two methods are employed together, e.g., in a paper by Bernadat et al. [53].

A large number of papers investigate the catalytic reaction occurring in the CA binding site, or to better understand the nature of the ligand–protein binding. For example, Chen et al. investigated CO₂ diffusion in the CA active site using Markov-state model and coarse-grained MD simulations [54]. Maupin et al. used multistate empirical valence bond (MS-EVB) method combined with MD to investigate proton transfer in CA [55, 56]. MD was used to deeper understand the hydrophobic effect [57] or the enthalpy/entropy compensation in protein–ligand binding [58]. Ganguly et al. combined molecular dynamics (MD) simulations, quantum mechanics/molecular mechanics (QM/MM) geometry optimizations, and QM/MM free energy simulations on a small protein which mimics CA to investigate hydrolysis of the *p*-nitrophenylacetate substrate [59]. Paul et al. used molecular dynamics and QM/MM calculations to explore intramolecular proton transfer reaction parameters in human CA II [60]. Koziol et al. used MD and *ab initio* density functional theory (DFT) calculations to investigate CO₂ hydration using Zn-bound tris(imidazolyl)

calix[6]arene aqua complex as a CA binding site mimetic [61]. This far from exhaustive list of applications shows that MD is a powerful tool for exploration of CA properties, as are quantum mechanics based calculations, which are briefly covered in the next section.

15.4 Quantum Mechanics

Similar in number to MD-related papers, Scopus showed up to 200 hits which combine “quantum” or “ab initio” calculations and “Carbonic Anhydrase” as the search terms. Quantum mechanical (QM) calculations have already been mentioned above, as they often were used in combination with other methods. In contrast with the methods based on force fields, QM calculations include the actual electronic structure of the molecules which are being investigated, and generally are very CPU and/or memory demanding. A variation of QM calculations where a smaller part of the system is represented by quantum theory governed nuclei/electrons, and the rest of the system described using empirical force fields is called QM/MM (quantum mechanics/molecular mechanics). Because QM allows for a relatively accurate representation of atoms, it is used to explore the reaction mechanisms at a great detail. Below we very briefly will mention some representative QM applications.

Jiao and Rempe used density functional theory (DFT) calculations coupled with a continuum model of the surrounding environment to understand the factors determining the pK_a of zinc-bound water in CA [62]. In several papers QM calculations were used to design and explore the behavior of biomimetics—compounds which mimic the active site of CA. Ma et al. used DFT calculations to study the mechanism of CO_2 hydrolysis by Co-(1,4,7,10-tetrazacyclododecane) in order to model the activity of cobalt containing CA [63]. QM was also used to derive force field parameters for zinc-containing systems, for example, for AMBER [64] and OPLS-AA [53] force fields. It can be used to clarify details of binding of inhibitors. For example, Pecina et al. used QM/MM calculations to understand the differences between the binding of two carborane sulfonamide inhibitors [65]. Ghiasi et al. used QM approach to investigate the thermodynamic properties of fullerene based inhibitor bound to CA binding site [66]. As the computer resources are becoming cheaper, and the QM methods are improving, we will be seeing more of this type of simulations in the future.

15.5 Quantitative Structure–Activity Relationship (QSAR)

The methods mentioned above have a common feature: they are structure-based approaches. They employ a known or a modeled structure of the receptor, and also they use the experimental or calculated structure of the ligand bound inside the receptor. In contrast, quantitative structure–activity relationship (QSAR) method usually (with some exceptions) does not require the receptor structure to be known, and is based on the ligand structure. For this reason, it is sometimes described as a ligand-based approach.

QSAR is an area of computational research that builds virtual models to predict quantities such as the binding affinity or the toxic potential of existing or hypothetical molecules [67]. QSAR finds the parameters of the compounds that govern their biological activities and elucidate their mechanism of action [68]. Both these aspects of QSAR greatly help in modifying the structures of the compounds leading to compounds of high therapeutic value [69]. The determination of binding energies in QSAR studies is by no means simple. Free energies of binding depend on the ligand–protein interactions as well as on the loss of energy associated with stripping solvent molecules off the small-molecule ligand while moving from the aqueous environment of a cell or a body fluid to a protein binding pocket during the binding process [67]. The first stage of QSAR modeling is descriptor calculation. A molecular descriptor “is the final result of a logic and mathematical procedure which transforms chemical information encoded within a symbolic representation of a molecule into a useful number or the result of some standardized experiment” [70]. Molecular descriptors are calculated for chemical compounds and used to develop QSAR models for predicting the biological activities of novel compounds [71]. Feature selection is an important but still poorly solved problem in QSAR modeling [72]. In the second stage the most relevant descriptors for model must be elected, and finally fitting between selected features/descriptors must be carried out to have the QSAR model with optimum prediction ability.

Some papers are dealing with descriptors and their fitness for CA. It was found that quantum descriptors are critical of the pyrazolo[4,3-*e*][1,2,4]triazine sulfonamides antiproliferative activity against human MCF-7 cells [73]. This can indicate a more complex mechanism of cytotoxicity than the inhibition of CA IX and CA XII isozymes [73]. A new *ad hoc* descriptor T(OH..Cl) was designed to improve the quality of the CA XII QSAR affinity model which was defined as the sum of the topological distances between the hydroxyl groups and chlorine atoms in the molecule [74].

A series of QSAR papers deal with the analysis of the inhibitor binding to CA and propose modifications of the compounds. All compounds more active than acetazolamide have hydrophobic groups in phenyl substituted part and because of this reason have a higher activity than acetazolamide towards CA II [75]. If there are hydrogen bond acceptors on one side of acetazolamide pyrazole ring, then the activity of compounds towards CA II can be increased [75]. The sum of the topological distances between the hydroxyl groups and chlorine atoms in the molecule is important in benzenesulfonamide affinity towards CA XII. Through 3D-QSAR it was shown that most of the benzenesulfonamide selectivity against CA isoforms is caused by the benzene ring substituents [74]. It was suggested that locating of a dual moiety with hydrophobic/hydrogen bond acceptors properties on compounds, at a 13.6 Å distance, can result in higher selectivity of the compounds for isoforms CA II and CA IX and that locating of a dual moiety with hydrophobic/hydrogen bond acceptors or hydrophobic/hydrogen bond donor properties on compounds, at a 9.6 Å distance, can improve the selectivity of the compounds towards isoform CA IX [76]. Investigated molecules with a larger number of oxo groups show better interactions with enzymes and receptors, which could be the consequence of their stronger

hydrophilicity [77]. Compounds lacking halide group to fulfill the hydrophobic feature in the designed pharmacophore model were seen as the main reason behind their imperfect CA inhibitor activity [9]. It was suggested that very close and very distant hydrophobic moieties are not in favor of ligand–receptor binding [78]. In a calibration set, the bond order and molecular orbital bonding have greater influence on aromatic/heterocyclic sulfonamide inhibitor activity value on β -CA [79]. The presence of the methyl, sulfur atom, and amino thiadiazole groups is not favorable to inhibitor activity on β -carbonic anhydrase [79].

Clinically important *Plasmodium falciparum* CA (*PfCA*) is a popular QSAR target, because its X-ray structure is not available. On the other hand, homology modeling was feasible. The QSAR model developed by the author concludes that the average free valence of H atoms and polarizabilities are favorable to *P. falciparum* CA inhibitory activity [80]. The large percentage in weight of CHNS, C, and F atom fragments seems to be favorable for the *P. falciparum* CA inhibitory activity, in contrast to C_8H_5O fragment [80]. In the absence of 3D-protein structure and the lack of sufficient experimental data using the *PfCA* target, QSAR models were developed for inhibitors of *P. falciparum* CA [81]. The 2D-QSAR modeling analysis suggested the importance of electro-topological, electronic, extended topochemical atom, and spatial (Jurs) indices for modeling the inhibitory activity against *PfCA* [81].

It was found that formal (negative) charge and molecular polar surface area on benzoic acid analogs overwhelm the other correlations with CA III affinity constants [82]. The QSAR model concluded that the maximum charge of H in H–C bonds is not favorable to CA IX inhibitory activity on ureido-substituted benzene sulfonamides, low percentage of atoms in aromatic circuits are favorable for inhibitory activity, polarity also influences the activity, and the number of aromatic carbon–nitrogen bonds play a dominant role for inhibitory activity [83].

QSAR was also used to propose novel inhibitors. ZINC database of purchasable compounds [84] was screened for possible new CA II inhibitors and three compounds were suggested as possible candidates, but the experimental assay on them was not performed [75]. QSAR was also performed on decorated nanotubes as CA inhibitors. It is possible that the entire CA enzyme interacts with the nanotube causing the enzyme to denature or prevent access to the active site. Another possibility is that the substituents on nanotube bind in the active site or at a secondary binding site on the CAs surface [85].

In some cases the analysis also used CA structural features to help explain the observed trends. It seems that compounds interact with the isoforms CA I and CA VII in a much less selective way than the remaining isoforms [78]. The highly potent cliff partner, dorzolamide (used as an antiglaucoma agent), shared the critically important sulfonamide group with its less potent partner, but formed two additional hydrogen bonds with residues Gln92 and Thr200 (PDB ID: **1kwr**, **1cil**), resulting in a 670-fold difference in potency [86]. Gln92 and Thr200 were identified as potency-modulating hot spots in CA II [86]. It was concluded that the entry of compounds with different sizes into the cavity of CA can be influenced by the bulkiness of the residue in position 131 [76].

CA inhibition data sets quite widely served as model data for QSAR method comparison and improvement. Compared to other methods, QSAR most effectively helped to quantify the subtle empirical relationship between the structure and the activity towards the CA II target [87]. Without filtration to remove all values from discordant sources/assays (with affinity differences greater than 2.0), no model whatsoever could be obtained for CA II [88]. Template CoMFA (comparative molecular field analysis), which was successfully applied to CA II, also has ease of use and versatility (having been developed with different applications in mind) that are superior to those of most other computer-aided molecular design methodologies [88]. The results show that for certain purposes genetic algorithm–multiple linear regressions are better than stepwise multiple linear regressions and for others, artificial neural network overcomes multiple linear regressions models [89]. Two six descriptor models were created for 22 benzenesulfonamides data set leading to R^2 as high as 0.99, and the leave-one-out (LOO) technique was used to establish the validity of the models [90]. The mathematical models revealed a poor relationship between the anticonvulsant activity related to CA inhibition and molecular descriptors obtained from DFT and docking calculations, so a QSAR model was developed using Dragon software [91] descriptors [92].

15.6 Concluding Remarks

In this chapter we described some highlights from the computational modeling of CA and its inhibitors. The computer simulations allowed to better understand the reasons for the observed binding affinities, help to reveal the reaction mechanisms, and to propose new and improved CA binders. CA is a challenging receptor due to difficulties in computational treatment of metals, sulfonamide compound rotamer problems, and the influence of the water solvent, among other issues. Nevertheless, the volume of theoretical calculations involving CA is increasing each year, witnessing a constant progress in designing better models for biomolecules.

References

1. Supuran, C.T., Scozzafava, A.: Carbonic anhydrases as targets for medicinal chemistry. *Bioorg. Med. Chem.* **15**, 4336–4350 (2007)
2. Fischer, E.: Einfluss Der Configuration Auf Die Wirkung Der Enzyme. *Ber. Dtsch. Chem. Ges.* **27**, 2985–2993 (1894)
3. Jones, G., Willett, P., Glen, R.C.: Molecular recognition of receptor sites using a genetic algorithm with a description of desolvation. *J. Mol. Biol.* **245**, 43–53 (1995)
4. Kramer, B., Rarey, M., Lengauer, T.: Evaluation of the FLEXX incremental construction algorithm for protein–ligand docking. *Proteins Struct. Funct. Bioinf.* **37**, 228–241 (1999)
5. Friesner, R.A., et al.: Glide: a new approach for rapid, accurate docking and scoring. 1. Method and assessment of docking accuracy. *J. Med. Chem.* **47**, 1739–1749 (2004)
6. Hartshorn, M.J., et al.: Diverse, high-quality test set for the validation of protein–ligand docking performance. *J. Med. Chem.* **50**, 726–741 (2007)

7. DesJarlais, R.L., et al.: Using shape complementarity as an initial screen in designing ligands for a receptor binding site of known three-dimensional structure. *J. Med. Chem.* **31**, 722–729 (1988)
8. Cvijetić, I.N., et al.: 5-Aryl-1H-pyrazole-3-carboxylic acids as selective inhibitors of human carbonic anhydrases IX and XII. *Bioorg. Med. Chem.* **23**, 4649–4659 (2015)
9. Imran, S., et al.: Synthesis of novel bisindolylmethanes: new carbonic anhydrase II inhibitors, docking, and 3D pharmacophore studies. *Bioinorg. Chem.* **68**, 90–104 (2016)
10. Akdemir, A., Güzel-Akdemir, Ö., Karalı, N., Supuran, C.T.: Isatin analogs as novel inhibitors of *Candida* Spp. β -carbonic anhydrase enzymes. *Bioorg. Med. Chem.* **24**, 1648–1652 (2016)
11. Eldehna, W.M., et al.: Novel indolin-2-one-based sulfonamides as carbonic anhydrase inhibitors: synthesis, in vitro biological evaluation against carbonic anhydrases isoforms I, II, IV and VII and molecular docking studies. *Eur. J. Med. Chem.* **127**, 521–530 (2017)
12. Iqbal, S., et al.: Carbohydrazones as new class of carbonic anhydrase inhibitors: synthesis, kinetics, and ligand docking studies. *Bioinorg. Chem.* **72**, 89–101 (2017)
13. De Luca, L., et al.: Inhibitory effects and structural insights for a novel series of coumarin-based compounds that selectively target human CA IX and CA XII carbonic anhydrases. *Eur. J. Med. Chem.* **143**, 276–282 (2018)
14. Morris, G.M., et al.: Automated docking using a Lamarckian genetic algorithm and an empirical binding free energy function. *J. Comput. Chem.* **19**, 1639–1662 (1998)
15. Corbeil, C.R., Williams, C.I., Labute, P.: Variability in docking success rates due to dataset preparation. *J. Comput. Aided Mol. Des.* **26**, 775–786 (2012)
16. Wu, G., Robertson, D.H., Brooks, C.L. III, Vieth, M.: Detailed analysis of grid-based molecular docking: a case study of CDOCKER-A CHARMM-based MD docking algorithm. *J. Comput. Chem.* **24**, 1549–1562 (2003)
17. Lang, P.T., et al.: DOCK 6: combining techniques to model RNA–small molecule complexes. *RNA* **15**, 1219–1230 (2009)
18. Chen, Y.-C.: Beware of docking! *Trends Pharmacol. Sci.* **36**, 78–95 (2015)
19. Tuccinardi, T., et al.: Analysis of human carbonic anhydrase II: docking reliability and receptor-based 3D-QSAR study. *J. Chem. Inf. Model.* **47**, 515–525 (2007)
20. Mori, M., et al.: Hit recycling: discovery of a potent carbonic anhydrase inhibitor by in silico target fishing. *ACS Chem. Biol.* **10**, 1964–1969 (2015)
21. Kontoyianni, M., McClellan, L.M., Sokol, G.S.: Evaluation of docking performance: comparative data on docking algorithms. *J. Med. Chem.* **47**, 558–565 (2004)
22. Santos-Martins, D., Forli, S., Ramos, M.J., Olson, A.J.: AutoDock4_{Zn}: an improved AutoDock force field for small-molecule docking to zinc metalloproteins. *J. Chem. Inf. Model.* **54**, 2371–2379 (2014)
23. David, L., Luo, R., Gilson, M.K.: Ligand-receptor docking with the mining minima optimizer. *J. Comput. Aided Mol. Des.* **15**, 157–171 (2001)
24. Čapkauskaitė, E., et al.: Design of [(2-pyrimidinylthio)acetyl]benzenesulfonamides as inhibitors of human carbonic anhydrases. *Eur. J. Med. Chem.* **51**, 259–270 (2012)
25. Krasavin, M., et al.: Probing the ‘bipolar’ nature of the carbonic anhydrase active site: aromatic sulfonamides containing 1,3-Oxazol-5-Yl moiety as picomolar inhibitors of cytosolic CA I and CA II isoforms. *Eur. J. Med. Chem.* **101**, 334–347 (2015)
26. Suthar, S.K. et al.: Design and synthesis of novel 4-(4-oxo-2-arylthiazolidin-3-yl) benzene-sulfonamides as selective inhibitors of carbonic anhydrase IX over I and II with potential anticancer activity. *Eur. J. Med. Chem.* **66**, 372–379 (2013)
27. Word, J.M., Lovell, S.C., Richardson, J.S., Richardson, D.C.: Asparagine and glutamine: using hydrogen atom contacts in the choice of side-chain amide orientation. *J. Mol. Biol.* **285**, 1735–1747 (1999)
28. Senger, S., Convery, M.A., Chan, C., Watson, N.S.: Arylsulfonamides: a study of the relationship between activity and conformational preferences for a series of factor Xa inhibitors. *Bioorg. Med. Chem. Lett.* **16**, 5731–5735 (2006)
29. Senger, S., et al.: Sulfonamide-related conformational effects and their importance in structure-based design. *Bioorg. Med. Chem. Lett.* **17**, 2931–2934 (2007)

30. Morkūnaitė, V., et al.: Saccharin sulfonamides as inhibitors of carbonic anhydrases I, II, VII, XII, and XIII. *BioMed Res. Int.* **2014**, 638902 (2014)
31. Brameld, K.A., Kuhn, B., Reuter, D. C., Stahl, M.: Small molecule conformational preferences derived from crystal structure data. A medicinal chemistry focused analysis. *J. Chem. Inf. Model.* **48**, 1–24 (2008)
32. Schwertz, G., et al.: Conformational aspects in the design of inhibitors for serine hydroxymethyltransferase (SHMT): biphenyl, aryl sulfonamide, and aryl sulfone motifs. *Chem. Eur. J.* **23**, 14345–14357 (2017)
33. Momany, F.A., Rone, R.: Validation of the general purpose QUANTA®3.2/CHARMM®force field. *J. Comput. Chem.* **13**, 888–900 (1992)
34. Vanommeslaeghe, K., et al.: CHARMM general force field: a force field for drug-like molecules compatible with the CHARMM All-atom additive biological force fields. *J. Comput. Chem.* **31**, 671–690 (2010)
35. MacKerell, A.D. Jr., et al.: All-atom empirical potential for molecular modeling and dynamics studies of proteins. *J. Phys. Chem. B* **102**, 3586–3616 (1998)
36. Smirnov, A., Zubrienė, A., Manakova, E., Gražulis, S., Matulis, D.: Crystal structure correlations with the intrinsic thermodynamics of human carbonic anhydrase inhibitor binding. *PeerJ* **6**, e4412 (2018)
37. Krishnamurthy, V.M., et al.: Carbonic anhydrase as a model for biophysical and physical-organic studies of proteins and protein-ligand binding. *Chem. Rev.* **108**, 946–1051 (2008)
38. Gelin, B.R., Karplus, M.: Side-chain torsional potentials: effect of dipeptide, protein, and solvent environment. *Biochemistry* **18**, 1256–1268 (1979)
39. Dudutienė, V., et al.: Functionalization of fluorinated benzenesulfonamides and their inhibitory properties toward carbonic anhydrases. *ChemMedChem* **10**, 662–687 (2015)
40. Olechnovič, K., Venclovas, Č.: Voronota: a fast and reliable tool for computing the vertices of the Voronoi diagram of atomic balls. *J. Comput. Chem.* **35**, 672–681 (2014)
41. Hünenberger, P.H., Helms, V., Narayana, N., Taylor, S.S., McCammon, J.A.: Determinants of ligand binding to cAMP-dependent protein kinase. *Biochemistry* **38**, 2358–2366 (1999)
42. Schulz-Gasch, T., Stahl, M.: Scoring functions for protein–ligand interactions: a critical perspective. *Drug Discov. Today Technol.* **1**, 231–239 (2004)
43. Liu, J., Wang, R.: Classification of current scoring functions. *J. Chem. Inf. Model.* **55**, 475–482 (2015)
44. Kišonaitė, M., et al.: Intrinsic thermodynamics and structure correlation of benzenesulfonamides with a pyrimidine moiety binding to carbonic anhydrases I, II, VII, XII, and XIII. *PLoS ONE* **9**, e114106 (2014)
45. Linkuvienė, V., et al.: Intrinsic thermodynamics of inhibitor binding to human carbonic anhydrase IX. *Biochim. Biophys. Acta Gen. Subj.* **1860**, 708–718 (2016)
46. Zubrienė, A., et al.: Intrinsic thermodynamics and structures of 2,4- and 3,4- substituted fluorinated benzenesulfonamides binding to carbonic anhydrases. *ChemMedChem* **12**, 161–176 (2017)
47. Özgeriş, B., et al.: Acetylcholinesterase and carbonic anhydrase inhibitory properties of novel urea and sulfamide derivatives incorporating dopaminergic 2-aminotetralin scaffolds. *Bioorg. Med. Chem.* **24**, 2318–2329 (2016)
48. Costa, G., Gidaro, M.C., Vullo, D., Supuran, C.T., Alcaro, S.: Active components of essential oils as anti-obesity potential drugs investigated by in silico techniques. *J. Agric. Food Chem.* **64**, 5295–5300 (2016)
49. Prakash, A., et al.: Elucidation of stable intermediates in urea-induced unfolding pathway of human carbonic anhydrase IX. *J. Biomol. Struct. Dyn.* **36**, 2391–2406 (2018)
50. Maupin, C.M., Voth, G.A.: Preferred orientations of His64 in human carbonic anhydrase II. *Biochemistry* **46**, 2938–2947 (2007)
51. Kovalevsky, A., et al.: “To be or not to be” protonated: atomic details of human carbonic anhydrase-clinical drug complexes by neutron crystallography and simulation. *Structure* **26**, 383–390 (2018)

52. Stote, R.H., Karplus, M.: Zinc binding in proteins and solution: a simple but accurate nonbonded representation. *Proteins* **23**, 12–31 (1995)
53. Bernadat, G., Supuran, C.T., Iorga, B.I.: Carbonic anhydrase binding site parameterization in OPLS-AA force field. *Bioorg. Med. Chem.* **21**, 1427–1430 (2013)
54. Chen, Z., et al.: Differential expression and function of CAIX and CAXII in breast cancer: a comparison between tumorgraft models and cells. *PLOS ONE* **13**, e0199476 (2018)
55. Maupin, C.M., McKenna, R., Silverman, D.N., Voth, G.A.: Elucidation of the proton transport mechanism in human carbonic anhydrase II. *J. Am. Chem. Soc.* **131**, 7598–7608 (2009)
56. Maupin, C.M., Voth, G.A.: Proton transport in carbonic anhydrase: insights from molecular simulation. *Biochimica et Biophysica Acta (BBA) - Proteins and Proteomics. Carbonic Anhydrase and Superoxide Dismutase* **1804**, 332–341 (2010)
57. Snyder, P.W., et al.: Mechanism of the hydrophobic effect in the biomolecular recognition of arylsulfonamides by carbonic anhydrase. *Proc. Natl. Acad. Sci. U S A* **108**, 17889–17894 (2011)
58. Breiten, B., et al.: Water networks contribute to enthalpy/entropy compensation in protein-ligand binding. *J. Am. Chem. Soc.* **135**, 15579–15584 (2013)
59. Ganguly, A., et al.: Elucidation of the catalytic mechanism of a miniature zinc finger hydrolase. *J. Phys. Chem. B* **121**, 6390–6398 (2017)
60. Paul, S., Paul, T.K., Taraphder, S.: Reaction coordinate, free energy, and rate of intramolecular proton transfer in human carbonic anhydrase II. *J. Phys. Chem. B* **122**, 2851–2866 (2018)
61. Koziol, L., et al.: Computational analysis of a Zn-bound tris(Imidazolyl) Calix[6]Arene aqua complex: toward incorporating second-coordination sphere effects into carbonic anhydrase biomimetics. *J. Chem. Theory Comput.* **9**, 1320–1327 (2013)
62. Jiao, D., Rempe, S.B.: Combined density functional theory (DFT) and continuum calculations of pK(a) in carbonic anhydrase. *Biochemistry* **51**, 5979–5989 (2012)
63. Ma, R., Schuette, G.F., Broadbelt, L.J.: Toward understanding the activity of cobalt carbonic anhydrase: a comparative study of zinc- and cobalt-cyclen. *Appl. Catal. A Gen.* **492**, 151–159 (2015)
64. Lin, F., Wang, R.: Systematic derivation of AMBER force field parameters applicable to zinc-containing systems. *J. Chem. Theory Comput.* **6**, 1852–1870 (2010)
65. Pecina, A., et al.: QM/MM calculations reveal the different nature of the interaction of two carborane-based sulfamide inhibitors of human carbonic anhydrase II. *J. Phys. Chem. B.* **117**, 16096–16104 (2013)
66. Ghiasi, M., Kamalinahad, S., Zahedi, M.: Complexation of nanoscale enzyme inhibitor with carbonic anhydrase active center: a quantum mechanical approach. *J. Struct. Chem.* **55**, 1574–1586 (2014)
67. Lill, M.A.: Multi-dimensional QSAR in drug discovery. *Drug Discov. Today* **12**, 1013–1017 (2007)
68. Singh, S., Supuran, C.T.: 3D-QSAR CoMFA studies on sulfonamide inhibitors of the Rv3588c β -carbonic anhydrase from mycobacterium tuberculosis and design of not yet synthesized new molecules. *J. Enzyme Inhib. Med. Chem.* **29**, 449–455 (2013)
69. Singh, S., Supuran, C.T.: Chemometric QSAR modeling and in silico design of carbonic anhydrase inhibition of a coral secretory isoform by sulfonamide. *Bioorg. Med. Chem.* **21**, 1495–1502 (2013)
70. Todeschini, R., Consonni, V.: *Handbook of Molecular Descriptors*. Wiley VCH Verlag GmbH, Weinheim, 2000
71. Yap, C.W.: PaDEL-descriptor: an open source software to calculate molecular descriptors and fingerprints. *J. Comput. Chem.* **32**, 1466–1474 (2011)
72. Burden, F.R., Winkler, D.A.: An optimal self-pruning neural network and nonlinear descriptor selection in QSAR. *QSAR Comb. Sci.* **28**, 1092–1097 (2009)
73. Matysiak, J., Skrzypek, A., Tarasiuk, P., Mojzycz, M.: QSAR study of pyrazolo[4,3-e][1,2,4]triazine sulfonamides against tumor-associated human carbonic anhydrase isoforms IX and XII. *Comput. Biol. Chem.* **71**, 57–62 (2017)

74. Raškevičius, V., Kairys, V.: Predicting isoform-specific binding selectivities of benzenesulfonamides using QSAR and 3D-QSAR. *Curr. Comput. Aided Drug Des.* **13**, 75–83 (2017)
75. Heravi, Y.E. et al.: 3D QSAR studies, pharmacophore modeling, and virtual screening of diarylpyrazole–benzenesulfonamide derivatives as a template to obtain new inhibitors, using human carbonic anhydrase II as a model protein. *J. Enzyme Inhib. Med. Chem.* **32**, 688–700 (2017)
76. Rasti, B., Namazi, M., Karimi-Jafari, M.H., Ghasemi, J.B.: Proteochemometric modeling of the interaction space of carbonic anhydrase and its inhibitors: an assessment of structure-based and sequence-based descriptors. *Mol. Inf.* **36**, 1600102 (2017)
77. Trifunović, J., Borčić, V., Mikov, M.: Bile acids and their oxo derivatives: potential inhibitors of carbonic anhydrase I and II, androgen receptor antagonists and CYP3A4 substrates. *Biomed. Chromatogr.* **31**, e3870 (2017)
78. Rasti, B., Karimi-Jafari, M.H., Ghasemi, J.B.: Quantitative characterization of the interaction space of the mammalian carbonic anhydrase isoforms I, II, VII, IX, XII, XIV and their inhibitors, using the proteochemometric approach. *Chem. Biol. Drug Des.* **88**, 341–353 (2016)
79. Singh, S., Supuran, C.T.: In silico modeling of β -carbonic anhydrase inhibitors from the fungus *Malassezia globosa* as antidandruff agents. *J. Enzyme Inhib. Med. Chem.* **31**, 417–424 (2016)
80. Singh, S.: Computational design and chemometric QSAR modeling of plasmodium falciparum carbonic anhydrase inhibitors. *Bioorg. Med. Chem. Lett.* **25**, 133–141 (2015)
81. Aher, R.B., Roy, K.: First report on two-fold classification of plasmodium falciparum carbonic anhydrase inhibitors using QSAR modeling approaches. *Comb. Chem. High Throughput Screen.* **17**, 745–755 (2014)
82. Alzweiri, M., Al-Balas, Q., Al-Hiari, Y.: Chromatographic evaluation and QSAR optimization for benzoic acid analogues against carbonic anhydrase III. *J. Enzyme Inhib. Med. Chem.* **30**, 420–429 (2015)
83. Singh, S., Supuran, C.T.: Chemometric modeling of breast cancer associated carbonic anhydrase IX inhibitors belonging to the ureido-substituted benzene sulfonamide class. *J. Enzyme Inhib. Med. Chem.* **29**, 877–883 (2014)
84. Irwin, J.J., Sterling, T., Mysinger, M.M., Bolstad, E.S., Coleman, R.G.: ZINC: a free tool to discover chemistry for biology. *J. Chem. Inf. Model.* **52**, 1757–1768 (2012)
85. Esposito, E.X., et al.: Exploring possible mechanisms of action for the nanotoxicity and protein binding of decorated nanotubes: interpretation of physicochemical properties from optimal QSAR models. *Toxicol. Appl. Pharmacol.* **288**, 52–62 (2015)
86. Furtmann, N., Hu, Y., Gütschow M., Bajorath, J.: Identification of interaction hot spots in structures of drug targets on the basis of three-dimensional activity cliff information. *Chem. Biol. Drug Des.* **86**, 1458–1465 (2015)
87. Raškevičius, V., Kairys, V.: Comparison of performance of docking, LIE, metadynamics and QSAR in predicting binding affinity of benzenesulfonamides. *Curr. Comput. Aided Drug Des.* **11**, 237–244 (2015)
88. Cramer, R.D.: Template CoMFA generates single 3D-QSAR models that, for twelve of twelve biological targets, predict all ChEMBL-tabulated affinities. *PLOS ONE* **10**, e0129307 (2015)
89. Maleki, A., Daraei, H., Alaei, L., Faraji, A.: Comparison of QSAR models based on combinations of genetic algorithm, stepwise multiple linear regression, and artificial neural network methods to predict K_d of some derivatives of aromatic sulfonamides as carbonic anhydrase II inhibitors. *Russ. J. Bioorg. Chem.* **40**, 61–75 (2014)
90. Alafeefy, A.M., et al.: Exploring QSARs of some benzenesulfonamides incorporating cyanoacrylamide moieties as a carbonic anhydrase inhibitors (Specifically against Tumor-Associated Isoforms IX and XII). *J. Enzyme Inhib. Med. Chem.* **30**, 519–523 (2015)
91. Mauri, A., Consonni, V., Pavan, M., Todeschini, R.: DRAGON software: an easy approach to molecular descriptor calculations. *MATCH Commun. Math. Comput. Chem.* **56**, 237–248 (2006)
92. Garro Martinez, J.C., et al.: Lacosamide derivatives with anticonvulsant activity as carbonic anhydrase inhibitors. Molecular modeling, docking and QSAR analysis. *Curr. Comput. Aided Drug Des.* **10**, 160–167 (2014)



Maps of Correlations Between Compound Chemical Structures and Thermodynamics of Binding to 12 Human Carbonic Anhydrases: Towards Isoform-Selective Inhibitors

16

Asta Zubrienė, Vaida Linkuvienė, and Daumantas Matulis

Abstract

In the design of target-based pharmaceutical compounds it is important to synthesize chemical compounds that would bind with high affinity to target protein and would not bind to any unintended protein. Thus, the compounds should possess high selectivity towards the target protein, a feature that is difficult to achieve because the correlations between compound structures and their affinities for the target are rather poorly understood. Here we build and analyze maps that compare between compounds of similar structures and demonstrate how small changes of compound functional groups influence their capability to bind a particular CA isoform and at the same time may improve selectivity over the remaining non-target 11 catalytically active CA isoforms. The analysis of such correlations has helped to synthesize compounds that possess picomolar affinities towards some CAs and demonstrate up to million-fold selectivities for the target isoform. In addition to the intrinsic affinities of the compounds, we have analyzed other thermodynamic parameters, the intrinsic enthalpy and entropy changes upon binding, providing information on the contacts and bonds between the compound and the protein.

16.1 Introduction

Novel compounds with pharmaceutical applications are aimed to perform their therapeutic function in the human body while showing no toxic side effects. In other words, the synthetic chemical compounds should bind strongly (with high affinity,

A. Zubrienė · V. Linkuvienė · D. Matulis (✉)

Department of Biothermodynamics and Drug Design, Institute of Biotechnology, Vilnius University, Vilnius, Lithuania

e-mail: astzu@ibt.lt; morkunaite@ibt.lt; matulis@ibt.lt

© Springer Nature Switzerland AG 2019

D. Matulis (ed.), *Carbonic Anhydrase as Drug Target*,
https://doi.org/10.1007/978-3-030-12780-0_16

233

with a large negative Gibbs energy change) to the intended target protein and at the same time it should not bind to any other protein in the cell or even entire body. There are more than 20,000 different proteins in every cell, so the task to achieve sufficient selectivity over all remaining non-target proteins is extremely difficult. In reality, the selectivity of tenfold for the target over non-target sometimes may be a significant achievement. However, such low selectivity is usually insufficient to avoid toxic side effects. We suppose that it is desirable to achieve the selectivity of at least 10,000-fold towards the target over non-target.

Primary sulfonamides have been known to possess significant affinity and selectivity towards CAs over other Zn-containing enzymes, such as histone deacetylases (HDACs) or matrix metalloproteinases (MMPs), that are weakly inhibited by primary sulfonamides, but instead are inhibited by hydroxamic-acid-bearing compounds [1, 2]. The presence of a pharmacophoric group such as sulfonamide increases the chance to build compounds with high affinity, because the pharmacophoric group already makes the compound a strong inhibitor that is selective towards a particular group of proteins such as CA.

However, in humans there are 12 catalytically active CA isoforms. They are present in every cell and perform vital functions of pH regulation and carbon metabolism [3]. Their full inhibition, even if it is temporary, would probably be detrimental for the body. Therefore, it is highly important to understand the principles and be able to build compounds that would inhibit just one target isoform of the whole family. For example, CA IX is often highly overexpressed in various cancers [4–7]. Thus it is thought that its inhibition could lead towards slowing the spread of cancer or even its treatment. In order to test such a hypothesis, it is necessary to design and synthesize a compound that would inhibit only CA IX and would not inhibit the remaining 11 CA isoforms. However, as it was shown in Chaps. 13 and 14, the structure of the active site pocket in all CAs is rather similar. Only several amino acids are specific for a particular CA isoform. Therefore, a hypothetical compound intended to bind CA IX, but not bind to any of the remaining 11 isoforms should exactly match the pocket of this isoform and simultaneously contain features that would prevent its binding to any other isoforms. Those features most often should be chemical groups that make steric clashes with some amino acids in the non-target isoforms.

Despite significant efforts and the synthesis of nearly 800 primary sulfonamides designed to test the influence of particular chemical groups on the compound affinity towards every CA isoform, we were not successful to design compounds that would bind, for example, CA IX while not binding at all to any remaining 11 isoforms. However, some of the most successful compounds bound CA IX hundreds of thousand-fold stronger over most crucial CA I and CA II [8–10]. Still, such compounds exhibited marginal selectivity over some not-as-crucial isoforms such as CA XIII or CA XIV. Therefore, even the best designed compounds should not be considered as fully free of binding to any unintended isoforms. Such compounds could be good tools used for the demonstration in biology of their potential as pharmaceuticals.

This chapter has several goals. First are application-oriented goals: to illustrate the chemical structures of compounds possessing highest affinities and selectivities towards several target CAs, and to show some principles on which chemical groups and at which positions provide highest increase in affinities and selectivities for some CAs. We also see this collection of compounds to be useful for scientists who search for basic principles that guide recognition between a chemical compound and a particular surface site on a protein. A large part of the binding data have been recently summarized [11] in a database format. It is important to remember that pharmaceutical design is still performed rather accidentally, primarily based on trial and error. Large compound libraries consisting of 100,000 to million compounds are usually screened by pharmaceutical companies in search of hit compounds that would bind new targets.

In our opinion, it is insufficient to limit protein–ligand binding studies by analyzing only affinities of compounds towards proteins. The affinity ($K_{d,int}$, ΔG_{int}) provides limited information about molecular recognition. For every protein–ligand binding reaction, additional thermodynamic and kinetic parameters can be estimated. The importance of kinetic parameters, the rate of association, the rate of dissociation, and the residence time has been discussed in Chap. 9 on SPR. The importance of the changes in enthalpy, entropy, and heat capacity has been introduced in Chap. 6 on ITC. In this chapter, we show enthalpic contributions by compound functional groups towards the overall intrinsic enthalpy of binding. The enthalpy–entropy compensation is also discussed.

16.2 Maps of Correlations Between Compound Chemical Structures and Intrinsic Binding Thermodynamics

Probably the first group that has accumulated data for a correlation map of compounds interacting with a CA led by Whitesides studied the binding thermodynamics of benzothiazole sulfonamide and its fluorinated derivatives to CA II [12–14]. They have determined the intrinsic Gibbs energies and enthalpies of binding that can be correlated with compound structures. Their motivation was to determine how the fluorination of compounds changes the binding thermodynamics with CA II. Based on their data we can draw a map of correlation between compound chemical structure and its binding thermodynamics (Fig. 16.1).

Thiazole sulfonamide (TA) bound CA II with the $\Delta G_{int} = -51.0$ kJ/mol. Addition of the benzene ring yielded benzothiazole (H4BTA) that bound CA II with the $\Delta G_{int} = -56.5$ kJ/mol. Thus the structural change from TA to H4BTA led to the change in $\Delta G_{int} = -5.4$ kJ/mol. Therefore, the change was favorable and H4BTA bound to CA II nearly tenfold more strongly than TA. Introduction of fluorine atoms at various positions, one, two, three, or even all four, led to minor changes in intrinsic affinity. The tetrafluoro-benzothiazole sulfonamide (F4BTA) bound to CA II with the $\Delta G_{int} = -54.4$ kJ/mol. Therefore, 2.1 kJ/mol Gibbs energy was lost and F4BTA bound weaker than H4BTA. It can be concluded that fluorines did not strongly affect how the compound recognizes the protein surface.

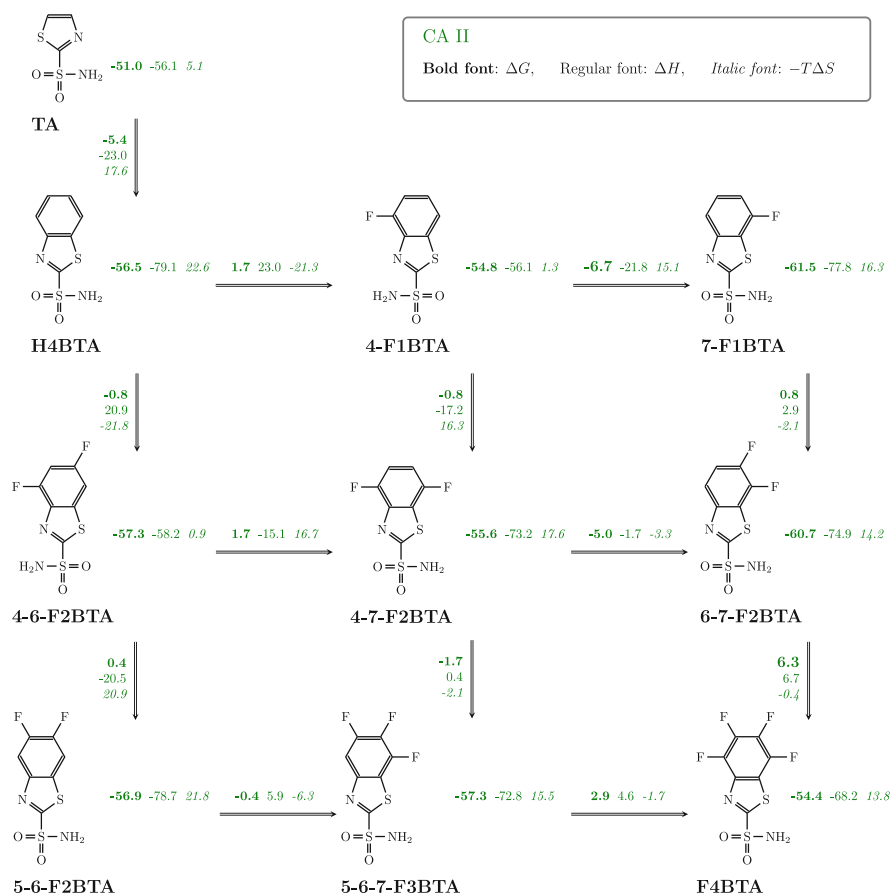


Fig. 16.1 Correlation map for the binding of benzothiazole sulfonamide derivatives with different fluorination patterns to human CA II. The intrinsic thermodynamic data obtained from ITC measurements at 25 °C were taken from [12–14]. The values next to compound structures list the intrinsic energies of binding of each compound, while the values on arrows show the differences in thermodynamic parameters between the adjacent compounds. The first number (bold) lists the Gibbs energy, the second (regular font)—enthalpy, and the third number (italic)—the negative entropy multiplied by the absolute temperature. All values are in kJ/mol

The fluorinated compound bound weaker, thus indicating that there may be a steric hindrance effect diminishing the affinity. It should be remembered that the observed affinity (ΔG_{obs}) increased significantly upon fluorination, but the reason for the increase was the change in $pK_{a,SA}$ and not the recognition between the protein and ligand surfaces.

The enthalpies of BTA compound binding to CA II (Fig. 16.1) were significantly different among the compounds. The compounds can be arranged in two groups. The first group containing TA, 4-F1BTA, and 4-6-F2BTA exhibited the enthalpy of binding (ΔH_{int}) in the range from -56.1 to -58.2 kJ/mol. The second group containing all remaining seven compound exhibited the ΔH_{int} in the range from -68.2 to -79.1 kJ/mol. There is no clear reason for this result. The increase in enthalpies was compensated by the decrease in entropies. In some cases introduction of a fluorine atom (e.g., H4BTA to 4-F1BTA) diminished the magnitude of the enthalpy, while in other cases it did not make much difference (e.g., H4BTA to 7-F1BTA). The compounds bound overall quite similarly to CA II, but the differences in enthalpies could have significant but so far unclear information on how each compound recognizes the protein surface. The authors have hypothesized that the change of water networks upon ligand binding most likely is the source of the compensating changes of ΔH_{int} and $T\Delta S_{int}$. Water molecules solvating the ligand and protein active site are as important as the contacts between the protein and the ligand for biomolecular recognition [15].

The presence of fluorine atoms in the benzene ring of benzenesulfonamide significantly increases the observed affinity of the compound over benzenesulfonamide because fluorines withdraw electrons and diminish the pK_a of the sulfonamide amino group (Chap. 8). In Fig. 16.2, a series of substituents have been introduced to the *para* position of the tetrafluorobenzenesulfonamide. The substituents have been introduced through N (upper two rows on the right and center) or S (bottom two rows) atoms. Introduction of the hydrazino group, for example, did not have major effects on binding, but the affinity for CA VB has diminished by $+12.6$ kJ/mol. Every 6 kJ/mol loss amounts to the loss of affinity of approximately tenfold. Therefore, the substituted compound VD10-14 bound to CA VB over 100-fold weaker than unsubstituted VD12-22.

Introduction of various substituents to *para* position of tetrafluorinated benzenesulfonamide VD12-22 led to the discovery of compound VD11-61 which bound CA I with 0.7 pM intrinsic affinity ($\Delta G_{int} = -72.3$ kJ mol $^{-1}$). These *para*-substituted compounds in general were good inhibitors of CA I. However, it is difficult to achieve any significant selectivity by applying *para* substitutions alone.

Several figures (Figs. 16.3, 16.4, 16.5, and 16.6) show parts of a large correlation map drawn to illustrate the search of CA IX-selective compounds. Various substituents are shown added to *ortho* and *meta* positions of a modified benzenesulfonamide. Some larger hydrophobic substituents especially cyclic aliphatic rings have significantly increased affinity for CA IX and led towards selectivity over remaining 11 CA isoforms. Several crystal structures have been solved of these compounds bound to CA IX as described in several other chapters of this book. The crystal structures have helped to determine which hydrophobic substituents have greater chances of making improved contacts with the protein surface.

CA I, CA II, CA III, CA IV, CA VA, CA VB, CA VI, CA VII, CA IX, CA XII, CA XIII, CA XIV

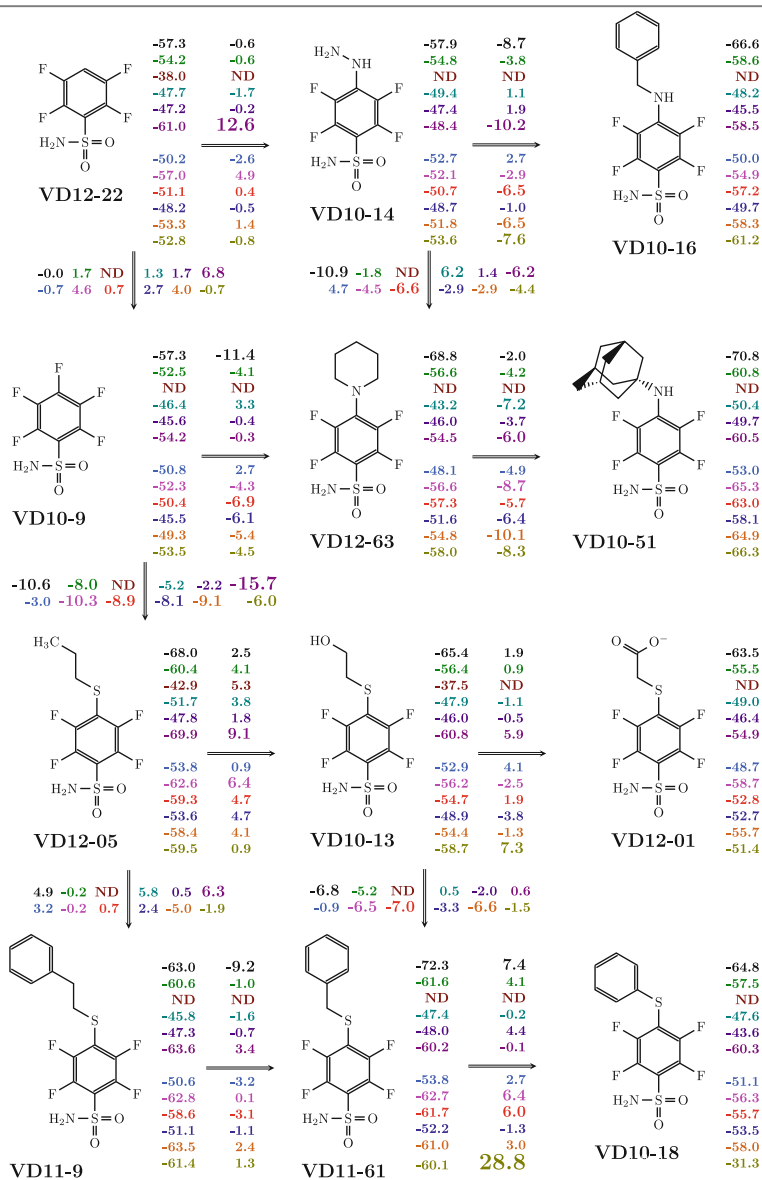


Fig. 16.2 Map of correlation between compound chemical structures and intrinsic Gibbs energies of binding to 12 human CA isoforms. A series of *para*-substituted tetrafluorobenzenesulfonamides are being compared. The values of intrinsic Gibbs energies of their binding to each CA isoform are presented near each compound structure in the order of increasing CA isoform number, while numbers near each arrow show the Gibbs energy differences ($\Delta\Delta G_{int}$) between neighboring compounds. Larger differences of Gibbs energies are depicted in larger font size to highlight the largest energy gains upon chemical modifications of the compounds

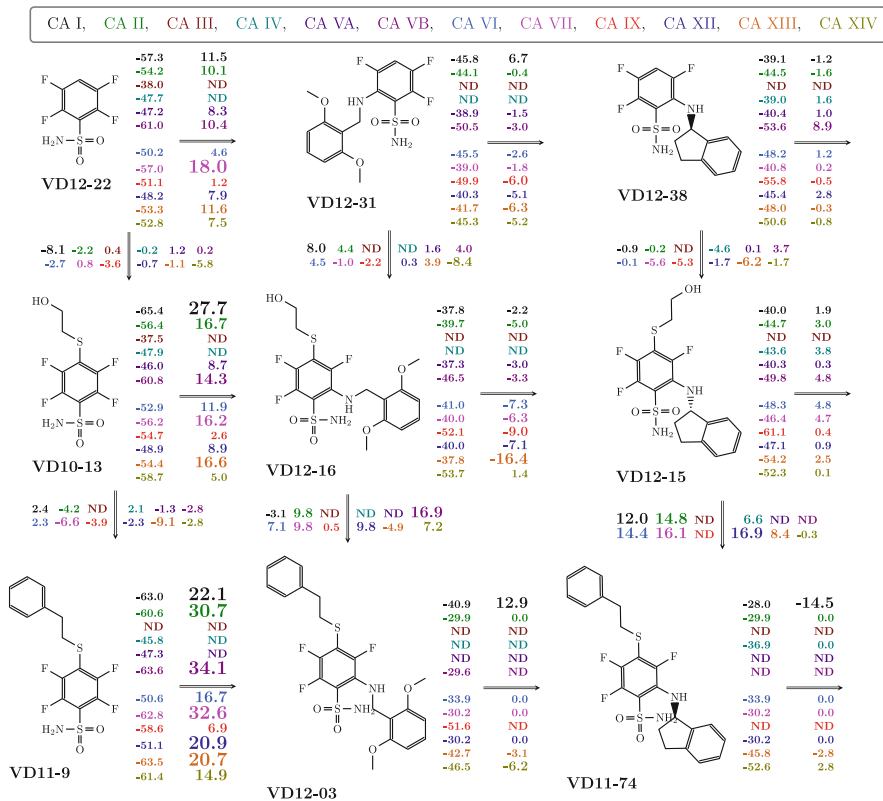


Fig. 16.3 Part I of the correlation map in search of CA IX-selective compounds. Introduction of these *ortho* substituents did not lead towards great inhibitors of CA IX. See previous figures for explanations

The next series (Fig. 16.7) compares compounds that have Cl atom at the *ortho* position relative to the sulfonamide headgroup and various substituents at *meta* and *para* positions. Beginning with the structurally simplest EA1-1 on the second row, we test contributions of larger hydrophobic substituents on the *para* position and some tails on the *meta* position. These series yielded inhibitors EA4-2 and EA4-2c that exhibited high affinity and selectivity for CA IV.

Compound E2 exhibited high affinity for CA VA (Fig. 16.8). Various compounds of highly similar structure are shown next to it, but in all cases the affinity for CA VA has reduced demonstrating that the E2 is a nicely optimized compound that recognizes CA VA. Unfortunately, there are no crystal structures of CA VA and it is not yet clear how this compound recognizes the protein surface.

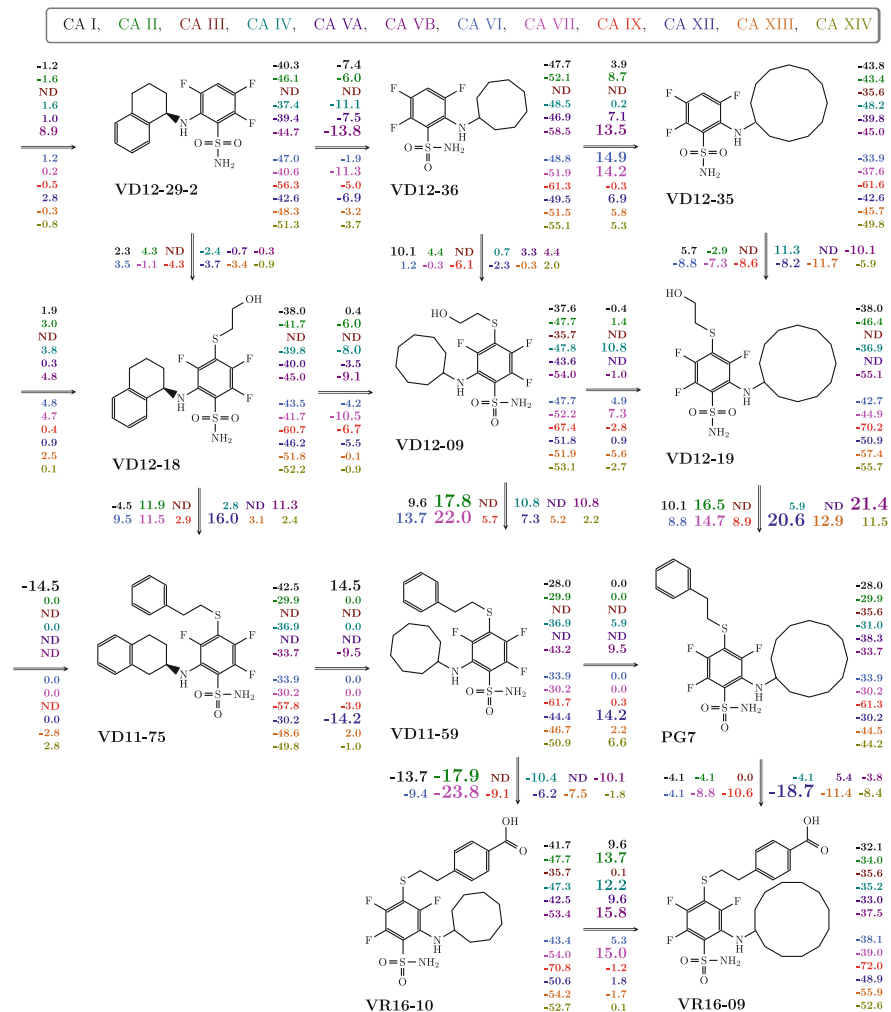


Fig. 16.4 Part II of the correlation map in search of CAIX-selective compounds. Addition of a bulky aliphatic ring at the *ortho* position led to some of the highest affinity compounds VR16-09 and VD12-19. See previous figures for explanations

16.3 Enthalpy and Entropy Correlation Maps

In addition to the Gibbs energy correlation maps that show compound affinities and also selectivities for particular CA isoforms, it is also important to draw correlation maps for other thermodynamic parameters, such as enthalpy and entropy of binding.

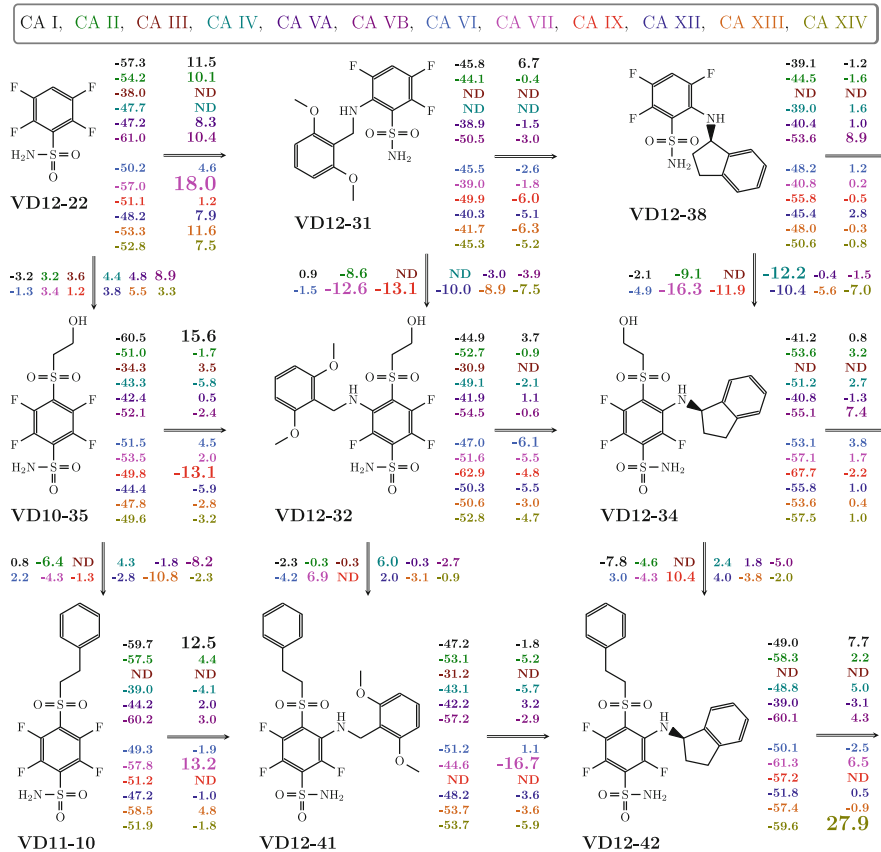


Fig. 16.5 Part III of the correlation map in search of CA IX-selective compounds. Compound VD12-34 possessed significant affinity and great selectivity towards CA IX. See previous figures for explanations

These parameters are not widely used, but in our opinion supported by a number of thermodynamicists, the enthalpies could provide significant additional insight in the understanding of the mechanism of interaction [15, 17–20]. Some of these examples will be provided in Chap. 17 describing correlations between crystal structures and thermodynamics of binding.

A correlation map that includes enthalpies and entropies of binding for compounds leading towards the best inhibitor of CA IX, VD11-4-2, is shown in Fig. 16.9. Introduction of *para* substituents to tetrafluorobenzenesulfonamide did not affect the enthalpy of binding. The ΔH_{int} for CA IX changed from -33.5 to -35.5 kJ/mol in VD10-35. However, the introduction of *meta*-substituted

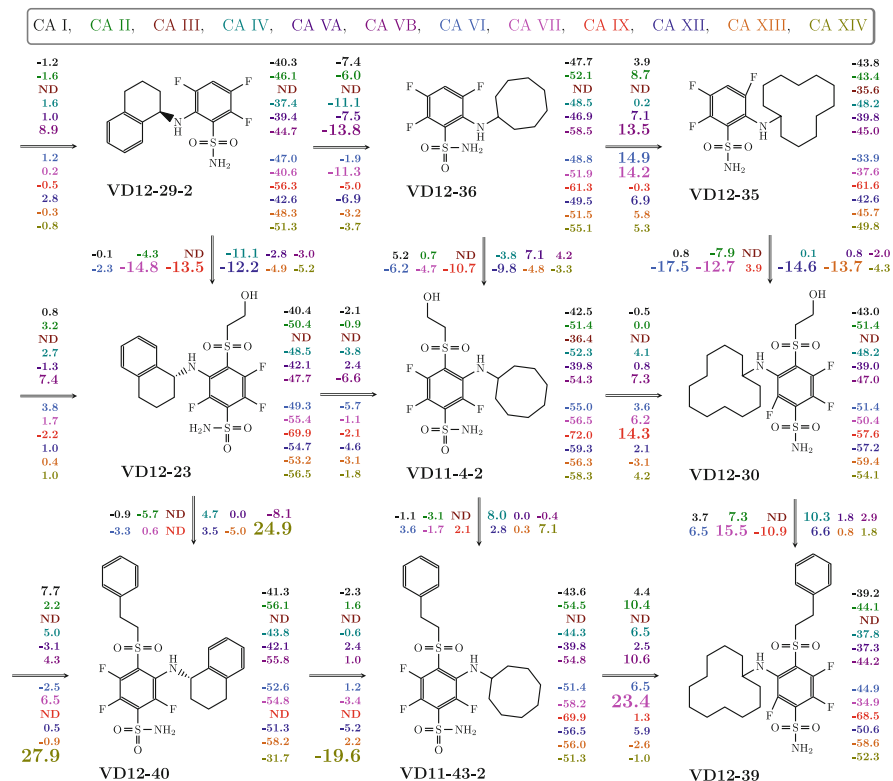


Fig. 16.6 Part IV of the correlation map in search of CA IX-selective compounds. Addition of a bulky aliphatic ring at the *meta* position also led to some of the highest affinity compounds such as VD11-4-2 (shown in the center). See previous figures for explanations

cyclooctylamino group diminished the magnitude of the enthalpy to -18.8 kJ/mol in VD12-36. The enthalpy of compound bearing both substituents (VD11-4-2) exhibited an intermediate enthalpy of -24.3 kJ/mol. Thus CA IX was recognized with a small change in enthalpy, but rather large change in entropy, a signature of the hydrophobic effect.

Figure 16.10 shows the enthalpy–entropy compensation plot for a large series of compound binding to eight CA isoforms. Compounds on the right top corner possess lowest affinities, while on the bottom left corner—the highest affinities. The compounds exhibit relatively similar affinities as compared to the spread in enthalpies and entropies of binding. Most compounds possess $K_{d,int}$ between 100 nM and 10 pM. This amounts to four orders of magnitude or approximately 24 kJ/mol of Gibbs energy. However, the enthalpies varied from -80 to 0 kJ/mol, thus spanning the range of 80 kJ/mol, some threefold greater than for Gibbs energies. This means that there is significant information in the enthalpies of binding that could be used to better understand the mechanism of recognition. More

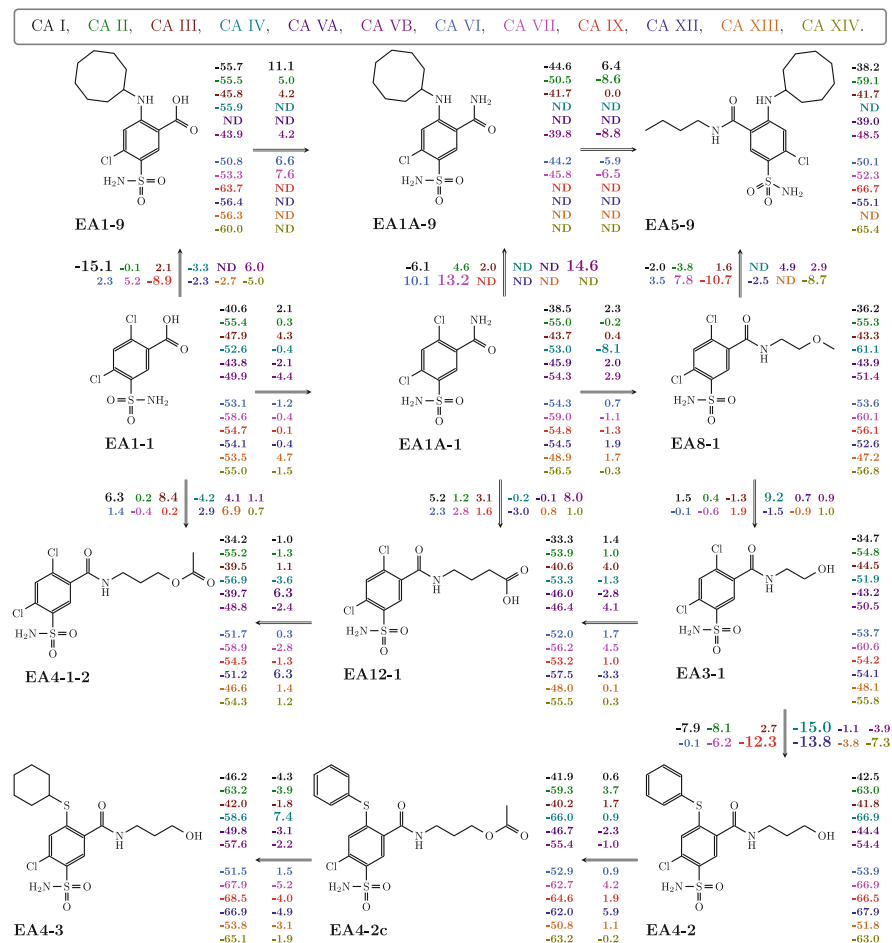


Fig. 16.7 Chlorinated compound functional group contribution to Gibbs energy of binding in the search of high affinity and selectivity CA IV inhibitor. The map shows a series of compounds connected by arrows beginning with the simpler compounds EA1-1 and EA1A-1 as the weakest inhibitors and ending with the best inhibitors of CA IV, i.e., EA4-2 and EA4-2c, displayed on the right bottom corner of the map. See previous figures for explanations

than half of the compounds are enthalpy-dominated, but many are also entropy-dominant binders. Compounds tend to group also according to CA isoform. For example, CA IX-binders are entropy-dominated, while CA I binders are much more dominated by the enthalpy of binding. Such compensation cannot be explained solely based on the contacts between the protein and the chemical compound. As previously hypothesized [15], most likely source of the compensation is hidden in the behavior of water molecules hydrating both the protein and the ligand.

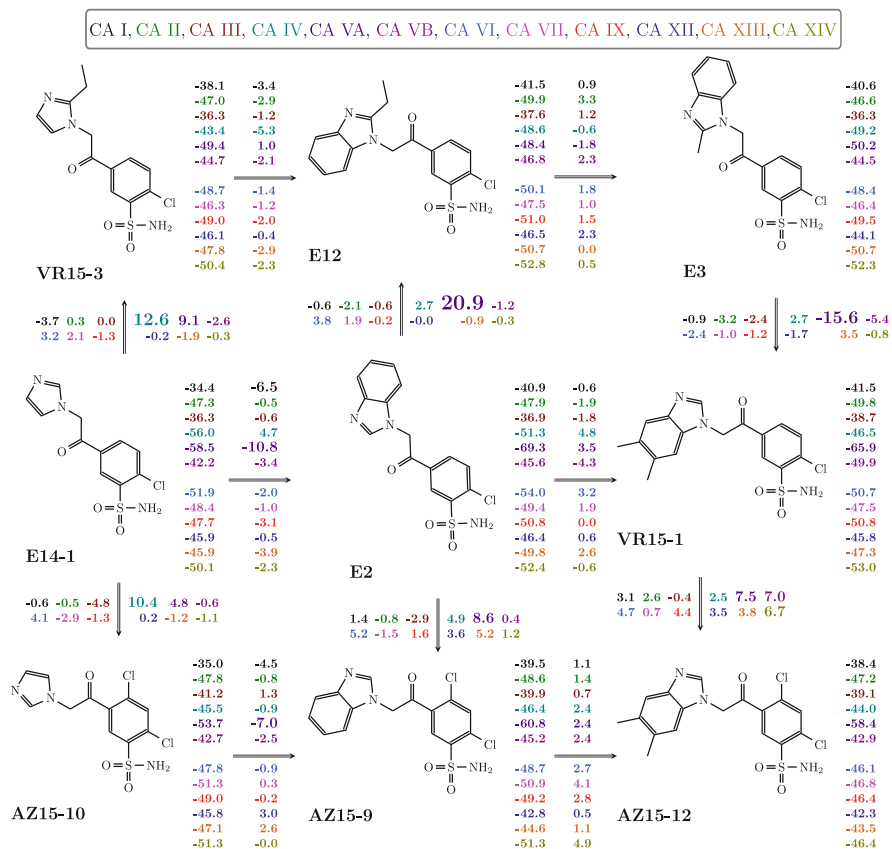


Fig. 16.8 Correlation map between thermodynamic of binding and the chemical structures of compound binding to CAs in the search of CA VA-selective compounds. The E2 compound in the center of the map exhibits highest affinity and great selectivity towards CA VA. The figure is adapted from [16]

16.4 Conclusions

Correlation maps between the compound chemical structures and their thermodynamic parameters of binding help understand the functional group contributions and forces driving the molecular recognition which facilitates the successful design of selective tight-binding inhibitors. Compounds of similar structure are drawn next to each other on the map and the differences in energies are listed between the adjacent structures showing the gain or loss in energy upon the introduction of a particular chemical change in the structure. Such maps illustrate the paths how compounds with highest affinities and selectivities towards a particular target CA isoform may be designed. Most important are the maps of Gibbs energy, but the maps of other

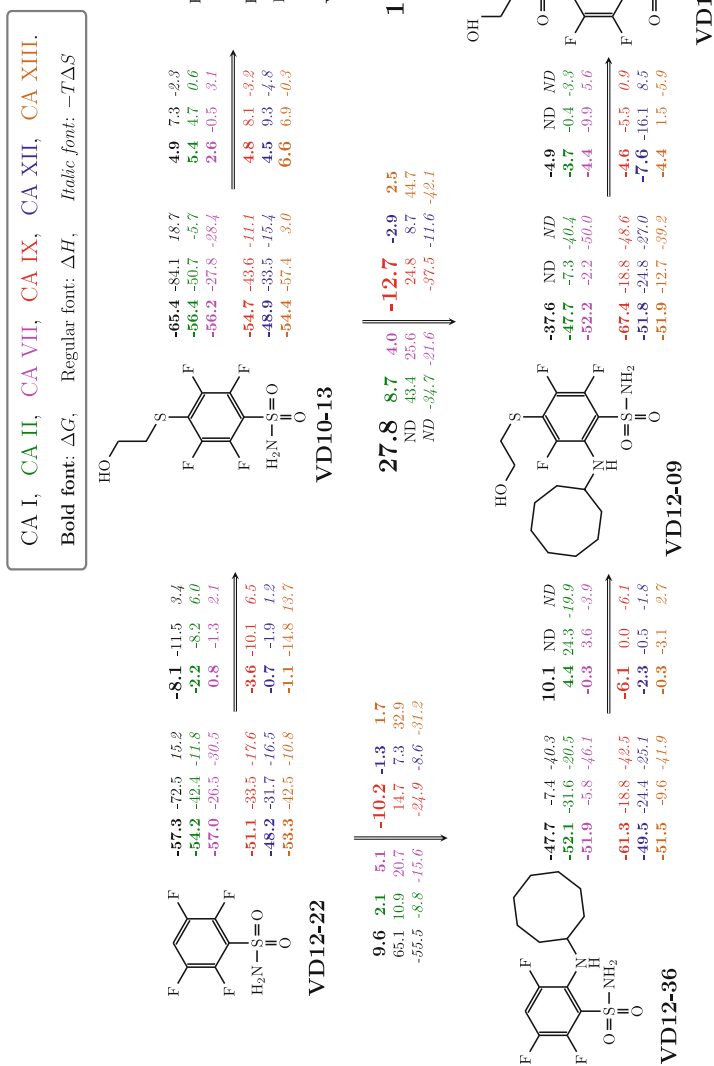


Fig. 16.9 Correlation map of compound chemical structures with intrinsic binding parameters (ΔG_{int} , ΔH_{int} , and $T\Delta S_{int}$) towards CA IX as determined by ITC. Intrinsic parameters of binding are shown next to the chemical structures. Differences in the binding parameters between chemically similar compounds are shown above the connecting arrows. Colors represent different CA isoforms. Intrinsic Gibbs energies of binding are shown in bold, enthalpies in regular font, and entropies are shown in italic. The figure is adapted from [21]

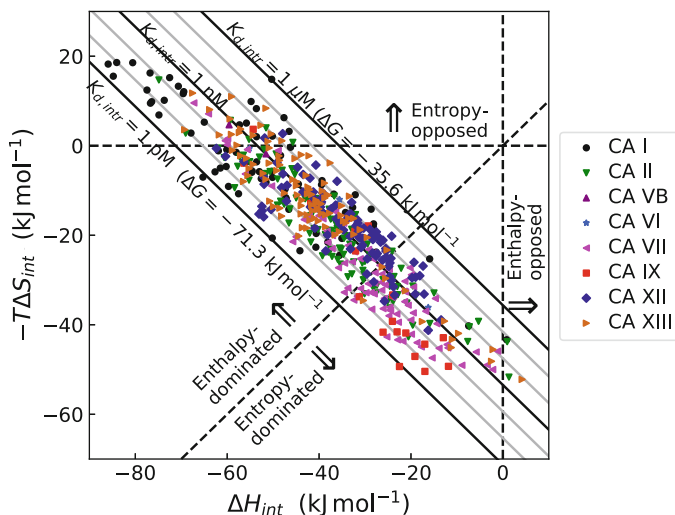


Fig. 16.10 Enthalpy–entropy correlation plot showing intrinsic enthalpies and entropies of binding of 150 compounds to 8 CA isoforms shown in different colors and symbol shapes. The compounds are significantly more different in enthalpies than Gibbs energies. Compounds tend to group according to CA isoform. The figure is reprinted from [11]

parameters such as enthalpy and entropy are useful for deeper understanding of the binding mechanism.

References

- Patil, V.M., Gupta, S.P.: Quantitative structure–activity relationship studies on sulfonamide-based MMP inhibitors, in *Matrix Metalloproteinase Inhibitors*, ed. by S.P. Gupta (Springer Basel, Basel, 2012), pp. 177–208
- Day, J.A., Cohen, S.M.: Investigating the selectivity of metalloenzyme inhibitors. *J. Med. Chem.* **56**, 7997–8007 (2013)
- Supuran, C.T.: Carbonic anhydrases—an overview. *Curr. Pharm. Des.* **14**, 603–614 (2008)
- Mahalingam, S.M., Chu, H., Liu, X., Leamon, C.P., Low, P.S.: Carbonic anhydrase IX-targeted near-infrared dye for fluorescence imaging of hypoxic tumors. *Bioconjug. Chem.* **29**, 3320–3331 (2018)
- Mahon, B., Pinard, M., McKenna, R.: Targeting carbonic anhydrase IX activity and expression. *Molecules* **20**, 2323–2348 (2015)
- Nocentini, A., Supuran, C.T.: Carbonic anhydrase inhibitors as antitumor/antimetastatic agents: a patent review (2008–2018). *Expert Opin. Ther. Pat.* **28**, 1–12 (2018)
- Swietach, P., Hulikova, A., Vaughan-Jones, R.D., Harris, A.L.: New insights into the physiological role of carbonic anhydrase IX in tumour pH regulation. *Oncogene* **29**, 6509–6521 (2010)
- Dudutienė, V., et al.: Discovery and characterization of novel selective inhibitors of carbonic anhydrase IX. *J. Med. Chem.* **57**, 9435–9446 (2014)
- Smirnovienė, J., Smirnovas, V., Matulis, D.: Picomolar inhibitors of carbonic anhydrase: importance of inhibition and binding assays. *Anal. Biochem.* **522**, 61–72 (2017)

10. Kazokaitė, J., et al.: Novel fluorinated carbonic anhydrase IX inhibitors reduce hypoxia-induced acidification and clonogenic survival of cancer cells. *Oncotarget* **9**, 26800–26816 (2018)
11. Linkuvienė, V., et al.: Thermodynamic, kinetic, and structural parameterization of human carbonic anhydrase interactions toward enhanced inhibitor design. *Q. Rev. Biophys.* **51**, 1–48 (2018)
12. Snyder, P.W., Lockett, M.R., Moustakas, D.T., Whitesides, G.M.: Is it the shape of the cavity, or the shape of the water in the cavity? *Eur. Phys. J. Spec. Top.* **223**, 853–891 (2013)
13. Breiten, B., et al.: Water networks contribute to enthalpy/entropy compensation in protein-ligand binding. *J. Am. Chem. Soc.* **135**, 15579–15584 (2013)
14. Lockett, M.R., et al.: The binding of benzoarylsulfonamide ligands to human carbonic anhydrase is insensitive to formal fluorination of the ligand. *Angew. Chem. Int. Ed. Engl.* **52**, 7714–7717 (2013)
15. Fox, J.M., Zhao, M., Fink, M.J., Kang, K., Whitesides, G.M.: The molecular origin of enthalpy/entropy compensation in biomolecular recognition. *Annu. Rev. Biophys.* **47**, 223–250 (2018)
16. Čapkauskaitė, E., et al.: Benzimidazole design, synthesis, and docking to build selective carbonic anhydrase VA inhibitors. *Bioorg. Med. Chem.* **26**, 675–687 (2018)
17. Martin, S.F., Clements, J.H.: Correlating structure and energetics in protein-ligand interactions: paradigms and paradoxes. *Annu. Rev. Biochem.* **82**, 267–293 (2013)
18. Klebe, G.: Applying thermodynamic profiling in lead finding and optimization. *Nat. Rev. Drug Discov.* **14**, 95–110 (2015)
19. Ferenczy, G.G., Keserű, G.M.: The impact of binding thermodynamics on medicinal chemistry optimizations. *Future Med. Chem.* **7**, 1285–1303 (2015)
20. Klebe, G.: The use of thermodynamic and kinetic data in drug discovery: decisive insight or increasing the puzzlement? *ChemMedChem* **10**, 229–231 (2015)
21. Zubrienė, A., et al.: Intrinsic thermodynamics of 4-substituted-2,3,5,6-tetrafluorobenzenesulfonamide binding to carbonic anhydrases by isothermal titration calorimetry. *Bio-phys. Chem.* **205**, 51–65 (2015)



Correlations Between Inhibitor Binding Thermodynamics and Co-crystal Structures with Carbonic Anhydrases

17

Alexey Smirnov, Elena Manakova, and Daumantas Matulis

Abstract

In order to be able to design chemical compounds that recognize a particular CA isoform, meaning that they would bind particular isoform with high affinity while not binding other isoforms, it is important to understand how compounds recognize the protein surface. To understand which structural features yield what types of changes in the binding energetics, we search for correlations between compound–isoform co-crystal structures and intrinsic thermodynamics of binding. The compounds are being compared by arranging them in matched molecular pairs that differ by a single functional group responsible for the change in binding thermodynamics. Part of the ligands bound in similar orientations of the benzenesulfonamide ring, while others bound in dissimilar orientation. All similar binders exhibited significant increase in entropic forces upon increase in the buried surface of the compounds, while dissimilar binders had various thermodynamics. Several mechanisms were identified, perfect geometry fit and a molecular trap. The softness of the CA active site and the water molecules are also discussed.

A. Smirnov · D. Matulis (✉)

Department of Biothermodynamics and Drug Design, Institute of Biotechnology, Life Sciences Center, Vilnius University, Vilnius, Lithuania

e-mail: Alexey.smirnov@bti.vu.lt; matulis@ibt.lt

E. Manakova

Department of Protein-DNA Interactions, Institute of Biotechnology, Life Sciences Center, Vilnius University, Vilnius, Lithuania

e-mail: lana@ibt.lt

© Springer Nature Switzerland AG 2019

D. Matulis (ed.), *Carbonic Anhydrase as Drug Target*,
https://doi.org/10.1007/978-3-030-12780-0_17

249

17.1 Introduction: The Energetics and Structure of Protein–Ligand Interactions

The first stage of drug design is the discovery of a chemical compound that tightly and specifically binds to the target protein and alters its function in a therapeutically beneficial way. The binding process is governed by the thermodynamics [1–3], where the standard equilibrium Gibbs energy change upon compound binding (ΔG) is the sum of contributions from the enthalpy (ΔH) or entropy ($-T\Delta S$) that drive the binding process. The process depends on many factors:

- (a) classical direct interaction between ligand and target protein resulting in hydrogen bonds, hydrophobic interactions, van der Waals contacts, salt bridges, and others;
- (b) water-related processes (solvation/desolvation and capture/release of water molecules from protein and ligand) during ligand–target complex formation;
- (c) the changes of conformational mobility of the ligand and the protein residues upon binding (conformational adaptation); and
- (d) shape, softness, and exposed molecular surface topography of the active site of the target protein.

It has been proposed that enthalpy-driven compounds are often preferred over entropy-driven ones due to the higher probability to obtain the good selectivity, high affinity, and other optimal characteristics of inhibitor such as its toxicology, adsorption, metabolism, and excretion [4]. However, the exact structural details determining the binding thermodynamics are not understood and thus it is difficult to rationally design compounds that bind target protein specifically and with desired energetics.

The change in binding enthalpy can be split into contributions [3]:

$$\Delta H_{obs} = \Delta H_{interactions} + \Delta H_{desolv} + \Delta H_{conf} + \Delta H_{exchange} \quad (17.1)$$

where $\Delta H_{interactions}$ is the enthalpy gain/loss associated with the formation of non-covalent interactions between binding partners, ΔH_{conf} is the enthalpy change associated with the conformational changes of ligand and protein, ΔH_{desolv} is the enthalpy gain/loss associated with the desolvation processes of the binding partners, and $\Delta H_{exchange}$ is the enthalpy change associated with the additional influence from interactions between ligand or protein and buffer components, protons (H^+), or other molecules. The pH influence to the binding process can be estimated and the $\Delta H_{exchange}$ eliminated from Eq. 17.1. The ΔH_{desolv} is often unfavorable for binding due to the disruption of “ligand–water” and “active site–water” interactions.

ΔH_{conf} is related to the energetics of conformational changes of the partners upon binding (conformational adaptation of interacting partners). The values of ΔH_{conf} may vary. $\Delta H_{interactions}$ is favorable for binding energetics and usually this impact compensates the unfavorable gain of desolvation process.

The change in binding entropy (multiplied by the absolute temperature) also can be split in a similar way:

$$\begin{aligned} -T \Delta S_{obs} = & -T \Delta S_{desolv} - T \Delta S_{conf} - T \Delta S_{exchange} \\ & -T \Delta S_{roto-translational} - T \Delta S_{vibrational} \end{aligned} \quad (17.2)$$

where new members $T \Delta S_{roto-translational}$ and $T \Delta S_{vibrational}$ are roto-translational (associated with degree of translational and rotational freedom) and vibrational (associated with covalent bonds) entropies, respectively. It was proposed to primarily focus on the optimization of desolvation and conformational entropies during drug design [3].

The conformational entropy change upon binding is usually unfavorable due to the reduction in freedom of bound partners. Thus restriction of conformational freedom of unbound ligand skeleton sometimes can be a successful trick which could minimize the values of unfavorable conformational entropy.

Water molecules at the ligand–protein interface play a crucial role in the enthalpy–entropy compensation effect [1,5]. The enthalpy–entropy compensation is a barrier in the design of selective and strong binders when the additional functional group does not improve the binding affinities but induce significant changes in the binding thermodynamics.

A ligand–protein binding event is characterized by binding affinity and selectivity. The binding affinity is the indicator of the binding strength between ligand and target, whereas the selectivity—an indicator of molecular discrimination among numerous other binding partners. Additional functional group may, for example, improve the binding selectivity to the target with negligible change in the binding affinity or vice versa. Thus high affinity may not be sufficient and high selectivity may be necessary to make a drug that binds the target protein and does not bind to other proteins, thus avoiding toxic side effects.

17.2 Matched Molecular Pairs of Similar Binders

In this chapter, we consider a series of structurally related chemical compounds bound to several human CA isoforms along with measurements of the intrinsic thermodynamics and co-crystal structures describing structural details of the interactions. The most interesting observations concerning two series of fluorinated and chlorinated benzenesulfonamide inhibitors of CAs are presented here based on [6]. Fifteen inhibitors have been grouped into 13 matched molecular pairs where compounds differ by hydrophobic substituents whose contribution is being studied. The 13 matched molecular pairs included six pairs with CA II, two with CA XIII, one with CA I, and four with CA XII. The compound VD12-10 binding mode was compared in the active site of CA II and CA XII.

A group of *similar* binders is defined by the same orientation of the benzene ring of compounds in the pair. Only the positions of substituents may be different in each pair. Figure 17.1 illustrates nine matched molecular pairs that exhibited *similar*

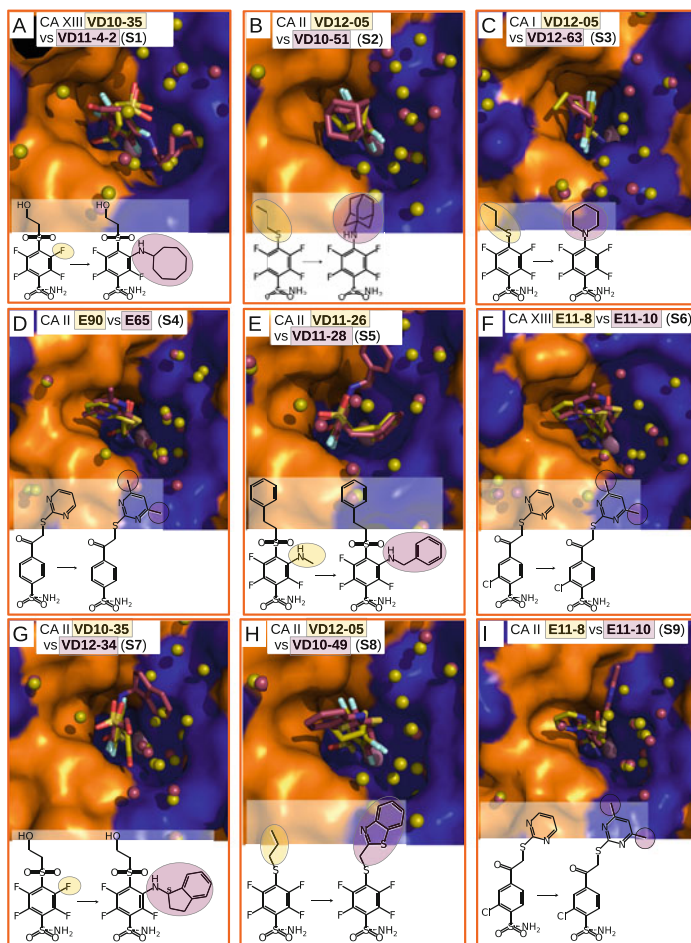


Fig. 17.1 Matched pairs of inhibitors which exhibit similar binding modes in the crystal structures of CA isoforms but have differences in the chemical structure by the presence of a functional group of interest. All CA active sites of the crystal structures are shown in the same orientation. The structural differences of the inhibitors in pairs are shaded by olive or raspberry color. The ligands and water molecules (spheres) found in crystal structures are colored the same. The Zn^{II} ion is shown as a pink sphere. The protein surface of CA active site is colored orange for hydrophobic residues (Val, Ile, Leu, Phe, Met, Ala, Gly, and Pro) and blue for amino acids with charged and polar side chains (Arg, Asp, Asn, Glu, Gln, His, Lys, Ser, Thr, Tyr, Trp, and Cys). (a) Compounds VD10-35 (olive, PDB 4HU1) and VD11-4-2 (raspberry, PDB 5E2N) bound to CA XIII (pair S1). (b) Compounds VD12-05 (olive, PDB 4WW6) and VD10-51 (raspberry, PDB 5LLE) bound to CA II (pair S2). (c) Compounds VD12-05 (olive, PDB 4WR7) and VD12-63 (raspberry, PDB ID 4WUQ) bound to CA I (pair S3). (d) Compounds E90 (green, PDB 3SBI) and E65 (raspberry, PDB 3SBH) bound to CA II (pair S4). (e) Compounds VD11-26 (olive, PDB 5LLC) and VD11-28 (raspberry, PDB 4QJM) bound to CA II (pair S5). (f) Compounds E11-8 (olive, PDB 4KNN) and E11-10 (raspberry, PDB 4KNM) bound to CA XIII (pair S6). (g) Compounds VD10-35 (olive, PDB 4PZH) and VD12-34 (raspberry, PDB 5DRS) bound to CA II (pair S7). (h) Compounds VD12-05 (olive, PDB 4WW6) and VD10-49 (raspberry, PDB 5LLH) bound to CA II (pair S8). (i) Compounds E11-8 (olive, PDB 4KNJ) and E11-10 (raspberry, PDB ID 4KNI) bound to CA II (pair S9)

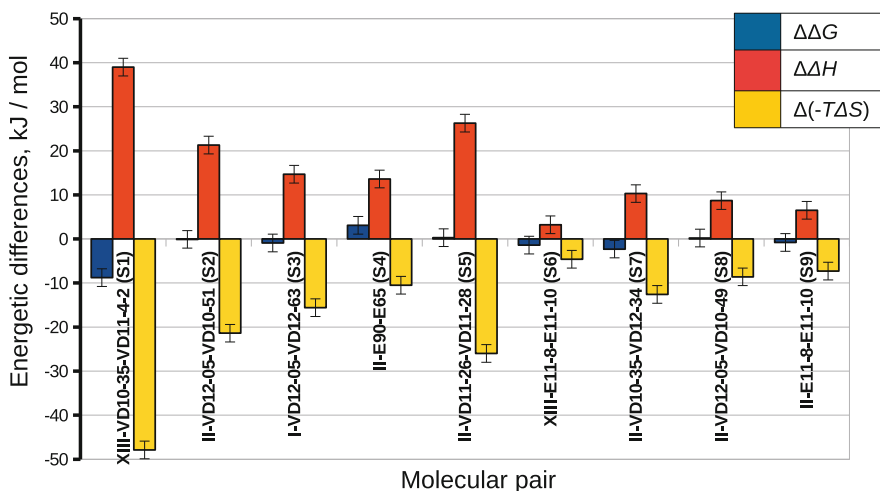


Fig. 17.2 The chart illustrates the changes of the intrinsic binding thermodynamics in the matched molecular pairs for similar binders. The enthalpy–entropy compensation effect described for similar binders is clearly evident. The additional hydrophobic surface did not significantly affect the binding affinity in most pairs. The unfavorable enthalpy change was always compensated by a favorable entropy change

binding mode. There were also numerous pairs that exhibited a nearly perpendicular orientation of the benzene ring in the pair and thus was termed *dissimilar* pair.

The analysis of the changes of binding thermodynamics between compounds in these pairs showed a distinct enthalpy–entropy compensation effect (Fig. 17.2). Comparison of the intrinsic Gibbs energy for similar molecular pairs showed that there was a relatively small increase in the affinity with an increase of additional hydrophobic molecular surface area. However, the intrinsic enthalpies of binding in all *similar* molecular pairs were significantly less exothermic for compounds bearing larger hydrophobic substituents. Additional contacts between the protein and the ligand did not make the enthalpy more favorable as could be expected. Instead, the intrinsic enthalpies of binding became less favorable. The entropies of binding mirrored the enthalpies and the enthalpy–entropy (H/S) compensation was evident.

We conclude that for a pair of *similar* binders the additional hydrophobic surface of the substituent does not substantially change the affinity but may significantly change the enthalpy and entropy of binding. The enthalpy–entropy compensation phenomenon is usually observed where unfavorable enthalpy change is compensated by the favorable entropy change.

In the case of *dissimilar* binders when the benzene ring of compounds in the pair was found in the different orientations, the changes of binding thermodynamics were much more varied. No generalization could be made such as in the case of similar binders.

17.3 The Case of Perfect Geometry Fit Between Protein and Ligand

A perfect geometry fit between drug and target as seen in the crystallographic data, when hydrogen bonds and van der Waals interactions are dense, may explain several ligand–CA binding cases when the binding affinity between interacting partners was extremely high ($K_{d,int}$ was approximately 1 pM). The fit geometry may never be perfect, but sometimes the fit could be called geometrically nearly perfect. Figure 17.3a illustrates the binding mode of compound VD12-05 in the active site of CA I exhibiting high binding affinity to CA I ($K_{d,int}$ value is 2.1 pM). In [7] we have described the structural reasons which possibly explain extremely

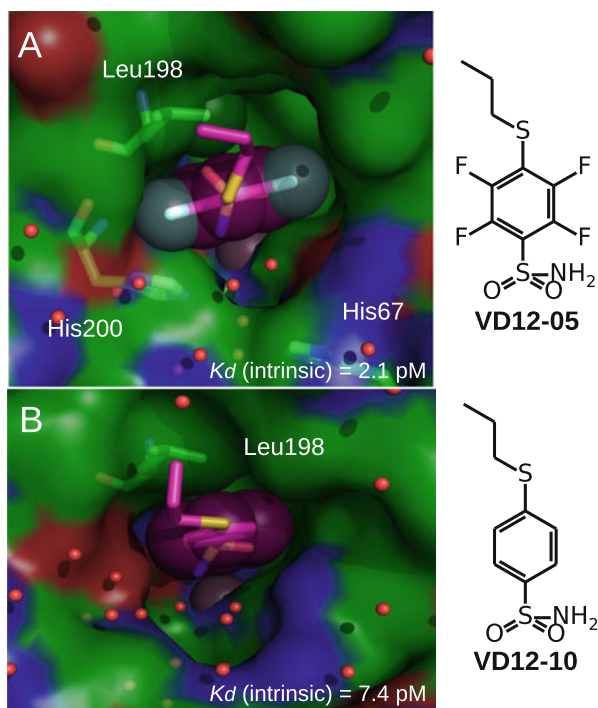


Fig. 17.3 Comparison of fluorobenzene and benzene ring positions in the active sites of two CA isoforms (CA I and CA II). The Zn^{II} is shown as a pink sphere, whereas the surface of protein is colored by element (C—green, O—red, and N—blue). (a) Compound VD12-05 in CA I active site (PDB 4WR7). The side chain of His200 restricted the motions of fluorinated ring, whereas Leu198 forms aliphatic–aromatic interaction with the fluorobenzene ring of the ligand from the opposite side. The atoms of fluorinated benzene and methyl group of Leu198 are shown in CPK. The aliphatic–aromatic interaction between benzene ring and methyl group of Leu198 is presented. (b) Compound VD12-10 in CA II active site (PDB 5LLG). Aliphatic–aromatic interaction between benzene ring and methyl group of Leu198 is presented. The atoms of fluorinated benzene and methyl group of Leu198 are shown in CPK

strong binding of this compound to CA I isoform that are clear in addition to the classical interactions of the compounds bearing primary sulfonamide moiety:

- (a) aliphatic–aromatic stacking interaction between fluorinated benzene ring of compound and methyl group of Leu198;
- (b) side chain of His200 restricted the motions of fluorinated benzene ring of compound VD12-05 which is fixed between the imidazole ring of His200 and side chain of Leu198; and
- (c) access of water molecules to interacting partners—sulfonamide and Zn^{II} ion—is restricted.

Another example of significant improvement of ligand binding to CA by aliphatic–aromatic stacking is shown in Fig. 17.3b. The compound VD12-10 is *para*-substituted benzenesulfonamide. Despite its relatively simple structure, this compound exhibited very high intrinsic affinities towards CA II and CA XII ($K_{d,int}$ values were 7.4 pM and 67 pM, respectively). The position of the benzenesulfonamide ring is similar, and the tight aromatic–aliphatic interaction between the benzene ring of VD12-10 and side chain of Leu198 (Leu197 in CA XII) was observed in both crystal structures.

This interaction along with classical bonds of sulfonamide formed by VD12-10 in the active site of CA and positioning of the *para*-substituent in the hydrophobic cavity in both CA isoforms could explain high binding affinity of this compound [6]. The space-filling model (CPK) of the first ring in both crystal structures exhibited a close fit in the active site (Fig. 17.3, where VD12-10 bound to CA II). The methyl group of conservative Leu198 in both cases is positioned against the center of benzene ring. We hypothesized that in both cases the tight aliphatic–aromatic interaction improved the binding affinity of the compound.

17.4 The Hydrophobic Barrier and Molecular Trap Mechanism of Strong Binders

The second possible mechanism, next to the case of perfect geometry, may be termed the hydrophobic barrier and molecular trap mechanism. Let us analyze the differences in the binding mode of compounds VD10-35 and VD11-4-2 in the active sites of CA XII and CA XIII.

Compounds VD10-35 and VD11-4-2 exhibited similar binding mode in the active site of CA XIII (the benzene ring was found in the same orientation, Fig. 17.4). Upon addition of cyclooctyl group to VD10-35 resulting in a modified compound VD11-4-2, the binding affinity increased 30-fold (corresponding values of $K_{d,int}$ are 8.9 nM and 0.29 nM). The binding mode of this pair of compounds has an interesting structural feature: the access of water molecules to sulfonamide changed after the increase of hydrophobic surface. The cyclooctyl group of VD11-4-2 replaced water molecules in the hydrophilic part of CA XIII active site. We have

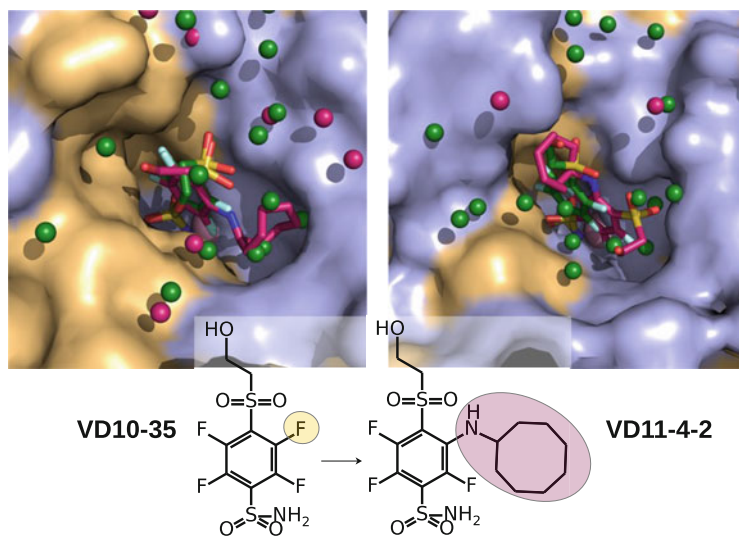


Fig. 17.4 Structural position of compounds VD10-35 (green) and VD11-4-2 (pink) bound CA XIII (left panel) and CA XII (right panel). The cyclooctyl group of VD11-4-2 replaced the green water molecules which are visible in the structure with VD10-35 (pink water molecules) of CA XIII. Both compounds are found here in similar orientation. However, in CA XII (right panel) the compounds are found in dissimilar orientation. The Zn^{II} ion is shown as a pink larger sphere. The protein surface of CA active site is colored olive for hydrophobic residues (Val, Ile, Leu, Phe, Met, Ala, Gly, and Pro) and blue for the residues with charged and polar side chains (Arg, Asp, Asn, Glu, Gln, His, Lys, Ser, Thr, Tyr, Trp, and Cys)

proposed that the barrier formed by the cyclooctyl group of VD11-4-2 complicates access of water molecules to the Zn^{II} ion during the dissociation process.

Several possibilities to displace water molecules upon compound binding are schematically drawn in Fig. 17.5. The dissociation of VD10-35 from CA XIII could be described by the mechanism shown in Fig. 17.5a, where water molecules can directly compete for interactions with sulfonamide and Zn^{II} .

The dissociation of VD11-4-2 could be described by the mechanism shown in Fig. 17.5b, where the hydrophobic group of the inhibitor acts as a temporary barrier for the penetration of water molecules to sulfonamide and Zn^{II} ion. The complicated path for water molecule access to displace the sulfonamide is a likely reason for the increase of binding affinity.

It is known that hydrophobic pocket of CA XII active site is larger than in CA XIII due to the bulky phenylalanine side chain which occupies part of the pocket in CA XIII (Phe133). The CA XII active site contains the alanine residue instead of phenylalanine in this position. Figure 17.4b compares the binding mode of compounds VD10-35 and VD11-4-2 in CA XII. The compound VD11-4-2 is bound to CA XII 320-fold stronger than VD10-35 ($K_{d,int}$ values are 0.11 nM for VD11-4-2 and 35 nM for VD10-35). These compounds have dissimilar binding modes in

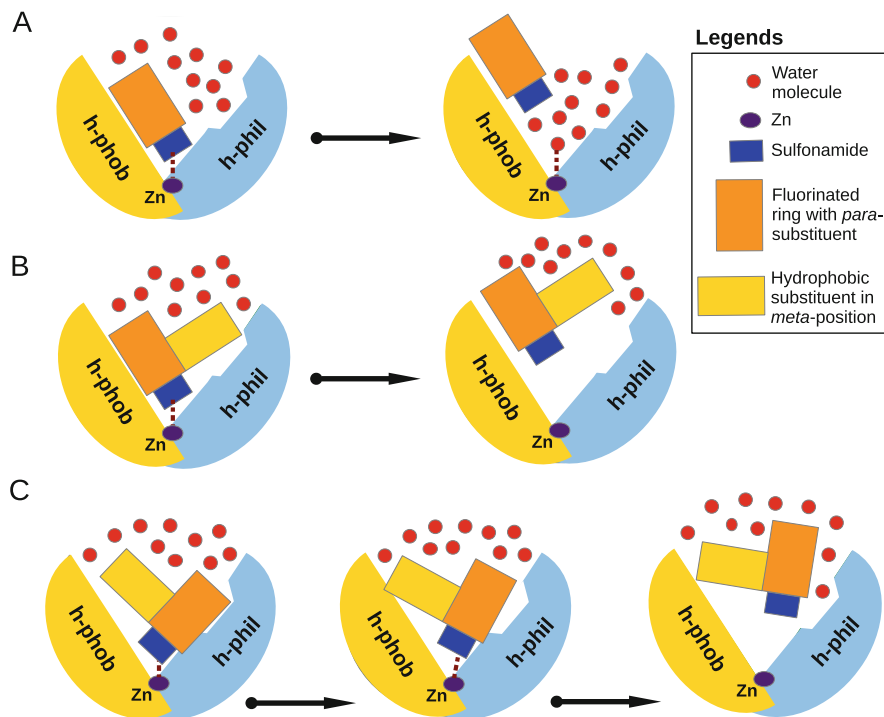


Fig. 17.5 Possible mechanisms of the impact of hydrophobic group to binding affinity. The CA active site is shown, where Zn^{II} ion is a small violet circle. The compound consists of the sulfonamide (blue rectangle), hydrophobic substituent (yellow rectangle), and benzene ring with *para*-group (orange rectangle). The small red circles represent the water molecules. The hphob and hphil labels mean the hydrophobic and hydrophilic parts of the active site. (a) Inhibitor dissociation process when water molecules in the active site compete for the binding to sulfonamide and Zn^{II} ion and participate in the compound dissociation out of the active site. (b) A large hydrophobic group in favorable orientation may create a temporary barrier for water molecules. (c) Dual mechanism of the ligand dissociation: when additional hydrophobic group displaces the other part of the ligand in the small active site cavities (molecular trap) and creates the steric barrier for water molecules to penetrate deeper into the active site

CA XII. The compound VD10-35 interacts with the hydrophobic part of CA XII active site, whereas the hydrophilic part is filled by water molecules. Such binding mode of VD10-35 is usual for *para*-substituted fluorinated benzenesulfonamides bound to CA II, CA IX, CA XII, and CA XIII isoforms. In the case of VD11-4-2 binding, the hydrophobic *meta*-substituent displaces the other part of compound in the hydrophilic part of CA XII.

In the crystal structure of CA XII-VD11-4-2, the *para*-substituent of the ligand is located under the side chains of Asn64 and Lys69 and such binding mode may explain the lower $K_{d,int}$ values. VD11-4-2 effectively displaced water molecules. The compound can exit the active site only after conformational changes of the

meta-cyclooctyl substituent, likely responsible for pushing of the *para*-group of the compound under the Asn64 and Lys69 side chains. The cyclooctyl group also creates a barrier for water molecules to enter the active site. Proposed mechanism explaining the high affinity of VD11-4-2 towards CA XII is schematically represented in Fig. 17.5c. The conformational change of cyclooctyl substituent is needed for the dissociation of VD11-4-2 from the active site.

However, we do not have full information about the dissociation process, its mechanism, and the triggers which enable the beginning of the dissociation process. We speculate that the role of water molecules in the binding process is significant and not yet fully understood.

17.5 The Softness of the CA Active Site

The ligands bound in CA active sites can induce significant conformational changes of protein amino acid side chains affecting the molecular surface of the active site. Ligand participates not only in the formation of the non-covalent interactions with the target molecular surfaces, but also in the rearrangement of the surface. Conformational adaptations of the active site residues could take place during the formation of ligand–protein complex.

Figure 17.6a illustrates the binding mode of VD10-35 (left panel) and VD11-4-2 (right panel) in CA II active site. The compound VD10-35 is a *para*-substituted fluorinated benzenesulfonamide, which did not affect the position of side chain of Phe131. Compound VD11-4-2 is a *meta*-position modified compound VD10-35. The orientation of fluorinated ring of these compounds is the same in CA II. The bulky hydrophobic group of VD11-4-2 pushed the side chain of Phe131 from its original position as in the complex CA II-VD10-35 (Fig. 17.6a).

Figure 17.6b illustrates the binding mode of VD11-4-2 in CA I active site. The compound occupies two alternative positions in CA I. The active site of CA I is narrower than CA II due to the presence of two histidine residues (one of them, His100, is shown in Fig. 17.6). In the crystal structure shown in the left panel of Fig. 17.6b the side chain of His100 was found in its original position, whereas in the right panel the fluorinated ring of compound VD11-4-2 affected the position of side chain of His100.

Adaptation to the ligand and amino acid side chains after complex formation is also illustrated in Fig. 17.6c. The binding mode of two ligands, VD10-35 and E11-8 (*para*-substituted fluorinated versus chlorinated benzenesulfonamide), was compared in the active site of CA XII. Both complexes are shown in the same orientation. In the structure shown in the left panel of Fig. 17.6c VD10-35 did not change the position of the side chain of Leu200, whereas the right panel shows that the chlorinated benzene of E11-8 changed the conformation of side chain of Leu200 in CA XII.

We conclude that the molecular surface and shape of the protein active site are changeable and the estimation of the active site softness is important for the

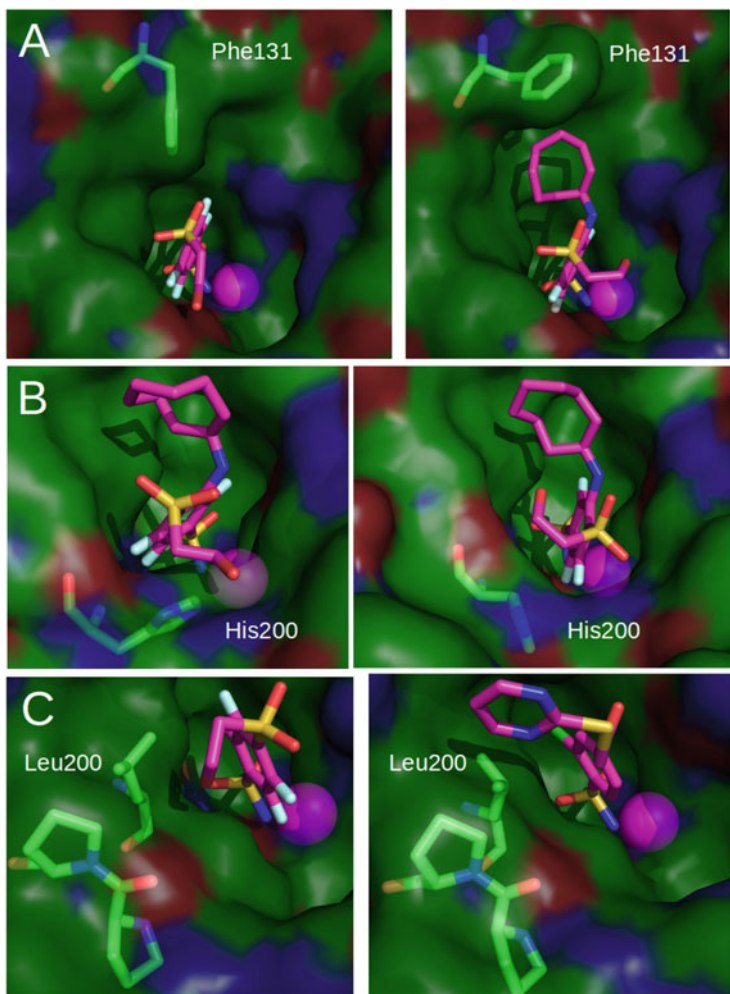


Fig. 17.6 The structures of fluorinated and chlorinated benzensulfonamides bound to the active sites of CA I, CA II, and CA XII. The Zn^{II} ion is shown as a pink sphere. (a) In the left, compound VD10-35 bound to CA II (PDB 4PZH). The side chain of Phe131 is found in the original position in CA II active site. On the right, compound VD11-4-2 bound to CA II (PDB 4PYY, alternative position of ligand model). (b) Two alternative conformations of compound VD11-2-4 bound CA I (PDB 5E2M, protein chain A). The shape of CA I active site is narrower as compared with CA II due to the presence of side chains of two histidine residues (His200, shown, and His67). Side chain of His200 is found in a different orientation. On the left, VD11-2-4 did not change the original position of His200, whereas on the right, VD11-2-4 is found in another binding mode and the position of side chain of His200 has changed. (c) Compounds VD10-35 and E11-8 bound to CA XII (PDB 5MSB and 4KP5, respectively). On the left, VD10-35 did not affect the original position of Leu200, whereas E11-8 (on the right) pushed and rotated the side chain of Leu200

structure-based drug design. It is difficult to estimate the impact of conformational adaptation to the binding thermodynamics.

17.6 Difficulties to Interpret the Crystallographically Visible Water Molecules

The crystal structures with resolution better than 1.8 Å contain electron-density peaks of sufficiently good quality to be interpreted as water molecules. Importance of the changes in local water structure of the active site after binding event is still an open question. The changes of local water network in the active site could be the reason for the entropy–enthalpy compensation effect [1, 5]. In principle, such changes can be a “cornerstone” of the protein–ligand binding thermodynamics. The resolution of CA–ligand complexes is often high enough (1.1–2.0 Å) and density peaks of water molecules in the active site can be correctly identified. Despite the suitable diffraction resolution of CA protein crystals, we cannot always accurately estimate the changes of crystallographic water molecule number in the active sites of CA–without ligand and CA–ligand complexes due to the following reasons:

- (a) the number of water molecules observed in the active site of crystal structure depends on the resolution and the interpretation of electron-density peaks. Weak peaks of electron-density map can be interpreted as peaks of more mobile water molecules. Different crystallographic software can generate partially different electron-density maps;
- (b) solvent molecules are often trapped and stabilized in the crystal structure between protein chains due to the crystal packing;
- (c) the crystal structure of CA XII often contains four subunits in the cell where the number and quality of solvent molecule peaks may have similar differences between active sites of the protein subunits;
- (d) the number of water molecules observed in the active site depends on the buffer composition resulting in buffer molecules observed at the protein surface instead of water molecules; and
- (e) the side chains of residues which form the surface of active site can have alternative positions that weaken the electron-density peaks of crystallographic waters and complicate the interpretation of density maps.

All these reasons influence the assumed correlations between the crystallographic water molecules in active sites and binding thermodynamic parameters. X-ray crystallography cannot yield the positions of hydrogen atoms of water molecules. Only the positions of oxygen atoms can be determined. The network of hydrogen bonds between crystallographic waters can be estimated by bioinformatic methods. As discussed in earlier chapter, the changes in the network of hydrogen bonds between water molecules could be investigated by neutron diffraction. Furthermore, the pH induces delicate rearrangements in the hydrogen bond network between water molecules in the active sites [8–11].

17.7 Conclusions

Full understanding of the correlations between the structure and thermodynamics of protein–ligand interactions is not yet possible. It is not clear why some ligands bind with highly enthalpy-dominating forces, while other structurally very similar compounds bind with highly entropy-dominating forces. However, structural crystallographic investigation of the high-affinity compounds bound to CA isoforms and arranged in matched molecular pairs that differ by a single functional group determining affinity and selectivity yielded several possible mechanisms such as perfect geometry and molecular trap. Compounds that bound similarly in matched molecular pairs (i.e., the orientation of the benzenesulfonamide ring was the same in both structures) exhibited decrease in the magnitude of enthalpy and increase in the magnitude of entropy in the driving of these binding reactions.

References

1. Klebe, G.: Applying thermodynamic profiling in lead finding and optimization. *Nat. Rev. Drug Discov.* **14**, 95–110 (2015)
2. Geschwindner, S., Ulander, J., Johansson, P.: Ligand binding thermodynamics in drug discovery: still a hot tip? *J. Med. Chem.* **58**, 6321–6335 (2015)
3. Claveria-Gimeno, R., Vega, S., Abian, O., Velazquez-Campoy, A.: A look at ligand binding thermodynamics in drug discovery. *Expert Opin. Drug Discov.* **12**, 363–377 (2017)
4. Freire, E.: Do enthalpy and entropy distinguish first in class from best in class? *Drug Discov. Today* **13**, 869–874 (2008)
5. Snyder, P.W., Lockett, M.R., Moustakas, D.T., Whitesides, G.M.: Is it the shape of the cavity, or the shape of the water in the cavity? *Eur. Phys. J. Spec. Top.* **223**, 853–891 (2013)
6. Smirnov, A., Zubrienė, A., Manakova, E., Gražulis, S., Matulis, D.: Crystal structure correlations with the intrinsic thermodynamics of human carbonic anhydrase inhibitor binding. *PeerJ* **6**, e4412 (2018)
7. Zubrienė, A., et al.: Intrinsic thermodynamics of 4-substituted-2,3,5,6-tetrafluorobenzenesulfonamide binding to carbonic anhydrases by isothermal titration calorimetry. *Bio-phys. Chem.* **205**, 51–65 (2015)
8. Fisher, Z., et al.: Neutron structure of human carbonic anhydrase II: a hydrogen-bonded water network “switch” is observed between pH 7.8 and 10.0. *Biochemistry* **50**, 9421–9423 (2011). PDB ID: 3TMJ
9. Michalczyk, R., et al.: Joint neutron crystallographic and nmr solution studies of tyr residue ionization and hydrogen bonding: implications for enzyme-mediated proton transfer. *Proc. Natl. Acad. Sci. U. S. A.* **112**, 5673–5678 (2015). PDB ID: 4Q49, 4Y0J
10. Kovalevsky, A., et al.: “To be or not to be” protonated: atomic details of human carbonic anhydrase-clinical drug complexes by neutron crystallography and simulation. *Structure* **26**, 383–390 (2018)
11. Aggarwal, M., et al.: Neutron structure of human carbonic anhydrase II in complex with methazolamide: mapping the solvent and hydrogen-bonding patterns of an effective clinical drug. *IUCrJ* **3**, 319–325 (2016)

Part IV

Biological Development of Lead Compounds Toward Drugs Targeting Carbonic Anhydrases



Efficacy of Novel CA IX Inhibitors in Biological Models

18

Justina Kazokaitė, Holger M. Becker, Harlan R. Barker,
Ashok Aspatwar, Seppo Parkkila, Ludwig J. Dubois,
and Daumantas Matulis

Abstract

Carbonic anhydrase (CA) IX belongs to a group of druggable targets which significantly affect cancer progression. Although many CA IX-targeting compounds have been reported, only a few sulfonamide derivatives progressed to clinical trials, and the results have been unfavorable, or unavailable, so far. Therefore, the design of different, more efficient CA IX-targeting inhibitors and their clinical benefits to patients are relevant issues to be studied. Here, the novel fluorinated benzenesulfonamides VD11-4-2, VD12-09, and VR16-09 were investigated in three different biological model systems, such as zebrafish embryos/larvae, *Xenopus laevis* oocytes, and human cancer cells. The results discussed in this chapter confirm that newly designed CA IX inhibitors are suitable for further development directed towards CA IX-specific anti-cancer therapy.

J. Kazokaitė · D. Matulis (✉)

Department of Biothermodynamics and Drug Design, Institute of Biotechnology,
Life Sciences Center, Vilnius University, Vilnius, Lithuania
e-mail: kazokaite@ibt.lt; matulis@ibt.lt

H. M. Becker

Department of Physiological Chemistry, University of Veterinary Medicine Hannover,
Hannover, Germany
e-mail: holger.becker@tiho-hannover.de

H. R. Barker · A. Aspatwar · S. Parkkila

Faculty of Medicine and Life Sciences, University of Tampere, Tampere, Finland
e-mail: harlan.barker@tuni.fi; ashok.aspatwar@tuni.fi; seppo.parkkila@tuni.fi

L. J. Dubois

Department of Precision Medicine, The M-Lab, GROW - School for Oncology and
Developmental Biology, Maastricht University Medical Centre, Maastricht, The Netherlands
e-mail: ludwig.dubois@maastrichtuniversity.nl

18.1 Introduction

Drug development follows a well-defined path. It is comprised of several steps, such as target validation, lead identification and optimization, preclinical testing, clinical trials, and marketing (Fig. 18.1). This process is highly regulated by national and international agencies for drug regulation and can take over 15 years and have a cost of \$2.6 billion per drug launch, as recently estimated [1].

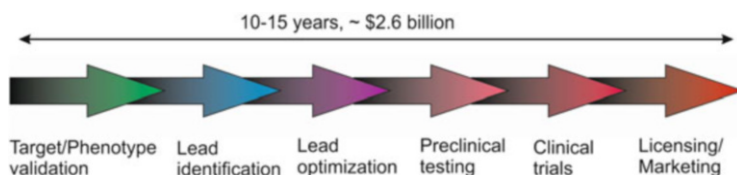


Fig. 18.1 A scheme representing the major steps of drug development

pH-modulating proteins have emerged as promising targets for cancer therapy [2]. Hypoxia, present in almost all solid tumors, significantly affects regulation of gene expression, thereby leading to a vast production and accumulation of lactate, H^+ , and CO_2 . These metabolites can compromise cellular pH homeostasis.

Several pH-regulatory proteins are essential to maintain the cellular acid–base balance in hypoxic cancer cells (Fig. 18.2). These proteins are responsible for H^+ extrusion and buffering of the intracellular pH (pH_i). The efflux of H^+ is carried

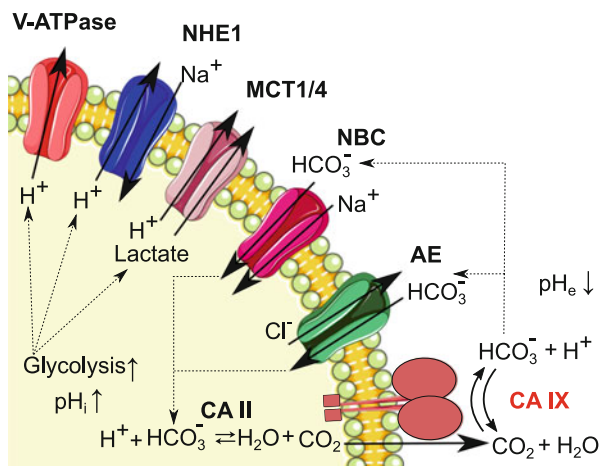


Fig. 18.2 A schematic model of major proteins involved in pH regulation (drawn not to scale). V-ATPase–vacuolar-type H^+ -adenosine triphosphatase, NHE1– Na^+/H^+ exchanger 1, MCT1/4–monocarboxylate transporter 1/4, NBC– Na^+/HCO_3^- co-transporter, AE–anion exchanger, CA IX–carbonic anhydrase IX, and CA II–carbonic anhydrase II

out by membrane-bound monocarboxylate transporters (MCTs), Na^+/H^+ exchangers (NHEs), and vacuolar-type H^+ -adenosine triphosphatases (V-ATPases) [3]. Carbonic anhydrases (CAs) belong to another important family of pH-regulatory enzymes. They catalyze the reversible hydration of CO_2 to HCO_3^- and H^+ ($\text{CO}_2 + \text{H}_2\text{O} \rightleftharpoons \text{HCO}_3^- + \text{H}^+$). There are twelve catalytically active human CA isoforms and three non-catalytic CA-related proteins (CARPs), both are linked with diverse physiological processes and diseases [4]. Among this family of proteins, the membrane-anchored CA IX has been associated with cancer progression due to its unique expression pattern. CA IX is only found in a handful of normal tissues [5], whereas CA IX is overexpressed in a broad spectrum of hypoxic tumors [6]. The extracellular catalytic domain of CA IX is responsible for the catalysis of CO_2 hydration to HCO_3^- and H^+ . Thus, a concentration gradient of CO_2 is created, enabling passive diffusion of CO_2 across the membrane. CA IX-produced H^+ ions increase extracellular acidification, contributing to an invasive tumor phenotype [7]. Moreover, HCO_3^- ions are transported into the cell via $\text{Na}^+/\text{HCO}_3^-$ co-transporters (NBCs) and anion exchangers (AEs) to alkalize pH_i and thereby promote cell survival [3, 8–10].

The interplay of enzymes involved in pH modulation is critical for tumor growth and therapeutic resistance. Therefore, pH regulators have become promising targets for cancer therapy. In the last decade, several chemical molecules and antibodies which bind MCT1, V-ATPase, or CA IX in tumor cells have been developed and are at various stages of clinical development (Table 18.1).

Recently, an alternative approach has been proposed which focuses on the simultaneous targeting of several proteins involved in H^+ flux. The combination of V-ATPase inhibitor lansoprazole with diverse CA IX inhibitors, such as the sulfamate S4 or the ureido-sulfamate derivative FC9-399A, was shown to be more promising than treatments with individual compounds in human melanoma cells [11]. However, the synergistic effects of NHE1 and CA IX combined knockout were

Table 18.1 Clinical trials of drug candidates targeting MCT1, V-ATPase, or CA IX

Target	Compound	Type of cancer	Phase	Identifier
MCT1	AZD3965	Solid tumors, prostate cancer, gastric cancer, diffuse large B cell lymphoma	Phase I	NCT01791595
V-ATPase	Esomeprazole	Esophageal cancer	Phase III	NCT00357682
		Breast cancer	Phase I	NCT00849329
	Pantoprazole	Prostate cancer	Phase II	NCT01748500
		Solid tumors	Phase I	NCT01163903
	Omeprazole	Colorectal cancer	Phase II	NCT02518373
		Breast cancer	Phase II	NCT01069081
CA IX	SLC-0111	Solid tumors	Phase I	NCT02215850
	SLC-0111	Metastatic pancreatic ductal adenocarcinoma	Phases I and II	NCT03450018
	3ee9-MMAE	Solid tumors	Phase I	NCT01028755

not determined *in vivo*, potentially due to the increase in CA XII expression, as a compensatory pH-regulating protein [12].

In conclusion, tumor acidosis is relevant for anti-cancer drug discovery and development. Key pH-regulatory proteins have become clinically important targets. However, deeper knowledge of the molecular basis of pH-dependent cell behavior could provide more profound for improved cancer treatment and patient outcomes.

18.2 Overview of CA IX

CA IX, originally called MN, was discovered as a tumor-associated antigen in 1992 using the monoclonal antibody (mAb) M75 [13]. This study was followed by the analysis of the CA IX cDNA [14] and gene [15] sequences. The results revealed a highly conserved CA catalytic domain. Therefore, MN was classified as the ninth member of CA family and renamed to CA IX. Another group found an antigen of renal cancer, termed G250 [16], it was later shown to be CA IX [17].

Mature CA IX is composed of several domains, such as a N-terminal proteoglycan-like (PG) domain, a conserved CA catalytic domain, a hydrophobic membrane-spanning helix, and a cytoplasmic tail at the C-terminus [15]. The PG domain features high conformational flexibility [18] and is a distinctive feature of CA IX because it is absent within other human CA isoforms. Thus, a selective detection of CA IX among other CAs can be accomplished through the application of mAb M75, which binds to a repetitive epitope in the PG domain [19]. The cytoplasmic tail of CA IX has three phosphorylation sites. They are significant for signaling and regulation of enzymatic activity [20, 21]. The expression of a shorter CA IX has also been reported as a consequence of alternative splicing [22, 23]. The crystal structure of recombinant CA IX supports a homodimeric configuration with two monomeric catalytic domains stabilized via an intermolecular disulfide bond [24].

The expression pattern of CA IX highlights its potential to be a cancer-specific target. In normal tissues, CA IX is only found in the epithelia of the gastrointestinal tract [5]. However, CA IX is strongly overexpressed in a wide range of solid tumors including malignancies of the brain, kidney, colon, head and neck, lung, breast, esophagus, ovary, and liver [6, 25, 26]. Transcription of the *CA9* gene can be induced by hypoxia [27] or other pathways [28–31]. Alternatively, CA IX also exists as a shed ectodomain (ECD) composed of CA catalytic and PG domains, which is formed after cleavage by metalloproteinases, such as TACE/ADAM17 [32]. ECD circulates in the serum and/or plasma of patients [33] and thus can be used for prognostic applications, but its clinical significance is inconclusive so far [34–37].

The important role of CA IX has been confirmed by *in vitro* and *in vivo* studies, which are listed in this paragraph. They have indicated that depletion of CA IX enzymatic activity or its expression leads to decreased cell viability and attenuated primary tumor growth. CA IX-selective inhibitors have reduced extracellular acidification [38, 39] or caused intracellular acidification [40] under hypoxic conditions, thereby increasing cell death. Clonogenic cell survival has been decreased after the depletion of CA IX via RNA interference [41]. In mouse models, the growth rates

of tumor xenografts have been reduced when the *CA9* gene was knocked down via short hairpin RNAs [42–44] or knocked out using the CRISPR–Cas9 system [12]. Furthermore, CA IX has been linked with several stem cell markers [45]. The inhibition of CA IX has been reported to reduce the expansion of cancer stem cells and thereby diminish tumor growth and metastasis formation [46]. Interestingly, the upregulation of CA XII after CA IX knockdown has been demonstrated [12, 42, 43], suggesting the cross-talk between CAs to maintain pH homeostasis.

Upon tumor cell migration, CA IX is involved in the maintenance of pH gradients inside and outside the cell. Recent studies have indicated that CA IX is localized in lamellipodia where it promotes migration via H^+ production, enhances bicarbonate uptake through interaction with specific transporters [47], and regulates collagen degradation mediated by matrix metalloproteinase isoform 14 [48]. Moreover, CA IX competes with E-cadherin for binding with β -catenin, causing the detachment of E-cadherin from the cytoskeleton, and thus supports cell motility [49]. CA IX has also been associated with several signaling pathways [20, 50, 51] which can influence migration rates. The invasiveness of cancer cells in vitro and in vivo has been reduced after elimination of CA IX via selective inhibitors or gene silencing methods [44, 48, 52, 53].

18.3 Novel CA IX Inhibitors

The modulation of catalytic activities of human CA isozymes has been widely investigated [54] with five different mechanisms of CA inhibition determined so far [55]. The aim of these human CA studies is to discover compounds exhibiting high affinity towards pathology-linked CAs and low affinity towards other CA isoforms. However, the design of CA-selective compounds is a challenging task because of the high structural homology among human CA isoforms, as shown in Fig. 18.3 [56].

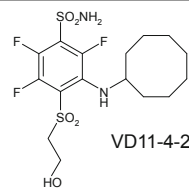
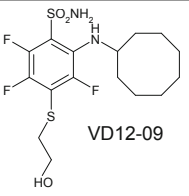
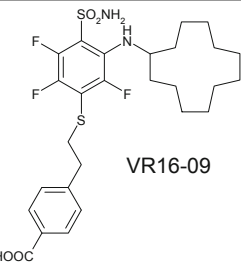
Here, research interest is focused on the derivatives of primary sulfonamides as classical CA inhibitors [57]. Three fluorinated benzenesulfonamides, named

Fig. 18.3 Overlay of available structures of catalytically active human CA monomers. PDB IDs: 1HCB for CA I (yellow), 3KS3 for CA II (green), 1Z93 for CA III (magenta), 1ZNC for CA IV (blue), 3FE4 for CA VI (orange), 3ML5 for CA VII (gray), 3IAI for CA IX (red), 1JCZ for CA XII (dark green), 3D0N for CA XIII (black), and 4LU3 for CA XIV (cyan)



VD11-4-2, VD12-09, and VR16-09, as lead CA IX inhibitors have been designed. Enzymatic and biophysical approaches confirmed that these compounds are strong binders and selective inhibitors of recombinant CA IX [58, 59]. Binding and inhibition affinities of inhibitors are shown in Table 18.2. For further development, studies applying zebrafish embryos/larvae [60], *Xenopus* oocytes [61], and human cancer cells [58] were carried out to confirm efficacy of novel lead CA IX inhibitors.

Table 18.2 Binding and inhibition affinities of novel lead CA IX-selective inhibitors

CA isoform	K_d (K_i), nM		
	 VD11-4-2	 VD12-09	 VR16-09
CA I	710	50,000	≥200,000
CA II	60	1,300	≥200,000
CA III	40,000	≥200,000	≥200,000
CA IV	25	1,700	≥200,000
CA VA	2,500	3,300	≥200,000
CA VB	5.6	210	45,000
CA VI	95	4,300	≥200,000
CA VII	9.8	330	37,000
CA IX	0.05 (<10)	1.1 (<5)	0.16 (<1)
CA XII	3.3	330	710
CA XIII	3.6	140	20
CA XIV	1.6	170	170

The dissociation constants (K_d) of VD11-4-2, VD12-09, and VR16-09 for the binding with twelve human recombinant CA isoforms were determined by fluorescent thermal shift assay (pH 7.0, extrapolated to 37 °C). The inhibition constants (K_i) evaluated by stopped-flow kinetic inhibition assay (pH 7.5, 25 °C) are shown in the parentheses. The synthesis, binding, and inhibition profiles of compounds VD11-4-2, VD12-09, and VR16-09 were previously published [58, 59]. The standard error of K_d measurements is ± 2 times

18.4 Toxic Effects of the CA IX Inhibitors on Zebrafish Embryos/larvae

The zebrafish has emerged as a versatile tool for human drug discovery [62]. For toxicological studies, zebrafish as a model system has been applied for over 60 years [63, 64]. Zebrafish exhibits numerous advantages, including transparency of embryo and larva, regenerative capacity, high fecundity, external fertilization, rapid develop-

ment, and they are relatively easy to maintain. Furthermore, zebrafish offers lower experimental costs and compound consumption compared with other animal models [65]. Despite the lack of a few mammalian organs, zebrafish shares a highly conserved, but not absolutely identical, physiology and anatomy with mammals [62].

Screening of CA inhibitors in zebrafish is a relatively novel scientific subject. The treatment of zebrafish with the membrane-impermeable human CA inhibitor F3500 was reported in 2009 for the first time [66]. Phenotypic abnormalities of zebrafish caused by acetazolamide, a non-selective CA inhibitor, were thereafter published [67], followed by several studies of zebrafish developmental toxicity induced by a handful of CA inhibitors [68,69]. Subsequently, the roles of zebrafish CA isozymes, including acatalytic CAs [70,71], CA II [72,73], and CA VI [74], were investigated during zebrafish embryonic development using gene silencing methods. In these studies, knockout/knockdown of CAs showed effect on phenotypes of zebrafish larvae giving insights into the structural and biological functions of these CAs in organisms.

The toxicological screening of the novel CA IX inhibitors VD11-4-2 and VD12-09 was performed employing over 2,300 zebrafish embryos. According to the survival rate, the half-maximal lethal concentration (LC_{50}) for each compound was determined using the sigmoidal dose-response Hill model. The results showed dose-dependent lethal effects of VD11-4-2, VD12-09, and ethoxzolamide (EZA), a non-selective CA inhibitor, on the development of 24–120h post-fertilized (hpf) zebrafish larvae (Fig. 18.4). Compounds VD12-09 and EZA exhibited similar impacts on mortality of zebrafish larvae (LC_{50} values were 13 and 9 μM , respectively). Inhibitor VD11-4-2 possessed the highest LC_{50} value (120 μM) among the tested compounds, showing tenfold lower capacity for inducing mortality of zebrafish larvae than EZA. The steepness of dose-response curves in this study can be compared with those of the recent exploration on the toxicity of anti-cancer compounds in zebrafish [75], suggesting that the investigated inhibitors may exhibit lower excretion or cause severe effects on multiple organ systems.

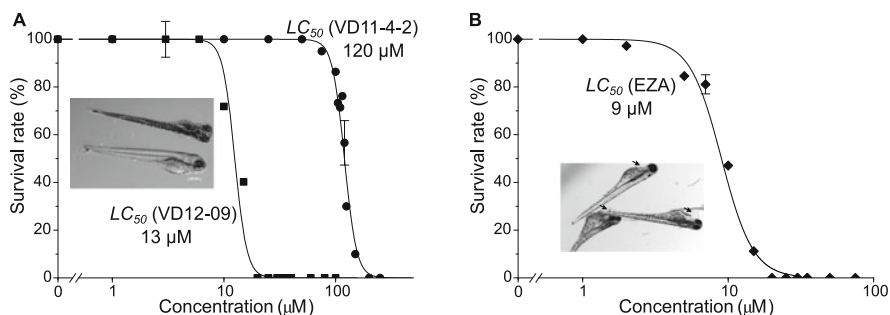


Fig. 18.4 Effect of inhibitor dose on zebrafish larval survival. Three inhibitors were applied: (a) VD11-4-2 (filled circle), VD12-09 (filled square); (b) EZA. Data points were obtained experimentally, while the solid lines were simulated according to the Hill model (Hill coefficient 4–8). Insets show zebrafish larvae after 5 days treatment with 100 μM VD11-4-2 (a) or 10 μM EZA (b). Arrows in the inset of panel (b) indicate pericardial edema

Analyses using light microscopy showed abnormalities in the phenotypes of zebrafish larvae to be less severe when treated with inhibitors VD11-4-2 or VD12-09 than EZA, as shown in the insets of Fig. 18.4. No phenotypic defects in the zebrafish larvae were detected after treatment with VD compounds (Fig. 18.4a). However, zebrafish larvae treated with EZA exhibited developmental abnormalities, such as pericardial edema, unutilized yolk sac, and abnormal body shape (Fig. 18.4b). Histochemical analysis did not reveal any apparent morphological changes to the tissues or internal organs of zebrafish larvae treated with the studied inhibitors compared with the DMSO-treated and untreated wild-type zebrafish. To summarize, both VD11-4-2 and VD12-09 caused lower toxicity than EZA in zebrafish larvae and therefore were suitable for further development.

18.5 Affinity and Selectivity Properties of the CA IX Inhibitors in *Xenopus* Oocytes

The clawed frog *Xenopus laevis* (*X. laevis*) is originally from South Africa. Until the 1960s, *X. laevis* was applied for the rapid diagnosis of early pregnancy [76]. Nowadays, *Xenopus* oocytes are often employed as a model system due to its many advantages, such as easy manipulations because of big cell size (1.1 mm to 1.3 mm), convenient laboratory maintenance, and a large number of offspring [77].

Structural and functional properties of eukaryotic proteins can be studied using *Xenopus* oocytes. Efficient transcription and translation of exogenous nucleic acid into protein are enabled by nuclear injections of cDNA, or mostly by cytoplasmic injections of in vitro synthesized cRNA [78]. Oocytes in developmental stages IV to VI are applied in molecular and physiological research because they feature the highest translational capacity [79]. Importantly, the activities of endogenous ion channels and membrane transporters are low in oocytes [80]. Thus, measurements in oocytes are affected by endogenous proteins, thereby emphasizing oocytes to be a convenient model system for a broad variety of biological and biochemical applications.

The absence of CA activity in native *Xenopus* oocytes has been previously noted [81]. Therefore, injecting oocytes with cRNA coding for particular human CA isoforms allows for expression of those CAs. This gives the opportunity for further investigations, in particular protein–protein interactions and selective inhibition. Several studies on targeting heterologous CA isoforms in oocytes have been reported, as discussed further below. CA inhibition was monitored with micro-electrodes by measuring the pH in the cytosol and at the outer membrane surface, and was subsequently confirmed by gas-analysis mass spectrometry (MS) [77]. The significant inhibitory properties of 10–30 μM EZA against heterologous CA II [82], CA IV [83], and CA IX [84] have been described in oocytes. Furthermore, oocytes have been used to reveal that heterologous CA II [85], CA IV [86], and CA IX [87] possess non-catalytic functions linked with the ability to increase lactate flux via interactions with monocarboxylate transporters. This non-catalytic function was unaffected by CA inhibitor EZA. Based on the listed observations, *Xenopus* oocytes

are promising models to study the roles of CAs and characterize the affinity and selectivity of CA inhibitors in a live eukaryotic cell with a fully matured target CA isozyme.

Recently, two different subcellular localizations have been shown for heterologous CA IX in *Xenopus* oocytes: ~80% intracellular and ~20% membrane-bound, with extracellular enzymatic activity [84]. Therefore, the novel inhibitors VD11-4-2 and VD12-09 were tested in native oocytes lacking CA activity and oocytes injected with CA IX-cRNA or CA II-cRNA. The rate of change in the intracellular $[H^+]$ ($\Delta[H^+]_i/\Delta t$) was measured with pH-sensitive microelectrodes. In comparison with native oocytes (25.4 ± 2.9 nM/min; Fig. 18.5c), the rate of acidification increased for both CA IX (82.0 ± 8.8 nM/min; Fig. 18.5b, e) and CA II (137.5 ± 14.7 nM/min; Fig. 18.5a, d) expressing oocytes. The effect of $10 \mu\text{M}$ VD11-4-2 on $\Delta[H^+]_i/\Delta t$ induced by heterologous CA II in oocytes was negligible (Fig. 18.5a, d). In CA IX-expressing oocytes, $\Delta[H^+]_i/\Delta t$ was reduced from 82.0 ± 8.8 to 20.3 ± 3.5 nM/min by $10 \mu\text{M}$ VD11-4-2 (Fig. 18.5e). This value matched the rate of 20.2 ± 1.4 nM/min measured in native cells when they were treated with the same dose of VD11-4-2 (Fig. 18.5c). Moreover, VD11-4-2 was not washable from CA IX after 15 and 45 min ($\Delta[H^+]_i/\Delta t$ were 26.4 ± 2.9 and 27.7 ± 3.5 nM/min, respectively). Thus, VD11-4-2 was demonstrated to be a membrane-permeable inhibitor that completely blocked the CA IX-generated rate of acidification at $10 \mu\text{M}$ in *Xenopus* oocytes.

The inhibitor VD12-09 was also studied in oocytes with heterologous CA II or CA IX isoforms. The $\Delta[H^+]_i/\Delta t$ was not influenced by $10 \mu\text{M}$ VD12-09 in CA II-expressing cells (Fig. 18.5f), whereas $\Delta[H^+]_i/\Delta t$ was reduced by $10 \mu\text{M}$ VD12-09 in CA IX-expressing cells, from 87.5 ± 17.8 to 40.6 ± 6.9 nM/min (Fig. 18.5g). Even though VD12-09 was selective against CA IX as compared with CA II, the CA IX inhibition effect was lower than that of $10 \mu\text{M}$ VD11-4-2. Thus, VD12-09 was not investigated further in oocytes.

According to crystallographic analysis, mature CA IX is a transmembrane protein displaying extracellular catalytic activity [24]. The impact of $10 \mu\text{M}$ VD11-4-2 on the extracellular activity of CA IX was determined in *Xenopus* oocytes by measuring extracellular $[H^+]$ at the outer membrane surface ($[H^+]_s$) using pH-sensitive microelectrodes (Fig. 18.6a). A transient decrease in $[H^+]_s$ was induced by the addition of $\text{CO}_2/\text{HCO}_3^-$ and an increase of $[H^+]_s$ was caused by removal of $\text{CO}_2/\text{HCO}_3^-$. The extracellular CA IX activity was evaluated by the amplitude of $\Delta[H^+]_s$ during the removal of $\text{CO}_2/\text{HCO}_3^-$. In the absence of inhibitors, $\Delta[H^+]_s$ was determined to be 15.6 ± 0.4 nM/min in native cells (Fig. 18.6b), which increased to 63.0 ± 3.1 nM/min in CA IX-expressing oocytes (Fig. 18.6a, c). The amplitude of the acid transient decreased to 22.1 ± 0.7 nM/min by $10 \mu\text{M}$ VD11-4-2 (Fig. 18.6a, c). This $\Delta[H^+]_s$ correlated with $\Delta[H^+]_i$ obtained in native cells after exposure to the same dose of VD11-4-2 (14.5 ± 0.5 nM/min, Fig. 18.6b). In line with the results of measuring intracellular pH, the interaction between heterologous extracellular CA IX and VD11-4-2 indicated high affinity and was determined to be essentially irreversible, with a $\Delta[H^+]_s$ of 34.0 ± 6.0 nM/min after 15 min of washing out (Fig. 18.6a, c).

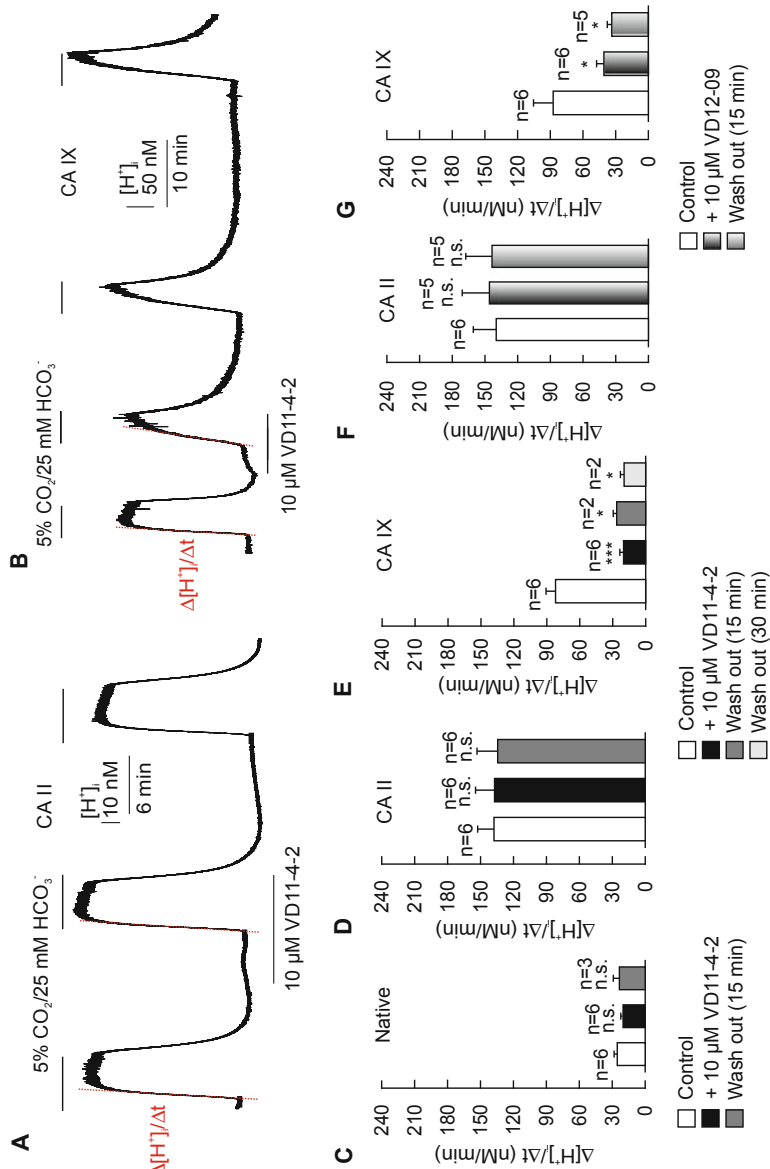


Fig. 18.5 Measurements of the rate of cytosolic H⁺ changes in *Xenopus* oocytes expressing target CA isoform (a, b, d–g) and native *Xenopus* oocytes (c). Cells were injected with CA II-cRNA (a, d, e and f) or CA IX-cRNA (b, e, and g) during application of CO₂/HCO₃⁻ (from a normally CO₂-free, HEPES-buffered solution) in the absence and presence of 10 μM VD11-4-2 or 10 μM VD12-09 and after 15 or 45 min of washing out. Red lines represent slopes which were used for the evaluation of Δ[H⁺]_i/Δt. Asterisks indicate significant difference in CA activity before and after addition of inhibitor and after washing it out (*p < 0.05, ***p < 0.001)

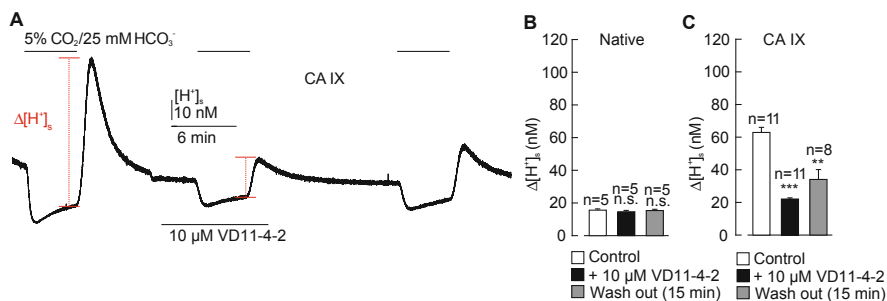


Fig. 18.6 Measurements of $[H^+]_s$ changes in *Xenopus* oocytes injected with CA IX-cRNA (a and c) and uninjected (native) oocytes (b) during application of CO_2/HCO_3^- (from a nominally CO_2 -free, Hepes-buffered solution) in the absence and in the presence of $10\ \mu M$ VD11-4-2 and after 15 min of washing out. Red lines represent amplitudes which were used for the evaluation of $\Delta[H^+]_s$. Asterisks indicate difference between CA activity before and after addition of inhibitor and after washing it out (** $p < 0.01$, *** $p < 0.001$)

Dose-response curves were determined for changes in the intracellular (Fig. 18.7a) and extracellular (Fig. 18.7b) CA IX activity, as a function on VD11-4-2 concentration. CA IX-expressing oocytes were treated with tenfold increasing doses of VD11-4-2 and $\Delta[H^+]_i/\Delta t$ (Fig. 18.7a) or $\Delta[H^+]_s$ (Fig. 18.7b) were measured. Half-maximal inhibitory concentrations (IC_{50}) for VD11-4-2 were determined using the sigmoidal dose-response Hill model. The IC_{50} of inhibiting intracellular CA IX by VD11-4-2 was found to be $15\ nM$ (Fig. 18.7a). This result was consistent with IC_{50} of $25\ nM$ for inhibition of extracellular CA IX by VD11-4-2 (Fig. 18.7b). Thus, VD11-4-2 exhibited high inhibitory potential towards both heterologous intracellular and extracellular CA IX in *Xenopus* oocytes.

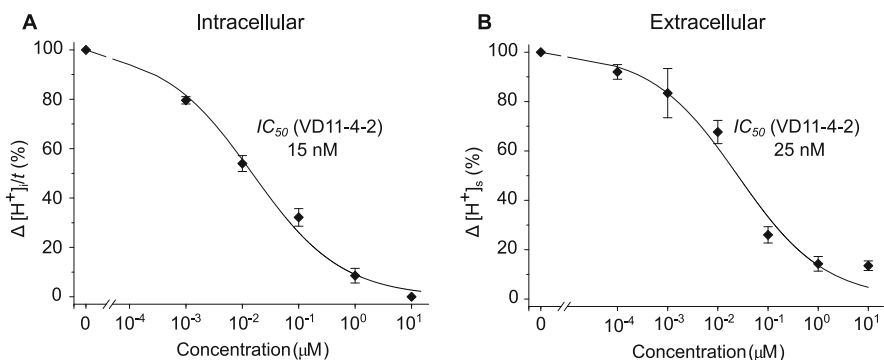


Fig. 18.7 The dependence of changes in $[H^+]_i/t$ (a) and $[H^+]_s$ (b) on the concentration of inhibitor VD11-4-2. Black data points were obtained experimentally, while solid lines were simulated according to the Hill model (Hill coefficient 0.5)

Two other extracellular heterologous CAs, CA IV and CA XII (Fig. 18.8), were involved in this study using *Xenopus* oocytes to evaluate selectivity of VD11-4-2 towards CA IX. The activities of CA IV or CA XII were not significantly

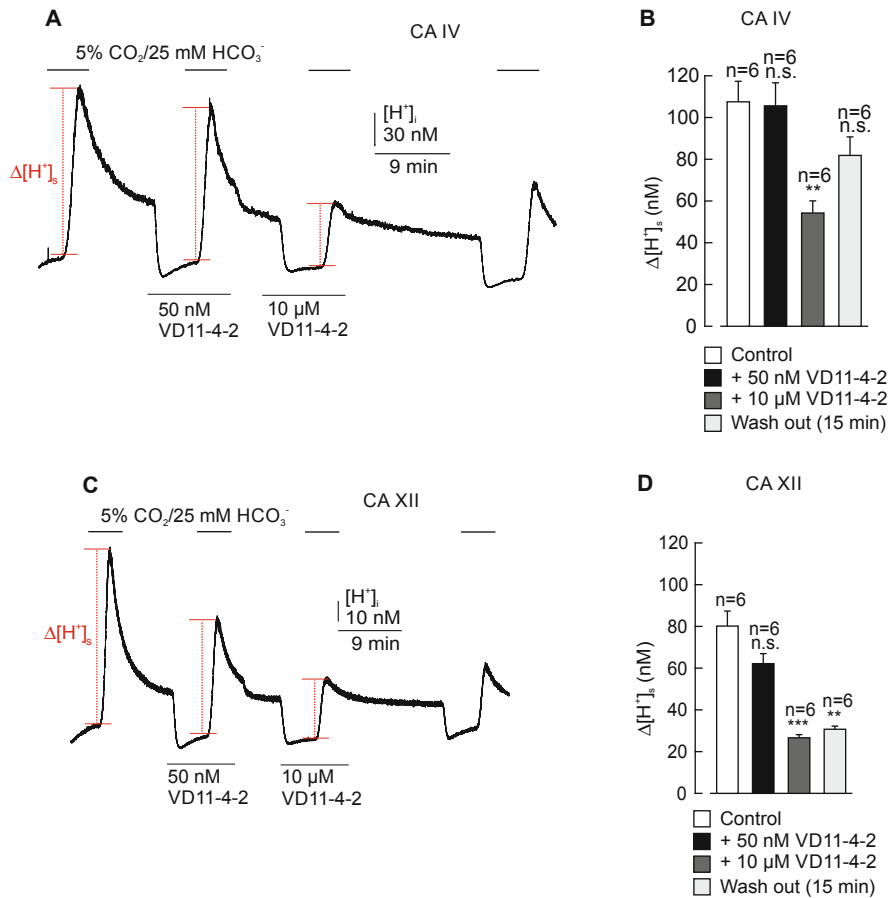


Fig. 18.8 Measurements of $[H^+]_i$ in oocytes injected with 1 ng CA IV-cRNA (a and b) or 5 ng CA XII-cRNA (c and d) during application of CO_2/HCO_3^- (from a nominally CO_2 -free, HEPES-buffered solution) in the absence and presence of 50 nM and 10 μ M VD11-4-2 and after 15 min of washing out. Asterisks indicate significant difference between CA activity before and after addition of inhibitor and after washing it out (** $p < 0.01$, *** $p < 0.001$)

affected by 50 nM VD11-4-2, while 10 μ M VD11-4-2 significantly reduced $\Delta[H^+]_i$, to 54.3 ± 5.7 and 26.5 ± 1.4 nM/min in oocytes expressing CA IV and CA XII, respectively (the rate of 20.2 ± 1.4 nM/min measured in native cells). Furthermore, VD11-4-2 was found to be washable for CA IV, while non-washable for CA XII. This result supports the conclusion that at nanomolar levels VD11-4-2 is highly selective for CA IX, but not CA II, CA IV, or CA XII.

The high affinity of VD11-4-2 against heterologous CA IX in *Xenopus* oocytes was confirmed by mass spectrometry (MS). This method is based on following the ^{18}O depletion of doubly labeled $^{13}C^{18}O_2$ through several hydration and dehydration steps of CO_2 and HCO_3^- [82, 88]. Three isotopic CO_2 species can be generated

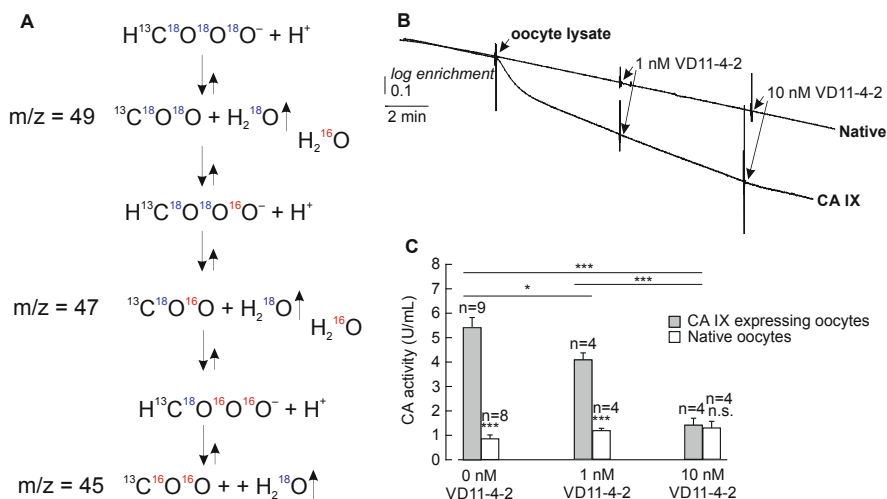


Fig. 18.9 Inhibition of heterologous CA IX in oocytes as determined by MS. **(a)** Reactions of ^{18}O exchange from doubly labeled $^{13}\text{C}^{18}\text{O}_2$ ($m/z = 49$) to $^{13}\text{C}^{16}\text{O}_2$ ($m/z = 45$) and H_2^{18}O . **(b)** Recordings of the degradation of ^{18}O -labeled CO_2 . **(c)** Evaluations of CA IX activity in the absence and presence of 1 and 10 nM VD11-4-2 in lysed oocytes. The addition of oocyte lysate made from 20 cells and different concentrations of VD11-4-2 are shown by arrows. In panel **(c)**, asterisks in the upper part of the graph indicate a significant difference between CA activity before and after addition of inhibitor using CA IX-expressing oocytes, while asterisks above the bars show a difference between CA activity in native and CA IX-expressing oocytes when applying the same dose of inhibitor (* $p < 0.05$, *** $p < 0.001$)

depending on the mass-to-charge ratio (m/z) (Fig. 18.9a). For the calculation of CA activity, the rate of ^{18}O depletion is evaluated and compared with the corresponding rate of the non-catalyzed reaction, as defined previously [89]. In this work, the total activity of intracellular and extracellular CA IX was decreased by $\sim 25\%$ using 1 nM VD11-4-2 in lysate of oocytes expressing CA IX (Fig. 18.9b, c). Moreover, complete inhibition of CA IX activity was measured using 10 nM VD11-4-2 as compared with results when the lysate of native cells were treated with the same dose of VD11-4-2 using same setup. Therefore, the characterization of VD11-4-2 activity by MS confirmed the outcome from intracellular and extracellular pH measurements revealing the nanomolar affinity of VD11-4-2 against heterologous CA IX in *Xenopus* oocytes.

18.6 Functional Activities of the CA IX Inhibitors in Human Cancer Cells

Human cancer cells are essential in vitro models in cancer research for diverse applications, including anti-cancer drug development. Here, functional activities of the inhibitors VD11-4-2, VD12-09, and VR16-09 were determined in a panel of

human cancer cell lines exhibiting increased expression of CA IX under hypoxic (0.2% O₂) conditions: A549 (lung), MDA-MB-231 (breast), H460 (lung), and HeLa (cervical).

First, compounds were evaluated by MS for their inhibitory potential of the total extracellular CA catalytic activity in hypoxic MDA-MB-231 cells. As in experiments with *Xenopus* oocytes, the rate of the CO₂/HCO₃⁻ hydration/dehydration reaction via ¹⁸O depletion from ¹³C¹⁸O₂ was determined. Pre-incubation of the cell suspension with VR16-09, VD11-4-2, or VD12-09 resulted in a dose-dependent decrease in CA activity with IC₅₀ values of 1.29 ± 0.11 nM, 2.95 ± 0.69 nM, and 167.4 ± 1.3 nM, respectively (Fig. 18.10a–c).

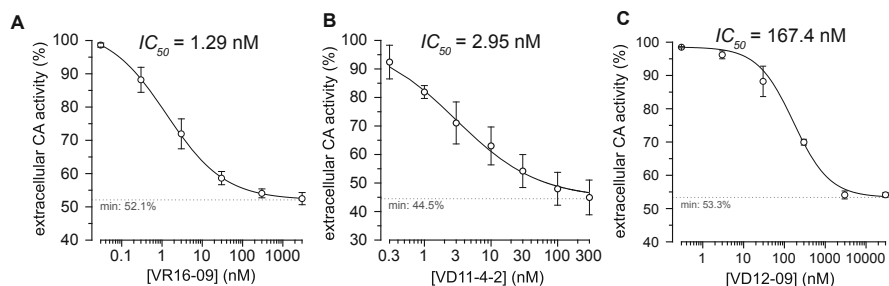


Fig. 18.10 Compound IC₅₀ evaluation representing inhibition capacity of total extracellular CA activity in hypoxic MDA-MB-231 cells as determined by MS. Cells were incubated under hypoxia (1% O₂) for 3 days and thereafter exposed to VR16-09 (a), VD11-4-2 (b), or VD12-09 (c) for up to 3 h. CA activity in the presence of inhibitor was normalized to the activity in the absence of inhibitor. Average ± SD of four independent experiments per cell line is shown

CA IX-selectivity of inhibitors was verified via MS using HeLa CA IX knockout (KO) cells. These cells were generated using CRISPR–Cas9 genome editing and selected according to Western blot analysis, followed by the genetic confirmation using single allele sequencing of KO-causing mutations in the CA9 gene in two alleles per clone. HeLa wild-type cells and two individual HeLa CA IX KO clones were treated with VR16-09 (300 nM), VD11-4-2 (300 nM), or VD12-09 (30 μM). These doses of compounds caused near maximum inhibition of extracellular CA activity in hypoxic MDA-MB-231 cells. The investigated inhibitors did not change the CA activity in either hypoxic HeLa CA IX KO clones (Fig. 18.11). However, considerable CA activity remained in hypoxic HeLa CA IX KO cells, emphasizing the activity of other extracellular CA isoforms. In HeLa wild-type cells, the tested inhibitors reduced CA activity to 30–40%. Similar CA activity was measured in untreated HeLa CA IX KO clones. Therefore, VR16-09, VD11-4-2, and VD12-09 selectively targeted CA IX in HeLa cells.

The functional activity of compounds was further confirmed by extracellular acidification assay measuring the rise in pH under normoxic conditions or directly inside a hypoxic chamber (Fig. 18.12a). An experimental scheme is shown in Fig. 18.12b. Cells were plated in 6 cm dishes and allowed to attach overnight in normoxia. The next day cells were exposed to inhibitors or DMSO for 72 h in

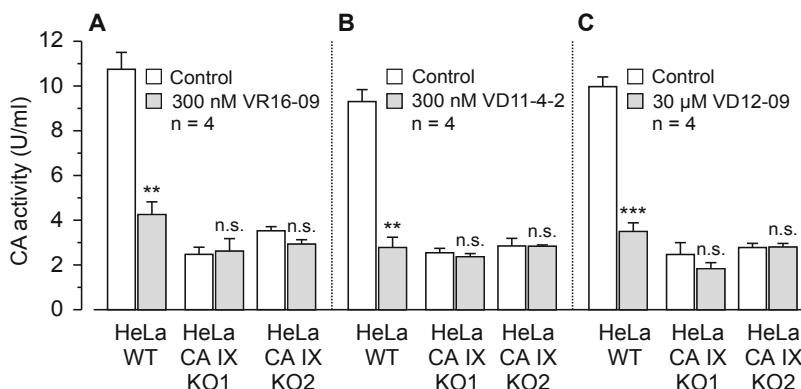


Fig. 18.11 CA IX-dependent mode of action for inhibitors in hypoxic HeLa cells. CA activity in HeLa wild-type and two HeLa CA IX KO clones before (white bars) and after addition of compound (gray bars) VR16-09 (a), VD11-4-2 (b), or VD12-09 (c) was determined by MS gas-analysis from the increase in the rate of log enrichment after addition of cell suspension. CA activity in the presence of inhibitor was normalized to the activity in the absence of inhibitor. Average \pm SD of four independent experiments per cell line is shown. Asterisks indicate significant difference between CA activity before and after addition of inhibitor (** $p < 0.01$, *** $p < 0.001$)

parallel under normoxic or hypoxic conditions and pH of the culture medium was measured at the end of each experiment. The results were evaluated as a difference between the pH of medium in the control plate (without seeded cells) and the pH of medium in the targeted plate (containing cells exposed to the compound or vehicle).

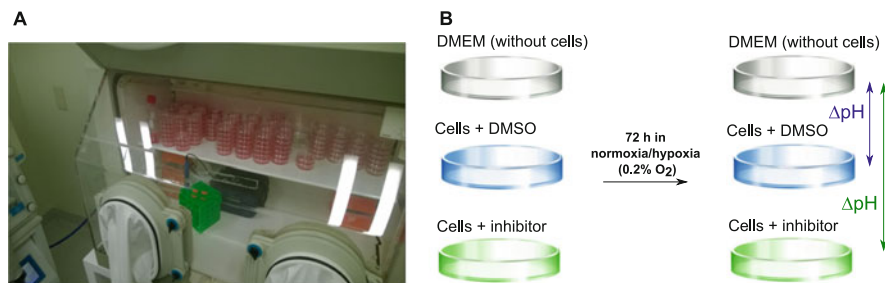


Fig. 18.12 Extracellular acidification assay. Experimental example representing hypoxic chamber (a) and experimental scheme (b)

Acidification in HeLa cells under hypoxic conditions was significantly reduced by VR16-09, VD11-4-2, and VD12-09 in a dose-dependent manner, while the impact on acidification of normoxic HeLa cells was negligible (Fig. 18.13). This functional activity was the most pronounced for VR16-09 at 50 μ M, whereas VD12-09 exhibited the lowest functional activity of the tested compounds in HeLa cells. Hypoxia-induced acidosis of three other cell lines was significantly reduced by 50 μ M VR16-09 (Fig. 18.14a) and 50 μ M VD11-4-2 (Fig. 18.14b). The extracellular

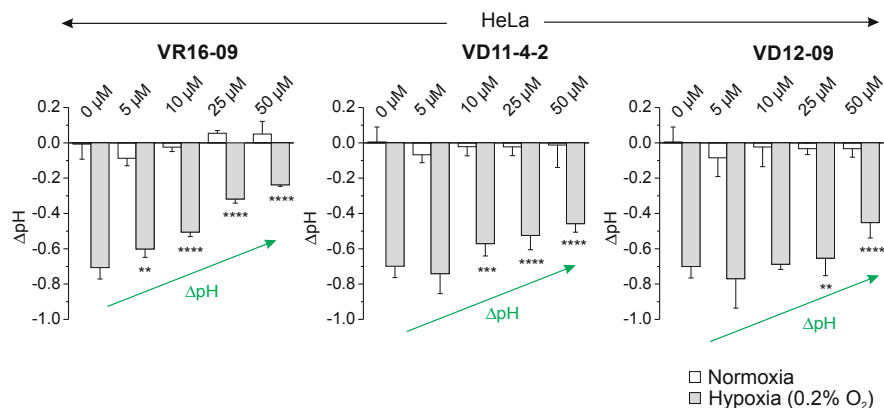


Fig. 18.13 Changes in extracellular acidification of HeLa cells after the treatment with VR16-09, VD11-4-2 or VD12-09 for 72 h under normoxia (21% O₂; white bars) or hypoxia (0.2% O₂; gray bars). Average \pm SD of at least three independent experiments is shown. Green arrows show the reduction of extracellular acidification under hypoxic conditions upon the application of increasing doses of each inhibitor. Asterisks indicate a significant difference between medium pH of cells exposed to DMSO and cells treated with various doses of inhibitor under hypoxic conditions (* p < 0.05, ** p < 0.01, *** p < 0.001, **** p < 0.0001)

pH of cells treated with DMSO and in parallel with 50 μM VR16-09 was elevated from 6.97 ± 0.06 to 7.44 ± 0.06 for HeLa, from 6.67 ± 0.13 to 7.19 ± 0.14 for H460, from 6.37 ± 0.11 to 6.83 ± 0.20 for MDA-MB-231, and from 6.70 ± 0.04 to 6.79 ± 0.07 for A549 cells. The inhibitor VD11-4-2 also significantly affected hypoxic acidification. The exposure of cells to 50 μM VD11-4-2 as compared with DMSO control caused an increase of pH from 6.97 ± 0.06 to 7.21 ± 0.05 for HeLa, from 6.67 ± 0.13 to 6.84 ± 0.14 for H460, from 6.37 ± 0.11 to 6.63 ± 0.07 for MDA-MB-231, and from 6.70 ± 0.04 to 6.81 ± 0.03 for A549 cells.

The inhibitor-induced cytotoxicity was investigated by the Alamar blue cell viability assay. Response to treatments was quantified by determining concentration of inhibitor which leads to half-maximum viability response (EC_{50}). When two-dimensional (2D) monolayer cells were employed, inhibitors VR16-09, VD11-4-2, and VD12-09 were more effective in reducing viability of normoxic cells without or with significantly lower CA IX expression than hypoxic CA IX-expressing cells. Therefore, cytotoxic ratios of selectivity to hypoxia for inhibitors were lower than 1 (Table 18.3). This result is in line with the previously published cytotoxicity profiles of several CA IX inhibitors, including SLC-0111 [90], sulfamate S4 [91], and dual-target derivatives [92]. These compounds were more cytotoxic under normoxic than hypoxic conditions, promoting a hypothesis for the relevance of inhibitor affinity towards CA XII. Since the upregulation of CA XII has been reported as a result of CA IX knockdown [12, 42, 43], new cellular models with both CA IX and CA XII KOs will be crucial to characterize CA IX- or CA XII-dependent activities of inhibitors.

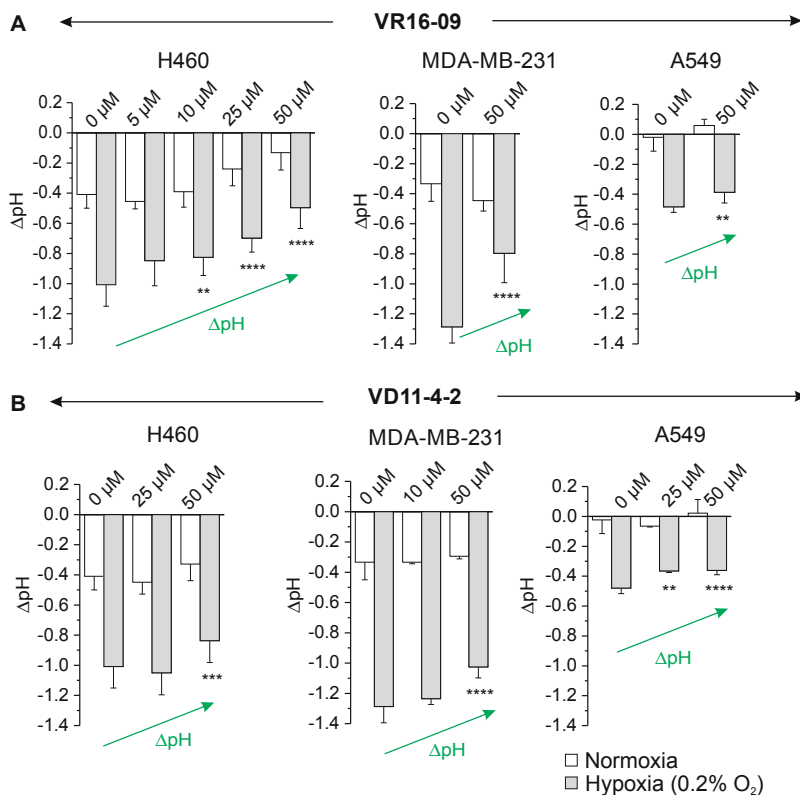


Fig. 18.14 Changes in extracellular acidification of H460, MDA-MB-231, and A549 cells after the treatment with VR16-09 (a) or VD11-4-2 (b) for 72 h under normoxia (21% O₂; white bars) or hypoxia (0.2% O₂; gray bars). Average \pm SD of at least three independent experiments is shown. Green arrows show the reduction of extracellular acidification under hypoxic conditions upon the application of increasing doses of inhibitor. Asterisks indicate significant difference between medium pH of cells exposed to DMSO and cells treated with various doses of inhibitor under hypoxic conditions (* $p < 0.05$, ** $p < 0.01$, *** $p < 0.001$, **** $p < 0.0001$)

Table 18.3 Cytotoxic ratios ($EC_{50,N}/EC_{50,H}$) of selectivity to hypoxia for inhibitors as determined by Alamar Blue assay

	VR16-09	VD11-4-2	VD12-09
HeLa	0.46 \pm 0.06	0.52 \pm 0.08	0.44 \pm 0.10
H460	0.49 \pm 0.04	0.48 \pm 0.05	0.46 \pm 0.09
A549	0.22 \pm 0.02	0.42 \pm 0.04	0.34 \pm 0.04
MDA-MB-231	0.88 \pm 0.03	0.83 \pm 0.08	0.82 \pm 0.09

The monolayer HeLa, H460, A549, and MDA-MB-231 cells were exposed to the compounds under normoxia (N, 21% O₂) or hypoxia (H, 0.2% O₂) for 72 h. The results of at least three independent repeats are shown (average \pm SD)

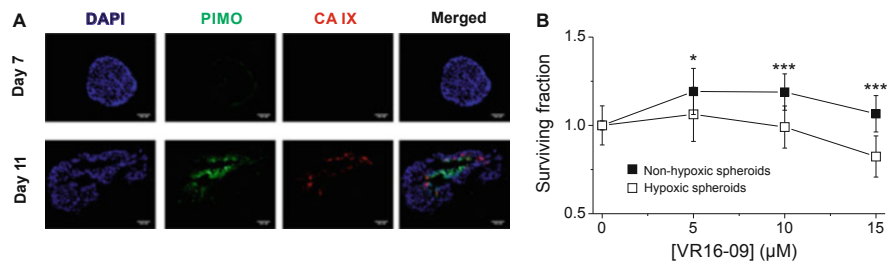


Fig. 18.15 The impact of VR16-09 on H460 spheroid clonogenic survival. **(a)** Immunofluorescence images of H460 spheroids stained for DAPI (blue), PIMO (green), and CA IX (red). The scale bar indicates 100 μM. **(b)** Survival of clonogenic cells derived from non-hypoxic (filled square) and hypoxic (open square) H460 spheroids exposed to VR16-09 for 24 h on day 4 or day 11, respectively. Single cell suspensions were prepared and cells were plated and allowed to form colonies which thereafter were quantified. Asterisks indicate statistically significant differences between the surviving fractions of clonogenic cells derived from normoxic or hypoxic spheroids after exposure to the same dose of inhibitor ($*p < 0.05$, $***p < 0.001$)

To determine the hypoxia-dependent efficacy of the compounds, H460 spheroids were employed. According to immunofluorescence analysis, hypoxic regions (shown using pimonidazole (PIMO)) and CA IX expression (indicated using mAb M75) were identified in sections of H460 spheroids grown for 11 days (Fig. 18.15a). Therefore, non-hypoxic and hypoxic H460 spheroids grown for 4 and 11 days, respectively, were treated with VR16-09 as it was the most effective inhibitor for reducing extracellular acidification during hypoxia, among the compounds investigated (Figs. 18.13 and 18.14a). Cells were plated for evaluation by clonogenic cell survival after exposure to inhibitor. A hypoxia-dependent effect on clonogenic survival of VR16-09 was found in H460 spheroids (Fig. 18.15b) which was not observed using 2D monolayer cells. This result emphasizes the importance of three-dimensional (3D) cell models to study CA IX-targeting compounds, with clonogenic survival as endpoint, because such cell models resemble the naturally occurring hypoxic microenvironment.

18.7 Conclusions and Future Perspectives

This chapter provides a novel concept to characterize compound efficacy via an integrative set of biophysical, biochemical, and cell biology-based approaches. Novel CA IX inhibitors exhibited low toxicity in zebrafish embryos/larvae, high affinity and selectivity towards heterologous CA IX in *Xenopus* oocytes, and CA IX-dependent nanomolar functional activities in human cancer cells. Thus, these newly designed compounds, especially VD11-4-2 and VR16-09, are promising agents for CA IX-specific therapy.

For future studies, the design of dual targeting compounds based on the combination of inhibitors VD11-4-2 or VR16-09 with various derivatives, including

nitroimidazoles, would be worth pursuing. This strategy was previously reported to be effective in both reducing tumor growth and sensitizing only CA IX-expressing tumors to irradiation without systemic toxicity [93]. Moreover, combinatorial experiments applying novel CA IX inhibitors with the standard treatment modalities, such as doxorubicin, in human cancer cells could result in improved in vitro biological efficacies. Prior to clinical trials, in vivo studies on VD11-4-2 or VR16-09 in tumors formed from CA IX-expressing and CA IX KO cells would be relevant for further development.

References

1. Davis, A.M., Plowright, A.T., Valeur, E.: Directing evolution: the next revolution in drug discovery? *Nat. Rev. Drug Discov.* **16**, 681–698 (2017)
2. Corbet, C., Feron, O.: Tumour acidosis: from the passenger to the driver's seat. *Nat. Rev. Cancer* **17**, 577–593 (2017)
3. Parks, S.K., Chiche, J., Pouyssegur, J.: Disrupting proton dynamics and energy metabolism for cancer therapy. *Nat. Rev. Cancer* **13**, 611–623 (2013)
4. Mboge, M.Y., Mahon, B.P., McKenna, R., Frost, S.C.: Carbonic anhydrases: role in pH control and cancer. *Metabolites* **8**, 19 (2018)
5. Pastoreková, S., et al.: Carbonic anhydrase IX, MN/CA IX: analysis of stomach complementary DNA sequence and expression in human and rat alimentary tracts. *Gastroenterology* **112**, 398–408 (1997)
6. van Kuijk, S.J.A., et al.: Prognostic significance of carbonic anhydrase IX expression in cancer patients: a meta-analysis. *Front. Oncol.* **6**, 69 (2016)
7. Svastová, E. et al.: Hypoxia activates the capacity of tumor-associated carbonic anhydrase IX to acidify extracellular pH. *FEBS Lett.* **577**, 439–445 (2004)
8. Gorbatenko, A., Olesen, C.W., Boedtkjer, E., Pedersen, S.F.: Regulation and roles of bicarbonate transporters in cancer. *Front. Physiol.* **5**, 130 (2014)
9. Lee, S., et al.: Na⁺/HCO₃⁻ cotransport is functionally upregulated during human breast carcinogenesis and required for the inverted pH gradient across the plasma membrane. *Pflugers Arch.* **467**, 367–377 (2015)
10. Hulikova, A., et al.: Stromal uptake and transmission of acid is a pathway for venting cancer cell-generated acid. *Proc. Natl. Acad. Sci. U S A* **113**, E5344–E5353 (2016)
11. Federici, C., et al.: Lansoprazole and carbonic anhydrase IX inhibitors synergize against human melanoma cells. *J. Enzyme Inhib. Med. Chem.* **31**, 119–125 (2016)
12. Parks, S.K., Cormerais, Y., Durivault, J., Pouyssegur, J.: Genetic disruption of the pH-regulating proteins Na⁺/H⁺ exchanger 1 (SLC9A1) and carbonic anhydrase 9 severely reduces growth of colon cancer cells. *Oncotarget* **8**, 10225–10237 (2016)
13. Pastoreková, S., Zavadová, Z., Kostál, M., Babusíková, O., Závada, J.: A novel quasi-viral agent, MaTu, is a two-component system. *Virology* **187**, 620–626 (1992)
14. Pastorek, J., et al.: Cloning and characterization of MN, a human tumor-associated protein with a domain homologous to carbonic anhydrase and a putative helix-loop-helix DNA binding segment. *Oncogene* **9**, 2877–2888 (1994)
15. Opavský, R., et al.: Human MN/CA9 gene, a novel member of the carbonic anhydrase family: structure and exon to protein domain relationships. *Genomics* **33**, 480–487 (1996)
16. Oosterwijk, E., et al.: Monoclonal antibody G 250 recognizes a determinant present in renal-cell carcinoma and absent from normal kidney. *Int. J. Cancer* **38**, 489–494 (1986)
17. Grabmaier, K., et al.: Molecular cloning and immunogenicity of renal cell carcinoma-associated antigen G250. *Int. J. Cancer* **85**, 865–870 (2000)

18. Langella, E., et al.: Biochemical, biophysical and molecular dynamics studies on the proteoglycan-like domain of carbonic anhydrase IX. *Cell. Mol. Life Sci.* **75**, 3283–3296 (2018)
19. Závada, J., et al.: Human tumour-associated cell adhesion protein MN/CA IX: identification of M75 epitope and of the region mediating cell adhesion. *Br. J. Cancer* **82**, 1808–1813 (2000)
20. Dorai, T., Sawczuk, I.S., Pastorek, J., Wiernik, P.H., Dutcher, J.P.: The role of carbonic anhydrase IX overexpression in kidney cancer. *Eur. J. Cancer* **41**, 2935–2947 (2005)
21. Ditte, P., et al.: Phosphorylation of carbonic anhydrase IX controls its ability to mediate extracellular acidification in hypoxic tumors. *Cancer Res.* **71**, 7558–7567 (2011)
22. Barathova, M., et al.: Alternative splicing variant of the hypoxia marker carbonic anhydrase IX expressed independently of hypoxia and tumour phenotype. *Br. J. Cancer* **98**, 129–136 (2008)
23. Malentacchi, F., et al.: Alternative splicing variants of carbonic anhydrase IX in human non-small cell lung cancer. *Lung Cancer* **64**, 271–276 (2009)
24. Alterio, V., et al.: Crystal structure of the catalytic domain of the tumor-associated human carbonic anhydrase IX. *Proc. Natl. Acad. Sci. U S A* **106**, 16233–16238 (2009)
25. Ivanov, S., et al.: Expression of hypoxia-inducible cell-surface transmembrane carbonic anhydrases in human cancer. *Am. J. Pathol.* **158**, 905–919 (2001)
26. Leibovich, B.C., et al.: Carbonic anhydrase IX is not an independent predictor of outcome for patients with clear cell renal cell carcinoma. *J. Clin. Oncol.* **25**, 4757–4764 (2007)
27. Wykoff, C.C., et al.: Hypoxia-inducible expression of tumor-associated carbonic anhydrases. *Cancer Res.* **60**, 7075–7083 (2000)
28. Kopacek, J., et al.: MAPK pathway contributes to density- and hypoxia- induced expression of the tumor-associated carbonic anhydrase IX. *Biochim. Biophys. Acta* **1729**, 41–49 (2005)
29. Simko, V., et al.: Dexamethasone downregulates expression of carbonic anhydrase IX via HIF1 α and NF κ B-dependent mechanisms. *Int. J. Oncol.* **49**, 1277–1288 (2016)
30. Andreucci, E., et al.: Carbonic anhydrase IX inhibition affects viability of cancer cells adapted to extracellular acidosis. *J. Mol. Med.* **95**, 1341–1353 (2017)
31. Panisova, E., et al.: Lactate stimulates CA IX expression in normoxic cancer cells. *Oncotarget* **8**, 77819–77835 (2017)
32. Zatovicova, M., et al.: Ectodomain shedding of the hypoxia-induced carbonic anhydrase IX Is a metalloprotease-dependent process regulated by TACE/ADAM17. *Br. J. Cancer* **93**, 1267–1276 (2005)
33. Závada, J., Zavadová, Z., Zat'ovičová, M., Hyršl, L., Kawaciuk, I.: Soluble form of carbonic anhydrase IX (CA IX) in the serum and urine of renal carcinoma patients. *Br. J. Cancer* **89**, 1067–1071 (2003)
34. Hyršl, L., et al.: Soluble form of carbonic anhydrase IX (CAIX) in transitional cell carcinoma of urinary tract. *Neoplasma* **56**, 298–302 (2009)
35. Ilie, M., et al.: High levels of carbonic anhydrase IX in tumour tissue and plasma are biomarkers of poor prognostic in patients with non-small cell lung cancer. *Br. J. Cancer* **102**, 1627–1635 (2010)
36. Woelber, L., et al.: Carbonic anhydrase IX in tumor tissue and sera of patients with primary cervical cancer. *BMC Cancer* **11**, 12 (2011)
37. Schütze, D., et al.: Relevance of cellular and serum carbonic anhydrase IX in primary breast cancer. *J. Cancer Res. Clin. Oncol.* **139**, 747–754 (2013)
38. Dubois, L., et al.: Imaging the hypoxia surrogate marker CA IX requires expression and catalytic activity for binding fluorescent sulfonamide inhibitors. *Radiother. Oncol.* **83**, 367–373 (2007)
39. Li, Y., et al.: Expression and activity of carbonic anhydrase IX Is associated with metabolic dysfunction in MDA-MB-231 breast cancer cells. *Cancer Invest.* **27**, 613–623 (2009)
40. Cianchi, F., et al.: Selective inhibition of carbonic anhydrase IX decreases cell proliferation and induces ceramide-mediated apoptosis in human cancer cells. *J. Pharmacol. Exp. Ther.* **334**, 710–719 (2010)
41. Robertson, N., Potter, C., Harris, A.L.: Role of carbonic anhydrase IX in human tumor cell growth, survival, and invasion. *Cancer Res.* **64**, 6160–6165 (2004)

42. McIntyre, A., et al.: Carbonic anhydrase IX promotes tumour growth and necrosis in vivo and inhibition enhances anti-VEGF therapy. *Clin. Cancer Res.* **18**, 3100–3111 (2012)
43. Chiche, J., et al.: Hypoxia-inducible carbonic anhydrase IX and XII promote tumor cell growth by counteracting acidosis through the regulation of the intracellular pH. *Cancer Res.* **69**, 358–368 (2009)
44. Lou, Y., et al.: Targeting tumor hypoxia: suppression of breast tumor growth and metastasis by novel carbonic anhydrase IX inhibitors. *Cancer Res.* **71**, 3364–3376 (2011)
45. Currie, M.J., et al.: Immunohistochemical analysis of cancer stem cell markers in invasive breast carcinoma and associated ductal carcinoma in situ: relationships with markers of tumor hypoxia and microvasculature. *Hum. Pathol.* **44**, 402–411 (2013)
46. Lock, F.E., et al.: Targeting carbonic anhydrase IX depletes breast cancer stem cells within the hypoxic niche. *Oncogene* **32**, 5210–5219 (2013)
47. Svastova, E., et al.: Carbonic anhydrase IX interacts with bicarbonate transporters in lamellipodia and increases cell migration via its catalytic domain. *J. Biol. Chem.* **287**, 3392–3402 (2012)
48. Swayampakula, M., et al.: The interactome of metabolic enzyme carbonic anhydrase IX reveals novel roles in tumor cell migration and invadopodia/MMP14-mediated invasion. *Oncogene* **36**, 6244 (2017)
49. Svastová, E., et al.: Carbonic anhydrase IX reduces E-cadherin-mediated adhesion of MDCK cells via interaction with beta-catenin. *Exp. Cell Res.* **290**, 332–345 (2003)
50. Kim, B.-R., et al.: Dickkopf-1 (DKK-1) interrupts FAK/PI3K/mTOR pathway by interaction of carbonic anhydrase IX (CA9) in tumorigenesis. *Cell. Signal.* **24**, 1406–1413 (2012)
51. Shin, H.-J., et al.: Carbonic anhydrase IX (CA9) modulates tumor-associated cell migration and invasion. *J. Cell. Sci.* **124**, 1077–1087 (2011)
52. Sansone, P., et al.: Cyclooxygenase-2/carbonic anhydrase-IX up-regulation promotes invasive potential and hypoxia survival in colorectal cancer cells. *J. Cell Mol. Med.* **13**, 3876–3887 (2009)
53. Radvak, P., et al.: Suppression of carbonic anhydrase IX leads to aberrant focal adhesion and decreased invasion of tumor cells. *Oncol. Rep.* **29**, 1147–1153 (2013)
54. Alterio, V., Di Fiore, A., D’Ambrosio, K., Supuran, C.T., De Simone, G.: Multiple binding modes of inhibitors to carbonic anhydrases: how to design specific drugs targeting 15 different isoforms? *Chem. Rev.* **112**, 4421–4468 (2012)
55. Supuran, C.T.: Structure and function of carbonic anhydrases. *Biochem. J.* **473**, 2023–2032 (2016)
56. Pinar, M.A., Mahon, B., McKenna, R.: Probing the surface of human carbonic anhydrase for clues towards the design of isoform specific inhibitors. *Biomed. Res. Int.* **2015**, 453543 (2015)
57. Lomelino, C., McKenna, R.: Carbonic anhydrase inhibitors: a review on the progress of patent literature (2011–2016). *Expert Opin. Ther. Pat.* **26**, 947–956 (2016)
58. Kazokaitė, J., et al.: Novel fluorinated carbonic anhydrase IX inhibitors reduce hypoxia-induced acidification and clonogenic survival of cancer cells. *Oncotarget* **9**, 26800–26816 (2018)
59. Dudutienė, V., et al.: Discovery and characterization of novel selective inhibitors of carbonic anhydrase IX. *J. Med. Chem.* **57**, 9435–9446 (2014)
60. Kazokaitė, J., Aspatwar, A., Kairys, V., Parkkila, S., Matulis, D.: Fluorinated benzenesulfonamide anticancer inhibitors of carbonic anhydrase IX exhibit lower toxic effects on zebrafish embryonic development than ethoxzolamide. *Drug. Chem. Toxicol.* **40**, 309–319 (2017)
61. Kazokaitė, J., Ames, S., Becker, H.M., Deitmer, J.W., Matulis, D.: Selective inhibition of human carbonic anhydrase IX in xenopus oocytes and MDA-MB-231 breast cancer cells. *J. Enzyme Inhib. Med. Chem.* **31**, 38–44 (2016)
62. MacRae, C.A., Peterson, R.T.: Zebrafish as tools for drug discovery. *Nat. Rev. Drug. Discov.* **14**, 721–731 (2015)
63. Battle, H.I., Hisaoka, K.K.: Effects of ethyl carbamate (Urethan) on the early development of the teleost brachydanio rerio. *Cancer Res.* **12**, 334–340 (1952)

64. Gamse, J.T., Gorelick, D.A.: Mixtures, metabolites, and mechanisms: understanding toxicology using zebrafish. *Zebrafish* **13**, 377–378 (2016)
65. He, J.-H., Gao, J.-M., Huang, C.-J., Li, C.-Q.: Zebrafish models for assessing developmental and reproductive toxicity. *Neurotoxicol. Teratol.* **42**, 35–42 (2014)
66. Esbaugh, A.J., Perry, S.F., Gilmour, K.M.: Hypoxia-inducible carbonic anhydrase IX expression is insufficient to alleviate intracellular metabolic acidosis in the muscle of Zebrafish, *Danio Rerio*. *Am. J. Physiol. Regul. Integr. Comp. Physiol.* **296**, R150–160 (2009)
67. Postel, R., Sonnenberg, A.: Carbonic anhydrase 5 regulates acid-base homeostasis in Zebrafish. *PLoS ONE* **7**, e39881 (2012)
68. Matsumoto, H., et al.: Carbonic anhydrase inhibitors induce developmental toxicity during Zebrafish embryogenesis, especially in the inner ear. *Mar. Biotechnol.* **19**, 430–440 (2017)
69. Aspatwar, A., et al.: Nitroimidazole-based inhibitors DTP338 and DTP348 are safe for Zebrafish embryos and efficiently inhibit the activity of human CA IX in xenopus oocytes. *J. Enzyme Inhib. Med. Chem.* **33**, 1064–1073 (2018)
70. Aspatwar, A., et al.: Abnormal cerebellar development and ataxia in CARP VIII morphant Zebrafish. *Hum. Mol. Genet.* **22**, 417–432 (2013)
71. Aspatwar, A., et al.: Inactivation of Ca10a and Ca10b genes leads to abnormal embryonic development and alters movement pattern in Zebrafish. *PLoS ONE* **10**, e0134263 (2015)
72. Lin, T.-Y., et al.: Carbonic anhydrase 2-like a and 15a are involved in acid-base regulation and Na⁺ uptake in Zebrafish H⁺-ATPase-Rich cells. *Am. J. Physiol. Cell Physiol.* **294**, C1250–1260 (2008)
73. Miller, S., Pollack, J., Bradshaw, J., Kumai, Y., Perry, S.F.: Cardiac responses to hypercapnia in larval Zebrafish (*Danio Rerio*): the links between CO₂ chemoreception, catecholamines and carbonic anhydrase. *J. Exp. Biol.* **217**, 3569–3578 (2014)
74. Patrikainen, M.S., et al.: Identification and characterization of a novel Zebrafish (*Danio Rerio*) pentraxin-carbonic anhydrase. *PeerJ* **5**, e4128 (2017)
75. Gao, X.-P., et al.: Toxicity assessment of 7 anticancer compounds in Zebrafish. *Int. J. Toxicol.* **33**, 98–105 (2014)
76. Shapiro, H.A., Zwarenstein, H.: A rapid test for pregnancy on *Xenopus Laevis*. *Nature* **133**, 762 (1934)
77. Becker, H.M.: In: Hirrlinger, J., Waagepetersen, H.S. (eds.) *Brain Energy Metabolism*, pp. 25–43. Springer, New York (2014)
78. Geib, S., et al.: A novel xenopus oocyte expression system based on cytoplasmic coinjection of T7-driven plasmids and purified T7-RNA polymerase. *Recept. Channels* **7**, 331–343 (2001)
79. Taylor, M.A., Johnson, A.D., Smith, L.D.: Growing xenopus oocytes have spare translational capacity. *Proc. Natl. Acad. Sci. U S A* **82**, 6586–6589 (1985)
80. Weber, W.: Ion currents of xenopus laevis oocytes: state of the art. *Biochim. Biophys. Acta* **1421**, 213–233 (1999)
81. Nakhoul, N.L., Davis, B.A., Romero, M.F., Boron, W.F.: Effect of expressing the water channel aquaporin-1 on the CO₂ permeability of xenopus oocytes. *Am. J. Physiol.* **274**, C543–548 (1998)
82. Becker, H.M., Hirnet, D., Fecher-Trost, C., Sültemeyer, D., Deitmer, J.W.: Transport activity of MCT1 expressed in xenopus oocytes is increased by interaction with carbonic anhydrase. *J. Biol. Chem.* **280**, 39882–39889 (2005)
83. Schneider, H.-P., et al.: GPI-anchored carbonic anhydrase IV displays both intra- and extracellular activity in cRNA-injected oocytes and in mouse neurons. *Proc. Natl. Acad. Sci. U S A* **110**, 1494–1499 (2013)
84. Klier, M., et al.: Catalytic activity of human carbonic anhydrase isoform IX is displayed both extra- and intracellularly. *FEBS J.* **283**, 191–200 (2016)
85. Becker, H.M., Deitmer, J.W.: Nonenzymatic proton handling by carbonic anhydrase II during H⁺-lactate cotransport via monocarboxylate transporter 1. *J. Biol. Chem.* **283**, 21655–21667 (2008)

86. Klier, M., et al.: Transport activity of the high-affinity monocarboxylate transporter MCT2 is enhanced by extracellular carbonic anhydrase IV but not by intracellular carbonic anhydrase II. *J. Biol. Chem.* **286**, 27781–27791 (2011)
87. Jamali, S., et al.: Hypoxia-induced carbonic anhydrase IX facilitates lactate flux in human breast cancer cells by non-catalytic function. *Sci. Rep.* **5**, 13605 (2015)
88. Tu, C.K., Silverman, D.N.: Solvent deuterium isotope effects in the catalysis of oxygen-18 exchange by human carbonic anhydrase II. *Biochemistry* **21**, 6353–6360 (1982)
89. Price, G.D., Badger, M.R.: Expression of human carbonic anhydrase in the cyanobacterium *synechococcus* PCC7942 creates a high CO₂-requiring phenotype 1. *Plant. Physiol.* **91**, 505–513 (1989)
90. Angeli, A., et al.: Discovery of new selenoureido analogues of 4-(4-fluorophenylureido) benzenesulfonamide as carbonic anhydrase inhibitors. *ACS Med. Chem. Lett.* **8**, 963–968 (2017)
91. Meehan, J., et al.: Inhibition of pH regulation as a therapeutic strategy in hypoxic human breast cancer cells. *Oncotarget* **8**, 42857–42875 (2017)
92. van Kuijk, S.J.A., et al.: New approach of delivering cytotoxic drugs towards CAIX expressing cells: a concept of dual-target drugs. *Eur. J. Med. Chem.* **127**, 691–702 (2017)
93. Dubois, L., et al.: Targeting carbonic anhydrase IX by nitroimidazole based sulfamides enhances the therapeutic effect of tumor irradiation: a new concept of dual targeting drugs. *Radiother. Oncol.* **108**, 523–528 (2013)



Use of Carbonic Anhydrase IX Inhibitors for Selective Delivery of Attached Drugs to Solid Tumors 19

Spencer Gardeen and Philip S. Low

Abstract

Central to the goal of precision medicine lies the ability to target an effective drug specifically to diseased cells, thereby avoiding the uptake and collateral toxicity that arises when good drugs accumulate in healthy cells. While antibody-drug conjugates (ADCs) have pioneered many efforts in this field, small molecule drug conjugates (SMDCs) with high specificities for diseased cell types are now displaying equal if not greater potential because of their improved abilities to penetrate solid tissues. For both technologies, however, success has invariably depended on an ability to identify a receptor that is overexpressed on the desired pathologic cell (e.g., cancer cell, virus-infected cell, inflammatory cell, etc.), but absent or weakly expressed on all other healthy cells. While few cell surface receptors can satisfy these criteria, one that has attracted considerable recent attention has been carbonic anhydrase IX (CA IX), a cell surface enzyme that is expressed in virtually all hypoxic tissues, but minimally expressed, if at all, in healthy tissues. Because most solid tumors are hypoxic, CA IX-targeted SMDCs are now being explored as broad-spectrum agents for the diagnosis and therapy of CA IX-expressing malignancies. The following chapter highlights some of the groundbreaking research in this area and provides key insights into how the design of a CA IX-targeted SMDC can impact efficacy.

S. Gardeen · P. S. Low (✉)

Department of Chemistry and Purdue Institute for Drug Discovery, Purdue University,
West Lafayette, IN, USA

e-mail: sgardeen@purdue.edu; plow@purdue.edu

19.1 Introduction

In the era of precision medicine, ligand-targeted drugs that can deliver an attached therapeutic payload selectively to diseased cells are receiving increased attention, because they frequently increase drug uptake by pathologic cells while suppressing its accumulation in healthy cells [1–3]. While antibody-drug conjugates that exploit an antibody's affinity for a disease-specific receptor have been explored for some applications, their inability to efficiently penetrate solid tumors and other dense tissues have limited their envisioned uses [4]. In contrast, small molecule drug conjugates that rely on low molecular weight targeting ligands to deliver attached imaging or therapeutic agents to diseased cells have attracted increasing interest, primarily because of their improved abilities to penetrate pathologic tissues and their rapid clearance from receptor-negative healthy tissues [5, 6]. Moreover, after binding to disease-specific receptors on target cells, many of these small molecule drug conjugates enter the target cells by receptor-mediated endocytosis [7], thereby trapping the drug conjugate within the target cell and reducing its chance of diffusing into adjacent healthy cells.

While many low molecular weight ligand-drug conjugates have entered clinical trials, the most successful ligand-targeted drugs to date have been targeted to either folate receptors [3] or prostate-specific membrane antigen [8]. Folate receptor alpha ($FR\alpha$), for example, is overexpressed on approximately 40% of human cancers [9], including cancers of the ovary, lung, endometrium, kidney, colon, bladder, and breast [9]. Folate receptor beta ($FR\beta$), in contrast, is upregulated on myelogenous leukemia cells (i.e., AML and CML) and also on activated but not resting macrophages [10, 11]. Due to its over-expression on activated macrophages, $FR\beta$ is abundantly observed in virtually all inflamed tissues, including lesions associated with rheumatoid arthritis, inflammatory bowel diseases, multiple sclerosis, idiopathic pulmonary fibrosis, psoriasis, osteoarthritis, sarcoidosis, scleroderma, and Sjogren's disease [12–17]. Prostate-specific membrane antigen, on the other hand, is overexpressed on almost all prostate cancer cells [18], and more recently, has been found to be upregulated on the neovasculature of many solid tumors [19–22]. While folate receptor and prostate-specific membrane antigen targeting ligands enable delivery of attached therapeutic and imaging agents to over half of all human cancers, there are still a large number of lethal malignancies for which no targeting ligands currently exist.

In an effort to identify targeting ligands for those malignancies not addressed by folate receptor or prostate-specific membrane antigen-targeted drugs, we have searched for other cell surface receptors that might be upregulated in multiple human cancers but largely absent from normal tissues [23–27]. After examination of the literature, we concluded that carbonic anhydrase IX (CA IX), a membrane-spanning CA isoform that catalyzes the interconversion of $H_2CO_3 \leftrightarrow H_2O + CO_2$, might constitute an attractive target for further evaluation [28]. Thus, CA IX is a membrane-spanning carbonic anhydrase whose active site is exposed on the extracellular surface of a cell and whose expression is normally negligible except under

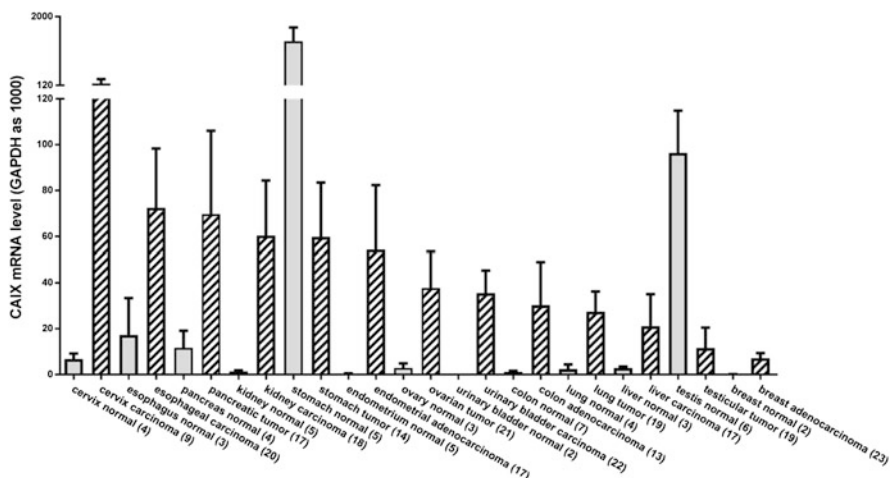


Fig. 19.1 Expression of CAIX relative to GAPDH in various human cancers and adjacent normal tissues. GAPDH gene expression in each tissue sample was set arbitrarily at 1000 and the cDNA level of CAIX gene expression was calculated from the threshold cycle (Ct) difference ($Ct_{CAIX} - Ct_{GAPDH}$). The numbers of each tissue type examined are provided in parentheses and values are expressed as mean \pm SEM. Reprinted with permission from Bioconjugate Chemistry [30]

hypoxic conditions where it is strongly induced [29]. Because most solid tumors are highly hypoxic, CA IX appears to be upregulated in most malignant masses, but largely absent from the corresponding normal tissues [23–27]. Quantitative rtPCR of multiple tissue samples from many human cancers has indeed confirmed this hypothesis. Thus, as shown in Fig. 19.1, expression of CA IX in most malignant lesions exceeds its expression in the corresponding normal tissues by anywhere from 5 to 100 fold. In fact, only stomach and testes exhibit greater expression in normal than cancer tissues. Based on this tumor specificity, we and others have elected to design, synthesize, and test a variety of CA IX targeted drugs for their tumor-selective uptake. The brief review below summarizes many of the results of these efforts.

19.2 CA IX Targeting with a Benzenesulfonamide Ligand

One of the more common groups of ligands used for targeting drugs to CA IX contains benzenesulfonamide as the central scaffold in the CA IX binding moiety. In this ligand, as in other CA IX ligands described in this and other articles in this book, the sulfonamide moiety binds to a catalytic zinc atom in the active site, whereas the other substituents on the ligand are designed to enhance affinity and confer specificity for the desired carbonic anhydrase isozyme. In the case of CA IX, the catalytic pocket is 20 Å deep [1], dictating that a linker must be inserted between the

targeting ligand and the desired payload in order to allow the sulfonamide moiety to engage the zinc at the bottom of the catalytic pocket. Moreover, because the catalytic pocket is narrow in places, if the linker is not optimally designed, its conjugation to the targeting ligand can reduce the ligand's affinity for CA IX. For example, whereas the bis-benzenesulfonamide inhibitor originally developed by Rami et al. displayed single digit nanomolar affinity for CA IX [31], an infrared dye and ^{99m}Tc conjugate of the same ligand were found to bind CA IX-expressing cancer cells with dissociation constants of 45 and 54 nM, respectively. This comparison indicates that care must be taken in the design of the linker to assure that neither the linker nor the attached payload interfere with binding to the enzyme [32, 33].

In general, the benzenesulfonamide ligands have been primarily exploited to deliver either SPECT (^{188}Re , ^{99m}Tc) or PET (^{68}Ga , ^{18}F) imaging agents to solid tumors [34–40]. While many of the benzenesulfonamide-based imaging agents retain excellent affinity for CA IX [34, 35, 40], there has been a general lack of specificity for tumor over normal tissue [34, 39], resulting in unfavorable biodistribution patterns that have led to complicated whole body images. Except for a trimeric ^{68}Ga conjugate produced by Lau et al., most compounds have displayed tumor-to-blood ratios less than 1 with considerable uptake in healthy organs such as liver, kidney, and intestines [38]. Given the much higher expression of CA IX in malignant than healthy tissues (Fig. 19.1), the question must be asked whether benzenesulfonamide-derived ligands might exhibit off-target affinities for other metal-containing enzymes or whether the imaging payload might significantly alter the biodistribution of the intact conjugate. Regarding the latter possibility, we have noticed that a strongly anionic aromatic payload exhibits much lower healthy tissue accumulation than the same benzenesulfonamide ligand linked via an identical PEG₁₂ spacer to a peptidic payload [41]. Thus, an EDTA-bridged bis-benzenesulfonamide connected via PEG₁₂ to the indocyanine dye, S0456, shows little nonmalignant tissue retention in tumor-bearing mice except in the kidneys, whereas the same EDTA-bridged bis-benzenesulfonamide-PEG₁₂ construct linked to a tetrapeptide payload displays considerable uptake in many normal tissues [41, 42]. While the cause of this difference in tissue retention has not been investigated, we hypothesize that the unwanted normal tissue retention exhibited by the peptidic conjugate might derive from widely expressed peptide scavenger receptors that are present in many healthy tissues [43].

In addition to the above imaging applications, the latter EDTA-bridged bis-benzenesulfonamide ligand has also been exploited for delivery of a therapeutic warhead for treatment of CA IX-expressing tumors [44]. Thus, Lv et al. have shown that an EDTA-bridged bis-benzenesulfonamide conjugate of tubulysin B hydrazide (Fig. 19.2) can prevent tumor growth in mice bearing human cancer xenografts [44]. Although the tumors were not completely eradicated, the ability of the conjugate to block tumor expansion without causing observable toxicity argued that the conjugate deserved further investigation [44]. This absence of detectable toxicity to healthy organs also suggested that the off-target uptake seen with several benzenesulfonamide-targeted imaging agents was probably replicated when the

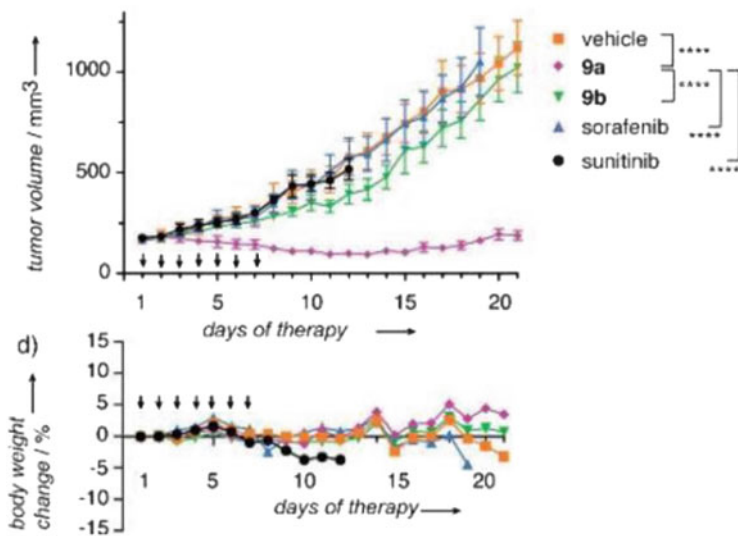


Fig. 19.3 In vivo efficacy of acetazolamide-targeted drug conjugates. Mice bearing SKRC52 xenografts were treated with 70 nmols acetazolamide-targeted (9a) untargeted (9b) DM1 and appropriate controls for 7 days, then monitored for 3 weeks. Arrows indicate days of dosing. Reprinted with permission from Angewandte Chemie [46]

stable, and have proper release kinetics to effectively deliver therapeutic levels of drug to the intended target. For more details on payload selection, please consult the following detailed reviews [32, 33].

Success in using acetazolamide to deliver cytotoxic drugs to CA IX-expressing cancers prompted Krall et al. to publish a subsequent paper in which they attached a peptide-based ^{99m}Tc chelating agent previously employed in EC20 [49] to create a SPECT radio imaging agent for localization of CA IX positive tumors [45]. Although tumor:blood ratios were acceptable, tumor to other tissue ratios revealed poor tumor specificity (Fig. 19.4) [45]. Given the apparent tumor specificity of the acetazolamide-targeted DM1 conjugate, we suspect that the strongly peptidic nature of this imaging agent may have diverted much of the conjugate to peptide scavenger receptors in the healthy tissues.

Acetazolamide has also been exploited to deliver attached near infrared fluorescent dyes to tumor tissues for intended use in fluorescence-guided surgery of cancer. As shown in Fig. 19.5, Bao et al. [50] were able to construct an acetazolamide-VivoTag 680 conjugate that displayed significant uptake in only the tumor and kidney, with little dye retention in most other tissues. Moreover, with a slight variation in linker length and the use of a phenyl-oxo-bridged S0456 NIR dye, Mahalingam et al. observed a similarly improved biodistribution pattern, except the uptake in the kidneys was still further reduced (Fig. 19.6) [2]. These data support the previously stated hypothesis that linker chemistry and payload composition can influence the biodistribution of a ligand-targeted drug conjugate.

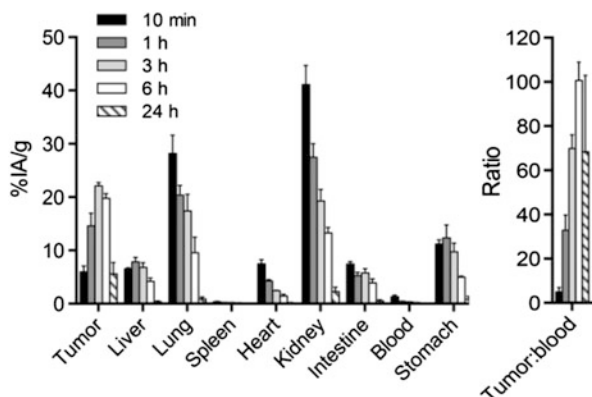
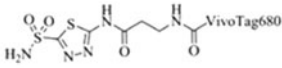



Fig. 19.4 Biodistribution of acetazolamide- ^{99m}Tc in mouse with SKRC-52 tumor. Mice bearing SKRC52 xenografts were injected with 0.17MBq of chelated ^{99m}Tc targeted with acetazolamide and subsequently sacrificed at the indicated time points to carry out biodistribution. Reprinted with permission from Journal of Nuclear Medicine [45](2 figures)

While variations in linker length/composition as well as dye choice can influence the eventual biodistribution, enhancing tumor uptake and improving tumor-to-healthy tissue ratios can also be achieved by increasing the affinity of the targeting ligand for its CA IX receptor. This principle demonstrated by Wichert et al. in a DNA encoded library of more than 100,000 compounds was used to identify moieties that might increase the binding affinity of acetazolamide. Thus, when a higher affinity CA IX targeting ligand was used to deliver a near infrared fluorescent dye, increased tumor accumulation, prolonged tumor retention, and greater tumor-to-background ratios were observed (Fig. 19.7) [51]. These data were interpreted to demonstrate that higher ligand affinity can also improve the performance of a ligand-drug conjugate [2]. Finally, in other studies it has been noted that the rate of tumor accumulation and healthy tissue clearance can also be impacted by the different components of the targeted drug [52]. Taken together, the above data argue that all components of a ligand-targeted drug conjugate (i.e., ligand, linker, and payload) must be independently optimized to achieve the most favorable pharmacokinetics, pharmacodynamics, and biodistribution of the final conjugate.

19.4 CA IX Targeting with 3-((2-(Cyclooctylamino)-3,5,6-Trifluoro-4-Sulfamoylphenyl)Sulfonyl)Propanoic Acid

The final class of CA IX-targeted conjugates (see Fig. 19.8, below) employs a high affinity, high specificity substituted benzenesulfonamide CA IX inhibitor originally developed by Matulis and colleagues for delivery of attached imaging and therapeutic agents [53]. As shown in Fig. 19.8, the CA IX targeting moiety distinguishes

	HS680	Control Agent
Structure		
MW	1372 g/mol	1341 g/mol
Absorbance	670 nm	670 nm
Emission	686 nm	685 nm

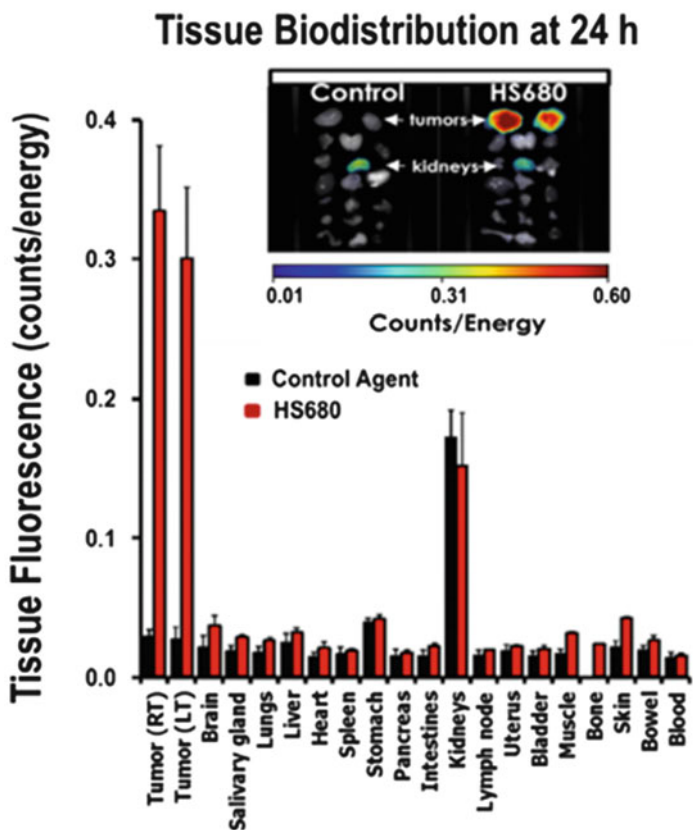


Fig. 19.5 Biodistribution of acetazolamide targeted and untargeted near infrared dye. Mice bearing HeLa tumor xenografts were injected with 2 nmols of acetazolamide targeted or untargeted NIR dye and sacrificed after 24 h for subsequent biodistribution analysis. Reprinted with permission from PLOS ONE [50]

itself from those described above in that the benzenesulfonamide is reprivatized with a cyclooctylamine-ring that presumably fills a hydrophobic pocket in the binding site of CA IX not occupied by other inhibitors and thereby increases the scaffold's affinity for CA IX by at least 1000-fold [53]. Use of the improved CA IX ligand for delivery of an attached cytotoxic drug (tubulysin B hydrazide) was found to generate

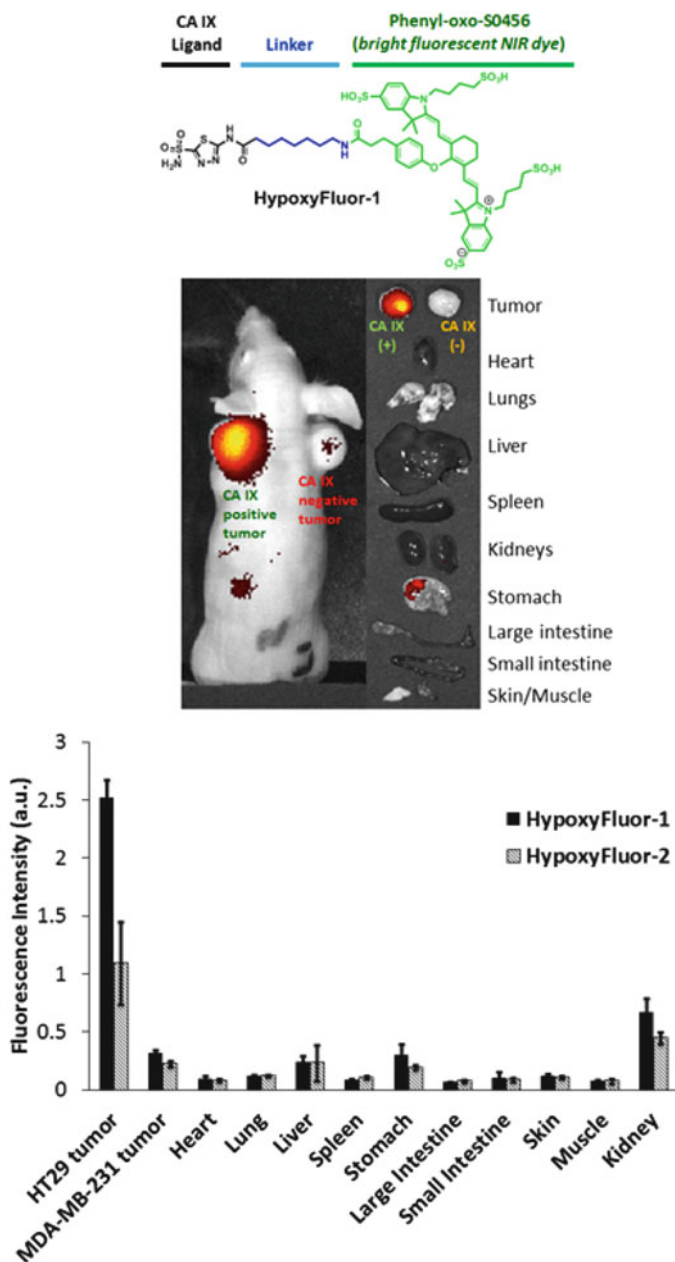


Fig. 19.6 Structure, imaging, and biodistribution of acetazolamide-targeted phenyl-oxo-S0456. The mouse in the image shown above bears both HT-29 (CA IX-positive) and MDA-MB0231 (CA IX-negative) tumor xenografts. The mouse was imaged 4h after being injected with 10 nmols of conjugate. The biodistribution above was done under similar conditions with either an acetazolamide (HypoxyFluor-1) or 6-aminosaccharin (HypoxyFluor-2) CA IX inhibitor and sacrificed at 24 h. Reprinted with permission from Bioconjugate Chemistry [2]

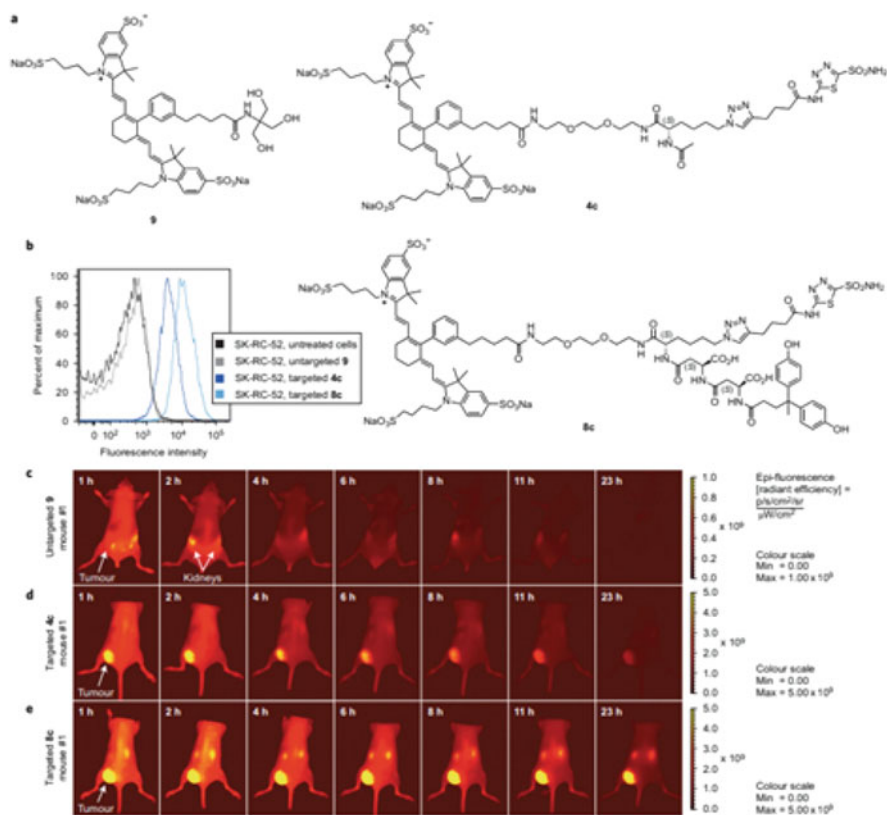
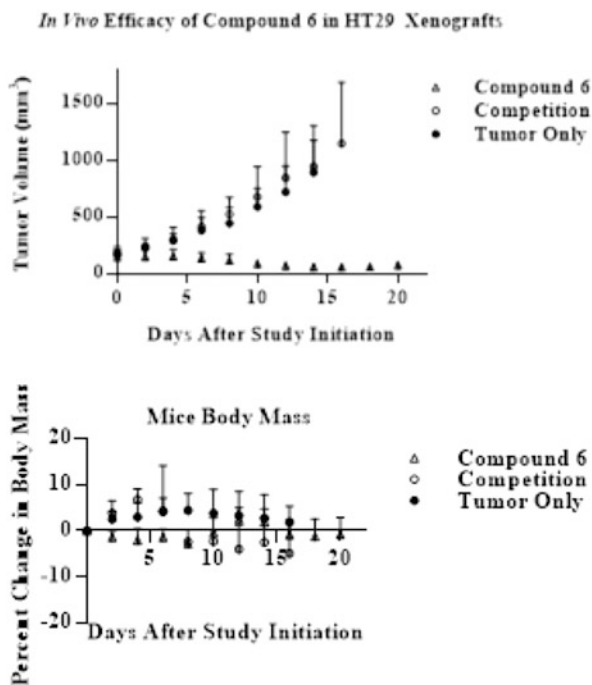


Fig. 19.7 Chemical structure and in vivo biodistribution of modified acetazolamide-targeted NIR conjugates. Mice bearing SKRC-52 tumor xenografts were injected with 3 nmol of the various compounds shown above and imaged periodically. Reprinted with permission from Nature Chemistry [51]



Fig. 19.8 Overall structure of FBSA targeted tubulysin B conjugate. Reprinted with permission from Molecular Pharmaceutics [1]

Fig. 19.9 In vivo testing of FBSA targeted tubulysin B conjugate. Mice bearing HT-29 colorectal tumor xenografts were treated twice per week with 1.25 $\mu\text{moles/kg}$ of compound shown in Fig. 19.8 and monitored for tumor size and body weight. Reprinted with permission from Molecular Pharmaceutics [1]



a highly potent antitumor agent that was able to block the growth of HT 29 colorectal cancer xenografts in athymic nude mice [1]. Thus, as shown in Fig. 19.9, $\approx 150 \text{ mm}^3$ tumors largely disappeared from mice treated $2\times$ per week with $1.25 \mu\text{moles/kg}$ without causing any unwanted weight loss (a measure of systemic toxicity) from the mice [1]. Because free tubulysin B is so toxic to healthy tissues that it kills mice before it induces any suppression of tumor growth, these data indicate that the cyclooctylamine-modified CA IX ligand has excellent tumor specificity with minimal uptake in normal tissues.

When compared to the bis-benzenesulfonamide tubulysin B studies carried out by Lv et al., the FBSA ligand was shown to be more efficacious at approximately half the amount of administered compound [1, 44]. This highlights the enormous benefits of using a selective sub-nanomolar binding targeting ligand. Generally, higher affinity targeting ligands require less administered compound, which reduces side effects associated with hepatically cleared conjugate, thereby rendering effective chemotherapy treatment with minimal to no side effects.

19.5 Conclusions

Because most solid tumors outgrow their blood supply, they are commonly poorly oxygenated, resulting in upregulation of HIF-1 α inducible genes [54]. One of the most prominent of these inducible genes is carbonic anhydrase IX, an enzyme

that helps mitigate the harmful effects of an acidic tumor microenvironment by catalyzing $\text{H}^+ + \text{HCO}_3^- \rightarrow \text{H}_2\text{CO}_3 \rightarrow \text{H}_2\text{O} + \text{CO}_2$ (which can be exhaled) [28]. Because virtually all healthy tissues are normoxic, expression of CA IX in normal tissues is limited primarily to those cells where its expression is induced by other stimuli (i.e., other than hypoxia such as stomach and testes). Interestingly, although the stomach constitutes the major healthy tissue in which carbonic anhydrase nine is measurably expressed, we saw only limited uptake of our imaging agents in the healthy stomachs of the mice we studied (Fig. 19.1) [30]. Taken together, these data suggest that a carbonic anhydrase IX specific ligand should constitute an excellent delivery vehicle for targeted drug delivery solid tumors.

Use of a CA IX targeting ligand to deliver attached drugs to solid tumors may come with still another unexpected benefit. That is, hypoxic regions of tumors constitute the major sites where cancer cells undergo an epithelial to mesenchymal transition (EMT) [55]. As a consequence of the hypoxic stress, these niches also form the microenvironment where cancer stem cells appear to be generated [55]. Thus, with judicious selection of the proper therapeutic payload, it might be possible to eradicate the slowly dividing cancer stem cells that are generally thought to be a major source of drug resistance.

In summary, a high affinity, high selectivity CA IX targeting ligand can be envisioned to perform multiple useful functions in the management of solid tumors. First, an appropriately designed CA IX-targeted PET or radio imaging agent should prove useful for systemic localization of malignant lesions. Second, where surgery is mandated, a CA IX-targeted near infrared dye could prove beneficial in locating and resecting all malignant nodules. In fact, the same targeted fluorescent dye might help avoid positive tumor margins that might otherwise remain undetected in the absence of an appropriate fluorescent contrast agent. Finally, a CA IX-targeted cytotoxic drug could contribute to the eradication of any residual diseased tissue not removed by fluorescence-guided surgery. In aggregate, a thoughtfully selected CA IX targeting ligand has the potential to contribute at multiple stages in the management of a cancer patient's disease.

References

1. Marks, I.S., et al.: Development of a small molecule tubulysin B conjugate for treatment of carbonic anhydrase IX receptor expressing cancers. *Mol. Pharm.* **15**, 2289–2296 (2018)
2. Roy, J., Kaake, M., Srinivasarao, M., Low, P.S.: Targeted tubulysin B hydrazide conjugate for the treatment of luteinizing hormone-releasing hormone receptor-positive cancers. *Bioconjug. Chem.* **29**, 2208–2214 (2018)
3. Shum, C.F., et al.: Novel use of folate-targeted intraoperative fluorescence, OTL38, in Robot-assisted laparoscopic partial nephrectomy: report of the first three cases. *J. Endourol. Case Rep.* **2**, 189–197 (2016)
4. Thurber, G.M., Schmidt, M.M., Wittrup, K.D.: Antibody tumor penetration: transport opposed by systemic and antigen-mediated clearance. *Adv. Drug Deliv. Rev.* **60**, 1421–1434 (2008)
5. Vlashi, E., Kelderhouse, L.E., Sturgis, J.E., Low, P.S.: Effect of folate-targeted nanoparticle size on their rates of penetration into solid tumors. *ACS Nano* **7**, 8573–8582 (2013)

6. Mahalingam, S.M., et al.: Evaluation of novel tumor-targeted near-infrared probe for fluorescence-guided surgery of cancer. *J. Med. Chem.* **61**(21), 9637–9646 (2018)
7. Paulos, C.M.: Ligand binding and kinetics of folate receptor recycling in vivo: impact on receptor-mediated drug delivery. *Mol. Pharmacol.* **66**, 1406–1414 (2004)
8. Paganelli, G., De Giorgi, U.: [177 Lu]-PSMA-617 for targeted prostate cancer treatment: a magic bullet? *Lancet Oncol.* **19**, 725–726 (2018)
9. Parker, N., et al.: Folate receptor expression in carcinomas and normal tissues determined by a quantitative radioligand binding assay. *Anal. Biochem.* **338**, 284–293 (2005)
10. Ross, J.F., et al.: Folate receptor type β is a neutrophilic lineage marker and is differentially expressed in myeloid leukemia. *Cancer* **85**, 348–357 (1999)
11. Shen, J., et al.: Folate receptor- β constitutes a marker for human proinflammatory monocytes. *J. Leukoc. Biol.* **96**, 563–570 (2014)
12. Nakashima-Matsushita, N., et al.: Selective expression of folate receptor β and its possible role in methotrexate transport in synovial macrophages from patients with rheumatoid arthritis. *Arthritis Rheum.* **42**, 1609–1616 (1999)
13. Low, P.: Folate receptor-targeted drugs for cancer and inflammatory diseases. *Adv. Drug Deliv. Rev.* **56**, 1055–1058 (2004)
14. Schupp, J.C., et al.: Macrophage activation in acute exacerbation of idiopathic pulmonary fibrosis. *PLoS One* **10**(ed Ryffel, B.), e0116775 (2015)
15. Han, W., et al.: Molecular imaging of folate receptor β -positive macrophages during acute lung inflammation. *Am. J. Respir. Cell Mol. Biol.* **53**, 50–59 (2015)
16. Chia, J.J., Lu, T.T.: Update on macrophages and innate immunity in scleroderma. *Curr. Opin. Rheumatol.* **27**, 530–536 (2015)
17. Zhou, D., et al.: Critical involvement of macrophage infiltration in the development of Sjögren's syndrome-associated dry eye. *Am. J. Pathol.* **181**, 753–760 (2012)
18. Wright, G.L., Haley, C., Beckett, M.L., Schellhammer, P.F.: Expression of prostate-specific membrane antigen in normal, benign, and malignant prostate tissues. *Urol. Oncol. Semin. Orig. Investig.* **1**, 18–28 (1995)
19. Heitkötter, B., et al.: Neovascular PSMA expression is a common feature in malignant neoplasms of the thyroid. *Oncotarget* **9**(11), 9867–9874 (2018)
20. Schmidt, L.H., et al.: Prostate specific membrane antigen (PSMA) expression in non-small cell lung cancer. *PLoS One* **12**(ed Ahmad, A.), e0186280 (2017)
21. Stock, K., et al.: Neovascular prostate-specific membrane antigen expression is associated with improved overall survival under palliative chemotherapy in patients with pancreatic ductal adenocarcinoma. *Biomed. Res. Int.* **2017**, 1–8 (2017)
22. Silver, D.A., Pellicer, I., Fair, W.R., Heston, W.D., Cordon-Cardo, C.: Prostate-specific membrane antigen expression in normal and malignant human tissues. *Clin. Cancer Res. Off. J. Am. Assoc. Cancer Res.* **3**, 81–85 (1997)
23. Smyth, L.G., et al.: Carbonic anhydrase IX expression in prostate cancer. *Prostate Cancer Prostatic Dis.* **13**, 178–181 (2010)
24. Genega, E.M., et al.: Carbonic anhydrase IX expression in renal neoplasms: correlation with tumor type and grade. *Am. J. Clin. Pathol.* **134**, 873–879 (2010)
25. İlie, M., et al.: High levels of carbonic anhydrase IX in tumour tissue and plasma are biomarkers of poor prognostic in patients with non-small cell lung cancer. *Br. J. Cancer* **102**, 1627–1635 (2010)
26. Loncaster, J.A., et al.: Carbonic anhydrase (CA IX) expression, a potential new intrinsic marker of hypoxia: correlations with tumor oxygen measurements and prognosis in locally advanced carcinoma of the cervix. *Cancer Res.* **61**, 6394–6399 (2001)
27. Ivanov, S., et al.: Expression of hypoxia-inducible cell-surface transmembrane carbonic anhydrases in human cancer. *Am. J. Pathol.* **158**, 905–919 (2001)
28. Mboge, M., Mahon, B., McKenna, R., Frost, S.: Carbonic anhydrases: role in pH control and cancer. *Metabolites* **8**, 19 (2018)

29. Chrastina, A.: High cell density-mediated pericellular hypoxia is a crucial factor inducing expression of the intrinsic hypoxia marker CA IX in Vitro in HeLa cells. *Neoplasma* **50**, 251–256 (2003)
30. Mahalingam, S.M., Chu, H., Liu, X., Leamon, C.P., Low, P.S.: Carbonic anhydrase IX-targeted near-infrared dye for fluorescence imaging of hypoxic tumors. *Bioconjug. Chem.* **29**, 3320–3331 (2018)
31. Rami, M., et al.: Carbonic anhydrase inhibitors: design of membrane-impermeant copper(II) complexes of DTPA-, DOTA-, and TETA-tailed sulfonamides targeting the tumor-associated transmembrane isoform IX. *ChemMedChem* **3**, 1780–1788 (2008)
32. Srinivasarao, M., Low, P.S.: Ligand-targeted drug delivery. *Chem. Rev.* **117**, 12133–12164 (2017)
33. Srinivasarao, M., Galliford, C.V., Low, P.S.: Principles in the design of ligand-targeted cancer therapeutics and imaging agents. *Nat. Rev. Drug Discov.* **14**, 203–219 (2015)
34. Lau, J., et al.: Synthesis and evaluation of ¹⁸F-labeled tertiary benzenesulfonamides for imaging carbonic anhydrase IX expression in tumours with positron emission tomography. *Bioorg. Med. Chem. Lett.* **24**, 3064–3068 (2014)
35. Asakawa, C., et al.: Radiosynthesis of three [¹¹C]ureido-substituted benzenesulfonamides as PET probes for carbonic anhydrase IX in tumors. *Bioorg. Med. Chem. Lett.* **21**, 7017–7020 (2011)
36. Lau, J., et al.: PET imaging of carbonic anhydrase IX expression of HT-29 tumor xenograft mice with ⁶⁸Ga-labeled benzenesulfonamides. *Mol. Pharm.* **13**, 1137–1146 (2016)
37. Lau, J., et al.: Trimeric radiofluorinated sulfonamide derivatives to achieve in vivo selectivity for carbonic anhydrase IX-targeted PET imaging. *J. Nucl. Med.* **56**, 1434–1440 (2015)
38. Lu, G., et al.: Synthesis and SAR of novel Re/^{99m}Tc-labeled benzenesulfonamide carbonic anhydrase IX inhibitors for molecular imaging of tumor hypoxia. *J. Med. Chem.* **56**, 510–520 (2013)
39. Akurathi, V., et al.: Synthesis and biological evaluation of a ^{99m}Tc-labelled sulfonamide conjugate for in vivo visualization of carbonic anhydrase IX expression in tumor hypoxia. *Nucl. Med. Biol.* **37**, 557–564 (2010)
40. Can, D., et al.: [(Cp-R)M(CO)₃] (M=Re or ^{99m}Tc) arylsulfonamide, arylsulfamide, and arylsulfamate conjugates for selective targeting of human carbonic anhydrase IX. *Angew. Chem. Int. Ed.* **51**, 3354–3357 (2012)
41. Lv, P.C., Putt, K.S., Low, P.S.: Evaluation of nonpeptidic ligand conjugates for SPECT imaging of hypoxic and carbonic anhydrase IX-expressing cancers. *Bioconjug. Chem.* **27**, 1762–1769 (2016)
42. Lv, P.C., Roy, J., Putt, K.S., Low, P.S.: Evaluation of a carbonic anhydrase IX-targeted near-infrared dye for fluorescence-guided surgery of hypoxic tumors. *Mol. Pharm.* **13**, 1618–1625 (2016)
43. Terada, T., Inui, K.i.: In: *Current Topics in Membranes*, pp. 257–274. Elsevier, Amsterdam (2012)
44. Lv, P.C., Roy, J., Putt, K.S., Low, P.S.: Evaluation of nonpeptidic ligand conjugates for the treatment of hypoxic and carbonic anhydrase IX-expressing cancers. *Mol. Cancer Ther.* **16**, 453–460 (2017)
45. Krall, N., Pretto, F., Mattarella, M., Muller, C., Neri, D.: A ^{99m}Tc-labeled ligand of carbonic anhydrase IX selectively targets renal cell carcinoma in vivo. *J. Nucl. Med.* **57**, 943–949 (2016)
46. Krall, N., et al.: A small-molecule drug conjugate for the treatment of carbonic anhydrase IX expressing tumors. *Angew. Chem. Int. Ed.* **53**, 4231–4235 (2014)
47. Krall, N., Pretto, F., Neri, D.: A bivalent small molecule-drug conjugate directed against carbonic anhydrase IX can elicit complete tumour regression in mice. *Chem. Sci.* **5**, 3640 (2014)
48. Reddy, J.A., et al.: Pre-clinical evaluation of EC1456, a folate-tubulysin anti-cancer therapeutic. *Sci. Rep.* **8**(1), 8943 (2018)
49. Fisher, R.E., et al.: Exploratory study of ^{99m}Tc-EC20 imaging for identifying patients with folate receptor-positive solid tumors. *J. Nucl. Med.* **49**, 899–906 (2008)

50. Bao, B., et al.: In vivo imaging and quantification of carbonic anhydrase IX expression as an endogenous biomarker of tumor hypoxia. *PLoS One* **7**, e50860 (2012)
51. Wichert, M., et al.: Dual-display of small molecules enables the discovery of ligand pairs and facilitates affinity maturation. *Nat. Chem.* **7**, 241–249 (2015)
52. Leamon, C.P., et al.: Reducing undesirable hepatic clearance of a tumor-targeted vinca alkaloid via novel saccharopeptidic modifications. *J. Pharmacol. Exp. Ther.* **336**, 336–343 (2011)
53. Dudutienė, V., et al.: Discovery and characterization of novel selective inhibitors of carbonic anhydrase IX. *J. Med. Chem.* **57**, 9435–9446 (2014)
54. Majmundar, A.J., Wong, W.J., Simon, M.C.: Hypoxia-inducible factors and the response to hypoxic stress. *Mol. Cell* **40**, 294–309 (2010)
55. Morandi, A., Taddei, M.L., Chiarugi, P., Giannoni, E.: Targeting the metabolic reprogramming that controls epithelial-to-mesenchymal transition in aggressive tumors. *Front. Oncol.* **7**, 40 (2017).



Development of Therapeutic Antibodies Against Carbonic Anhydrases

20

Dovilė Stravinskienė and Aurelija Žvirblienė

Abstract

Antibodies and their derivatives are used as immunotherapeutic substances for the treatment of different diseases by stimulating or suppressing certain components of the immune system or directly affecting the target. Treatment of allergies, autoimmune conditions, and various types of cancers are the main trends of antibody-based immunotherapy. Selection of an appropriate antigen target is one of the most important concerns to employ antibodies for therapy. Cell surface localization, importance to disease mechanism, and different expression levels in normal or abnormal cells and tissues are essential requirements for target antigens. Two membrane-associated carbonic anhydrases IX and XII (CA IX and CA XII), with their catalytic active center directed to extracellular milieu, are highly overexpressed in many types of cancers, which makes them promising cancer antigens for antibody-directed therapy. While antibodies recognizing CA XII are in the early stage of development and adaptation for cancer treatment, a few antibodies against CA IX are well characterized and chimeric form of mouse monoclonal antibody is being evaluated as an immunotherapeutic agent for kidney cancer. In this chapter, we focus on potential immunotherapeutic antibodies and their derivatives targeting carbonic anhydrases.

D. Stravinskienė · A. Žvirblienė (✉)

Department of Immunology and Cell Biology, Institute of Biotechnology, Life Sciences Center, Vilnius University, Vilnius, Lithuania

e-mail: dovile.stravinskiene@gmc.vu.lt; aurelija.zvirbliene@bti.vu.lt

© Springer Nature Switzerland AG 2019

D. Matulis (ed.), *Carbonic Anhydrase as Drug Target*,
https://doi.org/10.1007/978-3-030-12780-0_20

305

20.1 Introduction

The field of immunotherapy is progressing apace. Eleven years after description of hybridoma technology for monoclonal antibody (MAb) production [1], the first murine MAb OKT3 (Muromonab-CD3) [2] was approved by the FDA as a therapeutic agent for human use. At the same time, first attempts to generate recombinant antibodies (rAb) preventing the formation of immune response against murine antibodies leading to inactivation of their therapeutic function were reported [3, 4]. Chimerization, humanization, phage display, and transgenic mice technologies have resulted in several generations of antibodies of various structures and enabled their use in treating a wide range of human diseases [5]. Engineered T cells expressing chimeric antigen receptors (CAR-T) are the latest FDA-approved technology merging *ex vivo* gene therapy and immunotherapy by creating the so-called living drug [6, 7].

The efficiency of immunotherapy is highly dependent on the availability of the reliable disease-relevant antigens. The increasing need to develop precise biomarkers led to the emergence of a number of approved drugs and even more candidates in several disease scenarios [8, 9]. For instance, for the treatment of eosinophilic asthma, FDA has recently approved Bendralizumab, Mepolizumab, and Reslizumab targeting interleukin-5 (IL-5) responsible for eosinophil growth and activation [10, 11]. B-lymphocyte antigen CD19 expressed in many B cell tumors is targeted by a novel CAR T cell therapy that has shown high efficiency for the treatment of acute lymphoblastic leukemia [7, 12]. In solid tumors, easily attainable cell surface proteins which are abundantly expressed in tumor tissues with no or low expression in normal tissues could be ideal targets for immunotherapy. The biological function of the target antigen, its contribution to carcinogenesis, and homogeneous expression or minimal secretion are important factors that should be considered for selecting the target antigens [13, 14]. In addition, to increase the advantages of immunotherapy, patient stratification should be made and the subpopulations of antigen-expressing patients must be defined to separate patients responding to treatment from non-responders [11].

Despite already approved drugs for the treatment of cancer, there is still a demand of novel improved targets and therapeutic agents with less toxicity and application for wider population or different type of cancers. Here, we discuss the suitability of carbonic anhydrases as cancer antigens and their potential as targets for antibody-based cancer immunotherapy as well as development of CA-targeting antibodies of potential therapeutic relevance.

20.2 CA IX-Targeting Immunotherapy

Cell surface-exposed transmembrane carbonic anhydrase IX (CA IX) with its catalytic site directed to the intercellular space is considered as a reliable biomarker of hypoxic tumors and can be efficiently targeted by antibody-based cancer therapy

[15, 16]. Insignificant expression of CA IX in unaltered tissues reduces the risk of potential side effects and high protein level present in different tumor types (liver, gallbladder, kidney, colon, cervix, breast, lung, brain, head and neck, etc. [17–26]) enables application of CA IX-targeted immunotherapy in a variety of cases [27–29]. CA IX role in carcinogenesis is of great importance considering its involvement in tumor promotion, progression, and diffusion through intracellular and extracellular pH regulation, thus encouraging further development of anti-cancer agents to improve the current immunotherapeutic protocols in various kinds of tumor treatments [29, 30].

20.2.1 Mouse Monoclonal Antibodies and their Derivatives Targeting CA IX

During the last 30 years, different antibody production strategies were applied to generate CA IX-targeting antibodies suitable for cancer immunotherapy (extensive details and relevant references are given in Table 20.1). Several MAbs of mouse origin (G250, M75, and VII/20) were derived by hybridoma technology using different antigens for immunizations, either isolated CA IX protein or CA IX-expressing cells, such as tumor cells from renal-cell carcinoma (RCC) lesions, cervical cancer cells (HeLa), colorectal carcinoma cells (HT-29), or mouse NIH3T3 fibroblasts stably transfected with the wild-type CA9 cDNA. The obtained MAbs were directed against the functional (CA) or proteoglycan (PG) domains of CA IX and were reactive with native CA IX protein on the cell surface without any cross-reactivity with other CA isoforms. Antibody M75 is broadly used for detection of CA IX by different immunochemical methods, mainly immunohistochemistry. Antibody VII/20 showed anti-cancer effect in mouse xenograft model of colorectal carcinoma, therefore is considered as a potential immunotherapeutic tool. Meanwhile, MAb G250 and its chimeric derivative cG250 conjugated with different radionuclides were involved in various preclinical and clinical phase I/II studies for metastatic clear cell renal-cell carcinoma (ccRCC) treatment [31, 32]. However, iodine-131-labeled mouse MAb G250 (^{131}I -G250) rapidly failed phase I/II radioimmunotherapy trial as human anti-mouse antibodies (HAMA) developed after a single antibody infusion and there was no significant positive outcome [33]. Further clinical studies were performed with cG250 antibody conjugated to Iodine-131, Lutetium-177, or Yttrium-90 for radioimmunotherapy, or by infusion of either non-labeled cG250 alone or in combination with cytokines to initiate cancer cell killing through antibody-dependent cellular cytotoxicity (ADCC) (Fig. 20.1, A and B) [34]. To summarize the results of radioimmunotherapy studies, it was proposed to use ^{131}I -cG250 for low-volume lesions, while ^{177}Lu -cG250 was recommended to use to suspend the previously cumulative metastatic ccRCC. From the clinical point of view, no complete response was achieved by using G250-based radioimmunotherapy. Two partial remission cases and several patients with a stabilized disease have been reported, while the rest of patients had a progressive disease. On

Table 20.1 An overview of production, characterization, and application of CA IX-targeting antibodies

Antibody title, format, production technology	Properties	Application
<p>G250 [57–59] Mouse MAb, IgG1 subclass Hybridoma technology; antigen: cell homogenates from primary renal-cell carcinoma (RCC) lesions obtained from 4 different patients cG250, Girentuximab, RENCAREX [60] Human/mouse chimeric derivative of G250 MAb, IgG1 subclass Chimeric antibody is composed of the murine variable region from the G250 MAb and the constant region of the human IgG1 isotype domains</p>	<p>Interacts with the native CA IX protein; recognizes a conformational epitope in the CA domain, does not bind in or close to the active site; detects the soluble CA IX ectodomain (ECD), but not the splicing variant; does not cross-react with CA I, CA II, and CA XII isoforms or with mouse and rat CA IX orthologs cG250 functions principally via antibody-dependent cell-cytotoxicity (ADCC)</p>	<p>Immunohistochemical staining of cryostat tissue samples but not with formalin-fixed and paraffin-embedded tissue sections; immunofluorescence; ELISA; immunoprecipitation; radioimmunoscintigraphy with animal models with human tumor xenografts cG250 is currently being evaluated for the immunotherapy of kidney cancer</p>
<p>M75 [16, 20, 61–63] Mouse MAb, IgG2b subclass; Hybridoma technology; antigen: HeLa cells</p>	<p>Recognizes linear epitope GEEDLP which is located in the proteoglycan domain of CA IX; recognizes both native and denatured antigen</p>	<p>Western blot; ELISA; immunofluorescence using acetone fixation or vital staining; immunohistochemistry with snap-frozen, acetone-fixed sections, and formalin-fixed and paraffin-embedded tissues; immunoradiometric assay It is mainly used for diagnostic purposes in immunohistochemistry</p>

<p>A3 and CC7 [64] Humanized mAbs, expressed as scFv fragments in <i>E. coli</i> and in small immunoprotein (SIP) format in CHO-S cells Phage-display technology. Human MABs were isolated from the ETH-2-Gold phage antibody library. Affinity-maturation by combinatorial mutagenesis of residues in the CDR1 loops of VH and VL domains was used, yielding clone A3, following with additional mutagenesis of CDR2 providing the derivative antibody clone CC7</p>	<p>SIP antibodies recognize native human CA IX with affinities in the low nanomolar range, do not inhibit CA IX activity, and do not bind to CA XII; localize to hypoxic areas of tumor xenografts after i.v. administration into the tail vein of mice</p>	<p>Fluorescence-activated cell sorting (FACS); immunofluorescence with frozen tissue sections</p>
<p>VII/20 [65, 66] Mouse MAb, IgG2a subclass Hybridoma technology using CA IX-deficient mice. Antigen: different combination of mouse NIH3T3 fibroblasts stably transfected with the wild-type CA9 cDNA, HT-29 human colorectal carcinoma cells naturally expressing CA IX, and recombinant bacterial CA domain of CA IX fused to GST</p>	<p>Reacts with human, but not mouse CA IX; binds to the CA domain, recognizes conformational epitope, shows no cross-reactivity with CA I, CA II, and CA XII. After binding to CA IX on cell surface, the VII/20 MAb undergoes efficient receptor-mediated internalization, which has a significant influence on immunotherapy. It is able to induce anti-cancer effect in mouse xenograft model</p>	<p>ELISA, immunofluorescence (with cells fixed in ice-cold methanol), immunoprecipitation, immunohistochemistry (with tissue sections from paraffin-embedded tumor xenografts generated from HeLa cells)</p>
<p>MSC8 [27] Antigen-binding antibody fragment (Fab) and its corresponding full-length IgG Phage-display technology. A non-immunized human donor phage library expressing Fab antibodies was used for selection. Fab antibodies were produced in <i>E. coli</i> TG-1; variable domains of selected MSC8 were cloned into the plasmid to obtain a fully human IgG1, stably expressed in NS0 cells</p>	<p>Recognizes native CA IX protein; do not bind to other membrane-tethered isoforms (CA IV, CA XII, and CA XIV) or the cytosolic isoform CA II; MSC8 Fab is not competing with M75 or G250, which indicates non-overlapping epitopes; Fab and full-length IgG inhibited CA IX by up to 57 and 76%, respectively, with half-maximal inhibition at 6.5 nM for MSC8 Fab and 2.2nM for MSC8 IgG</p>	<p>ELISA, FACS</p>

(continued)

Table 20.1 (continued)

Antibody title, format, production technology	Properties	Application
<p>Collection of 14 scFv-Fc fusion antibodies (G10, G36, G37, G39, G45, G57, G106, G119, G6, G27, G40, G125, G9, G104) [67]</p> <p>Phage-display technology; two non-immune human scFv-phage display libraries were used to directly isolate CA IX specific antibodies by panning with CA IX-containing paramagnetic proteoliposomes; ScFvs were subcloned, expressed in 293FT cells, and purified as scFv-Fc fusion proteins</p>	<p>Thirteen (except G104) anti-CA IX scFv-Fcs specifically recognized native CA IX; antibodies interacted with the CA domain and the affinity binding constant (KD) ranged between 1.5 and 4.3 nM. Four antibodies (G6, G37, G39, and G125) were capable of inhibiting the CA activity and six (G45, G119, G10, G37, G36, and G106) induced surface CA IX internalization efficiently</p>	<p>ELISA, FACS, immunofluorescence</p>

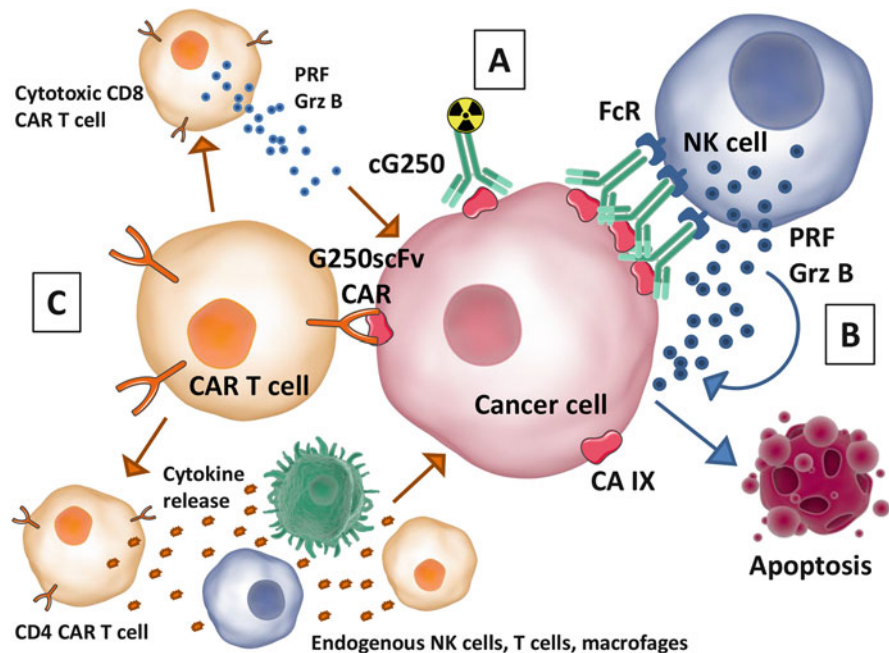


Fig. 20.1 Different approaches for G250 antibody-based targeting of CA IX-positive cancer cells. A—Radioisotopes (^{131}I , ^{177}Lu , ^{90}Y) conjugated to chimeric antibody cG250 can be delivered to tumor site and damage DNA of tumor cell, leading to cell death [34, 40]. B—Immune effector mechanisms such as antibody-dependent cellular cytotoxicity (ADCC) or complement-dependent cytotoxicity (CDC) can be engaged by cG250. After cG250 antibody binds to CA IX, the Fc domain is recognized by Fc receptor (FcR) expressed on natural killer (NK) cells, which triggers NK cells degranulation by releasing the content of cytotoxic granules with perforin (PRF) and granzymes (Grz B) and cytokine secretion promoting tumor cell lysis [34, 41]. C—Isolated patient's T cells can be activated ex vivo by transduction with a genetically engineered single-chain fragment variable of G250 (G250scFv) based chimeric antigen receptor (CAR), then expanded ex vivo and re-infused to patient. Modified CAR T cells are activated after binding to CA IX on tumor cells and can release PRF and Grz B for direct cell killing (CD8+ CAR T cells) or can attract other components of the immune system (endogenous NK cells, T cells, and macrophages) by cytokine release (CD4+ CAR T cells) [42–44]

the other hand, radioimmunotherapy resulted in grade 3–4 myelotoxicity in most patients, thus preventing the prolonged treatment efficiency [35–39].

As mentioned above, non-labeled cG250 entered a few clinical trials alone or along with a subcutaneous injection of cytokines interleukin-2 (IL-2) or interferon alpha 2b (IFN- α 2b) expecting an enhanced ADCC and elevated anti-tumor responses [34]. As a single agent, cG250 was safe and no serious adverse events were observed up to the highest dose, in contrast to radioimmunotherapy. During phase I/II clinical studies, two cases of complete anti-tumor response were attained, one patient had a partial response and a considerable number of patients with stable disease were observed [45, 46]. The ARISER double blind randomized phase III

study to evaluate the adjuvant monotherapy with cG250 was subsequently carried out for a total of 864 patients with high-risk clinically localized ccRCC. There was no statistically significant difference between cG250 ($n = 433$) and placebo ($n = 431$) treated patients in terms of disease-free survival and the overall survival. Still, cG250 therapy was well tolerated and a non-significant disease-free survival benefit was observed for those patients with higher expression of CA IX [47, 48].

The anti-tumor activity of cG250 is based on ADCC, so its efficacy is highly dependent on the capacity of patient's immune system, for example, when an immune response declines with age [49, 50]. The combined therapy with the regulators of the immune system, such as cytokines that control proliferation, differentiation, effector functions, and survival of leukocytes, should be preeminent than antibodies alone [51]. Cytokines IFN- α 2b or IL-2 co-administered with cG250 entered a few clinical studies to augment the ADCC by subcutaneous low-dose weekly injection schedule. To sum up the clinical benefit of these trials, in total one patient had a complete remission, four patients—partial remission, the disease was stabilized in 15 cases, and the rest of the patients had a progressive condition. Treatment was quite well tolerated with a modest toxicity and most recorded side effects were linked to the activity of cytokines. Although complete responses are still very rare, it is important to notice that patients receiving an extended treatment showed a significantly longer survival rate than the non-responders, and an increased overall survival rate compared to cG250 monotherapy [52–54]. Further randomized clinical trials are needed to approve these promising results.

20.2.2 Phage-Display Derived Various Formats of Human Antibodies Against CA IX

Next generation of antibody formats either humanized or fully human antibodies targeting CA IX are on their way. Researchers seek to create more innovative tools for immunodiagnostics and immunotherapy with improved qualities such as reduced immunogenicity, better tissue penetration, or direct inhibition of the target. Genetic engineering, recombinant protein production, combinatorial mutagenesis, and phage-display technologies are employed to obtain desirable candidates for cancer therapy [55]. Since the chimeric cG250 anti-CA IX antibody entered clinical trials, infrequent human anti-chimeric antibody (HACA) responses were recorded, causing rapid clearance of cG250 and suspending subsequent treatment [35, 36, 46, 56]. Humanized antibody fragments or fully human antibodies targeting CA IX (A3 and CC7, MSC8, collection of 14 scFv-Fc fusion antibodies) were generated by phage-display technology using non-immune human single-chain fragment variable (scFv) phage-display libraries, expecting to overcome the immunogenicity problem. High-affinity human monoclonal antibodies A3 and CC7 were selected after two rounds of combinatorial mutagenesis for affinity-maturation and were able to target CA IX *in vivo*. Collection of 14 human scFv-Fc fusion antibodies diverse in their functions was isolated using CA IX-containing paramagnetic proteoliposomes. Part of these antibodies were able to inhibit the enzymatic activity of CA IX (none of

the previously described antibodies had inhibitory effect) and others could induce receptor-mediated antibody internalization allowing tumor targeting by delivery of various therapeutic cytotoxins and radionuclides. Another inhibitory antibody MSC8 in antigen-binding antibody fragment (Fab) or full-length IgG format is highly perspective to interfere with tumor growth by combining target specificity with enzymatic inhibition (relevant references are presented in Table 20.1). However, there are a lot of aspects to be proved as, to the best of our knowledge, none of these antibodies are undergoing clinical evaluation.

20.2.3 CAR T Cell Immunotherapy Based on Anti-CA IX Single-Chain Fragment Variable

Beyond the antibody format, recently FDA-approved chimeric antigen receptor (CAR) T cell immunotherapy is being investigated for CA IX targeting in solid tumors (Fig. 20.1, C). The principle of this method is to induce expression of antibody-based artificial chimeric receptors in the membrane of autologous T cells by their transfection *ex vivo*. Modified T cells are expanded *in vitro* and re-infused into the patient for executing a targeted cytotoxic immune response against target cells [68]. In case of CA IX-based targeting, single-chain fragment variable of murine G250 (G250-scFv) was linked to different intracellular signaling molecules, such as γ -chain of immunoglobulin E receptor (Fc ϵ RI) or CD4 transmembrane region coupled to the signal transducing TCR/CD3 ζ chain to optimize membrane expression of CAR and specific cytolysis of target cells [69, 70]. Such modified receptor is sufficient to transfer activation signal to the T cell after scFv fragment binds to the antigen in MHC-independent manner [42]. CAR with G250-scFv transgene was inserted in a few different retroviral vectors (LXSN and pSTITCH) for efficient gene transduction and was co-transfected with plasmids (pHIT6016 and pCOLT-GALV) encoding genes for GAG (major structural polyprotein), Pol (reverse transcriptase), and Env (surface glycoprotein and transmembrane proteins) proteins to allow the formation of vector-containing viral particles. Two retrovirus culture supernatant batches containing gibbon ape leukemia virus-enveloped vector (GaLV) and Moloney murine leukemia virus-enveloped vector were produced in PG13 and Phoenix-Ampho packaging cell lines, respectively [70–74]. Phoenix clone 58 and PG13 clone 1.2 were evaluated for their potency to transduce primary human T cells by analyzing the expression of G250-scFv (flow cytometry), cytokines IFN- γ , TNF- α , IL-4, IL-5, and IL-10 production level (cytokine bead array) and antigen-specific cytotoxicity (^{51}Cr -release assay). A significantly higher transduction yield and an enhanced TNF- α production as well as cytolysis of RCC cells were achieved by using Phoenix clone 58 retrovirus culture supernatant, which was further applied in phase I/II clinical study [72].

No conventional treatment was available for 12 patients with progressive metastatic RCC involved in adoptive CAR T cells therapy. All patients had undergone nephrectomy and have been diagnosed with CA IX-positive primary tumors. An inpatient dose-escalation scheme of injected cells was intended

to be applied for the first eight patients to ascertain maximum tolerated dose; however, a liver enzyme dose-limiting toxicity occurred at the starting dose. Four out of eight patients had liver enzyme disturbances of grades 2–4 (according to Common Toxicity Criteria), which was shown to be antigen-related by the immunohistochemistry of liver biopsy. CA IX expression was observed using MAb M75 in the epithelial cells of the bile duct causing T cell accumulation around it or infiltrating the epithelium. Therefore, the rest four patients were pre-treated with the anti-CA IX MAb G250 to circumvent the interaction of G250-scFv transduced T cells with target antigen expressed on normal tissue. Afterwards, no toxicities were observed allowing increased T cell doses. However, the so-called first generation CAR T cells approach did not yield any positive clinical responses, thus suggesting the need for an improvement of future treatment strategies [44, 75].

Great efforts are being made to develop second generation CAR constructs for CA IX targeting by transduced human T cells to improve their proliferation, effector functions, and cytokine secretion or to overcome their anergic state *in vivo* [76, 77]. The previously mentioned high-affinity human anti-CA IX scFv G36 (Table 20.1) [67] derived by phage-display technology was coupled to truncated extracellular, hinge, transmembrane, and intracellular domains of CD8 α and signaling domain of human TCR ζ (first generation CAR: scFv(G36)-CD8-TCR ζ) or to costimulatory activating motifs from CD28 and the signaling motif from the TCR ζ chain (second generation CAR: scFv(G36)-CD28-TCR ζ). The transgenes were cloned into self-inactivating lentiviral vector pHAGE and transiently transfected into human primary T cells (293T) along with four HIV helper plasmids. After transduction of human primary T cells with lentivirus supernatants, both batches of modified T cells expressing first and second generation CARs were compared for cytokine secretion, *in vitro* specific cytotoxicity, *in vitro* proliferation, persistent effector function, suppression of established tumor in nude mice, and *in situ* cytotoxicity. Second generation CAR scFv(G36)-CD28-TCR ζ outperformed first generation receptors-bearing T cells, thus providing opportunities for more efficient treatment of cancer [77, 78].

Novel approach to improve the efficiency of CA IX-targeted CAR T cells was recently published by Suarez and colleagues. CAR T cells expressing second generation chimeric receptor scFv(G36)-CD28-TCR ζ were modified to secrete human IgG1 or IgG4 antibodies targeting programmed death ligand 1 (PD-L1) [79]. Many cancers upregulate PD-L1 (type I transmembrane glycoprotein) expression, thus leading to immune tolerance against cancer by activating the immune checkpoint receptor programmed death 1 (PD-1) protein expressed on the membrane of activated T cells. Negative signaling pathway of PD-1 is responsible for the induction of T cell anergy and the restriction of T cell activity. Several antibodies, suspending the interaction of PD-1/PD-L1 and therefore maintaining the anti-tumor potency of T cells, are already approved for cancer therapy [80–83]. Consequently, improved engineered T cells expressing the combination of membranous anti-CA IX CARs and secreted anti-PD-L1 antibodies are promising anti-cancer therapeutic agents. CAR T cells are guided to the site of CA IX-expressing tumor and are delivering secreted anti-PD-L1 antibodies, which efficiently block PD-L1/PD-1 binding, thus demonstrating superior properties to antibody non-secreting CAR T

cells. The engineered CAR T cells showed an enhanced resistance to exhaustion, anti-tumor activity, and employment of other immune cells, leading to reduced proliferation of tumor cells and decreased tumor growth in a mouse model [79]. Although a lot has to be confirmed, cancer immunotherapy is becoming more and more advanced and individualized, expecting to obtain positive clinical outcome for more patients.

20.3 Prospects of Antibodies Against CA XII for Immunotherapy

Besides CA IX, carbonic anhydrase XII (CA XII) is another cell surface membrane protein of carbonic anhydrase family, whose increased expression is linked to cancer or other pathological disorders, such as glaucoma [84], juvenile idiopathic arthritis [85], chronic low back pain [86], and advanced atherosclerosis [87]. In case of cancer, alterations in expression levels of CA XII in normal and malignant tissues are intensively investigated. Unlike CA IX, CA XII is found in broader range of normal tissues (breast, renal, uterus, sweat glands of the skin, and seminal vesicles), which might result in unwanted side effects in terms of CA XII-targeted therapy [88]. Despite that, many studies have shown an abnormal expression of CA XII in renal-cell carcinoma [89], diffuse astrocytomas and other brain tumors [90,91], ovarian tumors [92], non-small cell lung cancers [93], colorectal tumors [94], invasive breast cancer [95], and oral cancer [96], thus suggesting CA XII as a novel target for cancer therapy [97]. It has been demonstrated in previous reports that CA XII silencing or inhibition with chemical compounds, such as acetazolamide, sensitizes chemoresistant colon cancer cells [98], decreases invasion and migration of breast cancer cells [99], reduces proliferation, and entails apoptosis of T cell lymphoma cells [100]. Moreover, combined invalidation of both cancer-related CA XII and CA IX diminished the growth of cancer cells *in vitro* and *in vivo* more efficiently, compared to silencing CA IX alone, which was buffered by upregulation of CA XII [101]. This provides new strategies for cancer therapy, based not only on CA IX inhibition, but also on targeting CA XII or both CA isoforms.

While antibodies against CA IX are counting more than 30 years of exploitation and various derivatives are already in the trial stage for cancer immunotherapy, antibodies recognizing CA XII are still at the early stage of development. First publications analyzing CA XII expression in various normal tissues and cancer specimens were based on polyclonal rabbit antiserum [89], which was used to detect CA XII basically by immunohistochemical staining [23, 84, 88, 102]. Polyclonal antibodies are decent reagents for research or diagnostic purposes, as their production is straightforward and rapid process usually without much cost. However, prospects to use polyclonal serum for the treatment of infectious diseases or cancer are limited because of the inability to reproduce batches of equal characteristics or appearance of severe side effects related to significant amount of donor proteins injected to the patient. The nature of polyclonal antibodies recognizing numerous epitopes affects their ability to localize cancer in human body, thus application

of polyclonal antibodies for immunoimaging or immunotherapy is practically impossible [103, 104].

Highly specific monoclonal antibodies were obtained after rats were immunized with lung cancer cells A549 [105], which were previously reported for high CA XII expression [101]. MAb 6A10 was reactive with native CA XII protein on cell surface by flow cytometry and was not only able to inhibit recombinant CA XII by a stopped-flow method, but also inhibited the three-dimensional growth of tumor cells. Anti-tumor efficacy of MAb 6A10 was further investigated in a mouse xenograft model of human lung cancer, showing a significant MAb 6A10 interference with tumor growth [105, 106]. The following study demonstrated an enhanced chemosensitivity of chemoresistant cancer cells and reduction of metastases in mice xenograft model after MAb 6A10 was co-administered with doxorubicin [107]. Most recent report on 6A10 Fab (fragment antigen binding) fragment application for radioimmunotherapy and positron emission tomography indicated promising results for cancer imaging and therapy [108, 109].

Recently, we have reported generation of a large collection of murine MAbs against CA XII [110, 111]. In our studies, mice were injected with either synthetic peptide of the selected CA XII surface-located sequence conjugated with keyhole limpet hemocyanin (KLH) carrier [110] or purified recombinant extracellular domain of human CA XII expressed in *E. coli* cells [111] to generate MAbs against CA XII. Different strategies of immunization have resulted in MAbs of various characteristics and application potential. Production of MAbs based on the use of synthetic peptides, derived from the bioinformatics analysis of CA XII protein surface sequences, provides possibility to address antibodies to the desirable part of target protein, thus generating potentially inhibitory MAbs. We have demonstrated that MAbs 1D8 and 3C8 raised against synthetic peptide corresponding to 167–180 amino acid sequence of CA XII were able to inhibit the enzymatic activity of recombinant CA XII protein; moreover, clone 3C8 recognized cellular CA XII by immunohistochemistry in formalin-fixed and paraffin-embedded specimens of breast and lung cancer tissues [110]. Another set of antibodies was generated after mice were immunized with recombinant catalytic domain of CA XII expressed in bacterial expression system. *E. coli*-derived recombinant protein was highly immunogenic and the obtained MAbs were able to recognize various epitopes of CA XII. The MAbs were characterized by different immunochemical methods showing their broad applicability for CA XII immunodetection, in particular clone 15A4, which was reactive with cellular CA XII both by flow cytometry and immunohistochemistry [111]. However, these antibodies were not reactive with native CA XII protein on the surface of living cells (data not published), which limits their application to therapy. To overcome this limitation, we have improved our immunization strategy and generated a new collection of MAbs using as an immunogen recombinant CA XII extracellular domain produced in human HEK 293 cells. We expected to generate MAbs targeting native CA XII by using recombinant immunogen that was supposed to be more similar to cellular CA XII in terms of post-translational modification than previously used antigens. We succeeded in generating 24 MAbs against CA XII despite the low immunogenicity of recombinant

antigen. All MAbs were comprehensively analyzed for their ability to detect native CA XII on the cell surface and 12 MAbs were shown to recognize cellular CA XII by flow cytometry. Further investigations demonstrated an inhibitory activity of one clone by stopped-flow assay (publication in preparation). These findings encourage further investigation to elucidate perspectives of this MAb in terms of CA XII-based immunotherapy.

20.4 Conclusions

Antibody-based immunotherapy is currently going through a huge ascension as more and more antibodies or their derivatives are approved for the treatment of cancer and other diseases. Better understanding of the mechanisms of diseases provides more accurate targets for antibody-based treatment. Different strategies are applied for producing therapeutic antibodies or their derivatives with reduced side effects, improved tissue penetration, or longer half-life. Carbonic anhydrases IX and XII are now recognized as potential cancer antigens and targets for antibody-based therapy. Antibodies against CA IX, in particular clone G250, have already been tested in a number of clinical trials. Antibodies against CA XII are still at the early stage of development.

References

1. Köhler, G., Milstein, C.: Continuous cultures of fused cells secreting antibody of predefined specificity. *Nature* **256**, 495–497 (1975)
2. Abramowicz, D., et al.: Release of tumor necrosis factor, interleukin-2, and gamma-interferon in serum after injection of OKT3 monoclonal antibody in kidney transplant recipients. *Transplantation* **47**, 606–608 (1989)
3. Jones, P.T., Dear, P.H., Foote, J., Neuberger, M.S., Winter, G.: Replacing the complementarity-determining regions in a human antibody with those from a mouse. *Nature* **321**, 522–525 (1986)
4. Legouffe, E., et al.: Human anti-mouse antibody response to the injection of murine monoclonal antibodies against IL-6. *Clin. Exp. Immunol.* **98**, 323–329 (1994)
5. Beck, A., Wurch, T., Bailly, C., Corvaia, N.: Strategies and Challenges for the next Generation of Therapeutic Antibodies. *Nat. Rev. Immunol.* **10**, 345–352 (2010)
6. Fesnak, A.D., June, C.H., Levine, B.L.: Engineered T cells: the promise and challenges of cancer immunotherapy. *Nat. Rev. Cancer* **16**, 566–581 (2016)
7. Mullard, A.: FDA approves first CAR T therapy. *Nat. Rev. Drug Discov.* **16**, 669–669 (2017)
8. Ilyas, S., Yang, J. C.: Landscape of tumor antigens in T cell immunotherapy. *J. Immunol.* **195**, 5117–5122 (2015)
9. Judkowski, V. A., et al.: Antigen discovery for the identification of vaccine candidates and biomarkers using a T cell driven approach in combination with positional scanning peptide libraries. *Procedia in Vaccinology* **9**, 91–95 (2015)
10. Fritzsching, B.: Personalized medicine in allergic asthma: at the crossroads of allergen immunotherapy and “Biologicals”. *Front. Pediatr.* **5**(2017)
11. Rothenberg, M.E.: Humanized anti-IL-5 antibody therapy. *Cell* **165**, 509 (2016)
12. Wang, K., Wei, G., Liu, D.: CD19: a biomarker for B cell development, lymphoma diagnosis and therapy. *Exp. Hematol. Oncol.* **1**, 36 (2012)

13. Scott, A.M., Wolchok, J.D., Old, L.J.: Antibody therapy of cancer. *Nat. Rev. Cancer* **12**, 278–287 (2012)
14. Scott, A.M., Allison, J.P., Wolchok, J.D.: Monoclonal antibodies in cancer therapy. *Cancer Immun.* **12**, 8 (2012)
15. Li, Y., et al.: Expression and activity of carbonic anhydrase IX is associated with metabolic dysfunction in MDA-MB-231 breast cancer cells. *Cancer Investig.* **27**, 613–623 (2009)
16. Takacova, M., et al.: encapsulation of anti-carbonic anhydrase IX antibody in hydrogel microspheres for tumor targeting. *J. Enzyme Inhib. Med. Chem.* **31**, 110–118 (2016)
17. Chia, S.K., et al.: Prognostic significance of a novel hypoxia-regulated marker, carbonic anhydrase IX, in invasive breast carcinoma. *J. Clin. Oncol.* **19**, 3660–3668 (2001)
18. Kang, H.J., Kim, I.H., Sung, C.O., Shim, J.H., Yu, E.: Expression of carbonic anhydrase 9 is a novel prognostic marker in resectable hepatocellular carcinoma. *Virchows Arch. Int. J. Pathol.* **466**, 403–413 (2015)
19. Koukourakis, M.I., et al.: Hypoxia-regulated carbonic anhydrase-9 (CA9) relates to poor vascularization and resistance of squamous cell head and neck cancer to chemoradiotherapy. *Clin. Cancer Res.* **7**, 3399–403 (1994)
20. Liao, S.Y., Aurelio, O., Jan, K., Zavada, J., Stanbridge, E.: Identification of the MN/CA9 protein as a reliable diagnostic biomarker of clear cell carcinoma of the kidney. *J. Urol.* **159**, 1784–1785 (1998)
21. Liao, S.Y., et al.: Identification of the MN antigen as a diagnostic biomarker of cervical intraepithelial squamous and glandular neoplasia and cervical carcinomas. *Am. J. Pathol.* **145**(3), 598–609 (1994)
22. Liu, Z., et al.: Paxillin and carbonic anhydrase IX are prognostic markers in gallbladder squamous cell/adenosquamous carcinomas and adenocarcinomas. *Histopathology* **64**, 921–934 (2014)
23. Proescholdt, M.A., et al.: Expression of hypoxia-inducible carbonic anhydrases in brain tumors. *Neuro-Oncology* **7**, 465–475 (2005)
24. Saarnio, J., et al.: Immunohistochemical study of colorectal tumors for expression of a novel transmembrane carbonic anhydrase, MN/CA IX, with potential value as a marker of cell proliferation. *Am. J. Pathol.* **153**, 279–285 (1998)
25. Vermeylen, P., et al.: Carbonic anhydrase IX antigen differentiates between preneoplastic malignant lesions in non-small cell lung carcinoma. *Eur. Respir. J.* **14**, 806 (1999)
26. Závada, J., et al.: Expression of MaTu-MN protein in human tumor cultures and in clinical specimens. *Int. J. Cancer* **54**, 268–274 (1993)
27. Murri-Plesko, M.T., et al.: Antibody inhibiting enzymatic activity of tumour associated carbonic anhydrase isoform IX. *Eur. J. Pharmacol.* **657**, 173–183 (2011)
28. Said, H.M., et al. Distinct patterns of hypoxic expression of carbonic anhydrase IX (CA IX) in human malignant glioma cell lines. *J. Neuro-Oncol.* **81**, 27–38 (2006)
29. Thiry, A., Dogné, J.-M., Masereel, B., Supuran, C.T.: Targeting tumor-associated carbonic anhydrase IX in cancer therapy. *Trends Pharmacol. Sci.* **27**, 566–573 (2006)
30. Fang, J.S., Gillies, R.D., Gatenby, R.A.: Adaptation to hypoxia and acidosis in carcinogenesis and tumor progression. *Semin. Cancer Biol.* **18**, 330–337 (2008)
31. Lau, J., Lin, K.-S., Bénéard, F.: Past, present, and future: development of theranostic agents targeting carbonic anhydrase IX. *Theranostics* **7**, 4322–4339 (2017)
32. Supuran, C.T., et al.: Inhibition of carbonic anhydrase IX targets primary tumors, metastases, and cancer stem cells: three for the price of one. *Med. Res. Rev.* **38**, 1799–1836 (2018)
33. Divgi, C.R., et al.: Phase I/II radioimmunotherapy trial with iodine-131-labeled monoclonal antibody G250 in metastatic renal cell carcinoma. *Clin. Cancer Res.* **4**, 2729–2739 (1998)
34. Oosterwijk-Wakka, J., Boerman, O., Mulders, P., Oosterwijk, E.: Application of monoclonal antibody G250 recognizing carbonic anhydrase IX in renal cell carcinoma. *Int. J. Mol. Sci.* **14**, 11402–11423 (2013)
35. Brouwers, A.H.: Radioimmunotherapy with [¹³¹I]cG250 in patients with metastasized renal cell cancer: dosimetric analysis and immunologic response. *Clin. Cancer Res.* **11**, 7178s–7186s (2005)

36. Divgi, C.R., et al.: Phase I clinical trial with fractionated radioimmunotherapy using ¹³¹I-labeled chimeric G250 in metastatic renal cancer. *J. Nucl. Med.* **45**, 1412–21 (2004)
37. Muselaers, C.H., et al.: Phase 2 study of lutetium ¹⁷⁷-labeled anti-carbonic anhydrase IX monoclonal antibody girentuximab in patients with advanced renal cell carcinoma. *Eur. Urol.* **69**, 767–770 (2016)
38. Steffens, M.G., et al.: Phase I radioimmunotherapy of metastatic renal cell carcinoma with ¹³¹I-labeled chimeric monoclonal antibody G250. *Clin. Cancer Res. Off. J. Am. Assoc. Cancer Res.* **5**, 3268s–3274s (1999)
39. Stillebroer, A.B., et al.: Dosimetric analysis of ¹⁷⁷Lu-cG250 radioimmunotherapy in renal cell carcinoma patients: correlation with myelotoxicity and pretherapeutic absorbed dose predictions based on ¹¹¹In-cG250 imaging. *J. Nucl. Med.* **53**, 82–89 (2012)
40. Baskar, R., Lee, K.A., Yeo, R., Yeoh, K.W.: Cancer and radiation therapy: current advances and future directions. *Int. J. Med. Sci.* **9**, 193–199 (2012)
41. Wang, W.: NK cell-mediated antibody-dependent cellular cytotoxicity in cancer immunotherapy. *Front. Immunol.* **6**, 368 (2015)
42. Almásbak, H., Aarvak, T., Vemuri, M.C.: CAR T cell therapy: a game changer in cancer treatment. *J. Immunol. Res.* **2016**, 1–10 (2016)
43. Fan, M., et al.: Chimeric antigen receptors for adoptive T cell therapy in acute myeloid leukemia. *J. Hematol. Oncol.* **10**(1), 151 (2017)
44. Lamers, C.H., et al.: Treatment of metastatic renal cell carcinoma with CAIX CAR-engineered T cells: clinical evaluation and management of on-target toxicity. *Mol. Ther.* **21**, 904–912 (2013)
45. Bleumer, I., et al.: A phase II trial of chimeric monoclonal antibody G250 for advanced renal cell carcinoma patients. *Br. J. Cancer* **90**, 985–990 (2004)
46. Davis, I.D., et al.: A phase I multiple dose, dose escalation study of cG250 monoclonal antibody in patients with advanced renal cell carcinoma. *Cancer Immun.* **7**, 13 (2007)
47. Belldegrun, A.S., et al.: ARISER: a randomized double blind phase III study to evaluate adjuvant cG250 treatment versus placebo in patients with high-risk ccRCC—results and implications for adjuvant clinical trials. *J. Clin. Oncol.* **31**, 4507–4507 (2013)
48. Chamie, K., et al.: Adjuvant weekly girentuximab following nephrectomy for high-risk renal cell carcinoma: the ARISER randomized clinical trial. *JAMA Oncol.* **3**, 913–920 (2017)
49. Burns, E.A.: Effects of aging on immune function. *J. Nutr. Health Aging* **8**, 9–18 (2004)
50. Tomihara, K., Curiel, T.J., Zhang, B.: Optimization of immunotherapy in elderly cancer patients. *Crit. Rev. Oncog.* **18**, 573–583 (2013)
51. Waldmann, T.A.: Cytokines in cancer immunotherapy. *Cold Spring Harb. Perspect. Biol.* **10**(12), a028472 (2017)
52. Bleumer, I., et al.: A clinical trial with chimeric monoclonal antibody WX-G250 and low dose interleukin-2 pulsing scheme for advanced renal cell carcinoma. *J. Urol.* **175**, 57–62 (2006)
53. Davis, I.D., et al.: A pilot study of monoclonal antibody cG250 and low dose subcutaneous IL-2 in patients with advanced renal cell carcinoma. *Cancer Immun.* **7**, 14 (2007)
54. Siebels, M., et al.: A clinical phase I/II trial with the monoclonal antibody cG250 (RENCAREX®) and interferon-alpha-2a in metastatic renal cell carcinoma patients. *World J. Urol.* **29**, 121–126 (2011)
55. Laffly, E., Sodoyer, R.: Monoclonal and recombinant antibodies, 30 years after . . . *Hum. Antibodies* **14**, 33–55 (2006)
56. Steffens, M.G., et al.: Targeting of renal cell carcinoma with iodine-131-labeled chimeric monoclonal antibody G250. *J. Clin. Oncol.* **15**, 1529–1537 (1997)
57. Oosterwijk, E., Debruyne, F.M., Schalken, J.A.: The use of monoclonal antibody G250 in the therapy of renal-cell carcinoma. *Semin. Oncol.* **22**, 34–41 (1995)
58. Oosterwdk, E., et al.: Monoclonal antibody G 250 recognizes a determinant present in renal-cell carcinoma and absent from normal kidney. *Int. J. Cancer* **38**, 489–494 (1986)
59. Surfus, J.E., et al.: Anti-renal-cell carcinoma chimeric antibody G250 facilitates antibody-dependent cellular cytotoxicity with in vitro and in vivo interleukin-2-activated effectors. *J. Immunother. Emphasis Tumor Immunol. Off. J. Soc. Biol. Ther.* **19**, 184–191 (1996)

60. Zatovicova, M., et al.: Monoclonal antibody G250 targeting CA IX: binding specificity, internalization and therapeutic effects in a non-renal cancer model. *Int. J. Oncol.* **45**, 2455–2467 (2014)
61. Chrastina, A., et al.: Biodistribution and pharmacokinetics of ¹²⁵I-labeled monoclonal antibody M75 specific for carbonic anhydrase IX, an intrinsic marker of hypoxia, in nude mice xenografted with human colorectal carcinoma: tumor targeting by anti-CA IX MAB M75. *Int. J. Cancer* **105**, 873–881 (2003)
62. Pastoreková, S., Zavadová, Z., Košťál, M., Babušíková, O., Závada, J.: A novel quasi-viral agent, MaTu, is a two-component system. *Virology* **187**, 620–626 (1992)
63. Závada, J., et al.: Human tumour-associated cell adhesion protein MN/CA IX: identification of M75 epitope and of the region mediating cell adhesion. *Br. J. Cancer* **82**, 1808–1813 (2000)
64. Ahlskog, J.K.J., et al.: Human monoclonal antibodies targeting carbonic anhydrase IX for the molecular imaging of hypoxic regions in solid tumours. *Br. J. Cancer* **101**, 645–657 (2009)
65. Zatovicova, M., et al.: Carbonic anhydrase IX as an anticancer therapy target: preclinical evaluation of internalizing monoclonal antibody directed to catalytic domain. *Curr. Pharm. Des.* **16**, 3255–3263 (2010)
66. Zátovicová, M.: Monoclonal antibodies generated in carbonic anhydrase IX-deficient mice recognize different domains of tumour-associated hypoxia-induced carbonic anhydrase IX*1. *J. Immunol. Methods* **282**, 117–134 (2003)
67. Xu, C., et al.: Unique biological properties of catalytic domain directed human anti-CAIX antibodies discovered through phage-display technology. *PLoS One* **5**(ed Hofmann, A.), e9625 (2010)
68. Ventola, C.L.: Cancer immunotherapy. Part 1: Current strategies and agents. *P T.* **42**, 375–83 (2017)
69. Weijtens, M., Willemsen, R., Hart, E., Bolhuis, R.: A retroviral vector system ‘STITCH’ in combination with an optimized single chain antibody chimeric receptor gene structure allows efficient gene transduction and expression in human T lymphocytes. *Gene Ther.* **5**, 1195–1203 (1998)
70. Weijtens, M.E., Willemsen, R.A., Valerio, D., Stam, K., Bolhuis, R.L.: Single chain Ig/Gamma gene-redirceted human T lymphocytes produce cytokines, specifically lyse tumor cells, and recycle lytic capacity. *J. Immunol.* (Baltimore, Md.: 1950) **157**, 836–843 (1996)
71. Lamers, C.H., et al.: Long-term stability of T-cell activation and transduction components critical to the processing of clinical batches of gene-engineered T cells. *Cytotherapy* **15**, 620–626 (2013)
72. Lamers, C.H.J., et al.: Phoenix-ampho outperforms PG13 as retroviral packaging cells to transduce human T cells with tumor-specific receptors: implications for clinical immunogene therapy of cancer. *Cancer Gene Ther.* **13**, 503–509 (2006)
73. Lamers, C.H.J., Willemsen, R.A., Luiders, B.A., Debets, R., Bolhuis, R.L.H.: Protocol for gene transduction and expansion of human T lymphocytes for clinical immunogene therapy of cancer. *Cancer Gene Ther.* **9**, 613–623 (2002)
74. Morgan, R., Boyerinas, B.: Genetic modification of T cells. *Biomedicines* **4**, 9 (2016)
75. Lamers, C.H.J., et al.: Treatment of metastatic renal cell carcinoma with autologous T-lymphocytes genetically retargeted against carbonic anhydrase IX: first clinical experience. *J. Clin. Oncol. Off. J. Am. Soc. Clin. Oncol.* **24**, e20–22 (2006)
76. Hartmann, J., Schübler-Lenz, M., Bondanza, A., Buchholz, C.J.: Clinical development of CAR T cells—challenges and opportunities in translating innovative treatment concepts. *EMBO Mol. Med.* **9**, 1183–1197 (2017)
77. Lo, A.S.Y., Xu, C., Murakami, A., Marasco, W.A.: Regression of established renal cell carcinoma in nude mice using lentivirus-transduced human T cells expressing a human anti-CAIX chimeric antigen receptor. *Mol. Ther. Oncolytics* **1**, 14003 (2014)
78. Lee, D.W., Barrett, D.M., Mackall, C., Orentas, R., Grupp, S.A.: The future is now: chimeric antigen receptors as new targeted therapies for childhood cancer. *Clin. Cancer Res.* **18**, 2780–2790 (2012)

79. Suarez, E.R., et al.: Chimeric antigen receptor T cells secreting anti-PD-L1 antibodies more effectively regress renal cell carcinoma in a humanized mouse model. *Oncotarget* **7**(23), 34341–34355 (2016)
80. Alsaab, H.O., et al.: PD-1 and PD-L1 checkpoint signaling inhibition for cancer immunotherapy: mechanism, combinations, and clinical outcome. *Front. Pharmacol.* **8**, 561 (2017)
81. Bai, J., et al., Regulation of PD-1/PD-L1 pathway and resistance to PD1/PDL1 blockade. *Oncotarget* **8**(66), 110693–110707. (2017)
82. Jin, H.T., Ahmed, R., Okazaki, T.: Role of PD-1 in regulating T-cell immunity. *Curr. Top. Microbiol. Immunol.* **350**, 17–37 (2011)
83. Pardoll, D.M.: The blockade of immune checkpoints in cancer immunotherapy. *Nat. Rev. Cancer* **12**, 252–264 (2012)
84. Liao, S.Y.: Expression of cell surface transmembrane carbonic anhydrase genes CA9 and CA12 in the human eye: overexpression of CA12 (CAXII) in glaucoma. *J. Med. Genet.* **40**, 257–261 (2003)
85. Margheri, F., et al.: Overexpression of the transmembrane carbonic anhydrase isoforms IX and XII in the inflamed synovium. *J. Enzyme Inhib. Med. Chem.* **31**, 60–63 (2016)
86. Power, K.A., et al.: Identification of cell surface-specific markers to target human nucleus pulposus cells: expression of carbonic anhydrase XII varies with age and degeneration. *Arthritis Rheum.* **63**, 3876–3886 (2011)
87. Oksala, N., et al.: Carbonic anhydrases II and XII are upregulated in osteoclast-like cells in advanced human atherosclerotic plaques—Tampere vascular study. *Ann. Med.* **42**, 360–370 (2010)
88. Ivanov, S., et al.: Expression of hypoxia-inducible cell-surface transmembrane carbonic anhydrases in human cancer. *Am. J. Pathol.* **158**, 905–919 (2001)
89. Tureci, O., et al.: Human carbonic anhydrase XII: cDNA cloning, expression, and chromosomal localization of a carbonic anhydrase gene that is overexpressed in some renal cell cancers. *Proc. Natl. Acad. Sci.* **95**, 7608–7613 (1998)
90. Haapasalo, J., et al.: Identification of an alternatively spliced isoform of carbonic anhydrase XII in diffusely infiltrating astrocytic gliomas. *Neuro-Oncology* **10**, 131–138 (2008)
91. Nordfors, K., et al.: The tumour-associated carbonic anhydrases CA II, CA IX and CA XII in a group of medulloblastomas and supratentorial primitive neuroectodermal tumours: an association of CA IX with poor prognosis. *BMC Cancer* **10**, 148 (2010)
92. Hynninen, P., et al.: Expression of transmembrane carbonic anhydrases IX and XII in ovarian tumours. *Histopathology* **49**, 594–602 (2006)
93. Ilie, M.I., et al.: Overexpression of carbonic anhydrase XII in tissues from resectable non-small cell lung cancers is a biomarker of good prognosis. *Int. J. Cancer* **128**, 1614–1623 (2011)
94. Kivelä, A., et al.: Expression of a novel transmembrane carbonic anhydrase isozyme XII in normal human gut and colorectal tumors. *Am. J. Pathol.* **156**, 577–584 (2000)
95. Watson, P.H., et al.: Carbonic anhydrase XII is a marker of good prognosis in invasive breast carcinoma. *Br. J. Cancer* **88**, 1065–1070 (2003)
96. Chien, M.H., et al.: Tumor-associated carbonic anhydrase XII is linked to the growth of primary oral squamous cell carcinoma and its poor prognosis. *Oral Oncol.* **48**, 417–423 (2012)
97. Mboge, M., Mahon, B., McKenna, R., Frost, S.: Carbonic anhydrases: role in pH control and cancer. *Metabolites* **8**, 19 (2018)
98. Kopecka, J., et al.: Carbonic anhydrase XII is a new therapeutic target to overcome chemoresistance in cancer cells. *Oncotarget* **6**(9), 6776–6793 (2015)
99. Hsieh, M.J., Chen, K.S., Chiou, H.L., Hsieh, Y.S.: Carbonic anhydrase XII promotes invasion and migration ability of MDA-MB-231 breast cancer cells through the P38 MAPK signaling pathway. *Eur. J. Cell Biol.* **89**, 598–606 (2010)
100. Lounnas, N., et al.: Pharmacological inhibition of carbonic anhydrase xii interferes with cell proliferation and induces cell apoptosis in T-cell lymphomas. *Cancer Lett.* **333**, 76–88 (2013)

101. Chiche, J., et al.: Hypoxia-inducible carbonic anhydrase IX and XII promote tumor cell growth by counteracting acidosis through the regulation of the intracellular pH. *Cancer Res.* **69**, 358–368 (2009)
102. Karhumaa, P.: Identification of carbonic anhydrase XII as the membrane isozyme expressed in the normal human endometrial epithelium. *Mol. Hum. Reprod.* **6**, 68–74 (2000)
103. Lipman, N.S., Jackson, L.R., Trudel, L.J., Weis-Garcia, F.: Monoclonal versus polyclonal antibodies: distinguishing characteristics, applications, and information resources. *ILAR J.* **46**, 258–268 (2005)
104. Llewelyn, M.B., Hawkins, R.E., Russell, S.J.: Discovery of antibodies. *BMJ* **305**, 1269–1272 (1992)
105. Battke, C., et al.: Generation and characterization of the first inhibitory antibody targeting tumour-associated carbonic anhydrase XII. *Cancer Immunol. Immunother.* **60**, 649–658 (2011)
106. Gondi, G., et al.: Antitumor efficacy of a monoclonal antibody that inhibits the activity of cancer-associated carbonic anhydrase XII. *Cancer Res.* **73**, 6494–6503 (2013)
107. von Neubeck, B., et al.: An inhibitory antibody targeting carbonic anhydrase XII abrogates chemoresistance and significantly reduces lung metastases in an orthotopic breast cancer model in vivo: inhibition of carbonic anhydrase XII abrogates chemoresistance. *Int. J. Cancer* **143**, 2065–2075 (2018)
108. Fiedler, L., et al.: Fully automated production and characterization of ^{64}Cu and proof-of-principle small-animal PET imaging using ^{64}Cu -labelled CA XII targeting 6A10 Fab. *ChemMedChem* **13**, 1230–1237 (2018)
109. Fiedler, L., et al.: Evaluation of ^{177}Lu [Lu]-CHX-A''-DTPA-6A10 Fab as a radioimmunotherapy agent targeting carbonic anhydrase XII. *nuclear medicine and biology* **60**, 55–62 (2018)
110. Dekaminaviciute, D., et al.: Monoclonal antibodies raised against 167–180 Aa sequence of human carbonic anhydrase XII inhibit its enzymatic activity. *J. Enzyme Inhib. Med. Chem.* **29**, 804–810 (2014)
111. Dekaminaviciute, D., et al.: Development and characterization of new monoclonal antibodies against human recombinant CA XII. *Biomed. Res. Int.* **2014**, 1–11 (2014)



Aistė Imbrasaitė, Dovilė Stravinskienė, and Aurelija Žvirblienė

Abstract

Since the discovery of carbonic anhydrases (CAs), many studies have been done to learn more about their structure, functions, and distribution in different organisms. A variety of methods have been developed and applied for the detection of CAs, including chemical methods, based on CA enzymatic properties (histochemistry), autoradiography, immunological methods such as radioimmunoassay, immunohistochemistry, immunofluorescence, enzyme-linked immunosorbent assay (ELISA), and Western blot. It is now known that some isoforms of CA protein family are related to cancer (CA II, CA IX, and CA XII) and to other diseases, which makes detection of CAs in human organism highly important for the diagnostics of certain diseases as well as assessment of CA potential as a therapeutic target. In this chapter, we discuss various methods developed for CA detection starting from the first experimental approaches, and wide application of CA-specific antibodies which tremendously improved techniques for the CA analysis in different specimens or directly in human body.

21.1 First Analytical Methods for CA Detection

In 1932, CAs were first discovered in blood of various animals and described as a catalyst involved in the reversible hydration of carbon dioxide to bicarbonate. In 1933, this enzyme was detected in several lower marine organisms by measuring the velocity of reaction between CO_2 and NaHCO_3 solutions in various samples of different organisms. Phenol red was used as reaction indicator, which turned

A. Imbrasaitė · D. Stravinskienė · A. Žvirblienė (✉)

Department of Immunology and Cell Biology, Institute of Biotechnology, Life Sciences Center, Vilnius University, Vilnius, Lithuania

e-mail: aiste.imbrasait@gmc.vu.lt; dovile.stravinskiene@gmc.vu.lt; aurelija.zvirbliene@bti.vu.lt

into yellow, if the sample contained CA [1]. The chemical reaction ($\text{CO}_2 + \text{H}_2\text{O} \rightleftharpoons \text{HCO}_3^- + \text{H}^+$) catalyzed by these enzymes was used to develop new methods, dedicated for CA detection in certain samples. One of the first attempts to locate CAs was based on polyacrylamide gels. Carbon dioxide was used as the substrate and bromocresol purple as the indicator for hydrogen ions formed during the CA-catalyzed enzymatic reaction. In 1971, Patterson and others improved this experiment by using low-temperature fluorescence for better identification of CA bands in polyacrylamide gels [2]. Instead of using color indicators, conductivity measurements were used to detect CA in polyacrylamide gels by recording conductivity enhancement, which was caused by a rapid increase of ions formed during chemical reaction [3]. Chemical compound 5-dimethylaminonaphthalene-1-sulfonamide (DNSA) was used for the visualization of CA purified from the inner ear of the guinea pig after electrophoresis using non-denaturing polyacrylamide gels. It was shown that DNSA forms a highly fluorescent complex with CA and, more importantly, it was noticed that sulfonamides, in particular acetazolamide, strongly bind and inhibit CA activity [4]. Quantitative determination of CA in the rabbit cornea specimens was performed by mass spectrometry. The concentration of CA was linked to the rate of isotopic depletion of ^{18}O labeled bicarbonate during the catalyzed dehydration reaction [5].

Identification and visualization of proteins in cells or tissues is important for the understanding of their biological function or their involvement in the pathogenesis of certain disorders. First attempts to localize CA in tissues were published in 1953 by the histochemical method based on the catalytic activity of CA. Fresh tissues were placed in the solution of manganese bicarbonate, which was then dehydrated if the tissue contained an active CA. Manganese carbonate formed during the CA-catalyzed reaction accumulated at the active site of enzyme and, after section of tissue was incubated with the solution of potassium periodate, it was visualized as brown granules. The active CA was detected in red blood corpuscles, lens, gastric mucosa, pancreas cells, and the tubule of the kidney of several animals (rat, mouse, and guinea pig). This method overcame some limitations of biochemical methods previously used for CA enzyme analysis in tissues [6].

The reliability of the histochemical methods, based on the detection of CA enzymatic activity by visualizing the precipitates of reaction products, was subsequently questioned. The equivocal validity of these methods was demonstrated by showing that the staining was caused by the formation of an unknown reactive compound and it was enzyme-independent [7, 8]. The labeled inhibitor autoradiography was later proposed as a more reliable alternative to histochemical staining. The well-recognized CA inhibitor acetazolamide was labeled with radioactive hydrogen isotope ^3H and was used to detect CA in biological samples of avian tissues [9]. In addition, another CA-specific compound DNSA was used to detect CA in tissue specimens by fluorescence microscopy. As mentioned earlier, the light blue-specific fluorescence was observed at 470 nm after formation of CA-DNSA-complex and it was determined in chicken kidney, proventriculus, and bone [10].

The studies described above demonstrate an early interest on CA properties and expression in different organisms as well as improvement of detection methods, which initiated further CA-related research in fundamental and applied sciences. However, these techniques were not able to differentiate among the different isoforms of CA family, which have been identified later [11]. Afterwards, the most important goals were to determine the prevalence and distribution of CA isoforms in human body and reveal their significance for physiological and pathological processes. Many novel detection methods were developed since then, providing new knowledge about various isoforms of CAs.

21.2 Application of Antibodies for CA Detection

For many years, antibodies were used as a key component in different immunological methods like radioimmunoassay, immunohistochemistry, or immunofluorescence for the detection of various proteins [12, 13]. First studies focused to CA detection by antibodies were based on the use of antisera from immunized animal. CA purified from chicken erythrocytes was used to immunize rabbits, afterwards their blood was collected and the CA-specific antiserum was obtained. CA-specific immunoglobulin G was purified and then used in the indirect fluorescent immunohistologic technique as primary antibodies to detect CA in various chicken tissues. Secondary goat anti-rabbit antibodies conjugated with fluorescein isothiocyanate were used for the detection of the antigen–antibody complex. The antiserum was validated by using various controls and was demonstrated to be highly specific to CA [14]. Later on it became an important tool not only to determine if the sample contains CA, but also to distinguish between different isoforms of CA, particularly by analyzing normal and pathological tissues in case of various human disorders.

Rabbit antiserum to rat CA I and CA II and to bovine CA III was used to investigate these CA isoforms in rat and human tissues by a double immunodiffusion assay [15], immunofluorescence [16], or immunocytochemical staining [17] providing useful data on the presence and localization of the three isozymes in the muscles. At the same time, a radioimmunoassay based on a competitive binding of radiolabeled antigen and an unlabeled antigen to CA-specific antibodies, for the detection of rat and human CA III, has been developed. Rabbit antisera to human and rat CA III were generated using CA proteins purified from tissues and were employed to interact with iodinated or unlabeled CA III, subsequently counting radioactivity by an automatic gamma counter. An increased plasma CA III level was demonstrated in patients suffering from Duchenne muscular dystrophy compared to the control group [18, 19]. The radioimmunoassay was also developed to detect the secreted CA isoenzyme (CA VI) in sheep saliva and tissues [20].

The immunoperoxidase technique involves the use of secondary antibodies which interact with peroxidase–antiperoxidase (PAP) (peroxidase bound to an antiperoxidase antibody) complex and primary antibody–antigen complex. This method was applied to study localization of CA I and CA II isozymes in human eye tissues. The specimens were also analyzed by immunofluorescence using CA

isoform-specific antisera and secondary antibodies conjugated with fluorescein isothiocyanate [21]. In-house produced or commercially available antisera, also known as polyclonal antibodies (PAbs), to various CA isoforms were later involved in many other studies to determine the prevalence of CA in human organs and to analyze the differences of CA expression in normal and pathological tissues [22–24].

It has been often debated about the specificity and cross-reactivity of PAbs. Protein antigens such as CAs are complex molecules with a variety of linear and conformational epitopes, thus antisera obtained from the blood of immunized animals can recognize different epitopes. As the homology of CA family members is quite high, it is possible to get non-specific reactions while using antisera for the detection of CA proteins [25, 26]. Determination of potential cross-reactivity requires sensitive techniques and the specificity of antibodies must be validated with as many samples as possible in order to ensure the reliability of the results. An absorbed antigen radioimmunoassay was applied to study the cross-reactions among variety of PAbs derived against bovine CA III, human CA I, CA II, and CA III. In addition, 5 monoclonal antibodies (MAbs) were developed by hybridoma technique against human CA I, CA II and bovine CA III and their cross-reactivity was investigated. The reactivities of some PAbs with non-autologous CA from various species were as efficient as with the autologous isozyme. In contrast, cross-reactions of MAbs were determined less frequently or they were more individualized [27]. These findings emphasize the advantages of MAbs for identifying single members of protein families such as CA family [25].

Many previous studies have been focused on the investigation of CA expression level alterations during disease progression, thus PAbs and MAbs specific to CA were broadly applied for this purpose. Rabbit polyclonal anti-CA II antibodies were used to investigate CA II protein level by ELISA and Western blot methods in blood plasma samples from Alzheimer's disease patients. The levels of CA II were elevated in plasma samples of Alzheimer's disease patients, therefore considering CA II role in the pathogenesis of Alzheimer's disease [28]. The ELISA method has an advantage over the radioimmunoassay as it employs enzymes like horseradish peroxidase. Over the years, several types of ELISA have emerged for different purposes, like a direct ELISA for antigen detection with peroxidase-labeled primary antibodies or an indirect ELISA based on using horseradish peroxidase-labeled secondary antibodies interacting with target antibodies [29]. Another ELISA format, sandwich (or capture) ELISA, was developed for soluble CA IX detection in blood samples and will be discussed in more details later in this chapter.

Another immunoassay—Western blot—is based on the transfer of separated proteins from the polyacrylamide gel matrix to an adsorbent membrane, such as nitrocellulose, where they are visualized by antibodies. Specific immunodetection of target proteins from tissues, cell lysates, or blood samples depends on appropriate and high quality antibodies used for the analysis [30]. Western blot is widely used in CA research, for example, it was applied for the determination of CA VII protein in colorectal carcinoma clinical samples using primary antibody specific for CA VII [31].

Many modifications of immunoassays have been developed and used for the detection of CA family proteins. For example, positron emission tomography (PET) based on antibodies against cancer-associated CAs is under clinical evaluation to diagnose certain cancers and will be reviewed subsequently.

21.3 Immunoassays Based on the Use of Antibodies Against CA IX and CA XII

CA IX and CA XII are tumor-associated CA isoforms that contribute to the survival of cancer cells under hypoxia conditions. Both proteins are overexpressed in several cancer types (renal cell carcinomas, breast, bladder, glioblastomas, and head and neck cancers) and in some cases they are identified as cancer biomarkers. One of the main tools used for CA IX and CA XII detection in human tissues or blood samples are MAb [32, 33]. MAb G250 is one of the best known antibody against CA IX that was generated in 1986 after immunizing mouse with RCC cell homogenates [34]. This antibody is specific to CA IX and binds to its catalytic domain [35]. The application of the MAb G250 for CA IX detection in renal cell carcinoma (RCC) was demonstrated by visualization of RCC tumors in animal models using radiolabeled G250 antibody. Nude mice with human RCC xenografts were investigated by radioimmunodetection, using ^{99m}Tc -labeled MAb G250 preparations. RCC xenografts were clearly visualized in mice using new radiolabeled antibodies, indicating them as possible candidates for radioimmunodetection of RCC in patients [36]. The clear cell renal cell carcinoma (ccRCC) tumor was visualized by immuno-PET method in nude mice with CA IX-expressing ccRCC xenografts. The immuno-PET is a non-invasive method for radionuclide-labeled MAb visualization by a PET camera. The labeled antibody binds to a specific tumor cell surface marker and then is localized using PET imaging (Fig. 21.1). This allows to study in vivo tumor marker expression, its distribution in the cell, and obtain information about its possible diagnostic value. Mice were injected with ^{89}Zr and ^{124}I radiolabeled cG250 (chimeric version of MAb G250) antibodies and PET images were obtained using a special PET/CT scanner. The ccRCC tumors were clearly visualized by the radiolabeled antibody, indicating potential application of cG250 in immuno-PET for ccRCC diagnosis in patients [37]. To study possible diagnostic and therapeutic applications of the MAb G250, several clinical studies were initiated [38, 39].

MAb M75 is another MAb generated against CA IX in 1992 after mice were immunized with MaTu-infected HeLa cells [40]. MAb M75 specificity to CA IX was demonstrated using various methods, predominantly in immunohistochemistry studies (Fig. 21.2). CA IX protein detection on HT-29 cell surface was confirmed by the immunofluorescence method. Methanol-fixed cells were treated with the MAb M75 and later with fluoresoiothiocyanate (FITC)-conjugated swine anti-mouse secondary antibodies. The presence of CA IX in HT-29 cells and in nude mice bearing HT-29 human colorectal carcinoma xenografts was shown by Western blotting

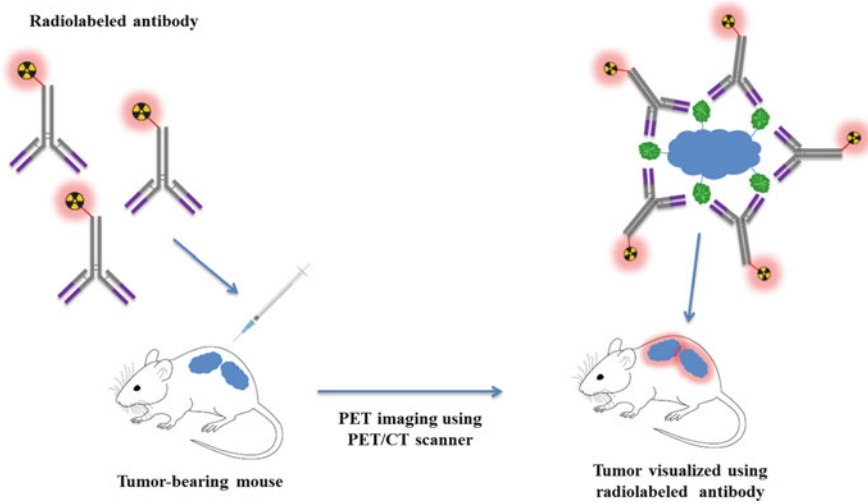


Fig. 21.1 Schematic illustration of immuno-PET imaging. Tumor-bearing mouse (tumors colored in blue) is injected with radiolabeled antibody that binds to a specific tumor marker located on the tumor cell surface. After scanning mouse with special PET/CT scanner, tumors are visualized because of the bound radiolabeled antibody (tumors colored in red)

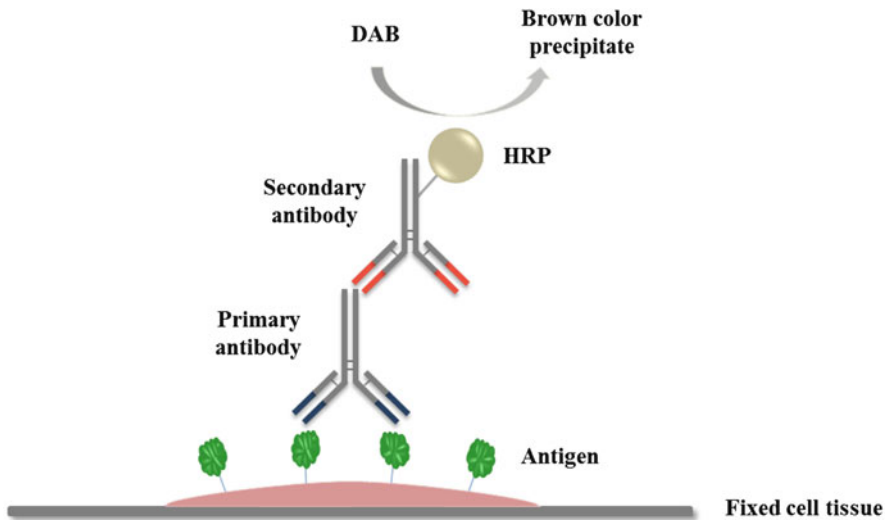
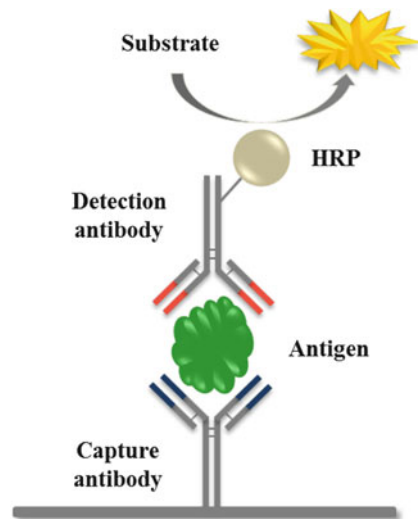


Fig. 21.2 Schematic illustration of immunohistochemistry assay. Tissue specimen is fixed to a glass slide and then is incubated with primary antibody that directly binds to the target antigen. After washing, the slide is incubated with secondary antibody that is labeled with horseradish peroxidase (HRP). Antigen localization in tissue is visualized using 3,3-o-diaminobenzidine tetrahydrochloride (DAB). Brown color precipitate is formed on the slide at the location of the antigen

using ^{125}I labeled M75 antibody [41]. Strong CA IX expression was detected by immunohistochemistry in tissue microarray (TMA) slides of ccRCC patients after staining them with the MAb M75 [42]. For CA IX detection in certain tumors using immuno-PET imaging, MAb M75 was labeled with the positron emitter ^{64}Cu to produce new radioimmunoconjugate ^{64}Cu -PS-IgG M75. The athymic mice inoculated with HT-29 cells were injected with the new conjugate and its biodistribution around the tumor was imaged using a $\mu\text{PET}/\text{CT}$ camera. Tumors were visualized using the radioimmunoconjugate, suggesting possible application of ^{64}Cu -PS-IgG M75 for CA IX *in vivo* imaging using the immuno-PET method in certain cancers [43].

Two forms of CA IX protein—membrane-bound and soluble—have been detected in human organism. The transmembrane protein was analyzed by immunohistochemistry, immunofluorescence, and Western blot methods as described above. A soluble form of CA IX can be detected by Western blot, immunoprecipitation, flow cytometry, and quantitative sandwich ELISA method developed using CA-specific MAbs. The soluble form of CA IX is released into the body fluids or in cancer cell culture medium by proteolytic cleavage of the CA IX extracellular domain. Low concentration of soluble CA IX is detectable in healthy people, but it is elevated in certain cancers and therefore is considered to have prognostic value [44, 45]. Soluble form of CA IX was detected in blood serum (0.02–3.6 ng/ml) and urine (0.02–3 ng/ml) of patients with RCC by capture ELISA method (Fig. 21.3). From the same biological samples of RCC patients, soluble CA IX form was immunoprecipitated using the MAb M75 and detected by Western blot using M75-Px conjugate [44]. Using a commercial ELISA kit, CA IX was quantified (23–499 pg/ml) in serum samples of patients with primary cervical

Fig. 21.3 Schematic illustration of sandwich ELISA method. The micro-well plate is coated with the capture antibody and then incubated with sample solution containing target antigen. After washing, horseradish peroxidase (HRP)-labeled detection antibody is added. The quantity of target antigen in sample solution is indicated by color change of the added substrate 3,3',5,5'-tetramethylbenzidine (TMB) as a result of HRP-catalyzed reaction



cancer [46]. These findings demonstrate the capture ELISA method as a promising tool for a non-invasive CA IX detection in biological samples.

Recently, large collections of MABs against CA IX and CA XII were developed [47, 48] and used to investigate target protein expression in tumor cells by flow cytometry. The MABs raised against recombinant CA IX recognized the native CA IX protein on the cell surface, demonstrating that the expression level of CA IX is strongly upregulated by hypoxia in several tumor cell lines (Stravinskiene et al., unpublished data). Application potential of these MABs, especially one clone, is very broad, as it recognizes CA IX in various assays such as Western blot, immunohistochemistry, immunofluorescence, flow cytometry, and sandwich (capture) ELISA for soluble CA IX. Sandwich ELISA was applied to investigate the levels of soluble CA IX in cancer cell culture medium. It was demonstrated that Ca Ski (cervical squamous cell carcinoma), U87 (glioblastoma), A549 (lung carcinoma), and HeLa (cervical adenocarcinoma) cancer cell lines grown under hypoxia conditions release the extracellular CA IX domain into growth medium (Stravinskiene et al., unpublished data).

CA XII expression in various cancers was primarily studied using PABs against CA XII. Analyzing human tumor tissue by immunohistochemistry method and using rabbit polyclonal antibody to CA XII protein, CA XII was immunostained in RCC, low-grade glioma, breast cancer, medulloblastoma, ovarian tumors, and in other tumor tissue specimens [49–51].

In 2011, one of the first MABs against CA XII was generated after immunizing LOU rats with A549 lung cancer cells, named as MAb 6A10. The analysis of A549 cells by flow cytometry confirmed that MAb 6A10 binds to CA XII protein located on A549 cells surface [52]. Using the same antibody, CA XII was immunoprecipitated from A549 whole-cell lysates and detected by Western blot using PAB against CA XII [53]. In 2014, the development of new collections of MABs against CA XII was reported using either recombinant CA XII or selected CA XII peptide as an immunogen [47, 48]. The reactivity of CA XII-specific MABs 15A4 and 4A6 raised against recombinant full-length CA XII with native CA XII protein expressed in human tissue specimens was studied by immunohistochemistry. The immunoreactivity of the MAB 15A4 to cellular CA XII was also confirmed by analyzing CA XII-positive human tumor cell lines by flow cytometry [47]. Two more MABs were generated against the selected CA XII sequence (167 aa to 180 aa) located in CA XII catalytic domain: MAB 1D8 and MAB 3C8. Both antibodies inhibited CA XII enzymatic activity, but only MAB 3C8 recognized cellular CA XII protein in human breast and lung cancer tissue specimens by immunohistochemistry assay [48]. These findings indicate that MABs to CA IX and CA XII are useful tools for the detection of target proteins in cancer cells and human biological samples thus providing possibilities for diagnostics and patient stratification.

21.4 Conclusions

After the discovery of CAs, different analytical methods were developed for CA detection that were later improved for better sensitivity and measurement performance. These methods provided new information about CA catalytic activity, distribution, and functions. Immunoassays based on the use of either polyclonal or monoclonal CA-specific antibodies improved CA detection and allowed discrimination of CA isoforms. Highly specific antibodies against different CA isoforms became very helpful tools for the analysis of CA expression in various biological samples and currently are widely used in different immunoassays, such as ELISA, Western blot, immunohistochemistry, flow cytometry, and in vivo imaging.

References

1. Brinkman, R.: The occurrence of carbonic anhydrase in lower marine animals. *J. Physiol.* **80**, 171–173 (1933)
2. Patterson, B., Atkins, C., Graham, D., Wills, R.: Carbonic anhydrase: a new method of detection on polyacrylamide gels using low-temperature fluorescence. *Anal. Biochem.* **44**, 388–391 (1971)
3. Wiedner, G., Simon, B., Thomas, L.: Carbonic anhydrase: a new method of detection on polyacrylamide gels using conductivity measurements. *Anal. Biochem.* **55**, 93–97 (1973)
4. Drescher, D.G.: Purification of blood carbonic anhydrases and specific detection of carbonic anhydrase isoenzymes on polyacrylamide gels with 5-dimethylaminonaphthalene-1-sulfonamide (DNSA). *Anal. Biochem.* **90**, 349–358 (1978)
5. Silverman, D.N.: Carbonic anhydrase catalyzed oxygen-18 exchange between bicarbonate and water. *Arch. Biochem. Biophys.* **155**, 452–457 (1973)
6. Kurata, Y.: Histochemical demonstration of carbonic anhydrase activity. *Stain. Technol.* **28**, 231–233 (1953)
7. Hansson, H.P.J.: Histochemical demonstration of carbonic anhydrase activity. *Histochemie* **11**, 112–128 (1967)
8. Muther, T.F.: A critical evaluation of the histochemical methods for carbonic anhydrase. *J. Histochem. Cytochem.* **20**, 319–330 (1972)
9. Gay, C.V., Mueller, W.J.: Cellular localization of carbonic anhydrase in avian tissues by labeled inhibitor autoradiography. *J. Histochem. Cytochem.* **21**, 693–702 (1973)
10. Pochhammer, C., Dietsch, P., Siegmund, P.R.: Histochemical detection of carbonic anhydrase with diemthylaminonaphthalene-5-sulfonamide. *J. Histochem. Cytochem.* **27**, 1103–1107 (1979)
11. Sly, W.S., Hu, P.Y.: Human carbonic anhydrases and carbonic anhydrase deficiencies. *Annu. Rev. Biochem.* **64**, 375–401 (1995)
12. Coons, A.H., Creech, H.J., Jones, R.N.: Immunological properties of an antibody containing a fluorescent group. *Exp. Biol. Med.* **47**, 200–202 (1941)
13. De Matos, L.L., Trufelli, D.C., De Matos, M.G.L., Da Silva Pinhal, M.A.: Immunohistochemistry as an important tool in biomarkers detection and clinical practice. *Biomark. Insights* **5**, BML.S2185 (2010)
14. Gay, C.V., Schraer, H., Faleski, E.J., Schraer, R.: Localization of carbonic anhydrase in avian gastric mucosa, shell gland and bone by immunohistochemistry. *J. Histochem. Cytochem.* **22**, 819–825 (1974)
15. Carter, N.D., Hewett-Emmett, D., Jeffrey, S., Tashian, R.E.: Carbonic anhydrase isozyme of rat liver is indistinguishable from skeletal muscle carbonic anhydrase III. *FEBS Lett.* **128**, 5 (1981)

16. Moyle, S., Jeffery, S., Carter, N.D.: Localization of human muscle carbonic anhydrase isozymes using immunofluorescence. *J. Histochem. Cytochem.* **32**, 1262–1264 (1984)
17. Jeffery, S., Carter, N.D., Smith, A.: Immunocytochemical localization of carbonic anhydrase isozymes I, II, and III in rat skeletal muscle. *J. Histochem. Cytochem.* **34**, 513–516 (1986)
18. Heath, R., Jeffery, S., Carter, N.: Radioimmunoassay of human muscle carbonic anhydrase III in dystrophic states. *Clin. Chim. Acta* **119**, 299–305 (1982)
19. Shiels, A., Jeffery, S., Wilson, C., Carter, N.: Radioimmunoassay of carbonic anhydrase III in rat tissues. *Biochem. J.* **218**, 281–284 (1984)
20. Fernley, R.T., Wright, R.D., Coghlan, J.P.: Radioimmunoassay of carbonic anhydrase VI in saliva and sheep tissues. *Biochem. J.* **274**, 313–316 (1991)
21. Wistrand, P.J., Schenholm, M., Lönnerholm, G.: Carbonic anhydrase isoenzymes CA I and CA II in the human eye. *Invest. Ophthalmol. Vis. Sci.* **27**, 419–428 (1986)
22. Kaufmann, P., et al.: Immunohistochemistry of carbonic anhydrase in human placenta and fetal membranes. *Histochemistry* **101**, 91–98 (1994)
23. Kummola, L., et al.: Expression of a novel carbonic anhydrase, CA XIII, in normal and neoplastic colorectal mucosa. *BMC Cancer* **5**, 41 (2005)
24. Kida, E., et al.: Carbonic anhydrase II in the developing and adult human brain. *J. Neuropathol. Exp. Neurol.* **65**, 664–674 (2006)
25. Lipman, N.S., Jackson, L.R., Trudel, L.J., Weis-Garcia, F.: Monoclonal versus polyclonal antibodies: distinguishing characteristics, applications, and information resources. *ILAR J.* **46**, 258–268 (2005)
26. Pradidarcheep, W., Labruyère, W.T., Dabhoiwala, N.F., Lamers, W.H.: Lack of specificity of commercially available antisera: better specifications needed. *J. Histochem. Cytochem.* **56**, 1099–1111 (2008)
27. Erickson, R.P., Kay, G., Hewett-Emmett, D., Tashian, R.E., Claffin, J.L.: Cross-reactions among carbonic anhydrases I, II, and III studied by binding tests and with monoclonal antibodies. *Biochem. Genet.* **20**, 809–819 (1982)
28. Jang, B.G., et al.: Plasma carbonic anhydrase II protein is elevated in Alzheimer's disease. *J. Alzheimers Dis.* **21**, 939–945 (2010)
29. Aydin, S.: A short history, principles, and types of ELISA, and our laboratory experience with peptide/protein analyses using ELISA. *Peptides* **72**, 4–15 (2015)
30. Kurien, B.T., Scofield, R.: Protein blotting: a review. *J. Immunol. Methods* **274**, 1–15 (2003)
31. Yang, G.Z., et al.: Prognostic value of carbonic anhydrase VII expression in colorectal carcinoma. *BMC Cancer* **15**, 209 (2015)
32. Supuran, C.T.: Carbonic anhydrase inhibition and the management of hypoxic tumors. *Metabolites* **7**, 48 (2017)
33. Mboge, M., Mahon, B., McKenna, R., Frost, S.: Carbonic anhydrases: role in pH control and cancer. *Metabolites* **8**, 19 (2018)
34. Oosterwjk, E., et al.: Monoclonal antibody G 250 recognizes a determinant present in renal-cell carcinoma and absent from normal kidney. *Int. J. Cancer* **38**, 489–494 (1986)
35. Zatovicova, M., et al.: Monoclonal antibody G250 targeting CA IX: binding specificity, internalization and therapeutic effects in a non-renal cancer model. *Int. J. Oncol.* **45**, 2455–2467 (2014)
36. Steffens, M.G., et al.: In vivo and in vitro characterizations of three ^{99m}Tc-labeled monoclonal antibody G250 preparations. *J. Nucl. Med.* **40**, 829–836 (1999)
37. Stillebroer, A.B., et al.: ImmunoPET imaging of renal cell carcinoma with ¹²⁴I- and ⁸⁹Zr-labeled anti-CAIX monoclonal antibody cG250 in mice. *Cancer Biother. Radiopharm.* **28**, 510–515 (2013)
38. Oosterwijk-Wakka, J., Boerman, O., Mulders, P., Oosterwijk, E.: Application of monoclonal antibody G250 recognizing carbonic anhydrase IX in renal cell carcinoma. *Int. J. Mol. Sci.* **14**, 11402–11423 (2013)
39. Lau, J., Lin, K.S., Bénard, F.: Past, present, and future: development of theranostic agents targeting carbonic anhydrase IX. *Theranostics* **7**, 4322–4339 (2017)

40. Pastoreková, S., Závadová, Z., Košťál, M., Babušíková, O., Závada, J.: A novel quasi-viral agent, MaTu, is a two component system. *Virology* **187**, 620–626 (1992)
41. Chrastina, A., et al.: Biodistribution and pharmacokinetics of ^{125}I -labeled monoclonal antibody M75 specific for carbonic anhydrase IX, an intrinsic marker of hypoxia, in nude mice xenografted with human colorectal carcinoma: tumor targeting by anti-CA IX MAb M75. *Int. J. Cancer* **105**, 873–881 (2003)
42. Al-Ahmadie, H.A., et al.: Carbonic anhydrase IX expression in clear cell renal cell carcinoma: an immunohistochemical study comparing 2 antibodies. *Am. J. Surg. Pathol.* **32**, 377–382 (2008)
43. Čepa, A., et al.: In vitro evaluation of the monoclonal antibody 64 Cu-IgG M75 against human carbonic anhydrase IX and its in vivo imaging. *Appl. Radiat. Isot.* **133**, 9–13 (2018)
44. Závada, J., Závadová, Z., Zat'ovičová, M., Hyršl, L., Kawaciuk, I.: Soluble form of carbonic anhydrase IX (CA IX) in the serum and urine of renal carcinoma patients. *Br. J. Cancer* **89**, 1067–1071 (2003)
45. Tafreshi, N.K., Lloyd, M.C., Bui, M.M., Gillies, R.J., Morse, D.L.: In: Frost, S.C., McKenna, R. (eds.) *Carbonic Anhydrase: Mechanism, Regulation, Links to Disease, and Industrial Applications*, pp. 221–254. Springer Netherlands, Dordrecht (2014)
46. Woelber, L., et al.: Carbonic anhydrase IX in tumor tissue and sera of patients with primary cervical cancer. *BMC Cancer* **11**, 12 (2011)
47. Dekaminaviciute, D., et al.: Development and characterization of new monoclonal antibodies against human recombinant CA XII. *Biomed. Res. Int.* **2014**, 1–11 (2014)
48. Dekaminaviciute, D., et al.: Monoclonal antibodies raised against 167–180 Aa sequence of human carbonic anhydrase XII inhibit its enzymatic activity. *J. Enzyme Inhib. Med. Chem.* **29**, 804–810 (2014)
49. Ivanov, S., et al.: Expression of hypoxia-inducible cell-surface transmembrane carbonic anhydrases in human cancer. *Am. J. Pathol.* **158**, 905–919 (2001)
50. Hynninen, P., et al.: Expression of transmembrane carbonic anhydrases IX and XII in ovarian tumours. *Histopathology* **49**, 594–602 (2006)
51. Nordfors, K., et al.: The tumour-associated carbonic anhydrases CA II, CA IX and CA XII in a group of medulloblastomas and supratentorial primitive neuroectodermal tumours: an association of CA IX with poor prognosis. *BMC Cancer* **10**, 148 (2010)
52. Battke, C., et al.: Generation and characterization of the first inhibitory antibody targeting tumour-associated carbonic anhydrase XII. *Cancer Immunol. Immunother.* **60**, 649–658 (2011)
53. Gondi, G., et al.: Antitumor efficacy of a monoclonal antibody that inhibits the activity of cancer-associated carbonic anhydrase XII. *Cancer Res.* **73**, 6494–6503 (2013)



Clinical Trials Involving Carbonic Anhydrase IX as a Target for Cancer Diagnosis and Treatment 22

Švitrigailė Grincevičienė and Daumantas Matulis

Abstract

Carbonic anhydrase IX (CA IX) has been identified as a potential target for cancer treatment over 20 years ago. Extensive efforts to develop drugs based on small molecules or antibodies have not yet yielded the FDA approval for use in clinical practice. Still, in clinical trials CA IX has been used as a marker for cancer diagnosis and prognosis, and some therapeutic benefit has been achieved. In this chapter we summarize the clinical trials involving CA IX for the visualization of tumor tissue, patient stratification, and anticancer therapy. Goals and major outcomes of the trials are summarized. Both the small-molecule and antibody-based approaches are discussed.

22.1 Introduction

Hypoxic solid tumors have poor blood supply in the tissue, causing problems for the delivery of chemotherapeutic agents resulting in more rapid spread of the disease and resistance to drugs [1] thus limiting efficacy of treatment [2]. Tissue hypoxia correlates with the overexpression of carbonic anhydrase IX (CA IX), a trans-membrane enzyme, predominantly found in solid hypoxic tumors and involved in balancing cellular pH [2]. This dimeric zinc-containing glycoprotein hydrates carbon dioxide to proton and bicarbonate which is released to intracellular matrix and decreases its pH. This promotes the proliferation of the tumor cells, degradation of extracellular matrix, and is important for cellular migration, invasion, and metastases [3].

Š. Grincevičienė · D. Matulis (✉)

Department of Biothermodynamics and Drug Design, Institute of Biotechnology, Life Sciences Center, Vilnius University, Vilnius, Lithuania

e-mail: svitrigaile.grinceviciene@bti.vu.lt; matulis@ibt.lt

© Springer Nature Switzerland AG 2019

D. Matulis (ed.), *Carbonic Anhydrase as Drug Target*,
https://doi.org/10.1007/978-3-030-12780-0_22

335

Since the elevated levels of CA IX actively contribute to the aggressiveness of tumor cells, inhibitors of the enzyme are analyzed as potential markers for disease visualization, stratification for possible treatment modalities, and as adjuvant drugs. In cancer research, every potential CA IX inhibitor undergoes the evaluation of usage in few or all areas, mentioned above. They are developed beginning with the visualization of CA IX in tumor tissue, and continued for diagnosis and patient stratification. Finally, some of them are selected for clinical trials as the treatment options. Clinical trials registered in <http://clinicaltrials.gov> (last revised on 3rd of June, 2018) are briefly reviewed in this chapter.

22.1.1 Visualization of Tumor Tissues

Visualization of tumor tissue is important in clinical practice, because it helps to detect the localization and limits of cancerous tissue as well as to gain information about specific characteristics of the cells. The maximum removal of tumor tissue cells is essential for patient treatment. This is possible through surgery/brachytherapy for solid masses and chemo/radiotherapy for remaining cells and distal metastases. However, too aggressive treatment (both chemotherapy and radiotherapy) or too much extended surgery is related to poor quality of life and higher complication rate. The ideal treatment should be precise in optimal dosing and tissue removing. The development of visualization markers could significantly contribute towards this aim. Table 22.1 summarizes the use of CA IX as a diagnostic marker.

22.1.2 Antibodies for Immunohistochemistry

Early detection of cancer is essential for the most effective cancer treatment, resulting in the lowest impact on the quality of life. According to International Agency for Research on Cancer, 2018 (www.iarc.fr) supported by World Health Organization, cervical cancer is a second gynecological tumor after breast cancer affecting women worldwide. Despite the fact that it is the most preventable cancer, the mortality is very high, especially in developing countries. Even in developed countries, some cases of false negative observations occur [8]. Human papillomavirus (HPV) testing could add to the accuracy of diagnosis. Cytology and HPV-negative cervical cases could be missed [9]. Molecular markers such as p16, Ki67 are under development [10].

Hybrid Capture II high-risk HPV-negative women diagnosed with AGC-NOS (atypical glandular cells, not otherwise specified [11]) in cervical cytology could safely undergo surveillance [12]. However, CA IX immunohistochemical staining together with Hybrid Capture II high-risk HPV and cytological testing did not improve the accuracy as compared to the two tests. Researchers found that mucinous adenocarcinoma with gastric phenotype has high concentration of CA IX even in the absence of high-risk HPV [13]. Based on this finding, Liao et al. developed diag-

Table 22.1 Clinical trials involving CA IX as a diagnostic marker. Prepared according to the <http://clinicaltrials.gov>

The trial no, stage, country	Topic	Study design	Marker	Outcomes
NCT00892866; recruiting, USA	Cervical cancer stage 0 AGUS diagnosis	Observational with non-probability sampling	Immunohistochemical staining of CA IX with M75 antibody	Not available
NCT02497599 recruiting, The Netherlands	ccRCC	Phase I	Indium-111-DOTA-girentuximab-IRDye800CW	Not available
NCT02883153 completed, The Netherlands	ccRCC	Phase II/III	Zirconium-89-girentuximab	Suspected ccRCC identification [4]
NCT00884520 completed, USA	Lung cancer Squamous cell carcinoma Head and neck cancer Hepatic carcinoma Renal cell carcinoma	Phase I	[¹⁸ F]VM4-037 in PET/CT (radioactive-fluorine-labeled (S)-3-(4-(2-[¹⁸ F]fluoroethoxy)phenyl)-2-(3-methyl-2-(4-(2-sulfamoylbenzo[d]thiazol-6-yloxy)methyl)-1H-1,2,3-triazol-1-yl)butanamide) propanoic acid)	High uptake in liver and kidney [5]
NCT01712685 terminated, USA	ccRCC	Phase II	¹⁸ F-VM4-037	Moderate signal uptake in primary tumors and excellent visualization of CAIX positive metastases [6]
NCT00606632, completed, USA	ccRCC	Phase III	124-Iodine-cG250	(124I)-girentuximab PET/CT can accurately and noninvasively identify ccRCC [7]
Completed, Sweden	Renal carcinoma	Open label	Anti-CAIX (APC) (R&D Systems) clone: 303123	Flow cytometry is able to detect micrometastases in lymph nodes

nostic methodology for CA IX in AGUS (patent No 2384744; US20020058251A1) [14, 15] (AGUS—atypical glandular cells of unknown significance). After running the model analysis [16], Liao and colleagues started the recruitment of patients for CA IX for the detection of atypical cells from liquid-based cytology, mainly in atypical endocervical or endometrial cells. Immunohistochemical staining with anti CA IX mouse monoclonal antibody M75 was used for CA IX visualization in cells (<http://clinicaltrials.gov> NCT00892866).

For cervical cancer prognosis after surgery, the immunohistochemically stained CA IX in tissues was used. A retrospective review identified 60 patients with cervical cancer [17] for positron emission tomography (PET) using 2-deoxy-2-[18F] fluoro-D-glucose (FDG) (F-18 FDG PET), and detected the expression of CA IX using immunohistochemical staining method (rabbit polyclonal antibody; Novus) [17]. CA IX was not superior prognostic marker in patients with surgically resected cervical cancer [17].

Immunohistochemically stained tissue evaluation was also used for other types of cancer—rectal and renal. Two population-based, multicenter, randomized controlled trials of different rectal cancer screening strategies were run [18]. The expression of CA IX was used as an endogenous hypoxia biomarker to assess the micro-regional distribution of hypoxia in the adenomatous tissue in colorectal cancer [18]. Serial paraffin sections, 3- μ m-thick, which were mounted on pre-coated slides were processed according to standardized automated procedures using pre-diluted antisera for CA IX (Novocastra, clone TH22, diluted 1:100) [18]. Authors concluded that CA IX expression was significantly higher in immunochemical fecal occult blood test and bleeding possibly occurs during periods of hypoxia [18]. This finding is also important for further colorectal marker development, because fecal occult blood test could be false positive because of dietary practice or non-cancer related gastrointestinal bleeding [19].

The detection of cancer cells in sentinel lymphatic node is an important diagnostic procedure. Despite the localization of cancer (breast, vulvar, etc.), the treatment recommendation and the extent of surgery as well as future prognosis for survival depends on this finding. The detection of metastatic cells of renal tumors in sentinel lymphatic nodes was performed using flow cytometry by combining a surface staining of CA IX (anti-CA IX (APC) (R&D Systems) clone: 303123). Cadherin 6 and intracellular staining of CK18 were performed in Sweden (trial was not registered in <http://clinicaltrials.gov>) [20]. They found that flow cytometry is able to detect micro-metastases in lymph nodes of renal tumor patients that were undetected under H&E examination [20]. Four out of five patients were diagnosed with positive MICs in lymph nodes by flow cytometry, whereas all of them were negative by H&E examination of CA IX, Cadherin 6, and intracellular staining of CK18 [20]. This finding is important for further development of sentinel node metastases detection and could be repeated in large sample for other solid tumors.

22.1.3 Antibodies and Small Molecules for PET

As described above, the immunohistochemically stained tissue analysis enhances clinician's ability to detect CA IX expression in the tissue. The biopsy or surgery material is necessary for this test. The procedure, the time from tissue sampling to pathologist examination, and the preservation type of the tissue could affect the results. Furthermore, patient must wait for the result and the treatment is delayed. Visualization *in vivo* is another rapidly developing advanced procedure for cancer patients. Computer tomography (CT) is used to visualize the extent of disease and metastases prior to surgery. Positron emission tomography (PET), a nuclear medicine functional imaging technique, is a perfect choice for cancer visualization because of the shift of metabolism in tumor cells. Both these methods are important for the detection of tumor stage and treatment choice.

CA IX antibodies were widely studied for the visualization of cancer in patients. One such studied solid cancer was clear cell renal cell carcinoma (ccRCC). Divgi et al group have been working with the chimeric antibody cG250 from the late 1980s [21–25]. The group developed the ^{124}I -girentuximab and ^{131}I -labeled chimeric G250 antibodies. The first successfully proved to be a good enhancer for ccRCC visualization prior to surgery [7]. ^{124}I -girentuximab was administered intravenously before PET/CT scan for the enhancement of contrast. Operation was performed 2–6 days after test and the tumor was resected [7]. The sensitivity was 86.2% (95% CI, 75.3% to 97.1%) for PET/CT with ^{124}I -girentuximab (compared with contrast enhanced CT 75.5% (95% CI, 62.6% to 88.4%); $P = 0.023$). The specificity increased to 85.9% (95% CI, 69.4% to 99.9%) (compared with contrast enhanced CT 46.8% (95% CI, 18.8% to 74.7%); $p = 0.005$) [7]. Sensitivity depended on tumor size and it was higher for tumors larger than 2 cm [7]. The method allowed to visualize all lesions below 1 cm [7]. The positive predictive value was 94.4% and negative predictive value was 69.4% [7]. The phase III trial for the same marker (Nr. NCT01762592) was withdrawn in 2017.

Researchers at the Abramson Cancer Center of the University of Pennsylvania (NCT00717587) initiated phase II trial to analyze sunitinib effect when used before and after surgery in treating patients with stage IV kidney cancer. I-124 girentuximab was planned to be used for visualization of tumor vascular permeability after 2 weeks of therapy, but no data has been published yet.

Zirconium-89-girentuximab PET/CT imaging was used for ccRCC imaging [26]. Only eight patients are still recruited with small renal masses or with suspected relapse of the disease. Seven patients benefited from the scan. One did not uptake the marker in solid lymph node which was a metastasis of CA IX expressing papillary ccRCC [26]. This trial is registered on <http://clinicaltrials.gov> (No: NCT02883153) as phase 2/3 trial and is still ongoing. Authors published updated data of 30 patients [4] with positive conclusion of efficacy in detection of ccRCC noninvasively. However, no data of sensitivity, specificity, and positive/negative predicted value are available.

Another molecular imaging study (NCT02228954) was performed aiming to compare FDG (fluoro-D-glucose)—PET and zirconium-89-girentuximab—PET results. These two tests were performed for patients with renal tumor before treatment to predict rapid progression (≤ 2 months after the baseline scan) or prolonged indolent (≥ 12 months after the baseline scan) under watchful waiting. This is not randomized, open-label study, still active. However, recruitment has been stopped and there are no published results.

Several new clinical trials are continuing. Indium-111-DOTA-girentuximab-IRDye800CW is under research of dual-labeled antibody for dual-modality image-guided surgery. The aim of this marker is to help intraoperative visualization of tumor (ccRCC). This is a phase I study to evaluate the safety and feasibility of intraoperative detection of tumor using Indium-111-DOTA-girentuximab-IRDye800CW (NCT02497599). Researchers are trying to answer whether the tumor could be visualized by fluorescence marker. No results have been published yet.

^{111}In -Girentuximab DOTA SPECT is used for the “early evaluation of the therapeutic effect by performing early follow-up imaging after percutaneous magnetic resonance—guided cryo-ablation of pT1a renal cell carcinoma” (NCT02411968). This is a minimal-invasion treatment related to higher quality of life and lower extent of surgery. It is an option of choice among developing surgical techniques and a good follow-up for progression/relapse detection, essential for patient safety. The study is still ongoing (recruiting subjects) and no data is available.

A small chemical molecule— ^{18}F VM4-037—a radiopharmaceutical substance consisting of a sulfonamide covalently attached to the positron-emitting isotope fluorine ^{18}F with CA IX-binding and radioisotope activities. It was used for the visualization of CA IX in the whole body scan in healthy volunteers (NCT00884520). Researchers found high uptake of the substance in the liver and kidneys [5]. Kidneys were the organs that received the highest radiation dose, demonstrating the importance to evaluate liver and kidney function during the usage of the substance [5].

Furthermore, ^{18}F -VM₄-037 was used to visualize ccRCC tumors (NCT01712685) in PET, phase II study. The study was terminated because the substance was no longer available for researchers. The primary results showed good results in differentiating metastases [6]. Visualization of primary tumor was challenging due to high activity of renal background parenchyma [6].

Authors decided to try the substance ^{18}F VM4-037 for neck and lung CA IX-positive tumors. They ran phase II study and tested the reproducibility of ^{18}F -VM4-037 uptake in tumors by imaging the same patient on sequential days in a test–retest protocol (NCT01075399). Researchers included histology-confirmed head/neck, lung, liver, rectal, or cervical cancers. The patients were about to receive chemotherapy or radiation according to the treatment protocol. Results were reported for head and neck cancer—the PET imaging with the ^{18}F VM4-037 was repeatable and reliable. The same results were received for lung cancer [27]. The ^{18}F VM4-037 was chosen to use for treatment of stage IV solid cancer (unspecified). Since the study enrolled 0 patients, it was withdrawn (NCT00935142).

22.2 CA IX as Patient Stratification Marker

Visualization of tumor before treatment is an important step for cancer staging. Even the same solid tumors have a wide heterogeneity and could respond differently to the same treatment. It is important to stratify the patients in accordance with molecular markers for predicting prognosis and adapting treatment modalities.

Enhanced CA IX expression was discussed as a marker for more aggressive, treatment resistance sign [3], so a number of trials were run to discover the CA IX value for patient stratification. This step is very important for CA IX-targeted drug development, because it provides evidence for CA IX hyper-expression in particular groups.

On the other hand, it was hypothesized that the decrease of CA IX expression in tissue during treatment was a positive outcome marker and could be used as an additional short-time evidence for treatment efficacy. The disease-free, overall survival was good, but long-term outcomes did not improve. It is important to have information of rapid effect during treatment, because it enables clinicians to change the strategy according to the results.

The CA IX detection was attempted to be used as a short-term treatment efficacy marker. The methods of CA IX detection involved immunohistochemical staining of tumor material, detection of soluble form, and radiological visualization. The targets were locally advanced or metastatic cancers. The localization of primary disease was rectal, breast, renal and cervical, lung, gliomas, etc. Diseases were mainly solid tumors. The trial with acute leukemia was run as well.

22.2.1 Radioactively Labeled CA IX Antibodies for Patient Stratification

Radiological uptake of radioactively labeled CA IX antibody was used for primary diagnosis and visualization of disease extent. The group working with cG250 antibody developed a substance for the evaluation of CA IX expression before and after treatment. The ¹¹¹Indium-cG250, a CA IX antibody with radiosensitive part accumulated in ccRCC (C. H. J. Muselaers et al. 2012). Based on these results, ¹¹¹Indium-cG250 was prescribed before and after sorafenib with the goal to investigate tumor uptake. Whole body scintigraphic images were recorded 1 week after both injections (NCT00602862). The ¹¹¹In-cG250 was compared to ¹¹¹In-bevacizumab uptake during whole body scintigraphic image before and after sorafenib treatment. However, data has not been published yet.

22.2.2 Immunohistochemistry Based on CA IX Staining for Patient Stratification

Immunohistochemistry was attempted to be used to stratify renal tumors because high level of CA IX was found in patients and optimistic results in visualization of

the disease were obtained as described above. The development of markers for renal cancer response to treatment was unsuccessful.

Muselaers et al. found that sorafenib treatment for metastatic ccRCC was associated with decreased uptake of chimeric CA IX antibody girentuximab (cG250) [28]. They did not find differences in immunohistochemically stained CA IX (CA IX mouse monoclonal antibody M75) between sorafenib treated and untreated groups [28] (NCT00602862).

CA IX was overexpressed in ccRCC, except papillary renal cell carcinoma [29]. The study on immunohistochemically stained CA IX (anti-CA IX antibody G250 (Wilex AG)) in metastatic renal clear cell carcinoma (ccRCC) patients aimed to analyze the predictive markers in the development of aggressive tumor [29]. The trial was withdrawn because primary investigator left the team (NCT00908739).

CA IX immunohistochemistry was used to assess the efficacy of tivozanib for non-ccRCC (NCT01297244) and sorafenib in phase II clinical trial for ccRCC (NCT00480389).

High-dose interleukin 2 (Proleukin, Novartis) was approved in the USA for the treatment of metastatic kidney cancer (NCT00554515). This is a standard treatment for this advanced disease, but not all patients benefit from it. McDermott with colleagues [30] tried to find a stratification marker for better response to the treatment. Vickers and colleagues [31] in their review concluded that immunohistochemically stained CA IX in tissue is associated with higher response rate to high-dose interleukin 2 treatment. It was found as a poor predictor marker for response to another drug temsirolimus (NCT00554515) [31]. In conclusion, CA IX marker is a part of “good” predictive pathological feature [30].

In some studies, CA IX was used as a standard marker for solid tumors. Immunohistochemically stained CA IX marker in rectal tissue was used for the evaluation of rectal cancer treatment by standard care plus oxygenation (NCT01189877). Similar study was performed with high grade glioma (NCT00826930). The CA IX was an immunohistochemically stained marker of cancer tissue. Patient was treated following the standard of care. In the residual tumor, the oxygenation was monitored and trans sodium crocetinate was injected. The study was terminated because of sponsor decision. In both studies, the data about CA IX usefulness was not published. CA IX immunohistochemistry together with other hypoxia markers was used in phase II clinical trial (NCT00381797). Researcher treated high grade pediatric brain glioblastomas with monoclonal antibody bevacizumab. The results are presented on drug pharmacokinetics [32] and no data about CA IX immunohistochemical staining correlation with outcomes.

Many studies on CA IX as a patient stratification marker are being performed, but the results are still unavailable. The solid tumors of prostate, head and neck, rectal, laryngeal, and cervical cancers were studied.

CA IX will be analyzed as immunohistochemically stained marker in prostate cancer comparing with the radiological technique (NCT03293602). In the trial, prostate MRI with blood oxygenation level dependent (BOLD) imaging sequences and ¹⁸F-misonidazole PET before surgery will be compared for stratification of a higher risk group. The aim of this comparison is to identify the patient group

with low oxygenation cancer. The study will be run in France and is now in a pre-recruiting phase.

Head and neck cancer validation and functional imaging trial is recruiting patients and CA IX immunohistochemistry is used for correlation with imaging PET-CT (<http://clinicaltrials.gov> NCT01827709). Head and neck cancer oxygenation is planned to be analyzed in patients receiving metformin (NCT03510390). Investigators will analyze RNA sequences, with special attention to hypoxia-responsive genes, CA IX being one of them. CA IX immunohistochemistry is planned as well. The study is at the recruitment phase.

There are some studies with promising results. Kim et al. [33] found that CA IX (immunohistochemically stained with rabbit monoclonal antibody EPR4151) could be used to stratify patients for hyperthermia to enhance the effect of preoperative radiochemotherapy in rectal cancer [34]. As hyperthermia is highly painful and damaging procedure, stratification of patients is essential. Women with CA IX-positive tumors and with poor response to therapy had the worst distance metastasis-free survival and cancer-specific survival. These findings are in line with other data showing that CA IX-positive tumors are more aggressive and resistant to treatment. Hyperthermic therapy increased tumor response in CA IX-positive cases and improved cancer-specific survival even after the recurrence of the disease.

CA IX expression was used to stratify patients with laryngeal carcinoma. Accelerated radiotherapy with carbogen breathing and nicotinamide ARCON improved regional control and metastasis-free survival only in patients with low CA IX expression [35]. Laryngeal carcinoma (NCT00147732) CA IX immunohistochemical staining (mouse anti-CAIX (E. Oosterwijk, Department of Urology, Radboud University Nijmegen Medical Centre)) and colocation with Ki-67 did not predict the response better than Ki-67 [36].

CA IX was used to stratify patients suffering from primary cervical cancer and receiving radiotherapy (NCT00980759). Extended-field irradiation (EFI) was compared with pelvic radiation expecting that EFI will have different effect on CA IX-positive (M75 antibody immunohistochemical staining) and CA IX-negative patients. EFI significantly reduced recurrences of CA IX-positive tumors, but the survival outcome did not improved, because of local recurrence and distant metastases [34]. Patients treated from cervical cancer with Cu 64-ATSM were followed for progression-free survival (NCT00794339) in phase II study. The correlation between CA IX immunohistochemistry and uptake of Cu 64-ATSM were measured. However, the results are not published yet.

CA IX immunohistochemistry was used not only for solid tumors. Changes in bone marrow hypoxia were measured using CA IX immunohistochemistry (NCT01555268) in phase I cytarabine study for acute leukemia treatment. The clinical trial NCT01037556 phase I/II study included relapsed/refractory acute myeloid leukemia ($n = 40$) after 1 or 2 prior treatments or acute lymphoblastic leukemia ($n = 10$) after any number of prior treatments [37]. They found a significant correlation between proportions of HIF-1 α - and CA IX-positive immunohistochemically stained cells before treatment. Expression of both markers significantly correlated with the percentage of BM blasts in pre-treatment and post-treatment samples [37].

No significant associations between biomarkers and dose or toxicity were found. The expression levels of the biomarkers did not directly correlate with the anti-leukemia efficacy of hypoxia-activated prodrug PR104 [37].

22.2.3 Detection of Soluble Form of CA IX for Patient Stratification

Markers found in blood are more user-friendly and require less intervention for the patient. The soluble form of CA IX was analyzed as a potential marker for patient stratification for breast, renal cancers, and solid tumors.

Ho et al. [38] analyzed serum CA IX (detected by an enzyme-linked immunosorbent assay (ELISA) from Oncogene Science/Nuclea Biotechnologies Inc.) as a pre-treatment marker for metastatic HER2+ breast cancer. They found that cut-off from 506 pg/ml was associated with higher progression-free survival (HR 1.16, CI 95% 1.22–2.11). Tolaney and colleagues [39] found that serum CA IX (detected by ELISA) was increasing during treatment of metastatic triple-negative breast cancer with cabozantinib in phase II study (NCT02260531). The clinical value of the finding is not fully clear.

Serum CA IX (detected by ELISA) level ((216.68 ± 67.02) pg/ml) was found to be a marker for postoperative recurrence of conventional renal cell carcinoma [40]. These findings were used to plan a study of possible use of serum protein CA IX and mRNA of CA IX level under medical treatment in trial NCT00942058. The blood and urine should be analyzed before treatment at 1, 3, 6, 9, and 12 months (NCT00942058). The CA IX levels were not published because the study was stopped (NCT00942058). The reason of termination was low recruitment rate.

Blood serum CA IX as a marker was investigated in phase I of drug BAY87-2243 in patients with advanced refractory to standard treatment of solid tumors (NCT01297530). The trial was terminated due to safety reasons [41]. Blood biomarker of CA IX (measured by ELISA) was not a useful marker to predict the overall survival in patients with non-small cell lung cancer treated with chemoradiotherapy (NCT01936571) [42]. The serum CA IX was used as marker in metastatic liver disease treatment with AZD2171 (cediranib) (NCT00427973). Overall survival was inversely correlated to circulating CA IX (measured by ELISA) [43]. However, the study was terminated.

22.3 Development of CA IX-Binders as Anticancer Drugs for Therapy

Only several studies were conducted to evaluate anti-CA IX medication efficacy for treatment. The drugs are being developed for very advanced disease. High-risk clear cell renal carcinoma, non-metastatic and metastatic solid tumors were studied. Table 22.2 summarizes CA IX binders used in trials for the treatment.

Table 22.2 CA IX inhibitors for treatment

The trial no, stage, country	Phase	Target	Medication	Conclusion
Antibodies				
NCT00087022 Completed The USA, Germany, UK, Russia, Finland, Brazil	Phase III	ccRCC	Girentuximab	No difference in disease-free or overall survival between patients receiving girentuximab and those receiving placebo [44]
NCT00142415 Completed The Netherlands	Phase I	Metastatic ccRCC	(177)Lu-cG250	Stabilized the progression [45]
NCT02002312 Completed The Netherlands	Phase II	Metastatic ccRCC	(177)Lu-cG250	Disease stabilization in 9 of 14 patients [46]
Completed The USA	Phase I	ccRCC	¹³¹ I-Labeled Chimeric G250	Not effective [21]
Small-molecule drug candidates				
NCT02216669 Withdrawn The Netherlands	Phase I	Head and neck neoplasms	DTP348	Not available
NCT02215850 Completed Canada	Phase I	Solid tumors	SLC-0111	Favorable results [47]
NCT03450018 Pre-recruiting Canada	Phase Ib	Metastatic pancreatic ductal adeno- carcinoma	SLC-0111	Not available

All trials are antibody-based except SLC-0111 that is a small-molecule-based trial. Prepared according to the <http://Clinictrials.gov>

22.3.1 Drugs Based on CA IX-Specific Antibodies

Girentuximab is a chimeric monoclonal antibody that binds CA IX. It showed good results in the visualization of renal tumor. It alone or with additions in the molecule was used for radio- or chemotherapy. The outcomes were not very promising—in some cases disease stabilization was achieved, but in others—non-effective.

¹³¹I-labeled chimeric G250 was used for radiotherapy both for clear cell renal carcinoma [21] and for biliary cancer [48] (trials were not registered in <http://clinicaltrials.gov>). For biliary cancer it was not effective due to small uptake of the agent [48]. Clinical trials stopped at phase I/II for renal cancer because of no clinical response. Some of the patients developed anti-antibody response [21, 22].

Stillebroer and colleagues [45] investigated patients suffering from metastatic ccRCC. Radioimmunotherapy (lutetium 177 ((177)Lu)-girentuximab) stabilized the disease during 3 month treatment period (NCT00142415). Based on the

study results, the same group ran phase II clinical trial for advanced clear cell renal carcinoma. They evaluated radioimmunotherapy (RIT) with lutetium 177 ((¹⁷⁷Lu)-girentuximab [46]. However, the trial was non-randomized. They achieved stable disease. Despite that, myelotoxicity was a burden for re-treatment (NCT02002312).

Phase III multi-central clinical trial was run with girentuximab (<http://clinicaltrials.gov> NCT00087022). They compared monoclonal CA IX antibody with placebo for treatment renal cancer. Girentuximab was used as adjuvant treatment after nephrectomy. The medication did not improve the disease-free and overall survival compared to placebo. Even in sub-group with high CA IX scores, the disease-free survival was improved statistically insignificantly [44].

22.3.2 Other Molecules Used as CA IX Inhibitors

Other molecules inhibiting CA IX have been used for very advanced cases of solid tumors. The knowledge about their efficacy in patients is lacking, except one molecule.

DTP 348 is an oral drug with dual mechanism of action: CA IX inhibitor and a radio sensitizer of hypoxic cells through its 5-nitroimidazole moiety which reduced the triple negative breast cancer growth in xenografts in mice [49]. DTP348 was used in head and neck cancer patients in combination with radiotherapy (randomized phase I clinical trial). The inclusion criteria were histologically or cytologically confirmed solid malignancy that was metastatic or unresectable. There were no standard curative measures for included patients (NCT02216669). Unfortunately, the study was withdrawn without any results because of financial disagreement.

The CA inhibitor (both of CA IX and CA XII) SLC-0111 was investigated for glioblastoma treatment in combination with temozolomide (NCT02215850) [50]. The authors determined an extended survival in mice. The same drug was investigated in humans. The SLC-0111 was used to treat solid advanced and/or metastatic or unresectable tumor(s) without standard curative measures (NCT02215850). In this prospective single arm study, researchers aimed to investigate safety and efficacy data of the drug. The study was completed in March, 2016, but data still is not published. McDonald with colleagues [47] has mentioned that the drug has favorable profile and has moved to phase Ib study of metastatic pancreas cancer.

The combination of SLC-0111 and gemcitabine was recommended for metastatic pancreatic ductal adenocarcinoma in CA IX positive patients (NCT03450018). The recruitment of patients has not started yet. The basis for treatment was the prediction of hypoxia for aggressive growth and spontaneous metastasis formation in patient-driven xenografts [51].

22.4 Conclusions

Both antibodies and small-molecule inhibitors of CA IX have been used in clinical trials for diagnosis of numerous cancers, patient stratification, and treatment. More than 46 clinical trials have been started. Most of them analyzed for the presence of CA IX by immunostaining in tissue. The most comprehensively investigated monoclonal antibody is G250 that has been attempted for visualization, stratification, and treatment. The clear cell renal cell carcinoma was the most common target. Other solid hypoxic tumors such as rectal and cervical cancers were also investigated. The CA IX was confirmed in many hypoxic tumors. Researchers showed that CA IX-positive and CA IX-negative neoplasms of the same localization have different response to the same treatment. Therefore, CA IX seems to be a promising marker in patient stratification. Other novel applications for the visualization of CA IX-positive tumors during surgery were started. CA IX antibodies or small molecules have not yet showed promising results in cancer treatment. Therefore, though there is no doubt that CA IX is an important marker of worse prognosis and more aggressive cancer and immunohistochemical staining of CA IX is a standard procedure in solid hypoxic tumor research, further ideas are necessary aiming at improved treatment outcomes.

References

1. Höckel, M., et al.: Association between tumor hypoxia and malignant progression in advanced cancer of the uterine cervix. *Cancer Res.* **56**, 4509–4515 (1996)
2. van Kuijk, S.J.A., et al.: Prognostic significance of carbonic anhydrase IX expression in cancer patients: a meta-analysis. *Front. Oncol.* **6**, 69 (2016)
3. Pastorek, J., Pastorekova, S.: Hypoxia-induced carbonic anhydrase IX as a target for cancer therapy: from biology to clinical use. *Semin. Cancer Biol.* **31**, 52–64 (2015)
4. Hekman, M.C.H., et al.: Positron emission tomography/computed tomography with ⁸⁹Zr-girentuximab can aid in diagnostic dilemmas of clear cell renal cell carcinoma suspicion. *Eur. Urol.* **74**(3), 257–260 (2018)
5. Doss, M., et al.: Biodistribution and radiation dosimetry of the carbonic anhydrase IX imaging agent [(18)F]VM4-037 determined from PET/CT scans in healthy volunteers. *Mol. Imaging Biol. MIB off. Publ. Acad. Mol. Imaging* **16**, 739–746 (2014)
6. Turkbey, B., et al.: PET/CT imaging of renal cell carcinoma with (18)FVM4-037: a phase II pilot study. *Abdom. Radiol. N. Y.* **41**, 109–118 (2016)
7. Divgi, C.R., et al.: Positron emission tomography/computed tomography identification of clear cell renal cell carcinoma: results from the REDECT trial. *J. Clin. Oncol. Off. J. Am. Soc. Clin. Oncol.* **31**, 187–194 (2013)
8. Sørbye, S.W., et al.: Accuracy of cervical cytology: comparison of diagnoses of 100 Pap smears read by four pathologists at three hospitals in Norway. *BMC Clin. Pathol.* **17**, 18 (2017)
9. Dillner, J., et al.: Long term predictive values of cytology and human papillomavirus testing in cervical cancer screening: joint European cohort study. *BMJ* **337**, a1754 (2008)
10. Ebisch, R.M., et al.: Evaluation of P16/Ki-67 dual-stained cytology as triage test for high-risk human papillomavirus-positive women. *Mod. Pathol.* **30**, 1021–1031 (2017)
11. Shoji, T., et al.: Clinical significance of atypical glandular cells in the Bethesda system 2001: a comparison with the histopathological diagnosis of surgically resected specimens. *Cancer Invest.* **32**, 105–109 (2014)

12. Carter, R.L., et al.: A modified latent class model assessment of human papillomavirus-based screening tests for cervical lesions in women with atypical glandular cells: a gynecologic oncology group study. *Cancer causes and control: CCC* **23**, 2013–2021 (2012)
13. Liao, S.Y., et al.: Endocervical glandular neoplasia associated with lobular endocervical glandular hyperplasia is HPV-independent and correlates with carbonic anhydrase-IX expression: a gynaecological oncology group study. *Br. J. Cancer* **108**, 613–620 (2013)
14. Government of Canada, I.C.: Canadian Patent Database / Base de Données. In: *Sur Les Brevets Canadiens*. <http://brevets-patents.ic.gc.ca/opic-cipo/cpd/eng/patent/2384744/summary.html> (2015). Accessed 15 June 2015
15. Liao, S.Y., Stanbridge, E.J.: US20020058251A1 (2002)
16. Kang, L., Carter, R., Darcy, K., Kauderer, J., Liao, S.Y.: A fast Monte Carlo EM algorithm for estimation in latent class model analysis with an application to assess diagnostic accuracy for cervical neoplasia in women with AGC. *J. Appl. Stat.* **40**, 2699–2719 (2013)
17. Yun, M.S., Kim, S.J., Pak, K., Lee, C.H.: Additional prognostic value of SUVmax measured by F-18 FDG PET/CT over biological marker expressions in surgically resected cervical cancer patients. *Oncol. Res. Treat.* **38**, 413–416 (2015)
18. Risio, M., et al.: Histological features of advanced colorectal adenomas detected by endoscopy and fecal immunochemical test. *Endoscopy* **47**, 903–909 (2015)
19. Hubbard, R.A., Johnson, E., Hsia, R., Rutter, C.M.: The cumulative risk of false-positive fecal occult blood test after 10 years of colorectal cancer screening. *Cancer Epidemiol. Biomark. Prev. Publ. Am. Assoc. Cancer Res. cosponsored Am. Soc. Prev. Oncol.* **22**, 1612–1619 (2013)
20. Hartana, C.A., et al.: Detection of micrometastases by flow cytometry in sentinel lymph nodes from patients with renal tumours. *Br. J. Cancer* **115**, 957–966 (2016)
21. Divgi, C.R., et al.: Phase I/II radioimmunotherapy trial with iodine-131-labeled monoclonal antibody G250 in metastatic renal cell carcinoma. *Clin. Cancer Res.* **4**, 2729–2739 (1998)
22. Divgi, C.R., et al.: Phase I clinical trial with fractionated radioimmunotherapy using 131I-labeled chimeric G250 in metastatic renal cancer. *J. Nucl. Med.* **45**, 1412–1421 (2004)
23. Divgi, C.R., et al.: Preoperative characterisation of clear-cell renal carcinoma using iodine-124-labelled antibody chimeric G250 (124I-cG250) and PET in patients with renal masses: a phase I trial. *Lancet Oncol.* **8**, 304–310 (2007)
24. Oosterwijk, E., et al.: Antibody localization in human renal cell carcinoma: a phase I study of monoclonal antibody G250. *J. Clin. Oncol.* **11**, 738–750 (1993)
25. Pryma, D.A., et al.: Correlation of in vivo and in vitro measures of carbonic anhydrase IX antigen expression in renal masses using antibody 124IcG250. *J. Nucl. Med.* **52**, 535–540 (2011)
26. Hekman, M., et al.: Zirconium-89-girentuximab PET/CT imaging in renal cell carcinoma: first in man results. *Eur. Urol. Suppl.* **15**, e1501 (2016)
27. Zegers, C.M.L., et al.: Repeatability of hypoxia PET imaging using [18F]HX4 in lung and head and neck cancer patients: a prospective multicenter trial. *Eur. J. Nucl. Med. Mol. Imaging* **42**, 1840–1849 (2015)
28. Muselaers, C.H.J., et al.: Tyrosine kinase inhibitor sorafenib decreases 111In-girentuximab uptake in patients with clear cell renal cell carcinoma. *J. Nucl. Med. Off. Publ. Soc. Nucl. Med.* **55**, 242–247 (2014)
29. Desar, I.M.E., et al.: 111In-Bevacizumab imaging of renal cell cancer and evaluation of neoadjuvant treatment with the vascular endothelial growth factor receptor inhibitor sorafenib. *J. Nucl. Med. Off. Publ. Soc. Nucl. Med.* **51**, 1707–1715 (2010)
30. McDermott, D.F., et al.: The high-dose aldesleukin “select” trial: a trial to prospectively validate predictive models of response treatment in patients with metastatic renal cell carcinoma. *Clin. Cancer Res. Off. J. Am. Assoc. Cancer Res.* **21**, 561–568 (2015)
31. Vickers, M.M., Heng, D.Y.C.: Prognostic and predictive biomarkers in renal cell carcinoma. *Target. Oncol.* **5**, 85–94 (2010)
32. Han, K., et al.: Bevacizumab dosing strategy in paediatric cancer patients based on population pharmacokinetic analysis with external validation. *Br. J. Clin. Pharmacol.* **81**, 148–160 (2016)

33. Kim, J.K., et al.: Active-site solvent replenishment observed during human carbonic anhydrase II catalysis. *IUCrJ* **5**, 93–102 (2018)
34. Kim, J.H., et al.: Prophylactic irradiation of para-aortic lymph nodes for patients with locally advanced cervical cancers with and without high CA9 expression (KROG 07-01): a randomized, open-label, multicenter, phase 2 trial. *Radiother. Oncol. J. Eur. Soc. Ther. Radiol. Oncol.* **120**, 383–389 (2016)
35. Rademakers, S.E., et al.: Pattern of CAIX expression is prognostic for outcome and predicts response to ARCON in patients with laryngeal cancer treated in a phase III randomized trial. *Radiother. Oncol. J. Eur. Soc. Ther. Radiol. Oncol.* **108**, 517–522 (2013)
36. Rademakers, S.E., et al.: Prognostic value of the proliferation marker Ki67 in laryngeal carcinoma: results of the accelerated radiotherapy with carbogen breathing and nicotinamide phase III randomized trial. *Head Neck* **37**, 171–176 (2015)
37. Konopleva, M., et al.: Phase I/II study of the hypoxia-activated prodrug PR104 in refractory/relapsed acute myeloid leukemia and acute lymphoblastic leukemia. *Haematologica* **100**, 927–934 (2015)
38. Ho, D., et al.: Impact of serum HER2, TIMP-1, and CAIX on outcome for HER2+ metastatic breast cancer patients: CCTG MA.31 (lapatinib vs. trastuzumab). *Breast Cancer Res. Treat.* **164**, 571–580 (2017)
39. Tolaney, S.M., et al.: Phase II and biomarker study of cabozantinib in metastatic triple-negative breast cancer patients. *Oncologist* **22**, 25–32 (2017)
40. Li, G., Feng, G., Gentil-Perret, A., Genin, C., Tostain, J.: Serum carbonic anhydrase 9 level is associated with postoperative recurrence of conventional renal cell cancer. *J. Urol.* **180**, 510–513 (2008)
41. Yu, T., Tang, B., Sun, X.: Development of inhibitors targeting hypoxia inducible factor 1 and 2 for cancer therapy. *Yonsei Med. J.* **58**, 489–496 (2017)
42. Carvalho, S., et al.: Prognostic value of blood-biomarkers related to hypoxia, inflammation, immune response and tumour load in non-small cell lung cancer—a survival model with external validation. *Radiother. Oncol.* **119**, 487–494 (2016)
43. Zhu, A.X., et al.: Efficacy, safety, pharmacokinetics and biomarkers of cediranib monotherapy in advanced hepatocellular carcinoma: a phase II study. *Clin. Cancer Res. Off. J. Am. Assoc. Cancer Res.* **19**, 1557–1566 (2013)
44. Chamie, K., et al.: Adjuvant weekly girentuximab following nephrectomy for high-risk renal cell carcinoma: the ARISER randomized clinical trial. *JAMA Oncol.* **3**, 913–920 (2017)
45. Stillebroer, A.B., et al.: Phase 1 radioimmunotherapy study with lutetium 177-labeled anti-carbonic anhydrase IX monoclonal antibody girentuximab in patients with advanced renal cell carcinoma. *Eur. Urol.* **64**, 478–485 (2013)
46. Muselaers, C.H.J., et al.: Phase 2 study of lutetium 177-labeled anticarbonic anhydrase IX monoclonal antibody girentuximab in patients with advanced renal cell carcinoma. *Eur. Urol.* **69**, 767–770 (2016)
47. McDonald, P.C., Swayampakula, M., Dedhar, S.: Coordinated regulation of metabolic transporters and migration/invasion by carbonic anhydrase IX. *Metabolites* **8**(1) (2018)
48. Hendrickx, B.W., et al.: Targeting of biliary cancer with radiolabeled chimeric monoclonal antibody CG250. *Cancer Biother. Radiopharmaceuticals* **21**, 263–268 (2006)
49. Ward, C., et al.: Evaluation of carbonic anhydrase IX as a therapeutic target for inhibition of breast cancer invasion and metastasis using a series of in vitro breast cancer models. *Oncotarget* **6**, 24856–24870 (2015)
50. Boyd, N.H., et al.: Addition of carbonic anhydrase 9 inhibitor SLC-0111 to temozolomide treatment delays glioblastoma growth in vivo. *JCI Insight* **2**, e92928 (2017)
51. Chang, Q., Jurisica, I., Do, T., Hedley, D.W.: Hypoxia predicts aggressive growth and spontaneous metastasis formation from orthotopically grown primary xenografts of human pancreatic cancer. *Cancer Res.* **71**, 3110–3120 (2011)

Index

- Ab initio calculations, 225
Acetazolamide, 16, 102, 293
Affinity, 251
1,8-Anilino-naphthalene sulfonate, 64
Association constant, 80
Association rate constant, 128
Autoradiography, 324
- Binding constant, 81
Brinzolamide, 72
- CA I, 17
CA II, 17
CA III, 17
CA IV, 17
CA VA, 17
CA VA-selective compounds, 147
CA VB, 17
CA VI, 17
CA VII, 17
CA IX, 204, 267
CA IX as a diagnostic marker, 337
CA IX knockout cells, 278
CA XII, 17
CA XIII, 17
CA XIV, 17
Calorie, 80
Calorimetric cell, 84
Calorimetry, 80
Cancer cells, 277
Carbonic acid hydro-lyase, 40
Carbonic anhydrase, 3
Catalytic domain of CA IX, 207
Center of spectral mass (CSM), 100
Cheng–Prusoff equation, 47
CRISPR-Cas9, 278
Cryo-electron microscopy, 180
- Crystal structures, 260
CSM, *see* Center of spectral mass
- Denaturation, 55
Density functional theory, 225
Detection of CA, 324
Differential scanning calorimetry (DSC), 52
Differential scanning fluorimetry (DSF), 63
Dimethylsulfoxide (DMSO), 56
Dissimilar binders, 253
Dissociation constant, 80, 81
Dissociation rate constant, 128
Docking, 216
Dose-response curves, 275
Dosing curve, 102
Drug development, 266
DSF, *see* Differential scanning fluorimetry
- Electron density, 181
ELISA, 326
Endothermic, 82
Enthalpy, 80
 change, 81
 of protonation of the CA Zn^{II}-bound
 hydroxide/water molecule, 118
 of sulfonamide amino group protonation,
 119
Entropy, 80
Entropy change, 82
Enzymatic activity inhibitors, 41
Epigenetics, 175
Equilibrium dissociation constant, 128
Esterase activity, 41
Ethoxzolamide, 16, 46, 271
Exergonic, 80
Exothermic, 82

- Fluorescence-guided surgery of cancer, 294
Fluorescent pressure shift assay (FPSA), 101
Fluorescent thermal shift assay (FTSA), 52, 63, 102, 108
Fluorinated benzenesulfonamides, 154
FPSA, *see* Fluorescent pressure shift assay
FTSA, 63, *see* Fluorescent thermal shift assay
- Gibbs energy change, 80
Gibbs energy of unfolding, 99
Glycerol, 56
Guanidine hydrochloride, 55
- Half-maximal inhibitory concentrations, 275
High-throughput screening, 163
Hill coefficient, 44, 45
Hill model, 45
His₆-tag, 17
Histochemical methods, 324
Hygromycin B, 32
Hypoxic, 279
Hypoxic chamber, 278
- Immunofluorescence, 325
Immunohistochemistry, 325
Immunotherapy, 306
Inhibition constant K_i , 47
Inhibitor dosing curves, 45
Intrinsic association rate constant, 136
Intrinsic dissociation rate constant, 136
Intrinsic enthalpy, 235
Intrinsic Gibbs energy, 235
Intrinsic rate constants, 135
Intrinsic reaction, 108
Isopropyl- β -D-thiogalactoside (IPTG), 29
Isothermal titration calorimetry, 80, 108
ITC, *see* Isothermal titration calorimetry
- Joule, 80
- Linked protonation reactions, 108
- Mass spectrometry, 276
Matched molecular pairs, 251
Matrix metallo-proteinase, 168
Melting temperature, 52
Molecular dynamics, 224
- Molecular mechanics, 225
Monoclonal antibody, 306
Monte-Carlo, 224
Morrison model, 42, 45
Multitarget epigenetic drugs, 175
- Neutron crystallography, 183
Ni²⁺-chelation chromatography, 17
Nitrophenylacetate, 41
Normoxic, 279
Nuclear magnetic resonance, 180
- Observed* dissociation constants, 108
Observed enthalpy upon binding, 113
Observed reaction, 108
- Patient stratification, 341
Pentafluorobenzenesulfonamide, 154
Peptidoglycan (PG) domain, 16
pET15b vector, 17
Phenol Red, 43, 44
pH-regulatory proteins, 266
Ping-pong mechanism, 6, 40
 pK_a of protonation of the CA Zn^{II}-bound hydroxide/water molecule, 118
 pK_a of sulfonamide, 119
Prostaglandin, 175
Protein crystallography, 180
Proteoglycan-like domain, 205
Proton-shuttle residue His64, 40
Protonography, 47
- Quantitative structure-activity relationship, 225
Quantum mechanical calculations, 225
Quantum mechanics, 225
- Recombinant antibodies, 306
Restriction nuclease, 25
- Sensorgram, 127
Similar binders, 251
Sodium chloride, 55
Standard conditions, 80
Stopped-flow assay of inhibition of CA enzymatic activity, 108
Surface plasmon resonance, 126
Sypro Orange, 65

-
- Therapy, [344](#)
Thermal shift assay, [52](#)
Thermodynamic parameters, [80](#)
ThermoFluor[®], [63](#)
Toxicological screening, [271](#)
Treatment, [344](#)
- Unfolding, [55](#)
Urea, [55](#)
- Voronoi cell, [221](#)
Voronota program, [221](#)
- Western blot, [326](#)
- Xenopus* oocytes, [272](#)
- Zonisamide, [42](#)